The Effects of Long-Term Isothermal Ageing on the Microstructure of HP-Nb and HP-NbTi Alloys

---

A thesis

submitted in partial fulfilment

of the requirements for the Degree

of

DOCTOR OF PHILOSOPHY IN MECHANICAL ENGINEERING
IN THE
UNIVERSITY OF CANTERBURY

BY

KARL GRAHAM BUCHANAN

University of Canterbury

2013

Preface

This thesis is submitted as a partial requirement for the degree of Doctor of Philosophy in Mechanical Engineering in the University of Canterbury. This research was conducted under the supervision of Professor Milo V. Kral in the Mechanical Engineering Department, University of Canterbury, between March 2008 and March 2013.

Acknowledgements

I would like to acknowledge the following people and organizations that have made this research work possible:

- Professor Milo V. Kral for supervision of thesis and for his technical support, knowledgeable critique, optimism and personal support of throughout this research program;
- The Ministry of Research, Science and Technology, New Zealand for the provision of The Technology for Industry Fellowships funding;
- Quest Integrity Group Ltd. (Wellington, New Zealand) for the supply of the as-cast and isothermally aged material characterized in this research and for generously funding of this research;
- Shell Global Solutions (Amsterdam, The Netherlands) for funding this research;
- Charles W. Thomas (Quest Integrity Group) and David M. Knowles for the many useful discussions and advice throughout the course of this research;
- Members of the Materials Engineering Group (MEG): Dr. Takanori Sato, Dr. Catherine Bishop, Emeritus Professor Les Erasmus, Dr. John Smaill, Mike Flaws and Kevin Stobbs; MEG visitor Dr. Chris Hutchinson (Monash University); in addition to fellow MEG student and Professor John Cahn (University of Washington), for all of their help, questions and critique;
- Technical staff of the Mechanical Engineering Department, Ken Brown, Julian Philips, Scott Amies, David Read, Gary Cotton and Paul Southward and the numerous Administrative staff for their skill, knowledge and kind assistance;
- Last but certainly not least, my parents and extended family for their significant support throughout this project.

Abstract

High alloy Fe-Cr-Ni-C austenitic stainless steels have become the principal alloys for use in steam-methane reforming furnaces within the petrochemical industry. Each furnace contains a large array of vertically oriented centrifugally cast tubes through which a mixture of methane and steam is flowed across a nickel-oxide catalyst in order to obtain a mixture of hydrogen, carbon monoxide and carbon dioxide and water commonly known as synthesis gas (or syngas). Generally, the tubes operate at temperatures between 850-1050°C, internal pressures between 1-3.5MPa and are expected to withstand service lives in excess of 100,000 hours. The combination of high temperatures and moderate stresses causes creep to be the dominant failure mechanism experienced by these tubes in service.

The HP austenitic alloys are the latest in a series of heat resisting (H-series) stainless steels developed to provide high temperature strength, ductility, and corrosion resistance in the oxygen, carbon, and sulphur rich environments typical of these furnaces. Extensive work has been carried out to optimise HP alloys' microstructure in order to maximise the alloy's creep resistance. Strength increases have largely been realized through the use of niobium and/or titanium additions, which modify the primary precipitates (formed during solidification) and secondary precipitates (formed during exposure to the service temperatures). These strength increases have typically been observed during laboratory accelerated creep testing of the 'modified' HP alloys where the temperature and/or stress is increased to achieve failure of the material within reasonable time period (typically between 1000-2000 hours). However, since the duration of typical accelerated creep tests often represent less than 2% of the tubes' actual service life, uncertainty surrounds the validity of using this testing method as the basis to predict the tubes actual service life. This uncertainty has largely arisen due to the significant microstructural evolution that occurs within these alloys during prolonged service exposure and is not captured within the typical accelerated testing time-frame.

In the present work, the microstructures of HP alloys modified with a single addition of niobium (HP-Nb) and dual additions of niobium and titanium (HP-NbTi) have been characterized in the as-cast condition and after long-term (10,000 hours) isothermal laboratory ageing at 1000, 1050 and 1100°C. The main focus of this study is to provide further insight into the microstructural features that increase the HP-NbTi alloy's creep resistance in comparison to the HP-Nb alloy when performing accelerated creep testing and determine if these microstructural features remain stable during long-

term ageing. The microstructure and crystallography of the primary and secondary precipitates in each alloy have been studied in detail using light optical microscopy, high resolution scanning electron microscopy, transmission electron microscopy, various electron diffraction methods (EBSD, SAD and CBED), Powder X-ray Diffraction and energy dispersive X-ray spectroscopy. Specific attention has been paid to the niobium-rich and niobium-titanium-rich phases that form as a direct result of HP alloy's modification with niobium and titanium.

The current research is part of a wider project conducted in collaboration with Quest Integrity Group Ltd. (Wellington, New Zealand) that aims to characterize the microstructural and mechanical properties of the HP-Nb and HP-NbTi alloys during long-term service exposure. The microstructural characterization presented in this thesis will subsequently be used by Quest Integrity Group to build a comprehensive understanding of the relationship between HP-Nb and HP-NbTi alloy's microstructure and creep properties. This understanding will allow Quest Integrity Group to more accurately predict the service life of HP-Nb and HP-NbTi alloy tubes within steam-methane reforming furnaces.

Contents

List of Figures

List of Tables

Chapter 1 **Introduction**

Heat resistant Fe-Cr-Ni-C austenitic stainless steels have become the principal alloys for use in steam-methane reforming and pyrolysis applications within the petrochemical industry. Generally, large arrays of vertically oriented centrifugally cast alloy tubes filled with nickel-oxide catalyst are utilised within reforming or pyrolysis furnaces to convert various feedstocks (e.g. methane, LPG or ethane) into hydrogen, lighter alkenes (e.g. ethylene or propylene) or aromatic hydrocarbons (e.g. benzene). Depending on the process requirements, these tubes typically operate at temperatures between 850-1050°C and internal pressures between 1-3.5MPa for a design life of at least 100,000 hours. The combination of high temperatures and moderate stresses causes creep to be the dominant failure mechanism experienced in service. The heat resisting (H-series) austenitic alloys were developed with high levels of chromium and nickel to provide high temperature strength, ductility, and corrosion resistance in the oxygen, carbon, and sulphur rich environments typical of these furnaces. Initially, the centrifugally cast HK (25%Cr, 20%Ni) alloy series replaced the wrought HT (18%Cr, 37%Ni) superalloys, providing tubes with comparable creep performance while reducing cost (due to the decrease in Ni). Increasing demand for tubes which could withstand more aggressive operating conditions while maintaining a similar service life expectancy subsequently resulted in the HK series being superseded by the HP series (25%Cr, 35%Ni), which has shown higher creep strength and oxidation resistance than its predecessors.

Extensive work has been carried out to optimise the HK and HP alloys' microstructure in order to maximise each alloy's high temperature strength. Typically, strength increases for both alloys have been realized through the use of niobium and/or titanium additions, which modify the primary precipitates (formed during solidification) and secondary precipitates (formed during exposure to the service temperatures). Accelerated creep tests performed on as-cast material and also material that had been aged for up to 1000 hours has shown that the creep resistance of modified HK and HP alloys was superior to the standard HK and HP compositions. However, as the tubes often experience service periods of between 60,000-100,000 hours, the significant microstructural evolution which occurs within these alloys during prolonged thermal exposure causes the 'in-service' microstructure to be considerably different to the microstructure present during accelerated creep tests. Consequently, the creep properties measured from accelerated testing of these alloys may not yield

accurate representations of the material's true creep performance during service. Accelerated creep testing of ex-service material suggests that long-term service exposure significantly reduces the HP alloy's creep properties. This reduction is typically greater than would be expected from the accumulation of creep damage within the material during service. Hence, the long-term damage to the HP alloy's creep resistance as a result of the thermally induced microstructural evolution must be taken into account in order to yield more accurate service life predictions.

In the present work, the microstructures of HP alloys modified with a single addition of niobium (HP-Nb) and dual additions of niobium and titanium (HP-NbTi) have been characterized in the as-cast condition and after long-term (10,000 hours) isothermal laboratory ageing at 1000, 1050 and 1100°C. The main focus of this study is to characterize the microstructural evolution of the HP-Nb and HP-NbTi alloys with respect to ageing temperature and time. A comprehensive understanding of each alloy's microstructural evolution is necessary to determine the microstructural changes that may decrease the alloy's creep resistance during service. It was also considered necessary to determine whether the microstructural evolution during service will lead to the convergence of each alloy's creep resistance during service. In parallel to the current microstructural research (performed at the University of Canterbury), accelerated creep testing of the laboratory aged HP-Nb and HP-NbTi samples was conducted at Quest Integrity Group's test facility located in Wellington, New Zealand. It was anticipated that the microstructural study presented in this thesis in combination with Quest Integrity Group's accelerated creep testing program would lead to a significantly improved understanding of the long-term creep performance of the HP-Nb and HP-NbTi alloys. It was envisioned that this increased understanding of the factors which influence each alloy's long-term creep properties would allow Quest Integrity Group to produce considerably more accurate service life predictions for HP-Nb and HP-NbTi alloy tubes within steam-methane reforming furnaces.

1.1 Research Background

The combination of high temperatures ($T > 0.6T_M$) and pressure induced stresses experienced by the austenitic alloy tubes during service within steam-methane reforming and cracking furnaces causes the tubes' service life to predominantly be limited by creep. Typically, creep deformation results in the gradual expansion of the tubes diameter during service. This permanent deformation occurs over an extended period of time and is dependent on the temperature and stress distributions across the tube's wall-thickness. Generally, the furnace temperature, process gas pressure, and tube geometry (i.e. tube diameter and wall-thickness) are designed to allow the HP alloy tubes to withstand service periods of up to 100,000 hours (11.4 years). Tubes are usually retired from service when excessive radial creep deformation is identified during scheduled plant shutdowns which, are primarily undertaken to replace the nickel-oxide catalyst contained within each tube (typically occurring at 2-4 year intervals). However, the accumulation of creep damage within the tube wall during service (i.e. void nucleation, growth and coalescence) can lead to the catastrophic rupture of tubes prior to the tube's expected service life, resulting in unscheduled plant shutdowns. The extensive cost of replacing each tube assembly (i.e. the centrifugally cast tube and catalyst) and considerably greater costs associated with unscheduled shutdowns makes premature tube failures extremely undesirable. Thus, accurate and reliable prediction of each tube's actual service life is of significant importance to plant operators. For example, the cost of a single steam-methane reforming tube assembly typically exceeds US$7000, while the cost of lost production due to unplanned outages costs in excess of US$250,000 per day (depending on the plant size) with the average disruption lasting between 7-10 days [1, 2]. In order to maximise a plant's profitability, plant operators must maximize the life of each tube while minimizing the probability of unexpected failures. In parallel, plant operators also desire increasingly aggressive operating conditions (which can significantly reduce the tubes' service life) in order to improve the plants thermodynamic efficiency. Maintaining the balance between a plant's reliability and efficiency is relatively complex and consequently requires a comprehensive understanding of the tube alloy's long-term creep performance with respect to the furnace operating conditions.

The HP alloy's creep resistance is heavily dependent on the macroscopic and microscopic structure. Macroscopically, the combination of columnar grains at the tube's outer diameter and equiaxed grains at the inner diameter as a result of the centrifugal casting technique increased the HP alloy's

creep resistance. Microscopically, the HP alloy's primary carbide network (formed during solidification) and the secondary distribution of carbides (formed once the material is subjected to elevated temperatures) control the creep properties of the material (discussed in detail in Chapter 2). The significant influence of the primary and secondary precipitates on the HP alloy's creep resistance has caused recent emphasis to be placed on the modification of these precipitates using small additions of niobium (0.5-2.0wt.%), titanium (0.04-0.3wt.%), tungsten (0.1-0.15wt.%) and rare earth elements (<0.1wt.%) in combination with the standard HP composition [3-10]. Accelerated creep tests where test samples are subjected to either higher load and/or temperature (in comparison to service conditions) have shown enhanced creep properties attributed to the addition of these elements. However, as the duration of accelerated testing (typically lasting between 1000-2000 hours) commonly represents less than 2% of a tube's typical service life, the long term effectiveness of these alloying elements on the creep properties is relatively unknown.

Current design of reformer tubing is based upon the materials stress rupture properties, the operating temperature, and the internal pressure. Based on knowledge of these parameters, designers predominantly use API 530 [11] to determine a minimum wall thickness that will last a specified lifetime (typically 100,000 hours). However, as the design of reformer tubes is largely based on creep properties which are extrapolated from data generated by short-term accelerated creep testing, the removal of tubes from service due to excessive creep strain (measured and removed during pre-determined plant shutdowns) or rupture (catastrophic failure of the tube while the plant is in operation) prior to the tube's 100,000 hour expected service life is not uncommon. Such failures likely arise as a result of accelerated creep testing's inability to accurately replicate the conditions experienced by the tubes during service. For example, the transient through-wall thermal stresses (often an order of magnitude greater than the pressure induced hoop stress [12]) that are induced during start-up and shutdown of the furnace are completely unaccounted for during constant load accelerated creep testing. Moreover, as previously stated, the duration of typical accelerated creep tests often represent less than 1-2% of the tubes actual service life. Hence, the significant microstructural evolution that occurs during prolonged service is not captured within the typical accelerated testing time-frame.

Figure 1.1 (a) to (c) demonstrate the significant microstructural evolution which occurs within the HP-Nb alloy during long-term thermal exposure. The micrograph shown in Figure 1.1 (b) is typical of the microstructures on which accelerated testing is conducted. The fragmented interdendritic

precipitate network and fine distribution of intragranular secondary precipitates present within the timeframe of accelerated creep tests leads to accelerated creep testing being performed on the alloy's most creep resistant microstructure. However, the significant growth and coalescence of the primary precipitates, depletion and coarsening of the secondary precipitates, coupled with other more sluggish phase transformations which occur during prolonged ageing (Figure 1.1 (c)) leads to a microstructure which is less resistant to creep deformation. Such unfavourable microstructures are rarely accounted for by accelerated testing. Therefore, the extrapolation of creep properties from short-term accelerated testing likely overestimates the actual creep properties of HP alloy tubes during high temperature service increasing the potential of unexpected tube failures.

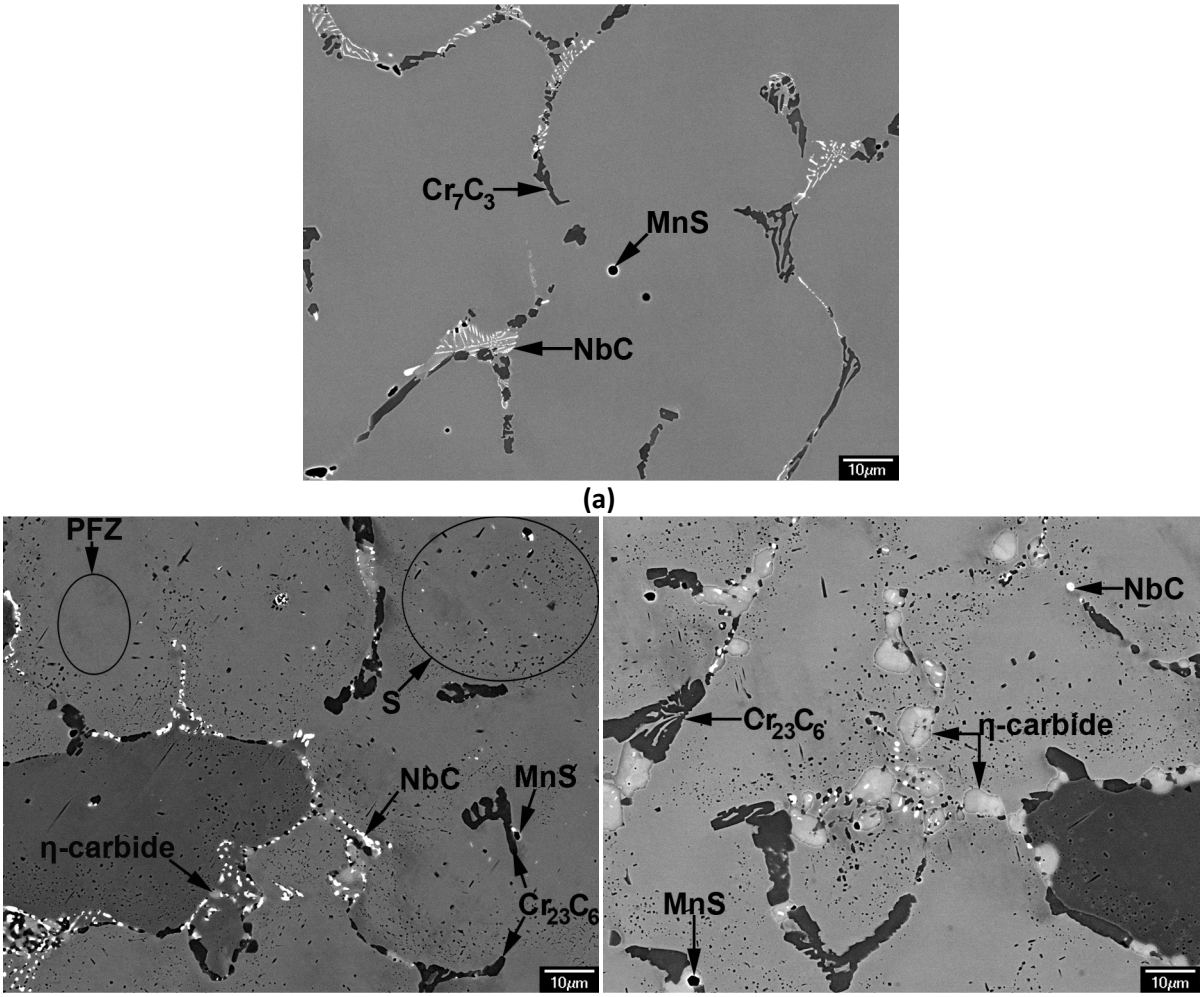

Figure 1.1 – Backscatter electron micrographs showing the significant microstructural evolution that occurs within the HP-Nb alloy during ageing at 1000°C. (a) as-cast condition, (b) 1000 hours and (c) 10,000 hours.

Although the API 530 standard contains inbuilt safety factors to account for any discrepancy between the 'design' and 'actual' material properties and furnace operation conditions, the reliability of these safety factors in accounting for the difference between the HP alloys' short-term creep resistance (as determined by laboratory accelerated creep testing) and long-term creep resistance (i.e. the tubes actual service performance) is currently unknown. Applying these safety factors to modified HP alloys is particularly contentious as it is currently unknown whether the initial increase in the modified alloys' creep resistance (i.e. as a result of the new alloying additions) actually remains present during long-term service exposure. Determining if there is a discrepancy between the modified alloys' short-term and long-term creep resistance is particularly important as the improved creep resistance observed when performing short-term accelerated creep testing has led to reductions in tube wall thicknesses while supposedly keeping similar calculated life expectancies [13]. Alternatively, the improved creep properties has allowed steam-methane reforming furnace designers to increase the maximum allowable furnace temperature and/or internal gas pressure while keeping the tube wall thicknesses unchanged in order to increase the plants thermodynamic efficiency. Consequently, if the observed short-term creep strength increase does not remain during long-term service exposure (i.e. the properties of tubes with the alloying additions becomes similar to tubes without the additions), the changes to the design parameters will undoubtedly increase the number of unexpected tube failures.

Accelerated creep testing of ex-service niobium modified HP alloy tubes (subjected to service for >70,000 hours) has shown a significant reduction in the alloy's creep rupture strength accompanied by an increase in creep ductility in comparison with the as-cast material properties [13]. While a reduction in the material's remaining creep life as a result of creep deformation during long-term service exposure can be expected, accelerated testing of the ex-service material suggested the tubes remaining creep life was significantly lower than would be expected when comparing the actual duration of the tubes service exposure with the tube's total design life (i.e. the service life calculated based on the maximum operating conditions and short-term creep properties). Microstructural examination of the ex-service material often indicated little or no creep damage (in the form of voids), but revealed extensive microstructural changes (in the form of transformation and subsequent coarsening of the primary carbide network and extensive Ostwald ripening of the secondary precipitation within the matrix) in comparison to the microstructures typically observed after accelerated testing of as-cast material. The significant microstructural changes observed in the ex-service material suggests that the observed reduction in the creep resistance of ex-service

modified HP alloys is partially attributed to the thermally induced microstructural evolution which also occurs during prolonged service. In order to prevent costly unexpected tube failures, subsequent research must focus on quantifying the extent to which thermally induced microstructural ageing affects the modified HP alloys' creep resistance.

Interestingly, comparisons made between the actual operating conditions experienced by ex-service steam-methane reforming tubes and the original design specification often reveals that the tubes were operated below their maximum design conditions. As a result, the tubes' theoretical life expectancy is markedly increased when recalculating life using the actual average temperature and pressure experienced by the tubes during service as design variables [12, 13]. However, the consistent reduction in the creep resistance of ex-service tubes (as determined by accelerated creep testing of the ex-service material) suggests the 'extra life' given by the operation of the furnaces below their maximum design conditions acts as an additional safety factor against failure which offsets any degradation in the materials properties due to microstructural ageing. Thus, this 'extra life' may be preventing the failure of many modified HP alloy tubes where the increased short-term creep resistance of these alloys originally lead to the specification of reduced tube wall thicknesses or more aggressive operating conditions in comparison to unmodified HP or HK alloys.

Recently, a growing interest in planned life extension programs has arisen to take advantage of the theoretical 'extra life' created by the reduced operating conditions. However, simply extending a tube's service life on the basis of inverse design calculations, which use the tube's service history and as-cast material properties to determine the tube's remaining creep life, without accounting for the tube's extensive microstructural evolution will likely result in the unexpected failure of the tube during the subsequent service period. Hence, in order to minimise the probability of tube failure during service, life extension programs must account for the degradation of the materials creep properties due to microstructural ageing. This degradation can be accounted for by performing accelerated creep testing and/or microstructural analysis on the ex-service material but these techniques usually require the partial destruction of the tube and potentially render it unusable for further service. Alternatively, non-destructive testing methods such as the measurement of creep strain (primarily the tubes diametral expansion), eddy current inspection or ultrasonic inspection can be used to assess a tube's remaining life. However, extensive research must be conducted on standardised samples which contain varying levels of creep damage in order to calibrate each method before they can produce reliable and interpretable results when assessing tubes in service.

Regardless of the testing method (i.e. destructive or non-destruction), a comprehensive understanding of the HP alloy's long-term creep properties (e.g. rupture life, minimum creep rate and creep ductility) is essential to reliably predict each tube's remaining life and minimise the probability of catastrophic failure if the tube's service life is to be extended. To gain such an understanding for the modified HP alloys requires extensive laboratory accelerated testing to be conducted over a wide range of temperatures, stresses and exposure times. In parallel, detailed characterization of the microstructural evolution within each modified alloy with respect to temperature, stress and time is necessary to determine the microstructural features which lead to the alloys' differing creep properties during service.

While a number of previous studies have characterized the short-term (typically less than 2000 hours) microstructural evolution and creep properties of the modified HP alloys [3-9], studies on the alloys' long-term microstructural evolution and creep properties are relatively limited. Consequently, the purpose of the present research was to significantly increase the understanding of the long-term microstructural evolution of two dominant modified HP variants currently used in service: the HP-Nb (typically 0.5-1.5wt.% Nb) and HP-NbTi (typically 0.5-1.5wt,%Nb, 0.02-0.1wt.% Ti) alloys. Similar to the previous short-term studies conducted on the HP-Nb and HP-NbTi alloys [3-7], the current study subjects each alloy to unstressed isothermal laboratory ageing followed by detailed microstructural characterization using optical microscopy, high resolution scanning electron and transmission electron microscopy, various electron and X-ray diffraction methods (EBSD, SAD, CBED and XRD), energy dispersive X-ray spectroscopy and inductively coupled plasma atomic emission spectroscopy. Laboratory ageing was carried out at 1000, 1050 and 1100°C for periods between 1000 to 10,000 hours, which represents between 1 to 10% of a tube's typical service life (in comparison to the 1 to 2% characterized by previous studies). The microstructural characterization presented in this work primarily focused on the following microstructural aspects:

- Identification of the primary carbide precipitates phases (i.e. the precipitates which form during solidification) in the as-cast HP-Nb and HP-NbTi alloys;

- Detailed characterization of the primary precipitates' evolution (e.g. phase transformations, coarsening and dissolution and precipitate-matrix crystallography) with respect to ageing temperature and time. Emphasis was placed on the characterization of the niobium-rich primary precipitate phases (i.e. the phases that form as a direct result of the alloys

modification) during ageing as the increased creep properties have been partially attributed to the presence of these precipitates;

- Identification of the secondary precipitates phases that form while isothermally ageing each alloy and characterization of the Ostwald ripening of these precipitates with respect to ageing temperature and time and alloy composition;

- Identification of the microstructural changes that lead to the degradation of each alloy's creep properties during prolonged thermal exposure.

The current study was conducted in collaboration with Quest Integrity Group[1] (QIG) and is part of a larger project that also subjects the aged samples to accelerated creep testing to determine the evolution of the HP-Nb and HP-NbTi alloys' creep properties with respect to ageing temperature and time. It was anticipated that QIG's creep testing program in combination with the detailed microstructural study presented in this thesis would significantly improve the current knowledge of the microstructural features which govern the long-term creep properties of the HP-Nb and HP-NbTi alloys and consequently further enhance QIG's ability to provide accurate remaining life assessments to the petrochemical industry. It was also expected that these two parallel studies would determine whether the initial increase in each alloys' creep resistance provided by the additions of niobium and titanium would remain after prolonged ageing. This knowledge will verify if the increased costs which are associated with the production of tubes incorporating these modifying alloying additions are justified and also provide a level of confidence that the reduction in the tube's wall thickness and/or increase in the furnace's operating conditions, which occurred as a direct result of modified alloys' increased short-term creep properties, will not result in unexpected failures during service.

[1] Quest Integrity Group Ltd. is a global engineering consultancy specialising in providing high level structural and metallurgical services to the petrochemical and energy industries. Refer to Section 1.2 for further information on QIG's involvement with the current project.

1.2 Research Overview

The as-cast and isothermally aged material studied in this work was supplied by Quest Integrity Group Ltd. (Wellington, NZ), which was one of the main sponsors for this project. Prior to the commencement of the microstructural study at the University of Canterbury, QIG subjected segments of centrifugally cast HP-Nb and HP-NbTi alloy tubing to unstressed isothermal ageing at 1000, 1050 and 1100°C for between 500 - 10,000 hours. Table 1.1 to Table 1.3 summarize the aged samples that were supplied by QIG for microstructural analysis at the University of Canterbury.

Due to the limited availability of as-cast HP-Nb material, ageing of this alloy had to be completed using material taken from two separately cast tubes. The niobium modified centrifugally cast tubes that were subjected to laboratory ageing were manufactured Kubota Metal Corporation Canada (alloy designation KHR35C) [14] and by Paralloy Limited U.K. (alloy designation H39W) [15]. For the purposes of this thesis, the KHR35C alloy is referred to as the 'HP-Nb1' alloy and was subjected to ageing at 1050 and 1100°C (Table 1.1). The H39W alloy is referred to as the 'HP-Nb2' alloy and was only aged at 1000°C (Table 1.2). As shown in Table 1.1, limitations on the availability of material caused QIG to not obtain samples of the HP-Nb1 alloy after ageing at 1050 and 1100°C for 6000 hours. Additionally, QIG did not obtain a sample of the HP-Nb2 alloy after ageing at 1000°C for 500 hours (Table 1.2).

Two separately cast HP-NbTi tubes were also studied in this thesis but both tubes were manufactured by Schmidt-Clemens Spain S.A.U. (alloy designation Centralloy 4852Micro) [16]. However, only one of these tubes was subjected to long-term isothermal ageing at 1000, 1050 and 1100°C (referred to as the 'HP-NbTi1' alloy). As shown in Table 1.3, QIG did not obtain samples after ageing at 1000°C for 500 hours and 1050°C for 6000 hours. The second tube (referred to as the 'HP-NbTi2' alloy) was solely used for the accelerated creep testing experiments that were performed at the University of Canterbury.

For convenience, the chemical composition and selected materials properties for each alloy have been reproduced in Appendix A of this thesis. All ageing was completed between December 2006 and February 2008 within QIG's Metallurgical laboratories located in Wellington, New Zealand prior to the commencement of the current research at the University of Canterbury.

Table 1.1– HP-Nb1 aged samples supplied by Quest Integrity Group

HP-Nb1 (KHR35C)	Time (h)				
Temperature (°C)	500	1000	3000	6000	10000
1000	Nb1 NOT AGED AT 1000°C				
1050	✓	✓	✓	✘	✓
1100	✓	✓	✓	✘	✓

Table 1.2– HP-Nb2 aged samples supplied by Quest Integrity Group

HP-Nb2 (H39W)	Time (h)				
Temperature (°C)	500	1000	3000	6000	10000
1000	✘	✓	✓	✓	✓
1050	Nb2 AGED AT 1050 & 1100°C				
1100					

Table 1.3 – HP-NbTi1 aged samples supplied by Quest Integrity Group

HP-NbTi1 (4582Micro)	Time (h)				
Temperature (°C)	500	1000	3000	6000	10000
1000	✘	✓	✓	✓	✓
1050	✓	✓	✓	✘	✓
1100	✓	✓	✓	✓	✓

The experimental process implemented for this project is shown schematically in Figure 1.2. On completion of the isothermal ageing program at QIG, small segments were cut from the as-cast and isothermally aged HP-Nb and HP-NbTi samples and shipped the Metallurgical Laboratories located within the University of Canterbury's Mechanical Engineering Department (Christchurch, New Zealand) for detailed microstructural analysis. All of the microstructural characterization was completed between March 2008 and June 2012. Metallographic samples for optical and scanning electron microscopy were immediately prepared from the as-cast and aged tube segments. The primary carbides in the as-cast HP-Nb and HP-NbTi alloys were then characterized using the light optical and high resolution scanning electron microscopes. Identification of the precipitate phases in the as-cast HP-Nb and HP-NbTi alloys was carried out using a combination of energy dispersive X-ray spectroscopy (EDS) and electron backscatter diffraction (EBSD). EBSD was also used to investigate the crystallographic relationship between the niobium-rich primary precipitates and austenite matrix. Thin foils were subsequently prepared from each alloy in order to perform high resolution transmission electron microscopy specifically on the niobium-rich primary carbides in each alloy (i.e. the precipitates that form as a result of the HP alloy's modification with niobium and titanium). The TEM was also used to search for sub-micron sized precipitates within the as-cast austenite grains.

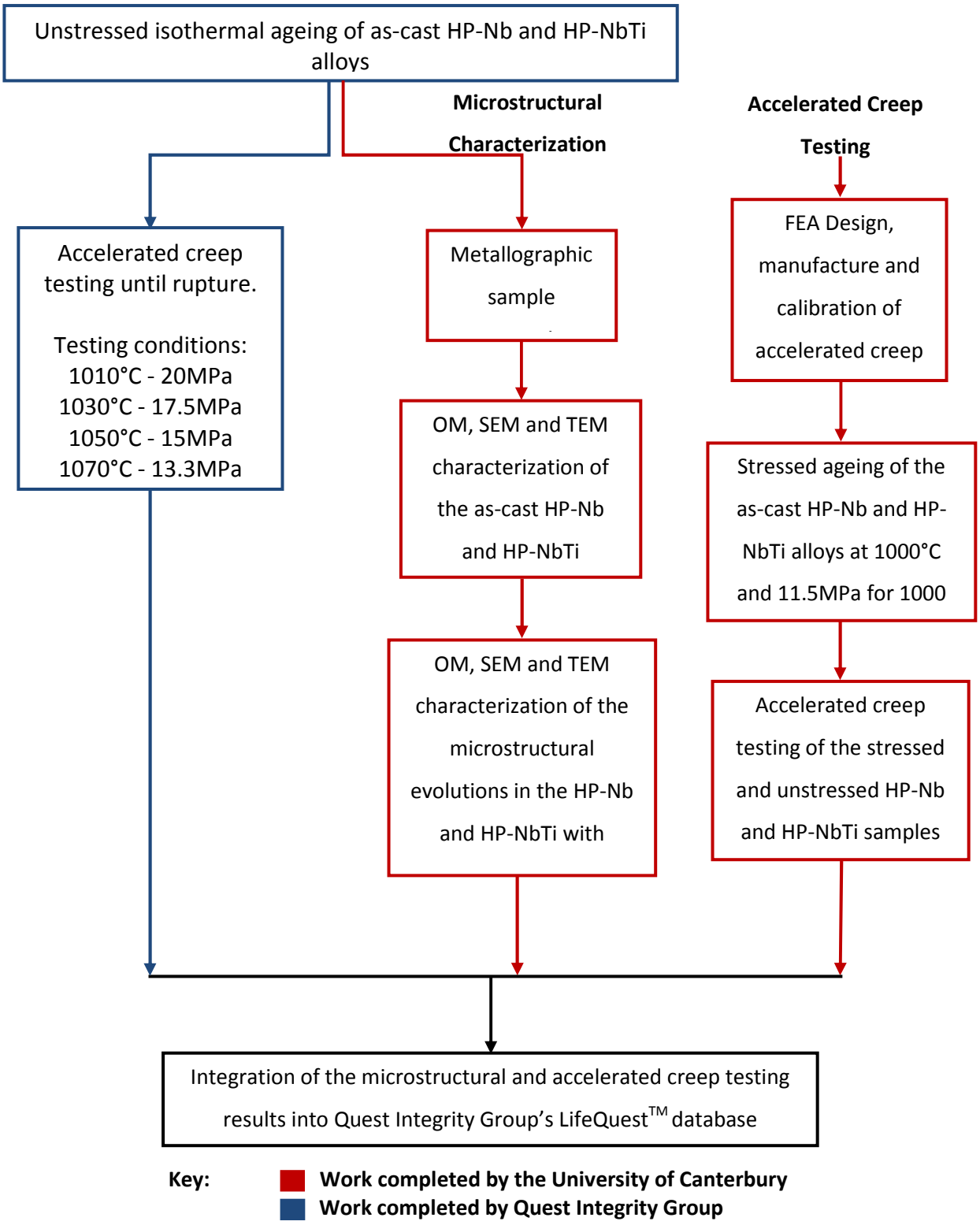

Figure 1.2 - Schematic showing the experimental process used for the microstructural characterization and accelerated creep testing presented in this thesis. The accelerated creep testing conducted in parallel at QIG is also shown. OM = Optical Microscope, SEM = Scanning Electron Microscope, TEM = Transmission Electron Microscope, FEA = Finite Element Analysis.

The numerous aged HP-Nb and HP-NbTi alloys were then progressively subjected to detailed microstructural analysis using optical and scanning electron microscopes with specific focus also being placed on the evolution of the niobium-rich precipitates in each alloy with respect to ageing temperature and time. The primary objective of the current research was to compare the microstructural evolution of the HP-Nb and HP-NbTi alloys with respect to ageing temperature and time. Image analysis, performed on backscatter electron micrographs, was also carried out to measure the average size and area fraction of the chromium and niobium rich carbides with respect to ageing temperature and time. Identification of the phases present in each aged sample was carried out using a combination of EDS and EBSD. Analysis of the crystallographic relationships between the primary precipitates and austenite matrix in the as-cast and aged samples was also performed using EBSD. Thin foils were produced from selected aged samples to characterize the sub-micron chromium and niobium rich secondary carbides and further analyse the niobium rich primary precipitates.

The remaining aged material was kept at QIG's Wellington laboratory where accelerated creep testing was conducted in parallel to the microstructural analysis. Ultimately, the results from the accelerated creep testing of the unstressed aged samples will be integrated into QIG's proprietary LifeQuest™ Reformer software suite [2]. The knowledge of the HP-Nb and HP-NbTi alloys' long-term creep properties (e.g. creep ductility and rupture life) is used by QIG's LifeQuest™ Reformer software suite in combination with measurements taken from the inner and outer diameter of service exposed service tubes using QIG's proprietary LOTIS® [2] and MANTIS™ [3] tube inspection systems to predict the remaining life of service exposed tubes. As the data obtained from accelerated creep testing of the laboratory aged samples forms the basis of the LifeQuest™ Reformer database, these creep results were considered by QIG to be commercially sensitive and could not be published or discussed in this thesis.

As previously mentioned, the HP-Nb and HP-NbTi samples used for the microstructural analysis and QIG's creep testing program were all aged without the application of any mechanically induced stress. Unstressed ageing was carried out in order to isolate and quantify any change in each alloy's creep properties due to the temperature induced microstructural evolution. However, ageing

[2] QIG's proprietary Laser Optical Tube Inspection System (LOTIS) which uses laser profilometry to measure each tube's internal diameter allowing for the accurate quantification of creep strain along the tubes length [2].
[3] An external tube 'crawler' containing QIG's proprietary sensors which measure creep strain along the tubes length and detects cracks using eddy current technology [2].

performed with the material unstressed is clearly not realistic in comparison to tubes in actual service. During service within reforming furnaces, the internal pressure of the process gasses results in stresses between 5-20MPa across the tube's wall thickness. The consumption of the material's creep life due to the presence of stress will likely cause the creep properties of stressed samples to reduce at a greater rate with respect to ageing temperature and time in comparison unstressed samples. Moreover, the addition of stress during ageing could alter the HP alloy's microstructural evolution during ageing (e.g. accelerating or decelerating the phase transformation kinetics). Hence, remaining life predictions based solely on the creep data obtained from the unstressed samples may overestimate the remaining life of service exposed tubes, increasing the risk of catastrophic failure if the tubes are subjected to further service.

Since the creep data derived from QIG's testing program will be used to predict the remaining creep lives of service exposed tubes (i.e. where stress induced creep damage cannot be neglected), it was considered necessary to compare the creep properties of samples that had undergone both stressed and unstressed ageing prior to accelerated creep testing. It was believed that this testing would help verify whether the creep properties of service exposed tubes could be accurately modelled using data produced from accelerated testing of samples that had been pre-aged without stress (i.e. QIG's creep testing program). If any significant discrepancy existed between the unstressed and stressed aged samples, this testing would provide a correction factor which could be applied in QIG's life prediction models to account for the accumulation of creep induced damage during service.

Initially, the accelerated testing of the stressed and unstressed aged samples was planned to be carried out in parallel to the microstructural analysis at the University of Canterbury (independently of the QIG's creep testing program which was performed at their Wellington laboratory). Consequently, three new accelerated creep testing rigs were designed and manufactured at the University of Canterbury specifically for the current this testing. The first rig was developed, manufactured and calibrated at the University of Canterbury between July 2009 and June 2010. This rig performed constant load accelerated creep testing of four samples positioned in series within a single tube furnace and was capable of obtaining high accuracy (~1µm resolution) measurements of each alloys' minimum creep rates (secondary creep). However, since the samples being connected in series, it could not test all four samples until failure. The first stressed ageing experiments began in August 2010 with accelerated creep testing of these samples commencing in late October 2010.

Unfortunately, this test was interrupted by the first Canterbury earthquake on September the 4th 2010. Ongoing aftershocks made testing during the September 2010-January 2011 period impossible as these tests require highly sensitive strain measurements to be performed over prolonged periods of time (60-70 days). Testing recommenced in late January (2011) as the aftershocks were thought to have reduced to a tolerable level. Unfortunately, a large aftershock struck on the 22nd of February rendering the rig largely unusable. Modifications were subsequently made to this rig and it was shipped to Quest Integrity Group's Wellington laboratory in order to carry out the stressed and unstressed ageing of the HP-Nb1 and HP-NbTi2 alloys. In parallel, two additional test rigs of a widely different design than the first rig were subsequently manufactured and calibrated at the University of Canterbury. Manufacturing of these rigs also suffered significant delays due to ongoing aftershocks causing the development of these rigs to take considerably longer than initially anticipated. While these new rigs incorporated design features similar to the first test rig, the capability of these rigs was expanded to allow for independent testing of four samples to rupture within a single furnace. Testing of the unstressed aged samples was restarted at the University of Canterbury during July 2012. Unfortunately, mechanical and electrical issues required modifications to be made to each rig causing further delay to the accelerated testing program. Testing was recommenced during December 2012.

Despite the considerable effort placed into the design and manufacture of each testing rig, the continued delays to the creep testing program made it impossible to perform accelerated testing on the stressed and unstressed aged samples within the time frame of the current project. Therefore, only a brief discussion that compares the creep properties of the HP-Nb1 and HP-NbTi2 alloys after ageing unstressed at 1000°C for 1000 hours will be presented in order to provide further insight into the microstructural features that result in the HP-NbTi alloys superior creep resistance in comparison to the HP-Nb alloy. Consequently, accelerated creep testing of the samples after stressed ageing has been placed in the future work section of this thesis and will be reported in a future journal publication.

Microstructural analysis of the samples subjected to ageing at 1000°C for 1000 hours with an applied stress was also not feasible. While, identical to the unstressed isothermal ageing experiments, stressed ageing was conducted within an air atmosphere, the comparatively smaller cross-section of the stressed samples (a 5mm diameter cylinder taken from the tubes 11-14mm wall thickness - Chapter 7) caused each sample's microstructure to be more greatly affected by the furnace

atmosphere in comparison to samples aged without the application of stress. Consequently, any effects of stress on the HP alloys' microstructural evolution during ageing could not be distinguished from the atmosphere induced phase transformations that occurred in parallel during stressed ageing. The effects of the furnace atmosphere on the HP alloys' microstructural evolution are discussed in detail in Chapter 8.

1.3 Research Scope

This study of the HP-Nb and HP-NbTi alloys' microstructural evolution during long-term ageing focused on the following academic and industrial interests:

- The effects of the single addition of niobium and dual additions niobium and titanium on the 'primary' carbides (present in the as-cast condition) and 'secondary' matrix precipitates (present after thermal exposure) and the stability of these precipitates during prolonged exposure to 1000, 1050 and 1100°C;

- Identification of the microstructural features within the HP-NbTi alloy which result in this alloy's increased short-term creep resistance in comparison to the HP-Nb alloy and determining if these features remain present in the HP-NbTi alloy during long-term exposure;

- Identification of the microstructural changes which lead to the degradation of each alloys' creep resistance during long-term service exposure;

- Obtaining a set of reference micrographs with known levels of microstructural ageing induced "damage" which can be compared to ex-service microstructures for life assessment;

- Verification that unstressed isothermal ageing of each alloy followed by accelerated creep testing is capable of producing creep properties representative of the alloys' properties during actual service.

Although numerous HP alloy compositions that contain a wide variety of modifying elements (e.g. Nb, Ti, W, Zr and Y) are currently used in service, this work was limited to the two most common HP-modified alloys currently found in service: HP-Nb (niobium modified) and HP-NbTi (niobium and titanium modified and also commonly known as HP-Micro or MA). Typical compositions for each alloy are given in Table 1.4.

While relating the accelerated creep testing results (performed by QIG at their Wellington laboratory) to the microstructural analysis (performed at the University of Canterbury) was part of the wider scope of this research project, the investigation of this relationship could not be published in the present thesis due to the commercial sensitivity of the creep testing results.

Table 1.4 - Typical compositions of the HP-Nb and HP-NbTi alloys

wt.%	C	Ni	Cr	Nb	Ti	Si	Mn
HP-Nb	0.4-0.5	34-37	24-28	0.6-1.5	-	1.5	1.5
HP-NbTi	0.4-0.5	35	25	1.5	0.02-0.1	1.4	1

1.4 Format of this Thesis

The contents of the nine chapters and three appendices presented in this thesis can be briefly summarized as follows:

Chapter 1 (current chapter) briefly discusses the background, overview and scope of the research presented in this thesis.

Chapter 2 gives a literature review addressing the development of steam-methane reformer tube alloy, the conditions within the reforming furnace that influence the tube's service life and the previous metallurgical characterization of the HK and HP alloys. This chapter was composed using work published within peer-reviewed journal articles, conference proceedings, technical reports, past doctoral theses and engineering/scientific textbooks that were available through bibliographic databases (such as Engineering Village [17]) and the University of Canterbury library prior to the publishing of the current thesis.

Chapter 3 explains the experimental techniques used to prepare the metallographic samples for optical microscopy (OM), scanning electron microscopy (SEM) and transmission electron microscopy (TEM). The equipment used to perform energy dispersive X-ray spectroscopy (EDS), electron backscatter diffraction (EBSD), selected area diffraction (SAD), convergent beam electron diffraction (CBED) and powdered X-ray diffraction (XRD) and the standard operating conditions for each piece of equipment are also briefly described.

Chapter 4 presents the comprehensive microstructural analysis performed on the as-cast HP-Nb alloy. Specific attention is paid to the morphology and crystallography of the primary NbC precipitates (i.e. the precipitates which form as a direct result of the alloy's modification with niobium).

Chapter 5 presents the detailed microstructural analysis performed on the as-cast HP-NbTi alloy. Emphasis is placed on the effects of titanium on the morphology and crystallography of the primary (NbTi)C precipitates.

Chapter 6 discusses the microstructural evolution that occurs at the mid-wall position of the HP-Nb alloy during unstressed isothermal ageing at 1000, 1050 and 1100°C. While the growth and crystallography of the chromium-rich precipitates has been investigated in detail, the characterization of the aged microstructures mainly focused on the evolution of the niobium-rich phases. Specifically, extensive characterization and discussion of the NbC/G-phase and NbC/η-carbide transformations with respect to ageing temperature is presented. Emphasis was placed on the characterization of the microstructural evolution at the tubes mid-wall position due to the gauge length of the QIG creep samples coinciding with the mid-wall position.

Chapter 7 discusses the microstructural evolution that occurs at the mid-wall position of the HP-NbTi alloy during unstressed isothermal ageing at 1000, 1050 and 1100°C. The increased stability of the primary (NbTi)C precipitates and presence of nano-scale (NbTi)C secondary precipitates (absent in the HP-Nb alloy) due to the combined addition of niobium and titanium is discussed. The microstructural evolution in the HP-Nb and HP-NbTi alloys with respect to ageing temperature and time is also compared and the microstructural features that are believed to increase the HP-NbTi alloy's creep resistance in comparison to the HP-Nb alloy are also discussed.

Chapter 8 shows the extensive nitridation and decarburization in the HP-Nb and HP-NbTi alloys as a result of ageing being carried out in an air atmosphere. The furnace atmosphere caused a number of phase transformations to occur at the tubes inner and outer diameter positions which were not observed at the mid-wall position. The types of phase transformation within the affected area and size of the affected area are discussed with respect to ageing temperature and time.

Chapter 9 concludes this thesis by summarizing the academic achievements and industrial relevance of the knowledge gained from the current research project.

Appendix A gives selected properties of the tube alloys (as published by the respective manufacturers).

Appendix B presents an overview of the design and development of the accelerated creep testing apparatuses used to perform the creep testing discussed in Chapter 7.

Appendix C presents time-temperature-transformation diagrams plotted for the $Cr_{23}C_6$-to-Cr_2(CN), MC-to-η-carbide and MC-to-Z-phase transformations discussed in Chapter 8.

Appendix D contains copies of the papers that were published during the course of this research project.

1.5 Research Achievements

This research project generated multiple academic contributions as listed below. The papers which have been published to date have been included in Appendix C of this thesis.

Buchanan, K. G. and Kral, M. V. (2009) *Effects of Long Term Aging on Creep Properties of HP Reformer Tubes,* presented at Characterization of Minerals, Metals and Materials, TMS 138th Annual Meeting & Exhibition, San Francisco, California, USA.

Knowles, D.; Buchanan, K. G and Kral, M. V. (2009) *Condition Assessment Strategies in Centrifugally Cast HP Steam Reformer Tube Alloys,* published in the Proceedings of the 2nd International ECCC Conference: Creep & Fracture in High Temperature Components – Design & Life Assessment, Dübendorf, Switzerland.

Buchanan, K. G. and Kral M. V. (2010) *Effects of Long Term Aging on Creep Properties of HP Reformer Tubes,* presented at The 7th Pacific Rim International Conference on Advanced Materials and Processing (PRICM), Cairns, Australia.

Kral M. V and Buchanan, K. G. (2012) *Effects of Long Term Aging on Creep Properties of HP alloy Hydrogen Reformer Tubes,* presented at Materials in Clean Power Systems VII: Clean Coal-, Hydrogen Based-Technologies, and Fuel Cells, TMS 141st Annual Meeting & Exhibition, Orlando, Florida, USA.

Buchanan, K.G. and Kral, M.V. (2012) *Crystallography and Morphology of Niobium Carbide in As-Cast HP-Niobium Reformer Tubes*, published in Metallurgical and Materials Transactions A 43(6): 1760-1769.

Buchanan, K. G. and Kral, M. V. (2013) *Detailed Characterization of the Various Morphologies obtained by MC Precipitates in Modified HP Alloy Reformer Tubes,* 26th New Zealand Conference on Microscopy, Christchurch, New Zealand.

Chapter References

[1] Wahab, A. A. (2007). *Three-Dimensional Analysis of Creep Void Formation in Steam-Methane Reformer Tubes.* Unpublished doctoral dissertation, University of Canterbury, Christchurch, New Zealand.

[2] Quest Integrity Group (2013). *Reformer Care: A Complete Asset Integrity Solution.* Retrieved January 2013, from http://www.questintegrity.com/technology/steam-reformer-tube-inspection

[3] Barbabela, G. D., de Almeida, L. H., da Silveira, T. L & Le May, I. (1991). *Role of Nb in Modifying the Microstructure of Heat-Resistant Cast HP Steel.* Materials Characterization, 26:pp. 193-197.

[4] de Almeida Soares, G. D., de Almeida, L. H., da Silveira, T. L. & Le May, I. (1992). *Niobium Additions in HP Heat-Resistant Cast Stainless Steels.* Materials Characterization, 29: pp. 387-396.

[5] Ibañez, R. A. P., Soares, G. D. A., de Almeida, L. H. & Le May, I. (1993). *Effects of Si Content on the Microstructure of Modified-HP Austenitic Steels.* Materials Characterization, 30: pp. 243-249.

[6] de Almeida, L. H., Ribeiro, A. F. & Le May, I. (2003). *Microstructural Characterization of modified 25Cr-35Ni centrifugally cast steel furnace tubes.* Materials Characterization, 49: pp. 219-229.

[7] Caballero, F. G., Imizcoz, P., Lopez, V., Alvarez, L. F. & Garcia de Andrés, C. (2007). *Use of titanium and zirconium in centrifugally cast heat resistant steel.* Materials Science and Technology, 23: pp. 528-534.

[8] Nunes, F. C., Dille, J., Delplancke J. -L & de Almeida, L. H. (2006). *Yttrium addition to heat-resistant cast stainless steel.* Scripta Materialia, 54: pp. 1553-1556.

[9] Laigo, J., Christien, F., Le Gall, R., Tancret, F. & Furtado, J. (2008). *SEM, EDS, EPMA-WDS and EBSD characterization of carbides in HP type heat resistant alloys.* Materials Characterization, 59: pp. 1580-1586.

[10] Davis, J. R. (Ed.). (1997). *ASM Specialty Handbook: Heat-Resistant Materials.* Materials Park, Ohio: ASM International, pp. 200-218.

[11] American Petroleum Institute. (2003). *Calculation of Heater Tube Thickness in Petroleum Refineries.* API 530, 5th Edition, ISO 13704:2001 (E).

[12] Thomas, C. W. (2007). *Factors influencing life of reformer furnace tubes.* Materials at High Temperatures, 24(3): pp. 233-240.

[13] Thomas, C. W., Stevens, K. J. & Ryan, M. J. (1996). *Microstructure and properties of alloy HP50-Nb: comparison of as cast and service exposed materials.* Materials Science and Technology, 12: pp. 469-475.

[14] Kubota Metal Corporation (1999). *KHR 35C alloy data sheet.* Revision 06/99. Kubota Metal Corporation: Ontario, Canada.

[15] ASM International (2002). *Paralloy H39Wmaterial datasheet.* Alloy Digest Inc.: Orange, New Jersey, U.S.A.

[16] Schmidt + Clemens Group (2001). *Centralloy CA4852 Micro material data sheet.* Schmidt + Clemens Group: Lindlar, Germany.

[17] Elsevier (2013), *Engineering Village*. Available from http://www.engineeringvillage.com

Chapter 2 **Literature Review**

The following chapter provides an overview of the previous work conducted on reformer tube alloys. This chapter will begin by discussing the use of austenitic stainless steel tubes within steam-methane reforming furnaces. Emphasis has been placed on the latest generation of reformer tube alloys: the HP series. The factors which influence the life of these tubes during service within reforming furnaces will be briefly discussed followed by a summary of the historical metallurgical development of reformer tube alloys. Finally, a detailed review of past work which studied the microstructure and creep properties of the HP-Nb and HP-NbTi alloys with respect to the laboratory ageing or service conditions will be presented.

Since the primary objective of the current research was to determine the effects of microstructural evolution on the HP-Nb and HP-NbTi alloys' creep properties during long-term service exposure within steam-methane reforming furnaces, only literature pertinent to this type of furnace has been included in the current review. While HP alloy tubes are also widely used within pyrolysis furnaces (also known as steam cracking furnaces), the severe carburization of the tubes internal bore during service (as a result of coke deposition [1]) causes the factors which influence the tube life during service within pyrolysis furnaces to be somewhat different than for reforming furnaces. Thus, the use of HP alloys in pyrolysis furnaces has been largely neglected in the following chapter.

2.1 The Use of Austenitic Tubes within Steam-Methane Reforming Furnaces

In general, reforming covers a wide range of chemical process used by the petrochemical industry to convert numerous unique gas mixtures into other new gas mixtures. During steam-methane reforming, a pressurized (1-3.5MPa) and preheated (~550°C) mixture of steam and methane gas is converted to hydrogen, carbon monoxide and carbon dioxide (Figure 2.1) [2, 3]. The reaction within each reformer tube can be summarized as follows:

$$CH_4 + H_2O \leftrightarrow CO + 3H_2 \qquad (2.1)$$

$$CO + H_2O \rightarrow CO_2 + H_2 \qquad (2.2)$$

This reaction is carried out within hundreds of vertically orientated catalyst (nickel-oxide) filled tubes that are heated within large furnaces typically held at temperatures between 850-1050°C (Figure 2.1). The combination of the internal gas pressure and elevated temperature causes the reformer tube's life to typically be limited by creep. The aggressive service environment within the reformer furnace necessitates the use of high alloy cast austenitic stainless steels tubes (such as the HK40 and HP40 alloy series) which exhibit good creep and oxidation resistance. Reformer tubes typically experience service lives of up to 100,000 hours [4] with tubes generally being retired from service when excessive radial expansion of the tubes is detected during planned furnace shutdown periods (generally to replace the nickel-oxide catalyst) or if a creep induced rupture of the tube has occurred during service.

Generally, reformer tubes have an internal diameter between 100-150mm with a wall thickness of 10-15mm. The exact dimensions of reformer tubes are dictated by the process requirements. For example, the tube's diameter must be designed to accommodate the required gas flow rate and catalyst volume whereas the tube's wall thickness must be balanced to maintain a creep life in excess of 100,000 hours (where thicker tube walls are beneficial) while also maintaining an acceptable heat transfer rate (where thinner tube walls are beneficial) [5]. The tubes are cast in 4.5 meter lengths which are welded together to give the typical reformer tube length of 13.5 meters.

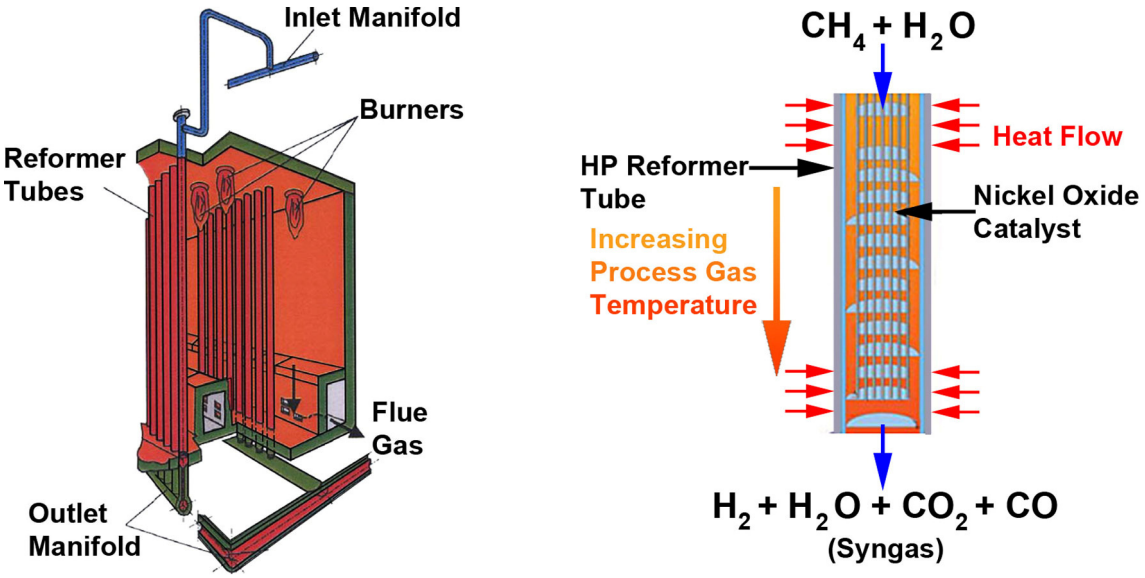

Figure 2.1 – Illustrations giving an example of (left) a typical reforming furnace layout and (right) the reaction occurring within each reformer tube.

The mixture of hydrogen, carbon monoxide and carbon dioxide produced by steam-methane reforming is commonly known as synthesis gas (also referred to as syngas). Synthesis gas is typically used as a feedstock gas for the production of numerous other chemicals such as methanol and ammonia. Alternatively, the hydrogen can be separated from the synthesis gas and used as a directly as fuel source. Specific details of each production process will not be given here as the current project focused solely on the tubes within the reforming furnace (which remains relatively similar for each process). However, the methanol production process has been shown in Figure 2.2 in order to give an example of the key role that the steam-methane reformer plays within the petrochemical industry. This example has been given as it is currently the most significant application of the steam-methane furnace in New Zealand.

Figure 2.2 gives an overview of the main processes used to produce methanol at Methanex's[1] Waitara Valley (NZ) methanol plant. In this case, the methanol production process can be split into three main sections (as shown in Figure 2.2) beginning with the steam-methane reforming furnace. Generally, the steam-methane reformer is regarded as one of the key components in the methanol production plant. The reformer is often the most expensive section of the production plant and one of the plant's primary energy consumers. Due to the aggressive environment within the reforming furnace, shutdowns of the entire plant are often a result of a problem with the reformer [2].

[1] Methanex (Vancouver, Canada) is the world's largest producer of methanol supplying methanol to major markets such as North America, Latin America, Europe and the Asian Pacific.

Consequently, considerable effort is often placed into the care and maintenance of the reforming furnace with particular attention paid to the reformer tubes. Monitoring of the tubes' external wall temperature, furnace combustion temperature and internal gas temperature, pressure and flow rates is typically carried out at regular intervals during normal operation to ensure the tube are kept within the maximum design conditions [6]. During planned plant shutdown periods (generally to replace the catalyst within each tube), non-destructive testing, such as measurement of the tubes diametral expansion, is often undertaken on each individual tube in order to assess the tube's remaining life and determine the likelihood of failure occurring within the next service period. Non-destructive testing, such as the preparation of metallographic samples for microstructural analysis, is often performed on a limited number of tubes (generally the tubes exhibiting the greatest level of creep deformation) to further ascertain the level of creep damage that can be expected within the entire set of tubes.

Ultimately, without a fundamental understanding of the relationship between the reformer tubes metallurgy and mechanical properties, each assessment technique is liable to produce inherently unreliable tube life predictions. Unfortunately, the tube's lengthy service life (up to 100,000 hours) causes research on long-term creep properties of the various HP alloys' to often be prohibitively awkward/difficult and expensive. Hence, despite the considerable effort placed into the correct operation and maintenance of reformer tubes, premature failure of reformer tubes during service remains a significant problem for plant operators.

The continuous evolution of new tube chemical compositions with increasingly greater creep properties has further increased the difficulty of performing long-term studies prior to the placement of the new alloys into service. Recently, HP alloy reformer tubes modified with differing additions of niobium, titanium, zirconium, tungsten and rare earth elements has resulted in a further increase in the tube's creep resistance in comparison to tubes without these alloying additions [7]. This strength increase has allowed plant operators to decrease the tube's wall thickness in order to reduce the tube's production cost and increase the heat transfer rate to the process gases [4]. Alternatively, operators can take advantage of this strength increase by keeping the tubes wall thickness unchanged while increasing the furnaces operating temperature.

While numerous studies have investigated the microstructural features that affect the creep resistance of modified HK and HP alloys during short-term exposure (typically <2000 hours or 2% of the tubes service life) [8-20], relatively few studies have currently been conducted on the factors

which influence the alloys' long-term creep resistance [4, 21-25]. The current poor understanding of the new generation of alloy's long-term creep resistance has led to an increased level of concern over the accuracy of life predictions made from the current regime of non-destructive and destructive testing in combination with the mechanical properties extrapolated from short-term testing. This concern has largely arisen due to the lack of knowledge surrounding the long-term effectiveness of these new alloying additions. In other words, "Does the short-term creep strength increase offered by these new alloying additions remain during long-term service?". Therefore, this uncertainty and the importance of the steam-methane reforming furnace in numerous petrochemical production plants have resulted in recent emphasis being placed on determining the microstructural factors which influence the tube's life during long-term service [4, 21-25]. This emphasis has led to the initiation of the current project.

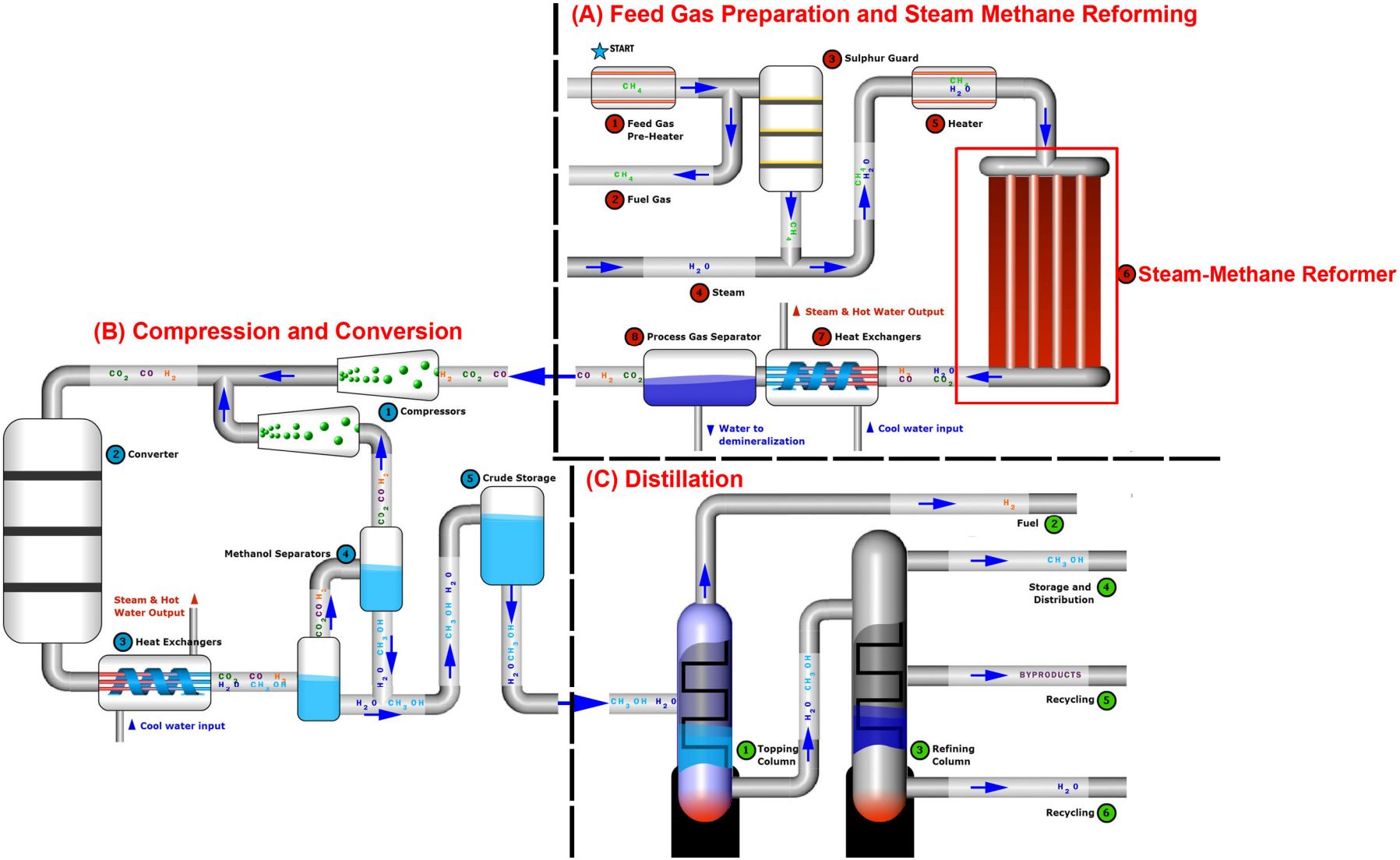

Figure 2.2 - Schematic showing the methanol production process. The dashed lines separate the three main stages of the process: (A) feed gas preparation and steam-methane reforming, (B) compression and conversion and (C) Distillation. Reproduced from [26].

2.2 Factors That Influence the Service Life of Reformer Tubes

Reformer tubes typically operate at temperatures between 850-1050°C with internal pressures between 1-3.5MPa. The high temperature is above the lower creep limit of high temperature stainless steels, hence the combination of temperature and moderate stresses cause creep to be the dominant failure mechanism. Reformer tubes are typically designed in accordance with standards such as API 530 [5]. Designs need to optimize the heat transfer rate through the tube wall, the processes thermodynamic efficiency and catalyst volumes while minimizing the stress within the tube wall in order to maintain a life expectancy of 100,000 hours. Initially the process parameters such as temperature, pressure, mass flow rate and catalyst volume are considered to determine the required tube diameter. Next the maximum permissible temperature and pressure that the tube will experience in steady state operation is used to calculate the required wall thickness. This calculation is typically done by calculating the Larson-Miller Parameter for the estimated temperature and service life (100,000 hours). Using the vendor supplied stress-rupture data, the Larson-Miller Parameter can be used to obtain the maximum allowable stress. Finally, this stress can be used to calculate the required tube wall thickness. The highest possible temperatures and pressures along with the minimum creep properties are used to ensure conservatism [5, 27-29].

Since the design of reformer tubing is based largely on the maximum internal pressure and external temperature during steady state operation of the furnace, other factors which influence the tubes service life, such as through wall temperature gradients, tube self weight, oxidation and microstructural ageing are typically accounted for by generous safety factors. Using safety factors in this manner potentially results in non-conservative life predictions (i.e. being above the tubes actual life) [27, 28]. Quantifying the effects of these factors on the tubes service life becomes particularly difficult when performing life assessments on ‘in-service’ tubes as it is often difficult to determine the extent to which each factor has reduced the tubes life without destructively testing the tube material (i.e. accelerated creep testing). Thus, the complex operating conditions experienced by the tubes causes unexpected tube failure to still be a significant problem for plant operators. The following briefly summarizes the main factors that influence the tube’s service life and the effort made to mitigate the effects of each factor.

2.2.1 Internal Pressure

As previously stated the reactants in the reformer tubes are held at pressures between 1-3.5MPa, depending on the process requirements. The hoop, radial and longitudinal stresses induced by the internal gas pressure is the major cause of creep damage in the tubes during steady state operation of the furnace. Lamé's equations to calculate stress for thick-walled tubes are shown in equations 2.3 to 2.5 [30] where the maximum stress is dependent on the wall thickness and gas pressure. It can also be seen that the stress varies with position in the tube wall (the greatest stress occurs the tubes inner diameter). The gradual radial expansion of the tubes during service indicates that the principle damage inducing stress can be approximated by the hoop stress which commonly ranges between 10-20MPa.

Hoop stress: $$\sigma_h = \frac{p r_i^{\,2}}{r_o^{\,2} - r_i^{\,2}} \left(1 + \frac{r_o^{\,2}}{r^2} \right) \qquad (2.3)$$

Radial stress: $$\sigma_r = \frac{p r_i^{\,2}}{r_o^{\,2} - r_i^{\,2}} \left(1 - \frac{r_o^{\,2}}{r^2} \right) \qquad (2.4)$$

Axial stress: $$\sigma_{ap} = \frac{p r_i^{\,2}}{r_o^{\,2} - r_i^{\,2}} \qquad (2.5)$$

Where: p = Internal pressure,
ri = Tube inner wall radius,
ro = Tube outer wall radius,
r = Radius to point of interest.

2.2.2 Self Weight

The significant size of the tube assemblies causes each to weigh a substantial amount. Thus, at the furnace's operating temperatures the stress induced due to self weight needs to be accounted for. Typically, the stress from the tubes self weight can be largely eliminated during design of the furnace. For example, Figure 2.3 shows a lever arm system that can be used to compensate for self weight. While many systems do not fully account for the self weight of the tubes, the level of stress induced by the tubes weight can be reduced to negligible levels by compensation systems [29].

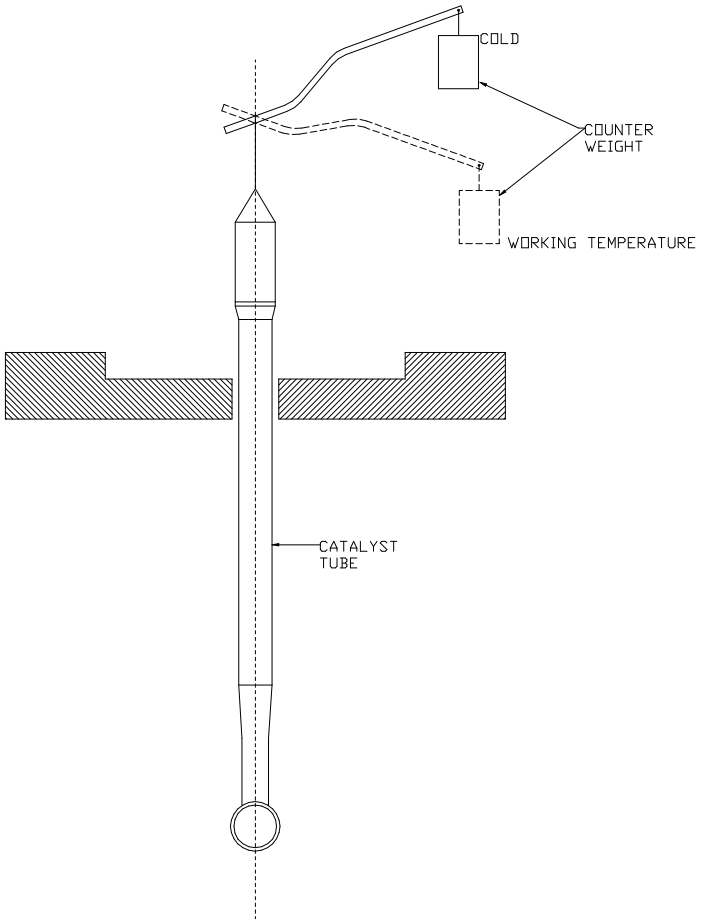

Figure 2.3 - Compensation for the tubes self weight

2.2.3 Thermal Elongation

As with any material operating over a range of temperatures, strain occurs due to thermal expansion. The high service temperatures involved causes significant elongation of the tubes. Stress will be induced if the tube's elongation is constrained by a design that does not account for this expansion. Most designs compensate for the elongation by the use of flexible inlet and outlet pigtails, and U-bends on the inlet and outlet lines, thus minimizing the induced stress [29]. Detailed design of flexible inlet and outlet tubing can reduce any thermal expansion induced stress within the reformer tube to a level that will have negligible effect on the tube's creep life.

2.2.4 Transient Through-wall Temperature Gradient

The lower inlet temperature of the reaction gases (~550°C) and endothermic reactions that occur within the tubes induces a temperature difference between the inner and outer diameter of the tube. The outer "skin" temperature of the tube can be as much as 50°C hotter than the temperature at the tube's inner surface [28, 29, 31]. This temperature difference causes a difference in thermal expansion across the tube wall and hence induces a through-wall stress distribution. Factors that affect this stress include the through-wall heat flux and the wall thickness. The stresses caused by the differential thermal expansion across the wall can be as much as an order of magnitude higher than the pressure induced stresses [28]. During steady state operation of the tubes the temperature gradient is relatively constant and hence the thermally induced strains are also constant [28, 29]. Therefore, due to stress relaxation, the elastic strain converts to plastic creep deformation at high temperatures, relieving the stress induced by the temperature gradient. However, any significant fluctuations in temperature during normal operation of the furnace and periodic shutdowns/startup cycling of the furnace will cause the re-emergence of the strain induced stress distribution through the tube's wall.

The presence of thermally induced stresses and their cyclic nature has been a significant concern when conducting remaining life calculations. Quantifying the effect of these stresses on the tube's creep life is relatively difficult since knowledge of the various HP alloys' stress relaxation properties in

the as-cast and aged conditions is relatively limited. Moreover, the reduction in the tube's life is heavily influenced by the number of cycles the tube has experienced and the temperature gradient across the tube wall during each cycle [28, 29]. The temperature gradient is particularly important during startup/ shutdown of the furnace. The temperature gradient across the tubes during these periods is heavily dependent on the heating rates experienced by the tubes. For example, a tube with a wall thickness of 10mm can experience peak stresses of approximately 200MPa when heating rates of 100°C/hour are used. When considering the room temperature yield stress of the material is approximately 220-250MPa, obviously the 200MPa stress level will cause localized yielding at elevated temperatures. Reducing the heating rate to 30°C/hour can result in a reduction of the peak stress to approximately 50MPa [29]. The consideration of the heating rate becomes much more important at later stages of the tubes life (i.e. once the degradation of the mechanical properties due to the effects of microstructural ageing becomes significant). While the formation of secondary carbides (which occurs during the tubes initial exposure to elevated temperatures) act to increase the material's creep resistance, they markedly reduce the tube's toughness [9, 28]. Growth and coalescence of the primary and secondary precipitates cause further reductions in the toughness of the tubes. The reduction in toughness causes acceptable heating rates for 'new' tubes to be unacceptable for use in plants with tubes that have seen service.

Previous work has attempted to quantify the effect of cyclic stresses on the service life of HP-Nb alloy reformer tubes based on the exhaustion of the material's creep ductility [28]. This concept assumes that a fraction of the material's creep ductility is consumed during each thermal cycle. Once the material's ductility is consumed, failure of the tube occurs. Using this method to quantify the effects of thermal cycling on a tube's service life is relatively complex as it requires a detailed understanding of the alloy's creep ductility and stress relaxation properties with respect to temperature, stress and exposure time in addition to accurate knowledge of the service conditions experienced by the tube (e.g. number of thermal cycles and heating rate). Since the HP-Nb alloys creep ductility varies significantly when comparing as-cast and aged material (3-19% as-cast, 17-39% aged [27, 28]), further analysis of the alloy's creep and stress relaxation properties in the as-cast and aged conditions is reportedly necessary to allow for reliable prediction of the effects of cyclic stresses on the tube's service life based on ductility exhaustion [28].

2.2.5 Non-Uniform Tube Wall Temperature Distributions during Steady-State Operation

Non-uniform temperature distributions along the length of individual tubes and between neighboring tubes or rows of tubes can exist during steady-state operation of the reforming furnace which causes variations in the tube's expected service lives [1, 31-33]. The considerable size of reforming furnaces presents a challenge to maintain a completely uniform temperature distribution between the numerous rows of tubes. Temperature variations between separate tubes causes the extent of creep damage and microstructural ageing to vary between each tube increasing the difficulty when producing remaining life predictions for the entire set of tubes. The temperature variation within the furnace can be minimized through detailed design of the furnace (e.g. the use of top fired or terrace-walled burners and correct spacing of the burners from the tubes). However, incorrect positioning of the burners with respect to the tube resulting in flame impingement or uneven firing can cause non-uniform temperature distributions around an individual tube's circumference [31]. Certain catalyst geometries are also known to create hot spots within individual tubes [2]. Localized overheating of the tube increases the creep rate, microstructural ageing and oxidation which often results in the tubes premature failure during service.

The comparatively low temperature of the process gases at the reformer tubes inlet (~550°C) results in a non-uniform temperature distribution along the tube's length. The wall temperature near the tube's inlet can be up to 300°C cooler in comparison the temperature near the base of the reforming furnace [2, 32]. Consequently, the creep deformation rate along the tube's length is non-uniform with the greatest level of creep deformation and microstructural ageing for each tube typically being greatest near the base of the reforming furnace.

2.2.6 Welding Induced Stresses

As mentioned previously, reformer tubes are a welded assembly. Typically, three 4.5 meter sections are welded together to produce the tubes 13.5 meter length [2]. Since any compositional difference between the weld filler material and tube parent material can result in a slight difference in each region's thermal expansion coefficients and creep strength, significant emphasis is placed on

matching the filler and parent materials when performing welding operations on these tubes [14]. If the filler material and parent material are not correctly matched, cracking can result in either the heat affected zone or weld filler material depending on whether the filler material is over or under matched to the high temperature properties of the parent material [29]. While matching on 'new' materials has been successful, it is much harder to match the filler material composition with that of older tubes [14, 29]. The stresses induced due to weld shrinkage must also be considered. However, these stresses can be minimized by preheating the parent material prior to carrying out welding.

2.2.7 Carburization, Nitridation and Oxidation

Aside from the high temperature and various stresses, the furnace atmosphere also affects the life of reformer tubes. Due to the heating medium being provided by the combustion of fossil fuels in air, the furnace atmosphere (typically a mixture of CO_2, CO, N_2 and H_2O depending on the air/fuel ratio) can cause carburization and nitridation at the tubes external surfaces. At the same time, the CO and CO_2 content within the process gases (typically between 35-40% CO and 25-35% CO_2 depending on the chemical composition of the feedstock gas) can cause carburization to occur at the tubes inner diameter. High temperature oxidation is another factor that can cause deterioration of material performance. Therefore, the tube material must include elements which give protection against environmental attack. The high level of nickel within the HP alloy and silicon additions is often used for this purpose [7].

2.2.8 Variations in the Tube's Dimensions

Wall thickness variations along the length of the reformer tube are relatively unavoidable due to the manufacture of the tubes by the centrifugal casting process. Slight wall thickness variations lead to non-uniform stress and temperature distributions along the tube's length. In extreme cases, eccentric bores can result in sections of the tube wall being thinner that the specified minimum 'safe' wall thickness [2]. Such manufacturing defects ultimately lead to early failure of the tubes during

service. To minimize tube geometry induced failures, variation below the tubes minimum specified 'safe' wall thickness is considered unacceptable and the tubes maximum wall thickness must not exceed 10% or 1.6mm (whichever is greater) of the specified wall thickness [34]. To minimize tube eccentricity (and also remove unwanted material) a honing operation is performed on the tubes internal surface.

2.2.9 Microstructural Evolution during Service Exposure

Long-term exposure of the tubes to the reforming furnace operating temperatures can be considered as an extremely prolonged heat treatment. This heat treatment results in the transformation and subsequent coarsening of the primary and secondary precipitates [4, 8-25, 27]. Unsurprisingly, this continuous evolution of the tube's microstructure causes the creep resistance to also continuously evolve during service. The effects of microstructural ageing on the tube's mechanical properties are often overlooked by the current design methodology as the tubes creep life is based on stress-rupture data which is extrapolated using parametric techniques such as Larson-Miller from data produced by accelerated creep testing on as-cast material. Consequently, numerous past studies have tried to quantify the effects of microstructural ageing on the creep properties (such as minimum creep rate, creep ductility and rupture time) of modified HK and HP alloys [4, 8-25]. As the effects of microstructural ageing are also the focus of the current project, a detailed review of previous work characterizing this evolution specific to the HP-Nb and HP-NbTi alloys has been presented separately in the following sections.

2.3 Metallurgical History of Reformer Tube Alloys

Prior to the 1960's, the aggressive environment within steam-methane reforming furnaces demanded the use of expensive wrought HT (Table 2.1) superalloys [35]. In an effort to reduce the cost of reformers, the centrifugally cast HK alloy series (Table 2.1) was introduced to replace the HT superalloys. The HK alloy tubes provided comparable creep performance to the HT alloy series while significantly reducing cost (due to the decrease in Ni and reduced production costs). The high carbon content in the HK series (0.4wt.%) induces the formation of eutectic Cr_7C_3 carbides along the grain and dendrite arm boundaries which significant improves the alloys creep properties in comparison to equivalent low carbon stainless steels [7]. During exposure to the reforming furnace's operating temperatures, the eutectic 'primary' carbides transform to $Cr_{23}C_6$ and a distribution of 'secondary' intragranular $Cr_{23}C_6$ precipitates forms within the austenite grains [35]. While the combination of primary and secondary precipitates initially increases the alloy's creep resistance, this increase is progressively lost due to continued coarsening of these precipitates during prolonged service (100,000 hours). Despite the gradual embrittlement of the HK alloy during long-term service, this alloy became the industry standard and basis of subsequent reformer alloy development as it was the only comparatively inexpensive alloy which exhibited reasonable creep strength at temperatures up to 1000°C.

The first significant improvement to the HK alloy was reportedly found by modifying the cooling rate during casting to produce tubes which contained a mixed columnar (OD)/equiaxed (ID) grain structure [36]. However, as discussed in detail in Section 2.4.1, the exact relationship between the tube's grain size/shape distribution and mechanical properties (such as creep rupture life and ductility) remains relatively contentious. Machining of the tubes inner diameter was also introduced to reduce the possibility of crack initiation at the tube's inner surface as a result of the non-metallic inclusions which typically segregated to the tube's inner diameter during centrifugal casting.

In general, subsequent developments focused on the alloy's chemical composition. Based on the use of niobium within American stainless steel production, International Nickel Ltd. developed a modified HK alloy (named IN519) which incorporated niobium additions and an increased nickel content [9, 35, 36]. The addition of niobium, a strong carbide former, to Alloy IN519 (Table 2.1) resulted in a mixed primary carbide network containing alternating groups of Cr_7C_3 and NbC precipitates (with the NbC

partially replacing the Cr_7C_3) in the as-cast condition [9, 36]. This modification to the as-cast microstructure markedly increased the alloys creep rupture strength and creep ductility (Figure 2.4).

Continued demand for materials capable of withstanding increasingly more aggressive service conditions resulted in the development of the HP alloys series (Table 2.1) [7, 36]. As shown in Figure 2.4, the unmodified HP alloy's creep strength is similar to the unmodified HK alloy. Consequently, manufacturers immediately introduced niobium to the HP composition (0.5-1.5wt.%), yielding an alloy with greater creep strength than the IN519 alloy. The enhanced creep strength and carburization resistance led to the HP-Nb alloy becoming the industry standard for use in reforming furnaces [36]. However, coarsening of the primary and secondary $Cr_{23}C_6$ precipitates and the transformation of the primary NbC precipitates to G-phase ($Ni_{16}Nb_6Si_7$) [11-13] during service exposure raised concerns into the long-term effectiveness of niobium additions.

In an effort to increase the alloys microstructural stability and further increase the HP alloy's creep strength, manufacturers began to produce "micro-alloyed" HP compositions that contained various combinations of niobium, titanium, zirconium, tungsten, rare earths or other proprietary combinations of elements. The use of multiple alloying additions is largely based on the work carried out by Hou and Honeycombe in 1985 [9]. In addition to niobium, Hou and Honeycombe used small additions of titanium and zirconium to significantly increase the creep strength of the IN519 alloy. As shown in Figure 2.4, the use of micro-alloying additions further increased the HP alloys creep strength in comparison to the HP alloys containing sole additions of niobium. Although manufacturers often keep the exact combination of micro-alloying elements and the quantity of each element as closely guarded secrets, previous work conducted on micro-alloys have commonly reported the combined use of niobium (up to 1.5wt.%) and titanium (up to 0.1wt.%) [7, 14, 16, 22]. Typically, the HP-Micro alloy's increased creep strength has been attributed to the increased complexity of the precipitate networks and their increase stability during service exposure [14, 16].

While the use of single and multiple modifying elements has resulted in a notable increase in the HP alloy's creep strength during short-term accelerated creep testing, questions still remain about modified HP alloy's creep performance during long-term service exposure (100,000 hours). Section 2.4 below reviews in detail the previous work which has characterized the microstructural evolution within the current generation of modified HP alloys during exposure to elevated temperatures and the effect of this evolution has on each alloy's creep strength.

Table 2.1 – Chemical composition of selected heat resistant stainless steels. Balance Fe.

wt.%	C	Cr	Ni	Si	Mn	Reference
HT	0.35-0.75	13-17	33-37	2.5	-	[7]
HK	0.2-0.6	23-27	19-22	1.75	1	[7]
IN519	0.3-0.4	23-24	24-25	0.7-0.8	0.5-0.7	[9]
HP	0.35-0.75	24-28	33-37	1.5	1.5	[7]

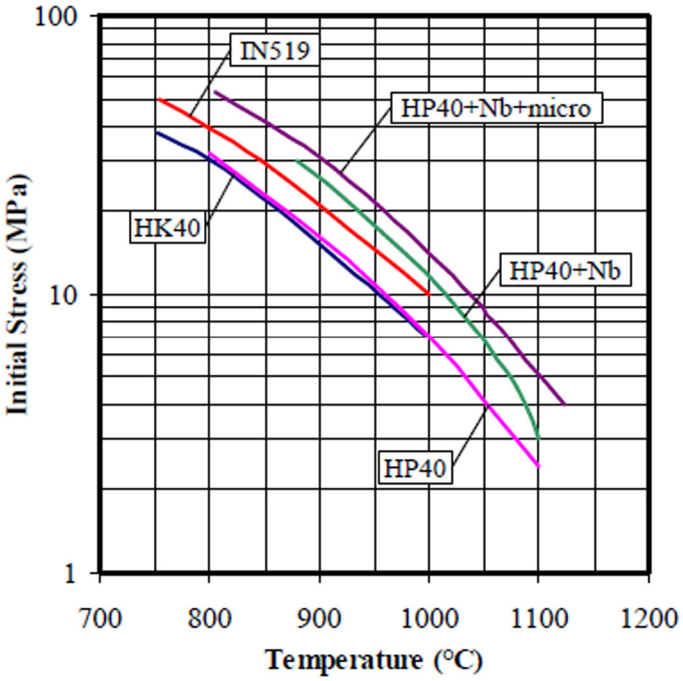

Figure 2.4 – Comparison of the 1000 hour rupture strength of several reformer tube alloy [2].

2.4 Metallurgy of Modified HK and HP Reformer Tubes

2.4.1 Macrostructure

Due to the centrifugal casting technique, the cross-section of the reformer tubes typically consists of small equiaxed (chill) grains (a), followed by columnar grains (b), and finally equiaxed grains (c) (Figure 2.5) [16, 37]. Except for the outer equiaxed grains, the proportion of columnar and inner equiaxed grains depends on the melt pouring temperature, mould material, and the rotational speed of the mould during pouring. Tube walls containing almost completely columnar grain structures can be produced if the cooling rate during casting is sufficiently high. As a result of centrifugal forces generated during casting, the comparatively lighter oxides or inclusions get segregated to the centre of the tube. These defects are subsequently removed by machining [16]. Thus, due to the consistent improvement in purity, creep properties and lower production cost, the centrifugal casting technique has become the industry standard for manufacture of reformer tubes.

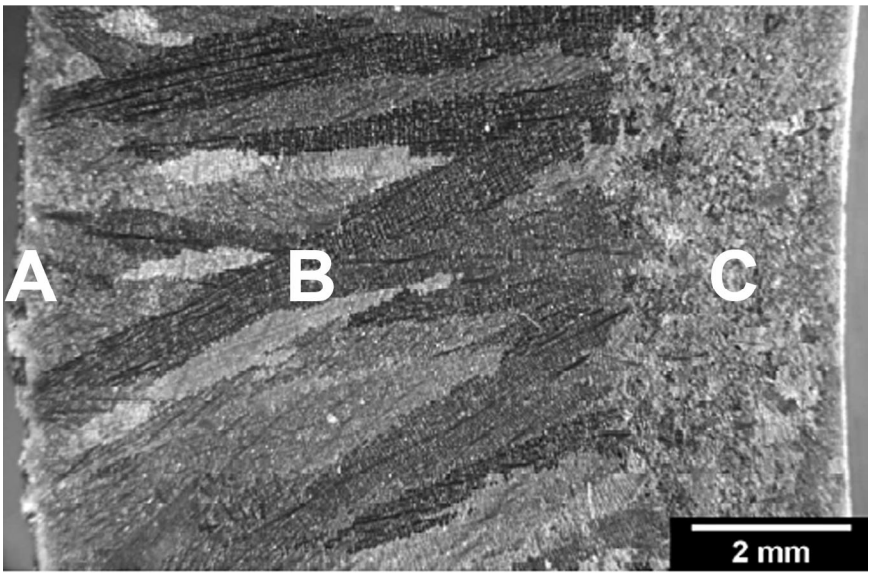

Figure 2.5 - Cross-section of a typical HP reformer tube macroscopic structure due to the Centrifugal casting method [2].

Although the centrifugal casting technique has become the industry standard for the tube's manufacture, the optimum columnar-equiaxed grain structure with respect to the tube's creep strength, in the published literature at least, remains relatively unclear. Many of the advancements in casting practice are known to be kept as industrial secrets [2]. Literature published by manufacturers specify that the inner diameter occupies a minimum of 30% equiaxed grains, stating that creep damage normally starts at the inner third section of the wall thickness [36]. Casting tubes with an equiaxed grain structure at the inner diameter reportedly increases the tube's resistance to creep crack propagation in comparison to tubes which contain completely columnar grain structures. However, little evidence was found in the literature to support this increased crack resistance at the tube's inner diameter.

Currently only a limited number of studies characterizing the effects of the grain structure on the HK and HP alloy's creep properties have been reported in the literature [23, 24, 37, 38]. These studies fall into two categories: i) controlled solidification studies followed by microstructural characterization and uni-axial accelerated creep testing [37, 38], ii) damage accumulation studies of ex-service tubes [23, 24]. Controlled solidification studies investigating the grain structure/creep properties relationship have focused solely on unmodified HK alloys. Zaghloul *et al.* [37] used graphite, cast iron and copper molds in combination with varying the rotational speed of the mold (between 1400-1700rpm) to modify the cooling rate during solidification. The columnar-equiaxed ratio, columnar grain size, refinement of the primary carbide network and carbide morphology was determined by the cooling rate during solidification. In general, the average size of the columnar grains and the proportion of the tube wall occupied by columnar grains increased with the cooling rate during casting. When performing uni-axial accelerated rupture testing at 950°C, the tube's rupture life was relatively unaffected by the cooling rate during casting suggesting that the rupture life was also independent of the grain structure. However, when conducting rupture testing at 1000 and 1100°C, the rupture life increased (~310% greater at 1000°C and ~30% greater at 1100°C) for tubes which experienced higher cooling rates during casting (804 versus 240°C/min).

While the tubes' grain size progressively increased with the cooling rate during casting, the volume fraction of the primary precipitates and average size of the secondary precipitates decreased (from 5-2.1% and 0.35-0.3µm respectively). Overall, the number of secondary precipitates increased with the cooling rate. The refinement of the secondary network would provide a superior dispersion strengthening effect and contribute to an improved rupture life. Hence, since the casting conditions

affect both the grain size/shape and precipitate distribution, it is inherently difficult to isolate the exact effect of grain size and shape on the creep properties of the precipitation hardened HK and HP alloys.

Wu *et al.* [38] similarly modified the HK alloy's grain structure within two separately cast tubes by using graphite (lower cooling rate) and cast iron (higher cooling rate) molds while keeping the molds rotational speed constant. In addition, a third tube was cast within a cast iron mold while also magnetically stirring the melt during solidification. All three tubes were subjected to uni-axial creep testing which was performed at 871 and 950°C over a range of stresses between 20-100MPa. Testing conducted on creep samples where the gauge length was populated with either 100% columnar (cast iron mold) or 100% equiaxed (graphite mold) grain structures indicated negligible difference in the rupture life when comparing each tube. However, magnetic stirring during solidification increased the third tube's rupture life by approximately 53%. This increase was partially attributed to the considerable refinement of the columnar and equiaxed grains as a result of magnetic stirring. However, in parallel to the refinement of the columnar and equiaxed grains, magnetic stirring also increased the volume fraction of primary precipitates by 2.6% within the columnar region and 2.3% within the equiaxed region of the tube. Consequently, the interdependence of the grain structure and precipitate distribution made it impossible to solely quantify the effects of the tube's grain structure on the creep properties.

Studies focusing on the accumulation of creep damage (e.g. creep voids) within service exposed HP alloy tubes (90,000 hours, 875-895°C, 2.65MPa internal pressure) indicated that the level of creep damage is lowest within the tube's equiaxed region [24]. Three dimensional reconstructions (through serial sectioning) of the columnar and equiaxed zones revealed the void density and accumulated volume was lowest at the tube's inner-wall (equiaxed) and highest at the outer-wall (columnar). However, due to the presence of through-wall temperature and stress gradients during service, the outer-wall was measured to be 20°C hotter while the hoop stress was calculated to be 1.9MPa lower at the outer-wall in comparison to the inner-wall. Therefore, the differences in the service conditions experienced by the tubes inner and outer diameter makes it difficult to directly compare the tolerance of columnar and equiaxed grains to creep damage. So far, similar three-dimensional reconstructions of ex-service tubes that have experienced similar service conditions and contained 100% columnar grain structures has not been completed. An observed increase or decrease in the void density at the inner diameter of service exposed reformer tubes with 100% columnar grain

structures in comparison to mixed columnar-equiaxed grain structures would allow for an understanding between the tube's grain distribution and creep life to be developed.

Obtaining a comprehensive understanding of the relationship between a tube's creep life and grain size/shape distribution is potentially impossible if the tube material is solely subjected to uni-axial accelerated creep testing. Currently, the tubes creep properties are largely determined through uni-axial accelerated creep testing of samples that are machined from the center of the tubes wall thickness [4, 9, 12, 35, 37, 38]. Therefore, it is impossible to produce tensile test samples that accurately represent tubes containing mixed grain structures. Moreover, even if it was possible to produce tensile creep samples containing representative grain structures, the complex stress state and non-uniform temperature distribution through the tubes wall thickness during service [2, 28] may negate the validity of performing uni-axial accelerated testing to predict the tubes in-service creep strength. Consequently, laboratory testing of pressurized tubes cast with varying combinations of columnar and equiaxed grain structures may be required in order to obtain a more representative test of the tubes actual creep strength. Such testing would possibly also allow for the stresses induced by through-wall temperature gradients to be simulated by flowing pressurized gas through the tube during testing. However, it must be noted that accurate measurement of the minimum creep rate, the shape of the creep curve and the creep ductility (standard measurements when performing uni-axial testing) is often prohibitively difficult when performing pressurized pipe testing. Since the current research was primarily concerned with the effects of differing alloying content and ageing conditions on the HP-Nb and HP-NbTi alloys' creep properties (which could be easily compared using uni-axial testing), pressurized pipe testing to investigate the relationship between the grain size/shape distribution and creep properties was outside the scope of the current project, but may be the subject of future research efforts in this area.

2.4.2 Microstructural Evolution of Niobium Modified HP Alloys

As-Cast Condition

Niobium is added to the HP composition to specifically modify the alloy's as-cast primary precipitate network. The rapid diffusion of chromium through the austenitic matrix (in comparison to vanadium,

niobium and titanium) reportedly causes the chromium-rich carbides to possibly be the least effective of the available carbides for strengthening high temperature stainless steels [37]. Niobium, being a stronger carbide former than chromium, causes the partial replacement of the as-cast chromium carbides with niobium carbides. Figure 2.6 (a) and (b) give representative optical and scanning electron micrographs of the HP-Nb alloy in the as-cast condition. The as-cast microstructure of these alloys is comprised of a typical austenite matrix with alternating groups of primary chromium (Cr_7C_3) and niobium (NbC) carbides located in the interdendritic positions. The chromium carbides appear dark grey while the niobium carbides appear white due to atomic number contrast in the backscatter electron image in Figure 2.6 (b). Generally, the matrix is believed to be free of precipitates based on observations of the as-cast microstructure at the magnifications in Figure 2.6 (a) and (b).

The relatively high cooling rates involved with the centrifugal casting technique causes the formation of the metastable Cr_7C_3 carbide, and results in the matrix being supersaturated with carbon [13]. However, $Cr_{23}C_6$ precipitates have been identified in statically cast HP-Nb alloys which contained niobium concentrations of greater than 1.97wt.% [12]. Note the chromium carbides (Cr_7C_3 and $Cr_{23}C_6$) typically contain small amounts of iron and nickel, and thus are often referred to as M_7C_3 and $M_{23}C_6$.

In addition to the replacement of the primary Cr_7C_3 with NbC, niobium additions have been shown to refine and fragment the primary carbide network [11-14]. The amount of replacement, refinement and fragmentation is a function of the niobium content. Accelerated testing showed that niobium-modified HP alloys have increased rupture life and lower minimum creep rates in comparison to the standard HP composition (i.e. without niobium) [12, 36]. The refinement and fragmentation of the primary precipitate network in the as-cast condition is reported to be partially responsible for the increased creep properties due to absence of a continuous crack propagation path along the precipitate/matrix interface [11-14]. The as-cast primary niobium carbides obtain a lamellar or "Chinese-script" morphology (identical to the NbC precipitates in the niobium modified HK alloy) [9, 11-14]. The lamellar NbC precipitates in the HK-Nb alloy have been shown to obtain a cube-cube (i.e. $[100]_{NbC}//[100]_{\gamma}$) orientation relationship (OR) with the matrix [9]. While the lamellar NbC precipitates in the HP-Nb alloys likely obtain the same OR, analysis of this OR (such as EBSD) has not been published in the literature.

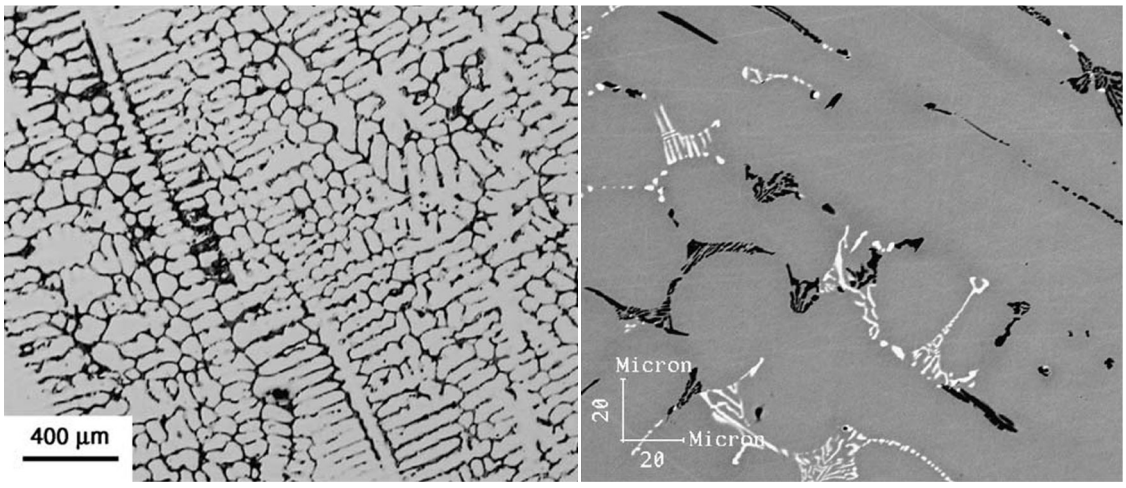

(a) **(b)**

Figure 2.6 – (a) Optical and (b) backscatter electron micrographs showing the as-cast HP-Nb primary carbide network [14].

Microstructural Evolution during Short-Term Ageing (<1000 hours)

Figure 2.7 (a) and (b) show optical and scanning electron micrographs of the HP-Nb alloy after exposure to 900°C for 1000 hours. Ageing the HP-Nb alloy at temperatures above 700°C causes the primary network of Cr_7C_3 to transform to the more stable $Cr_{23}C_6$ carbide and the formation of fine distributions of secondary $Cr_{23}C_6$ carbides within the austenite matrix. NbC precipitates similar in size to the $Cr_{23}C_6$ have also been reported within the secondary precipitate distribution [11, 12]. However, the number of NbC precipitates is typically insignificant in comparison to the $Cr_{23}C_6$. In total, the number of secondary precipitates is reportedly lower in the HP-Nb alloy in comparison to the standard HP alloy. The formation of the primary niobium carbides in the HP-Nb alloy reportedly increases the carbon consumption during solidification, resulting in a lower percentage of carbon being held in solution within the solidified austenite matrix [12].

The $Cr_{23}C_6$ and NbC secondary carbides are mainly concentrated near the primary network of grain boundary and interdendritic carbides. This non-uniform distribution of secondary carbides is believed to be due to the high dislocation densities located in these regions of the as-cast matrix, which provide ample heterogeneous nucleation sites [12, 37]. In service, the secondary precipitates vicinal to the grain boundary are believed to inhibit the creep deformation that is typically concentrated in this area [16].

The secondary $Cr_{23}C_6$ typically obtain a cuboidal morphology and share a cube-cube ($[100]_{Cr23C6}//[100]_{\gamma}$) OR with the austenite matrix [9, 14]. Less commonly, the secondary $Cr_{23}C_6$ precipitates obtain a Widmanstätten morphology (needle-like shape). The Widmanstätten morphology is reportedly induced when the alloy has an excess chromium concentration with respect to carbon in solid solution [11, 12]. However, the exact chromium and carbon ratio which causes the formation of this morphology is relatively unclear for the HP-Nb alloys as the ratio is influenced by the niobium content.

Ageing between 700-1000°C (depending on silicon and niobium content) causes the transformation of the primary and secondary niobium carbide precipitates to a nickel-niobium-silicon rich intermetallic. The composition of this face centered cubic (FCC) intermetallic has been reported in the literature as $Ni_{16}Nb_6Si_7$ and is more commonly known as G-phase [11-14]. Typically, the transformation is complete after 1000 hours and the G-phase retains the prior lamellar morphology. Ageing for longer than 1000 hours causes growth of the G-phase and eventual loss of the lamellar morphology.

The transformation from NbC to G-phase is thought to occur by carbon being rejected from and diffusion of nickel and silicon to the existing NbC precipitate [11-14]. Thus, the transformation rate is heavily dependent on the temperature at which the sample is aged and also the relative contents of silicon, niobium, and nickel. Increasing the silicon content increases the transformation rate for a given temperature, and the temperature range over which the G-phase transformation occurs [13]. The transformation rate also increases with the nickel and niobium content although the effect of these elements is much less pronounced than that of silicon. $Cr_{23}C_6$ is often found in close association with the G-phase and is believed to form a direct result of carbon's rejection from the transforming NbC to the surrounding chromium-saturated matrix [12, 13]. The converse has also been observed, with the formation of secondary G-phase being found at the $Cr_{23}C_6$/matrix interface [12, 14].

Based on the 1000 hour ageing limit and regardless of silicon and niobium contents, the transformation to G-phase has not been seen when ageing above 1100°C [11-13]. Instead the primary chromium and niobium carbides experience growth. The formation of sigma or ferrite phases have not been seen in any HP-Nb or HK-Nb alloy studied at any temperature for the ageing periods discussed here [8-14].

Regardless of the ageing temperature, the primary chromium carbide and secondary matrix precipitates are thought to coarsen to a lesser extent during ageing due to the addition of niobium [11-13]. This lower coarsening rate is thought to be due to the lower carbon content in solution caused as a result of the niobium and also the precipitation of chromium carbides at the G-phase/matrix interface.

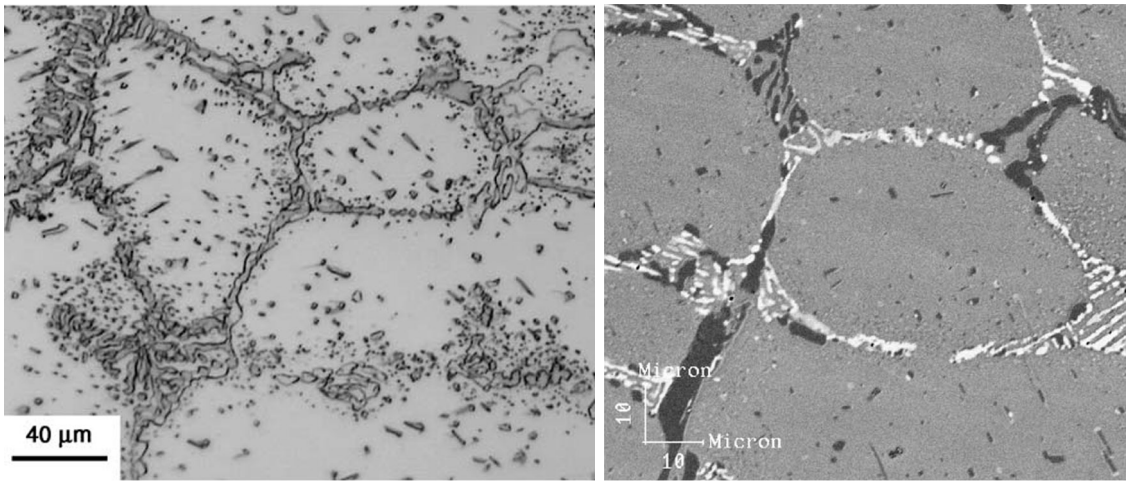

(a) **(b)**

Figure 2.7 – HP-Nb alloy after ageing at 900°C for 1000 hours (a) optical image (b) scanning electron micrograph using backscatter electrons [14].

Microstructural Evolution during Prolonged Ageing and Service Exposure

Currently, studies into the effects of long-term ageing on HP reformer tubes have largely involved analysing samples of material removed from service. Typically, the sample material is taken from tubes that have not failed in service and were removed as a result of excessive creep strain being identified during a scheduled plant shutdown [4, 25]. Previous work by Nishimoto *et al.* [22] characterized the HP-Nb alloy's microstructural evolution during long-term (10,000 hours) laboratory ageing at 1050°C. However, as the phase transformations that occur within the HP-Nb alloy during thermal exposure are strongly dependent on the ageing temperature, considerable further work is necessary to determine the HP-Nb alloy's microstructural evolution with respect to ageing temperature and time.

In general, the microstructural evolution during long-term thermal exposure involves the coalescence of the initially fragmented primary carbide network and depletion of the secondary

precipitates. The study of a HP-Nb (1.54 wt.% Nb) alloy in service for 105,000 hours at temperatures between 927-1066°C showed a matrix completely free of precipitates and an almost continuous primary precipitate network [25]. The depletion, coarsening and coalescence of the primary precipitates results in a significant reduction in the material's creep performance due to the increased likelihood of continuous crack propagation path at the precipitate/matrix interface [9, 11-14, 37].

The phases present in the HP-Nb alloy after long-term service exposure are subject to significant variance, with chromium carbide ($Cr_{23}C_6$) being the only typical phase present [4, 22, 25]. Generally, the variance is associated with the primary NbC precipitates which transform to silicon or nitrogen rich phases. The primary networks of two ex-service tubes subjected to 1100°C for 26,277 hours [22] and 927-1066°C for 105,000 hours [25] were comprised of chromium carbides ($Cr_{23}C_6$), an unidentified niobium-rich phase (which was considered to be a niobium carbo-nitride), and the silicon-rich η-phase [25]. The η-phase was also identified in a HP-Nb alloy after laboratory ageing the HP-Nb alloy at 1050°C for 10,000 hours [22]. Typically, the η-phase precipitates were found to be silicon-rich and carbon-lean indicating it is not the M_6C precipitate commonly reported in other stainless steel alloys [39, 40]. Furthermore, the Cr/Ni ratio of the phase was found to be appreciably higher in comparison to those reported for G-phase [11-13, 25]. The η-phase crystal structure was reported as diamond cubic; as opposed to G-phase's superlattice face centered cubic structure [9, 11-14]. The η-phase also differed from sigma phase due to η-phases' enrichment of nickel and silicon.

Studies of a HP-Nb alloy in service for 70,000 hours at ~920°C [4] showed that few coarse secondary precipitates remained within the austenite matrix while considerable coalescence of the primary carbide network had occurred. Similar to the previous studies, the primary NbC precipitates had participated in multiple unique phase transformations. Most commonly, a silicide having the η-phase crystal structure was identified followed by a nitride commonly known as Z-phase (NbCrN) which had a tetragonal unit cell (a=b=0.303nm, c=0.735nm). TEM observations of the secondary matrix precipitates also revealed precipitates which obtained a rhombohedral structure and were referred to as R-phase (a=b=1.09nm, c=1.93nm, α=β=γ=74°). The R-phase precipitates were high in niobium, chromium and nickel, but low in iron and silicon. Due to the low presence of the R-phase precipitates they were not able to be identified by X-ray diffraction.

In general, the niobium contents within ex-service HP-Nb alloys [4, 22, 25] were similar to the compositions of the material used to study the effects of short-term ageing [11-14]. As previously discussed, the only reported precipitate phases after ageing for 1000 hours at temperatures between 700-1100°C were $Cr_{23}C_6$, NbC and G-phase. In contrast, prolonged service exposure resulted in HP-Nb alloys containing a combination of $Cr_{23}C_6$, η-phase, Z-phase, and R-phase. Since the η, Z, and R phases were only present after such long ageing periods, the slow nucleation/growth kinetics of these phases make it unlikely that these phases will form in the time frame of accelerated creep tests (typically ~1000-2000 hours). Consequently, their absence in accelerated creep tests immediately casts doubt on the validity of the creep properties generated using this method of testing.

2.4.3 Microstructural Evolution of Niobium and Titanium Modified HP Alloys (HP-Micro)

As-Cast Condition

Combined additions of niobium and titanium have been used to further increase the HP alloy's creep resistance. HP alloys modified with multiple additions of alloying elements such and Nb and Ti are commonly referred to in industry as HP-Micro alloys. However, for the purposes of this thesis the alloy will be referred to as HP-NbTi since the -Micro designation has also been applied to alloys with additional elements such as zirconium. Much like the niobium-modified alloy, the HP-NbTi alloy's as-cast primary carbide network (Figure 2.8 (b)) is comprised of chromium carbide (dark grey) and the MC carbide (white), where the M represents the combination of titanium and niobium. Interestingly, the chromium-rich primary carbides in separately cast HP-NbTi alloys have been reported to solely obtain either the Cr_7C_3 (orthorhombic) crystal structure [22] or the $Cr_{23}C_6$ (FCC) crystal structure [14].

The addition of titanium is believed to cause further fragmentation of the primary carbide network (see Figure 2.8 (a)) [14, 16]. The addition of titanium to the niobium-rich primary carbides causes the precipitates to obtain a large blocky morphology (as opposed to the lamellar morphology in the HP-Nb alloy). This change in the MC morphology is not well documented for the HP series, but in the Nb-Ti modified HK series it has been attributed to the more complex composition of the carbide, which causes a higher interfacial energy between the MC carbide and austenite matrix. The interfacial area

of the precipitate is reduced by obtaining the blocky morphology, thus minimizing the energy associated with the precipitate [8, 9]. At the magnification given in Figure 2.8 (b), the austenite matrix appears to be is relatively free of precipitates. However, titanium carbide precipitates have been reported within the as-cast HP-NbTi alloy's austenite matrix [16].

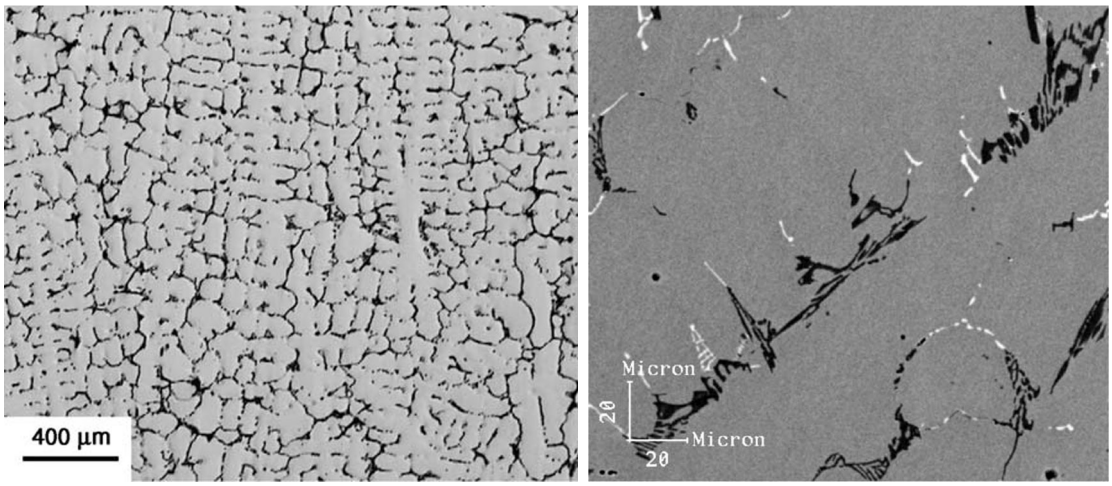

(a) **(b)**

Figure 2.8 – Representative (a) optical and (b) backscatter electron micrographs, showing the as-cast condition in the HP-NbTi alloy [14].

Microstructural Evolution during Short-Term Ageing (<1000 hours)

The transformation of the primary precipitates from Cr_7C_3 to $Cr_{23}C_6$ and secondary precipitation of $Cr_{23}C_6$ that occurred in the HP-Nb alloy also occurs when using dual additions of niobium and titanium. The secondary $Cr_{23}C_6$ typically obtain a cuboidal morphology and share a cube-cube OR with the austenite matrix. In addition to niobium-titanium rich secondary precipitation, the formation of fine titanium carbides on stacking faults and dislocations near the grain boundaries has been reported in HK-NbTi and HP-NbTi alloys [9, 14, 16]. Identical to the HP-Nb alloy, the secondary precipitates are predominantly confined to the matrix directly adjacent to the primary precipitates. During prolonged ageing, the TiC which has precipitated on stacking faults is thought to coarsen at a slower rate in comparison to the secondary $Cr_{23}C_6$ [9].

The combination of $Cr_{23}C_6$, (NbTi)C and TiC secondary precipitates is reported to cause the secondary precipitate distribution in the HP-NbTi alloy to be “finer” and “more evenly distributed” than the HP-Nb secondary precipitate distribution (Figure 2.9 (a) and (b)) [14, 16]. The finer distribution of carbides in the HP-NbTi alloy is thought to provide an increased dispersion strengthening effect, thus increasing the alloys’ creep resistance [14, 16]. However, the reported increased refinement and stability of the secondary carbides in the HP-NbTi alloy is often not obvious and requires statistical confirmation.

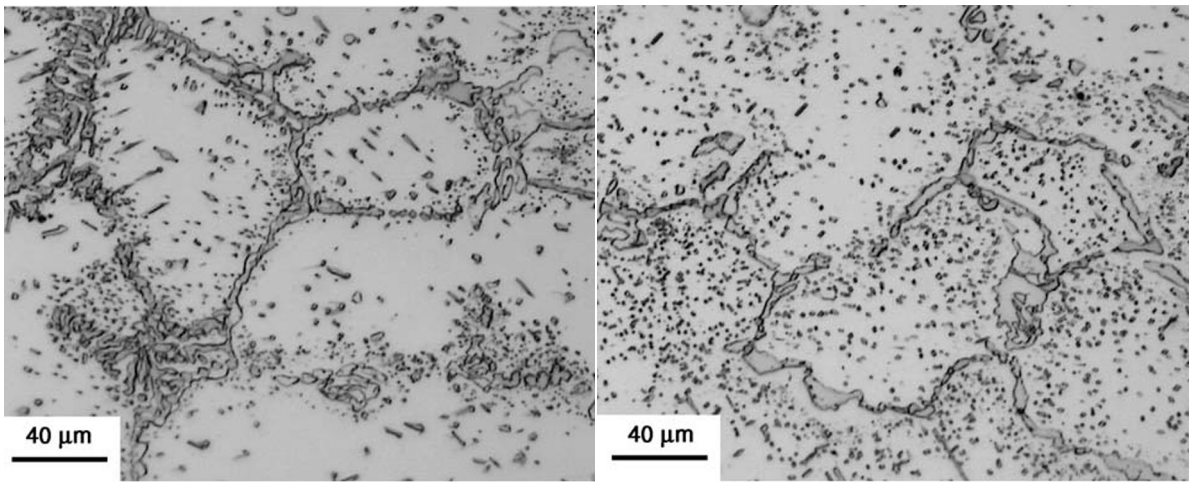

(a) **(b)**

Figure 2.9 – Optical Micrographs showing (a) HP-Nb alloy after 1000 hours at 900°C and (b) the HP-NbTi alloy after 1000 hours at 900°C [14].

The transformation of the MC carbide to G-phase has been reported when ageing the HP-NbTi alloy at 900°C for 1000 hours, but at a much reduced rate in comparison to the NbC-to-G-phase transformation in the HP-Nb alloy [14]. This decreased transformation rate was believed to be due to the insolubility of titanium in G-phase. Therefore, titanium along with carbon must diffuse from the G-phase particle for the transformation to occur. To illustrate this, TiC particles have been found in the centre of transforming precipitates (see Figure 2.10 (b)). After similar periods of ageing time, the transformation reaches completion in the HP-Nb alloy but not in the HP-NbTi alloy [14]. The MC-to-G-phase transformation was not observed after ageing the HP-NbTi alloy at 1000°C for 1000 hours [16]. The improved creep resistance of the HP-NbTi alloy in comparison to the HP-Nb alloy when performing accelerated creep testing has been attributed to the partial transformation of G-phase in combination with the less continuous nature of the primary precipitate network [14, 16].

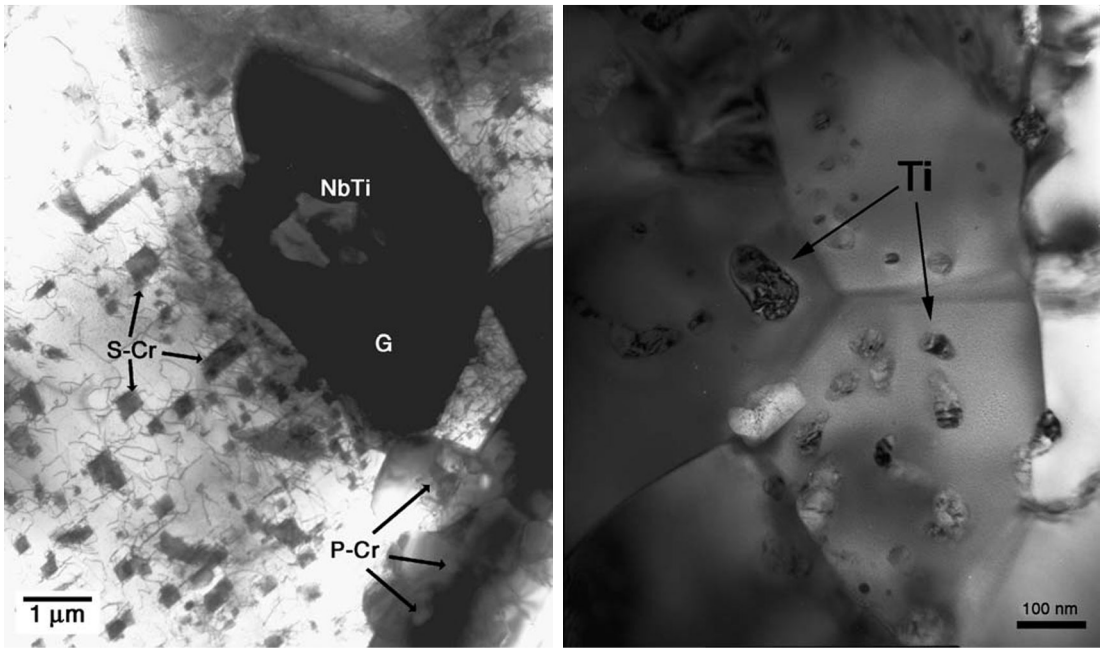

Figure 2.10 – (a) & (b) Transmission electron bright field micrographs showing the presence of the MC carbide and Ti rich particles within a primary (NbTi)C precipitate which has partially transformed to G-phase [14].

Microstructural Evolution during Prolonged Ageing and Service Exposure

Similar to the HP-Nb alloys, the relatively few studies which have characterized the effects of long-term ageing on the HP-NbTi alloy's microstructure have mainly focused on reformer tubes that were retired from service [22, 23, 24, 41]. While previous work by Nishimoto *et al.* [22] characterized the HP-NbTi alloy after laboratory ageing at 1050°C for 10,000 hours, further laboratory ageing of the HP-NbTi alloy at temperatures between 900°C to 1100°C is necessary as the phase transformations that occur in the HP-NbTi alloy during ageing are strongly dependent on the ageing temperature.

Generally, the effects of ageing the HP-NbTi alloy for periods greater than 1000 hours is even less clear than for the HP-Nb alloy. Similar to the HP-Nb alloy, the $Cr_{23}C_6$ precipitates remained stable within ex-service HP-NbTi tubes regardless of the ageing temperature, but underwent coarsening. The MC precipitates also remained stable during service at temperatures between 875 to 895°C for 90,000 hours [23, 24]. However, the MC-to-η-phase transformation was identified after laboratory ageing of a HP-NbTi alloy at 1050°C for 10,000 hours [22]. Studies of the HK alloy modified with additions of niobium and titanium found that the primary carbide network in the HK-NbTi alloy experience growth similar to the HK-Nb alloy, but at a reduced rate [9]. The coalescence of the HK-

NbTi alloy's primary carbide network was reduced compared to the HK-Nb alloy, but the increased as-cast fragmentation of the HK-NbTi carbide network is thought to be partially responsible for this difference. The secondary TiC within the HK-NbTi alloy's matrix also coarsened at a lesser rate during ageing in comparison to the $Cr_{23}C_6$, which was believed to possibly be due to the nucleation of the TiC precipitates on stacking faults and lower diffusion rate of titanium through the austenitic matrix (in comparison to chromium).

2.4.4 Creep Properties of the HP-Nb and HP-NbTi Alloys after Ageing

As shown in Figure 2.4, the creep properties of the HP-Nb alloy are generally greater than that of the plain HP alloy. The creep properties are even further improved in the HP-NbTi alloy (based on accelerated creep testing). This trend is also generally true after ageing both modified HK and HP alloys for up to 3000 hours at temperatures between 700-1200°C [7, 9, 13, 36]. Testing of the HP-Nb alloy after ageing at temperatures between 700-1100°C for 1000 hours generally showed increased creep properties over the as-cast condition [13]. Considering the resulting fragmented primary grain boundary carbides and fine dispersion of secondary matrix carbides present in the HP-Nb alloy after ageing for 1000 hours, an increase in properties is unsurprising. However, prolonged ageing should cause the growth and coalescence of the primary network, depletion and coarsening of the secondary precipitates, coupled with other more sluggish phase transformations, possibly leading to a significant loss of material properties.

The effect of G-phase on HP-Nb and HP-NbTi alloys' creep properties is not well known in the literature. HK-Nb alloy tubes surviving 60,000 hours of service without failure and having G-phase present have been documented [10] suggesting G-phase is not necessarily detrimental to the alloy's creep properties. Accelerated creep tests on aged HP-Nb samples with G-phase present have also shown increased creep properties in comparison to those aged above the upper limit of G-phase formation [12]. However, other studies conducted on the HP-NbTi alloy [14, 15] have suggested that there is a volume expansion associated with the transformation to G-phase causing an increased interfacial energy between the matrix and precipitate which could cause creep damage to preferentially occur at this interface.

Whether the η, Z, and R phases are beneficial or detrimental to the HP-Nb and HP-NbTi alloys' high temperature properties is unknown. These phases were observed exclusively in ex-service HP-Nb [4] and HP-NbTi [41] material. The long service life of HP-Nb and HP-NbTi tubes without failure could indicate the η, Z, and phases are not necessarily detrimental [4, 41]. However, as discussed in Chapter 1, many furnaces are operated below their maximum design conditions giving an additional safety factor. Thus, any negative effect of the η, Z, and R phases may be offset by this safety factor. Accelerated creep testing of ex-service HP-Nb tubes [4] has shown a significant reduction in alloy's creep resistance, with no evidence of creep damage present (in the form of voids). Although it is difficult to separate the effects of service induced creep damage and microstructural evolution on alloy's remaining creep life, the reduction was believed to be above that which could be credited to the creep damage that occurred during service.

Overall, the difference between the short and long term microstructures and creep properties for the HP-NbTi alloy appears to be less significant in comparison to the HP-Nb alloy. However, considering the typical design life of HP-Nb and HP-NbTi alloy tubes is approximately 100,000 hours, the effects of microstructural ageing on both alloys' long-term creep properties could potentially lead to disastrous tube life predications if the alloys' creep life continues to be predicted largely from the properties measured during short-term accelerated testing. Increasing the maximum design stress and/or temperature for new tubes to take advantage of the improved short-term creep properties offered by the HP-Nb and HP-NbTi alloys could also lead to similar unexpected failures due to the absence of the more sluggish η, Z, and R phase transformations during accelerated testing. Moreover, life extension programs which allow reformer tubes to remain in service without considering the effects of these more sluggish phase transformations will potentially increase the risk of unexpected tube failures during the subsequent service period. Hence, until significant further research has been conducted to determine the relationship between the HP-Nb and HP-NbTi alloys' long-term microstructural evolution and creep properties, a high level of conservatism is necessary when extrapolating the short-term properties to predict each alloy's long-term creep life.

Chapter References

[1] Wu, X. Q., Yang, Y. S., Zhan, Q. & Hu, Z. Q. (1998). *Structure Degradation of 25Cr35Ni Heat Resistant Tube Associated with Surface Coking and Internal Carburization.* Journal of Materials Engineering and Performance, 7(5): pp. 667-672.

[2] Wahab, A. A. (2007). *Three-Dimensional Analysis of Creep Void Formation in Steam-Methane Reformer Tubes.* Unpublished doctoral dissertation, University of Canterbury, Christchurch, New Zealand.

[3] Jakobi, D., Karduck, P. & von Richthofen, A. (2010). *Superior Spun Cast Material for Steam Reformer Furnaces: Alloy Centralloy® 4852 Micro R.* Ammonia Technical Manual, 51: pp. 65-76.

[4] Thomas, C. W., Stevens, K. J. & Ryan, M. J. (1996). *Microstructure and properties of alloy HP50-Nb: comparison of as cast and service exposed materials.* Materials Science and Technology, 12: pp. 469-475.

[5] American Petroleum Institute. (2003). *Calculation of Heater Tube Thickness in Petroleum Refineries.* API 530, 5th Edition, ISO 13704:2001 (E).

[6] Knowles, D., Buchanan, K. & Kral, M. (2009). *Condition Assessment Strategies in Centrifugally Cast HP Steam Reformer Tube Alloys.* Proceedings of the 2nd International ECCC Conference: Creep & Fracture in High Temperature Components – Design & Life Assessment, Dübendorf, Switzerland.

[7] Davis, J. R. (Ed.). (1997). *ASM Specialty Handbook: Heat-Resistant Materials.* Materials Park, Ohio: ASM International, pp. 200-218.

[8] Shinoda, T., Zaghloul, M. B, Kondo, Y. & Tanaka, R. (1978). *The Effect of Single and Combined Additions of Ti and Nb on the Structure and Strength of the Centrifugally Cast HK40 Steel.* Transactions of the Iron and Steel Institute of Japan, 18: pp. 139-148.

[9] Hou, W. T. & Honeycombe, R. W. K. (1985). *Structure of Centrifugally cast austenitic steels: Part 2 Effects of Nb, Ti and Zr.* Materials Science and Technology, 1(5): pp. 390-397.

[10] Barbabela, G. D., de Almeida, L. H., da Silveira, T. L., Le May, I. (1991). *Phase Characterization in Two Centrifugally Cast HK Stainless Steel Tubes.* Materials Characterization, 26: pp. 1-7.

[11] Barbabela, G. D., de Almeida, L. H., da Silveira, T. L & Le May, I. (1991). *Role of Nb in Modifying the Microstructure of Heat-Resistant Cast HP Steel.* Materials Characterization, 26:pp. 193-197.

[12] de Almeida Soares, G. D., de Almeida, L. H., da Silveira, T. L. & Le May, I. (1992). *Niobium Additions in HP Heat-Resistant Cast Stainless Steels.* Materials Characterization, 29: pp. 387-396.

[13] Ibañez, R. A. P., Soares, G. D. A., de Almeida, L. H. & Le May, I. (1993). *Effects of Si Content on the Microstructure of Modified-HP Austenitic Steels.* Materials Characterization, 30: pp. 243-249.

[14] de Almeida, L. H., Ribeiro, A. F. & Le May, I. (2003). *Microstructural Characterization of modified 25Cr-35Ni centrifugally cast steel furnace tubes.* Materials Characterization, 49: pp. 219-229.

[15] Ribeiro, A. F., Borges, R. M. T. & de Almeida, L. H. (2002). *Phase Transformation in Heat Resistant Steels Observed by Stem. (NbTi)C – NiNbSi (G-phase).* Acta Microscopica, 11(1): pp. 59-63.

[16] Caballero, F. G., Imizcoz, P., Lopez, V., Alvarez, L. F. & Garcia de Andrés, C. (2007). *Use of titanium and zirconium in centrifugally cast heat resistant steel.* Materials Science and Technology, 23: pp. 528-534.

[17] Nunes, F. C., Dille, J., Delplancke J. -L & de Almeida, L. H. (2006). *Yttrium addition to heat-resistant cast stainless steel.* Scripta Materialia, 54: pp. 1553-1556.

[18] Nunes. F. C., de Almeida, L. H., Dille, J., Delplancke, J. -L., Le May, I. (2007). *Microstructural Changes caused by yttrium addition to NbTi-modified centrifugally cast HP-type stainless steels.* Materials Characterization, 58: pp. 132-142.

[19] Ribeiro, A. F., de Almeida, L. H., dos Santos, D. S., Fruchart, D. & Bobrovnitchii, G. S. (2003). *Microstructural modifications induced by hydrogen in a heat resistant steel type HP-45 with Nb and Ti additions.* Journal of Alloys and Compounds, 356-357: pp. 693-696.

[20] Laigo, J., Christien, F., Le Gall, R., Tancret, F. & Furtado, J. (2008). *SEM, EDS, EPMA-WDS and EBSD characterization of carbides in HP type heat resistant alloys.* Materials Characterization, 59: pp. 1580-1586.

[21] Voicu, R., Andrieu, E., Poquillon, D., Furtado, J. & Lacaze, J. (2009). *Microstructure evolution of HP40-Nb alloys during aging under air at 1000°C.* Materials Characterization, 60: pp. 1020-1027.

[22] Nishimoto, K., Saida, K., Inui, M. & Takahashi, M. (2001). *Changes in microstructure of HP-modified, heat-resisting cast alloys under long-term aging. Repair weld craking of service exposed, HP-modified, heat-resisting cast alloys (2nd report).* Welding International, 15(7): pp. 1-9.

[23] Wahab, A. A. & Kral, M. V. (2005). *3D analysis of creep voids in hydrogen reformer tubes.* Materials Science & Engineering A, 412: pp. 222-229.

[24] Wahab, A. A., Hutchinson, C. R. & Kral, M. V. (2006). *A three-dimensional characterization of creep void formation in hydrogen reformer tube.* Scripta Materialia, 55: pp. 69-73.

[25] Kenik, E. A., Maziasz, P. J., Swindeman, R. W., Cervenka, J. (2003). *Structure and phase stability in a cast modified-HP austenite after long-term ageing.* Scripta Materialia, 49: pp. 117-122.

[26] *Making Methanol* [Image]. Retrieved January 2013, from http://www.methanex.com/education/english/main.html

[27] Thomas, C. W. (2007). *Factors influencing life of reformer furnace tubes.* Materials at High Temperatures, 24(3): pp. 233-240.

[28] Thomas, C. W., Tack, A. J. & Briggs, N. (1997). *Stress relaxation properties of alloy HP50Nb and their application to life assessment of reformer furnace tubing.* International Journal of Pressure Vessels and Piping, 70: pp. 59-68.

[29] Walter, M., Schlichthärle, G. (1998). *Stress Analysis for Improving Primary Reformer Performance*. Ammonia Technical Manual, 38: pp. 90-103.

[30] Muvdi, B. B. & McNabb, J. W. (1991). *Engineering Mechanics of Materials.* 3rd Edition. New York: Springer-Verlag.

[31] Swaminathan, J., Guguloth, K., Manojkumar, G., Roy, P. & Ghosh, R. (2008). *Failure analysis and remaining life assessment of service exposed primary reformer heater tubes.* Engineering Failure Analysis, 15: pp. 311-331.

[32] Alvino, A., Daniela, L., Giacobbe, F., Mazzocchi, V. & Rinaldi, A. (2010). *Damage characterization in two reformer heater tubes after nearly 10 years of service at different operative and maintenance conditions.* Engineering Failure Analysis, 17: pp. 1526-1541.

[33] Rani, B. (2006). *Catastrophic Failure of Reformer Tubes at Courtright Ammonia Plant.* Ammonia Technical Manual, 47: pp. 187-196.

[34] American Society for Testing and Materials. (2012). *Standard Specification for Centrifugally Cast Iron-Chromium-Nickel High-Alloy Tubing for Pressure Application at High Temperatures.* ASTM A608/A608M-12.

[35] Hou, W. T. & Honeycombe, R. W. K. (1985). *Structure of Centrifugally cast austenitic steels: Part 1. HK 40 as cast and after creep between 250 and 1000 degree C.* Materials Science and Technology, 1(5): pp. 385-389.

[36] Kirchheiner, R. & Woelpert, P. (2001). *Niobium in centrifugally cast tubes for petrochemical applications.* Proceedings of the International Symposium Niobium, Orlando, U.S.A.

[37] Zaghloul, M. B., Shinoda, T. & Tanaka, R. (1977). *Relation between Structure and Creep Rupture Strength of Centrifugally Cast HK40 Steel.* Transactions of the Iron and Steel Institute of Japan, 17(1): pp. 28-36.

[38] Wu, X. Q., Jing, Y. G., Zheng, Z. M., Yao, W. Ke. & Hu, Z. Q. (2000). *The eutectic carbides and rupture strength of 25Cr20Ni heat-resistant steel tubes centrifugally cast with different solidification conditions.* Materials Science and Engineering A, 293: pp. 252-260.

[39] Powell, D. J., Pilkington, R. & Miller, D. A. (1988). *Precipitation characteristics of 20%Cr/25%Ni-Nb stabilised stainless steel.* Acta Metallurgica, 36(3): pp. 713-724.

[40] Sourmail, T. (2001). *Precipitation in creep resistant austenitic stainless steels.* Materials Science and Technology, 17: pp. 1-14.

[41] Berghof-Hasselbacher, E., Gawenda, P., Schorr, M. & Schutze, M. (2008). *Atlas of Microstructures.* St. Lous: Materials Technology Institute.

Chapter 3 Metallographic Sample Preparation for Macro- and Micro-analysis of the HP alloys

In order to characterize the microstructural evolution of HP alloys during long-term isothermal ageing, numerous samples had to be prepared for optical, scanning electron and transmission electron microscope analysis. In general, the HP alloy can be polished to an acceptable surface finish for optical microscopy without the need for any significant prior experience with austenitic alloys. However, preparation of high quality samples for higher resolution techniques such as field emission scanning electron microscopy without prior experience or guidance can be very arduous and often frustrating. This difficulty is largely due to the significant surface deformation that occurs within the austenite matrix during mechanical polishing of the HP alloys with silicon carbide paper and diamond pastes. This deformation results in an unsightly polished section which often obscures the alloy's microstructure. Removal of this deformation during the final polishing stage was typically difficult and time consuming and extensive experimentation with the preparation procedure was necessary to determine a method which consistently yielded an acceptable surface finish.

Fortunately, the methodology for the preparation of thin foils from the HP alloy for transmission electron microscopy has been well documented in previous studies [1-4]. However, a trial and error approach was still necessary to determine the electropolishing and ion milling parameters which produced defect-free foils with large electron transparent regions. Slight divergence from the ideal voltage and electrolyte temperature during electropolishing or too aggressive ion milling conditions (e.g. high accelerating voltages) would induce significant pitting of the foil and led to a reduction in the total electron transparent area thus increasing the difficulty to obtain and subsequently analyze specific precipitates within the foil's thin area.

The following chapter has been written to provide guidance for the future preparation of the HP alloys for metallurgical analysis. Focus has been placed on the most successful sample preparation techniques that were determined for the HP-Nb and HP-NbTi alloys when performing light optical microscopy (LOM), scanning electron microscopy (SEM), electron backscatter diffraction (EBSD), X-ray diffraction (XRD) and transmission electron microscopy (TEM). The standard operating conditions for each of the aforementioned analysis techniques have also been briefly summarized.

3.1 Sample Preparation for Optical and Scanning Electron Microscopy

Figure 3.1 gives a schematic outlining the experimental procedure used to prepare all metallographic samples that were subjected to optical and scanning electron microscopy. In total, 35 individual HP-Nb and HP-NbTi samples were prepared for metallurgical analysis. While same process was implemented for each when cutting, mounting, grinding and polishing up to a 1µm surface finish, the final polish differed depending on the purpose of the subsequent analysis. Cutting and mounting of each sample was only performed once. However, each sample underwent many grinding, polishing and etching cycles in order to optimize the final surface finish specifically for the subsequent analysis technique. Sections 3.1.1 - 3.1.3 outline the most successful methods used in the current research to prepare metallographic samples for light optical microscopy (LOM), high resolution scanning electron microscopy (HR-SEM), electron backscatter diffraction (EBSD) and energy dispersive X-ray spectroscopy (EDS).

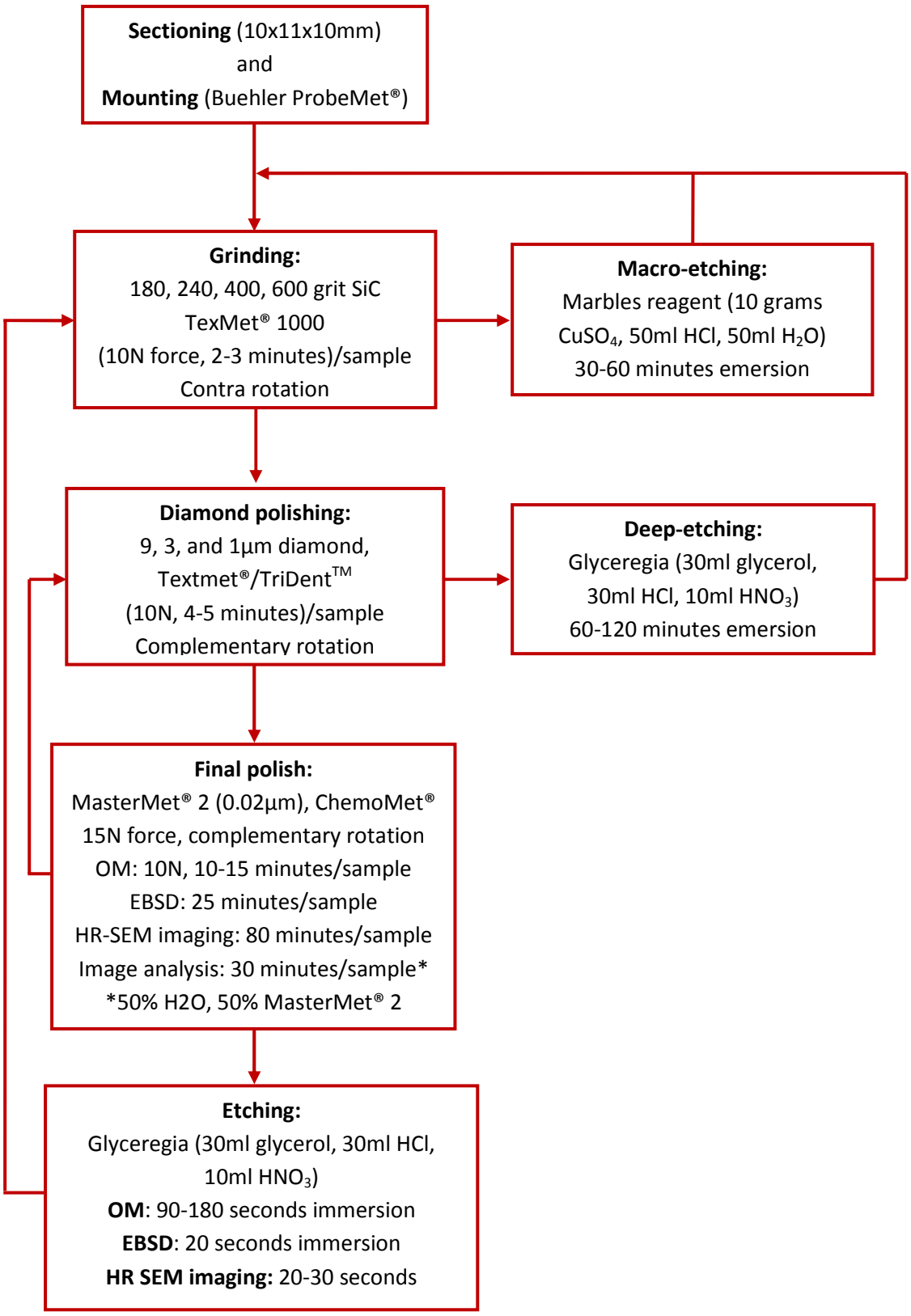

Figure 3.1 – Schematic of the preparation procedure used to prepare samples for optical and scanning electron microscopy.

3.1.1 Cutting, Mounting, Grinding and Polishing to a 1µm Surface Finish

Initially, blocks approximately 10 x 11 x 10mm (arc-length x tube wall thickness x depth) were cut from the as-cast and aged tube segments using a Buehler[1] Delta™ AbrasiMet® water cooled grinder. These segments were then individually mounted in 25.4mm diameter moulds using Buehler ProbeMet® and the Buehler SimpliMet® 1000 automatic compression mounting system. All samples were mounted for radial view (through wall).

All samples then underwent grinding steps using 180, 240, 400 and 600 grit silicon carbide paper (SiC) using the Buehler Beta grinder/polisher equipped with the Vector® automated polishing head. When possible, multiple samples were polished using the automatic polishing head. A pressure of approximately 10N was applied to each sample while the rotating the samples in a direction contra to the grinding platen's rotation. Each stage was typically performed for 2-3 minutes or until a flat surface without any scratches from the previous grinding stages was obtained.

While electropolishing of samples was attempted after completing grinding to a 600 grit finish, electropolishing typically produced highly topographic surfaces which were unsuitable for analysis using the OM and SEM. Topographic surfaces occurred regardless of the electrolyte composition or polishing voltage and current as generally the matrix was preferentially attacked while the precipitates remained relatively intact. Therefore, mechanical polishing (i.e. using diamond suspensions or paste in combination with polishing cloth) was exclusively used to prepare the samples for OM and SEM analysis. Polishing steps using 9 and 3µm Buehler MetaDi® Supreme diamond polishing suspension were performed in combination with a Buehler TexMet® 1000 polishing cloth. Approximately 10N of force was applied to each sample for 4 minutes while rotating the samples in a complementary direction to the polishing platen's rotation. The TexMet® 1000 cloth was specifically used for the 9 and 3µm polishing stages for its relatively high material removal rate and ability to minimize relief between the hard carbides and soft austenite matrix. When replacing polishing pads, it was important to ensure the new pad was given a base of Engis Hyprez® diamond compound and broken-in by polishing an unwanted sample for 1-2minutes. Using a new TexMet® 1000 cloth without this base would typically result in the cloth inducing scratches greater than could be attributed to the size of diamond being applied to the cloth.

[1] Buehler (an Illinois Tool Works Company), Lake Bluff, Illinois, USA.

Further polishing using the 1µm MetaDi® Supreme diamond polishing suspension in combination with a Buehler TriDent™ polishing cloth was subsequently performed for 5 minutes (using the same pressure and polishing direction as the 9 and 3µm stages). The TriDent™ polishing cloth was used for this stage as it effectively removed the scratches and surface deformation induced during the previous stage while typically producing a finish of higher quality in comparison to the finishes obtained when using the more aggressive TexMet® 1000 polishing cloth.

3.1.2 Final polish and Etching

The final polish was carried out using Buehler MasterMet® 2 0.02µm colloidal silica in combination with a Buehler ChemoMet® polishing cloth (the MasterMet® 0.06µm solution can substituted for MasterMet® 2). While the numerous combinations of different polishing solutions and cloths were experimented with, the Buehler MasterMet® 2 0.02µm colloidal silica solution in combination with a Buehler ChemoMet® polishing cloth generally gave the best finish. Approximately 15N of force was applied to each sample while rotating the samples in a direction complementary to the polishing platen's rotation. In contrast to the previous stages the polishing time varied significantly depending on the nature of the subsequent analysis (e.g. optical or scanning electron microscopy). The varied polishing times were a result of the significant surface deformation that was induced during the diamond polishing stages. Figure 3.2 shows a high resolution scanning electron micrograph of the HP-NbTi alloy where the duration of the final polishing stage was insufficient to remove the surface deformation (arrowed) from the previous 1µm stage. While surface deformation appeared similar to scratches on the samples surface, the absence of topography within the matrix clearly distinguished the deformation from scratches (scratches were also observable if the final polish was particularly poor). The deformation was predominantly an issue when performing high resolution scanning electron imaging of the samples as it commonly obscured the precipitates (particularly the smaller secondary precipitates) when viewing the sample with backscatter electrons.

Generally, the surface deformation could be removed by increasing the polishing time. The following paragraphs detail the final polishing procedures which were found to be the most successful for LOM, ESBD, HR-SEM, and image analysis. Where applicable, the etching procedures have also been

included. For ease of reference, the polishing and etching conditions have also been summarized in Figure 3.1.

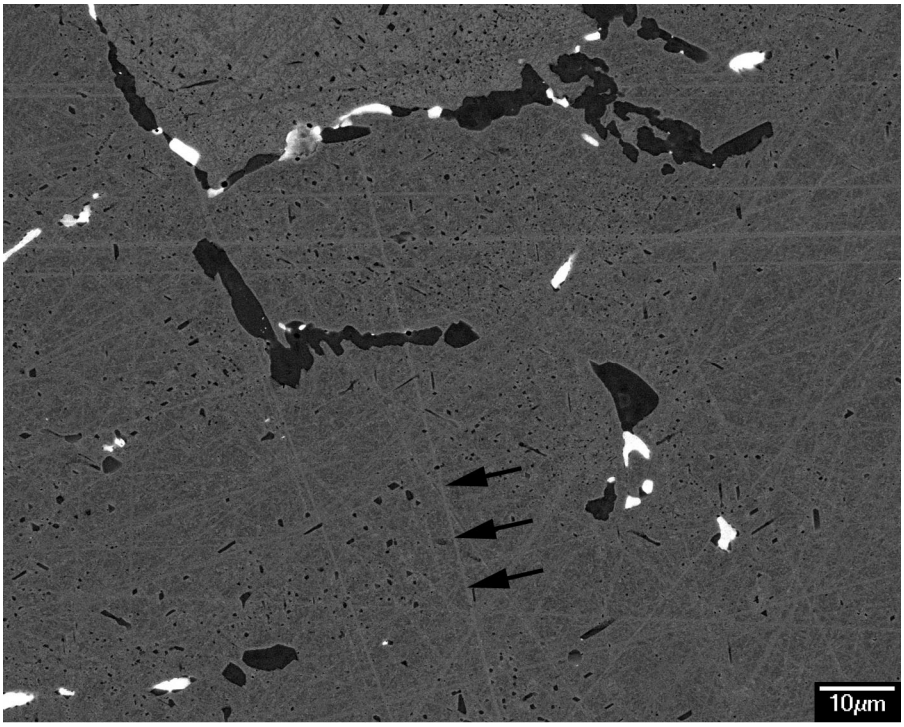

Figure 3.2 – High resolution backscatter electron micrograph of the HP-NbTi alloy showing the remaining surface deformation when the final polish duration is not sufficient.

Light Optical Microscopy (LOM)

Performing a final polish with colloidal silica for 10 minutes generally removed sufficient surface deformation to produce a finish which appeared scratch-free when observing the sample in the as-polished condition using the LOM. Following the final polish, all samples were etched by individually immersing and vigorously agitating each sample in glyceregia (30ml glycerol, 30ml HCl, 10ml HNO_3) for 90-180 seconds. The samples were then thoroughly rinsed with water and ethanol prior to observing the sample using the LOM. Typically, the effects of any remaining surface deformation were unobservable at the resolution capability of the LOM. However, in some cases the etching process would cause the re-emergence of scratches as a result of the remaining surface deformation being preferentially attacked by the etchant. Rarely, the extent of scratching after etching was

sufficient to impair the quality of the LOM images taken from the sample. Thus, grinding and polishing of the sample was repeated beginning from the 600 grit stage.

Electron Backscatter Diffraction (EBSD)

In general, the surface deformation only affected the quality of the electron backscatter diffraction patterns (or EBSPs) produced by the austenite matrix. Poor polishing procedure typically made the austenite's EBSPs diffuse causing indexing to be inaccurate or occasionally impossible. Consequently, the duration of the final polish was initially increased to 60 minutes in an attempt to completely remove the surface deformation. While the prolonged polishing time significantly improved the quality of the austenite's EBSPs, the quality of the EBSPs from the primary Cr_7C_3 and $Cr_{23}C_6$ precipitates decreased considerably. Through trial and error, a final polishing duration of 25 minutes was found to give surface finishes where the quality of the EBSPs produced by the austenite and chromium carbides was sufficient to allow for accurate and reliable indexing of each phase.

Since the contrast of the precipitates and matrix converged after tilting the sample for EBSD analysis (70°C from horizontal), light etching (~20 seconds) of the samples in glyceregia was performed to increase the visibility of the precipitates when performing EBSD analysis. Comparison between as-polished and etched samples indicated that etching did not have any adverse affect on the EBSPs produced by the precipitates or matrix.

High Resolution Scanning Electron Microscopy (HR-SEM)

To achieve high quality scanning electron microscope images of the as-cast and aged HP alloys the surface deformation had to be completely removed. Therefore, when preparing samples for HR-SEM analysis, the duration of the final polish was extended to 80 minutes. Generally, this extended final polish was adequate to remove the surface deformation while the ChemoMet® cloth was relatively new. However, the performance of the ChemoMet® cloth would progressively degrade with each polishing cycle. This degradation lowered the material removal rate and necessitated that the cloth be replaced at regular intervals (between 10-15 cycles). If too much surface deformation remained

after completing the final polish, the 1μm diamond and final polish (with a new ChemoMet® cloth) stages were repeated.

Typically, the samples were observed after performing light etching of each sample in glyceregia. Light etching significantly improved the appearance of the precipitates/matrix interface without causing excessive pitting of the matrix. Emersion of the sample and vigorous agitation for 20-30 seconds ensured that the etchant uniformly attacked the austenite (as opposed to the preferential attack of the matrix directly adjacent to the precipitates). However, it was important to ensure that etching was not continued for longer than 30 seconds as the image quality would rapidly decline as if the dissolution of the matrix was too great.

Image Analysis

The method of preparation for image analysis had to be designed to render all features of interest (i.e. the precipitate network) clearly visible without introducing any polishing artifacts which could be mistaken as part of the particle distribution. In general, poor final polishes would affect the thresholding[2] of the backscatter electron image which would subsequently induce error when measuring the average size and area fraction of each precipitate type from the binary image. Typical sources of error included surface deformation, surface pitting, precipitate fallout, staining of the surface from the polishing solution and excessive relief (surface topography) between the precipitates and matrix.

Generally, the surface deformation could be eliminated by increasing the duration of the final polish while surface pitting could be minimized by maintaining a pressure of 15N per sample while polishing. However, prolonged final polishes would increase the level of surface relief between the precipitates and matrix and also increased the number of precipitates which would fallout during polishing. Surface relief between the precipitate and matrix was a direct result of the carbides being considerably harder than the austenite matrix. As illustrated in Figure 3.3 (a), precipitate phases in relief typically appear larger in the image of the cross-sectioned surface than they would appear in an image of a planar section. In order to minimize these artifacts, the duration of the final polish had to

[2] Thresholding is the process used to segment the microstructure based on the difference in contrast between the precipitates and matrix. The resulting binary image is comprised of 1 and 0 values where the precipitates appear as either black (0) or white (1) pixels.

be a compromise between the removal of surface deformation and minimization of surface relief. A final polishing duration of 30 minutes (determined through trial and error) generally gave the best balance. While it was impossible to completely eliminate the surface relief, the use of the Buehler ChemoMet® polishing cloth which is a relatively low nap cloth also helped to minimize the level of surface relief while maintaining a higher material removal rate in comparison higher nap cloths (such as Buehler's MicroCloth or MasterTex cloths).

Imaging of the samples in the as-polished condition using backscatter electrons generally gave sufficient contrast between the precipitates and matrix to allow for precipitates to be accurately segmented during thresholding of the backscatter electron image. Etching of the samples was not carried out as the etchant preferentially attacks the matrix directly surrounding the precipitates. As shown in Figure 3.3 (b), the resulting surface topography induces similar measurement errors to polishing-induced surface relief as the removed material would often appear similar in contrast to the chromium carbide precipitates and artificially increasing the measured average size and area fraction of these precipitates.

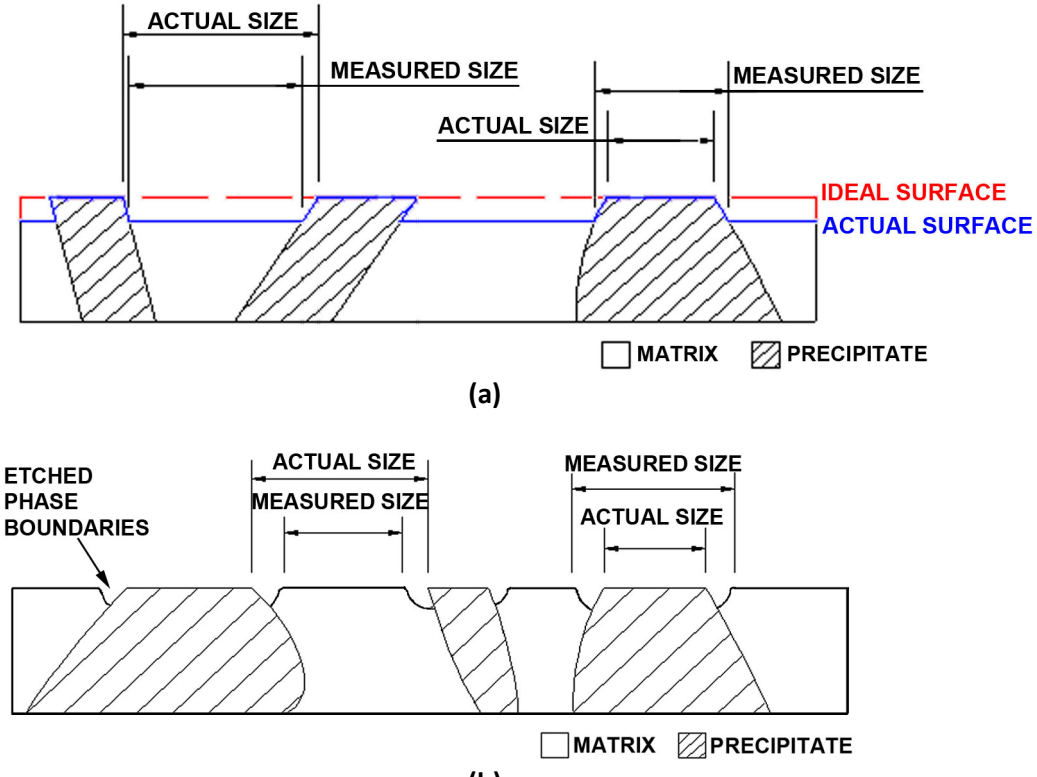

Figure 3.3 - Illustrations depicting (a) the surface relief which occurred between the carbides (hard) and austenite matrix (soft) during polishing and (b) similar surface relief induced by etching of the samples.

Prolonged final polishes using solely the MasterMet® 2 polishing solution also induced considerable contrast between individual grains (Figure 3.4 (a) and (b)). While this effect made grain boundaries easily identifiable, the considerable darkening of certain grains (e.g. grain 1 in Figure 3.4 (b)) often caused the matrix to become very similar in contrast to the chromium-rich precipitates. Consequently, the chromium carbides within these grains could not be segmented from the matrix during thresholding. Since the location of each field of view for image analysis was dependent on a predefined grid (used to prevent any user induced bias when selecting the field of view - Figure 3.5), these darkened grains would commonly be coincident with points on the analysis grid. Therefore, polishes where the darkened grains were common would result in a number of images that were completely unusable. Further experimentation with the final polishing conditions determined that the grain contrast could be reduced significantly by using a 50/50 mixture of water and the MasterMet® 2 polishing solution and liberally applying the mixture (at a rate of approximately 20ml per minute).

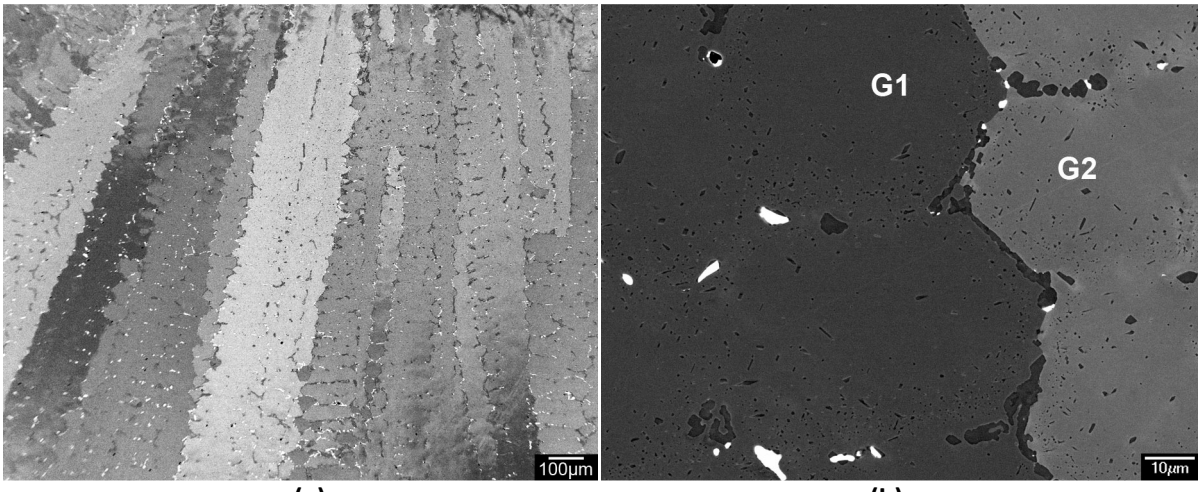

(a) **(b)**

Figure 3.4 - (a) & (b) Backscatter electron micrographs showing the contrast between individual grains which is accentuated after prolonged final polishes using solely the MasterMet® 2 solution.

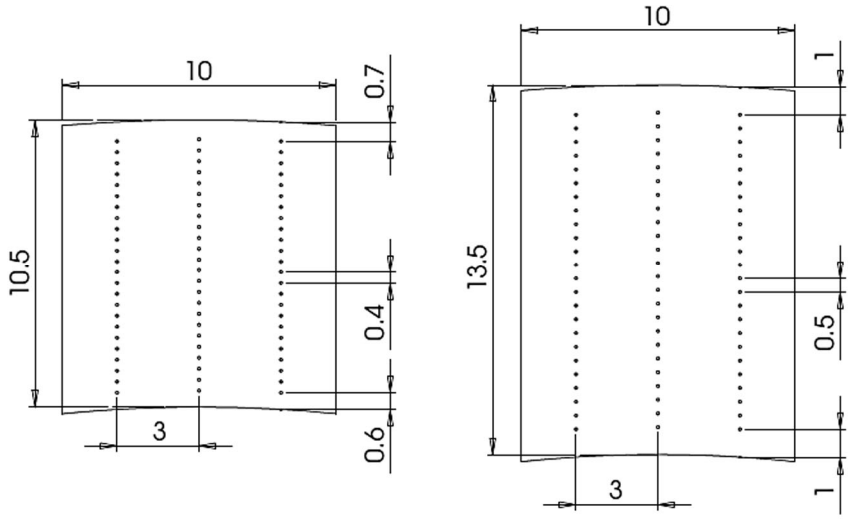

(a) **(b)**

Figure 3.5 - Schematics showing the grids (72 points each) used to select the fields of view for the image analysis of the (a) HP-Nb and (b) HP-NbTi alloys.

3.1.3 Deep Etching for Macro- and Micro-analysis

As shown in Figure 3.1, deep etching of the HP alloys was performed in order to observe the HP-Nb and HP-NbTi alloys' macroscopic grain structure in the as-cast condition (Chapters 4 and 5) and the three-dimensional morphology of the alloys' precipitates in the as-cast and aged conditions (Chapters 4, 5, 6 and 7). For macro-analysis, grinding of the samples was halted after the 600 grit stage. In this case, it was only necessary to obtain a 600 grit surface finish as the scratches and surface deformation were completely dissolved during the etching process leaving only the tubes grain structure. Macro-etching was carried out by immersing the samples in Marbles reagent (10 grams $CuSO_4$, 50ml HCl, 50ml H_2O) for 30-60 minutes without agitating the etchant. The samples were subsequently submerged in concentrated HNO_3 for 1-2 minutes to increase the reflectivity of the macro-etched surface. Finally, the surface was thoroughly rinsed with water and ethanol. After imaging the samples were re-ground (starting from 180 grit SiC) and polished to a mirror finish to allow for further microstructural analysis.

For micro-analysis, the samples were typically polished to 1µm finish prior to deep etching in glyceregia (30ml glycerol, 30ml HCl, 10ml HNO_3) for periods between 60-120 minutes. In this case, polishing to a 1µm finish was performed as the polished surface of the precipitates was completely retained and clearly observable in the SEM after deep etching. This surface often helped to

understand the relationship between the appearances of each precipitate in two- and three-dimensions. All etching with glyceregia was carried out using the apparatus shown in Figure 3.6 (a). Immersion of the samples in a beaker containing stagnant glyceregia was not successful since a thin transparent film would form during etching. This film would obscure the precipitates in the scanning electron microscope (Figure 3.6 (b)). Gentle agitation of the etchant with a magnetic stirrer was introduced to prevent the film's formation without any adverse affects on the primary precipitate network (e.g. fracture and fallout of the precipitates). Although all samples were oriented with the polished surface face-down in the etchant, the relatively high connectivity of the primary precipitate network in three dimensions caused precipitate fallout to be insignificant during etching. After etching the samples were given a thorough rinse using hot water followed by an ethanol prior to performing SEM analysis.

Progressive etching of samples (i.e. observing samples in the as-polished condition and after etching for set intervals of time) was also performed to confirm that the glyceregia etchant only dissolved the austenite matrix and left the precipitates completely intact. This process ensured that the microstructural features observed in three-dimensions were not an etching induced artifact. Prior to etching, each sample was polished to the same level as that used for HR-SEM. Micro-hardness indents were then placed at fixed intervals across the tubes wall thickness to give a set of fiducial markers which would allow the same region of the sample to be located in the as-polished and etched conditions. Multiple regions containing the primary chromium and niobium rich precipitates were subsequently imaged in the as-polished condition and after etching for 45 seconds and 5, 10 and 30 minutes using the backscatter and secondary electrons.

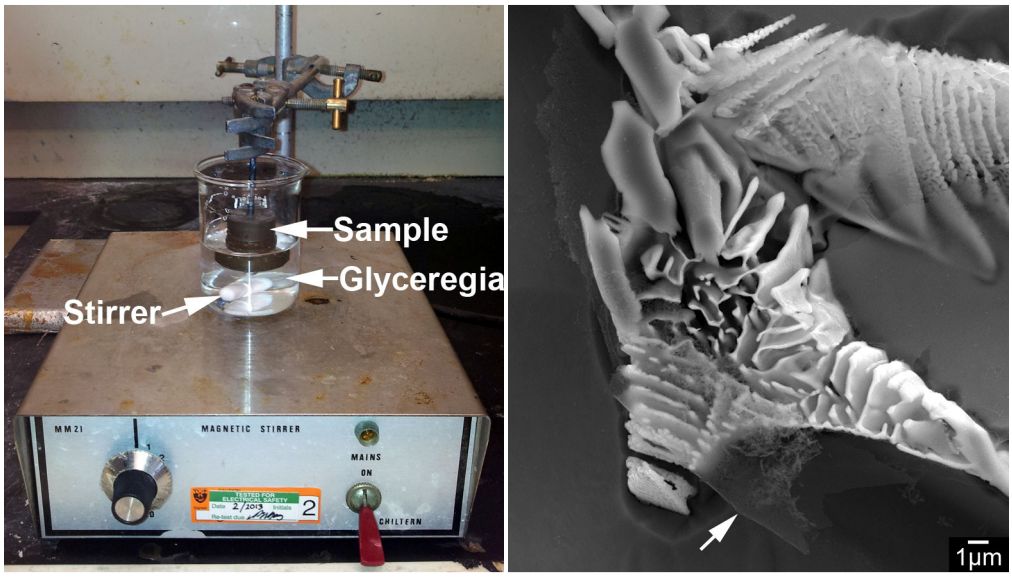

(a) **(b)**

Figure 3.6 - (a) Apparatus used to agitate the glyceregia etchant during deep etching of the HP alloys and (b) the transparent film which would form when etching in stagnant glyceregia.

3.2 Sample Preparation for Powder X-ray Diffraction

Powder X-ray diffraction (XRD) was performed on the HP-Nb 1000°C-3000 hours aged sample and an ex-service HP-Nb alloy to identify the precipitate phases within each sample. This analysis required the conversion of the samples into a powdered form. This conversion was achieved by firstly cutting thin slices approximately 5 x 11 x 0.4 mm (arc-length x tube wall thickness x depth) using the Buehler IsoMet® low speed saw. The thin slices from each alloy were then separately submerged in glyceregia for approximately 12 hours to completely dissolve the austenite matrix. As the precipitates within each sample were the primary focus of this analysis, the etching reagent had to solely attack the austenite while leaving the precipitates intact. Progressive etching experiments performed on each sample (prior to the powder's preparation) determined that the precipitates within each alloy were unaffected by the etching process. Since glyceregia becomes increasingly volatile with time, the solution had to be replaced at two hour intervals. While care had to be taken to ensure that the loss of any loose precipitate fragments was kept to a minimum during replacement of the etchant, fortunately the primary precipitate networks within each sample were fairly continuous. Hence, the total loss of precipitates could be kept to a minimum if sufficient care was taken to prevent the fracture of this network during exchange of the etchant.

The reaction between the matrix and etchant was judged to be nearing completion once bubbles stopped being emitted from the sample. After pouring out the final glyceregia solution, each sample was gently rinsed (while being kept in their respective beakers) using water followed by ethanol. Once the samples had been thoroughly washed with ethanol, the remaining liquid in each beaker was given time to evaporate. The dry precipitate networks were then separately crushed into a fine powder using a clean mortar and pestle.

3.3 Sample preparation for Transmission Electron Microscopy

3.3.1 Cutting, Grinding and Punching TEM Disks

For transmission electron microscopy (TEM), 3mm diameter foils had to be prepared from the as-cast and aged tube segments. Initially, thin slices approximately 5 x 11 x 0.6mm (arc-length x tube wall thickness x depth) were cut from each tube segment. All slices were cut so that the face of each foil was parallel to the OM and SEM samples polished surface (i.e. cut for radial or through-wall view in the TEM). The slices were then ground to a thickness of approximately 0.3mm using 400 and 600 grit SiC paper followed by mechanical punching of 3mm disks from each slice. These disks were subsequently ground using 1200 and 4000 grit SiC paper until foils with a thickness of approximately 100µm was obtained. Grinding was performed on both sides the disks to remove any surface deformation induced during mechanical punching.

3.3.2 Mechanical Dimpling

Prior to ion milling, the center of each sample was pre-thinned by using either mechanical dimpling or electropolishing. Simply ion milling the foil from a 100µm thickness to electron transparency (<500nm) was not practical as it would take approximately 8-10 hours per sample. Additionally, the aggressive milling conditions (accelerating voltage of 5keV, and sputtering angle of 6°) required to maintain an acceptable material removal rate induced considerable damage during the prolonged ion milling period (Figure 3.9 (a) and (b)). This damage caused the total electron transparent area

within each sample to be relatively low. Thus, mechanical dimpling or electropolishing was used to rapidly reduce the thickness at the disks center and ultimately minimizing the duration of the subsequent ion milling stage.

Mechanical dimpling was carried out using the Gatan[3] 656 dimple grinder. Initially, thinning of the sample was carried out using a 15mm diameter phosphor-bronze polishing wheel in combination with 6µm Buehler MetaDi® Supreme diamond polishing suspension. This wheel cut a hemispherical dimple into one side of the foil. Once the dimple reached a diameter of approximately 1.5mm, a thin strip Buehler NanoCloth® was fitted to the circumference of a separate phosphor-bronze polishing wheel and used in combination with a 1µm diamond polishing suspension to increase the diameter of the dimple to between 2.1-2.2mm. After this stage, the thickness at the foil's center was typically reduced below 25µm (depending on the initial thickness of the disk). As the removal of material during mechanical dimpling induces surface deformation, increasing the size of the dimple further increased the likelihood of inducing artifacts (such as dislocations) into the samples electron transparent area. Thus, mechanical dimpling was halted as this stage and ion milling was subsequently used to remove any surface deformation and reduce the foil's thickness until perforation occurred.

3.3.3 Eletropolishing

In parallel to mechanical dimpling, electropolishing of separate foils was carried out a using the E.A. Fischione[4] automatic twin-jet electropolishing apparatus. Pre-thinning of the samples center through electropolishing was typically faster than mechanical dimpling (3-4 versus 10-15 minutes/sample respectively). However, electropolishing required significantly greater control of the conditions (e.g. electrolyte temperature, voltage and current) in order to obtain consistently successful polishes. Electropolishing was performed from both sides of the foil using a solution of 6% (by volume) perchloric acid, 35% n-butyl alcohol, and 59% methanol. Significant trial and error found that the best polishes were obtained when holding the electrolyte at approximately -40°C while applying a voltage of 40V and current of 25mA.

[3] Gatan, Inc, Pleasanton, California, USA.
[4] E. A. Fischione Instruments, Inc, Pittsburgh, Pennsylvania, USA.

Generally, for each electropolishing session, it was necessary to produce 2-3 additional foils that could be sacrificed in order to ensure the polishing settings were correct. On average, if the apparatus was setup correctly (i.e. correct sample alignment and jet speed), and a relatively fresh electrolyte was used with the electrolyte temperature strictly controlled within $^{+}/_{-}$ 5°C (to allow for a potential of 40V and current of 25mA to be maintained), a polish similar to that shown in Figure 3.7 (a) would be obtained. However, slight divergence of any of these parameters from the 'ideal' conditions would result in significant pitting of the samples (Figure 3.7 (b)). While these highly topographic polishes did not necessarily render the sample unusable, a considerable amount of ion milling was subsequently required to obtain sufficient thin area for analysis in the TEM. Though, such topographic samples would be undesirable as the resulting thin area would be less than for foils where the electropolishing process was successful. Through trial and error, the following factors were found to help minimize the prevalence of pitting during electropolishing:

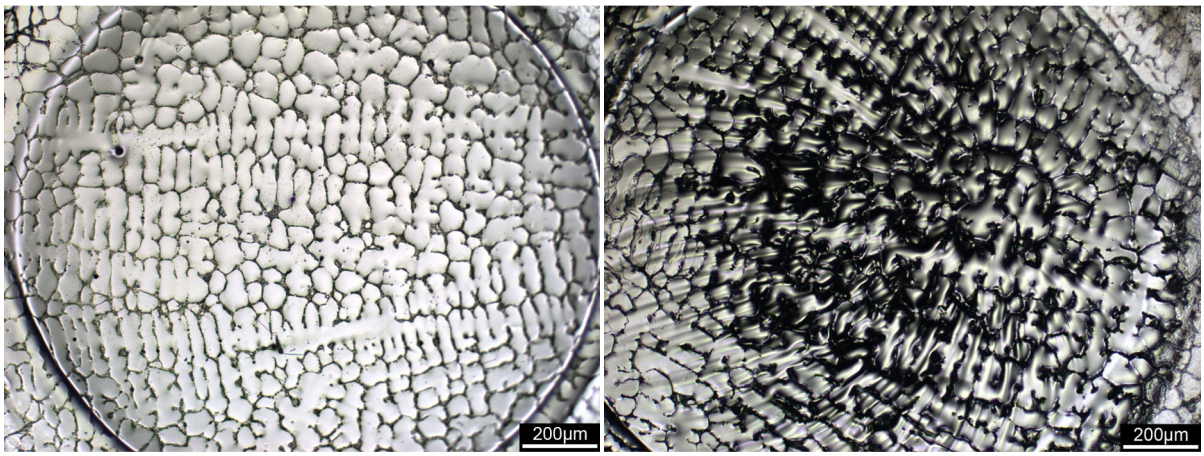

(a) **(b)**

Figure 3.7 – Optical micrographs showing examples of TEM foil specimens after (a) successful and (b) unsuccessful (pitting) electropolishing.

Setup of the Electrolyte Jets

During setup of the electropolishing apparatus, it was important to ensure that the nozzles (which directed the two separate jets of electrolyte to the foil - Figure 3.8) were equally spaced from each side of the foil. If the distance of the nozzles from the foil differed by greater than 2-3mm, the flow conditions experienced by each side of the foil would differ. This small offset would typically cause pitting on one side of the foil. Increasing the jet speed in attempt to reduce the pitting risked having a too aggressive jet speed on other side of the foil, increasing the risk of bending the center of the

foil once perforation occurred. Therefore, care was taken at the beginning of each polishing session to ensure that the nozzles were equally spaced at approximately 8mm from the samples surface. It was also important to ensure that the centreline of the two nozzles were parallel and aligned to direct the jet streams at the foil's center.

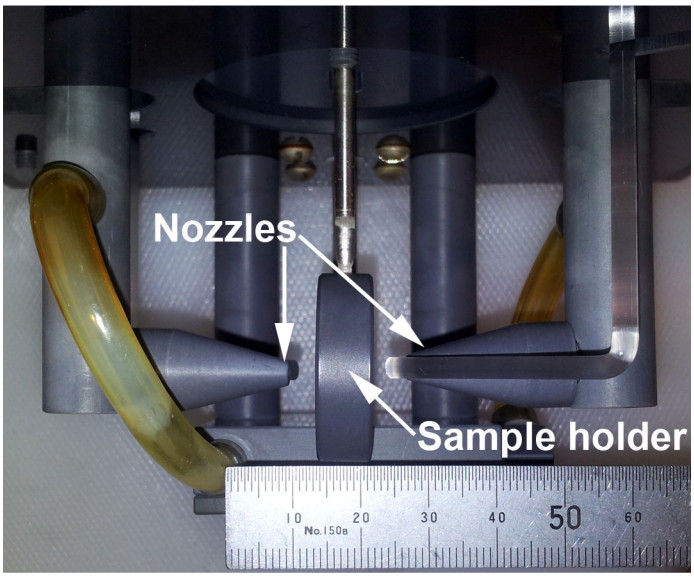

Figure 3.8 – The portion of the Fischione twin-jet electropolishing apparatus which is submerged in the electrolyte.

Jet Speed

It was important to adjust the jet speed at the beginning of the session and prior to polishing the first test foil. Without a consistent flow of fresh electrolyte to the foils surface, heavy pitting of the foil would occur. However, excessive jet speeds would bend the foil once electropolishing perforated the foil's center. The jet speed on the Fischione twin-jet electropolishing apparatus is controlled by a knob which defines the flow rate over an arbitrary range of 0 (minimum) to 10 (maximum). Initially, the nozzles were held slightly above the electrolyte and the jet speed was adjusted (without the sample holder in place) so that the two electrolyte jet streams just impinged on each other. After increasing the speed so that the jet streams impinged on each other, the nozzles were submerged in the electrolyte and the jet speed was increased by one additional graduation. If pitting was found after polishing the first test foil, the jet speed was increased by another 0.5 of a graduation whereas

the jet speed would be decreased by the same amount if bending of the foil's perforation was observed.

Voltage and Current and Electrolyte Temperature

As previously stated, the best foil specimens were produced when the voltage and current was maintained at 40V and 25mA during polishing. Increasing the voltage (>42V) would typically increase the prevalence of pitting while decreasing the voltage (<35V) would cause etching of the foil to occur. The current was dependent on both the applied voltage and the temperature of the electrolyte. Generally, maintaining the electrolyte temperature at -40°C ($^{+}/_{-}$.5°C) in order to obtain a current of approximately 25mA would reduce the prevalence of pitting. Allowing the electrolyte temperature to rise would also increase the polishing rate (due to the greater current) and often led to topographic foils with multiple perforations throughout the polished area of the foil.

Electrolyte

As previously stated, all polishing was carried out using a mixture of 6% (by volume) perchloric acid, 35% n-butyl alcohol, and 59% methanol. Generally, this mixture had a relatively long shelf life and was used to successfully polish a 6-8 separate batches of samples (5-10 samples/batch) over a 6-12 month period. However, if poor polishes continued to occur after ensuring the correct setup procedure and operating conditions had been used, the electrolyte would be replaced. The electropolishing apparatus would subsequently be thoroughly washed with methanol ensuring that there was no polishing residue on the platinum electrical wire which contacts the foil. The apparatus would then be setup once again with fresh electrolyte. This process typically resolved any unknown problem which was disrupting the electropolishing process.

3.3.4 Ion Milling

The use of ion milling to reduce each foil's thickness until electron transparency was necessary regardless of the pre-thinning technique. All ion milling was carried out using the Gatan Precision Ion

Polishing System (PIPS). Generally, a foil containing a relatively large electron transparent area could be obtained by using accelerating voltages and sputtering angles lower than 3.5keV and 6° respectively. Milling using more aggressive milling conditions (such as 5keV and 6°C) would result in a highly topographic surface similar to that shown in Figure 3.9 (a). This topography was highly undesirable as perforation of the foil first occurred at the base the pits shown in Figure 3.9 (b). Further milling increased the number of perforations and eventually the individual pits would coalesce to form a larger hole. The highly uneven surface surrounding the hole as a result of the pitting would considerably reduce the foil's electron transparent area in comparison to foils which experienced less aggressive ion milling conditions (Figure 3.9 (c)). Similar topography could also be induced if milling was continued for prolonged periods (>5 hours) at lower accelerating voltages (3-4keV). Such prolonged milling periods would only be necessary if the material removed during the pre-thinning process was insufficient.

As stated in Section 3.3.2, ion milling was required to remove the surface deformation produced within the foil during mechanical dimpling and reduce the foil's thickness to electron transparency. Typically, 3-4 hours of ion milling at an accelerating voltage of 3.5keV and sputtering angle of 6°C was necessary to thin the sample until a perforation formed. After perforation of the foil had occurred, milling was continued for 30-60 minutes at an accelerating voltage of 1.5keV and sputtering angle of 4.5° in order to increase the foil's electron transparent area. Once the perforation had increased to a size of between 0.2-0.5mm in diameter, a final milling operation at 0.5keV and sputtering angle at 4.5° was performed for 30-60 minutes to further increase the size of the thin area without significantly increasing the size of the perforation.

In contrast to mechanical dimpling, electropolishing could be continued until perforation of the foil occurred. However, as the precipitates and matrix polished at differing rates (regardless of the polish quality), the precipitates were considerably thicker than the austenite matrix after electropolishing was complete. Typically, the matrix was electron transparent in the as-electropolished condition. However, ion milling was always necessary to bring the precipitates to electron transparency and ultimately produce foils containing precipitates suitable for TEM analysis. As shown in Figure 3.9 (c), preferential milling of the thicker primary precipitates occurred during ion milling and could often be observed by the apparent increase in the size of the interdendritic network in comparison to the network shown in Figure 3.7 (a) (i.e. prior to ion milling).

Optimally, electropolishing was stopped just prior to the foil's perforation to avoid any bending of the foil by the electrolyte jets. As a result, an initial accelerating voltage of 3.5keV and sputtering angle of 6° was often used to perforate the sample. If the electropolishing stage was performed correctly, perforation of the foil would occur within the first hour of ion milling. Further milling at these conditions was performed until the perforation began to noticeably increase in size. The accelerating voltage was reduced to 1.5keV and sputtering angle to 4.5° to grow the perforation to a suitable size (~0.2-0.5mm diameter). A final milling stage at 0.5keV and sputtering angle at 4.5° was carried out for 30-60 minutes to further increase the samples electron transparent area.

While both mechanical dimpling and electropolishing prior to ion milling produced foils suitable for TEM analysis, the electropolished samples generally contained the greatest amount of electron transparent area. The comparatively lower area in mechanically dimpled foils was believed to be due to the longer ion milling times needed to perforate these foils (which resulted in a greater prevalence of surface pitting). As a result, electropolishing was the main technique used for the preparation of TEM foils in for the current research.

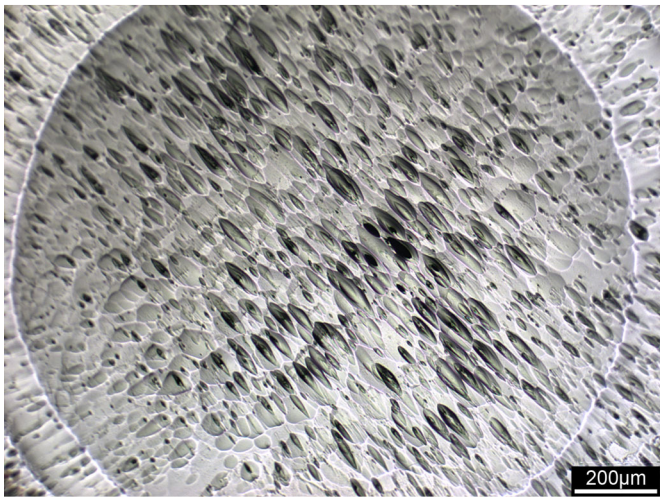

(a)

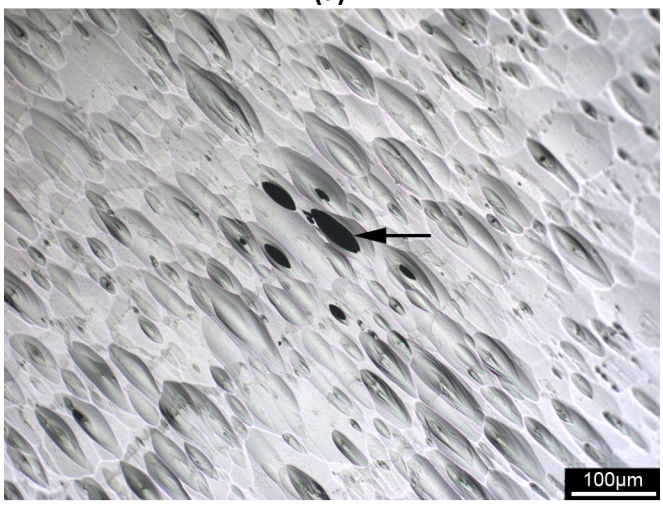

(b)

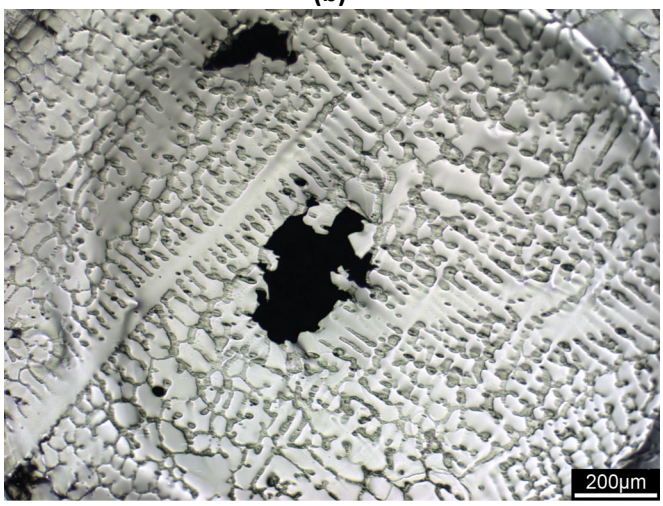

(c)

Figure 3.9 - Optical micrographs showing (a) & (b) a highly topographic TEM foil after ion milling at 5keV and 6° and (c) a comparatively less topographic foil after ion milling at 4keV and 3.5°.

3.4 Analysis Equipment and Typical Operating Conditions used for the Characterization of the HP-Nb and HP-NbTi Alloys

The following sections give a general overview of the analysis equipment and standard operating conditions which were used to characterize the HP-Nb and HP-NbTi alloys. The methods used for specific analysis techniques such as image analysis of the precipitates (Chapters 6 and 7), EDS and EBSD phase identification, EBSD analysis of the crystallographic relationship between various precipitates and the matrix (Chapters 4-7) and TEM trace analysis of linear precipitates (Chapter 4) have been presented in further detail with the relevant results in each respective chapter.

3.4.1 Optical Microscopy

All optical microscopy was performed using the Leica DM-Inverted Research Microscope. Brightfield images were captured digitally using a Nikon[5] Digital Sight DS-Fi1 camera and NiS-Elements F (version 3.2) software.

3.4.2 Scanning Electron Microscopy

For electron backscatter diffraction (EBSD) and energy dispersive X-ray spectroscopy (EDS) samples examined at 20keV using a JEOL[6] JSM 6100 scanning electron microscope (SEM) equipped with the Oxford eXL EDS and HKL Technology EBSD systems[7]. Secondary electron images and electron backscatter diffraction patterns (EBSPs) were captured using HKL Technology's Flamenco software. The experimentally determined EBSPs were indexed using the Flamenco software by comparing each pattern with a reference database of known crystal structures. This reference database was generated specifically for the HP-Nb and HP-NbTi alloys by selecting known phases (which had similar chemical composition that determined for each phase using EDS) from the Pearson's Crystal

[5] Nikon Corporation, Tokyo, Japan.
[6] JEOL is a trademark of Japan Eletron Optics Ltd, Tokyo, Japan.
[7] Oxford Instruments, Bucks, UK.

database [1]. The crystallography of each phase was individually entered into HKL Technology's Twist software and the phases were subsequently compiled in Flamenco.

High resolution scanning electron microscopy (HR-SEM) and energy dispersive X-ray spectroscopy (EDS) was carried out using a JEOL 7000F field emission scanning electron microscope equipped with a JEOL JED-2300 EDS detector. All observations were made at 20keV. This microscope was used to obtain high resolution images of the HP alloy's primary precipitate network for the image analysis (from two-dimensional polished sections); obtain high resolution images of the precipitates in the as-cast and aged condition (from two-dimension polished sections); and image the three-dimensional morphology of the precipitates in the as-cast and aged condition after the polished samples had been subjected to deep etching. EDS was also performed in parallel to the image analysis in order to determine the chemical composition of the phases present in the as-cast and aged condition prior to performing EBSD.

When performing detailed analysis of the precipitates in the HP-Nb and HP-NbTi alloys using the JEOL 7000F scanning electron microscope, imaging was performed using both secondary and backscatter electrons. In general, secondary electrons produced images with high spatial resolution but poor contrast (Figure 3.10 (a)). As a result, the precipitates morphology appeared clearly defined, but the contrast between the neighboring phases (e.g. the NbC precipitate and austenite matrix) was relatively low. Conversely, backscatter electron images offered better contrast between the phases (due to the difference in atomic number) but comparatively lower spatial resolution than the secondary electron image (Figure 3.10 (b)). The lower resolution of backscatter electron images (due to the large volume of material which generates the backscatter electron signal) was particularly evident when observing the HP alloy's precipitates at higher magnifications (>2000x). As shown in Figure 3.10 (a) and (b), certain features along the precipitate/matrix interface (arrowed) often appeared diffuse and difficult to observe in the backscatter electron image in comparison to the secondary electron image. However, the characteristically low contrast in Figure 3.10 (a) within the secondary electron image causes the two chemically and crystallographically unique phases which form the overall plate-like morphology to be almost indistinguishable.

In order to combine the high resolution offered by secondary electrons and the compositional information offered by backscatter electrons, both secondary and backscatter electron images of the same field of view were captured when imaging at magnifications above 2000x. The secondary electron image was used as a base image which was subsequently rendered using the compositional

information within the backscatter electron image, resulting in the composite image shown in Figure 3.10 (c). This composite image was created by overlaying the secondary electron image with the backscatter electron image followed by blending the two images using the "Screen" function in Adobe Photoshop CS5[8]. The "Screen" blending operation increases the brightness of the pixels in the lower secondary electron layer based on the brightness of the pixels in the upper backscatter electron layer. As a result, the high resolution of the secondary electron image is largely retained while the chromium-rich precipitates (arrowed) can be clearly distinguished from the niobium rich precipitates (white) and austenite matrix (light grey).

Composite images were only produced when imaging at magnifications in excess of 2000x where the relatively poor spatial resolution within the backscatter electron images caused blurring of the precipitate/matrix interface. When producing each composite image, significant care was taken to ensure that the blending process did not modify or obscure any of the true microstructural features within the raw secondary and backscatter electron images. Images where this technique has been used in this thesis have been referred to as "composite scanning electron micrographs" whereas images composed of solely secondary or backscatter electrons have been referred to as "secondary electron micrographs" or "backscatter electron micrographs".

When analysing the three-dimensional morphology of the precipitates in the as-cast and aged condition, imaging was carried out using solely secondary electrons.

[8] Adobe Systems Incorporated, San Jose, California, USA.

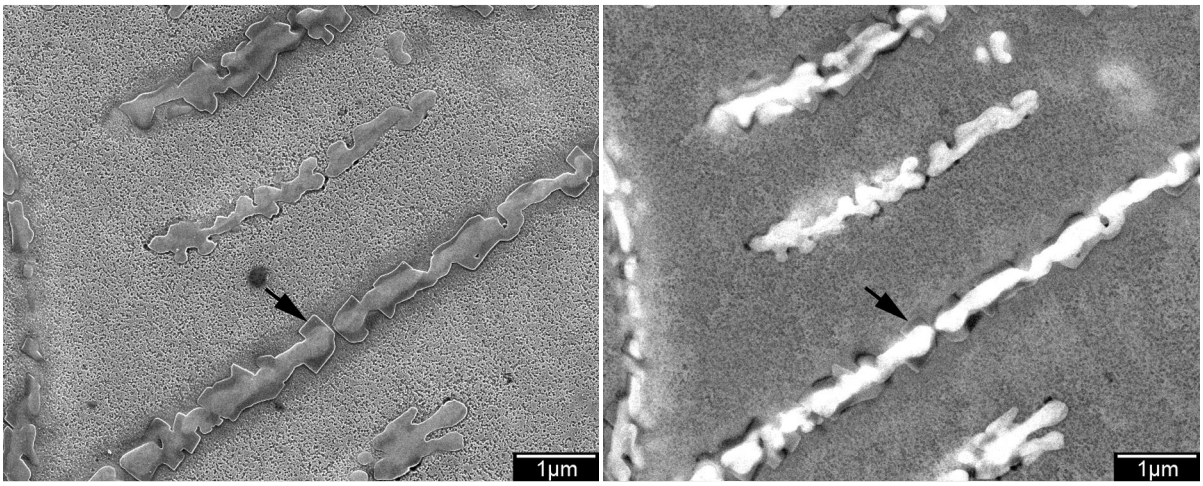

(a) **(b)**

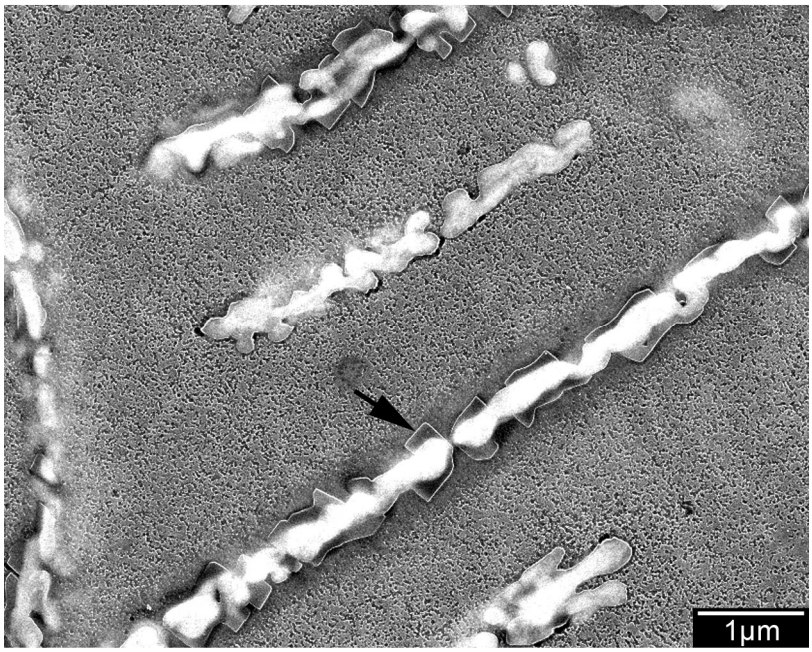

(c)

Figure 3.10 - Scanning electron micrographs taken using (a) secondary electrons, (b) backscatter electrons and (c) a composite image produced by combining the secondary and backscatter electron images.

3.4.3 Powder X-ray Diffraction (XRD)

XRD was performed using a Philips[9] X-ray Diffractometer system consisting of a Philips PW 1729 X-ray generator, PW 1820 Goniometer, PW 1710 Diffractometer control and a PW 2283/20 Copper X-ray tube. The X-ray tube was operated at 50keV and 40mA producing copper Kα X-rays with a wavelength of 0.154178nm. Scanning of the powder was performed at 0.02° intervals over a range of 10-100°. The precipitates were identified by comparing the experimentally determined spectrum against a set of simulated spectra generated in the Desktop Microscopist software suit[10] (version 2.2a) using phases of known crystal structure and chemical composition from the Pearson's Crystal Database [5].

3.4.4 Transmission Electron Microscopy (TEM)

Analysis of thin foils was performed using a Philips CM200 transmission electron microscope equipped with the Oxford INCA x-sight EDS system. All samples were observed at an accelerating voltage of 200keV. Predominantly, bright field images (BF), selected area diffraction (SAD) and convergent beam electron diffraction (CBED) patterns were captured on Kodak[11] SO163 electron microscope film. After developing the films in a darkroom, the negatives were digitized using an Epson[12] Perfection 1200U Flatbed scanner. Alternatively, BF images were captured digitally using the Gatan Orius™ SC 200 CCD camera. Analysis of the BF, SAD and CBED images was performed in Adobe Photoshop CS5.

[9] Philips is a trademark of the FEI Company, Hillsboro, Oregon, USA.
[10] Lacuna Laboratories, Beaverton, Oregon, USA.
[11] Eastman Kodak Company, Rochester, New York, USA.
[12] Seiko Epson Corporation, Suwa, Nagano, Japan.

Chapter References

[1] Wahab, A. A. & Kral, M. V. (2005). *3D analysis of creep voids in hydrogen reformer tubes.* Materials Science & Engineering A, 412: pp. 222-229.

[2] de Almeida Soares, G. D., de Almeida, L. H., da Silveira, T. L. & Le May, I. (1992). *Niobium Additions in HP Heat-Resistant Cast Stainless Steels.* Materials Characterization, 29: pp. 387-396.

[3] de Almeida, L. H., Ribeiro, A. F. & Le May, I. (2003). *Microstructural Characterization of modified 25Cr-35Ni centrifugally cast steel furnace tubes.* Materials Characterization, 49: pp. 219-229.

[4] Nunes, F. C., Dille, J., Delplancke J. -L & de Almeida, L. H. (2006). *Yttrium addition to heat-resistant cast stainless steel.* Scripta Materialia, 54: pp. 1553-1556.

[5] Villars, P. (Ed.) & Cenzual, K. (Ed) (2008). *Pearson's Crystal Data: Crystal Structure Database for Inorganic Compounds.* (Version 1.0) [Computer software]. Materials Park, Ohio, U. S. A.: ASM International®.

Chapter 4 Microstructural Characterization of the As-Cast Niobium Modified HP Alloys

Originally the main objective of this project was to characterize the microstructural evolution of the HP-Nb and HP-NbTi alloys after long-term isothermal ageing. It was initially considered that these as-cast structures had been well characterised in the literature. As a result, the initial focus of the as-cast analysis was merely to confirm the primary precipitate phases, precipitate morphologies and relative quantities of each constituent with those reported in the literature. However, during this analysis, it became evident that many aspects of the NbC precipitates (i.e. the phases which form as a direct result of the alloy's modification with niobium) had been overlooked by previous studies. As the addition of these precipitates to the primary carbide network are widely thought to be responsible for the increased creep resistance of the HP-Nb alloy (in comparison to the standard HP composition), it was deemed necessary to perform a more in-depth analysis of the as-cast microstructures before completing the analysis of the aged samples.

Section 4.1 focuses on the macroscopic properties of the HP-Nb alloy. Section 4.2 presents a detailed analysis of the HP-Nb microstructure where specific attention has been paid to the NbC precipitates. The characterization methods employed include optical microscopy (OM), high resolution scanning electron microscopy (SEM), energy dispersive X-ray spectroscopy (EDS), electron backscatter diffraction (EBSD), high resolution transmission electron microscopy (TEM), selected area diffraction (SAD), and convergent beam electron diffraction (CBED). TEM trace analysis of linear/planar features was also performed to determine whether any of the NbC precipitates obtained a specific habit plane.

A portion of this chapter has been published in a paper entitled *"Crystallography and Morphology of Niobium Carbide in As-Cast HP-Niobium Reformer Tubes"* by Karl G. Buchanan and Milo V. Kral, in Metallurgical and Materials Transactions A 43 (2012) pp. 1760-1769.

4.1 Macroscopic Observations of the Niobium Modified HP Alloys

4.1.1 Chemical Compositions of the HP-Nb1 and HP-Nb2 Tubes

Two separate centrifugally cast niobium modified HP reformer tubes were subjected to detailed microstructural analysis. The two alloys were manufactured by Kubota Metal Corporation [1] (alloy designation KHR35C) and Paralloy [2] (alloy designation H39W). The chemical composition, as determined by inductively coupled plasma atomic emission spectroscopy (ICP-AES), and manufacturers' specification are shown in Table 4.1. For the purposes of this thesis these two alloys have been arbitrarily named HP-Nb1 (KHR35C) and HP-Nb2 (H39W). The limited availability of as-cast HP-Nb material necessitated the use of two independently cast HP-Nb alloy tubes for the laboratory ageing and accelerated creep testing programs.

Each tube material is based on the heat resistant HP alloy standard containing 0.35-0.75 weight percent (wt.%) C, 2wt.% (max) Si, 24-28wt.%Cr, 33-37wt.% Ni and 2wt.% (max) Mn [3]. As suggested by the HP-Nb1 and HP-Nb2 titles, these alloys are produced by modifying the HP base composition using a single addition of niobium to produce these variants. Typically, this alloy variant is referred to in the literature as HP-Nb or HP-modified. As these alloys will be compared with other HP alloy variants in this thesis, the –Nb1 and –Nb2 identifiers were considered to provide a clear and simple naming convention in comparison to using either the HP–modified or manufacturers' alloy designations as identifiers.

Table 4.1 - Chemical composition of the as-cast HP-Nb alloys as determined by inductively coupled plasma atomic emission spectroscopy (ICP-AES). Balance Fe.

	wt.%	C	Ni	Cr	Nb	Si	Mn	Mo	V	W	Co	S
HP-Nb1 KHR35C	**Specified**	0.4-0.5	34-37	24-28	0.6-1.5	< 1.5	< 1.5	-	-	-	-	<0.03
	ICP-AES	0.41	33	25	0.44	1.26	0.6	0.24	0.07	0.35	0.11	0.01
HP-Nb2 H39W	**Specified**	0.4	35	25	0.7-1.5	1.5	1	-	-	-	-	-
	ICP-AES	0.38	32.2	24.5	0.92	1.53	1.09	0.12	0.06	0.08	0.17	0.01

In general, both alloys were within the manufacturers' specified chemical composition range. However, the niobium content in HP-Nb1 alloy was below the specified 0.6-1.5wt.% range. Although the niobium content in the HP-Nb1 was outside that specified by Kubota Metal Corporation, it must be noted the composition of these cast materials varies slightly over the 4.5 meter length of the tubes. Due to the limited quantity of material available, further composition analysis of other sections of the HP-Nb1 tube to confirm the average chemical composition was not possible. However, compositional analysis of four samples taken at 0.9 meter intervals along the length of the HP-NbTi2 tube (Chapter 5) indicated the niobium content within the HP-NbTi2 tube varied by a maximum of $^{+}/_{-}$ 0.11wt.%. Since similar variance likely existed along the length of the HP-Nb1 tube, the niobium content could have been close to or within the specified range at other sections of the tube.

As stated in Chapter 2, niobium causes the partial replacement of the as-cast primary Cr_7C_3 network with NbC. Barbabela *et al.* [4] and Soares *et al.* [5] determined the relative volume fractions of the primary Cr_7C_3 and NbC in the as-cast microstructure was directly dependent on the niobium content. The minimum creep rate and rupture life were also shown to be affected by the niobium content. When performing accelerated creep testing (all tests were performed using a stress of 45MPa and temperature of 925°C) on as-cast material, alloys modified with 0.69wt.% niobium exhibited a lower minimum creep rate and higher rupture life in comparison to alloys modified with 1.23 and 1.97wt.% niobium. However, ageing the alloys for 1000 hours at temperatures between 700-1100°C prior to creep testing revealed the creep properties were highly dependent on the ageing temperature. For example, ageing at 700°C caused the 1.23wt.% alloy to have a significantly higher rupture life than the 0.69 and 1.97wt.% alloys (~480 hours 1.23wt.%, ~300 hours 0.69wt.%, ~160 hours 1.97wt.%). In contrast, after ageing the material at 900°C the 1.97wt.% alloy exhibited the highest rupture life whereas the 0.69wt.% alloy had the lowest rupture life (~240 hours 1.97wt.%, ~60 hours 0.69wt.%).

Determining the microstructural features which influenced the creep properties in the aged HP-Nb alloys was relatively complex. Ageing of the alloys at 700 and 900°C caused the NbC to partially transform to G-phase and extensive secondary precipitation to occur within the matrix. The decreased rupture life of the 1.97wt.% alloy after ageing at 700°C was attributed to a decrease in the volume fraction of secondary precipitates which occurred with increasing niobium content. Based on this theory the 0.69wt.% alloy would be expected to exhibit the greatest rupture life. However, as previously stated, the rupture life of the 1.23wt.% alloy was considerably higher. Interestingly, the minimum creep rate was lowest in the 0.69wt.% alloy after ageing at 700°C. The lower creep rate in

the 0.69wt.% alloy is likely attributed to the greater volume fraction of secondary precipitates which would impeded dislocation motion through the austenite matrix.

Ageing at 900°C reportedly caused the secondary precipitates to coalesce, with the level of coalescence being lowest in the 1.97wt.% alloy. Thus, the greater rupture life of the 1.97wt.% alloy after ageing at 900°C was partially attributed to the lower secondary network coalescence. The observed increase in the as-cast primary precipitate networks fragmentation with respect to the increased niobium content was also thought to be partially responsible for the increased rupture life of the 1.97wt.% alloy. The level of primary network fragmentation in combination with the volume fraction of secondary precipitates present in the 1.23wt.% alloy could possibly explain the greater rupture life exhibited by this alloy in comparison to the 0.69 and 1.97wt.% alloys after ageing at 700°C.

In addition to niobium, the relative silicon content in each alloy reportedly affects the as-cast NbC volume fraction and NbC-to-G-phase transformation rate [6]. Alloys with higher silicon contents (1.84 and 2.62wt.% Si) exhibited higher as-cast NbC volume fractions. As the niobium content in each alloy was kept constant (1.97wt.%), the solubility of niobium in austenite was believed to decrease with increasing silicon content, resulting in the increased volume fraction of NbC. During ageing at temperatures between 850-980°C, increased silicon levels accelerated the NbC-to-G-phase transformation. Since, the G-phase ($Ni_{16}Nb_7Si_6$) transformation requires the diffusion of silicon to the transforming NbC precipitate, the driving force for the transformation is increased by a higher abundance of silicon within the austenite matrix [6].

Based on previous studies, the decreased niobium and silicon contents in the HP-Nb1 alloy will likely result in a reduction of the as-cast NbC volume fraction in comparison to the HP-Nb2 alloy. During ageing, the NbC-to-G-phase transformation rate can be expected to be greater in the HP-Nb2 alloy due to the higher silicon content in this alloy. Given the knowledge available in the current literature, it is unknown which of the two alloys will have superior creep properties (e.g. minimum creep rate, rupture life and creep ductility). It must be stressed that ageing of the HP-Nb1 and HP-Nb2 tubes was carried out to determine the overall effects of the microstructural evolution during prolonged thermal exposure on the HP-Nb alloy's creep properties. The current study was not aimed at determining the microstructural features that maximised the HP-Nb alloy's creep resistance in the as-cast and aged conditions. While the specific rate at which the primary precipitate phase transformations occur was expected to differ between the HP-Nb1 and Nb2 alloys, the alloys overall microstructural evolution (e.g. the types of primary phase transformations and secondary

precipitation) was expected to be similar for each alloy when ageing at a constant temperature. The specific rate at which the HP-Nb1 and HP-Nb2 alloys' creep resistance evolved with respect to ageing temperature and time was also expected to be dependent on the alloys composition. However, the overall evolution of each alloy's creep properties (e.g. an increase or reduction in both alloys rupture life with increasing ageing time at a constant ageing temperature) was expected to be similar for the HP-Nb1 and HP-Nb2 alloys. Thus, the general microstructural evolution and creep resistance observed with respect to ageing temperature and time in the aged HP-Nb1 and HP-Nb2 samples is expected to be representative for all HP-Nb alloys.

Although not specified by the manufacturers, molybdenum, vanadium, tungsten and cobalt were also present in the HP-Nb alloys, each of which may have an effect of the alloys creep properties. Intentional additions of molybdenum, tungsten and cobalt have been used in other HP alloy variants to improve the alloys carburisation resistance and high temperature strength [3]. However, higher concentrations (0.5-1.5wt.% Mo, 0.5-5wt.% W, 3-15wt.% Co) are typically used in comparison to those present in the HP-Nb1 and HP-Nb2 alloys. In alloys where molybdenum additions are unintentional, concentrations of <0.5wt.% are commonly reported. During solidification of single crystal nickel-based superalloys, tungsten, molybdenum and cobalt have been shown to remain within solid-solution. Tungsten in particular is used for solid-solution strengthening of the matrix [7-9]. Therefore, the presence of these elements is likely to be beneficial to the alloys creep properties. In addition, as these elements likely remain in solid solution with the HP austenite matrix, they are unlikely to alter the intended effects of niobium on the primary carbide network.

4.1.2 HP-Nb Tube Macrostructures

Figure 4.1 (a) and (b) show the through-wall grain structure of the as-cast HP-Nb1 and HP-Nb2 tubes. Depending on the centrifugal casting conditions (for example casting temperature and cooling rate), reformer tubes exhibit either a completely columnar or a mixed columnar-equiaxed grain structure [10, 11]. The high cooling rate induced during casting of the HP-Nb1 and HP-Nb2 alloys has resulted in 100% columnar grain structures. Qualitatively, the HP-Nb1 alloy can be seen to have a significantly larger grain size than the HP-Nb2 alloy. Higher cooling rates during casting have been shown to increase the columnar grain size in unmodified HK alloys [12], suggesting the HP-Nb1 cooling rate during solidification was greater than that experienced by the HP-Nb2 alloy.

Unfortunately it was not possible to take quantitative measurements of the grain size from the images shown in Figure 4.1 (a) and (b). The number of individual grains which were visible in the captured macroscopic images was highly dependent on the manner in which the samples were illumined. Typically, grains which were not visible in the captured image would merge with a neighbouring grain increasing the apparent grain size. Altering the illumination conditions (i.e. illumination angle, number of illumination sources and light colour filters) would reveal unseen grains while merging other grains which were originally visible. Numerous combinations of illumination were attempted to maximize the number of visible grains with limited success. Figure 4.1 (a) and (b) show the best macroscopic images that were obtained from each sample. Although the images show a large number of the grains which were present in each sample, additional grains which appeared hidden in the captured image were typically visible when viewing the samples by eye. Therefore, it was considered inaccurate to take measurements from the macro-etched samples.

Due to the large grain size observed in the HP-Nb1 alloy, it was considered impractical to perform EBSD mapping of the samples to determine the average grain size. Furthermore, the evolution of the primary and secondary precipitates during ageing of the HP-Nb1 and HP-Nb2 alloys was the main focus of the current project, thus no further effort was placed into the measuring the as-cast grain size of the HP-Nb1 and HP-Nb2 alloys.

The rupture strength, minimum creep rate and creep ductility of HK and HP reformer tubes are dictated by the grain structure (e.g. size and shape) and the properties of the primary and secondary precipitates (e.g. the number of phases present and the average size, distribution and volume fraction of each constituent) [5, 10, 12, 13]. The as-cast grain structure and properties of the primary precipitate network (e.g. dendrite arm spacing and volume fraction) are influenced by the casting conditions[1] [10, 12]. Previous work conducted by Zaghloul *et. at.* [12] on unmodified HK alloys determined the dendrite arm spacing approximately doubled when increasing the cooling rate from 240-804°C/minute during casting. Moreover, the volume of primary precipitates (typically $Cr_{23}C_6$) located on both dendrite arm and grain boundaries approximately halved due to the increased cooling rate. Interestingly, the effect of the cooling rate on the as-cast material's creep rupture life was dependent on the accelerated creep testing conditions. Accelerated testing at 950°C and 29.5MPa revealed no significant difference in the rupture life with respect to the cooling rate experienced by each tube during casting. In contrast, when testing at 1000°C and 9.8MPa, the

[1] While the grain structure is largely dictated by the casting conditions, the properties of the as-cast primary precipitate network in the HP-Nb alloys are influenced by both the casting conditions and the chemical composition of the alloy.

rupture life increased from ~220 to 900 hours when increasing the cooling rate from 240-804°C/minute.

The size of the secondary precipitates in samples aged at 950-1100°C for up to 1000 hours was also found to be dependent on the cooling rate experienced by each tube during casting. Regardless of the ageing temperature, the secondary precipitates were generally finer in tubes which experienced higher cooling rates during casting. For example, after ageing at 950°C for 1000 hours, the average secondary precipitate size in material cooled at 804°C/minute was ~0.05µm smaller in comparison to material cooled at 240°C/minute. However, ageing at higher temperatures or for prolonged periods (<4500 hours) caused the average secondary precipitate size in all tubes to converge.

Despite the HP-Nb1 and HP-Nb2 tubes being based on similar alloy specifications, the differing casting conditions (as evidenced by the differing grain structures in Figure 4.1 (a) and (b)), will likely cause slight differences in the as-cast HP-Nb1 and HP-Nb2 tubes rupture life, minimum creep rate and creep ductility. Based on the preceding observations in the HK alloys, the larger grain size observed in HP-Nb1 alloy indicates this tube will exhibit a higher rupture life. However, it must be noted that primary precipitate network present in the unmodified HK alloy are considerably different in comparison to HK-Nb and HP-Nb alloys. The primary precipitate network in unmodified HK alloys is composed of Cr_7C_3 and $Cr_{23}C_6$ precipitates [10, 12]. The addition of niobium to the HK and HP alloys causes the partial replacement of the primary Cr_7C_3/$Cr_{23}C$ with NbC precipitates, resulting in a mixed Cr_7C_3-NbC or $Cr_{23}C_6$-NbC primary precipitate network in the as-cast alloys [5, 13]. Unfortunately, studies on the effects of the cooling rate during casting on the creep properties of modified HK or HP alloys currently have not been published in the widely available literature. Consequently, it is currently unknown how the differing casting conditions experienced by the HP-Nb1 and HP-Nb2 alloys affects the creep resistance of each alloy in the as-cast and aged conditions.

The purpose of the current study was to determine the effects of long-term isothermal ageing on the HP-Nb alloy's creep properties with respect to ageing temperature and time. While the as-cast grain structure and properties of the primary precipitate network in the HP-Nb1 and HP-Nb2 alloys will influence the microstructural evolution during ageing (and hence each alloy's creep resistance), overall the evolution of the primary and secondary precipitates is expected to relatively similar for these two alloys when ageing at constant temperature. For example, based on previous studies of HP-Nb alloys [4 5], the NbC-to-G-phase transformation and precipitation of secondary $Cr_{23}C_6$ within the matrix was expected to occur when ageing the HP-Nb1 and HP-Nb2 alloys at 1000°C. However, the differing casting conditions experienced by each alloy will likely cause the NbC-to-G-phase

transformation rate, volume fraction of the primary constituents and the size and number of secondary precipitates to differ in the HP-Nb1 and HP-Nb2 alloys.

As discussed in Chapter 1, the HP-Nb1 alloy was subjected to long-term unstressed isothermal ageing at 1050 and 1100°C. Ageing of the HP-Nb2 was conducted at 1000°C. Due to the limited amount of material available, long-term ageing of the HP-Nb1 and HP-Nb2 alloys at the same temperature was not possible. While the differing cooling rates experienced by the HP-Nb1 and HP-Nb2 alloys during casting will affect the absolute magnitude to which each alloy's microstructure and creep resistance changes when ageing at constant temperature, the overall evolution of these properties for each alloy is expected to be similar. Therefore, the general evolution of the HP-Nb2 alloy's microstructure and creep resistance during ageing at 1000°C (e.g. an increase or decrease in the alloys rupture life) was expected to be closely followed by the HP-Nb1 alloy if ageing of this alloy was also performed at 1000°C.

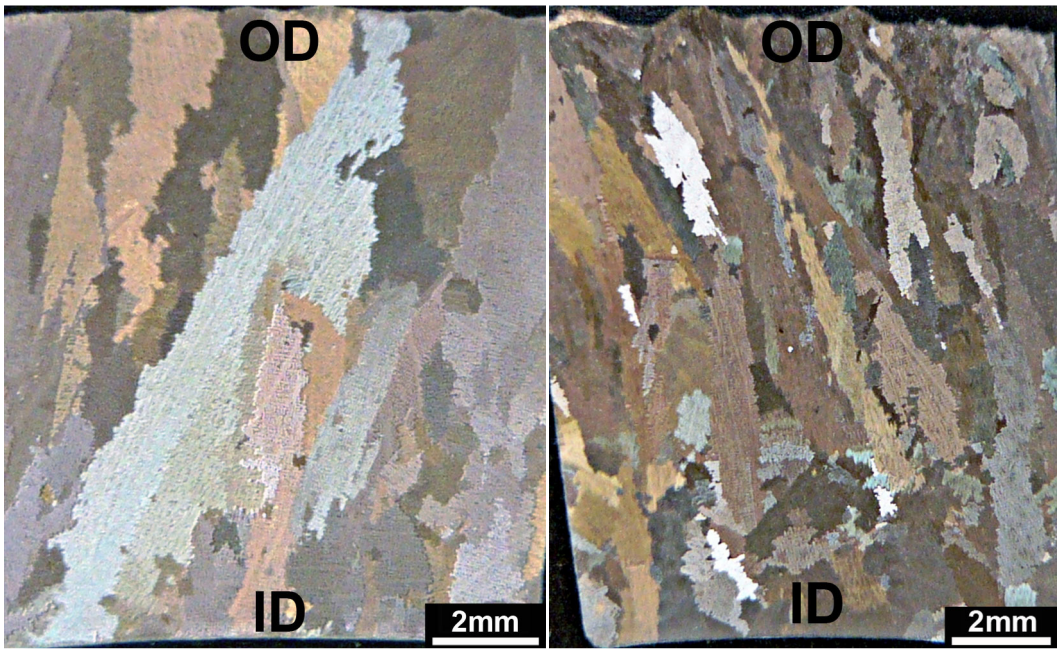

(a) **(b)**

Figure 4.1 - Low magnification optical micrographs showing the macrostructure of (a) HP-Nb1 and (b) HP-Nb2. (Etchant: Marbles reagent)

4.2 Microscopic Observations of the Niobium Modified HP Alloys

4.2.1 Identification of the As-Cast Primary Precipitates

Figure 4.2 (a) and (b) show representative optical and scanning electron micrographs of the HP-Nb microstructure taken at the mid-wall position. The dendritic structure, typical of these centrifugally cast alloys, contains alternating interdendritic groups of chromium (dark grey) and niobium (white) rich primary carbides (Figure 4.2 (b)). In addition to the primary carbides network, manganese sulfide inclusions (arrowed) were also observed within the as-cast microstructures of both HP-Nb alloys. At the magnifications shown, no secondary intragranular precipitation was present within the matrix.

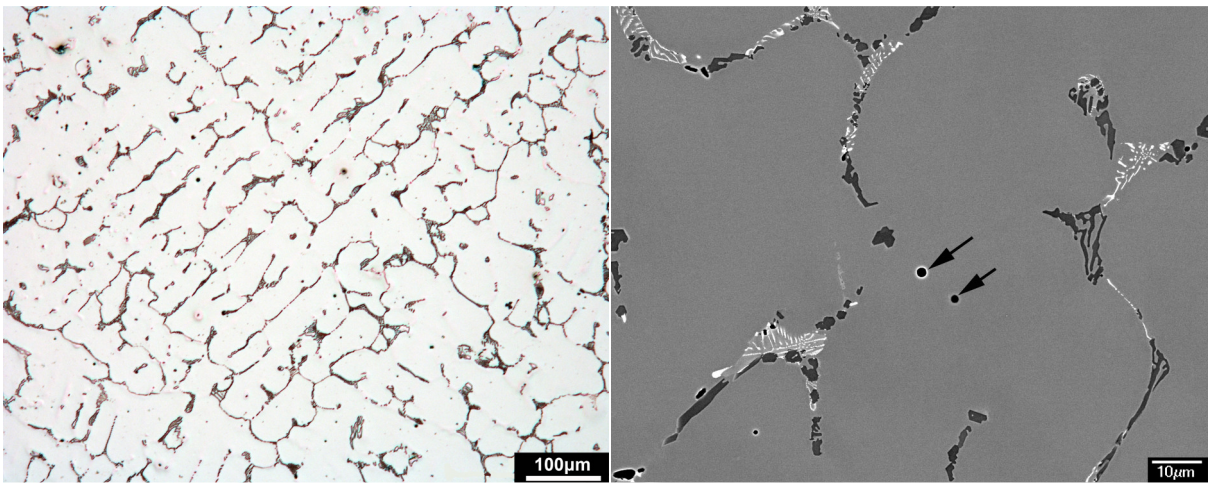

(a) **(b)**

Figure 4.2 - Representative optical (a) and backscatter electron (b) micrographs of the HP-Nb alloys. Due to the atomic number contrast in (b) the niobium rich phases appear white and chromium rich phases appear dark grey in the austenite matrix.

Figure 4.3 (b)-(d) show representative EDS spectra for the primary precipitate phases labelled A and B and the matrix (C) in Figure 4.3 (a). The primary precipitates were predominately chromium (A) and niobium (B) rich causing the atomic number contrast when observing the backscatter electron signal in the SEM. Both phases contained concentrations (typically less than 10at.%) of iron and nickel. Aside from silicon, all other minor elements detected within the iron-nickel-chromium matrix (C) by ICP-AES (Table 4.1), were below the detection capability of the JEOL JED-2300 EDS detector.

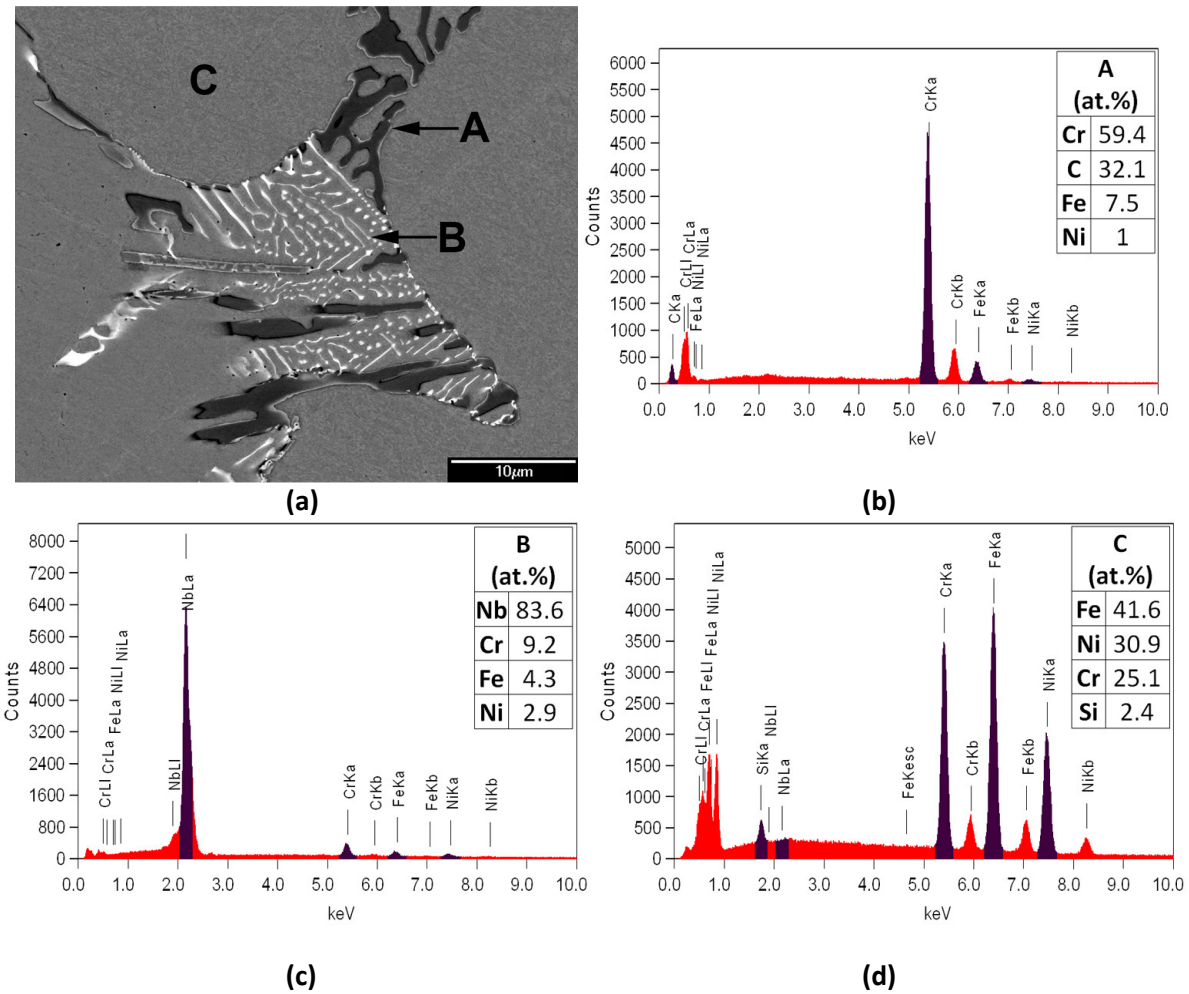

Figure 4.3 - (a) Backscatter electron micrograph of the HP-Nb primary precipitates, (b)-(d) chemical compositions of the phases labelled in (a) as determined by energy dispersive X-ray spectroscopy (EDS).

As previously mentioned, manganese-rich inclusions were observed in the as-cast condition for both alloys. These inclusions were commonly observed in contact with the primary carbide network (Figure 4.4 (a)) and exhibited morphologies similar to the Type I 'globular' and Type III 'random angular particles' described for MnS inclusions in cast plain carbon steels [14, 15]. On average the

inclusions were approximately 1µm in diameter and the total area fraction of MnS for both HP-Nb alloys was less than 0.1%. EDS analysis of the inclusions confirmed the inclusions largely contained manganese and sulfur (Figure 4.4 (b)). Interestingly, the inclusions consistently contained low concentrations (<5wt.%) of selenium. Additions of selenium have been reportedly used in plain carbon steels to improve machinability, resulting in MnS precipitates with selenium concentrations between 8-10wt.% [16]. However, the purpose of selenium additions in steels similar to the cast HP alloy is not well covered in the literature.

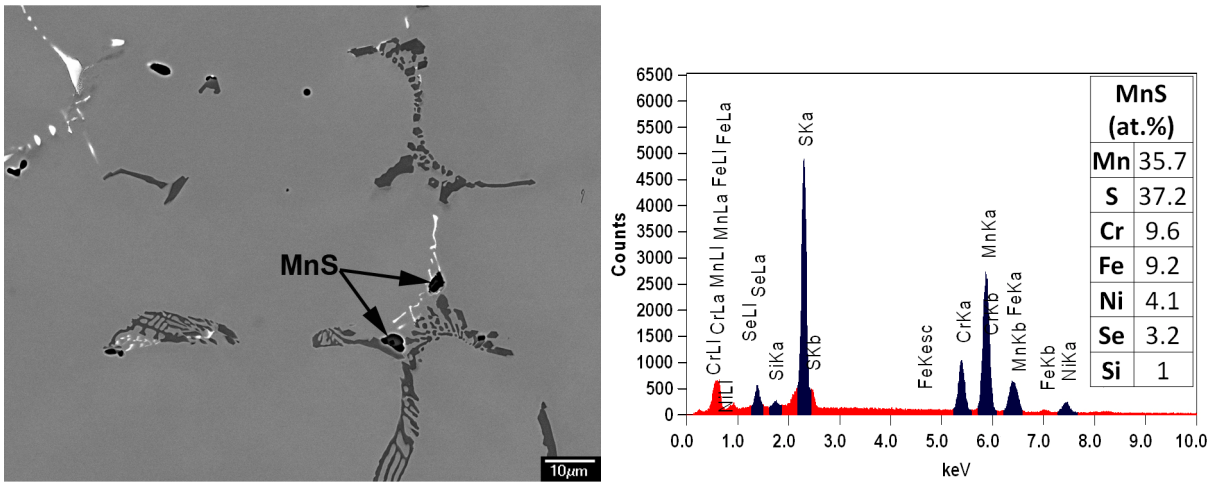

(a) (b)

Figure 4.4 - Backscatter electron micrograph showing the MnS inclusions observed in the as-cast HP-Nb alloys; (b) EDS spectra taken from the precipitates shown in (a).

From knowledge of the chemical composition of each phase, a list of candidate phases could be generated using the Pearson's Crystal database [17]. Table 4.2 lists the crystal structures used for phase identification of primary precipitate in the HP-Nb1 and HP-Nb2 alloys. Based on the available literature for centrifugally cast HP-Nb reformer tubes the Cr_7C_3, NbC and austenite phases were expected in the as-cast condition [4, 5]. The Cr_7C_3 phase was more commonly referred to as M_7C_3 in the literature to account for the low concentration of elements such as nickel and iron present within this phase. Although these elements were also dissolved in the NbC precipitates, the MC terminology was not typically implemented in the literature when referring to the NbC in HP-Nb alloys. Alternatively, authors typically chose to use MC to refer to the (NbTi)C precipitates in the HP-NbTi alloys. To avoid confusion, these phases will be referred to as Cr_7C_3 and NbC, and (NbTi)C (i.e. based on the important elements contained within each phase).

Table 4.2 - List of candidate crystal structures used for EBSD identification of the primary precipitates.

Phase	Crystal System	Space Group	Lattice parameters a, b, c (nm)			α, β, γ (°)			Ref.
CrC	Cubic	$Fm\bar{3}m$	0.403	0.403	0.403	90	90	90	18
Cr_3C	Orthorhombic	*Pnma*	0.512	0.68	0.458	90	90	90	19
Cr_3C_2	Orthorhombic	*Pnma*	1.146	0.552	0.282	90	90	90	20
Cr_3C_2	Orthorhombic	*Cmcm*	0.285	0.926	0.697	90	90	90	21
Cr_7C_3	Hexagonal	$P6_3mc$	1.401	1.401	0.453	90	90	120	22
Cr_7C_3	Orthorhombic	*Pnma*	0.701	1.215	0.453	90	90	90	23
$Cr_{23}C_6$	Cubic	$Fm\bar{3}m$	1.065	1.065	1.065	90	90	90	24
NbC	Cubic	$Fm\bar{3}m$	0.446	0.446	0.446	90	90	90	25
$NbC_{0.8}$	Hexagonal	$R\bar{3}m$	0.314	0.314	3.01	90	90	120	26
$NbC_{0.75}$	Hexagonal	$P3_1$	0.546	0.546	1.542	90	90	120	27
Nb_2C	Hexagonal	$P6_3$/mmc	0.31	0.31	0.5	90	90	120	28
Nb_2C	Hexagonal	$P\bar{3}1m$	0.542	0.542	0.497	90	90	120	29
Nb_2C	Orthorhombic	*Pnma*	1.091	0.31	0.497	90	90	90	29
Nb_6C_5	Monoclinic	C12/m1	0.545	0.944	0.545	90	109.5	90	30
Iron FCC	Cubic	$Fm\bar{3}m$	0.361	0.361	0.361	90	90	90	31
Iron BCC	Cubic	$Im\bar{3}m$	0.287	0.287	0.287	90	90	90	32
MnS	Cubic	$Fm\bar{3}m$	0.522	0.522	0.522	90	90	90	33

EBSD was subsequently used to determine the crystal structures of the as-cast phases. Figure 4.5 (a), (c), (e) and (g) show electron backscatter diffraction patterns (or EBSPs) obtained from the chromium and niobium rich carbides, austenite matrix and manganese-rich inclusions. Examples of the best matching simulated crystal structures (generated by HKL Technology's[2] Flamenco software using the crystallographic parameters in Table 4.2) for phases A, B, C (Figure 4.3 (a)) and the manganese-rich inclusions are shown overlaying the corresponding experimental patterns in Figure 4.5 (b), (d), (f) and (h). For each phase, EBSPs were obtained from at least 20 different precipitates located at separate positions across the wall thickness of the HP-Nb1 and HP-Nb2 tubes. The chromium-rich (A) and niobium-rich (B) precipitates were all confirmed as Cr_7C_3 (*Pnma*) and NbC ($Fm\bar{3}m$) respectively. The iron-nickel-chromium matrix (C) was confirmed as austenite ($Fm\bar{3}m$). Finally the manganese-sulfur rich inclusions were confirmed as MnS ($Fm\bar{3}m$).

[2] HKL Technology is a member of the Oxford Instruments Group (Abingdon, Oxfordshire, U.K.).

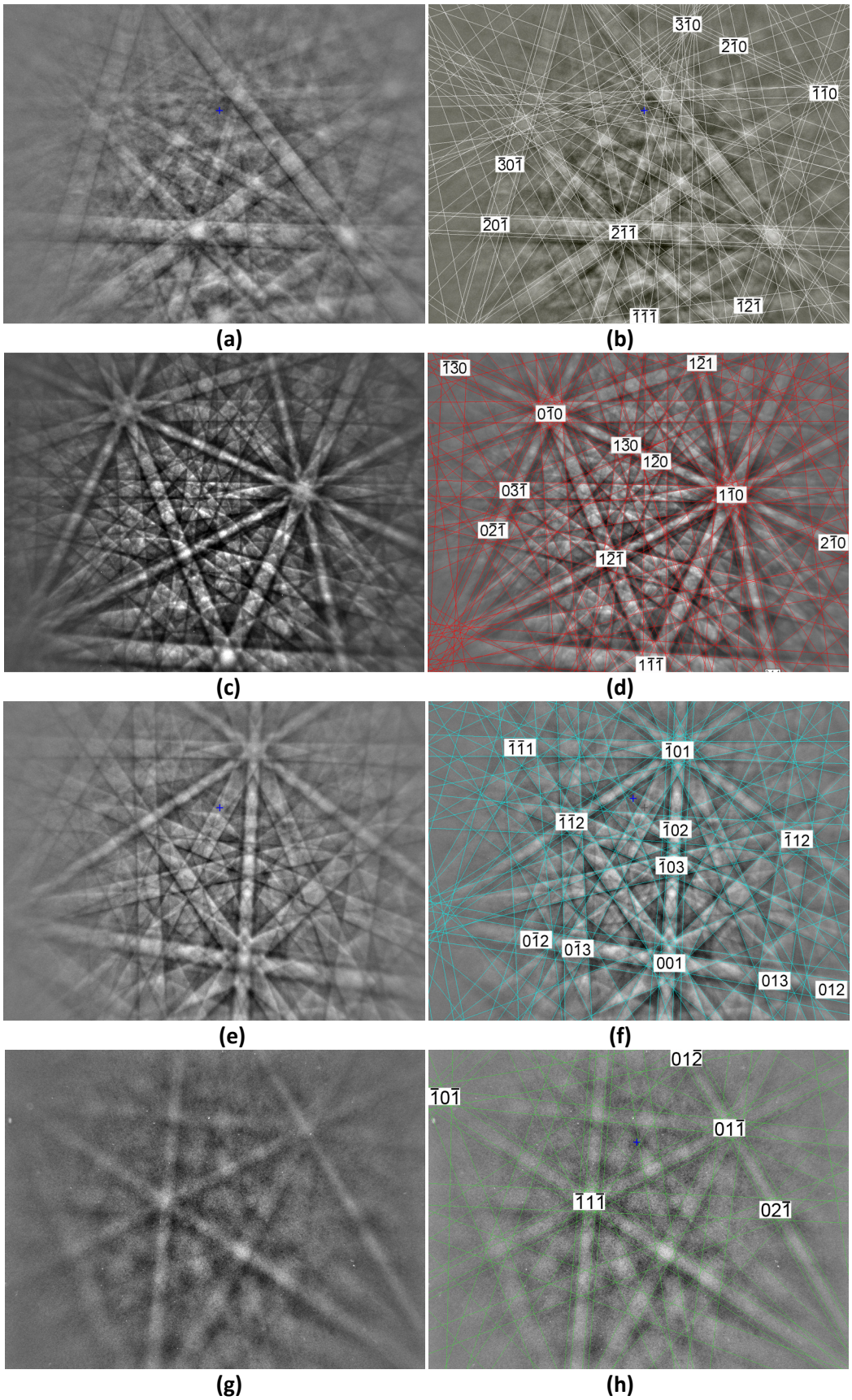

Figure 4.5 - Experimentally determined electron backscatter diffraction patterns (EBSP) and the corresponding simulated patterns for the (a) & (b) Cr_7C_3. (c) & (d) NbC, (e) & (f) Austenite and (g) & (h) MnS crystal structures.

4.2.2 Detailed Analysis of the Primary NbC Precipitates in HP-Nb1 and HP-Nb2 Alloys

Observations of the primary NbC at the magnifications shown in Figure 4.2 confirmed the typical lamellar or "Chinese–script" morphology as described by previous studies [4, 5]. However, observations of the primary NbC at higher magnifications revealed the existence of two significantly different morphologies of individual plate lamella (Figure 4.6 (a) and (b)). Type I lamellae, shown in Figure 4.6 (a), obtain a relatively planar interface with the austenite. In contrast, Type II lamellae (Figure 4.6 (b)) exhibit significant undulations along the lamellae's surfaces. In two-dimensions the Type II lamellae obtain an overall plate-like appearance; however, a degree of fragmentation was apparent along the length of the plates. Both morphologies were grouped in colonies of similar lamellae. Cases where the two lamellae were found adjacent to each other occurred only when two colonies of different morphology impinged on each other.

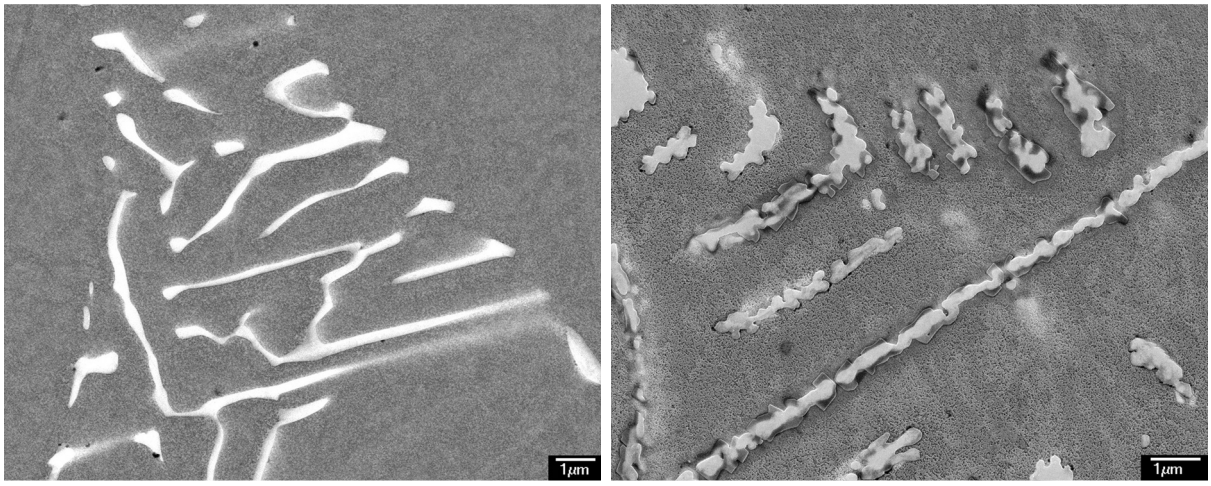

(a) **(b)**

Figure 4.6 – Composite scanning electron micrographs showing the two-dimensional morphology of (a) Type I lamellae and (b) Type II lamellae.

SAD and CBED analysis of thin foils confirmed that both morphologies have the face centred cubic NbC ($Fm\bar{3}m$) crystal structure. However, EDS consistently revealed small concentrations of molybdenum in the Type II (Table 4.3), but none in the Type I. During solidification, partitioning molybdenum could have influenced the growth morphology of the NbC precipitate. However, further investigation is required to prove this theory. Small concentrations (<5wt.%) of elements such as titanium (commonly utilised in combination with niobium in the HK- NbTi and HP-NbTi variants) have

been reported to cause the NbC morphology to change from lamellar to blocky [13, 34]. Similar changes to (TaTiNb)C (or MC) precipitates have been attributed to small concentrations of hafnium and zirconium in directionally solidified Ni-based alloys [35, 36]. Such additions are thought to increase the MC/matrix interfacial energy, causing the precipitates to obtain the blocky morphology to minimize the interfacial area. Thus, the small molybdenum concentration within the Type II lamellae may have a similar modifying effect on the NbC morphology.

Table 4.3 - SAD and CBED determined crystal structure and EDS chemical composition for the Type I and II NbC morphologies.

	Crystal System	Space Group	a(nm)	Nb	Cr	Fe	Ni	V	Mo
Type I	FCC	$Fm\bar{3}m$	0.438	87.9	7.6	2.3	1.5	0.7	-
Type II	FCC	$Fm\bar{3}m$	0.440	87.2	7.4	2.5	1.7	0.6	0.6

A small (typically <0.5µm^2) chromium-carbon rich phase was observed between the Type II lamellae and austenite phases (Figure 4.7 (a) and (b)). CBED analysis of this phase confirmed the orthorhombic Cr_7C_3 crystal structure (the same structure as the larger primary Cr-rich carbides). The Cr_7C_3/austenite interface was highly faceted whereas the NbC/Cr_7C_3 interface was dictated by the shape of the NbC precipitate. Although the interdendritic groups of primary Cr_7C_3 and NbC are commonly interlinked (Figure 4.3 (a)), it is believed that the interfacial Cr_7C_3 is independent of the primary Cr_7C_3 network (i.e. the interfacial Cr_7C_3 is not caused by two-dimensional sectioning of small segments of the primary Cr_7C_3 network).

Studies of material subjected to unstressed ageing for 1000 hours at 900°C [6] have previously reported the presence of $Cr_{23}C_6$ precipitates on the interface of NbC lamella which had partially transformed to G-phase. This $Cr_{23}C_6$ precipitation was said to have formed due to the rejection of carbon from the transforming NbC precipitate into the chromium-rich austenite. While the NbC interface likely represents an energetically favourable site for secondary precipitation of $Cr_{23}C_6$, the observed $Cr_{23}C_6$ precipitates are believed to more commonly arise from the transformation of the interfacial Cr_7C_3 precipitates in association with the Type II lamellae (shown in Figure 4.7 (a) and (b)). Analysis of the aged HP-Nb1 and HP-Nb2 samples determined the interfacial $Cr_{23}C_6$ precipitates were unique to the Type II lamellae (Chapter 6). Therefore, the interfacial $Cr_{23}C_6$ observed in the literature can also be largely attributed to transformation of the pre-existing Cr_7C_3 to $Cr_{23}C_6$ during ageing.

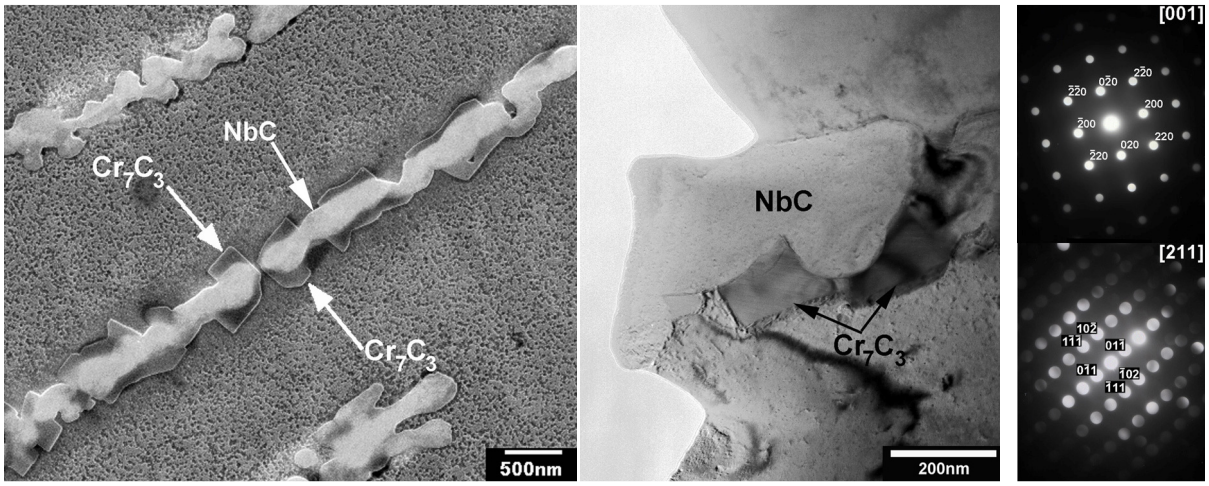

(a) (b) (c)

Figure 4.7 - (a) Composite scanning electron and (b) Bright field transmission electron micrographs showing the Cr_7C_3 located between the precipitate/matrix interface of Type II lamellae. (c) Indexed $[001]_{NbC}$ and $[211]_{Cr7C3}$ zone axis patterns (CBED) for the FCC NbC and orthorhombic Cr_7C_3.

Table 4.4 - CBED determined crystal structure and EDS chemical composition for the interfacial Cr_7C_3

	Crystal System	Space Group	Lattice parameters (nm)			EDS composition (at.%)				
			a	b	c	Cr	C	Fe	Ni	V
Cr_7C_3	Orthorhombic	*Pnma*	0.45	0.7	1.22	66	25.1	7.5	1.1	0.3

The difference between morphologies becomes more apparent after deep etching (Figure 4.8 (a)-(d)). Type I lamellae are revealed as smooth solid plates in three-dimensions (Figure 4.8 (a)), where the broad faces exhibit varying degrees of curvature. Small steps or facets on the broad faces of the plates (which would be associated with the curvature) were not resolved by SEM (Figure 4.8 (b)).

Figure 4.8 (c) and (d) show the web-like or reticulated shape of the Type II lamellae in three dimensions. The fragmentation of the lamellae observed in two-dimensions (Figure 4.6 (b)) corresponds to the three-dimensional pores within the plane of the plates. The undulations commonly occurred at a near-constant length scale causing pore size of plates within and between separate groups to also remain consistent (typically 0.2-0.5µm). Many lamellae adhered to a particular plane of growth causing the overall plate-like morphology. After deep etching, the interfacial Cr_7C_3 could not be distinguished from the Type II lamellae due to the lack of contrast between the two phases in scanning electron microscopy.

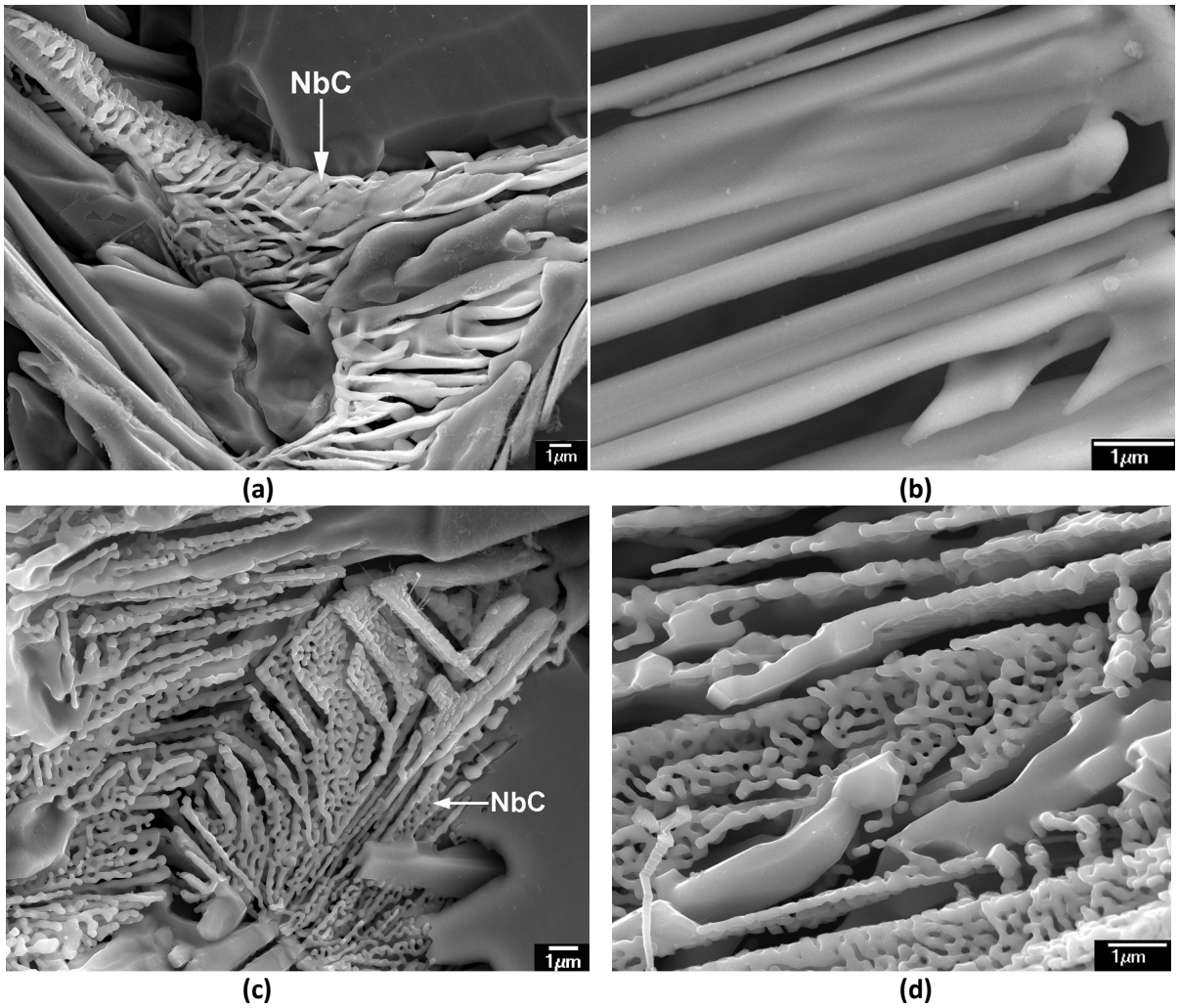

Figure 4.8 –Secondary electron micrographs showing the three-dimensional morphology of (a)-(b) Type I lamellae, (c)-(d) Type II lamellae

Progressive etching experiments on the as-cast material determined that deep etching with glyceregia (30ml glycerol, 30ml HCl, 10ml HNO_3) caused the sole dissolution of the austenite matrix while leaving the primary carbides completely intact (i.e. the carbide morphologies observed were not influenced by the etching process). Figure 4.9 (a) to (f) show scanning electron micrographs of the Type I and II morphologies in the as-polished condition and after etching for 10 and 30 minutes (taken from the same respective areas). The primary NbC and Cr_7C_3 precipitates increasingly protrude from the surface as the dissolution of the austenite matrix progresses. The features of the precipitates, as observed on the polished plane, correspond on a one-to-one basis in successive micrographs. Any discrepancy between the appearances of the precipitates during progressive etching was typically due to precipitate fallout.

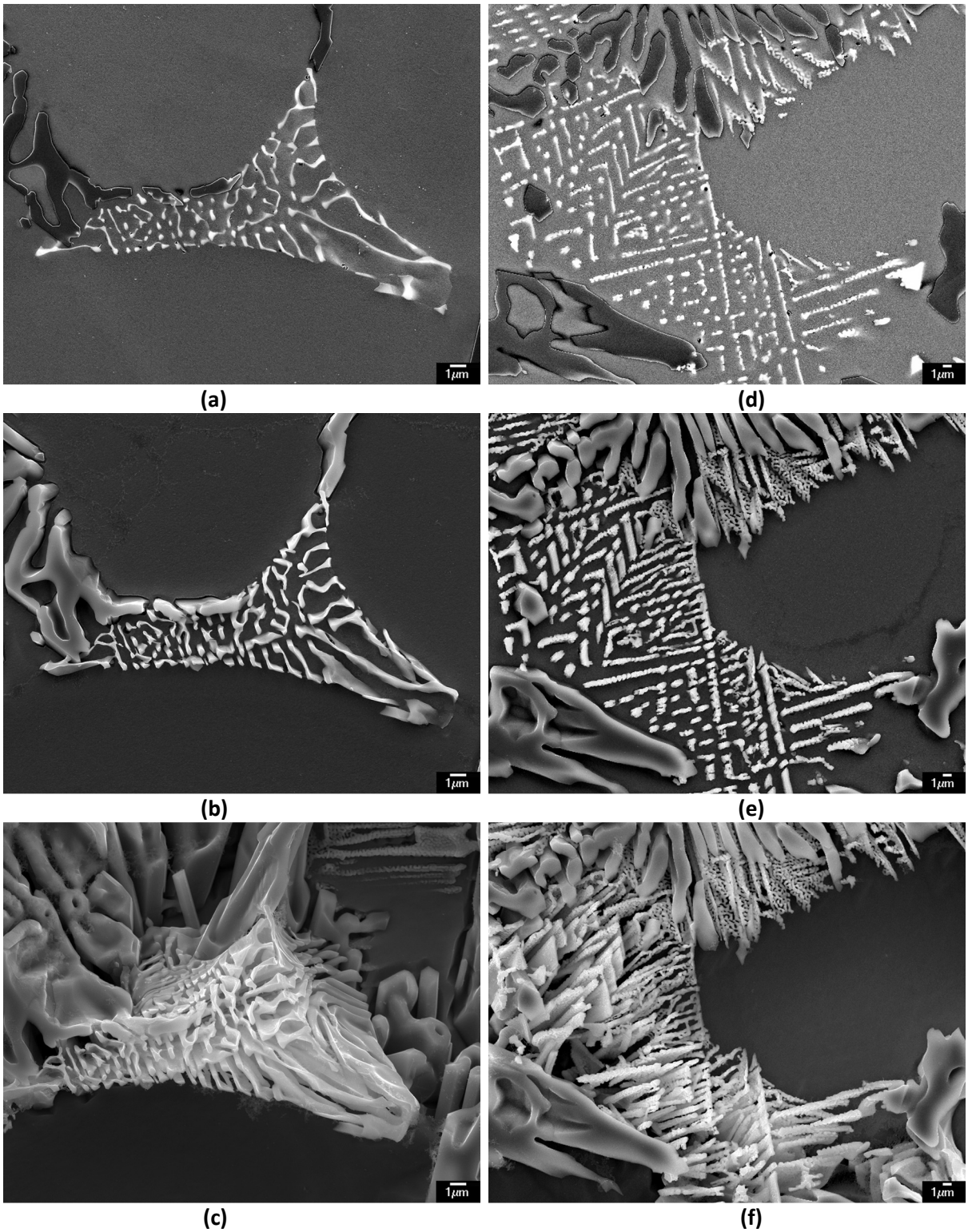

Figure 4.9 - Scanning electron micrographs of the Type I (a-c) and Type II (d-f) lamellae in the (a) & (d) as-polished condition (observed using backscatter electrons) and after etching for (b) & (e) 10 and (c) & (f) 30 minutes (observed using secondary electrons). Glyceregia etchant (30ml HCl, 30ml Glycerol, 10ml HNO_3).

For the HP-Nb2 alloy, the Type II lamellae appeared to be more prevalent than the Type I lamellae (approximately 65% Type II – 35% Type I). However, the Type I and II lamellae appeared to be equally abundant in the HP-Nb1 alloy (i.e. 50% Type II – 50% Type I). Neither morphology appeared to be preferentially located, e.g., at dendrite, grain boundaries or relative position within the tube wall. The Type II lamellae appear to exhibit a higher surface area to volume ratio in comparison to the Type I lamellae. However, further work (such as serial sectioning) would be required to quantify this ratio. Exposure of the HP-Nb alloy to temperatures between 700-1050°C typically causes the NbC-to-G-phase transformation to occur [4-6]. The total surface area and properties (i.e. interfacial structure and free energy) of the as-cast NbC/austenite interface will likely influence the kinetics of the G-phase transformation. Therefore, the two morphologies should exhibit different transformation kinetics during ageing.

The G-phase transformation did not occur when ageing the HP-Nb alloy at 1100°C (i.e. the NbC remained stable). At temperatures where the NbC remains stable, the high surface area to volume ratio exhibited by the Type II morphology could cause the lamellae to be unstable. Therefore, the lamellae would likely undergo spheriodization (Chapter 6) during prolonged ageing at 1100°C to reduce the total interfacial energy.

Accelerated creep testing has shown that laboratory aged samples with G-phase present have increased creep ductility in comparison to samples without G-phase [5]. Thus, the characteristics of the NbC-to-G-phase transformation are important to predicting the service behaviour of these alloys. However, since the existence of these two morphologies was previously unknown in the HP-Nb alloy, no effort to date has been made to determine the transformation characteristics specific to each morphology.

Following confirmation of the relative similarities of the crystal structure and chemical composition of these two lamellae, additional analysis was required to provide further insight into their origin. In a study of niobium modified HK alloys, Hou and Honeycombe [13] established the existence of a cube-cube crystallographic orientation relationship (OR) between the primary NbC and austenite:

$$<100>_{NbC} \,||\, <100>_{\gamma}$$

$$\{100\}_{NbC} \,||\, \{100\}_{\gamma}$$

Although not explicitly stated, the micrographs presented suggested this OR was exhibited by lamellae similar to the Type I morphology. The Type II lamellae were possibly not present in this alloy or overlooked by the authors. Subsequently, the precipitate/matrix orientation relationships between the Type I and II lamellae and austenite matrix in the HP-Nb1 and HP-Nb2 alloys were analyzed using EBSD. EBSPs were obtained from the primary NbC precipitates and the austenite matrix directly adjacent to each precipitate. Using HKL Technology's Flamenco software the Euler angles (ϕ_1, ϕ_2, Φ) describing the crystallographic orientation of the phase with respect to a reference axis system, could be calculated from the indexed EBSPs. These angles were used to calculate a 3x3 orientation matrix for each analysis point and subsequently the misorientation between any two points could be calculated using the following matrix operation:

$$[A][B]^{-1} = [M]$$

Where A and B are the orientation matrices of locations in phases A and B and M is the misorientation matrix:

$$[M] = \begin{bmatrix} m_{11} & m_{12} & m_{13} \\ m_{21} & m_{22} & m_{23} \\ m_{31} & m_{32} & m_{33} \end{bmatrix}$$

The orientation relationship (OR) between location A and B is then:

$$[m_{11} \quad m_{21} \quad m_{31}]_A \quad // \quad [1 \quad 0 \quad 0]_B$$
$$[m_{21} \quad m_{22} \quad m_{23}]_A \quad // \quad [0 \quad 1 \quad 0]_B$$
$$[m_{31} \quad m_{32} \quad m_{33}]_A \quad // \quad [0 \quad 0 \quad 1]_B$$

The misorientation angle θ and axis [u v w] between points A and B can also be calculated using the following equation:

$$\theta = \cos^{-1}\left(\frac{m_{11}+m_{22}+m_{33}-1}{2}\right)$$

$$[u\ \ v\ \ w] = [m_{23} - m_{32}\ \ \ m_{31} - m_{13}\ \ \ \ \ m_{12} - m_{21}]$$

By considering the 24 crystallographic equivalents for the cubic system, the disorientation (i.e. the variant with the smallest value of θ about axis UVW) can be determined [37]. Alternatively, the Euler angles can be converted to a quaternion representation of the crystals orientation with respect to the reference axis. The misorientation and disorientation can subsequently be calculated following the procedures used by Sutton and Balluffi [38] and Hanson [39].

Indexing of the EBSPs was carried out in the same manner used during the primary carbides phase identification. However, greater care was required when fitting the experimental and simulated patterns. Small rotations or translations of the simulated pattern with respect to the experimental pattern (which were less important during phase identification) introduced error into the calculated disorientation. The main source of error originated from the initial determination of the Kikuchi band positions. Determination of the band positions can be carried automatically using a Hough transform of the captured EBSP. The Hough transform converts the bands to geometrically related bright regions in a greyscale image which can be digitally detected. The relative positions of these bright regions are then used to calculate band lines representative of the original EBSP Kikuchi bands. Alternatively the bands positions can be entered manually by the user drawing reference lines directly on the captured EBSP. Following the determination of the band line positions, the crystallographic orientation of the phase (with respect to the sample reference axis) can be calculated. Therefore, as these lines are used when indexing the patterns, slight discrepancies during their positioning induces error when calculating the disorientation for the precipitate-matrix pair.

Quantification of the magnitude of disorientation error was carried out by first indexing a representative precipitate-matrix pair manually and calculating the disorientation. In general,

inputting the reference lines manually was more accurate in comparison to the automated method, allowing the simulated and experimental patterns to be matched almost exactly (i.e. creating a reference precipitate-matrix pair for comparison). Manually positioning of the band lines and indexing of each pattern was repeated a further 10 times. Repetitive manual indexing was necessary to quantify the user induced error and determine the level of diligence required to maintain an acceptable standard during indexing of a large number of patterns. Finally, the patterns were indexed automatically. The disorientation calculated for each indexing cycle was then compared to the reference precipitate-matrix disorientation. For manual indexing, the error in the calculated disorientation ranged from 0.5-2 degrees. Provided that care was taken during positioning of the band lines the error could be maintained below 2 degrees. The error for automatic indexing was found to be highly dependent on the quality of the experimental EBSP. The error was typically less than 5 degrees for EBSPs where the contrast between separate Kikuchi bands was high (for example the patterns shown in Figure 4.5(c)). The error was exacerbated when the pattern quality was poor (for example Figure 4.5(g)) and could be as large as 10 degrees. Overall, defining the position of the Kikuchi bands manually was more accurate and relatively less dependent on the quality of the EBSP; thus it was used when indexing all EBSPs.

For both morphologies, a minimum of two precipitate-matrix pairs were analysed within each colony of lamellae. In total over 100 colonies were analysed (Type I-40, Type II-62). Since separate plates within a particular colony were similarly orientated, an average orientation was calculated for each group. Generally disorientations between grains of less than 10-15 degrees are considered to be low angle grain boundaries where the disorientation can be accounted for by an array of tilt and screw dislocations [37, 40]. For this work, a near cube-cube orientation relationship was defined by a disorientation of less than 10 degrees.

The histogram in Figure 4.10 (a) shows the magnitude of disorientation for each Type I precipitate-matrix pair. Calculation of the OR using EBSD and the matrix operations described previously confirmed that all Type I lamellae located at dendrite boundaries obtain a cube-cube OR (on all sides of the lamella) with the austenite matrix. In cases where the lamellae were located on grain boundaries, the OR was exhibited with the grain which contained the associated colony of lamellae (i.e. the grain where nucleation of the colony occurred). 37 of the 40 Type I colonies analysed were found to deviate from the ideal cube-cube relationship by less than 10 degrees. Two of the three remaining colonies were within 0.5° of the 10 degree limit and the greatest value of disorientation

was 13.7 degrees. All precipitates within a single colony had the same crystallographic OR with a typical variance of less than 1 degree. Selected area diffraction of the Type I lamella and adjacent matrix confirmed the cube-cube OR (Figure 4.11). The slight rotation of the $\{220\}_{\gamma}$ reflections with respect to the $\{220\}_{NbC}$ reflections indicates some of the variance (from the ideal cube-cube OR) as determined from the EBSD OR data was a result of true disorientation between the two crystals as opposed to pattern indexing inaccuracies.

Analysis of the Type II lamellae using the previously explained matrix operations yielded complex expressions of OR such as:

$$[\overline{25}\ \overline{13}\ 25]_{NbC} \,||\, [1\ 0\ 0]_{\gamma}$$

$$[11\ \overline{25}\ 0]_{NbC} \,||\, [0\ 1\ 0]_{\gamma}$$

Although a consistent (but complex) crystallographic orientation relationship may exist between this example precipitate-matrix pair, rational pairs of parallel planes and directions from this information are not obvious. Therefore, calculation of the disorientation for each precipitate-matrix pair was performed to determine if clustering around a common angle occurred. Crystallographic orientation relationships with disorientations matching this common disorientation angle could then be confirmed or rejected by plotting the crystal pair with respect to each other in a stereographic projection and checking if the candidate poles were coincident.

Precipitates within each single colony of Type II lamellae were found to share a similar orientation with respect to the matrix (typical disorientation variance of less than 1 degree). However, between groups the disorientation varied significantly (Figure 4.10 (b)). The high level of variance between groups of these precipitates indicates that they are not likely to obtain a consistent orientation relationship with the matrix. Though there may seem to be slight clustering around 55 degrees, it must be noted that these plots only display the magnitude of disorientation and not the axis of rotation. This axis was found to vary considerably when comparing precipitate-matrix pairs with a disorientation of approximately 55°.

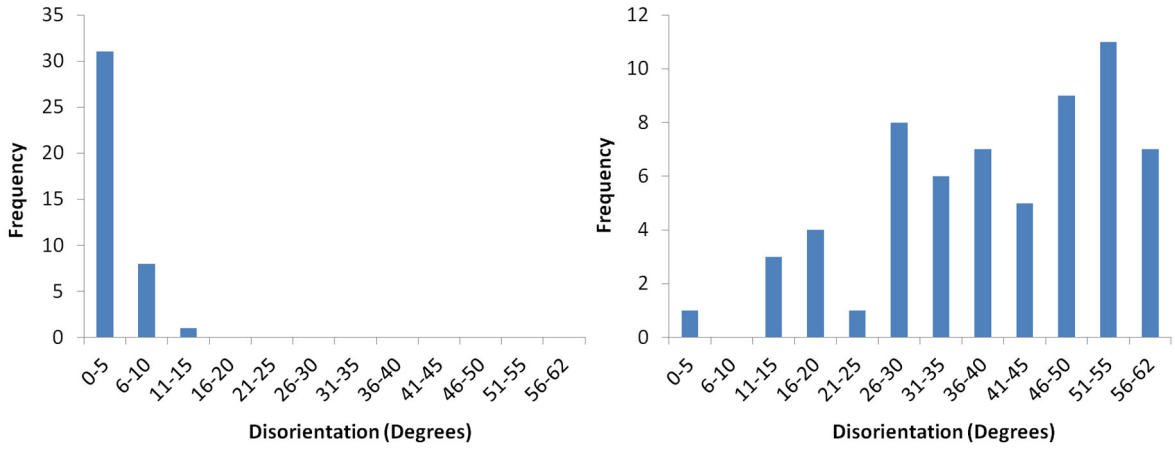

(a) (b)

Figure 4.10 - Histograms showing the frequency of occurrence of disorientation measured between NbC-matrix pairs for the (a) Type I lamellae (b) Type II lamellae.

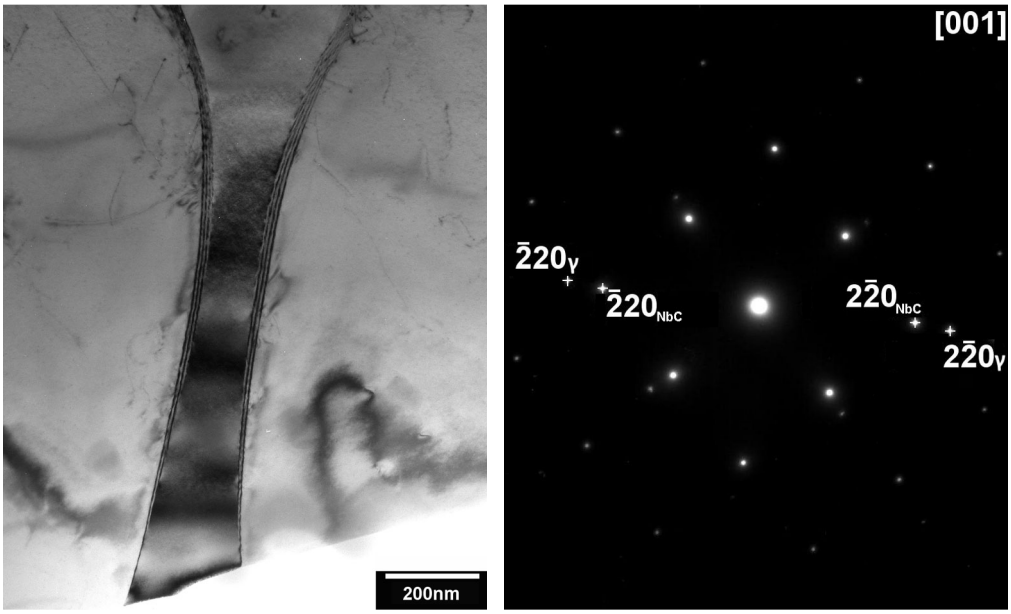

(a) (b)

Figure 4.11 - (a) TEM brightfield image of a Type I lamellae; (b) SAD [001] zone axis pattern taken with the selected area aperture overlapping the lamella and directly adjacent austenite shown in (a).

Deep etching of the samples indicated that both morphologies adhere to an overall growth plane. TEM trace analysis of linear/planar features was performed to determine if the Type I and II lamellae obtain a specific crystallographic 'habit plane'. Trace analysis was performed on precipitates three Type I and five Type II lamellae (with each lamellae belonging to a separate dendrite group) following the processes described by Hirsch *et al.* [41] and Loretto [42]. A minimum of three and maximum of four zone axes were indexed for each precipitate and, after correction for rotation, superimposed onto the TEM bright field image taken at each orientation.

For the Type I lamellae, traces were taken along the broad faces of lamella which had a sufficient linear edge (such as the precipitate shown in Figure 4.12 (a)). The traces taken from four widely separated zone axes for this precipitate are plotted on the stereographic projection shown in Figure 4.12 (b). Each trace can be seen to intersect at the (100) pole. The linear edges of three Type I lamellae were examined, all of which exhibited a {100} habit plane. Unique crystallographic habit planes are commonly observed in lamellar eutectics, a low energy interfacial plane between the precipitate and matrix is obtained to minimise the total interfacial energy [43]. Such low energy interfaces allow the lamellar morphologies to achieve relatively large interfacial areas (in comparison to rod-like eutectics).

The traces determined from the Type II lamella shown in Figure 4.13 (a) and (b) are plotted in Figure 4.13 (c). As the precipitates had no linear edge from which to take the traces, an estimated centreline for each lamella was defined as the trace direction. As shown in Figure 4.13 (c), the general area of intersection of the traces shows no strong association with any low index habit plane. Furthermore, the area of intersection for each set of traces was inconsistent. Trace analysis was performed on five Type II lamellae each showing similar inconsistencies indicating that it is unlikely that these plates obtain a rational habit plane over large areas. However, the complex shape of these precipitates and presence of the interfacial Cr_7C_3 causes great difficultly when attempting to consistently determine the trace direction when viewing the precipitate from different crystallographic orientations. Analysis of deviations in measured trace direction of approximately 5 degrees resulted in a worst case intersection deviation on the stereographic projection of between 10-15 degrees. Therefore, the sum of small errors in defining the trace for each zone could be largely contributing to the resulting ambiguities on the stereographic projection.

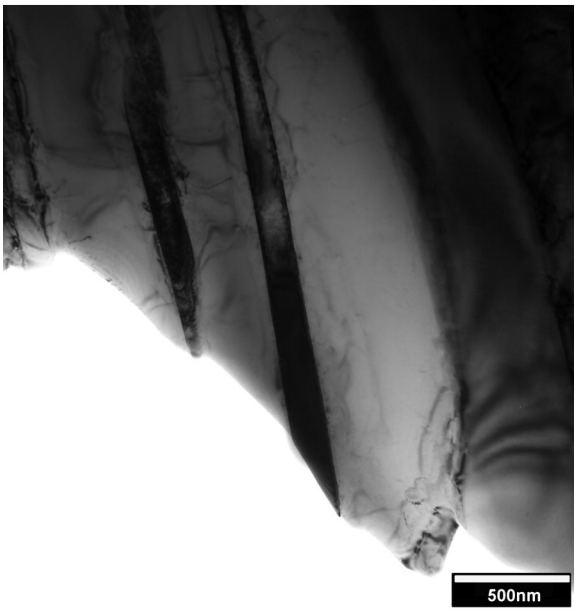

(a)

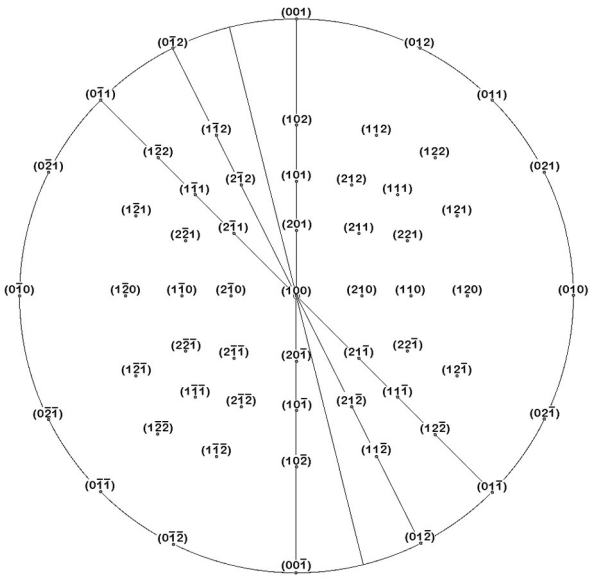

(b)

Figure 4.12 - (a) Representative bright field transmission electron micrograph of the Type I lamellae (b) Stereographic projection centered about $(100)_{NbC}$ showing the intersection of four traces taken from (a).

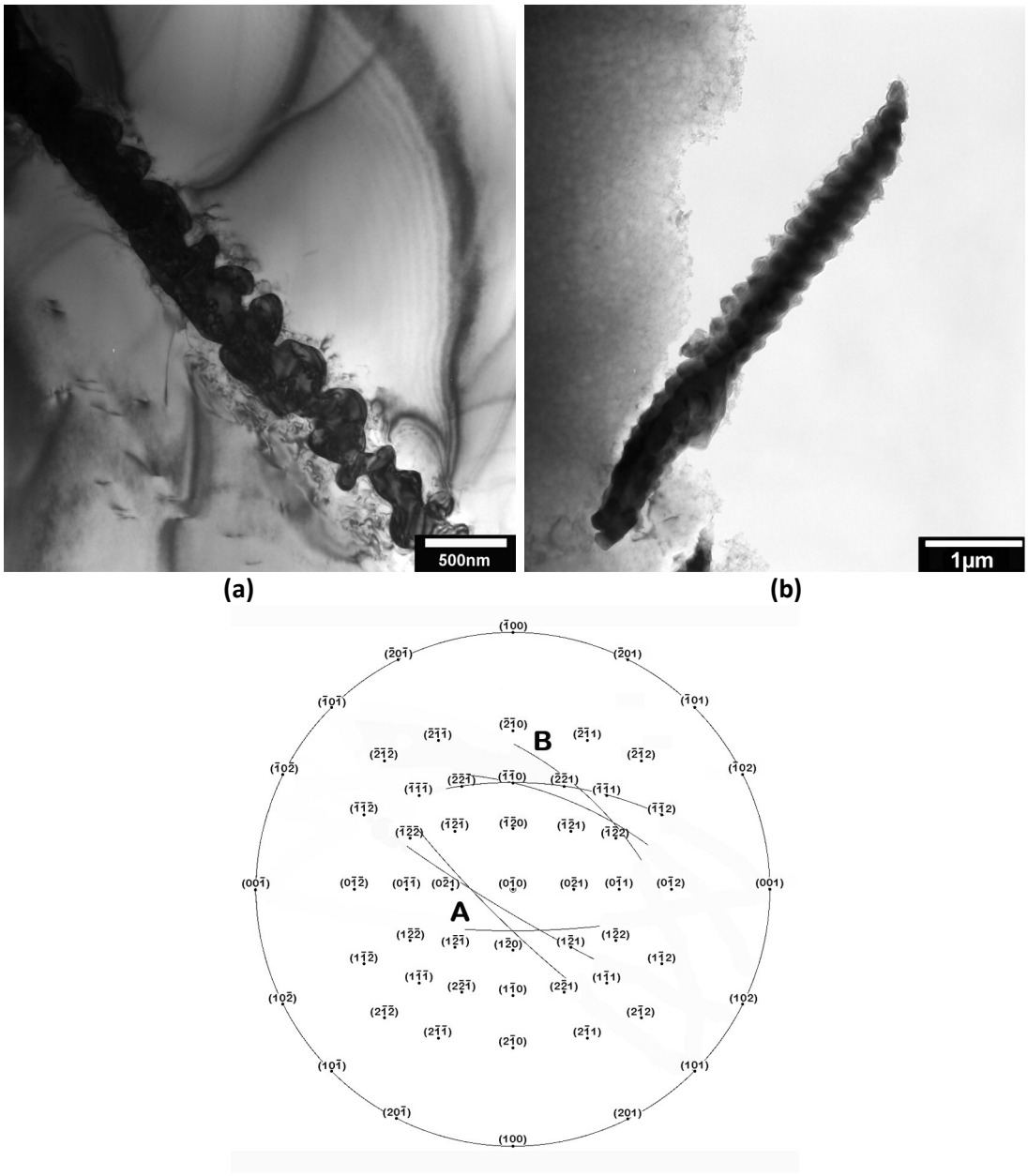

Figure 4.13 - (a)&(b) Representative bright field transmission electron micrographs of the Type II lamellae; (c) Stereographic projection centered about $(0\bar{1}0)_{NbC}$ showing the intersections of the three traces from precipitate (a) and of the three traces from precipitate (b).

High magnification observations of the Type I lamellae revealed the ledged appearance of the NbC interface (Figure 4.14 (a) and (b)). Figure 4.14(b) shows a TEM bright-field image of the Type I lamella with the beam direction parallel to the $[1\bar{1}4]_{NbC}$ zone axis, where the ledges appear to be viewed end-on. Ledges similar in appearance to the Type I ledges have been presented by Garmong and Rhodes in Al-$CuAl_2$ eutectic composites [44]. The eutectic interface was thought to consist of broad faces of low-energy orientation interface separated by relatively higher energy ledges. The broad faces were typically misoriented with respect to the macroscopic lamellar interface. Therefore, deviations of the apparent macroscopic interface (such as the observed curvature of the Type I lamellae in Figure 4.8(a)) from a hypothetical low-energy orientation would not necessarily negate the boundary being low energy. On average the broad faces of Type I ledges were misoriented by approximately 12 degrees with respect to the lamella's macroscopic habit plane. Due to slight angular deviations between successive ledges, no conclusive habit plane could be determined when performing trace analysis on the broad face the ledges. The misorientation observed between the broad faces of these ledges (Figure 4.14 (b)) and the low magnification habit plane, indicates the ledges do not obtain the same (100) habit plane.

Arrayed ledges allow the macroscopic interfacial plane to deviate, resulting in the curved appearance exhibited by the lamellae in three-dimensions (Figure 4.8 (a) and Figure 4.9 (a) to (c)). Without these ledges the crystallographic orientation of the lamellae with respect to the matrix would need to rotate significantly in order to achieve the observed interfacial curvature. EBSD analysis of individual lamella determined the average maximum disorientation variance (with respect to the matrix) along the curved regions of each plate was less than 1 degree. Although the variation along the length of the plates could be attributed to error during indexing of the EBSPs, visible rotation between subsequent patterns taken along the length of the same lamella was common. As previously discussed, true disorientation between the NbC and austenite was also apparent when performing selected area diffraction (Figure 4.13 (b)). These slight deviations from the ideal cube-cube orientation relationship can be explained by the association of dislocations with the ledges [44]. Arrays of edge and screw dislocations (similar to those used to describe low-angle tilt or twist grain boundaries [40] would accommodate slight rotations of the NbC lattice with respect to the austenite matrix. While not shown in Figure 4.14 (a) and (b), dislocations were often observed within the matrix surrounding the Type I lamellae.

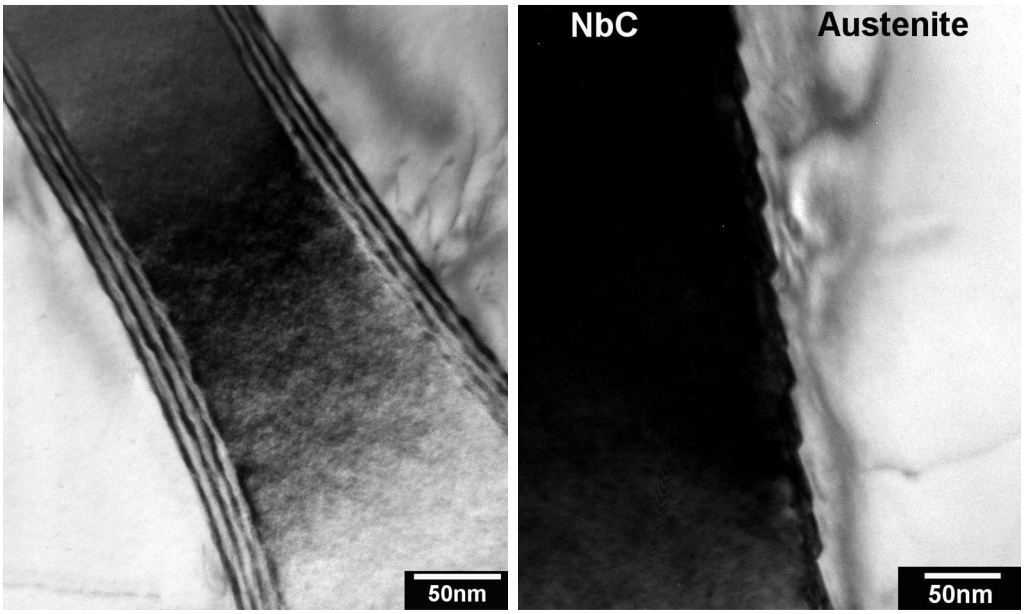

(a) (b)

Figure 4.14 - (a) & (b) High magnification bright field TEM images of the Type I lamellae showing the ledged appearance of the of the lamellae's broad faces.

While the Type II morphology has not been reported for Nb-rich MC precipitates in HP or HK alloys, similar morphologies have been observed in directionally solidified and single crystal Ni-based alloys [7-9, 45, 46]. Tin and Pollock [7-9] identified three distinctly different morphologies (blocky, Chinese-script and nodular) that Ta-rich MC precipitates exhibited in various single crystal Ni-based alloys. The nodular morphology appeared similar to the Type II lamellae when viewing the TaC precipitates in two and three dimensions. However, in three-dimensions, the nodular precipitates did not exhibit the same level of porosity observed for the Type II lamellae. In alloys containing carbon additions, the script and nodular lamellae were dominant, with only few blocky precipitates typically observed. The ratio of script to nodular precipitates varied significantly with respect to overall alloy composition. However, no single alloying element could be attributed to altering the script-nodular preference. While both morphologies existed throughout the cross-section, the nodular TaC precipitates were the sole precipitates situated around freckle chain defects[19]. These defects are a direct result of compositional gradients within the "mushy-zone", indicating the importance of local

[19] Large compositional gradients within the solid/liquid "mushy zone" of high-refractory content alloys often develop due to microsegregation within uni-directional single crystal castings. This compositional gradient can cause the density of the solute contained within the mushy zone to be less than the density of the bulk liquid. Since single crystal castings are typically uni-directionally solidified in an orientation opposite to gravity, a liquid-density inversion can evolve between the solute and bulk liquid. Once the buoyancy forces associated with the lower density solute reach a critical value (unknown), the system becomes unstable and localized plumes of flowing solute erupt from within the mushy zone. These plumes subsequently cause erosion and/or fracture of the secondary dendrite arms which leads to the formation of freckle chains upon solidification [7].

melt composition with respect to morphology. While the overall solidification conditions were kept constant, local compositional variations were present due to the turbine blades complex geometry. However, these local variations did not significantly affect the script-nodular preference.

The morphological dependence of MC carbides with respect to the solidification conditions has been studied extensively in directionally solidified (DS) Ni-based alloys [45-53]. Typically, individual studies kept the overall alloy composition constant while varying the solidification conditions at the γ/L interface. Due to the large range of Ni-based alloys, the MC composition varied significantly between studies (for example, (TaTi)C [45], (TiMo)C [46], (NbTi)C [50], (NbTiW)C [53]). Although composition is known to affect the MC morphology [34, 35, 36], generally all MC compositions followed similar trends with respect to the solidification conditions.

Previous work has shown that the thermal gradient at the γ/L interface (G_L) and overall growth rate (R) play an important role in determining morphology of the advancing γ/L interface, thus influencing the MC growth characteristics. In general, blocky morphologies dominated at high G_L/R ratios while low ratios promoted script morphologies similar to the Type I lamellae. When G_L remained constant, the MC precipitates formed blocky morphologies at growth rates below 5μm/s which progressively transitioned to script morphologies at growth rates between 5-100μm/s [8, 45-47, 49]. The exact growth rate where the transition occurred in each Ni-based alloy was specific to the composition of the MC precipitate. Under splat cooling conditions, fine faceted blocks (thought to be present in the melt prior to quenching) were dominant [36, 48]. Melt treatments such as superheating have also been reported to induce the blocky to script transition [51].

Low growth rates (R<1μm/s) induced planar growth fronts where nucleation and growth of the blocky precipitates occurred in the liquid ahead of the advancing γ/L interface. These blocky MC precipitates typically exhibited the equilibrium octahedral shape [8, 35, 36, 48]. Cellular growth fronts occurred at intermediate growth rates (1<R<5μm/s) with the MC precipitates exhibiting irregular blocky or elongated platelet morphologies [36, 45, 48-50]. This irregular shape often appeared to be a transitional morphology where both blocky and script-like features could be identified. In some cases the irregular morphologies contained titanium-nitrogen or hafnium rich cores which had heterogeneously nucleated on aluminium and/or magnesium oxide melt inclusions [48, 49, 52]. Dendritic growth fronts associated with higher growth rates (R>5μm/s) resulted in higher levels of solute super-saturation within the interdendritic regions, promoting the formation of a MC/γ eutectic. The favourable conditions for the growth of dendritic carbide branches results in

the Chinese-script morphology [36, 45, 48, 49]. Existing octahedral precipitates were also observed to preferentially grow along the $<100>_{MC}$ direction, resulting in arrowhead-shaped plates or rods [8, 36, 47].

Although script morphologies similar to the Type I lamellae were commonly observed in DS Ni-based alloys, morphologies similar to the Type II lamellae were rare. Nodular rods rich in titanium and tantalum were observed on the grain boundaries of a DS alloy when the growth rate was reduced below 0.5µm/s [46]. These rods were thought to have grown ahead of the γ/L interface into the solute rich liquid until the MC + γ eutectic composition was reached. Coarsening of the rod due to the eutectic reaction subsequently formed the nodules. However, no significant compositional or structural analysis was performed on the blocky, script or nodular morphologies observed in this alloy. Thus, it is difficult to attribute the nodular rods formation to either the local solidification rate or local melt composition.

Based on the preceding observations, the Type I lamellae are believed to be formed during eutectic solidification. The orientation relationship, crystallographic habit plane, and interfacial ledges exhibited by the lamellae are commonly observed attributes of lamellar eutectics [43]. Initially, rejection of niobium and carbon to the melt during dendritic growth of the austenite occurs until the MC + γ eutectic composition is reached. Nucleation of the Type I lamella likely occurs on the existing austenite dendrite; setting the NbC/austenite orientation relationship. The {100} habit plane is formed during cooperative growth of the NbC lamellae and austenite, thus allowing the precipitates to obtain a high surface area while minimising the total free energy associated with the boundary. These observations are consistent with those exhibited by the TaC, (TaTiNb)C and (TiNb)C script morphologies in Ni-based alloys [7-9, 47, 52-54]. Preferred orientation relationships and habit planes have also been observed in other alloy systems containing lamellar precipitates (for example, the Bagaryatsky or Pitsch-Petch relationships of pearlite [55]). Selection of these unique OR's and habit planes is thought to be influenced by the nucleation site, interfacial energy and relative growth rates of the constituents [43].

For the Type II lamellae, nucleation and growth is not well understood. Similar to the blocky morphology in Ni-based alloys [7-9], the Type II lamellae neither obtained a rational or consistent OR with the matrix suggesting these precipitates also form in the liquid ahead of the γ/L interface. The higher Type II prevalence in the HP-Nb2 alloy indicates that higher niobium contents (when comparing the HP-Nb1 and HP-Nb2 alloys- Table 4.1) further promotes nucleation in the liquid. The

differing solidification conditions (as suggested by the differing grain size) may also influence the morphology preference. However, controlled solidification studies (where the solidification rate, thermal gradient, alloy composition and inclusion content are systematically varied) are necessary to determine the factors which dominate the final morphology preference. While the overall alloy composition and solidification conditions likely influence the relative proportion of the Type II lamellae, the present evidence (i.e. no consistent NbC/γ OR, overall planar growth and undulations within the plates) suggests the morphology is determined by the nucleation site and local solidification conditions.

In alloy systems favouring lamellar growth, fibrous or degenerate structures (similar to the Type II lamellae) have been observed when the precipitates nucleation event appears to have not occurred on the already solidified dendrites [43]. Nucleation of the Type II lamellae possibly occurs heterogeneously on oxide inclusions within the liquid. Spherical Ti-rich nuclei surrounded by blocky (NbTi)C precipitates have been observed in the HP-NbTi alloy (Chapter 5) and IN718 Ni-based alloys [10, 48, 50, 56]. Sub-micron aluminium, magnesium and zirconium oxide inclusions were detected within these Ti-rich nuclei, indicating the presence of Al_2O_3, MgO or ZrO melt inclusions [10, 50, 56]. These Ti-rich nuclei acted as the nucleation site for the blocky (NbTi)C precipitates. Optical examination of the directionally solidified IN718 casting revealed that both blocky and 'script-like' carbides were present within the directional casting. Blocky carbides were more prevalent at the start of the casting with the emergence of the script carbides only being observed approximately 27mm from the start of the casting. Initially, the blocky and script carbides existed simultaneously. However, the script carbides became the sole morphology as distance from the start of the casting increased. Differential thermal analysis (DTA) indicated that precipitation of the blocky carbides occurred in the liquid at ~1563K while precipitation of the script carbides proceeded as a eutectic reaction at ~1443K. The disappearance of the blocky carbides was attributed to the consumption of available nucleation sites within the remaining melt. The precipitation sequence of the Type I and II morphologies in the present alloys is thus believed to occur in a similar manner. Nucleation of the Type II morphology proceeds until the available nucleation sites are exhausted. Sufficient niobium subsequently remains in solution to promote formation of the eutectic Type I morphology. The different Type I/Type II ratios can be explained by an initial disparity between the inclusion content within each alloy.

While no evidence of oxide inclusions associated with the Type II lamellae has been found, it is unlikely these sub-micron inclusions are isolated to the HP-NbTi alloy. The surrounding TiC nuclei in the HP-NbTi alloys (Chapter 5) typically causes the inclusions to be easily distinguishable within the blocky (NbTi)C. Nucleation of blocky (TiMo)C precipitates on alumina inclusions was also observed in directionally solidified IN100 alloys [46]. Therefore, the absence of titanium could make it inherently difficult to locate these oxide inclusions in the HP-Niobium alloys.

During growth of the blocky morphology in HP-NbTi alloys, the addition of titanium possibly increases the (NbTi)C/L interfacial energy. Therefore, the blocky morphology is formed to minimise the surface area to volume ratio. The Type II NbC/liquid interfacial energy in the HP-Nb alloys is possibly comparatively lower than the (NbTi)C/L interface, allowing the Type II lamellae to form a morphology with a significantly higher surface area.

Alternatively, the array of undulations within the plane of the plates is possibly influenced by partitioning molybdenum concentrating at the advancing NbC/L interface. Once a threshold concentration capable of affecting the growth profile has been reached the growth direction may be forced to alter. Similar modifications of eutectic morphologies (faceted to fibrous) due to elemental poisons (such as sodium or strontium in the Al-Si system) are well known in the literature [43]. The overall planar growth of the Type II lamellae is likely related to a preferred growth direction aligning with local melt thermal and chemical gradients.

Summary and Conclusions

Two compositionally unique HP-Nb alloys were subjected to detailed microstructural analysis. Generally, the base compositions of the two as-cast HP-Nb alloys were similar and within the manufacturers specified compositional tolerances. However, the HP-Nb1 niobium content (0.44wt.%Nb) was below the manufacturer's minimum specified concentration (0.6wt.%Nb). The niobium content between the alloys also varied significantly with the HP-Nb2 alloy (0.92wt.%Nb) containing approximately double the concentration present in the HP-Nb1 alloy.

Macroscopically, each alloy exhibited completely columnar grain structures, with the HP-Nb1 alloys grain size appearing significantly coarser than the HP-Nb2 alloy. Microscopically both alloys consisted of a interdendritic network of primary precipitates surrounded by an austenite matrix. A combination of EDS, and EBSD phase identification was used to confirm that the primary network was composed of alternating groups of chromium-rich Cr_7C_3 and niobium-rich NbC precipitates. No evidence of precipitation within the austenite matrix was observed (through SEM and TEM observations) in the as-cast condition.

When viewed at magnifications below 1000x the NbC appeared to exhibit the reported 'Chinese-script' morphology consisting of lamellar NbC plates surrounded by austenite. Higher magnification observations of two-dimensional as-polished and three-dimensional deep etched samples revealed the primary NbC distribution contained two distinctly different morphologies. Both had a FCC ($Fm\bar{3}m$) crystal structure (a=0.44nm). No location preference with respect to dendrite boundary, grain boundary or wall position was observed for either morphology. The attributes for each morphology can be summarised as follows:

Type I

- Has solid lamellar plates which share a relatively planar interface with the adjacent austenite,
- $<100>_{NbC}||<100>_{\gamma}$, $\{100\}_{NbC}||\{100\}_{\gamma}$ orientation relationship,
- Broad faces of the plates exhibited a {100} habit plane,
- No Cr_7C_3 located between the NbC/austenite interfaces
- Nano-scale ledges observed on the broad faces of the lamellae.

Type II

- Has web-like or reticulated plates,
- No consistent, rational NbC/matrix orientation relationship,
- The plates often adhered to an overall growth plane, but exhibit no crystallographically rational habit plane,
- More prevalent than the Type I lamellae, particularly so in the Nb2 alloy which contained a higher niobium content,
- Molybdenum was found present in the NbC composition,
- Cr_7C_3 was identified between the NbC and austenite,
- NbC interface did not exhibit nano-scale ledges.

The preceding observations suggest the morphological difference is determined by the solidification conditions that each type of lamellae experience. In the case of Type I lamellae, nucleation occurs on the existing austenite dendrite followed by eutectic growth of the lamellae with the austenite. The Type II lamellae likely nucleate in the liquid ahead of the γ/L interface, prior to the formation of the Type I lamellae. Local melt thermal and chemical gradients subsequently dominate growth of the Type II lamellae resulting in the observed array of undulations within the plates and overall planar growth.

Chapter References

[1] Kubota Metal Corporation (1999). *KHR 35C alloy data sheet.* Revision 06/99. Kubota Metal Corporation: Ontario, Canada.

[2] ASM International (2002). *Paralloy H39Wmaterial datasheet.* Orange, New Jersey: Alloy Digest Inc., ASM International®.

[3] Davis, J. R. (Ed.). (1997). *ASM Specialty Handbook: Heat-Resistant Materials.* Materials Park, Ohio: ASM International, pp. 200-218.

[4] Barbabela, G. D., de Almeida, L. H., da Silveira, T. L & Le May, I. (1991). *Role of Nb in Modifying the Microstructure of Heat-Resistant Cast HP Steel.* Materials Characterization, 26:pp. 193-197.

[5] de Almeida Soares, G. D., de Almeida, L. H., da Silveira, T. L. & Le May, I. (1992). *Niobium Additions in HP Heat-Resistant Cast Stainless Steels.* Materials Characterization, 29: pp. 387-396.

[6] Ibañez, R. A. P., Soares, G. D. A., de Almeida, L. H. & Le May, I. (1993). *Effects of Si Content on the Microstructure of Modified-HP Austenitic Steels.* Materials Characterization, 30: pp. 243-249.

[7] Tin, S., Pollock, T. M. & Murphy, W. (2001). *Stabilization of Thermosolutal Convective Instabilities in Ni-Based Single-Crystal Superalloys: Carbon Additions and Freckle Formation.* Metallurgical and Materials Transactions A, 32A: pp. 1743-1751

[8] Tin, S. & Pollock, T. M. (2003). *Stabilization of Thermosolutal Convective Instabilities in Ni-Based Single-Crystal Superalloys: Carbide Precipitation and Rayleigh Numbers.* Metallurgical and Materials Transactions A, 34A: pp. 1953-1967.

[9] Tin, S & Pollock, T. M. (2003). *Phase instabilities and carbon additions in single-crystal nickel-base superalloys.* Materials Science and Engineering A, 348: pp. 111-121.

[10] Wu, X. Q., Jing, Y. G., Zheng, Z. M., Yao, W. Ke. & Hu, Z. Q. (2000). *The eutectic carbides and rupture strength of 25Cr20Ni heat-resistant steel tubes centrifugally cast with different solidification conditions.* Materials Science and Engineering A, 293: pp. 252-260.

[11] Caballero, F. G., Imizcoz, P., Lopez, V., Alvarez, L. F. & Garcia de Andrés, C. (2007). *Use of titanium and zirconium in centrifugally cast heat resistant steel.* Materials Science and Technology, 23: pp. 528-534.

[12] Zaghloul, M. B., Shinoda, T. & Tanaka, R. (1977). *Relation between Structure and Creep Rupture Strength of Centrifugally Cast HK40 Steel.* Transactions of the Iron and Steel Institute of Japan, 17(1): pp. 28-36.

[13] Hou, W. T. & Honeycombe, R. W. K. (1985). *Structure of Centrifugally cast austenitic steels: Part 2 Effects of Nb, Ti and Zr.* Materials Science and Technology, 1(5): pp. 390-397.

[14] Krauss, G. (2005). *Steels: Processing, Structure, and Performance.* 2nd ed. Materials Park, Ohio: ASM International®.

[15] Bhadeshia, H. K. D. H. & Honeycombe, R. W. K. (2006). 3rd ed. Amsterdam, Boston: Elsevier, Butterworth-Heinemann.

[16] Rayaprolu, D. B. & Jaffrey, D. (1990). *Kinetics of Ostwald ripening – an analysis of models and errors with reference to MnS inclusions in steel.* Materials Characterization, 24(3): pp. 245-273.

[17] Villars, P. (Ed.) & Cenzual, K. (Ed) (2008). *Pearson's Crystal Data: Crystal Structure Database for Inorganic Compounds.* (Version 1.0) [Computer software]. Materials Park, Ohio, U. S. A.: ASM International®.

[18] Lui, B. X., Wang, J., Cheng, X. Y. & Fang, Z. Z. (1991). *Two Metastable Simple Structured Metal Carbides Formed by Carbon Ion Implantation.* Physica Status Solidi A, 128: pp. 71-75.

[19] Fuchart, D., Chaudouet, P., Fruchart, R., Rouault, A. & Sénateur, J. P. (1984). *Etudes structurales de composes de type cémentite: Effet de l'hydrogène sur Fe_3C suivi par diffraction neutronique. Spectrométrie Mössbauer sur $FeCo_2B$ et Co_2B dopes au ^{57}Fe.* Journal of Solid State Chemistry, 51: pp. 246-252.

[20] Hellbom, K. & Westgren, A. (1933). *Den rombiska kromkarbiden kristallbyggnad.* Sven. Kem. Tidskr, 45: pp. 141-150.

[21] Bouzy, E., Bauer Grosse, E. & Le Caer, G. (1993). *NaCl and filled Re_3B-type structures for two metastable chromium carbides.* Philosophical Magazine B, 68: pp. 619-638.

[22] Berkane, R., Gachon, J. C., Charles, J. & Hertz, J. (1987). *A THERMODYNAMIC STUDY OF THE CHROMIUM-CARBON SYSTEM.* Calphad: Computing Coupling Phase Diagrams Thermochemistry, 11: pp. 375-382.

[23] McClune, F. (1986). *New X-Ray Powder Diffraction Patterns from the JCPDS Associateship.* Powder Diffraction, 1: pp.77-99.

[24] Yakel, H. L. (1987). *Atom distributions in Tau-Carbide Phases: Fe and Cr Distributions in $(Cr_{23-x}Fe_x)C_6$ with $x=0, 0.7_4, 1.7_0, 4.1_3$, and 7.3_6.* Acta Crystallographica, 43: pp. 230-238.

[25] Lönnberg, B. & Lundström, T. (1988). *Crystal Growth of Solid Solutions of the Group IV-VI Transition Metals Monocarbides from Molten Aluminium.* Chemica Scripta, 28(1): pp. 25-32.

[26] Yvon, K. & Parthé, E. (1970). *On the Crystal Chemisty of the Close Packed Transition Metal Carbides. I. The Crystal Structure of the ζ-V, Nb and Ta Carbides.* Acta Crystallographica, 26: pp. 149-153.

[27] Christensen, A. N. (1985). *Vacancy Order in Nb_6C_5.* Acta Chemica Scandinavica, 39: pp. 803-804.

[28] Savitskii, E. M., Efimov, Y. V., Mikhailov, B. P. & Moroz, E. A. (1979). *REACTION OF SILICIDE, GERMANIDES, AND OTHER PHASES OF THE A15 STRUCTURAL TYPE WITH CARBON.* Inorganic Materials, 15: pp. 515-518.

[29] Lönnberg, B. & Lundström, T. (1985). *THERMAL EXPANSION AND PHASE ANALYTICAL STUDIES OF Nb_2C.* Journal of Less-Common Metals, 113: pp. 261-268.

[30] Khaenko, B. & Sivak, O. P. (1990). *Order structure of niobium monocarbide.* Soviet Powder Metallurgy and Metal Ceramics, 35: 653-655.

[31] Li, F., Yang, J., Xue, D. & Zhou, R. (1995). *X-ray Diffraction and Mössbauer studies of the $(Fe_{1-x}Ni_x)_4$ compounds ($0 \leq x \leq 0.5$).* Journal of Magnetism and Magnetic Materials, 151: pp. 221-224.

[32] Karen, P. (2004). *Chemistry and Thermodynaics of the Twin Charge-Ordering Transitions in $RBaFe_2O_{5+z}$ Series.* Journal of Solid State Chemistry, 177: pp. 281-292.

[33] Knitter, S. & Binnewies, M. (1999). *Chemical vapour transport of Solid Solution. 5 Chemical Transport of MnS/ZnS, FeS/ZnS, and FeS/MnS Mixed Crystals.* Zeitschrift für Anorganische und Allgemeine Chemie, 625: pp. 1582-1588.

[34] de Almeida, L. H., Ribeiro, A. F. & Le May, I. (2003). *Microstructural Characterization of modified 25Cr-35Ni centrifugally cast steel furnace tubes.* Materials Characterization, 49: pp. 219-229.

[35] Chen, Q. Z., Jones, C. N. & Knowles, D. M. (2002). *Effect of alloying chemistry on MC carbide morphology in modified RR20720 and RR2086 SX superalloys.* Scripta Materialia, 47: pp. 669-675.

[36] Bhambri, A. K., Kattamis, T. Z. & Morral, J. E. (1975). *Cast Microstructure of Inconel 713C and its Dependence on Solidification Variable.* Metallurgical Transactions B, 6B: pp. 523-533.

[37] Randle, V. (1993). *The Measurement of Grain Boundary Geometry.* Bristol, Philadelphia: Institute of Physics Publications, pp. 22-28.

[38] Sutton, A. P. & Balluffi, R. W. (1996). *Interfaces in Crystalline Materials.* Gloucestershire: Oxford Science Publications, pp. 17-20.

[39] Hanson, A. (2006). *Visualizing Quaternions.* San Francisco: Morgan Kaufmann, pp. 52-54.

[40] Porter, D. A., Easterling, K. E. & Sherif, M. Y. (2009). *Phase Transformations in Metals and Alloys.* 3rd ed. Boca Raton, Florida: CRC Press, pp. 117-121.

[41] Hirsch, P. B., Howie, A., Nicholson, R. B., Pashley, D. W. & Whelan, M. J. (1965). *Electron Microscopy of Thin Crystals.* 2nd ed. London: Butterworths, pp. 311-315.

[42] Loretto, M. H. (1994). *Electron Beam Analysis of Materials.* 2nd ed. London: Chapman & Hall, pp. 252-253.

[43] Elliott, R. (1977). *Eutectic Solidification.* International Metal Reviews, 22(1): pp. 161-186.

[44] Garmong, G., Rhodes, C. G. & Spurling, R. A. (1973). *Crystallography and Morphology of As-Grown and Coarsened Al-Al_3Ni Directionally Solidified Eutectic.* Metallurgical Transactions, 4(3): pp. 707-714.

[45] Sun, W. R., Lee, J. H., Seo, S. M., Choe, S. J. & Hu, Z. Q. (1999). *The eutectic characteristic of MC-type carbide precipitation in a DS nickel-base superalloy.* Materials Science and Engineering A, 271: pp. 143-149.

[46] Fernandez, R., Lecomte, J. C. & Kattamis, T. Z. (1978). *Effect of Solidification Parameters on the Growth Geometry of MC Carbide in IN-100 Dendritic Monocrystals.* Metallurgical Transactions A, 9A: pp. 1381-1386.

[47] Chen, J., Lee, J. H., Jo, C. Y., Choe, S. J. & Lee, Y. T. (1998). *MC carbide formation in directionally solidified MAR-M247 LC superalloy.* Materials Science and Engineering A, 247: pp. 113-125.

[48] Lui, L. & Sommer, F. (1994). *EFFECT OF SOLIDIFICATION CONDITIONS ON MC CARBIDES IN A NICKEL-BASE SUPERALLOY IN 738 LC.* Scripta Metallurgica et Materialia, 30: pp. 587-591.

[49] Seo, S. M., Kim, I. S., Lee, J. H., Jo, C. Y., Miyahara, H. & Ogi, K. (2008). *Microstructural Evolution in Directionally Solidified Ni-Base Superalloy IN792 + Hf.* Journal of Materials Science & Technology, 24(1): pp. 110-114.

[50] Formenti, A., Eliasson, A., Mitchell, A. & Fredriksson, H. (2005). *Solidification Sequence and Carbide Precipitation in Ni-Base Superalloys IN718, IN625 and IN939.* High Temperature Materials and Processes, 24: pp. 239-258.

[51] Yin, F. S., Sun, X. F., Li, J. G., Guan, H. R. & Hu, Z. Q. (2003). *Effects of melt treatment on the cast structure of M963 superalloy.* Scripta Materialia, 48: pp. 425-429.

[52] Al-Jarba, K. A. & Fuchs G. E. (2004). *Effect of carbon additions on the as-cast microstructure and defect formation of a single crystal Ni-based superalloy.* Materials Science and Engineering A, 373: pp. 255-267.

[53] Yang, J., Zheng, Q., Sun, X., Guan, H. & Hu, Z. (2006). *Morphological evolution of MC carbide in K 465 superalloy.* Journal of Materials Science, 41: 6476-6478.

[54] Wills, V. A. & McCartney, D. G. (1991). *A comparative study of solidification features in nickel-base superalloys: microstructural evolution and microsegregation.* Materials Science and Engineering A, 145: pp. 223-232.

[55] Zhou, D. S. & Shiflet, G. J. (1992). *Ferrite: Cementite Crystallography in Pearlite.* Metallurgical Transactions A, 23A: pp. 1259-1269.

[56] Nunes. F. C., de Almeida, L. H., Dille, J., Delplancke, J. -L., Le May, I. (2007). *Microstructural Changes caused by yttrium addition to NbTi-modified centrifugally cast HP-type stainless steels.* Materials Characterization, 58: pp. 132-142.

Chapter 5 Microstructural Characterization of the As-cast Niobium and Titanium Modified HP Alloys

'Micro-additions' of titanium to the HP-Nb composition are used to produce the HP-NbTi alloy (or more commonly known in industry as the HP-Micro grade). As discussed in Chapter 2, the use of 'micro-additions' further increased the HP alloy's creep strength in comparison to HP alloys containing sole additions of niobium. The HP-NbTi alloy's increased creep resistance has been partially attributed to the modifying effect that titanium has on the as-cast primary precipitate network. Similar to the analysis of the HP-Nb alloy, analysis of the as-cast HP-NbTi alloy initially focused on identifying the primary chromium and niobium rich phases, the precipitate morphologies and quantities of each constituent for comparison with those reported in the literature. However, it became apparent that many aspects of the niobium-titanium rich precipitates had been overlooked by previous studies. Due to the importance of these precipitates with respect to the HP-NbTi alloy's creep resistance, a more comprehensive analysis of the (NbTi)C precipitates was completed before continuing with the characterization of the aged HP-Nb and HP-NbTi microstructures.

The format for the following chapter parallels that used in Chapter 4. Section 5.1 discusses the HP-NbTi alloy's macrostructure. Section 5.2 presents detailed analysis of the HP-NbTi alloy's microstructure where particular attention has been paid to the (NbTi)C precipitates (i.e. the precipitates specifically affected by the addition of titanium). The characterization methods employed include optical microscopy (OM), high resolution scanning electron microscopy (SEM), energy dispersive X-ray spectroscopy (EDS), electron backscatter diffraction (EBSD), high resolution transmission electron microscopy (TEM) and selected area diffraction (SAD).

5.1 Macroscopic Observations of the Niobium and Titanium Modified HP Alloys

5.1.1 Chemical Composition of the HP-NbTi1 and HP-NbTi2 Tubes

Two separate centrifugally cast HP-NbTi reformer tubes were subjected to detailed microstructural analysis. The two HP-NbTi alloys were manufactured in separate heats by Schmidt + Clemens (alloy designation CA4852-Micro [1]). Schmidt + Clemens specify the CA4852-Micro alloy as a "25Cr-35Ni-Nb(Cb) alloy with micro-alloyed constituents". This specification has led to the CA4852-Micro alloy being commonly referred to industry as the HP-MA or HP-Micro alloy. Although these 'micro' alloying elements are not stated in the alloy's specification, Kirchheiner and Woelpert [2] suggest these micro-additions could include titanium, zirconium, and rare earth elements such as cerium. The 'micro' identifier supposedly refers to the comparatively small quantity (proprietary) of these additions.

The chemical composition of each tube, as determined by inductively coupled plasma atomic emission spectroscopy (ICP-AES), and the manufacturer's specification are shown in Table 5.1. Similar to the HP-Nb alloys the ICP-AES analysis was performed on a limited amount of material, thus the composition is expected to vary slightly from point-to-point within the length of the tubes. Since the –MA or –Micro modifiers can refer to numerous different combinations of 'micro' additions, this naming convention was considered too imprecise for the purposes of this thesis. Alternatively, the –NbTi convention used in the ASM Heat Resisting Materials Handbook [3] has been implemented. Niobium and titanium have been included as these elements were the major additions observed in the two CA4852-Micro tubes. These elements also have a significant influence on the HP alloy's primary carbide network. As the two HP-NbTi tubes were produced from two separate heats (i.e. each tube has a slightly different chemical composition and experienced different solidification conditions) the two tubes have been designated as HP-NbTi1 and HP-NbTi2 alloys.

Table 5.1 - Chemical composition of the as-cast HP-NbTi1 and HP-NbTi2 alloys as determined by ICP-AES. Balance Fe. A = 'Additions' (as specified by Schmidt + Clemens), N/S = not specified.

wt.%	C	Ni	Cr	Nb	Ti	Si	Mn	W	V	Co	Mo
Specified	0.43	35	25	1.5	A	1.4	1	N/S	N/S	N/S	N/S
HP-NbTi1	0.42	33.9	24.8	0.9	0.05	1.18	1.1	0.5	0.03	0.02	0.01
HP-NbTi2	0.44	35.6	25.1	0.85	0.08	1.72	0.45	0.49	0.03	0.02	0.02

Typical of cast materials, the 25Cr/35Ni base compositions of the HP-NbTi1 and HP-NbTi2 tubes did not match the manufacturer's specification exactly. However, the base composition lies within the acceptable range specified for HP alloys stated in the ASTM A608 standard [4]. The niobium content for both HP-NbTi alloys was below the specified 1.5wt.%. Compositional analysis of four samples taken at 0.9 meter intervals along the length of the HP-NbTi2 tube indicated the niobium within this tube varied by a maximum of +/- 0.11wt.%. Thus, it is considered unlikely that the average niobium content within each HP-NbTi tube was near the specified content. Niobium concentrations reported for similar alloys in the literature ranged from 0.3-1.27wt.%, indicating the concentrations shown in Table 5.1 are typical of HP-NbTi alloys [3, 5-8]. However, as niobium and titanium causes the partial replacement of the primary Cr_7C_3 network with (NbTi)C precipitates [5], the niobium content in the HP-NbTi1 and HP-NbTi2 alloys will reduce the level of Cr_7C_3 replacement with (NbTi)C precipitates in comparison to an alloy containing 1.5wt.%Nb.

As shown in Table 5.1, the only 'micro' addition used in the two CA4852-Micro tubes was titanium. The concentration of titanium observed in the HP-NbTi1 and HP-NbTi2 alloys was similar to the concentrations reported for HP-NbTi alloys in the literature (0.02-0.1wt.%) [3, 5]. In general, the optimum level of niobium and titanium with respect to the HP-NbTi alloy's creep properties is relatively unknown. Shinoda *et al.* [9] determined the maximum creep rupture strength was obtained for HK alloys with Ti/(Ti + Nb) or (Ti + Nb)/C ratios approximately equal to 0.3. However, accelerated creep testing of the HK-NbTi alloys was conducted solely on as-cast material. Since the HK and HP alloys undergo significant microstructural evolution during high temperature exposure (including transformation of the primary MC precipitates to G-phase and widespread precipitation of $Cr_{23}C_6$ and TIC within the matrix), the optimum niobium to titanium ratio likely differs depending on the ageing conditions experienced by each alloy prior to accelerated creep testing. Thus, currently it is unknown if the Ti/(Ti + Nb) or (Ti + Nb)/C ratios within the alloys studied in this research (0.05, 2.26 – HP-NbTi1, 0.09, 2.11 – HP-NbTi2) represent the alloying content which maximizes the HP-NbTi alloy's

high temperature strength during service in reforming furnaces or if further strength increases can be gained by varying the niobium and titanium content.

Interestingly each alloy contained approximately 0.5wt.% of tungsten. As stated in Chapter 4, intentional additions of tungsten have been used in other HP alloy variants to improve the alloy's high temperature strength [3]. Generally, niobium and/or titanium are absent in HP alloys where additions of tungsten between 4-5wt.% have been used. However, alloys containing between 0.25-0.5wt.% niobium, 0.1-0.3wt.% titanium and 0.5wt.% tungsten have been reported in the literature [3, 8].

Segregation of tungsten to the austenite matrices of various nickel-based superalloys has been detailed by Tin and Pollock [10, 11]. Tungsten was believed to provide increased creep resistance through solid-solution strengthening of the matrix. Assuming the tungsten similarly segregates to the austenite matrix during solidification of the HP-NbTi alloy, the tungsten would likely be beneficial to the alloy's creep resistance. Additionally, since the tungsten is believed to be largely confined to the matrix, it is unlikely that the tungsten will significantly alter the intended effects of niobium and titanium on the primary carbide network.

Other 'micro' additions, such as zirconium and rare earths, were not detected in these particular CA4952-Micro alloy tubes.

5.1.2 HP-NbTi Tube Macrostructures

Figure 5.1 (a) and (b) are low magnification optical micrographs showing the through-wall grain structure of the as-cast HP-NbTi1 and HP-NbTi2 alloys. The HP-NbTi1 tube was the only alloy in the present work that exhibited a mixed columnar-equiaxed grain structure (~80% columnar, 20% equiaxed). It must be noted that the wall thickness of the HP-NbTi1 tube was 2mm greater than the three other tubes (approximately the size of the equiaxed region). Thus, the larger section size of the HP-NbTi1 alloy possibly contributed to the emergence of equi-axed grains on the tube's inner wall. The casting conditions experienced by the HP-NbTi2 induced a 100% columnar grain structure.

As discussed in Chapter 4, the rupture strength, minimum creep rate and creep ductility of HK and HP reformer tubes are dictated by the grain structure (e.g. size and shape) and the properties of the primary and secondary precipitates (e.g. the number of phases present and the average size, distribution and volume fraction of each constituent) [5, 9, 12-15]. These properties of the as-cast structure are influenced by the alloys chemical composition and the casting conditions. Therefore, although the HP-NbTi1 and HP-NbTi2 tubes originated from the same manufacturer and are based on an identical alloy specification, the differing casting conditions (as evidenced by the differing grain structures in Figure 5.1 (a) and (b)) and chemical compositions (Section 5.1.1) will affect each tube's rupture life, minimum creep rate and creep ductility. While the absolute magnitude of the creep resistance of individual HP-NbTi castings is likely affected by the casting conditions and chemical composition, the general evolution of each separate casting's creep properties with respect to ageing temperature and time (e.g an increase or decrease in the tubes rupture life) is expected to be similar to the properties observed in the as-cast and aged HP-NbTi1 and HP-NbTi2 samples.

Both the columnar and equiaxed regions of the tubes were subjected to microstructural analysis. All creep samples were taken from the center of the tube wall (i.e. the columnar regions of the tubes). As stated in Chapter 1, only the HP-NbTi1 alloy was subjected to long-term unstressed isothermal ageing. The aged HP-NbTi1 samples were subsequently subjected to microstructural analysis (conducted at the University of Canterbury) and accelerated creep testing (performed by Quest Integrity Group Ltd., Wellington, New Zealand). In contrast to the HP-NbTi1 alloy, the HP-NbTi2 was only subjected to accelerated creep testing. Testing of this alloy was completed at the University of Canterbury and will be discussed in Chapter 7.

(a)

(b)

Figure 5.1 - Low magnification optical micrographs showing the macrostructure of (a) HP-NbTi1 (b) HP-NbTi2. (Etchant: Marbles reagent)

5.2 Microscopic Observations of the Niobium and Titanium Modified HP Alloys

5.2.1 Identification of the As-Cast Primary Precipitates

Representative optical and scanning electron micrographs of the primary precipitate network in the HP-NbTi alloys are shown in Figure 5.2 (a) and (b). Similar to the HP-Nb alloy, the interdendritic network consists of groups of chromium (dark grey) precipitates separated by and blocky niobium-titanium rich (white) precipitates. At the magnifications shown the matrix appears to be free of intragranular precipitation. Manganese sulfide inclusions (arrowed) were also present in the HP-NbTi alloys. These inclusions were of similar size to those observed in the HP-Nb alloys (~1µm in diameter) and represented less than 0.1% of the total analysed area.

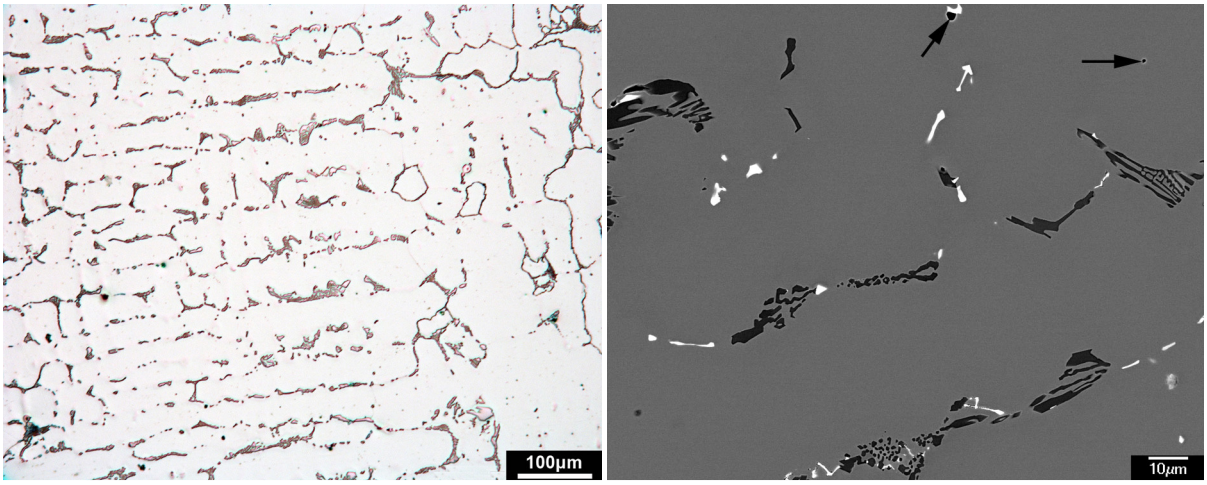

(a) **(b)**

Figure 5.2 - Representative optical (a) and backscatter electron (b) micrographs of the HP-NbTi alloys. As a result of the atomic number contrast in (b) the niobium-titanium rich phases appear white while the chromium rich phases appear dark grey in the austenite matrix.

Figure 5.4 (a)-(d) shows the chemical composition (as determined by EDS) of the phases labelled A, B, C and D in Figure 5.3 (a) and (b). The composition of phases A and B were nearly identical to that determined from the Cr_7C_3 and austenite matrix in the HP-Nb alloys. Analysis from the blocky niobium-rich phase revealed the presence of titanium (typically 2-4wt.%). The change in morphology from lamellar (HP-Nb) to blocky has been attributed to the additional titanium increasing the

precipitate/matrix surface energy, causing these precipitates to obtain the blocky morphology to minimise the total surface area [5, 7]. Generally, the 0.05wt.% titanium addition to the HP-NbTi1 alloy was contained within the blocky precipitates (i.e. no TiC precipitates were observed). However, as shown in Figure 5.4 (b), cuboidal TiC precipitates identical in contrast to the MnS inclusions were observed in the HP-NbTi2 alloy. Typically the MnS and TiC precipitates could be easily distinguished by their different morphologies (MnS globular, TiC cuboidal).

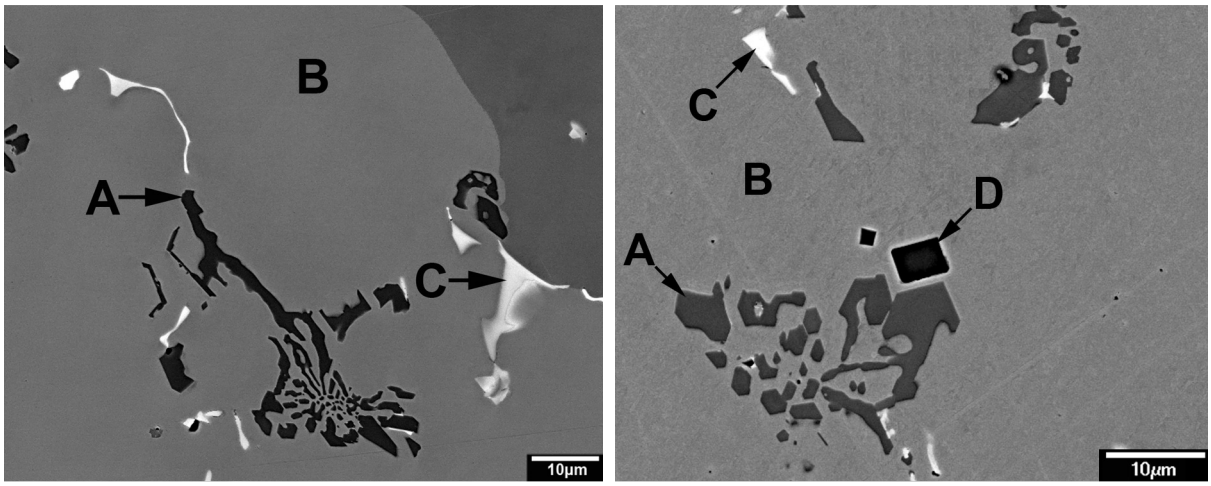

(a) (b)

Figure 5.3 – (a) & (b) Backscatter electron images of as-cast HP-NbTi primary precipitates in the as-polished condition.

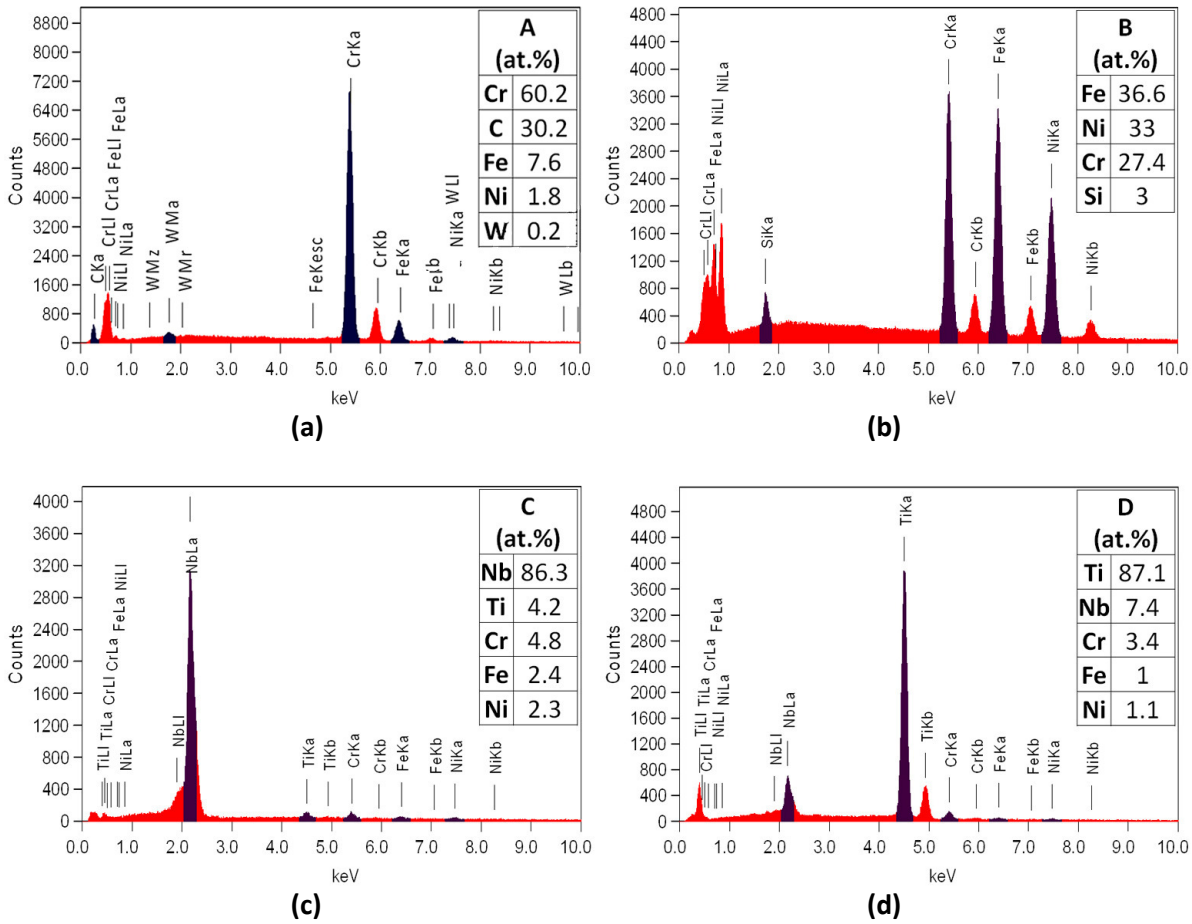

Figure 5.4 – (a)-(d) Chemical composition of phases A-D as determined by energy dispersive X-ray spectroscopy.

EBSD was used to identify the phases present in the as-cast HP-NbTi1 and HP-NbTi2 alloys. A total of 20 EBSPs were obtained from each phase at separate positions across each tube's wall thickness. Since the composition of the primary precipitate phases and matrix were similar in both the HP-Nb and HP-NbTi alloys, the crystal structure database compiled for the HP-Nb alloys (Chapter 4) could be also used for phase identification in the HP-NbTi alloys. However, due to the presence of titanium carbides in the HP-NbTi2 alloy, the additional Ti-rich crystal structures shown in Table 5.2 were added to the database. All phases in Table 5.2 were compiled using the Pearson's Crystal Database [16].

Figure 5.5 (a) to (h) show representative examples of the EBSPs taken from the phases labelled A, B C and D in Figure 5.4 (a) and (b). In agreement with the HP-Nb alloys, all chromium-rich precipitates (A) obtained the Cr_7C_3 crystal structure. In contrast, the chromium rich phase has been identified as either Cr_7C_3 or $Cr_{23}C_6$ in previous studies of centrifugally cast HP-NbTi alloys [5, 17, 18]. The

chromium-rich precipitates were exclusively identified as the orthorhombic Cr_7C_3 phase in independent studies by Voicu *et al.* [17] (using X-ray diffraction) and Laigo *et al.* [18] (using EDS, WDS and EBSD). Conversely, De Almeida, Ribeiro, and May identified the face centered cubic (FCC) $Cr_{23}C_6$ structure using selected area diffraction [5].

Studies conducted on the HP-Nb alloys determined the crystal structure obtained by chromium-rich precipitates is dependent on the solidification rate during casting and the concentration of niobium [19]. The Cr_7C_3 crystal structure (*Pnma*) was solely identified in statically cast HP-Nb alloys with niobium concentrations of 0.69 and 1.23wt.%. Increasing the niobium content from 1.23 to 1.97wt.% (in statically cast alloys) caused the chromium-rich precipitates obtain the $Cr_{23}C_6$ ($Fm\bar{3}m$) crystal structure. In contrast, the higher cooling rate experienced by centrifugally cast HP-Nb alloys containing 1.97wt.% niobium resulted in the chromium-rich precipitates obtaining the Cr_7C_3 crystal structure [20]. The slight differences between the HP-NbTi1 and HP-NbTi2 alloys' casting conditions (based on their respective macrostructures - Figure 5.1 (a) and (b)) and chemical composition (Table 5.1) was not sufficient to induce a similar Cr_7C_3/$Cr_{23}C_6$ transition observed in the literature.

The niobium-titanium rich (C) and titanium-rich precipitates (D) showed good agreement with the simulated diffraction patterns for the NbC and TiC face centred cubic (FCC) crystal structures ($Fm\bar{3}m$). EBSD is not able to distinguish between phases with similar lattice parameters (a_{NbC}=0.446nm, a_{TiC}=0.433 [16]) and crystal structures, thus the complementary used of EDS is useful when differentiating between phases C ((NbTi)C) and D (TiC). Reported values for the (NbTi)C lattice parameter typically lie between the NbC and TiC values ($a_{(NbTi)C}$=0.437nm [5]).

As expected, (regardless of wall position and grain morphology) EBSD confirmed the matrix (B) was austenite ($Fm\bar{3}m$). Identical to the HP-Nb alloys, the Mn-S rich inclusions obtained the MnS ($Fm\bar{3}m$) crystal structure.

Table 5.2 - List of candidate crystal structures used for EBSD identification of the primary precipitates.

Phase	Crystal System	Space Group	Lattice parameters a, b, c (nm)			α, β, γ (°)			Ref.
TiC	Cubic	$Fm\bar{3}m$	0.433	0.433	0.433	90	90	90	21
TiC	Hexagonal	$R\bar{3}m\ h$	0.294	0.294	0.734	90	90	120	21
$TiC_{0.62}$	Hexagonal	$R\bar{3}m\ h$	0.306	0.306	1.491	90	90	120	22
Ti_2C	Cubic	$Fd\bar{3}m$	0.86	0.86	0.86	90	90	90	23
Ti_8C_5	Hexagonal	$R\bar{3}m\ h$	0.612	0.612	1.49	90	90	120	24
TiC_2	Cubic	$Pm\bar{3}m$	0.313	0.313	0.313	90	90	90	25

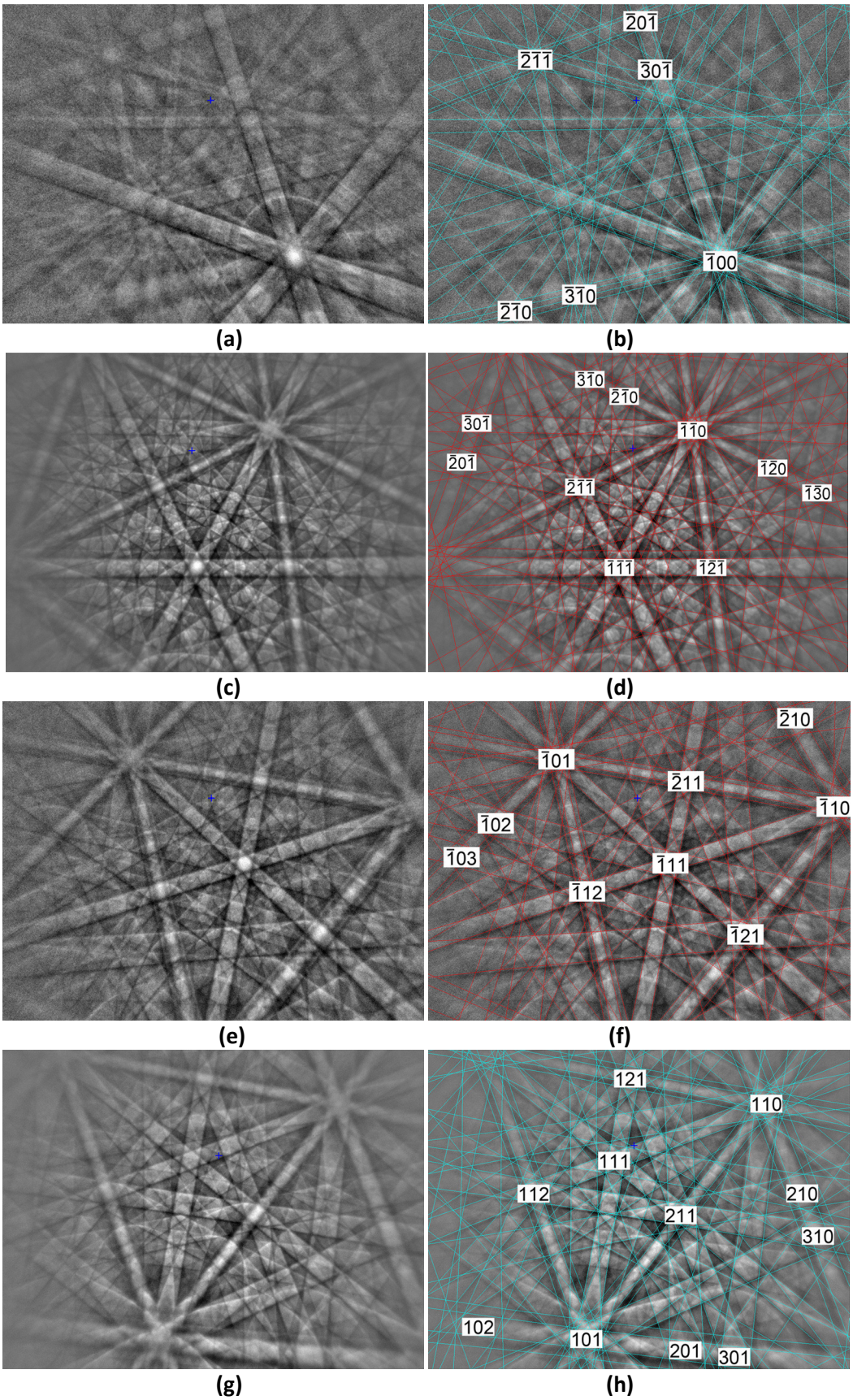

Figure 5.5 - Experimentally determined electron backscatter diffraction patterns (EBSP) and the corresponding simulated patterns for the (a) & (b) Cr_7C_3. (c) & (d) (NbTi)C, (e) & (f) TiC and (g) & (h) austenite crystal structures.

5.2.2 Fragmentation of the HP-Nb and HP-NbTi alloys' As-cast Primary Precipitate Networks

Previous studies [5] have partially attributed the superior creep resistance exhibited by the HP-NbTi alloy (in comparison to the HP-Nb alloys) to the "less continuous" (or more fragmented) as-cast primary carbide network. Towards the end of the tubes creep life, nucleation and growth of creep voids occurs on the primary precipitate/matrix interface. The growth and coalescence of these voids leads to the production of macroscopic cracks, which ultimately lead to failure of the tube [26, 27]. Alloying additions which increase the fragmentation of the as-cast primary network are believed to be beneficial to the HP alloy's creep properties [28] as it results in a less continuous path for creep crack growth during tertiary creep in comparison to HP alloys with highly connected primary precipitate networks.

Judgements of the primary precipitate network fragmentation (or alternatively network connectivity) have typically been based on qualitative comparison of low magnification optical images taken from two-dimensional polished sections of the HP-Nb and HP-NbTi alloys. Figure 5.6 (a) and (b) show representative optical micrographs (similar to those reported by previous studies [5]) taken at the mid-wall position of the HP-Nb1 and HP-NbTi1 alloys. Qualitative comparison of these micrographs suggests the primary precipitate network in the HP-NbTi1 alloy is less continuous than the HP-Nb1 alloy. However, it must be noted that the perception of the primary network's fragmentation can change significantly depending on how the microstructure is being observed. For example, precipitates that appear connected at the magnification shown in Figure 5.6 (a) and (b) often show no connection when viewed at higher magnifications. As discussed in Chapter 4, the as-cast primary precipitate network within the HP-Nb alloy is composed of alternating groups of Cr_7C_3 and NbC precipitates (Figure 5.7 (a)). Similarly, the HP-NbTi alloy's primary precipitate network is also composed of alternating groups of Cr_7C_3 and (NbTi)C precipitates (Figure 5.7 (b)). These alternating groups are often indistinguishable at magnification given in Figure 5.6 (a) and (b). Hence, at low magnifications these groups can appear as larger continuous precipitates, masking the fragmentation within each group.

Although the area fraction of NbC and (NbTi)C precipitates was similar in the HP-Nb and HP-NbTi alloys (~0.85-0.9%), there were significantly fewer (NbTi)C precipitates (~25% of the NbC population).

Thus, the individual blocky (NbTi)C precipitates were significantly larger than the NbC lamella (~3.5μm^2 and 0.5μm^2 respectively). However, as a group, the fine colonies of NbC lamellae were larger than the individual (NbTi)C precipitates (based on qualitative comparisons). As shown in Figure 5.6 (a), the NbC lamellae merge when viewing the HP-Nb alloy's primary precipitate network at low magnifications using the optical microscope (i.e. the colony appears as a single large precipitate). Similarly, individual precipitates within the Cr_7C_3 groups are indistinguishable in Figure 5.6 (a). Thus, the close association of the relatively large alternating groups of Cr_7C_3 and NbC precipitates causes the HP-Nb alloy's primary network to appear highly connected. In contrast, the (NbTi)C precipitates can often be individually resolved in Figure 5.7 (b) (arrowed). As a result, the fragmentation between individual (NbTi)C precipitates was generally more easily noticeable in comparison to the NbC lamellae reducing the apparent connectivity of the primary precipitate network in the HP-NbTi alloy.

While the fragmentation of the chromium and niobium rich precipitates becomes more apparent in Figure 5.7 (a) and (b), the NbC colonies generally appear more effective at linking the groups of Cr_7C_3 precipitates together than the blocky (NbTi)C precipitates creating a perception of a more connected primary precipitate network. However, increasing the magnification further revealed that individual NbC and (NbTi)C precipitates were equally rarely connected to the Cr_7C_3. Hence, the HP-Nb and HP-NbTi alloys' primary precipitate network could potentially be equally fragmented despite the more connected appearance of the HP-Nb alloy's network at lower magnifications.

Interestingly, both the lamellar and blocky niobium rich precipitates often shared common interfaces with the Cr_7C_3 in three-dimensions (i.e. the niobium and chromium rich primary precipitates typically came into contact in three-dimensions in both alloys). In some cases, individual (NbTi)C precipitates contacted Cr_7C_3 precipitate that belonged to separate groups. Figure 5.8 (a) and (b) show secondary electron micrographs of the as-cast HP-Nb1 and HP-NbTi1 alloys after deep etching of the samples in glyceregia for 10 hours (note: Figure 5.6 to Figure 5.8 are not taken from the exact same region). Unfortunately, due to the complexity of the primary precipitate networks in each alloy, it was impossible to determine which alloy exhibited the least continuous primary network when observing the deep etched samples. However, observations of the polished surfaces of the Cr_7C_3, NbC and (NbTi)C precipitates were similarly common in both deep etched samples suggesting that precipitate fall-out due to the networks fragmentation was rare for both alloys (i.e. each alloys network appeared relatively well connected).

While the addition of titanium to the niobium-rich precipitates clearly modifies the size and shape of these precipitates which may lead to an increase in the overall fragmentation of the primary network in the HP-NbTi alloy, it is unknown if the modification to the niobium-rich precipitates has any effect on the fragmentation of the Cr_7C_3 precipitates. Simply assuming that any increase in the primary network's fragmentation is beneficial to the alloy's creep properties is possibly misleading as this assumption suggests that all precipitate/matrix interfaces within the HP alloy (regardless of the precipitate phase) are equally intolerable to creep damage. However, previous work characterizing creep voids in ex-service HP-NbTi tubes determined that voids preferentially nucleate on low registry $Cr_{23}C_6$/austenite interfaces [26, 27]. Therefore, the overall fragmentation of the primary precipitate network may not directly influence the alloy's creep properties. Instead, the fragmentation of niobium and chromium rich precipitate networks (and susceptibility of each phase to creep damage) may have to be considered separately.

Although serial sectioning of the as-cast HP-Nb and NbTi alloys could provide further useful insight into the three-dimensional fragmentation of the HP-Nb and HP-NbTi alloy's primary precipitate network, such time consuming analysis specifically on the as-cast material was impractical within the timeframe of the current project. It also needs to be realised that the as-cast primary precipitate phases participate in multiple phase transformations (e.g. Cr_7C_3-to-$Cr_{23}C_6$, MC-to-G-phase and MC-to-η-carbide – Chapter 6 and 7) depending on the alloy composition and ageing temperature. Thus, it is likely necessary to analyze both the as-cast and aged precipitate networks in order to determine if the fragmentation of the as-cast primary precipitate network has an effect of the network's fragmentation after ageing. However, prior to attempting such time consuming and complex analysis of the primary precipitate networks' in the HP-Nb and HP-NbTi alloys, it is strongly believed that focus must be initially placed on gaining a detailed understanding of the susceptibility of each precipitate/matrix interface combination to creep damage (i.e. void nucleation, coalescence and macroscopic crack growth).

Based on the preceding evidence, it is believed that there is no conclusive evidence to suggest the primary precipitate network is more fragmented in the HP-NbTi alloy than in the HP-Nb alloy. Obtaining a link between primary network fragmentation and creep performance is beyond the scope of this project. While there appears no doubt that HP-NbTi alloys outperform HP-Nb alloys in accelerated creep tests (which could be related to the level of primary network fragmentation in each alloy), it is also possible that other factors (such as the fine distribution of stable secondary precipitates [5, 8, 15]) dominate the improved creep performance of HP-NbTi alloy.

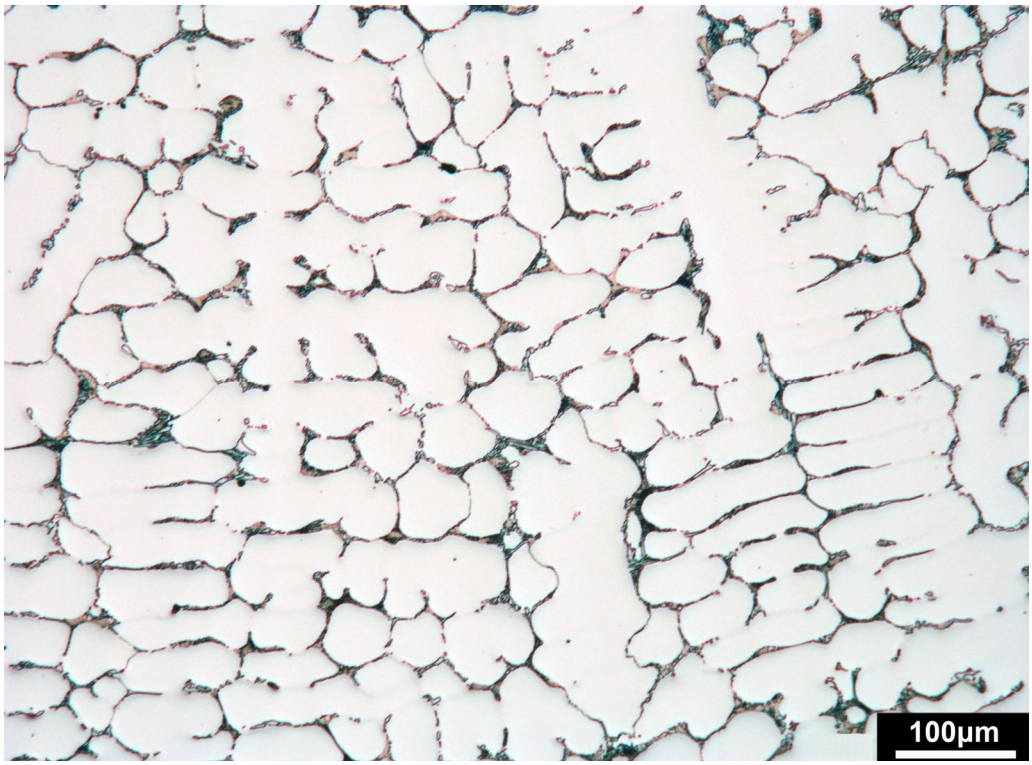

(a)

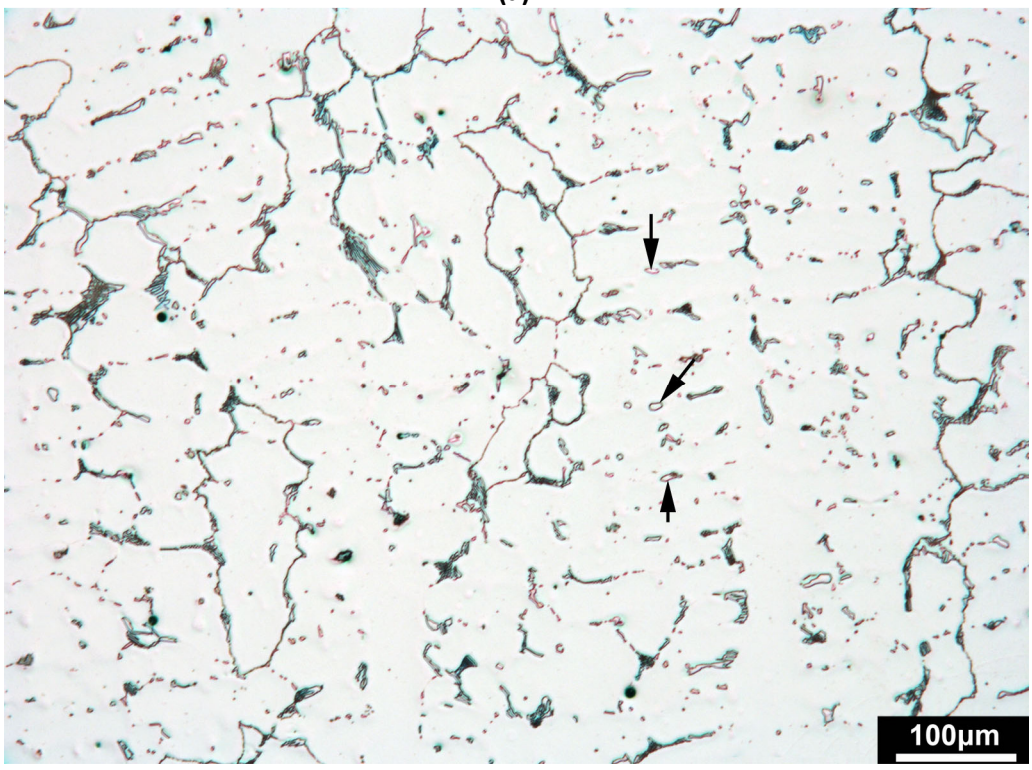

(b)

Figure 5.6 – Optical Micrographs showing the primary precipitate networks at the mid-wall position in the as-cast (a) HP-Nb1 and (b) HP-NbTi1 tubes. The arrows in (b) indicate the blocky (NbTi)C precipitates.

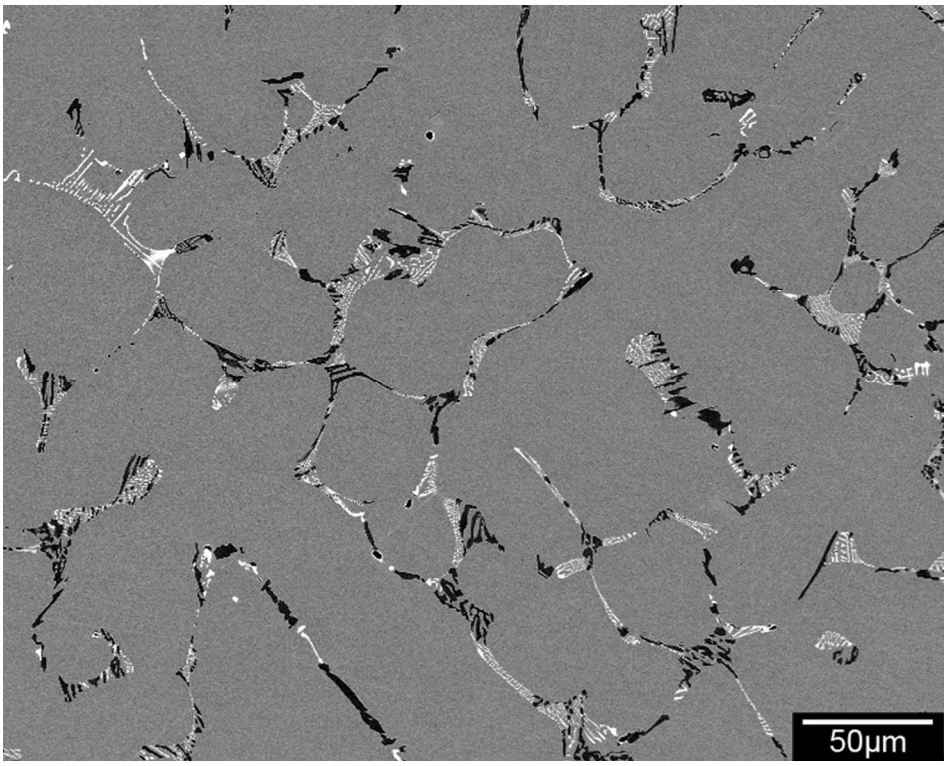

(a)

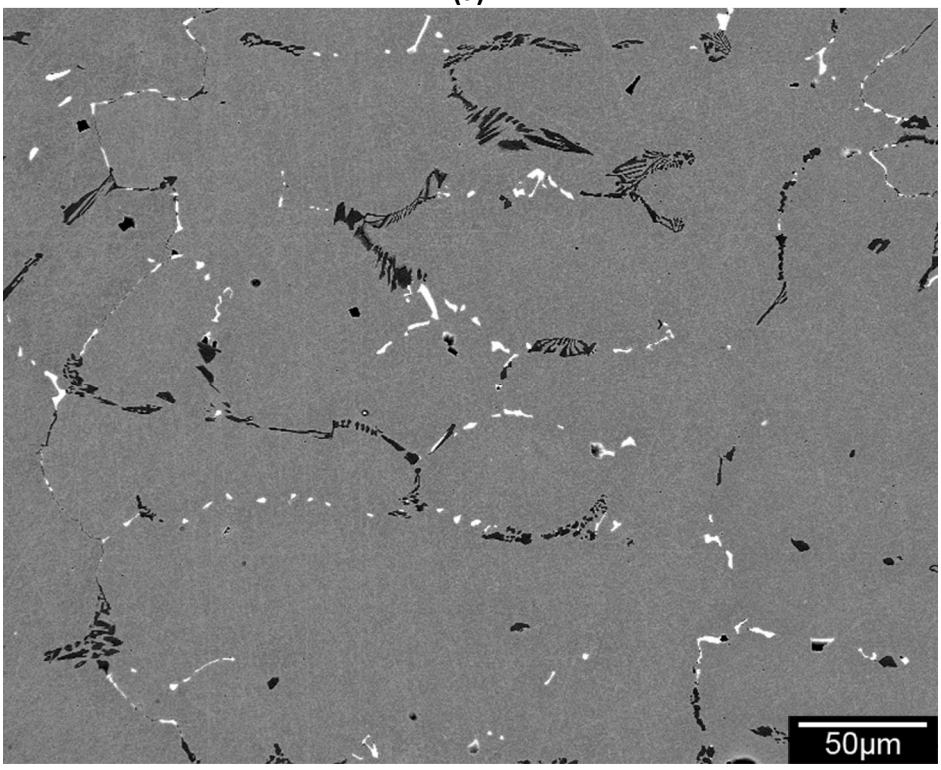

(a)

Figure 5.7 – Backscatter electron micrographs showing the primary precipitate networks at the mid-wall position in the as-cast (a) HP-Nb1 and (b) HP-NbTi1 tubes. The primary precipitate network in the HP-Nb alloy appears to be less fragmented in comparison to the HP-NbTi alloy.

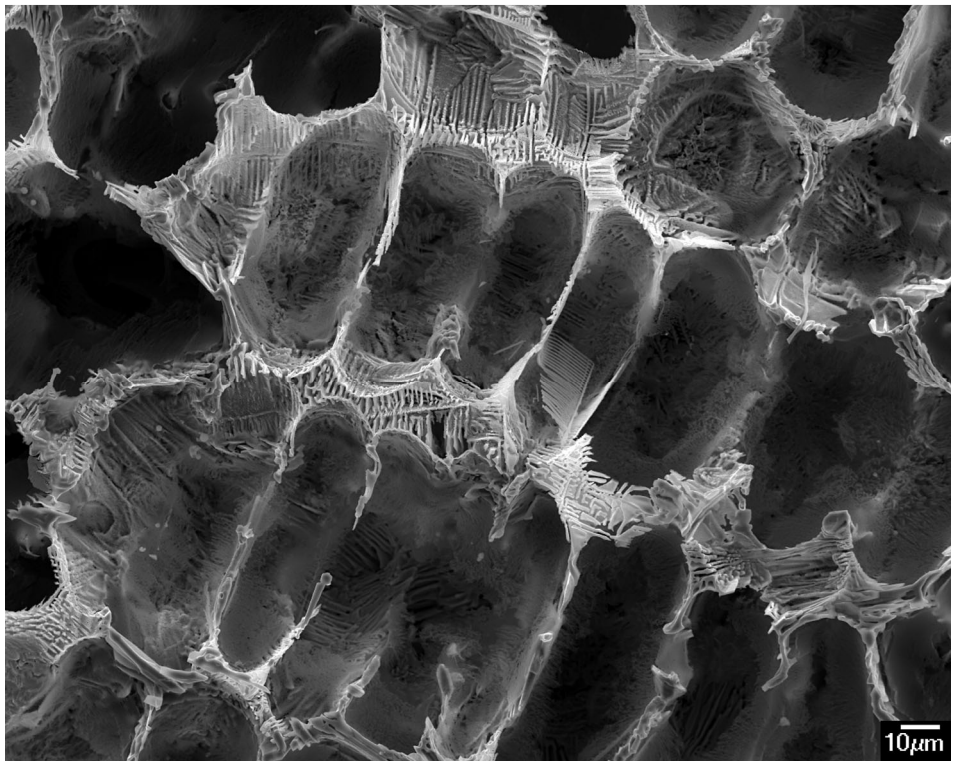

(a)

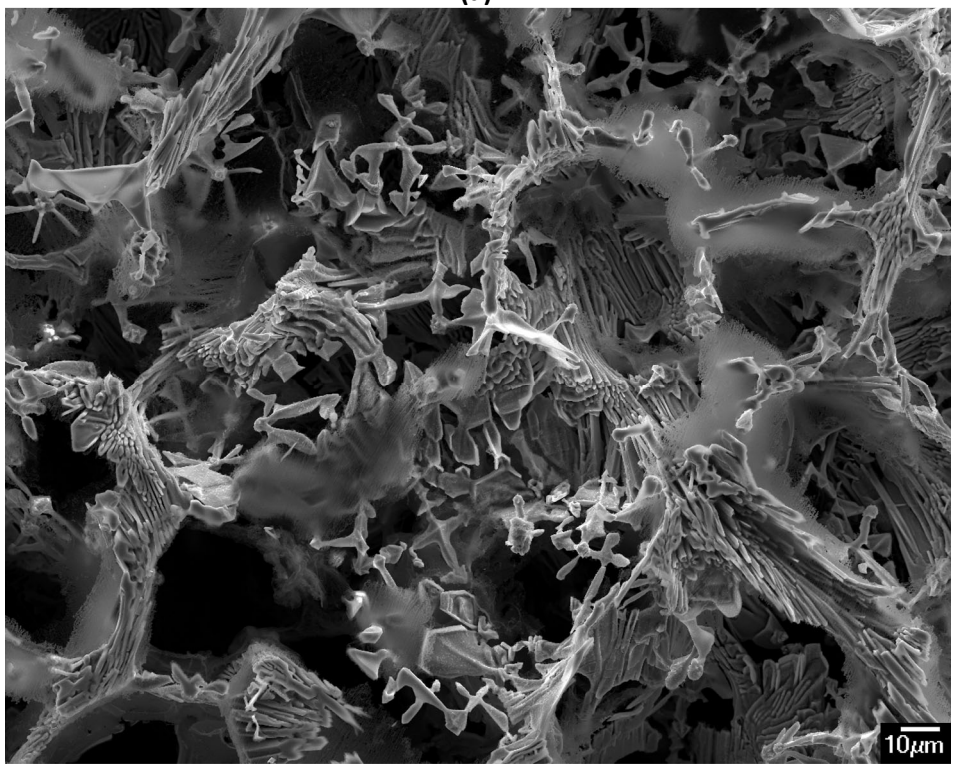

(b)

Figure 5.8 – Secondary electron micrographs of the primary precipitate networks at the mid-wall position in the as-cast (a) HP-Nb2 and (b) HP-NbTi1 tubes after deep etching for approximately 8 hours in glyceregia. The complex morphology of the primary precipitate network in three-dimensions causes quantitative measurements on the network's fragmentation to be inherently difficult.

5.2.3 Detailed Analysis of the Primary (NbTi)C Precipitates in the HP-NbTi1 and HP-NbTi2 Alloys

As stated in Section 5.2.1, the addition of titanium to the HP-Nb alloy composition caused the (NbTi)C precipitate to obtain a blocky morphology (a lamellar morphology was exhibited by the NbC precipitates in the HP-Nb alloy). During ageing of the HP-NbTi alloy at temperatures between 900-1050°C, the additional titanium within the (NbTi)C precipitates has been associated with reducing the (NbTi)C-to-G-phase transformation rate, hence increasing the stability of the primary carbide network [5]. Since the improvements in the tubes rupture life (in comparison to the HP-Nb alloys) has been partially attributed to this increased stability, it was considered necessary to further investigate the characteristics of these precipitates in the as-cast condition.

In general, low magnification (<1000x) observations of the HP-NbTi1 and HP-NbTi2 alloys confirmed the (NbTi)C precipitates obtained a blocky morphology (Figure 5.9 (a)) instead of the lamellar morphology obtained by the NbC precipitates in the HP-Nb alloy. However, similar to the HP-Nb alloys, detailed observations of these precipitates revealed the existence of two distinctly different morphologies (Figure 5.9 (a) and (b)). The (NbTi)C precipitate in Figure 5.9 (a) exhibits the typical blocky morphology as described in previous studies [5, 7]. In contrast, the (NbTi)C precipitates shown in Figure 5.9 (b) appear to obtain a morphology similar to the Type II lamellae in the HP-Nb alloys. Since each niobium-rich MC precipitate in the HP-Nb and HP-NbTi alloys obtain the same crystal structure, the same naming convention used for the NbC morphologies will be used for the (NbTi)C morphologies. Thus, for the purposes of this thesis, the morphologies shown in Figure 5.9 (a) and (b) will be referred to as the Type III and Type IV morphologies. For clarity, Table 5.3 summarises the general properties of the four MC precipitate morphologies.

In both the HP-NbTi1 and HP-NbTi2 alloys the blocky morphology was strongly dominant with the morphology shown in Figure 5.9 (b) representing less than 1% of the total (NbTi)C population. Neither of the morphologies appeared to be located preferentially with respect to grain, dendrite or wall position. Although the number of precipitates that obtained the Type IV morphology was relatively insignificant in comparison to the total (NbTi)C population, it was considered that the presence of this morphology in the HP-NbTi alloy could provide further insight into the origin of the Type II lamellae in the HP-Nb alloy.

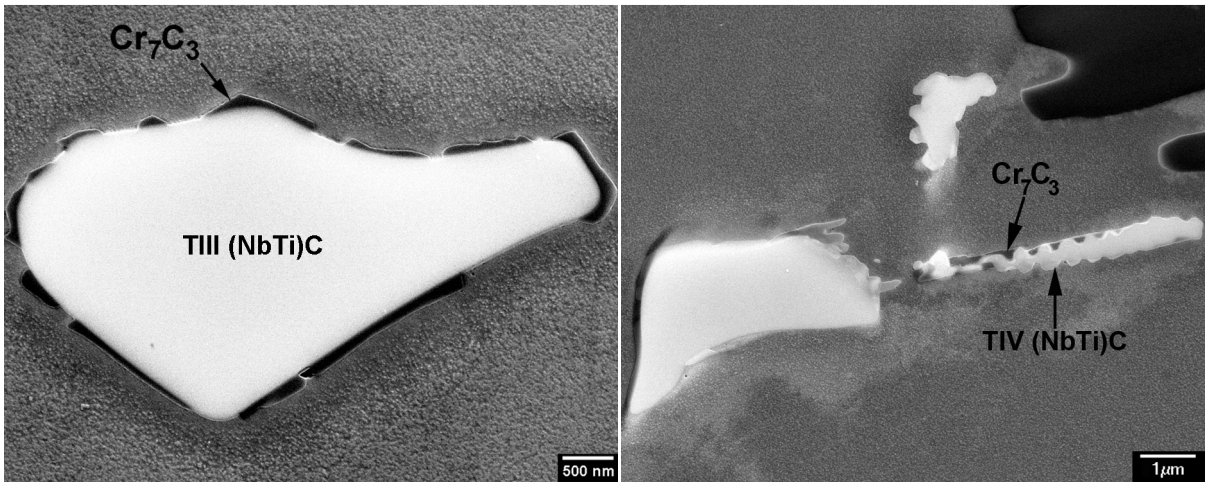

(a) **(b)**

Figure 5.9 – Composite scanning electron micrographs showing the two-dimensional morphology of the (a) Type III and (b) Type IV (NbTi)C precipitates in the HP-NbTi alloys.

Table 5.3 – Summary of the NbC and (NbTi)C precipitate morphologies in the HP-Nb and HP-NbTi alloys

Alloy	Phase	Morphology	Identification	Space Group	Representative Examples
HP-Nb	NbC	Lamellar eutectic	Type I	$Fm\bar{3}m$	Figure 4.6 (a)
	NbC	Reticulated plates	Type II	$Fm\bar{3}m$	Figure 4.6 (b)
HP-NbTi	(NbTi)C	Blocky	Type III	$Fm\bar{3}m$	Figure 5.9 (a)
	(NbTi)C	Nodular	Type IV	$Fm\bar{3}m$	Figure 5.9 (b)

Table 5.4 shows the average chemical composition as determined by EDS for the two morphologies. The composition was averaged from a minimum of 10 precipitates located across the wall thickness of the HP-NbTi tubes. All EDS was performed using a JEOL 7000F scanning electron microscope operating at an accelerating voltage of 10keV and the JEOL JED-2300 EDS detector. Due to the width of the Type IV plates typically being less than 0.5μm, the level of chromium, iron and nickel measured from these precipitates was significantly higher in comparison to the Type III precipitates. The iron, nickel and chromium concentrations were due to the interaction volume of the electron probe exciting characteristic X-rays from the adjacent austenite matrix and/or interfacial Cr_7C_3. While the TEM could have been used to obtain a more accurate measure of the Type IV precipitates chemical composition, the low occurrence of this morphology within the HP-NbTi alloy's microstructure caused such analysis to be unfeasible as without the use of preparation techniques where this phase could be specifically targeted (for example using a dual beam FIB/SEM), it was highly unlikely that a

sample would be obtained where these precipitates were located within the electron transparent area. Consequently, none of these precipitates were observed within the thin area of the HP-NbTi1 and HP-NbTi2 foils that were subjected to TEM analysis.

When comparing the Nb:Ti ratio for the two morphologies, the average titanium content in the Type IV morphology was consistently lower in comparison to the Type III morphology. Previous studies have attributed the lamellar (Type I) to blocky (Type III) morphology change to the addition of titanium to the HP-NbTi alloy [5, 7]. Partial substitution of titanium for niobium in the (NbTi)C lattice reportedly increases the precipitate/matrix interfacial energy causing the large interfacial surface area exhibited by the Type I lamellae to become energetically unfavourable. Therefore, the precipitates obtain the Type III morphology in an effort to reduce the precipitates total interfacial surface area and hence the interfacial energy associated with the precipitate/matrix interface.

The undulations along the surfaces of the Type IV morphology appear to increase the total surface area relative to that exhibited by the Type III morphology. Thus, the differing Nb:Ti ratios and interfacial surface areas associated with these two morphologies suggest the precipitate/matrix interfacial energy scales with the local titanium concentration during solidification. During growth of these precipitates, regions with lower titanium concentrations would be associated with relatively lower interfacial energies, thus allowing the formation of morphologies with higher interfacial surface areas (i.e. the Type IV morphology). Above a minimum threshold level of titanium, such high surface areas likely become energetically unstable causing the precipitate to minimise the total surface area leading to the formation of the Type III morphology.

Table 5.4 – Chemical composition of the Type III and IV morphologies as determined by EDS.

at.%	Ti	Cr	Fe	Ni	Nb	Nb:Ti
Type III (blocky)	4.4	7.8	5.4	4.2	78.2	18:1
Type IV (nodule)	0.7	18.3	17.8	14.8	48.4	69:1

Selected area diffraction (SAD) analysis confirmed the Type III precipitates obtained the FCC ($Fm\bar{3}m$) MC crystal structure common to the NbC and TiC phases (Figure 5.10 (a) and (b), and Table 5.5). As previously explained, the Type IV precipitates were not observed within the thin area of the TEM samples. However, alternatively EBSD analysis of the Type IV morphology confirmed that these precipitates also obtained the FCC ($Fm\bar{3}m$) MC crystal structure. Therefore, the expense of preparing numerous additional foils in order to analyse of the Type IV precipitates was considered unnecessary.

Table 5.5 shows the average lattice parameters measured from the Type III (NbTi)C precipitates. In total, measurements were taken from three separate Type III precipitates which contained titanium concentrations of between 3-5wt.%. Typically, the (NbTi)C lattice parameters were slightly larger than determined for the NbC precipitates in the HP-Nb alloys (a_{NbC} = 0.439nm, $a_{(NbTi)C}$=0.446nm). The (NbTi)C precipitate's larger lattice parameters in comparison to the NbC precipitates was in agreement with a similar study conducted using SAD an as-cast HP-NbTi alloy by De Almeida, Ribeiro and May [5]. In contrast, (NbTi)C lattice parameters reported in the Pearson's crystal database [16] (as determined by X-ray diffraction) were typically less than the NbC value. Generally, mixed Nb-Ti carbides with FCC crystal structures obtain lattice parameters that are a weighted average of the NbC (a_{NbC} = 0.446nm [29]) and TiC (a_{TiC} = 0.432nm [21]) parameters. For example, the lattice parameters for the $Nb_{0.8}Ti_{0.2}C_{0.96}$ and $Nb_{0.2}Ti_{0.8}C_{0.96}$ phases are 0.443nm and 0.434nm respectively [30].

For the HP-NbTi1 and HP-NbTi2 alloys the Nb:Ti ratio varied considerably within individual precipitates and between separate precipitates. Since the (NbTi)C lattice parameters are related to the Nb:Ti ratio, the lattice parameter for these precipitates will also be subject to a high degree of variance. However, the compositional variance does not account for the (NbTi)C lattice parameter being larger than the NbC lattice parameter. Alternatively, the larger lattice parameters in the current study could be a result of errors induced during SAD analysis of these precipitates. The total difference between the experimentally determined NbC and (NbTi)C lattice parameters was 0.007nm (i.e. a difference of 1.6%). Such a small difference could easily be reversed by the multiple sources of error associated with TEM diffraction (for example, errors induced by electron lens hysteresis). As the current project's focus was centred on characterising the evolution of the HP-Nb and HP-NbTi alloys during long-term isothermal ageing, further detailed analysis of each precipitate's lattice parameters using X-ray diffraction was considered unnecessary. However, throughout the course of the current research, significant effort was made to identify and control the major sources of error associated with electron diffraction in the TEM.

The following gives a short description of the main sources of error that were strictly controlled when performing SAD and CBED analysis on the precipitates in the as-cast and aged HP-Nb and HP-NbTi alloys:

- Calibration of the camera length (using gold ring patterns) was carried out on multiple occasions over a twelve month time period yielding a maximum variation of less than 0.5%.

- The effects of lens hysteresis was minimised by using the Philips CM200 lens normalisation function before capturing each diffraction pattern. The normalisation function momentarily increases the excitation of all magnifying lenses to the maximum level possible before returning to the excitation required for the selected magnification. Typically, reproducibility to within 1.5% of the calibrated magnification value is possible when using this process on the same zone axis pattern. In contrast, approaching a given magnification from slightly above or below the required lens excitation level (i.e. simply increasing or decreasing the magnification to achieve a set value) resulted in errors greater than 3%.

- Consistent focus between individual SAD patterns was achieved by using the same point on the objective aperture to focus on the back focal plane. A variance of less than 1% could be obtained when repeating the focusing process on the same zone axis when using the objective aperture as the focal point.

- Any errors induced by the digitisation of the film images were determined to be insignificant.

- When indexing each diffraction pattern, significant care was taken when measuring the distance between reflections. Repeated measurements taken from the same reflections on a single zone axis pattern generally resulted in a maximum D-spacing variance of less than 0.5%. Generally, the lattice parameters for each phase were calculated as an average of multiple measurements which were taken from the reflections on three widely separated zone axis.

Similar to the Type II morphology in the HP-Nb alloys, a small chromium-rich phase (<200nm in thickness) was present between the Type III/austenite and Type IV/austenite interfaces (Figure 5.9 (a) and (b)). When observing the interfacial precipitates in two-dimensions, the level of precipitation varied between individual (NbTi)C precipitates. Figure 5.9 (a) gives an example of a typical (NbTi)C precipitate where the interface was highly populated with the chromium-rich phase. However, (NbTi)C precipitates without any interfacial precipitate were also less commonly observed. SAD and CBED were used to confirm that the interfacial precipitates share the same Cr_7C_3 crystal structure as obtained by the larger chromium-rich primary precipitates (Figure 5.10 (a) & (c) and Table 5.5). While the primary Cr_7C_3 and (NbTi)C precipitates were infrequently connected, the interfacial chromium-rich precipitates were not believed to be part of the larger primary Cr_7C_3 precipitate network (i.e. the interfacial precipitates were not present due to two-dimensional sectioning of small portions of the primary Cr_7C_3 network).

Previous studies have identified similar chromium-rich interfacial precipitates between the (NbTi)C and austenite interfaces after subjecting the HP-NbTi alloy to isothermal ageing at 900°C for 1000 hours [7]. Although no chemical or crystallographic analysis of these precipitates was performed, the precipitates appeared similar in contrast to the primary $Cr_{23}C_6$ when observing the microstructure using backscatter electrons. Similar chromium-rich interfacial precipitates located between the Type II NbC and austenite interfaces after ageing the HP-Nb alloys were identified as $Cr_{23}C_6$ (Chapter 4, 6). Thus, the chromium-rich precipitates in the aged HP-NbTi material likely obtain the same $Cr_{23}C_6$ crystal structure. Based on the observation of the interfacial Cr_7C_3 precipitates in the as-cast HP-NbTi1 and HP-NbTi2 alloys, these precipitates are believed to have largely originated from the transformation the as-cast Cr_7C_3 to $Cr_{23}C_6$ during thermal exposure. However, additional precipitation of secondary $Cr_{23}C_6$ at the (NbTi)C/austenite interface cannot be ruled out as this interface likely represents an energetically favourable site for heterogeneous nucleation during ageing.

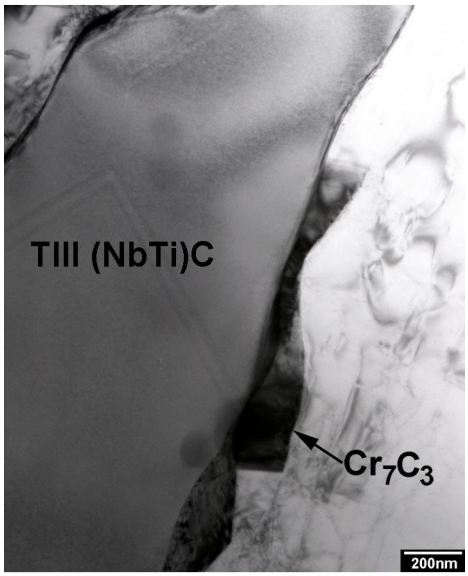

(a)

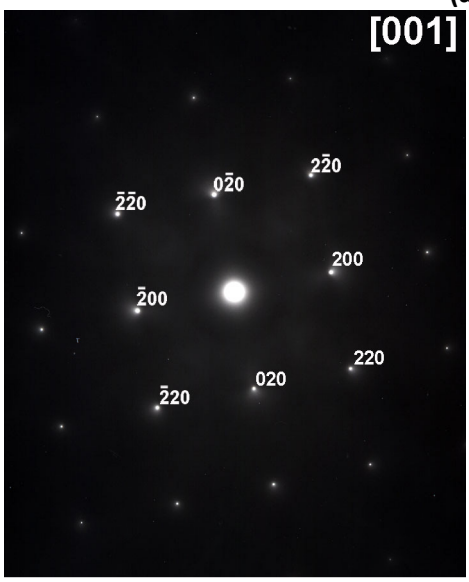

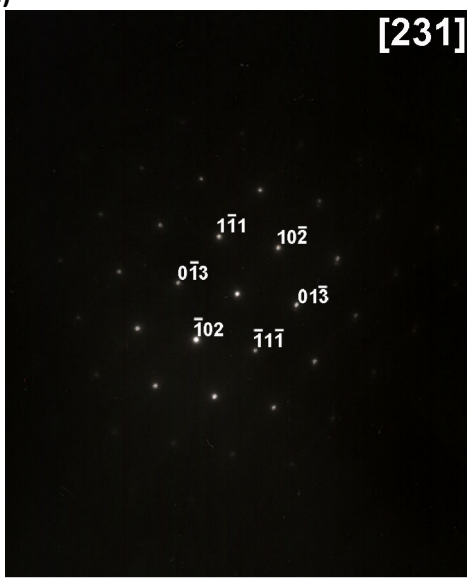

(b) (c)

Figure 5.10 - (a) Bright field transmission electron micrograph showing the Type III (NbTi)C and Cr_7C_3 located between the precipitate/matrix interface of Type III (NbTi)C. (b) $[001]_{NbC}$ and (c) $[231]_{Cr7C3}$ zone axis patterns (SAD) for the face centred cubic (NbTi)C and orthorhombic Cr_7C_3 phases respectively.

Table 5.5 - SAD determined crystal structures and lattice parameters for the primary (NbTi)C and interfacial Cr_7C_3 precipitates.

	Crystal system	Space group	a(nm)	b(nm)	c(nm)
(NbTi)C	FCC	$Fm\bar{3}m$	0.446	0.446	0.446
Cr_7C_3	Orthorhombic	$Pnma$	0.456	0.708	1.224

To further investigate the Type III and IV (NbTi)C and the Cr_7C_3 interfacial precipitates, the three-dimensional morphology of these precipitates was revealed by deep etching the as-cast HP-NbTi alloys in glyceregia (Figure 5.11 (a)-(d)). Similar to the HP-Nb alloys, progressive etching experiments performed on the HP-NbTi alloys determined the glyceregia etchant preferentially attacked the austenite matrix while leaving the carbide network completely intact. Generally, as-cast samples of the HP-NbTi1 and HP-NbTi2 alloys (mounted in Buehler Probemet^{TM}) were submerged in the etchant for 1-2 hours using the method described in Chapter 3.

Representative examples of the Type III morphology are shown in Figure 5.11 (a) and (b). In three-dimensions, multiple branches can be seen to radiate from a central nucleus. The blocky appearance of these precipitates in two-dimensions (Figure 5.9 (a)) results from radial and longitudinal sectioning of these branches. In general, the branching directions varied significantly between precipitates suggesting the local melt thermal and compositional gradients played a dominant role in determining the three-dimensional morphology of these precipitates. The influence of the local solidification conditions is evidenced in Figure 5.11 (a) and Figure 5.16 (b) where the growth of the branches was confined to particular conical or planar regions. As shown in Figure 5.11 (a) and (b) the tips of the (NbTi)C branches commonly terminated within groups of primary Cr_7C_3 precipitates. Aside from surface irregularities caused by the interfacial Cr_7C_3 (Figure 5.12), the Type III interfaces appeared to be relatively uniform (i.e. small steps or facets on the (NbTi)C interface were not resolved by SEM).

Figure 5.11 (c) and (d) show the three-dimensional morphology of the Type IV (NbTi)C precipitates. The undulations along the faces of the (NbTi)C plates in two dimensions (Figure 5.9 (a)) are a result of the nodular appearance of the plates broad faces in three-dimensions. The correspondence between plate's undulations in two-dimensions and the nodules in three-dimensions confirmed that the Type IV morphology's surface topography was part of the (NbTi)C precipitate as opposed to being a result of the interfacial Cr_7C_3. Generally the nodules were approximately 0.5μm in diameter and appeared to protrude from the surfaces of plate-like precipitates. Unlike the Type II morphology in the HP-Nb alloy, the Type IV morphology in the HP-NbTi alloy did not show any level of porosity.

Transition morphologies, where the precipitates exhibited attributes from both the Type III and IV morphologies, were also revealed by deep etching (Figure 5.11 (d)). In this case, a gradual transition from Type III to the Type IV morphology can be observed with the nodules appearing to coarsen with increasing distance from the TIII-TIV transition region. EDS of the nodules within the Type IV region indicated they were rich in niobium. Thus, the surface topography was not a result of particularly

coarse interfacial Cr_7C_3 precipitates. In contrast, the texture on the surface of the Type III region is due to the (NbTi)C interface being highly populated with Cr_7C_3 precipitates.

As previously discussed, the emergence of the nodules was believed to be related to the precipitate's titanium content. The hybrid precipitate in Figure 5.11 (d) further suggests the origin of the Type IV morphology is unlikely related to any difference in the nucleation site or the precipitate/matrix crystallography as shown for the Type I and II NbC lamellae in the HP-Nb alloy (Chapter 4). Alternatively, the titanium in solution likely becomes increasingly depleted as the formation of the (NbTi)C precipitate progresses. Growth of the nodular morphology proceeds once the titanium content remaining in solution falls below a threshold value (unknown).

As discussed in Chapter 4, nodular morphologies similar to the Type IV precipitates were identified by Tin and Pollock in single-crystal nickel-based superalloys [10, 11]. Similar to the HP-NbTi alloy, the sub-micron size nodules were observed on the surfaces of rod and plate shaped tantalum-rich MC precipitates. The Ni-based alloys typically contained three separate MC morphologies: octahedral blocks, script, and nodular (depending on alloying additions). Although all three morphologies reportedly contained small quantities of hafnium, cobalt, nickel and chromium, quantitative comparison of the concentration of each constituent within the three morphologies was not published. However, only nodule precipitates were observed around freckle chains (which are induced by large compositional gradients within the "mushy-zone" during solidification), suggesting the nodular precipitates were influenced by the local melt composition. Additionally, preferential formation of the nodular morphology occurred at the edges of the castings where Si, N and O were thought to be present in slightly higher quantities due to the use of investment casting molds. These compositional gradients further stress the influence of local solidification conditions on the carbides morphology.

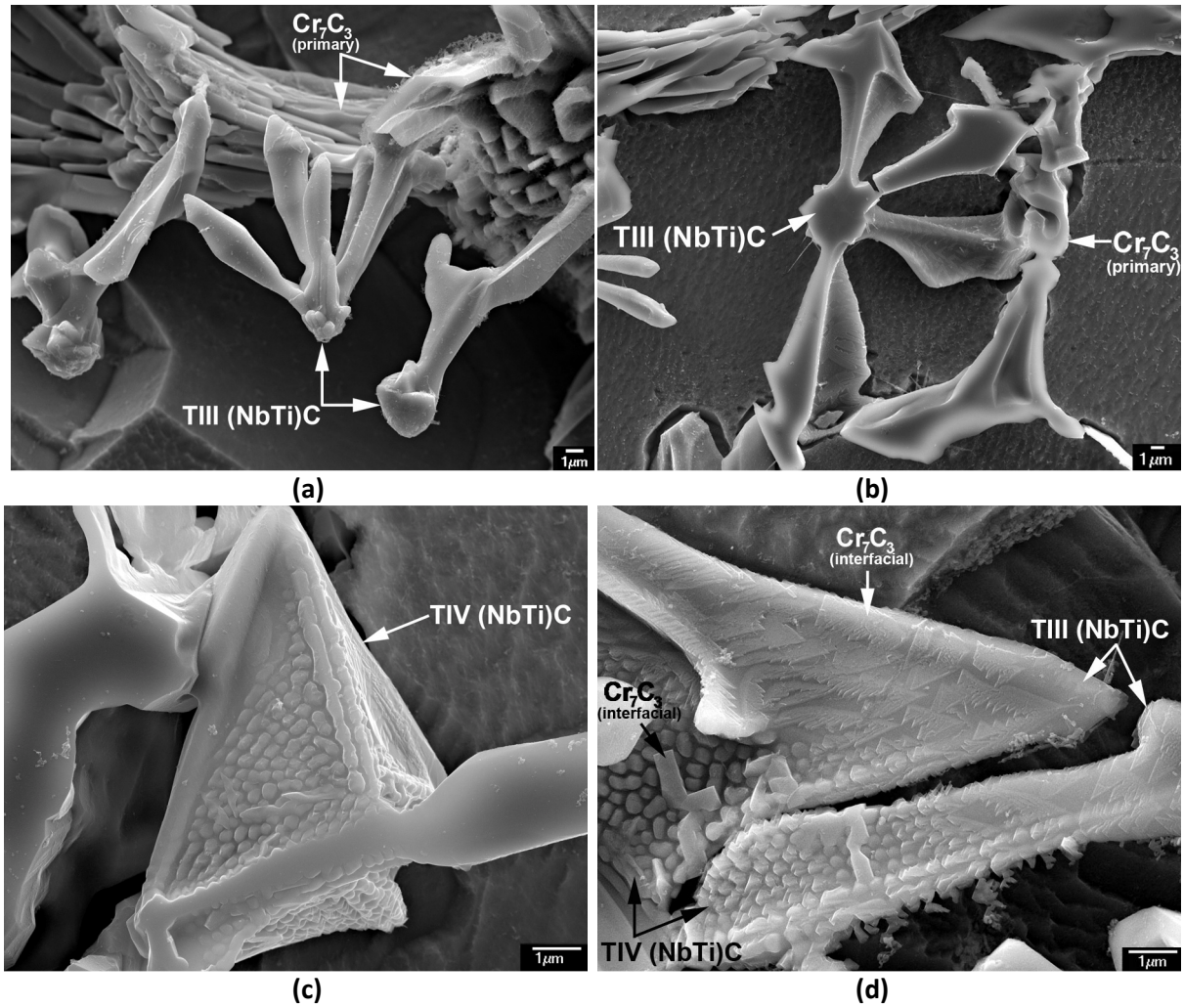

Figure 5.11 – Secondary electron micrographs showing the three-dimensional morphology of the (a)-(b) Type III, (c) Type IV and (d) mixed Type III/IV (NbTi)C precipitates.

As shown in Figure 5.12 (a), the interfacial Cr_7C_3 was easily distinguishable on the surface of the Type III morphology after deep etching. Higher magnification observations of the Type III morphology revealed the interfacial Cr_7C_3 precipitates were typically present as a thin film which coated large sections of the (NbTi)C interface (Figure 5.12 (a) and (b)). Generally this film exhibited a dendritic appearance, but larger faceted precipitates were also observed. Although the total proportion of the Type III interface which was occupied by Cr_7C_3 varied between individual Type III (NbTi)C precipitates, the highly populated in (NbTi)C interfaces shown in Figure 5.12 (a) and (b) were typical for the Type III morphology.

The film's morphology appeared to be dependent on the orientation of the (NbTi)C interface. As shown in Figure 5.12 (a) and (b), Cr_7C_3 precipitates shared a similar morphology when located on a

constantly oriented (NbTi)C interface. However, the Cr_7C_3 morphology varied significantly between adjoining (NbTi)C interfaces which exhibited widely differing orientations. For example, the change in the orientation of the (NbTi)C precipitates interface in Figure 5.12 (b) causes the Cr_7C_3 to transition to a fern-like morphology. In this instance, the apparent growth direction of the Cr_7C_3 ferns was constant between individual precipitates indicating that each interfacial precipitate originated from the Cr_7C_3 on located the adjoining (NbTi)C interface. Such directional growth of the Cr_7C_3 from the (NbTi)C precipitate's interfacial edges was common. However, it is unknown if the (NbTi)C edges act as preferential sites for the nucleation and growth of the Cr_7C_3.

The high level of surface topography exhibited by the Type IV morphology typically obscured the interfacial Cr_7C_3 precipitates when viewing these precipitates in three-dimensions using secondary electrons. However, highly faceted interfacial precipitates were observed on the Type IV (NbTi)C interface after deep etching (Figure 5.11 (d)). All Cr_7C_3 precipitates observed in association with the Type IV morphology obtained a similar faceted morphology. These faceted Cr_7C_3 precipitates were generally larger (0.5-1μm^2) than the Cr_7C_3 interfacial precipitates (<0.5μm^2) in association with the Type III morphology.

Previous studies reported the transformation of the (NbTi)C precipitates to G-phase during isothermal ageing of the HP-NbTi alloys at 900°C for 1000 hours [5, 6]. This transformation relies on diffusion of titanium, carbon, silicon and nickel across the (NbTi)C/austenite interface. The (NbTi)C-to-G-phase transformation rate was reportedly lower in comparison to the NbC-to-G-phase transformation rate in the HP-Nb alloys due to the insolubility of titanium within G-phase. Thus, the titanium within the (NbTi)C precipitates had to be rejected as the G-phase transformation progressed.

The current research suggests that this reduction could also be partially attributed to the large proportion of the (NbTi)C interface which is populated by chromium-rich precipitates. During ageing, the chromium-rich precipitates (which transform to $Cr_{23}C_6$) remain relatively stable [7]. If the $Cr_{23}C_6$ precipitates occupy a similar proportion of the (NbTi)C interface after ageing as observed for the Cr_7C_3 in the as-cast condition, the relatively stable $Cr_{23}C_6$ would likely act as a barrier to diffusion of Ti, Si, and Ni across the (NbTi)C/austenite interface unless these elements are able to rapidly diffuse through the $Cr_{23}C_6$. The low concentrations of Si, Ni and Ti typically observed in the $Cr_{23}C_6$ (Chapter 7) suggests the diffusion of these elements through the $Cr_{23}C_6$ is negligible. Thus, the $Cr_{23}C_6$ precipitate likely acts as a further barrier to the G-phase transformation in the HP-NbTi alloy.

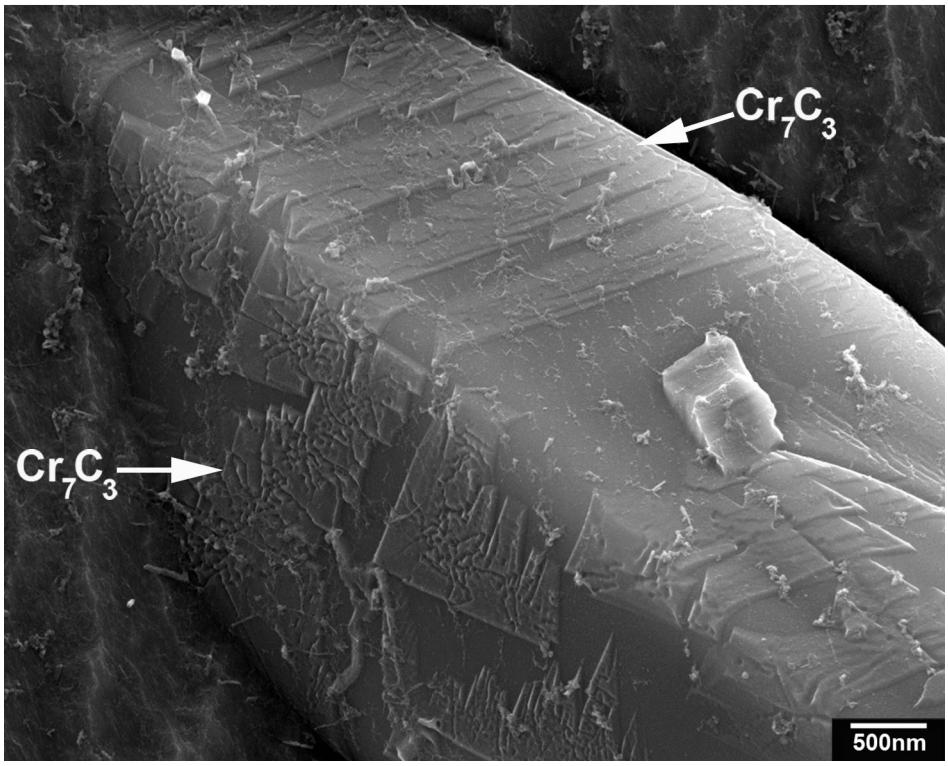

(a)

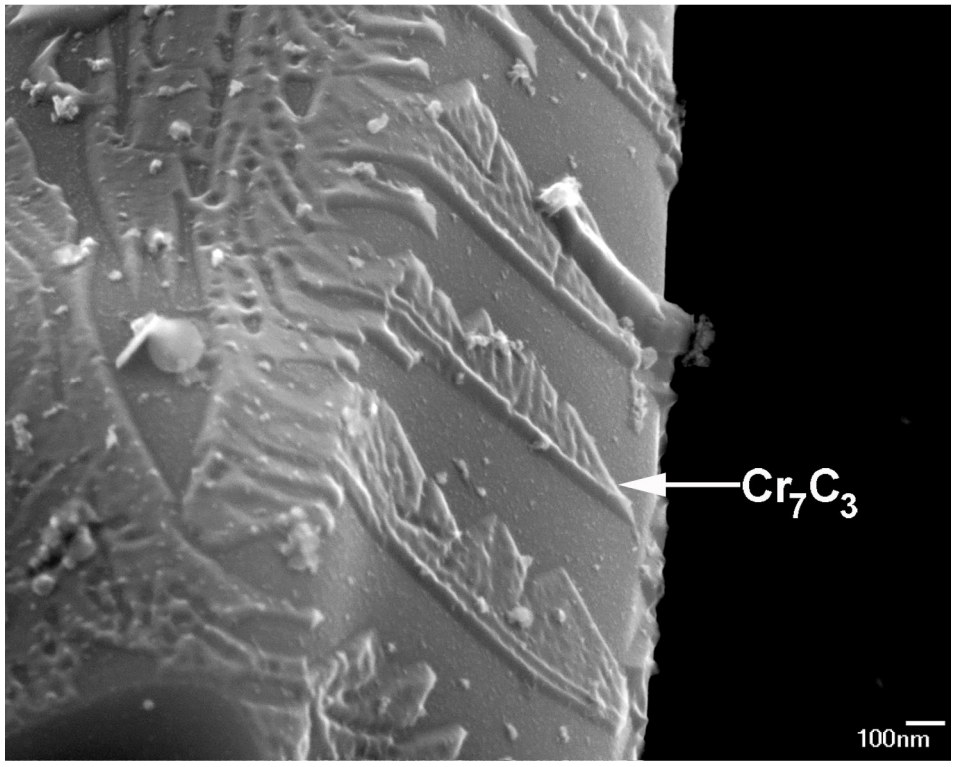

(b)

Figure 5.12 - High magnification secondary electron micrographs of the interfacial Cr_7C_3 located on the Type III (NbTi)C interface.

As mentioned previously, the three-dimensional branches of the Type III precipitates could typically be traced back to common nuclei. Further detailed observations of the HP-NbTi1 and HP-NbTi2 alloys in two-dimensions revealed that each three-dimensional nucleus contained a single spherical precipitate that was approximately 1-2µm in diameter (Figure 5.13 (a) and (b)). When observing the HP-NbTi alloys' microstructures in two-dimensions, generally less than 10% of the total population of Type III precipitates contained these spherical precipitates. However, since each Type III precipitate's branches consistently radiated from common nuclei when viewing the precipitates in three-dimensions, it was believed that all (NbTi)C precipitates contained the spherical precipitates shown in Figure 5.13.

EDS analysis determined the spherical particles were predominantly rich in aluminium, titanium and oxygen causing the distinct atomic number contrast (in comparison to the surrounding (NbTi)C precipitate) when imaging the HP-NbTi alloy's microstructure using backscattered electrons. Rarely, separate particles rich in aluminium and oxygen were observable within the Ti-rich sphere (Figure 5.13 (b)). EDS analysis of the material adjacent to these aluminium-oxide inclusions (Table 5.6) determined the sphere was predominately rich in titanium and oxygen suggesting the spherical particles were composed of both aluminium and titanium oxides. Similar mixed aluminium and titanium oxide inclusions have been reported in titanium killed carbon-manganese steels [31]. Ti_2O_3 inclusions were believed to have nucleated heterogeneously on the Al_2O_3 during cooling. It is currently unknown if the titanium-oxide sphere similarly nucleates on aluminium-oxide melt inclusions during solidification of the HP-NbTi1 and HP-NbTi2 alloys.

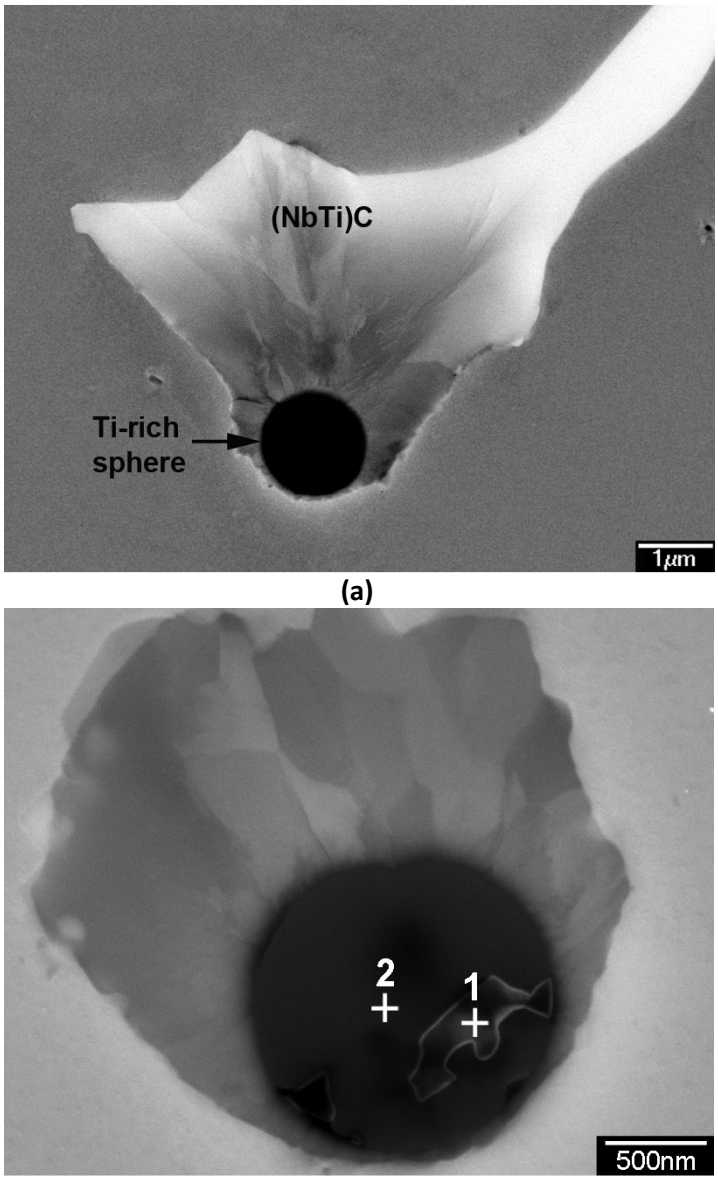

Figure 5.13 – (a) Backscatter electron micrograph showing a spherical Ti-rich precipitate contained within the primary (NbTi)C precipitates. (b) Secondary electron image showing an aluminium-oxide inclusion in the titanium-rich sphere.

Table 5.6 - Chemical composition of points 1 and 2 in Figure 6 (b) (as determined by EDS).

at.%	Al	Ti	O	Si	Cr
1	26	11	60.8	-	2.2
2	3.7	29.2	62.7	0.4	4.0

When observing the primary (NbTi)C precipitates with backscattered electrons, additional contrast could be observed within the region of the (NbTi)C precipitate which directly surrounded the Ti-rich sphere (Figure 5.13 and Figure 5.14 (a)). The darkened contrast within the (NbTi)C precipitate rapidly diminished with distance from the Ti-rich sphere (points 2-5, Figure 5.14 (a)).

Figure 5.14 (b) shows the relative concentrations of Nb, Ti, Al and O along the length of the (NbTi)C precipitate in Figure 5.14 (a) as determined by EDS. The profile was determined by generating (and subsequently quantifying) separate EDS spectra from 10 equidistant points (~1µm apart). For simplicity, minor elements such as iron, nickel and chromium (typically present in concentrations between 1-5wt.%) were neglected from Figure 5.14 (b) and the quantity of all remaining elements has been normalised to equal 100.

The region of the (NbTi)C precipitate which directly surrounded the Ti-rich sphere (point 2, Figure 5.14 (a)), was significantly enriched in titanium (41.1wt.%) in comparison to the level of titanium typically observed within the (NbTi)C branches. With increasing distance from the inclusion, the concentration of titanium in the (NbTi)C precipitate markedly decreased until eventually reaching the 3-5wt.% of Ti commonly observed in the Type III (NbTi)C precipitates. In extreme cases, the continued reduction of titanium within the (NbTi)C branch likely results in the transition to the Type IV morphology as shown in Figure 5.11 (d).

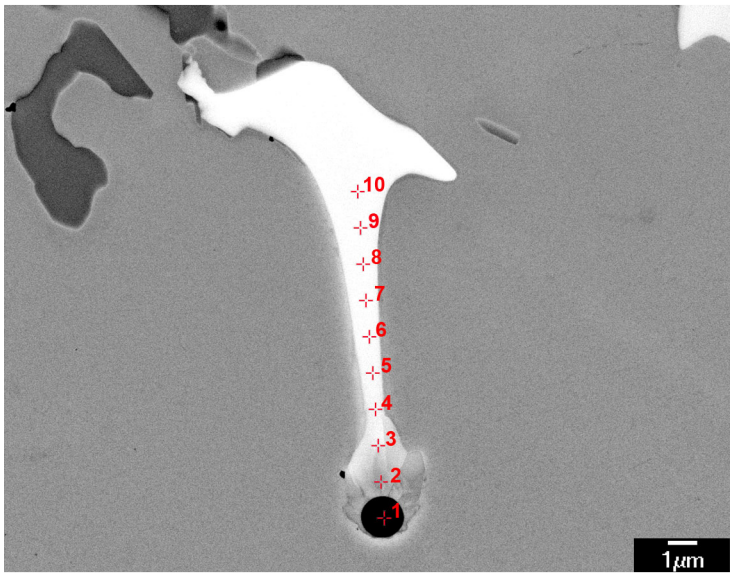

(a)

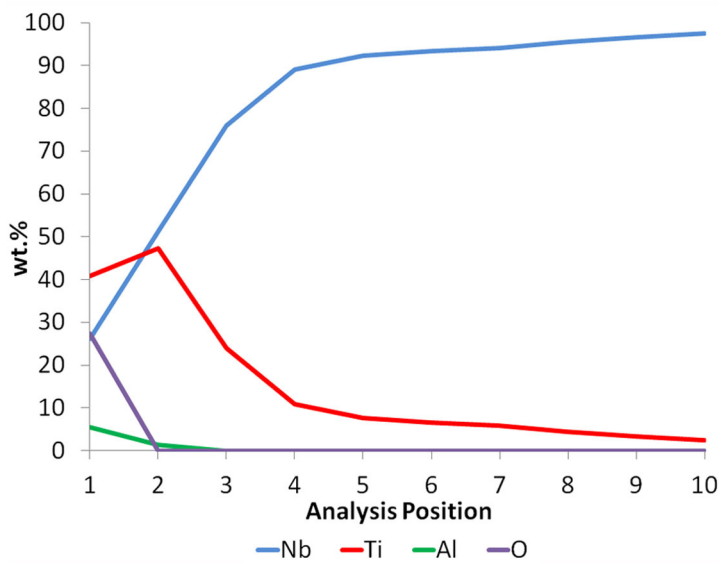

(b)

Figure 5.14 - (a) Backscatter electron micrograph of a Type III (NbTi)C precipitate containing a spherical Ti-Al rich particle. (b) Relative concentrations of Nb, Ti, Al, and O with respect to distance from the Ti-rich sphere.

Blocky morphology (NbTi)C precipitates containing titanium carbo-nitride "cores" were also observed in directionally solidified IN718 nickel-based superalloys [32]. EDS detected the presence of magnesium, aluminium and oxygen within these cores. These elements were attributed to MgO or Al_2O_3 particles that were present within the melt prior to casting of the alloys. During solidification, the titanium carbo-nitride cores were believed to have nucleated on oxide inclusions present within the liquid in the "mushy-zone". Subsequent nucleation of the blocky morphology (NbTi)C precipitates occurred on these cores with growth of the (NbTi)C precipitate progressing into the remaining liquid.

Nucleation of the titanium carbo-nitride cores was partially attributed to the presence of nitrogen within the melt. The strong affinity between titanium and nitrogen reportedly promoted heterogeneous nucleation on the oxide inclusions. However, no compositional analysis capable of detecting the nitrogen within these cores was presented. No detectable nitrogen peak was present when performing EDS analysis on the spherical titanium-rich sphere (or 'cores') observed in the HP-NbTi1 and HP-NbTi2 alloys. It must be stressed that the nitrogen Kα peak resides a region of the EDS spectrum which, for this phase, is relatively clustered. As a result, the nitrogen Kα peak is masked by the titanium Lα and LI peaks. If nitrogen was present within the spherical titanium-rich precipitates, the low concentration could not be resolved using the JEOL JED-2300 EDS detector. However, both the HP-NbTi1 and HP-NbTi2 alloys contained approximately 0.05wt.% of nitrogen (as determined using LECO combustion analysis). Caballero *et al.* [7] also reported low concentrations of nitrogen (0.036-0.037wt.%) in two separately cast HP-niobium and HP-niobium-titanium-zirconium modified alloys. Nucleation of titanium carbo-nitrides on zirconium oxide inclusions was solely reported within the HP-NbTiZr alloy. Therefore, it is possible that nitrogen in combination with titanium induces the heterogeneous nucleation of titanium carbo-nitride precipitates on the oxide inclusions in the HP-NbTi alloys.

Additional contrast was observed within the region of the (NbTi)C precipitate surrounding the Ti-rich sphere when observing the HP-NbTi alloy's microstructure using secondary electrons (Figure 5.15 (a)). This contrast delineated interfaces within the (NbTi)C precipitate, indicating the presence of sub-grain or grain boundaries. EBSPs taken from the individual grains (points 1-4 in Figure 5.15 (a) and (b)) visually demonstrate (by the relative displacements of each subsequent EBSP) the crystallographic misorientation between each grain. EBSD was performed on three individual precipitates each of which had a minimum of three visible grains located on the polished section. Performing the same procedures used when calculating the NbC/matrix orientation relationship in Chapter 4 determined the disorientation between neighbouring grains was typically greater than 15° (i.e. the interfaces were high angle grain boundaries). Therefore, EBSD confirmed the contrast was induced by the nucleation of multiple (NbTi)C grains on the spherical titanium-rich precipitates.

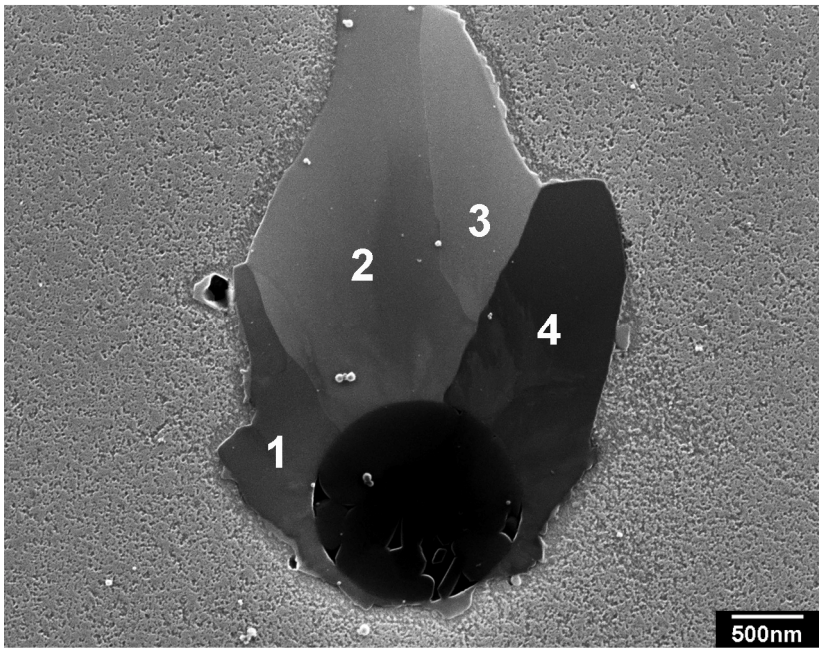

(a)

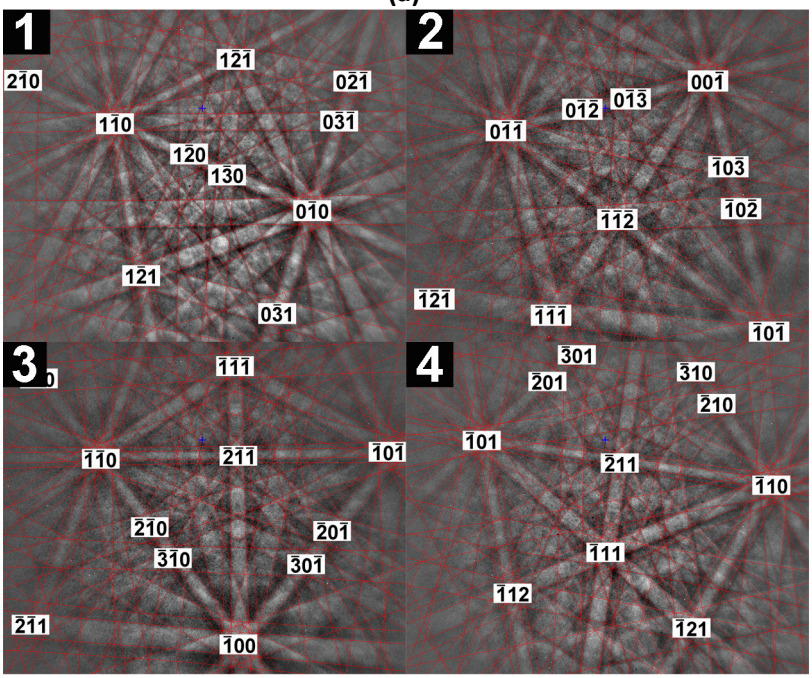

(b)

Figure 5.15 - (a) High magnification secondary electron micrograph of the (NbTi)C precipitate surrounding the Ti-rich sphere. (b) EBSD patterns taken from the areas in (a).

Figure 5.16 (a) shows a (NbTi)C precipitate after deep etching where the Ti-rich sphere is still observable on the originally polished surface. The individual grains in Figure 5.15 (a) (which nucleated on the Ti-rich sphere) correspond to branches in three dimensions. Regions where large branches did not protrude from the nucleus typically appeared highly topographic (Figure 5.16 (b)),

indicating that although nucleation of multiple (NbTi)C grains occurs on the Ti-rich sphere, only grains which are favourably oriented with respect to local melt composition and thermal gradients subsequently grow.

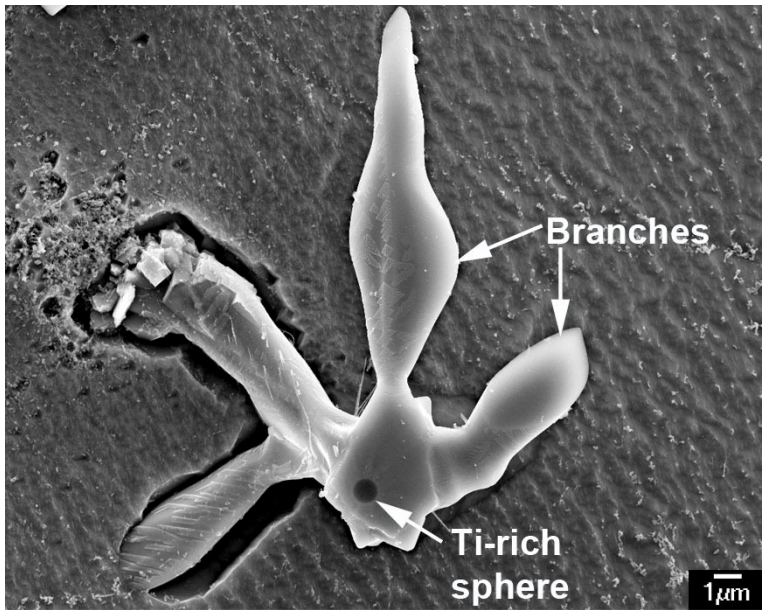

(a)

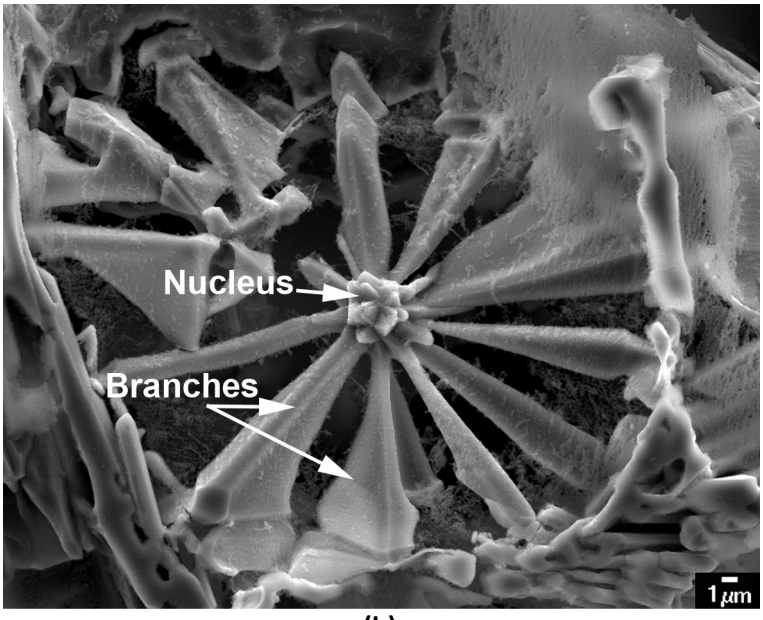

(b)

Figure 5.16 – Three-dimensional morphology of the Type III (NbTi)C showing the Ti-rich sphere (a) and (a) & (b) the branches corresponding to the individual grains observed in Figure 5.15.

The observation of oxide inclusions within the (NbTi)C precipitates strongly indicated that nucleation and growth of these precipitates occurred in the liquid ahead of the solidifying austenite dendrites. As a result, it was expected that these precipitates would not obtain a consistent orientation relationship (OR) with the austenite matrix. To determine if any consistent OR existed between the Type III and Type IV (NbTi)C precipitates and austenite matrix, EBSD analysis was performed on these precipitates using the same procedure discussed in Chapter 4 for the Type I and II lamellae in HP-Nb alloy. EBSPs were taken from both the Type III and Type IV morphologies and the matrix directly adjacent to each precipitate. A maximum of four EBSPs were obtained from each precipitate/matrix pair (i.e. two from the precipitate and two from the adjacent matrix). Although a total of 53 precipitate/matrix pairs were analysed, only five of these pairs were taken from the Type IV morphology due to the relatively low occurrence of this morphology in the HP-NbTi tubes.

The magnitudes of disorientation for the Type III/austenite and Type IV/austenite pairs are plotted in Figure 5.17. As discussed in Chapter 4, the presence of a precipitate/matrix OR is typically observed through clustering around a specific disorientation magnitude. Neither the Type III nor Type IV morphologies exhibited any strong level of clustering around a particular disorientation. Thus, the disorientation values for both morphologies have been consolidated onto one plot. Although clustering may seem somewhat apparent between 50-55°, it must be stressed that the graph only shows the magnitude of disorientation and not the rotation axis. Typically, the rotation axis varied significantly when comparing disorientations of a similar magnitude. Consequently, the significant disorientation variance between the primary (NbTi)C precipitates and austenite indicates that these phases are not likely to obtain a consistent OR.

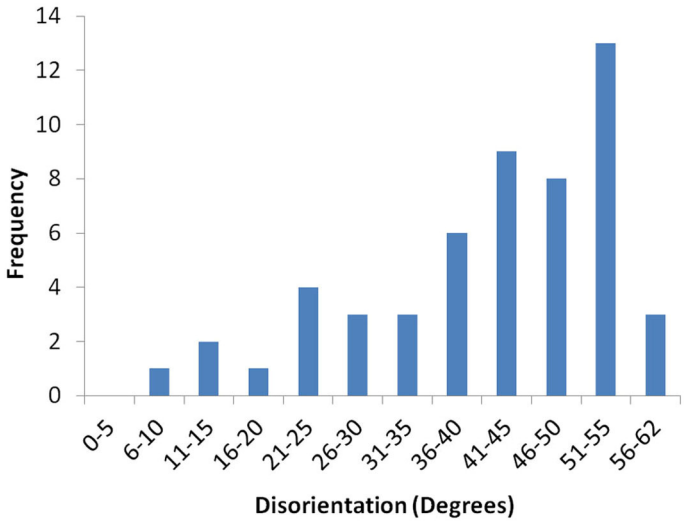

Figure 5.17 - Histogram showing the frequency of occurrence of disorientation measured between the primary (NbTi)C and adjacent austenite.

Identical to the (NbTi)C precipitates, the Type II NbC lamellae in the HP-Nb alloy did not obtain a consistent OR with the matrix. Interestingly, only 2% of the precipitate/matrix pairs from the Type II, III and IV data sets fell within the 10° upper limit defined for a cube-cube OR. Therefore, all three morphologies favoured high angle disorientations with respect to the matrix. Nucleation of the Type II lamellae in the HP-Nb alloy was also believed to occur on oxide inclusions (Chapter 4). Although oxide inclusions were commonly observed in association with the (NbTi)C precipitates, no evidence of similar inclusions was observed in association with the Type II NbC lamellae. However, it is considered unlikely that these inclusions are confined to the HP-NbTi alloys. Thus, the crystallographic similarities between the Type II, III and IV morphologies further suggest nucleation of the Type II lamellae is associated with oxide inclusions. The absence of titanium in the HP-Nb alloys (i.e. the element which highlighted the presence of the sub-micron oxide inclusion within the surrounding (NbTi)C precipitate in the HP-NbTi alloy) possibly attributed to these inclusions being difficult to observed in the HP-Nb alloys.

Based on the preceding evidence, nucleation of the Type III and Type IV morphologies in the HP-NbTi alloy is believed to occur in the liquid ahead of the solidifying austenite dendrites. Initially solidification of the austenite dendrites occurs causing the rejection of niobium, titanium, carbon and nitrogen to the remaining liquid. The aluminium oxide inclusions subsequently act as viable heterogeneous nucleation sites for the titanium-oxide spheres. These spheres subsequently act as prolific heterogeneous nucleation sites for the (NbTi)C precipitates, causing multiple (NbTi)C grains to

form on each sphere. Nucleation of both the Type III and Type IV morphologies is believed to occur on these spheres.

After nucleation, the growth of the (NbTi)C precipitate proceeds into the remaining liquid. The morphology preference is believed to be determined by the availability of titanium during solidification rather than any difference in the nucleation site or precipitate-matrix crystallography. Regions with relatively high concentrations of titanium promoted the formation of the Type III morphology. Generally, precipitates with titanium contents exceeding 2wt.% exhibited this blocky morphology. These precipitates likely have a higher (NbTi)C/liquid interfacial energy causing the individual branches to obtain the blocky morphology in an effort to minimize the total interfacial surface area. While the morphology of individual branches remained relatively consistent, the arrangement of these branches differed significantly in three-dimensions. The growth direction of the branches is likely dominated by local thermal and compositional gradients. After nucleation, (NbTi)C grains which have their crystallographic 'fast grow direction' favourably orientated with respect to these gradients grow preferentially causing the multitude of uniquely shaped precipitates observed after deep etching. Similar directional growth of MC precipitates has been observed in single crystal and directionally solidified nickel-based superalloys [10, 11, 33-39]. Faceted plates with their $<100>_{MC}$ direction aligned with the direction of maximum compositional gradient were believed to grow preferentially from octahedral shaped precipitates [10, 11, 36, 39].

The formation of the Type IV morphology is believed to progress in regions of the melt which contain a comparatively low concentration of titanium. The higher Nb:Ti ratio within the Type IV morphology in comparison to the Type III morphology suggests the (NbTi)C/liquid interfacial energy scales with the precipitate's titanium concentration. Therefore, when the titanium concentration falls below a threshold level (currently unknown), the associated decrease in the (NbTi)C/liquid interfacial energy allows the growth of precipitates with comparatively higher interfacial surface areas (i.e. the nodular morphology). The observed titanium gradient along the length of the (NbTi)C branches (as shown in Figure 5.14 (b)) and the observation of precipitates progressively transitioning from the Type III to Type IV morphology (Figure 5.11 (d)) demonstrate the compositionally induced change of the precipitate's morphology.

Since the Type IV morphology only represented a small fraction of the total (NbTi)C population in the HP-NbTi alloy, these precipitates will likely have little effect on the alloy's creep properties. Therefore, when considering the long-term life of the HP-NbTi reformer tubes, this morphology is of

comparatively low importance. However, the Type IV morphology provides significant further evidence on the nucleation and growth mechanisms of the Type II morphology in the HP-Nb alloys. The Type II morphology represented 50-65 percent (depending on alloy's chemical composition) of the total NbC population and is considered important to the creep properties of HP-Nb reformer tubes. The crystallographic and morphological similarities between the Type II and IV morphologies suggest that each precipitate follows a similar solidification path, thus supporting the nucleation and growth theory proposed for the Type II lamellae in Chapter 4.

Previous studies have attributed the lamellar to blocky morphology change in the HP-Nb and HP-NbTi alloys to the addition of titanium to the niobium-rich precipitates. The addition of titanium was believed to increase the (NbTi)C precipitates interfacial free energy causing the precipitates to obtain a morphology that has a comparatively lower surface area to volume ratio [5, 7]. The evidence presented in this chapter further demonstrates the role of titanium with respect to the (NbTi)C precipitate morphology. Titanium causes the nucleation of all (NbTi)C precipitates to occur on oxide inclusions and subsequently controls the morphology of the (NbTi)C precipitates during growth resulting in the Type III and IV morphologies.

Interestingly, the co-existence of (NbTi)C precipitates with lamellar (similar to the Type I) or blocky (similar to the Type III) morphologies has been documented in directionally solidified IN718 nickel-based superalloys [32]. Nucleation and growth of the blocky morphology initially proceeded until the oxide nucleation sites were believed to be depleted. Further solidification of the directional casting resulted in the emergence of the lamellar morphology. In the HP-NbTi1 and HP-NbTi2 alloys, the formation of the Type III and IV (NbTi)C was likely sufficient to largely consume the available niobium and titanium. Thus, suppressing any subsequent solidification of precipitates which exhibit the Type I or lamellar morphology.

The presence of Cr_7C_3 precipitates between the (NbTi)C and austenite interfaces suggests that once the local concentrations of niobium and titanium are exhausted, sufficient carbon remains in solution for the nucleation and growth of additional carbides. The relatively variable degree of interfacial precipitation observed between individual (NbTi)C precipitates corresponds to regions where the remaining carbon content was relatively high or low.

Currently, it is unknown if the nucleation and growth of these interfacial precipitates occurs within the melt or after solidification of the austenite matrix (i.e. as a liquid-solid or solid-solid phase

transformation). While the dendritic appearance of the interfacial precipitates may suggest that nucleation and growth of the Cr_7C_3 occurs in the melt, similar morphologies have been documented for $Cr_{23}C_6$ precipitates located on the austenite grain boundaries in sensitised austenitic stainless steels [40, 41]. Nucleation and growth of these precipitates occurred within the plane of the austenite grain boundaries while isothermally sensitising the steels at various temperatures between 595-815°C. Similar grain boundary precipitate morphologies have also been reported for Cr_7C_3 and $Cr_{23}C_6$ precipitates in the nickel-based 600 and 690 superalloys [42, 43] and for cementite (Fe_3C) precipitates in a austenitic Fe-1.3C-13Mn alloy [44]. Each type of precipitate formed through a solid-solid reaction on the austenite grain boundaries during isothermal ageing of the alloys at 1010-1093°C (Alloy 600), 718°C (Alloy 690) and 650-750°C (Fe-1.3C-13Mn). Typically, the growth of each precipitate remained confined to the grain boundary planes in each alloy.

The interfacial Cr_7C_3 in the HP-Nb and HP-NbTi alloys only formed on NbC and (NbTi)C precipitates which did not share a consistent orientation relationship with the austenite (i.e. the Type II, III and IV precipitates). Based on the disorientation data, approximately 95% of these precipitates shared high angle interfaces with the austenite. Thus, the NbC and (NbTi)C precipitates' phase boundaries share a level of crystallographic similarity with the high angle austenite grain boundaries in the sensitized stainless steel and Ni-based superalloys. The similar morphology of the Cr_7C_3 precipitates and confinement of these precipitate to the NbC and (NbTi)C phase boundaries suggests the Cr_7C_3 precipitates in the HP-Nb and HP-NbTi alloys also form through a solid-solid reaction.

Although it is believed that the Cr_7C_3 in each alloy forms through a solid-solid reaction, it must be noted that nucleation and growth of the Type II, III and IV precipitates was believed to occur in the liquid. During this time the MC/liquid interface would also act as a viable nucleation site for the Cr_7C_3. Thus, without further investigation, the specific mechanism through which these precipitates form cannot be confirmed.

Summary and Conclusions

The microstructures of two different heats of HP-NbTi alloys were investigated in the as-cast condition. Niobium and titanium were the major micro-alloying constituents present in each alloy that directly affected the primary carbide network. Tungsten was also observed in each alloy, but this was expected to remain within the austenite matrix (providing solid solution strengthening). Generally, the composition of each alloy complied with similar niobium-titanium alloys reported in the literature. Similar to the HP-Nb1 and HP-Nb2 alloys, the elements such as molybdenum and cobalt were also observed in the HP-NbTi1 and HP-NbTi2 composition. However, due to their low concentrations in both HP-NbTi alloys, the addition of these elements was considered to be of lesser importance to the alloy's creep properties.

The HP-NbTi1 alloys exhibited a mixed columnar/equi-axed grain structure (80% columnar/20% equi-axed), whereas the HP-NbTi2 alloy exhibited a completely columnar grain structure. Similar to the HP-Nb alloy, the HP-NbTi microstructure consisted of a interdendritic network of chromium-rich Cr_7C_3 precipitates separated by blocky niobium-titanium-rich (NbTi)C precipitates. These precipitates were surrounded by an austenite matrix which was relatively free of any intragranular precipitation. In addition to the (NbTi)C precipitates, cuboidal titanium carbides were also present in the HP-NbTi2 alloy, but relatively rare.

Observations of the (NbTi)C precipitates in the HP-NbTi alloy determined that two distinct morphologies existed. Both morphologies obtained an FCC crystal structure and showed no grain boundary, dendrite boundary or wall position preference. Neither type of morphology obtained a consistent orientation relationship with the matrix. Further attributes for the two morphologies can be summarised as follows:

Type III

- Blocky morphology when observed on two-dimensional polished sections,
- Spherical titanium-rich particles with oxide cores observed within the blocky (NbTi)C precipitates,

- The region of (NbTi)C precipitate directly adjacent to the Ti-rich sphere was significantly enriched with titanium. The level of titanium enrichment decreased with distance from the Ti-rich sphere,
- Multiple grains were observed to have nucleated on the spherical Ti-rich sphere. In three-dimensions these grains represented multiple blocky branches which radiated outwards from a centralised nucleus containing the oxide inclusions,
- Cr_7C_3 precipitates which obtained a dendritic morphology coated large proportions of the (NbTi)C interface.

Type IV

- Generally present as thick plates with significant undulations along the broad faces,
- Nodular appearance in three-dimensions,
- Represented <1% of the total (NbTi)C population in each alloy,
- Higher Nb:Ti ratio in comparison to the Type III morphology,
- Cr_7C_3 precipitates located between the (NbTi)C and austenite interface

Based on the previous observations both morphologies were believed to nucleate and grow ahead of the γ/liquid interface. Initially, nucleation of the spherical titanium carbo-nitrides occurs on aluminium oxide inclusions present in the melt. These Ti-rich spheres subsequently act as prolific nucleation sites for the (NbTi)C precipitates, resulting in nucleation of multiple titanium-rich (NbTi)C grains. Grains favourably oriented with respect to local thermal and compositional gradients grow preferentially, forming the blocky Type III branches. The Type IV morphology only emerges once the melt becomes relatively poor in titanium. The low concentration of titanium causes the Type IV precipitates to have a higher Nb:Ti ratio which reduces the (NbTi)C/liquid interfacial free energy. Thus, the Type IV precipitates are able obtain a higher total surface area than the Type III morphology.

Chapter References

[1] Schmidt + Clemens Group (2001). *Centralloy CA4852 Micro material data sheet.* Schmidt + Clemens Group: Lindlar, Germany.

[2] Kirchheiner, R. & Woelpert, P. (2001). *Niobium in centrifugally cast tubes for petrochemical applications.* Proceedings of the International Symposium Niobium, Orlando, U.S.A.

[3] Davis, J. R. (Ed.). (1997). *ASM Specialty Handbook: Heat-Resistant Materials.* Materials Park, Ohio: ASM International, pp. 200-218.

[4] American Society for Testing and Materials. (2012). *Standard Specification for Centrifugally Cast Iron-Chromium-Nickel High-Alloy Tubing for Pressure Application at High Temperatures.* ASTM A608/A608M-12.

[5] de Almeida, L. H., Ribeiro, A. F. & Le May, I. (2003). *Microstructural Characterization of modified 25Cr-35Ni centrifugally cast steel furnace tubes.* Materials Characterization, 49: pp. 219-229.

[6] Ribeiro, A. F., de Almeida, L. H., dos Santos, D. S., Fruchart, D. & Bobrovnitchii, G. S. (2003). *Microstructural modifications induced by hydrogen in a heat resistant steel type HP-45 with Nb and Ti additions.* Journal of Alloys and Compounds, 356-357: pp. 693-696.

[7] Caballero, F. G., Imizcoz, P., Lopez, V., Alvarez, L. F. & Garcia de Andrés, C. (2007). *Use of titanium and zirconium in centrifugally cast heat resistant steel.* Materials Science and Technology, 23: pp. 528-534.

[8] Nishimoto, K., Saida, K., Inui, M. & Takahashi, M. (2001). *Changes in microstructure of HP-modified, heat-resisting cast alloys under long-term aging. Repair weld craking of service exposed, HP-modified, heat-resisting cast alloys (2nd report).* Welding International, 15(7): pp. 1-9.

[9] Shinoda, T., Zaghloul, M. B, Kondo, Y. & Tanaka, R. (1978). *The Effect of Single and Combined Additions of Ti and Nb on the Structure and Strength of the Centrifugally Cast HK40 Steel.* Transactions of the Iron and Steel Institute of Japan, 18: pp. 139-148.

[10] Tin, S., Pollock, T. M. & Murphy, W. (2001). *Stabilization of Thermosolutal Convective Instabilities in Ni-Based Single-Crystal Superalloys: Carbon Additions and Freckle Formation.* Metallurgical and Materials Transactions A, 32A: pp. 1743-1751

[11] Tin, S. & Pollock, T. M. (2003). *Stabilization of Thermosolutal Convective Instabilities in Ni-Based Single-Crystal Superalloys: Carbide Precipitation and Rayleigh Numbers.* Metallurgical and Materials Transactions A, 34A: pp. 1953-1967.

[12] Zaghloul, M. B., Shinoda, T. & Tanaka, R. (1977). *Relation between Structure and Creep Rupture Strength of Centrifugally Cast HK40 Steel.* Transactions of the Iron and Steel Institute of Japan, 17(1): pp. 28-36.

[13] de Almeida Soares, G. D., de Almeida, L. H., da Silveira, T. L. & Le May, I. (1992). *Niobium Additions in HP Heat-Resistant Cast Stainless Steels.* Materials Characterization, 29: pp. 387-396.

[14] Wu, X. Q., Jing, Y. G., Zheng, Z. M., Yao, W. Ke. & Hu, Z. Q. (2000). The eutectic carbides and rupture strength of 25Cr20Ni heat-resistant steel tubes centrifugally cast with different solidification conditions. Materials Science and Engineering A, 293: pp. 252-260.

[15] Hou, W. T. & Honeycombe, R. W. K. (1985). Structure of Centrifugally cast austenitic steels: Part 2 Effects of Nb, Ti and Zr. Materials Science and Technology, 1(5): pp. 390-397.

[16] Villars, P. (Ed.) & Cenzual, K. (Ed) (2008). *Pearson's Crystal Data: Crystal Structure Database for Inorganic Compounds.* (Version 1.0) [Computer software]. Materials Park, Ohio, U. S. A.: ASM International®.

[17] Voicu, R., Andrieu, E., Poquillon, D., Furtado, J. & Lacaze, J. (2009). *Microstructure evolution of HP40-Nb alloys during aging under air at 1000°C.* Materials Characterization, 60: pp. 1020-1027.

[18] Laigo, J., Christien, F., Le Gall, R., Tancret, F. & Furtado, J. (2008). *SEM, EDS, EPMA-WDS and EBSD characterization of carbides in HP type heat resistant alloys.* Materials Characterization, 59: pp. 1580-1586.

[19] de Almeida Soares, G. D., de Almeida, L. H., da Silveira, T. L. & Le May, I. (1992). *Niobium Additions in HP Heat-Resistant Cast Stainless Steels.* Materials Characterization, 29: pp. 387-396.

[20] Ibañez, R. A. P., Soares, G. D. A., de Almeida, L. H. & Le May, I. (1993). *Effects of Si Content on the Microstructure of Modified-HP Austenitic Steels.* Materials Characterization, 30: pp. 243-249.

[21] Dubrovinskaia, N. A., Dubrovinsky, L. S., Saxena, S. K., Ahuja, R. & Johansson, B. (1999). *High-pressure study of titanium carbide.* Journal of Alloys and Compounds, 289: pp. 24-27.

[22] Khaenko, B. V. & Kukol', V. V. (1989). *Real order structure of titanium carbide.* Soviet Physics, Crystallography, 34: pp. 905-908.

[23] Goretzki, H. (1967). Neutron Diffraction Studies of Titanium-Carbon and Zirconium-Carbon Alloys. Physica Status Solidi A, 20: pp. K141-K143.

[24] Khaenko, B. V., Golub, S. Y. & Arbuzov, M. P. (1980). The order structure of titanium carbide. Soviet Physics, Crystallography, 25: pp. 63-67.

[25] Raman, S. & Ramachandran, G. N. (1962). STRUCTURE OF A NEW CARBIDE OF TITANIUM. Current Science, 31 : pp. 321-322.

[26] Wahab, A. A. & Kral, M. V. (2005). *3D analysis of creep voids in hydrogen reformer tubes.* Materials Science & Engineering A, 412: pp. 222-229.

[27] Wahab, A. A., Hutchinson, C. R. & Kral, M. V. (2006). *A three-dimensional characterization of creep void formation in hydrogen reformer tube.* Scripta Materialia, 55: pp. 69-73.

[28] Nunes, F. C., Dille, J., Delplancke J. -L & de Almeida, L. H. (2006). Yttrium addition to heat-resistant cast stainless steel. Scripta Materialia, 54: pp. 1553-1556.

[29] Lönnberg, B. & Lundström, T. (1988). Crystal Growth of Solid Solutions of the Group IV-VI Transition Metals Monocarbides from Molten Aluminium. Chemica Scripta, 28(1): pp. 25-32.

[30] Shveikin, G. P., Tskhai, V. A. & Mitrofanov, B. V. (1987). DEPENDENCE OF MICROHARDNESS ON THE PARAMETERS OF THE ELECTRONIC STRUCTURE OF CUBIC CARBIDES AND NITRIDES OF GROUP IV-VI TRANSITION METALS. Inorganic Materials, 23: pp. 837-841.

[31] Byun, J. –S, Shim, J. –M, Cho, Y. W. and Lee, D. N. (2003). *Non-metallic inclusion and intragranular nucleation of ferrite in Ti-killed C-Mn steel.* Acta Materialia, 51:pp. 1593-1606.

[32] Formenti, A., Eliasson, A., Mitchell, A. & Fredriksson, H. (2005). Solidification Sequence and Carbide Precipitation in Ni-Base Superalloys IN718, IN625 and IN939. High Temperature Materials and Processes, 24: pp. 239-258.

[33] Tin, S & Pollock, T. M. (2003). Phase instabilities and carbon additions in single-crystal nickel-base superalloys. Materials Science and Engineering A, 348: pp. 111-121.

[34] Bhambri, A. K., Kattamis, T. Z. & Morral, J. E. (1975). Cast Microstructure of Inconel 713C and its Dependence on Solidification Variable. Metallurgical Transactions B, 6B: pp. 523-533.

[35] Chen, J., Lee, J. H., Jo, C. Y., Choe, S. J. & Lee, Y. T. (1998). MC carbide formation in directionally solidified MAR-M247 LC superalloy. Materials Science and Engineering A, 247: pp. 113-125.

[36] Seo, S. M., Kim, I. S., Lee, J. H., Jo, C. Y., Miyahara, H. & Ogi, K. (2008). Microstructural Evolution in Directionally Solidified Ni-Base Superalloy IN792 + Hf. Journal of Materials Science & Technology, 24(1): pp. 110-114.

[37] Lui, L. & Sommer, F. (1994). EFFECT OF SOLIDIFICATION CONDITIONS ON MC CARBIDES IN A NICKEL-BASE SUPERALLOY IN 738 LC. Scripta Metallurgica et Materialia, 30: pp. 587-591.

[38] Fernandez, R., Lecomte, J. C. & Kattamis, T. Z. (1978). Effect of Solidification Parameters on the Growth Geometry of MC Carbide in IN-100 Dendritic Monocrystals. Metallurgical Transactions A, 9A: pp. 1381-1386.

[39] Chen, Q. Z., Jones, C. N. & Knowles, D. M. (2002). Effect of alloying chemistry on MC carbide morphology in modified RR20720 and RR2086 SX superalloys. Scripta Materialia, 47: pp. 669-675.

[40] Wilson, F. G. (1971). THE MORPHOLOGY OF GRAIN- AND TWIN- BOUNDARY CARBIDES IN AUSTENITIC STEELS. Journal of the Iron and Steel Institute, 209(2): pp. 126-130

[41] Mahla, E. M., & Neilsen, N. A. (1951). CARBIDE PRECIPITATION IN TYPE 304 STAINLESS STEEL – AN ELECTRON MICROSCOPE STUDY. American Society for Metals, 43: pp. 290-322.

[42] Webb, G. L. & Burke, M. G. (1995). Stress Corrosion Cracking Behaviour of Alloy 600 in High Temperature Water. Conference Proceeding: Presented at Seventh International Symposium on Environmental Degradation of Materials in Nuclear Power Systems –Water Reactors, August 6-10, 1995.

[43] Symons, D. M. (1998). *The Effect of Carbide Precipitation on the Hydrogen-Enhanced Fracture Behaviour of Alloy 690.* Metallurgical and Materials Transactions A, 29A: pp. 1265-1277.

[44] Kral, M. V. & Spanos, G. (1997). *THREE DIMENSIONAL MORPHOLOGY OF CEMENTITE PRECIPITATES.* Scripta Materialia, 36(8): pp. 875-882.

Chapter 6 Mid-Wall Microstructural Evolution of the HP-Nb Alloys during Unstressed Isothermal Ageing

The following chapter describes in detail the microstructural evolution observed at the mid-wall position of the HP-Nb1 and HP-Nb2 alloys after isothermal ageing at 1000, 1050 and 1100°C for 500, 1000, 3000, 6000 and 10,000 hours respectively. Ageing of all samples was performed in an air atmosphere resulting in significant decarburisation and nitridation to occur at each samples exposed surfaces. The effects of the ageing atmosphere became particularly apparent in all 10,000 hour samples resulting in multiple phase transformations which were not observed at the mid-wall position. In the present work, emphasis has been placed on the mid-wall microstructure as the samples subjected to accelerated creep testing by Quest Integrity Group (QIG) contained solely the mid-wall microstructure (i.e. the gauge length of creep samples was coincident with the tube's mid-wall position). Therefore, the creep properties of the aged alloys were dictated solely by the microstructural evolution which occurred at the mid-wall position.

While phase transformations similar to those observed at the inner and outer diameter of the HP-Nb1 and HP-Nb2 alloys have been observed at the same locations in ex-service reformer tubes, theses phases are typically present in lower volume fractions in the ex-service material than was observed after laboratory ageing [1]. Since these phases have been observed within ex-service reformer tubes, the affected material at the inner and outer diameter positions of the laboratory aged samples was also subjected to microstructural analysis. However, a detailed discussion of these phase transformations will be presented separately in Chapter 8.

6.1 Overview of the HP-Nb Alloy's Mid-Wall Microstructural Evolution during Isothermal Ageing

Figure 6.1 to Figure 6.6 show optical and scanning electron micrographs depicting the microstructural evolution of the HP-Nb2 alloy after unstressed isothermal ageing at 1000°C and the HP-Nb1 alloy after ageing at 1050 and 1100°C for between 500-10,000 hours. All images were taken from the mid-wall position of each aged sample as these regions are representative of the microstructure within the gauge length of QIG's accelerated creep test samples. The magnifications used in Figure 6.1 - Figure 6.6 have been presented specifically to give a general overview of the HP-Nb alloy's microstructural evolution with respect to the ageing temperature and time. Due to the significant microstructural changes which occur in the HP-Nb alloy during thermal exposure, a general understanding of the HP-Nb microstructural evolution with respect to temperature and time was considered necessary before presenting the detailed discussion of each phase's evolution during ageing. Therefore, detailed analysis and discussion of each phase labelled in Figure 6.2, Figure 6.4 and Figure 6.5 is given separately in Sections 6.2 and 0. For ease of reference the phases observed at the mid-wall position with respect to ageing temperature and time have been summarised in Table 6.1.

Due to the limited availability of as-cast HP-Nb material, the HP-Nb1 alloy was subjected to ageing at 1050 and 1100°C while the HP-Nb2 alloy was subjected to ageing at 1000°C. As discussed in Chapter 4, both alloys fell within the generally accepted specification for niobium modified HP alloys [2], but the differing casting conditions experienced by the HP-Nb1 and HP-Nb2 alloys resulted in differences in the tubes' macro- and micro- structures. Consequently, these differences had to be taken into account when comparing the microstructural evolution of the two alloys.

The difference between the alloys chemical composition and respective as-cast primary carbide networks (i.e. total precipitate area fraction and Type I and II NbC precipitates) were considered to be the most significant factors which could influence the microstructural evolution of each alloy when ageing at a constant temperature. Soares *et al*. [3] and Ibañez *et al.* [4] conducted similar laboratory ageing at temperatures between 700-1100°C on HP-Nb alloys with varying concentrations of niobium and silicon (0-1.97wt.% Nb, 1.84-2.62wt.% Si). Ageing at temperatures between 700-1050°C caused the Cr_7C_3-to-$Cr_{23}C_6$ and NbC-to-G-phase ($Ni_{16}Nb_6Si_7$) transformations to occur. While

these transformations remained consistent regardless of the ageing temperature and alloy composition, the NbC-to-G-phase transformation rate varied significantly. While the NbC-to-G-phase transformation rate was generally greatest when ageing the alloys at approximately 950°C, alloys with greater niobium and silicon contents exhibited higher NbC-to-G-phase transformation rates during ageing [3, 4].

The greater niobium and silicon content in the HP-Nb2 alloy was expected to slightly enhance the NbC-to-G-phase transformation in comparison to the HP-Nb1 alloy when ageing at a constant temperature. However, as the relative compositional difference between the HP-Nb1 and HP-Nb2 alloys (0.44 vs. 0.92wt.% Nb and 1.26 vs. 1.53wt.% Si, respectively) was considerably lower than those studied in the literature, the difference in the NbC-to-G-phase transformation rate was expected to be less pronounced in the HP-Nb1 and HP-Nb2 alloys than seen in the literature.

Overall, it was believed that the microstructural evolution within the HP-Nb1 and HP-Nb2 alloys (e.g. the types of phase transformations) would be the similar if each alloy had been aged at the same temperature. Hence, if isothermal ageing of the HP-Nb1 alloy was carried out at 1000°C for 500 to 10,000 hours, the same phase transformations that were observed in the HP-Nb2 alloy would also be expected to occur in the HP-Nb1 alloy. However, the rate at which each transformation occurred would be influenced by the alloy's chemical composition. Short-term ageing (1000 hours) of the HP-Nb1 alloy at 1000°C confirmed the types of phase transformations were consistent for each alloy when ageing at constant temperatures.

It must also be stressed that the HP-Nb1 and HP-Nb2 alloys were commercially produced using a centrifugal casting process. Thus, the observed compositional difference is typical of tubes used in service. Consequently, the microstructural evolutions of these alloys during isothermal ageing at temperatures between 1000-1100°C are considered to be representative of all HP-Nb tubes which fall within the manufactures specified tolerances presented in Appendix A.

6.1.1 Unstressed Isothermal Ageing of the HP-Nb2 Alloy at 1000°C

Figure 6.1 (a) to (c) show representative optical micrographs taken from the HP-Nb2 alloy in the as-cast condition and after ageing at 1000°C for 1000 and 10,000 hours respectively. Comparison of the as-cast and 1000 hours micrographs demonstrates the marked microstructural evolution which occurs in the HP-Nb alloy during short-term ageing. After 1000 hours, the as-cast interdendritic primary carbide network appears relatively unchanged at the given magnification (100x). However, extensive secondary precipitation occurred within the previously precipitate free as-cast matrix. Coarsening of the primary and secondary precipitates during prolonged ageing at 1000°C was unapparent based on observations each sample's microstructure using the light optical microscope (LOM).

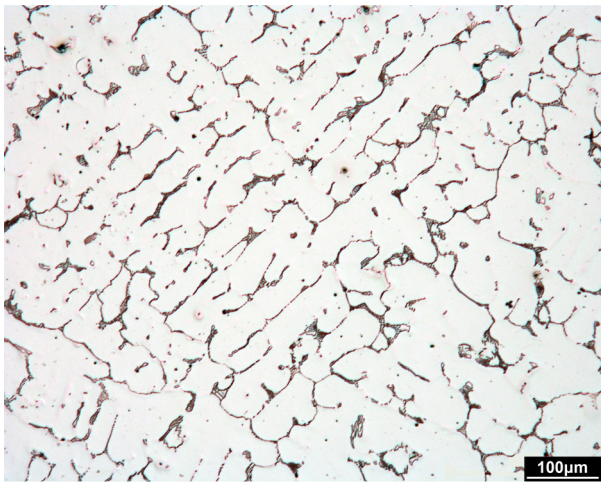

(a)

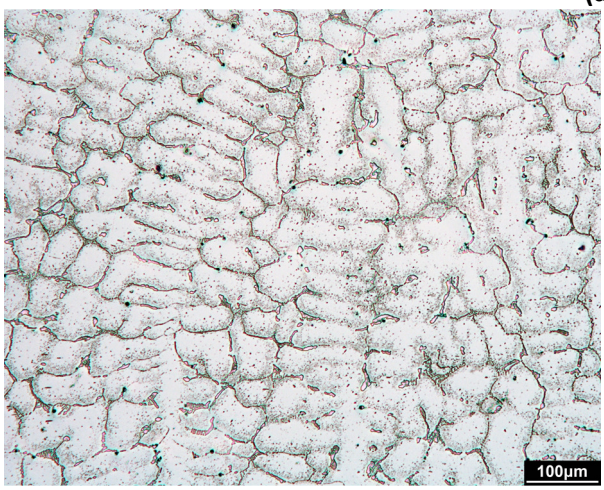

(b)

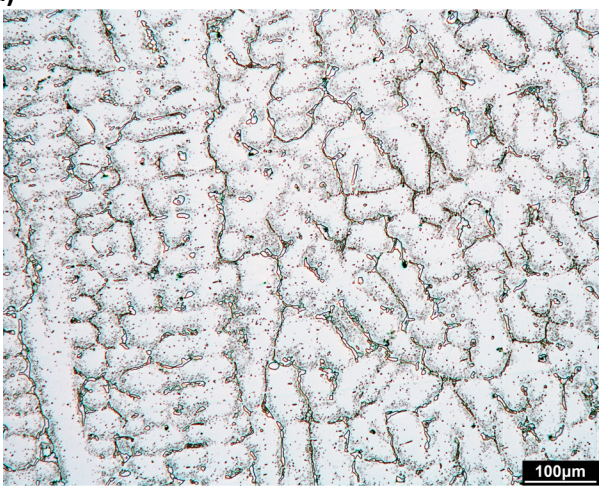

(c)

Figure 6.1 - Low magnification optical micrographs showing the HP-Nb2 alloy in the (a) as-cast condition and after unstressed isothermal ageing at 1000°C for (b) 1000 and (c) 10,000 hours.

The backscatter electron micrographs shown in Figure 6.2 (a) and (b) further demonstrate the considerable microstructural changes that occur in the HP-Nb alloy within the first 1000 hours of exposure to 1000°C (representing approximately 1% of a reformer tube's typical service life). Exposure for 1000 hours was sufficient to cause the complete transformation of the as-cast Cr_7C_3 to $Cr_{23}C_6$ and partial transformation of the NbC to η-carbides. Additionally, the austenite matrix was densely populated with fine secondary precipitates (typically <1μm^2 and denoted S in Figure 6.2 (b)). The secondary precipitates predominantly exhibited the $Cr_{23}C_6$ crystal structure and appeared dark grey when observing the aged microstructures using backscattered electrons. Niobium-rich (NbC) secondary precipitates (white) similar in size to the secondary $Cr_{23}C_6$ were also present after 1000 hours (shown in Figure 6.10).

Typically, the secondary $Cr_{23}C_6$ precipitates were preferentially located adjacent to the primary network. The secondary precipitate number density progressively decreased with increasing distance from the primary precipitates. As a result, the centres of the austenite dendrite arms (i.e. farthest from the primary precipitates) were often devoid of secondary precipitation (also highlighted in Figure 6.2 (b) as a "precipitate free zone", or PFZ). Generally, the secondary $Cr_{23}C_6$ and NbC exhibited a cuboidal morphology, but larger needle-like $Cr_{23}C_6$ precipitates were also present within the matrix. The cuboidal $Cr_{23}C_6$ precipitates were significantly more abundant than the NbC and the needle-like $Cr_{23}C_6$ with typically less than 30 of the latter morphologies observable within the 120 x 95μm field of view shown in Figure 6.2 (b) - (e) (estimated to be less than 1% of the total secondary precipitate population).

Further microstructural evolution, although less dramatic, was apparent when ageing for between 1000 to 10,000 hours. Comparison of Figure 6.2 (b) and (e) indicates the primary[20] and secondary $Cr_{23}C_6$ precipitates noticeably coarsen. Generally, the density of secondary precipitation reduced with increasing exposure time suggesting that coarsening and dissolution of the secondary precipitates supported the observed coarsening of the primary $Cr_{23}C_6$ precipitates. The NbC-to-η-carbide transformation also progressed during prolonged ageing, with approximately 50% of the as-cast NbC

[20] The term 'primary' typically refers to the interdendritic precipitates which form on solidification of the HP-Nb alloys. During ageing the interdendritic 'primary' Cr_7C_3 precipitates transform to $Cr_{23}C_6$. Although this transformation causes the interdendritic $Cr_{23}C_6$ precipitates to not strictly be 'primary' precipitates, using this term allows the interdendritic $Cr_{23}C_6$ to be clearly and simply distinguished from the intragranular 'secondary' $Cr_{23}C_6$ precipitates which also form during ageing.

(by area fraction) transformed to η-carbide after 10,000 hours. The η-carbides were considerably larger than the original NbC lamellae with many precipitates being comparable in size to the primary $Cr_{23}C_6$ precipitates after 10,000 hours (Figure 6.2 (e)). The number of secondary NbC precipitates also reduced during prolonged exposure likely due to these precipitates also transforming to η-carbides.

The MnS inclusions (present in the as-cast condition) remained stable during ageing. Qualitative comparisons between the as-cast and aged samples indicated the number, average size and area fraction of these inclusions remained relatively constant during ageing. Overall, the volume fraction of MnS precipitates was insignificant within all of the aged HP-Nb alloys (regardless of ageing temperature) in comparison to the primary carbide network.

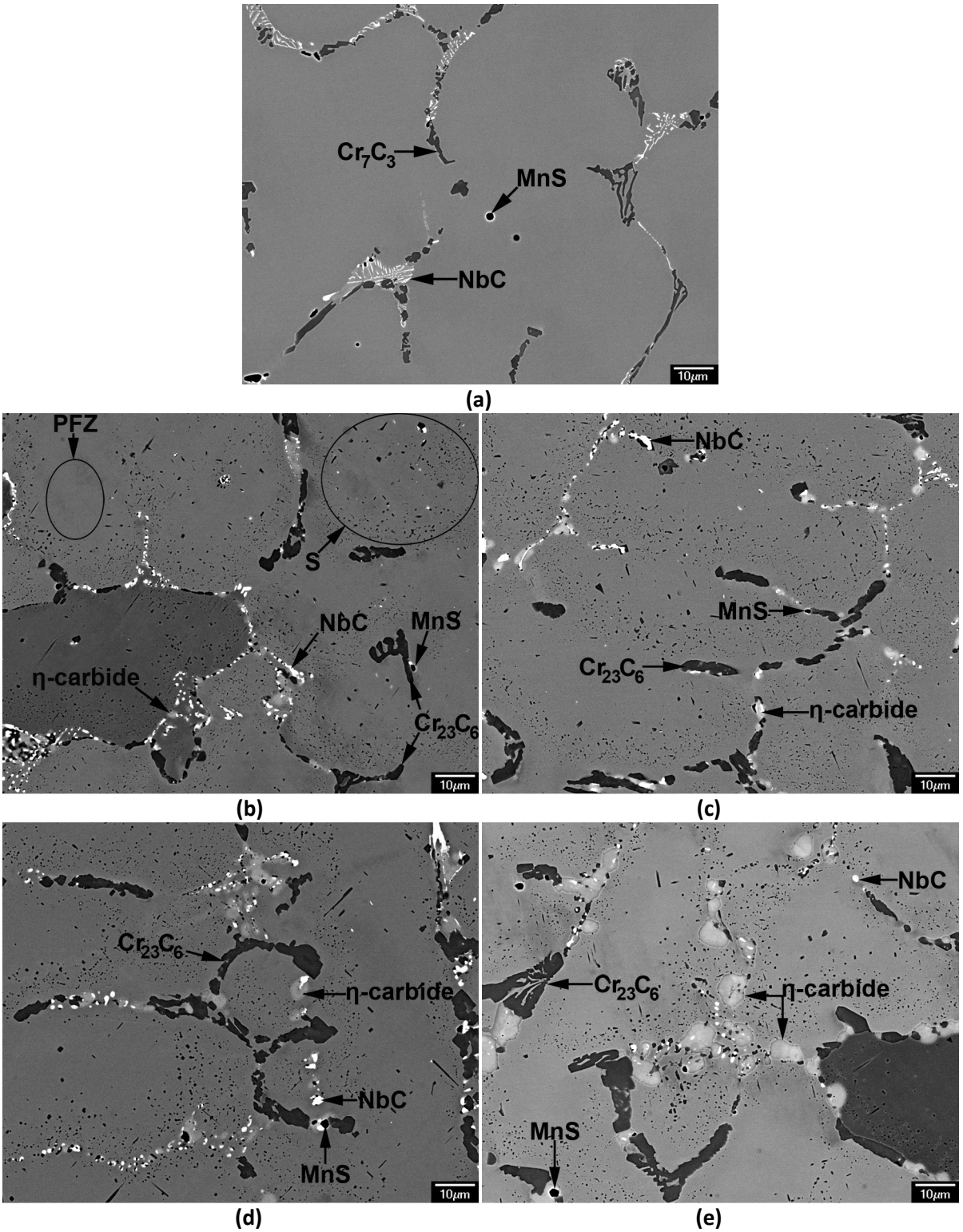

Figure 6.2 - Backscatter electron micrographs of the HP-Nb2 alloy in the (a) as-cast condition and after ageing at 1000°C for (b) 1000 hours (c) 3000 hours (d) 6000 hours (e) 10,000 hours.

6.1.2 Unstressed Isothermal Ageing of the HP-Nb1 Alloy at 1050°C

Optical micrographs taken from the HP-Nb1 alloy in the as-cast condition and after ageing at 1050°C for 500 hours and 10,000 hours are shown in Figure 6.3 (a) to (c). As observed in the HP-Nb2 samples after ageing at 1000°C, the interdendritic primary precipitate network remained largely intact after ageing at 1050°C for between 1000-10,000 hours. Comparison between primary precipitates in the as-cast and 10,000h samples at low magnifications (100x) indicated that notable coarsening of this network occurred during prolonged ageing at 1050°C. While a reduction in the primary network's fragmentation during ageing seems qualitatively evident through optical analysis of the as-cast and 1050°C-10,000h samples, quantitative analysis of optical micrographs was ultimately inconclusive.

As discussed in Chapter 5, quantitative analysis of the primary precipitate network's fragmentation is inherently complex. While numerous regions of the primary network in the aged sample appeared connected at the magnifications between 50-200x, this connection was often not observed when viewed at 500-1000x. Furthermore, due to the complex three-dimensional morphology of the primary carbide network, precipitates which appear fragmented on two-dimensional sections often exhibited connectivity in three-dimensions. Therefore, performing quantitative measurements on two-dimensional sections was considered to be inaccurate and was not performed on any of the aged samples.

Widespread secondary precipitation within the austenite matrix was also observable after 500 hours. Coarsening of the secondary precipitates is apparent when comparing the 1000 and 10,000 hour micrographs. The secondary precipitates present in the 1050°C-10,000 hours sample were also visibly coarser in comparison to the secondary precipitates observed in the HP-Nb2 1000°C-10,000h sample (Figure 6.1 (c)).

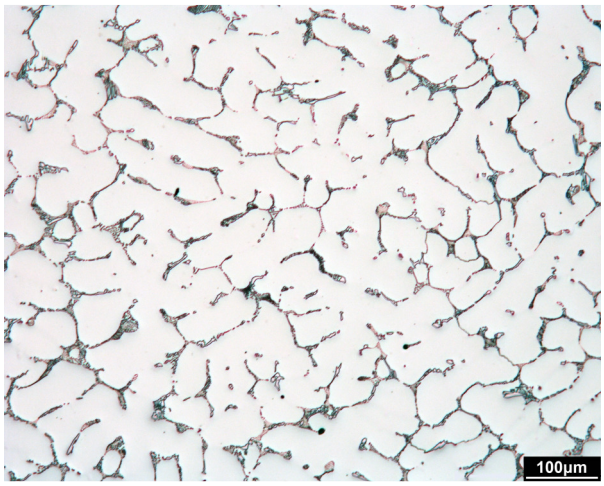

(a)

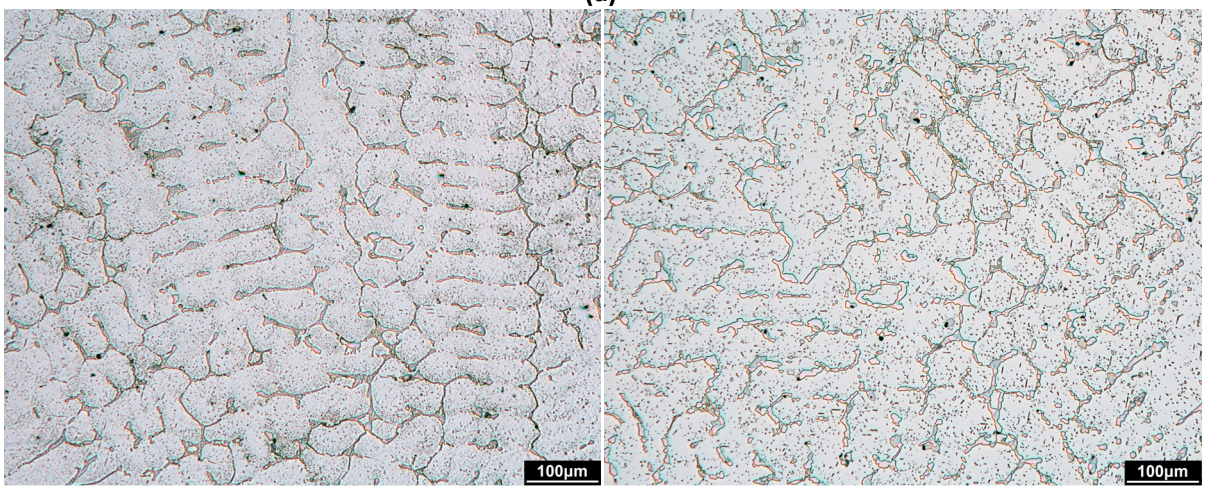

(b) (c)

Figure 6.3 - Low magnification optical micrographs showing the HP-Nb1 alloy in the (a) as-cast condition and after unstressed isothermal ageing at 1050°C for (b) 1000 and (c) 10,000 hours.

The scanning electron micrographs in Figure 6.4 (b) to (e) illustrate the microstructural evolution of the HP-Nb1 alloy after ageing at 1050°C for 500, 1000, 3000 and 10,000 hours. Due to the limited quantity of material for the ageing experiments, Quest Integrity Group did not take a sample after 6000 hours.

Transformation of the as-cast primary Cr_7C_3 to $Cr_{23}C_6$ was complete after 500 hours exposure to 1050°C. During prolonged ageing at 1050°C, the primary $Cr_{23}C_6$ coarsened significantly (Figure 6.3 (e)). In fact, ageing at 1050°C resulted in notably coarser $Cr_{23}C_6$ precipitates in comparison to those observed in the HP-Nb2 1000°C-10,000 hours aged sample (Figure 6.2 (e)).

In contrast to the HP-Nb2 1000°C samples, the NbC precipitates in the HP-Nb1 alloy remained stable when ageing for up to 3000 hours at 1050°C. The NbC-to-η-carbide transformation was only

observed at the mid-wall position after ageing for 10,000 hours at 1050°C (Figure 6.4 (e)). However, as discussed in Chapter 8, the NbC-to-η-carbide transformation at the mid-wall position of the HP-Nb1 alloy during ageing at 1050°C was believed to have been induced by the furnace atmosphere.

Overall, approximately 40% of the NbC area fraction observed after 3000 hours of ageing had transformed to η-carbides after 10,000 hours. However, the transformation rate varied significantly between individual NbC colonies. For colonies undergoing the NbC-to-η-carbide transformation, the transformation was often nearly complete after 10,000 hours. Generally, the transformed η-carbides encompassed the entire prior NbC colony, causing these precipitates to be comparable in size to the primary $Cr_{23}C_6$ (Figure 6.4 (e)). Conversely, for colonies where the NbC-to-η-carbide transformation did not occur, the Type I and II NbC lamellae simply coarsened.

Widespread precipitation of secondary carbides occurred within the austenite matrix after 500 hours exposure at 1050°C (Figure 6.4 (b)). The secondary precipitate distribution was mainly comprised of $Cr_{23}C_6$ (dark grey) precipitates with comparatively rare NbC precipitates (white) also present. Identical to the secondary precipitates present after ageing at 1000°C, the secondary $Cr_{23}C_6$ precipitates exhibited cuboidal and needle-like morphologies after 1000 hours exposure to 1050°C. The cuboidal morphology was clearly dominant in the HP-Nb1 1050°C samples. As shown in Figure 6.4 (b) to (e), considerable Ostwald ripening of the secondary precipitate distribution occurred during prolonged ageing at 1050°C.

Similar to the 1000°C samples, the MnS inclusions remained stable during ageing at 1050°C.

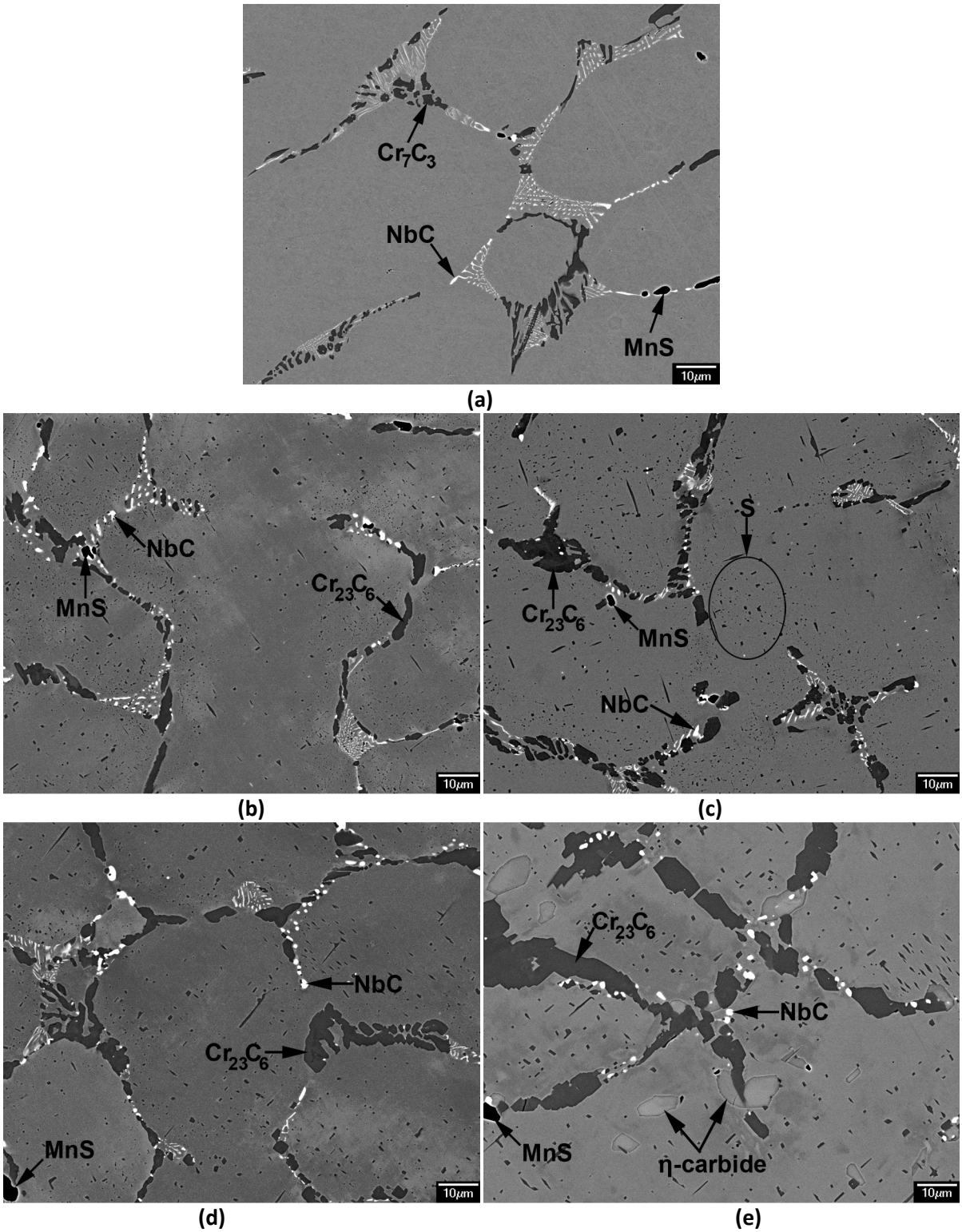

Figure 6.4 - Backscatter electron micrographs of the HP-Nb1 alloy in the (a) as-cast condition and after ageing at 1050°C for (b) 500 hours (c) 1000 hours (d) 3000 hours (e) 10,000 hours.

6.1.3 Unstressed Isothermal Ageing of the HP-Nb1 alloy at 1100°C

Figure 6.5 (a) to (c) show low magnification optical micrographs of the HP-Nb1 alloy in the as-cast condition and after ageing at 1100°C for 1000 and 10,000 hours. Identical to the 1000 and 1050°C aged sample, the primary precipitate network appeared to remain relatively intact but somewhat coarser after ageing at 1100°C for 1000 hours. Widespread secondary precipitation can also be observed within the austenite matrix after ageing for 1000 hours.

Long-term ageing of the HP-Nb1 alloy at 1100°C can be seen to have caused the primary precipitate network to coarsen significantly (Figure 6.5 (c)). Any reduction in the primary network's fragmentation as a result of the significant coarsening experienced by these precipitate during prolonged ageing was not obvious when observing the samples by optical microscopy. The extensive secondary precipitation present within the austenite matrix after 1000 hours had largely dissolved after 10,000 hours, suggesting that Ostwald ripening of this distribution at 1100°C had resulted in these precipitates being completely absorbed by the larger primary precipitate network.

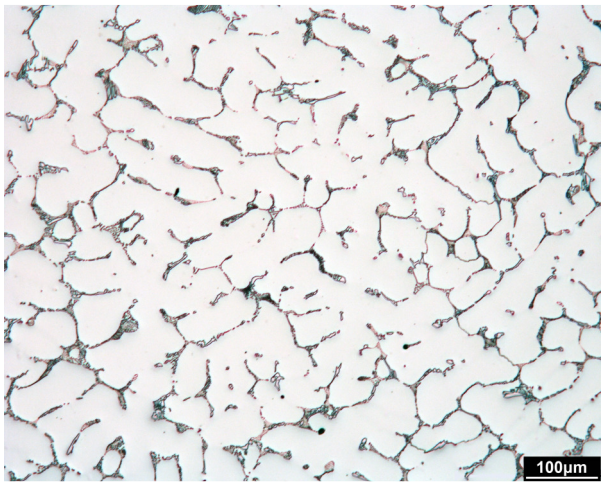

(a)

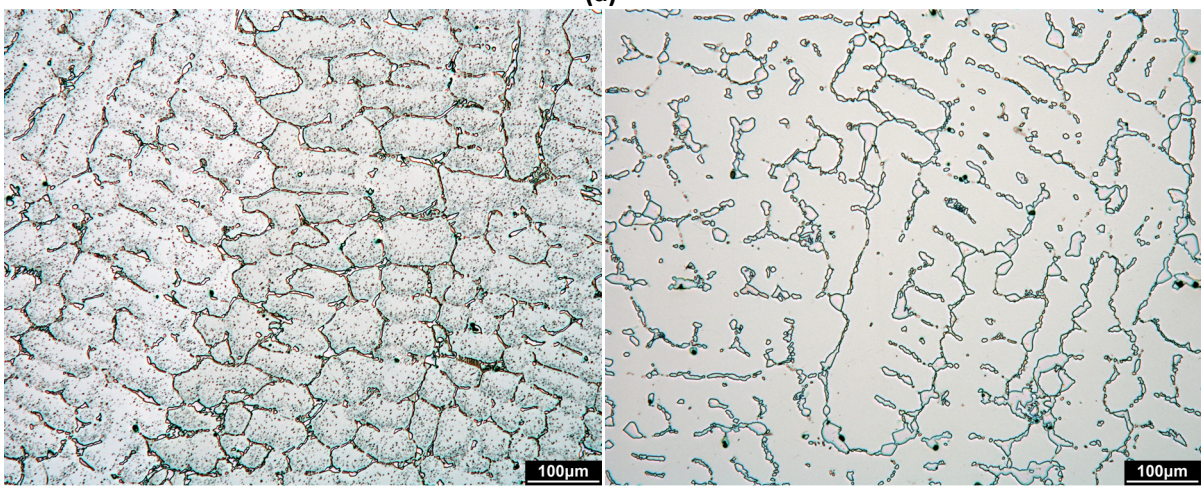

(b) (c)

Figure 6.5 - Low magnification optical micrographs showing the HP-Nb1 alloy in the (a) as-cast condition and after unstressed isothermal ageing at 1100°C for (b) 1000 and (c) 10,000 hours.

The microstructural evolution of the HP-Nb1 alloy after ageing at 1100°C for 500, 1000, 3000 and 10,000 hours as observed using backscattered electrons are shown in Figure 6.6 (b) to (e). Identical to the 1000 and 1050°C samples, complete transformation of the as-cast Cr_7C_3 to $Cr_{23}C_6$ occurred within the first 500 hours of ageing at 1100°C. The increased ageing temperature caused the primary $Cr_{23}C_6$ to coarsen at a greater rate than observed in the 1000 and 1050°C samples. For example, ageing the HP-Nb1 at 1100°C for 1000 hours resulted in primary $Cr_{23}C_6$ precipitates similar in size to those observed in the HP-Nb2 1000°C-10,000h sample (~18µm^2). The air ageing atmosphere also caused partial transformation of the primary $Cr_{23}C_6$ precipitate network to Cr_2N in the 10,000 hour sample (not shown in Figure 6.6 (e)). However, this transformation was typically confined to $Cr_{23}C_6$ precipitates located on the grain boundaries (as opposed to dendrite boundaries) and was relatively rare at the mid-wall position. This transformation has discussed in further detail in Chapter 8.

Regardless of the ageing time, the NbC did not transform during ageing at 1100°C and underwent significant coarsening during prolonged ageing. The average size of the NbC precipitates approximately doubled within the first 3000 hours of exposure to 1100°C (0.5-1.2μm^2). A similar size increase was also observed when ageing between 3000-10,000 hours ageing (~1.2-2μm^2). However, while the size of the NbC precipitates increased during prolonged ageing, the area fraction remained relatively constant (~0.9%)

Widespread precipitation of cuboidal $Cr_{23}C_6$ secondary precipitates was observed after ageing at 1100°C for 500 hours. However, ageing at 1100°C for caused the secondary $Cr_{23}C_6$ precipitate distribution to become visibly sparser in comparison to those observed after ageing at 1000 and 1050°C for 500 hours. Interestingly the higher ageing temperature caused the secondary precipitate distribution in the HP-Nb1 1100°C-1000h sample to be notably coarser in comparison to the HP-Nb2 1000°C-10,000h sample. Secondary NbC precipitates were rare in all 1100°C aged samples. The 500-3000 hours samples typically contained less than three secondary NbC precipitates within the field of view shown in Figure 6.6 (b) - (e). As shown in Figure 6.6 (e) the entire secondary precipitate distribution had completely disappeared after ageing at 1100°C for 10,000 hours with the chromium and carbon ejected from the dissolving secondary precipitates contributing to the coarsening of the primary $Cr_{23}C_6$ network.

As observed in the 1000 and 1050°C aged samples, the MnS inclusions remained relatively stable during ageing of the HP-Nb1 alloys at 1100°C.

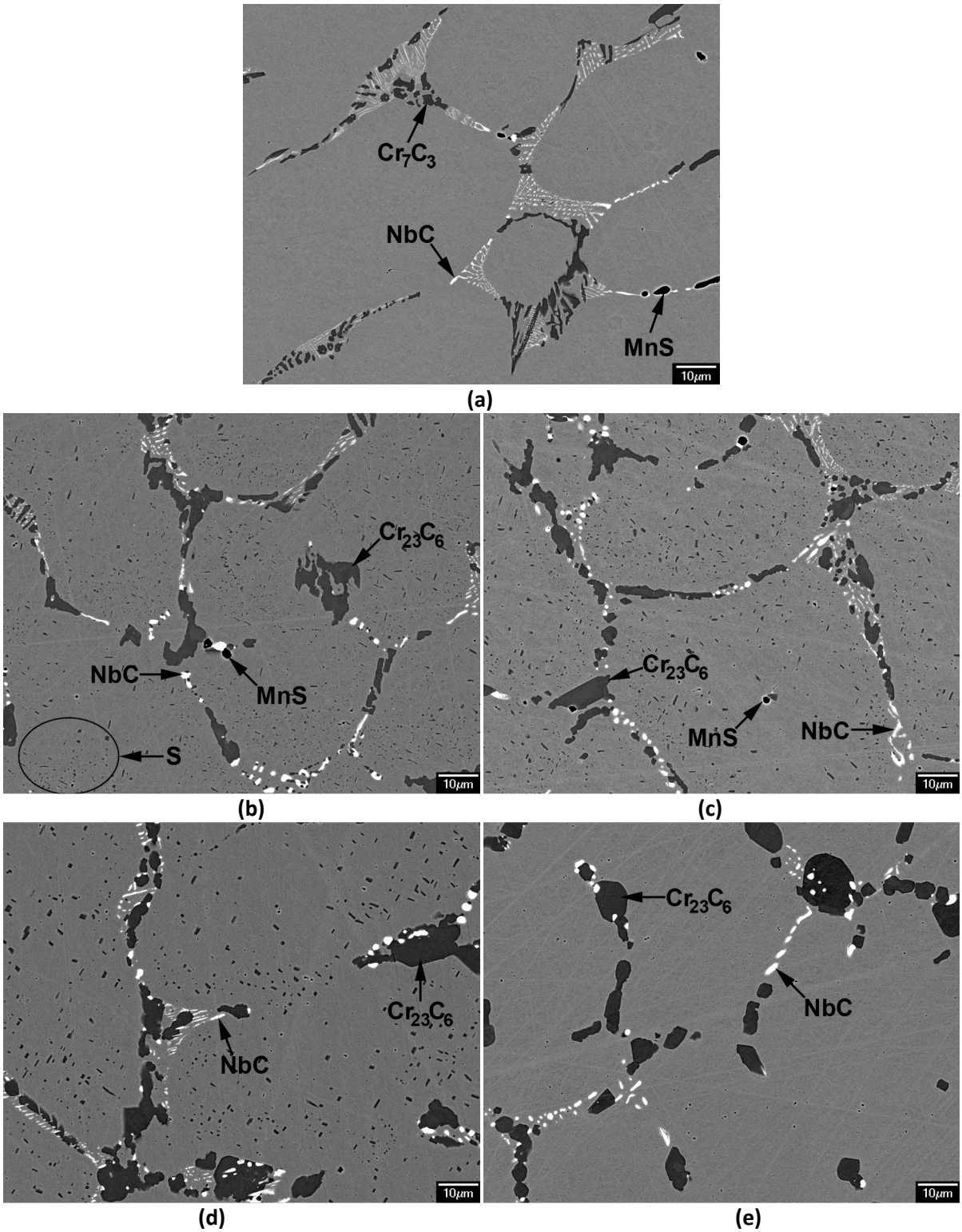

Figure 6.6 - Backscatter electron micrographs of the HP-Nb1 alloy in the (a) as-cast condition and after ageing at 1100°C for (b) 500 hours (c) 1000 hours (d) 3000 hours (e) 10,000 hours.

6.1.4 Summary of the Phases Observed in each Aged Sample

Table 6.1 gives a summary of the phases identified at the mid-wall position for each aged sample. Identification of these phases using EDS, EBSD, SAD and XRD is discussed in Sections 6.2 and 0.

Table 6.1 - Summary of the primary and secondary precipitate phase identified in the HP-Nb1 and HP-Nb2 alloys with respect to ageing temperature and time.

<table>
<tr><th rowspan="2">T (°C)</th><th rowspan="2">Network</th><th colspan="6">Aging Time (hours)</th></tr>
<tr><th>AC</th><th>500</th><th>1000</th><th>3000</th><th>6000</th><th>10,000</th></tr>
<tr><td rowspan="2">1000 (Nb2)</td><td>Primary</td><td>Cr_7C_3, NbC</td><td rowspan="2">No sample taken</td><td colspan="3">$Cr_{23}C_6$, NbC, η-carbide, MnS</td></tr>
<tr><td>Secondary</td><td>No precipitates</td><td colspan="2">$Cr_{23}C_6$, NbC</td><td>$Cr_{23}C_6$</td></tr>
<tr><td rowspan="2">1050 (Nb1)</td><td>Primary</td><td>Cr_7C_3, NbC</td><td colspan="2">$Cr_{23}C_6$, NbC, MnS</td><td rowspan="2">No sample taken</td><td>$Cr_{23}C_6$, NbC, η-carbide, MnS</td></tr>
<tr><td>Secondary</td><td>No precipitates</td><td colspan="2">$Cr_{23}C_6$, NbC</td><td>$Cr_{23}C_6$</td></tr>
<tr><td rowspan="2">1100 (Nb1)</td><td>Primary</td><td>Cr_7C_3, NbC</td><td colspan="2">$Cr_{23}C_6$, NbC, MnS</td><td rowspan="2">No sample taken</td><td>$Cr_{23}C_6$, NbC, MnS</td></tr>
<tr><td>Secondary</td><td>No precipitates</td><td colspan="2">$Cr_{23}C_6$, NbC</td><td>No precipitates</td></tr>
</table>

6.2 Evolution of the Chromium-Rich Phases during Isothermal Ageing

6.2.1 Primary Precipitate Network

Phase Identification

EDS and EBSD phase identification (Figure 6.8 and Figure 6.8 (a) & (c)) confirmed the as-cast Cr_7C_3 (*Pnma*) precipitates had completely transformed to $Cr_{23}C_6$ ($Fm\bar{3}m$) within 1000 hours for all ageing temperatures. Further short-term ageing experiments (6, 12 and 24 hours) carried out on the HP-Nb1 and HP-Nb2 alloys at 1000°C determined the Cr_7C_3-to-$Cr_{23}C_6$ phase transformation was complete within 6 hours of exposure. Rarely Cr_2(CN) precipitates were also identified on the grain boundaries at the mid-wall position of the HP-Nb1 alloy after ageing at 1100°C for 10,000 hours. Further analysis determined these precipitates formed as a result of the furnace atmosphere. Thus, this transformation will be discussed in Chapter 8.

Similar short-term ageing experiments performed on unmodified HK-40 alloys also observed the complete transformation of the Cr_7C_3 network to $Cr_{23}C_6$ within 10 hours of exposure to temperatures above 900°C [1]. Generally, the rapid decomposition of the as-cast Cr_7C_3 to $Cr_{23}C_6$ has been reported for centrifugally cast HK and HP alloys after exposure to temperatures exceeding 700°C [1, 2, 5].

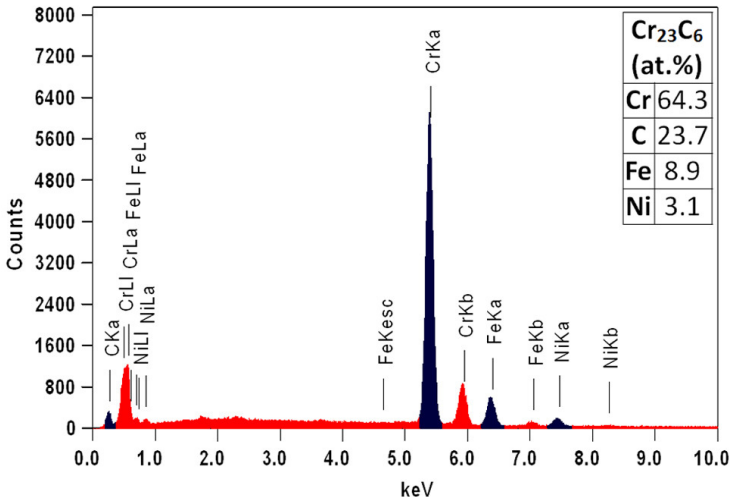

Figure 6.7 – Chemical composition of the primary $Cr_{23}C_6$ precipitates as determined by EDS.

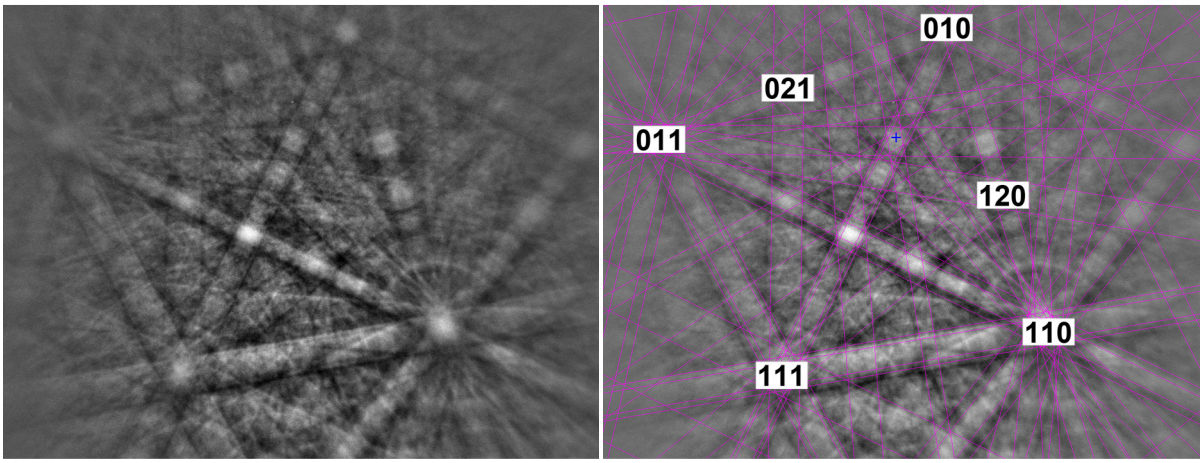

(b) (c)

Figure 6.8 – (a) Representative EBSP taken from the Primary $Cr_{23}C_6$ and (b) Simulated pattern for the $Cr_{23}C_6$ crystal structure overlaying the EBSP in (b).

Coarsening of the $Cr_{23}C_6$ Primary Precipitates during Prolonged Ageing

As discussed in Section 6.1, prolonged ageing of the HP-Nb1 and HP-Nb2 alloys at temperatures between 1000-1100°C caused the $Cr_{23}C_6$ precipitates to notably coarsen. To quantify the coarsening rate with respect to ageing temperature and time, image analysis was performed on the primary precipitate network. In total, 72 backscattered electron images (identical to those shown in Figure 6.2, Figure 6.4 and Figure 6.6) were taken from each aged sample and subjected to image analysis. Segmentation of the individual precipitates within each backscatter electron image was subsequently performed by thresholding the grayscale image in the NIH ImageJ software[21] to produce binary images. The thresholding process segmented the microstructure based on the difference in contrast between the precipitates and matrix. The resulting binary image is comprised of 1 and 0 values where the precipitates appear as either black (0) or white (1) pixels. The average size and area fraction of each phase were subsequently measured by counting the number of black (0) or white pixels (1) which were associated with each phase in the binary images using a code written specifically for this project within the MATLAB software package[22].

Figure 6.9 (a) and (b) show the average precipitate size and area fraction measured specifically from the primary $Cr_{23}C_6$ network (i.e. the secondary precipitates were excluded from this analysis).

[21] National Institutes of Health, Bethesda, Maryland, USA.
[22] Mathworks®, Natick, Massachusetts, USA.

Regardless of the ageing temperature, the average size and area fraction both drastically increased with time. For example, ageing of the HP-Nb2 alloy at 1000°C for 10,000 hours caused the average size and area fraction of the $Cr_{23}C_6$ to be double that of the as-cast Cr_7C_3. Due to the increasingly greater diffusion rates of chromium and carbon with increasing temperature, the highest coarsening rate was typically observed when ageing at 1100°C. However, the average $Cr_{23}C_6$ area fraction in the HP-Nb1 1050°C and 1100°C samples can be seen to converge when ageing between 3000-10,000 hours.

As shown in Figure 6.9 (c), the greatest coarsening rate was observed within the first 1000 hours of ageing (independent of the ageing temperature). The coarsening rate was significantly lower after 1000 hours of ageing with coarsening of the primary $Cr_{23}C_6$ appearing to cease in the 1000 and 1050°C samples when ageing between 1000-3000 hours. In contrast, no coarsening rate plateau was observed in the 1100°C samples. As evidenced by the convergence of average size and area fraction of the $Cr_{23}C_6$ precipitates in the 1050 and 1100°C samples (Figure 6.9 (a) and (b)), the $Cr_{23}C_6$ coarsening rate at 1100°C was noticeably lower than at 1050°C when ageing from 3000-10,000 hours.

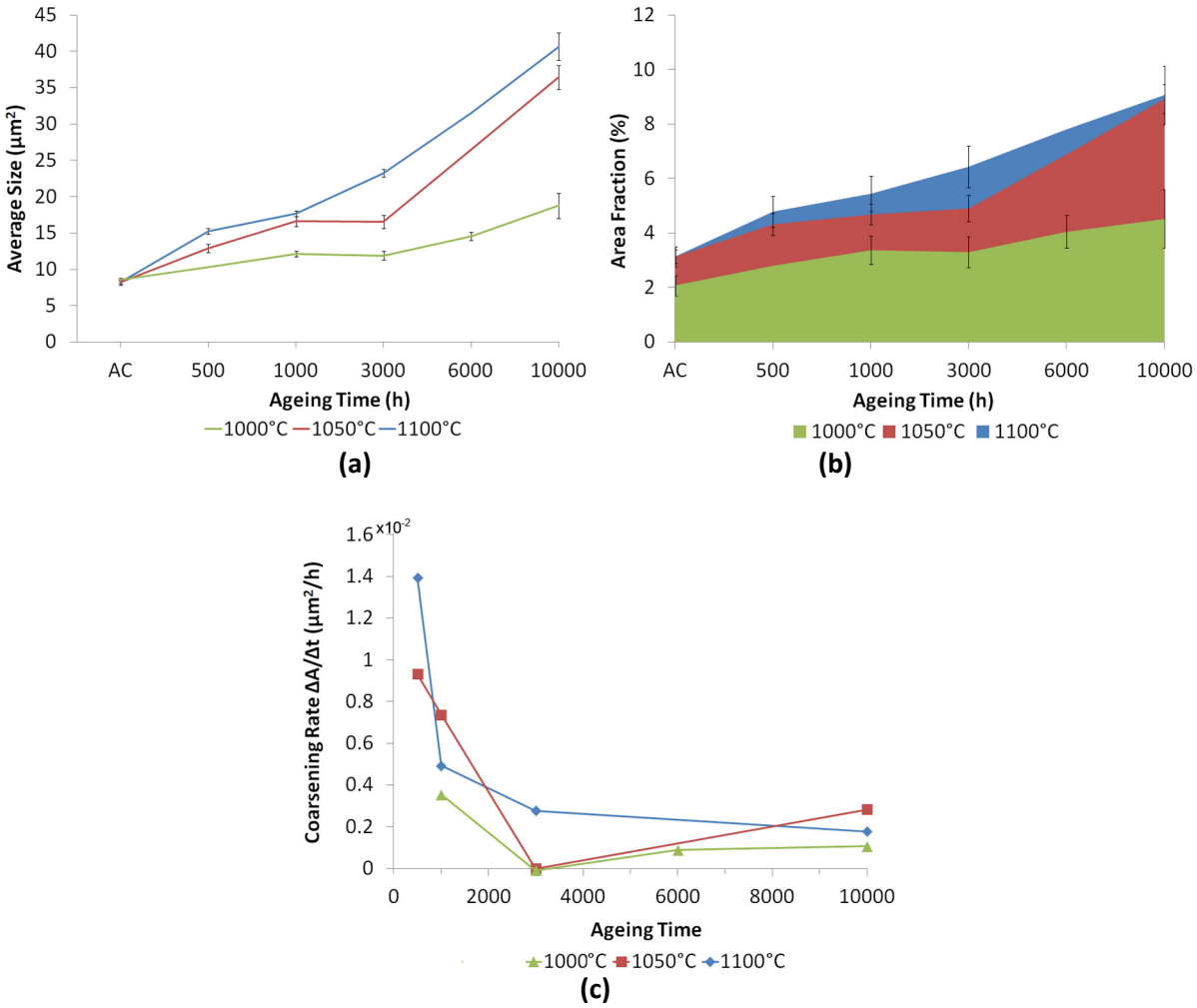

Figure 6.9 - The evolution of the primary chromium carbide network's (a) average size, (b) area fraction and (c) coarsening rate (precipitate size/ageing time) with respect to the ageing temperature and time.

The high coarsening rate observed within the first 1000 hours is likely due to a combination of the higher carbon content contained within the Cr_7C_3 crystal structure in comparison to the $Cr_{23}C_6$ (~33 and 21at.% respectively) structure and the relatively high carbon content in the as-cast matrix (as evidenced by the extensive secondary intragranular precipitation). In order for the Cr_7C_3 to transform to $Cr_{23}C_6$, the primary Cr_7C_3 precipitates must either absorb chromium from the matrix or reject carbon to the matrix. The chromium concentration within the as-cast austenite matrix directly adjacent to the primary Cr_7C_3 precipitates was typically between 25-28at.%. Thus, ample supply of chromium is available to diffuse across the Cr_7C_3/austenite interface if the transformation proceeds by the Cr_7C_3 precipitates absorbing chromium. In this case, the transformation rate would likely be limited by a combination of the rate of chromium diffusion across the precipitate/matrix interface

and short-range diffusion of chromium within the adjacent austenite. Alternatively, if the Cr_7C_3 precipitates rejects carbon, the carbon concentration within the adjacent matrix may become sufficient to induce secondary precipitation of $Cr_{23}C_6$ on the existing Cr_7C_3/austenite interface (similar to the $Cr_{23}C_6$ precipitation observed between the NbC/austenite interface – Section 6.3.5). Unfortunately, due to the rapid decomposition of the primary Cr_7C_3 precipitates during exposure to 1000, 1050 and 1100°C (reportedly less than 3 hours at 1000°C [1]), insight into the mechanism through which the Cr_7C_3-to-$Cr_{23}C_6$ transformation proceeds was unable to be deduced from the ageing periods studied in the current project (6-10,000 hours).

As shown in Figure 6.10, a precipitate-free-zone (PFZ) approximately 1.8µm thick surrounded the primary $Cr_{23}C_6$ after ageing at 1000°C for 1000 hours (no significant precipitate-free-zone was observed surrounding the primary NbC precipitates). PFZ's surrounding the chromium-rich primary precipitates was observed after 1000 hours regardless of the ageing temperature. The PFZ indicates the Cr_7C_3-to-$Cr_{23}C_6$ transformation and subsequent coarsening of the primary $Cr_{23}C_6$ during the first 1000 hours exhausts either the chromium and/or carbon in the immediately adjacent austenite. In general, no evidence of significant chromium depletion was observed within the matrix directly adjacent to the $Cr_{23}C_6$ precipitates in comparison to the center of the austenite dendrite arms when analysing samples aged at 1000°C for 12, 24 and 1000 hours (typically between 22-25at.%). Therefore, the transformation and subsequent growth of the primary $Cr_{23}C_6$ has likely consumed the carbon within this region. In order for the area fraction of the primary $Cr_{23}C_6$ to continue to increase during ageing (as shown in Figure 6.9 (b)), carbon must be released from secondary $Cr_{23}C_6$ precipitates and diffuse across the PFZ. Without the dissolution of the secondary precipitates during prolonged ageing, the average size of primary $Cr_{23}C_6$ would likely have increased while the area fraction remained relatively constant.

The continued increase of the primary $Cr_{23}C_6$ area fraction during prolonged ageing occurs due to Ostwald ripening of the primary and secondary chromium-rich precipitates. As show in Figure 6.1 to Figure 6.6, Ostwald ripening of the primary and secondary $Cr_{23}C_6$ precipitates occurs in parallel during ageing. Thus, the primary and secondary precipitates must initially compete for the chromium and carbon released from precipitates which are dissolving. The initial fine distribution of the secondary precipitates likely causes the carbon liberated from dissolving secondary precipitates to be predominantly re-absorbed by larger neighbouring secondary precipitates (which are spatially closer that the primary precipitates). After ageing at 1000°C for 1000 hours, the average spacing between

the secondary precipitates (<0.5μm) was significantly smaller than the thickness of the PFZ (~1.8μm). Consequently, the local compositional gradient in the direction of neighbouring secondary precipitates in comparison to the gradient across the PFZ allows the secondary precipitates to undergo coarsening.

Since the secondary precipitates do not reach a size which is comparable to the primary precipitates, secondary precipitates which initially underwent ripening will subsequently begin to dissolve once the average inter-particle spacing between the secondary precipitates distribution becomes comparable to the size of the PFZ and hence the local compositional gradients begin to favour the growth of primary $Cr_{23}C_6$ precipitates. Due to the Gibbs-Thomson effect [6], the considerably larger size of the primary precipitates causes the concentration of solute (i.e. carbon) to be lower within the matrix immediately adjacent to the primary precipitates in comparison to the matrix surrounding the remaining secondary precipitates. Thus, given sufficient ageing time at each temperature, the secondary $Cr_{23}C_6$ precipitates will ultimately be completely absorbed by the primary $Cr_{23}C_6$ precipitates (Figure 6.6 (e)).

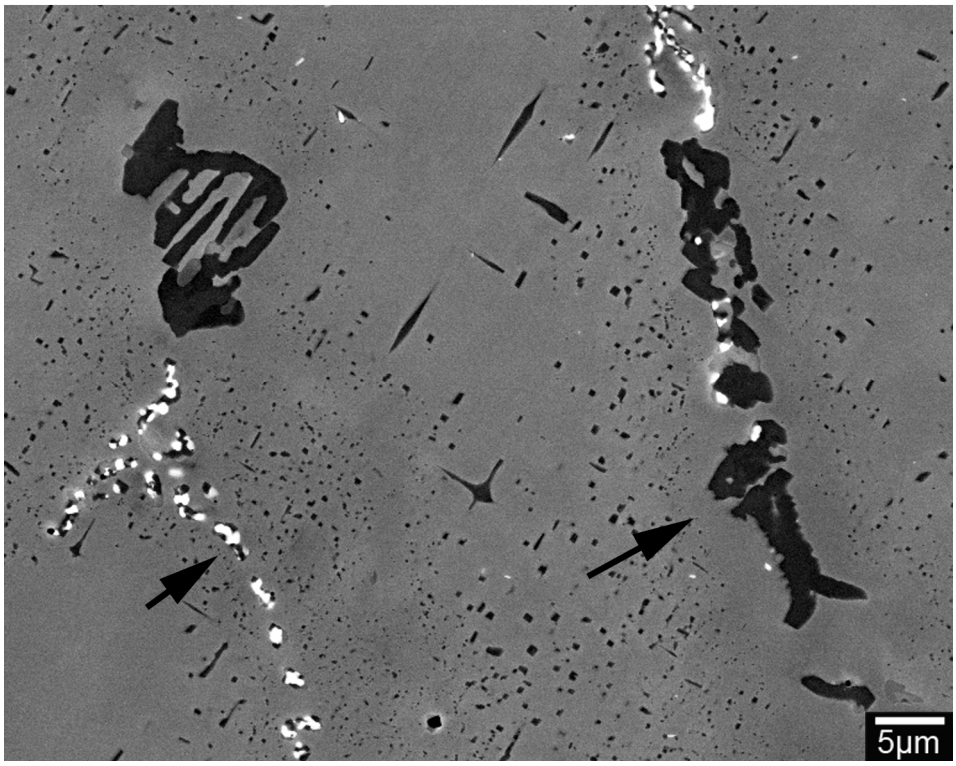

Figure 6.10 - Backscatter electron micrograph showing the precipitate-free-zone surrounding the primary $Cr_{23}C_6$ precipitates after ageing at 1000°C for 1000 hours (arrowed). Note that no significant PFZ is observed adjacent to the NbC precipitates (arrowed).

Based on the preceding observations, the average size and area fraction of primary $Cr_{23}C_6$ precipitates would be expected to be greatest in the 1100°C-10,000h sample. The secondary $Cr_{23}C_6$ network had completely dissolved in the 1100°C-10,000h sample (Figure 6.6 (e)) whereas numerous secondary precipitates remained in the 1050°C-10,000h sample (Figure 6.6 (d)). Thus, if the carbon liberated from the dissolution of the secondary precipitates solely contributed to the coarsening of the primary network, the complete dissolution of these precipitates in the 1100°C-10,000h sample would be expected to result in the greatest $Cr_{23}C_6$ area fraction for all of the aged samples. However, as shown in Figure 6.9 (b), the $Cr_{23}C_6$ area fraction in the HP-Nb1 alloy converged when ageing for between 3000-10,000 hours at 1050 and 1100°C. Given sufficient time, the gradual dissolution of the secondary $Cr_{23}C_6$ precipitates in favour of the primary $Cr_{23}C_6$ precipitates growth at each temperature should result in the convergence of the primary $Cr_{23}C_6$ area fractions. Yet, if the 1050°C-10,000h sample was to be subjected to further ageing, the primary $Cr_{23}C_6$ area fraction would likely increase as the remaining secondary precipitates dissolve. Conversely, as the dissolution of the secondary precipitates in the 1100°C-10,000h sample is complete, further ageing would unlikely cause a similar (or even noticeable) increase in the primary $Cr_{23}C_6$ area fraction. Consequently, the observed $Cr_{23}C_6$

area fraction convergence when ageing at 1050 and 1100°C despite of the complete loss of the secondary precipitates in the 1100°C-10,000h sample suggests the coarsening rate of the primary $Cr_{23}C_6$ was not solely influenced by the dissolution of the secondary $Cr_{23}C_6$ precipitates when ageing the HP-Nb1 alloy at 1050 and 1100°C

It must be stressed that the same alloy was aged at 1050 and 1100°C resulting in the area fraction and average size of the as-cast Cr_7C_3 primary precipitates in each sample prior to ageing to be almost identical (slight variations in these properties existed between the aged samples which were taken from slightly different locations of the tube). Therefore, the properties of the as-cast primary Cr_7C_3 network would not have affected the area fraction and average size of the $Cr_{23}C_6$ precipitates in the aged samples. Although the NbC transforms to η-carbides during ageing at 1050°C, the enhanced $Cr_{23}C_6$ coarsening rate between 3000 to 10,000 hours is not believed to be solely attributed to any possible rejection of carbon (the level of carbon released by the transformation is currently unknown) from the transforming NbC precipitates.

Additional analysis performed on the microstructural evolution at the tube's inner and outer diameter positions determined that the convergence of the $Cr_{23}C_6$ precipitate size when ageing at 1050 and 1100°C for 3000-10,000 hours was mainly attributed to the furnace atmosphere (air). Generally, the effects of the ageing atmosphere were restricted to the material directly adjacent of the samples exposed surfaces. Thus, the mid-wall microstructure within the majority of the aged samples was relatively unaffected. However, ageing of the HP-Nb1 alloy at 1050 and 1100°C for 10,000 hours was sufficient to modify the precipitates located at the tube's mid-wall position.

The effects of the furnace air atmosphere were most pronounced in the 1100°C-10,000h sample resulting in the primary $Cr_{23}C_6$ located at the mid-wall position also being affected by the ageing atmosphere. During the early stages of ageing, diffusion of carbon and chromium to the samples surfaces is believed to have accelerated the dissolution of the secondary precipitates within the material immediately adjacent to the exposed surfaces. During prolonged ageing, these solute-lean exposed surfaces act as an additional sink for the carbon and chromium released from the secondary precipitates. Thus, these elements subsequently contribute less to coarsening of the primary $Cr_{23}C_6$. Given sufficient ageing time, the continued loss of these elements at the exposed surfaces will affect the precipitates located at the mid-wall position (i.e. as observed after ageing at 1100°C for 10,000 hours). Further comprehensive analysis and discussion regarding the effects of air ageing atmosphere with respect to temperature, time and alloy composition is presented separately in Chapter 8.

Analysis of the Sub-grain and Grain Boundaries Observed within individual $Cr_{23}C_6$ Precipitates

Interestingly, while performing image analysis on the HP-Nb alloy's primary precipitate network, faint variations in contrast were consistently noticed across individual $Cr_{23}C_6$ precipitates (regardless of the ageing temperature or time). Figure 6.11 (a) shows a scanning electron micrograph of a primary $Cr_{23}C_6$ precipitate after etching the HP-Nb2 1000°C-1000h aged sample in glyceregia (30 seconds immersion). Generally, the slight variations in contrast gave the $Cr_{23}C_6$ precipitates a granular appearance indicating the presence of sub-grain or grain boundaries. EBSD analysis of numerous $Cr_{23}C_6$ precipitates confirmed that the contrast was indeed induced by crystallographic misorientation. Figure 6.11 (b) shows the crystallographic disorientation calculated from individual grains within 35 separate $Cr_{23}C_6$ precipitates. Typically, the disorientation between adjacent regions of differing contrast was less than 5 degrees. Of all regions analysed, 67% were below the 10-15 degree limit proposed in the literature for low-angle grain boundaries [6]. Although high angle (>15°) disorientations were also observed between adjacent regions, the predominance of low angle disorientations indicated the contrast variance was mainly due to the $Cr_{23}C_6$ precipitates being comprised of numerous sub-grains.

As shown in Figure 6.12 (a), clusters of individual Cr_7C_3 precipitates were often observed in the as-cast HP-Nb microstructures (circled). TEM observations of the as-cast microstructure showed no evidence of a sub-grain structure existing within each individual Cr_7C_3 precipitate. However, disorientations of typically less than 10 degrees were observed between individual precipitates within each cluster. Figure 6.12 (b) gives an example of four EBSP's taken from a single group of as-cast Cr_7C_3 similar to that in Figure 6.12 (a). The disorientation between each individual Cr_7C_3 precipitate can be seen visually by the translation of the [100] zone axis in each respective EBSP. EBSD analysis was performed on a total of five separate groups all of which yielded similar results. Although less common, disorientations greater than 10° were also observed between neighbouring Cr_7C_3 precipitates. No consistent orientation relationship between the Cr_7C_3 and austenite was observed.

The groups of individual Cr_7C_3 precipitates (Figure 6.12 (a)) decreased dramatically within 1000 hours of exposure to 1000, 1050 and 1100°C. Typically, the size and morphology of the $Cr_{23}C_6$ precipitates in the aged microstructures suggested the Cr_7C_3-to-$Cr_{23}C_6$ transformation and subsequent growth of each precipitate caused these clusters to coalesce, thus forming a large single $Cr_{23}C_6$ precipitate. During the Cr_7C_3-to-$Cr_{23}C_6$ transformation, the rejection of carbon from a transforming Cr_7C_3

precipitate to the chromium-rich matrix could induce secondary precipitation of $Cr_{23}C_6$ on the prior Cr_7C_3/austenite interface. This secondary precipitation of $Cr_{23}C_6$ on the Cr_7C_3/austenite interface possibly contributes to the granular structure show in Figure 6.11 (a) and subsequent coalescence of the individual precipitates in Figure 6.12 (a). As will be show in following section, the $Cr_{23}C_6$ precipitates typically obtain a cube-cube OR (i.e. $<100>_A//<100>_B$, $\{100\}_A//\{100\}_B$) with the austenite matrix (identical to the intragranular cuboidal $Cr_{23}C_6$ secondary precipitates). However, precipitates that did not share a consistent orientation relationship with the matrix were also observed. Precipitates that obtain the cube-cube OR with the matrix possibly correspond to secondary precipitates whereas precipitates that share high angle disorientations with the matrix are possibly either the original Cr_7C_3 precipitates which transformed to $Cr_{23}C_6$ and retained the Cr_7C_3 precipitates original crystallographic orientation or secondary precipitates that obtain an orientation based on that of the original Cr_7C_3 precipitates orientation. Subsequent growth and coalescence of these precipitates that share varying disorientations would result in the granular $Cr_{23}C_6$ precipitate shown in Figure 6.11 (a).

Since the Cr_7C_3-to-$Cr_{23}C_6$ transformation was complete after all ageing periods analyzed in the current study, significant further analysis of samples aged for shorter time periods is necessary to capture the early stages of this transformation and hence provide further insight into the origin of these grains.

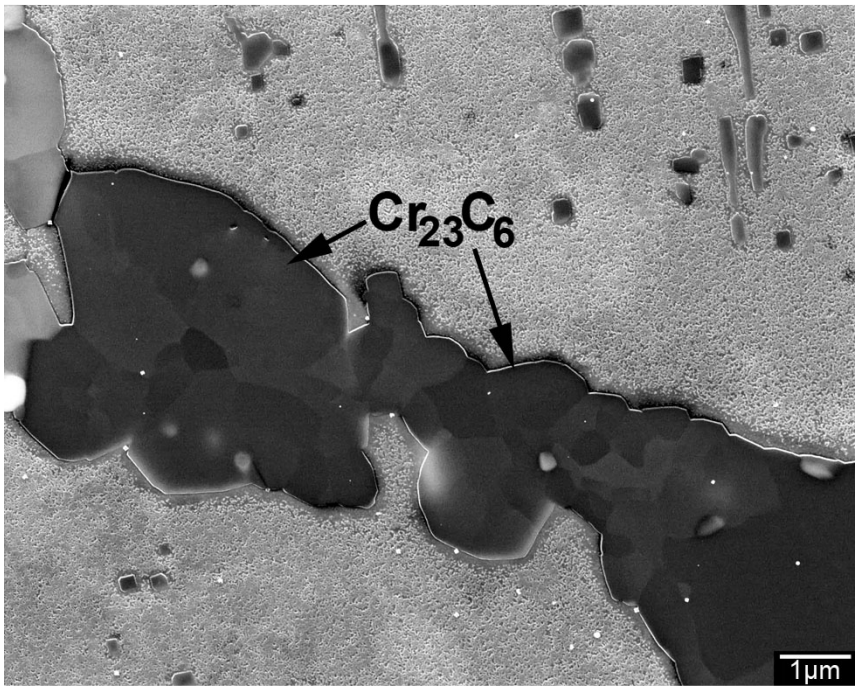

(a)

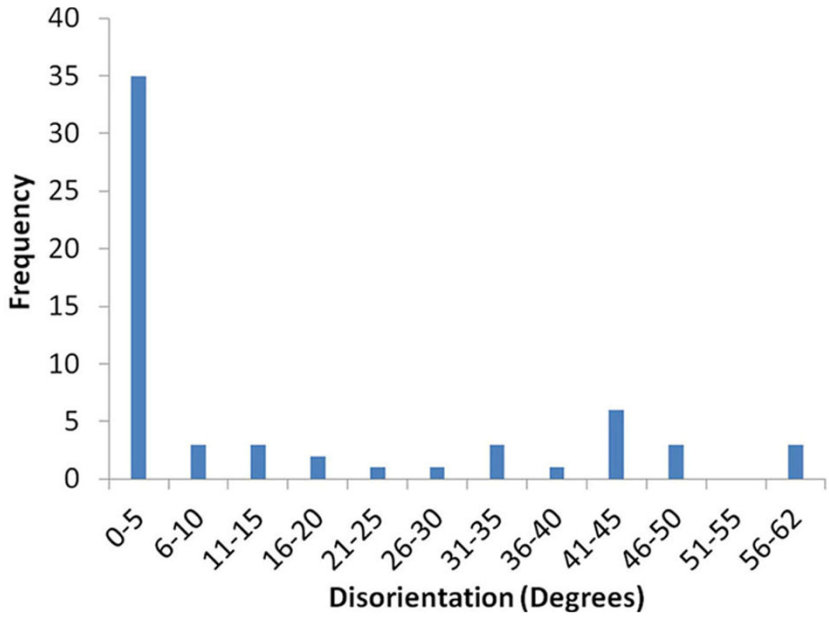

(b)

Figure 6.11 - (a) High magnification composite scanning electron micrograph of a primary $Cr_{23}C_6$ precipitate where the faint contrast within the precipitate delineates low and high angle grain boundaries. (b) Histogram showing the frequency of occurrence of disorientation measured between adjacent grains within 35 separate $Cr_{23}C_6$ precipitates.

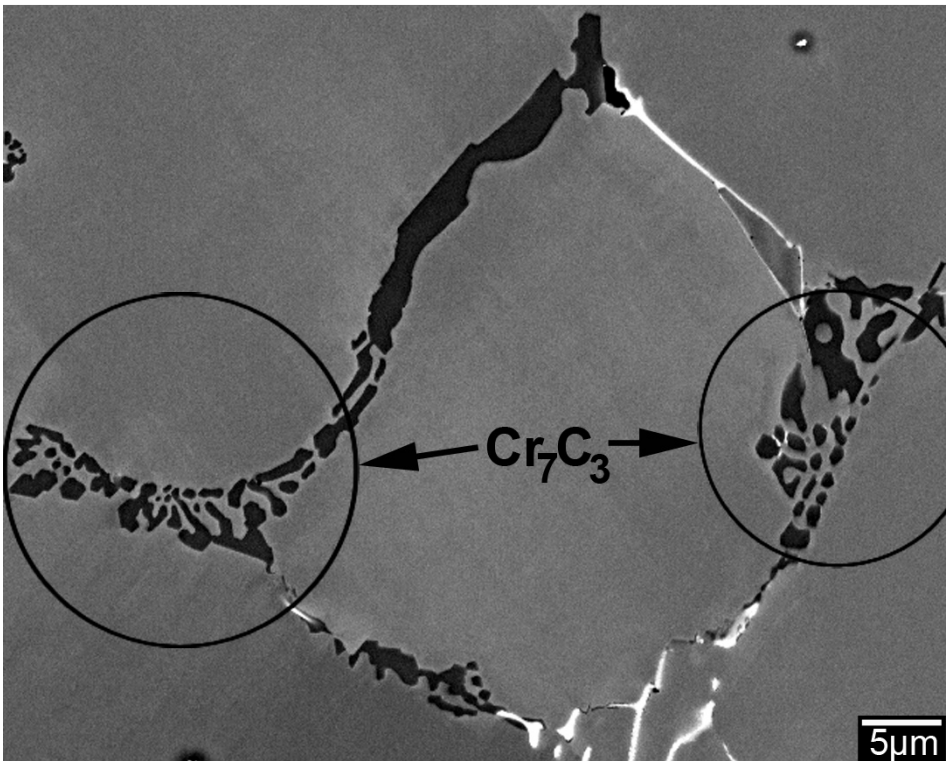

(a)

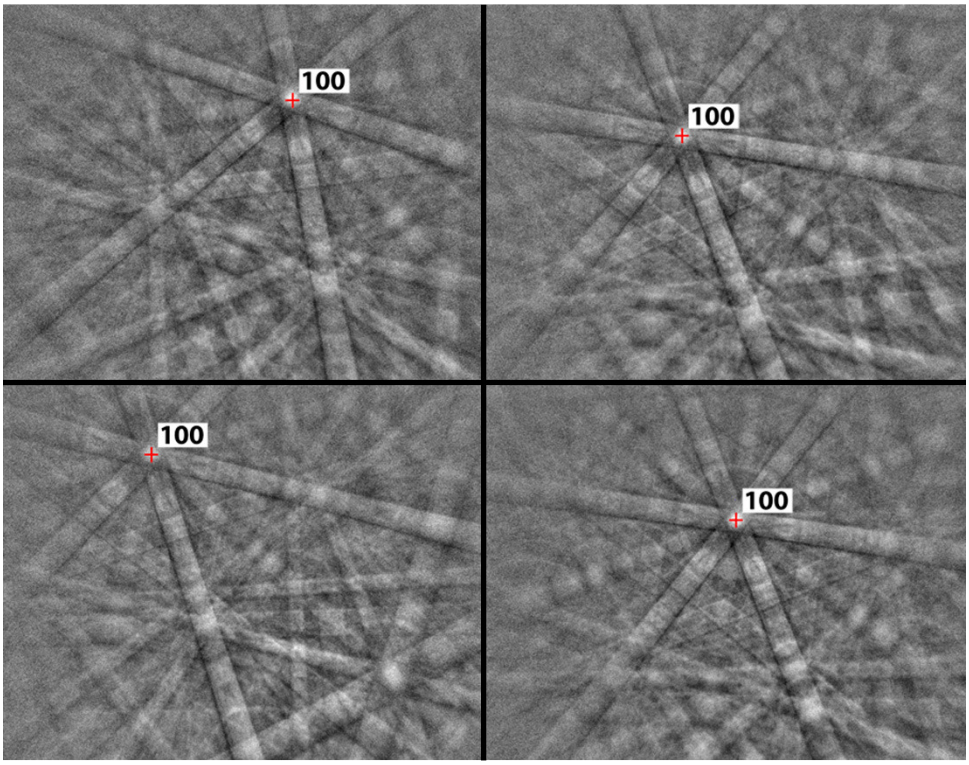

(b)

Figure 6.12 - (a) Backscatter electron micrograph showing the groups of as-cast Cr_7C_3. (b) EBSPs from adjacent (but separate) Cr_7C_3 precipitates within groups identical to those shown in (a). Disorientation between the adjacent Cr_7C_3 can be observed by the movement of the [100] zone axis in each EBSP.

Analysis of the Orientation Relationship between the Primary $Cr_{23}C_6$ and Austenite with respect to Ageing Temperature and Time

Previous work by Wahab and Kral [7, 8] reported preferential formation of creep voids at $Cr_{23}C_6$/austenite boundaries in ex-service HP-NbTi alloys (~940°C, ~12MPa, 60,000 hours). Three-dimensional reconstructions of serial sectioned material showed that all voids within the inspected volumes came into contact with primary $Cr_{23}C_6$ precipitates at some point along the voids perimeter. Moreover, approximately 80% of all voids situated between the prior $Cr_{23}C_6$/austenite interfaces were located on low registry boundaries (i.e. on boundaries where no consistent precipitate/matrix orientation relationship (OR) existed). The remaining 20% of voids were located on the prior $Cr_{23}C_6$/austenite of precipitates which obtained a cube-cube ($<100>_{Cr23C6}//<100>_{\gamma}$) OR with the austenite matrix.

Such preferential damage accumulation on specific combinations of precipitate type and interfacial crystallography indicates the importance of the primary carbide network with respect to the tubes in-service creep performance. Regardless of the ageing temperature and time, the primary $Cr_{23}C_6$ was the most abundant precipitate type in both the HP-Nb1 and HP-Nb2 alloys. Thus, it was considered necessary to perform further analysis of the orientation relationship obtained between the primary $Cr_{23}C_6$ and austenite matrix in the aged HP-Nb1 and HP-Nb2 alloys.

Identical to the analysis of the NbC/austenite OR in the as-cast HP-Nb alloy (Chapter 4), EBSD was used to determine the OR between the $Cr_{23}C_6$ and austenite with respect to ageing temperature and time. Due to the time consuming nature of this analysis, focus was placed on the samples aged at 1000°C as this temperature is closest to the typical operating temperatures experienced by reformer tubes during actual service. In total, 60 precipitate-matrix pairs were analysed for each ageing period using the same procedure described in Chapter 4. A minimum of three separate points within each precipitate was analysed in order to obtain an overall orientation. Disorientation values of less than 10° were defined as a cube-cube OR (i.e. $<100>_A//<100>_B$, $\{100\}_A//\{100\}_B$). The relatively random distribution of the disorientation values for precipitates which did not obtain a cube-cube OR with the matrix suggested that no other unique OR existed between the $Cr_{23}C_6$ and austenite. Since the majority of $Cr_{23}C_6$ formed at dendrite arm boundaries rather than grain boundaries, preference was placed on the analysis of precipitates located at dendrite arm boundaries (i.e. the location of the greatest area fraction of $Cr_{23}C_6$). EBSD of precipitates located on grain boundaries determined that these $Cr_{23}C_6$ precipitate typically obtained a cube-cube OR with one of the adjoining austenite grains.

While the cube-cube $Cr_{23}C_6$/austenite OR was also confirmed after ageing the HP-Nb1 alloy at 1050 and 1100°C, only 5-10 precipitate/matrix pairs were analysed in each of these samples.

Figure 6.13 shows the relative frequency of occurrence of disorientation between the primary $Cr_{23}C_6$ and directly adjacent austenite for the HP-Nb2 alloy after ageing at 1000°C for between 1000 to 10,000 hours. Regardless of the ageing time, the disorientation between the $Cr_{23}C_6$ precipitates and austenite matrix was typically less than 5 degrees. Therefore, these precipitates often obtained a $<100>_{Cr23C6}//<100>_{\gamma}$, $\{100\}_{Cr23C6}//\{100\}_{\gamma}$ orientation relationship with the matrix.

In agreement with the HP-Nb1 and HP-Nb2 alloys, analysis conducted by Wahab and Kral [7, 9] on a short-term laboratory aged HP-NbTi sample (1030°C, 500 hours, unstressed) determined that 45% of the primary $Cr_{23}C_6$ precipitates obtained a cube-cube OR with the austenite. However, only 20% of the $Cr_{23}C_6$ precipitates obtained cube-cube OR with the matrix in an ex-service HP-NbTi alloy (~940°C, ~12MPa, 60,000 hours) that was also studied by Wahab and Kral, suggesting that long-term service exposure results in the randomisation of the $Cr_{23}C_6$/austenite OR. Conversely, long-term unstressed isothermal ageing of the HP-Nb2 alloy at 1000°C caused a significant increase in the relative number of precipitates which obtain a cube-cube OR with the matrix (from 57 to 70% respectively).

The convergence of the $Cr_{23}C_6$ precipitates orientation towards a near cube-cube OR with austenite during prolonged ageing was previously predicted by Lewis and Hattersley [9] in austenitic steels. The OR was believed to be obtained between the $Cr_{23}C_6$ and austenite in order to minimise the total surface energy associated with the precipitate. While the minimisation of the precipitates total surface energy may explain the driving force for the increased prevalence of the cube-cube OR after 10,000 hours, it does not explain how precipitates sharing initially high disorientations with the matrix (i.e. greater than 10°) achieve the crystallographic rotation necessary to obtain the cube-cube OR. Analysis of the precipitates with disorientations greater than 10° with respect to ageing time indicated that these precipitates did not physically rotate during ageing to progressively lower disorientations until the cube-cube OR was obtained. If progressive re-orientation of these precipitates occurred, higher disorientations (e.g. 40-62°) would gradually become less prevalent while mid-range disorientations (e.g. 10-30°) would become increasingly prevalent with increased ageing time. However, as shown in Figure 6.13, no clear trend could be observed (at least within the current data set) for precipitates with disorientations greater than 10° with respect to ageing time. Thus, physical crystallographic rotation of the $Cr_{23}C_6$ precipitates during prolonged ageing was considered highly unlikely.

The increasing prevalence of the cube-cube OR in Figure 6.13 is more likely a result of the primary $Cr_{23}C_6$ precipitates being agglomerates of individual grains. As shown in Figure 6.11 (b), adjacent grains typically exhibited low angle disorientations (<10°), but high angle disorientations (>10°) were also observed. Measurement of the $Cr_{23}C_6$/austenite OR variance within a single $Cr_{23}C_6$ precipitate that on average obtained a cube-cube OR with the matrix showed that the sub-grains predominantly remained within 10 degrees of this OR. However, each $Cr_{23}C_6$ precipitate often contained a small number of grains which would not obtain the cube-cube OR with the matrix.

Conversely, primary $Cr_{23}C_6$ precipitates where the grains on average did not initially obtain the cube-cube OR also contained a small proportion of grains which obtained the cube-cube OR with the matrix. During prolonged ageing, grains sharing cube-cube OR with matrix possibly grew at the expense of grains without a consistent OR (with respect to the matrix and adjacent $Cr_{23}C_6$ grains). This preferential growth of favourably orientated grains at the expense of highly disorientated grains would cause the apparent number of primary $Cr_{23}C_6$ precipitates which share the OR with the matrix to progressively increase (as observed in Figure 6.13). Since these highly disorientated $Cr_{23}C_6$ grains likely share relatively high energy boundaries with each adjoining phase, such preferential growth of the favourably orientated grains would reduce the total precipitate/matrix surface energy (as predicted by Lewis and Hattersley [9]). However, it must be stressed that measurement of the size and number of $Cr_{23}C_6$ grains with and without the cube-cube OR (using EBSD) is necessary to confirm the preferential growth of favourably orientated $Cr_{23}C_6$ grains during prolonged ageing of the HP-Nb alloys.

Interestingly, the observation of high angle grain boundaries within individual $Cr_{23}C_6$ precipitates (Figure 6.11), suggests that precipitates which obtain a cube-cube OR (on average) with the matrix may also exhibit regions of low registry. Therefore, while 20% of voids in the ex-service material studied by Wahab and Kral [7, 8] were situated adjacent to what appeared to be rationally oriented $Cr_{23}C_6$ precipitates, the voids possibly nucleated on the $Cr_{23}C_6$ grains which exhibited comparatively high angle (>10-15°) disorientations with respect to the surrounding $Cr_{23}C_6$ grains and austenite matrix. However, high resolution EBSD mapping $Cr_{23}C_6$ precipitates three-dimensional grain structure (i.e. through serial sectioning) during the early stages of void formation is necessary to provide further evidence to determine if such preferential nucleation with respect to the local precipitate crystallography occurs.

Further analysis must also be conducted to determine why the frequency of the $Cr_{23}C_6$/austenite OR observed in the ex-service material studied by Wahab and Kral differed from the laboratory aged material studied in the current research (which did not experience stress during ageing). Analysis of $Cr_{23}C_6$ precipitates within material which has experienced simulated service conditions over the same time periods studied in the current research would confirm if the presence of stress during ageing causes the precipitate-matrix crystallography to become increasingly random with increasing ageing time.

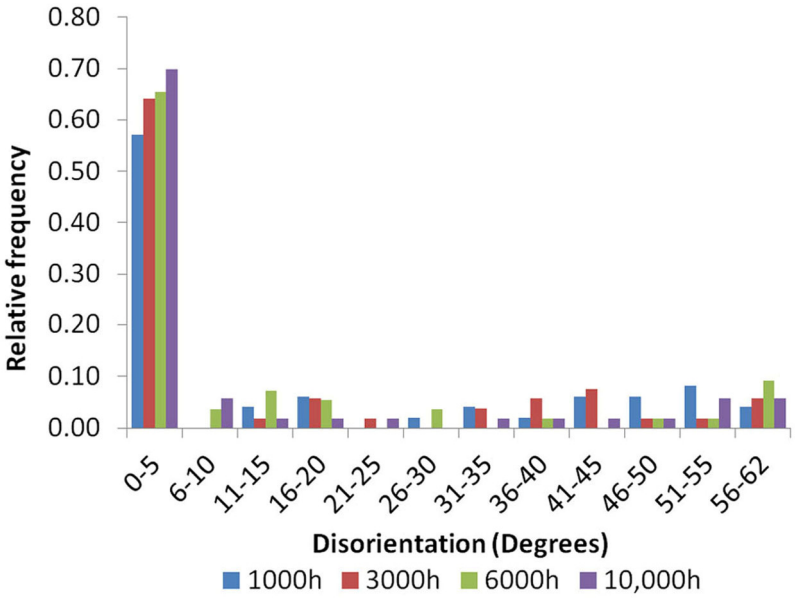

Figure 6.13 - Histograms showing the relative frequency of occurrence of disorientation measured between $Cr_{23}C_6$ and austenite with respect to ageing temperature and time

6.2.2 Secondary Precipitate Distribution

Figure 6.14 (a) to (f) show backscatter electron micrographs of the secondary precipitate distributions within the HP-Nb1 and HP-Nb2 alloys after ageing at 1000, 1050 and 1100°C for 1000 and 10,000 hours respectively. Regardless of the ageing temperature, the secondary precipitate distribution in the HP-Nb alloys was predominantly composed of $Cr_{23}C_6$ precipitates (dark grey). For both alloys, the nucleation and growth of secondary $Cr_{23}C_6$ precipitates occurred within 6 hours of exposure to 1000, 1050 and 1100°C. NbC secondary precipitates (white) were also observed in the aged samples. However, the number of these precipitate was insignificant in comparison to the $Cr_{23}C_6$ (estimated to be less than 1% of the total secondary precipitate population). Moreover, the NbC precipitates became increasingly rare as the ageing time increased.

For all ageing temperatures, the secondary $Cr_{23}C_6$ precipitates were mainly concentrated near the primary network of grain boundary and interdendritic carbides. The differing thermal expansion coefficients between the primary carbide network (which forms during solidification) and austenite matrix reportedly induces stresses within the austenite directly surrounding the primary precipitates during centrifugal casting of the HK and HP alloys [3, 5, 10] resulting in high dislocation densities within this region in the as-cast matrix (in comparison to the center of the dendrite arms). The subsequent nucleation of $Cr_{23}C_6$ on these dislocations during ageing results in the non-uniform secondary precipitate distribution typically observed in HP alloys [3, 5]. In contrast to the $Cr_{23}C_6$, the NbC precipitates did not appear to be preferentially located with respect to the primary precipitates.

Chromium and carbon concentration gradients within the austenite matrix likely also contribute to the non-uniform secondary $Cr_{23}C_6$ precipitate distribution. As discussed in Section 6.2.1, the transformation of the primary Cr_7C_3 precipitates to $Cr_{23}C_6$ consumes sufficient chromium from the matrix directly surrounding each primary precipitate to cause the observed precipitate-free-zone (PFZ) directly adjacent to the $Cr_{23}C_6$ (a similar PFZ was not observed surrounding the primary NbC precipitates). In general, the greatest density of secondary $Cr_{23}C_6$ precipitates occurred directly adjacent to the PFZ with the number of secondary precipitates decreasing with increasing distance from the PFZ. This decrease in the number of precipitates is possibly attributed to the concentration of carbon within the austenite matrix also decreasing with increasing distance from the primary precipitates eventually leading to the precipitate free region within the center of the austenite dendrite arms (i.e. the first region of austenite to solidify).

The average size and number of secondary precipitates was heavily dependent on the ageing temperature and time. After ageing for 1000 hours, the secondary precipitates can be seen to become increasingly coarser when comparing the 1000, 1050 and 1100°C samples. As shown in Figure 6.14 (b), (d) and (f), Ostwald ripening of the secondary precipitates occurred during prolonged ageing.

In general, dispersions of secondary particles within a matrix increase a material's overall energy due to the interfacial energy associated with the precipitate/matrix interface [11]. The fine dispersions of secondary precipitates in the HP-Nb alloy (which form due to the reported super-saturation of the as-cast matrix with carbon [12]) are likely associated with a relatively high degree of interfacial energy. Consequently, Ostwald ripening of the secondary precipitate distribution occurs during prolonged thermal exposure to reduce the total interfacial area and thus the interfacial energy associated with these precipitates. Ultimately, as the secondary precipitates never become comparable in size to the primary $Cr_{23}C_6$ precipitates, the Gibbs-Thomson effect [6] causes the dissolution of secondary precipitates in favour of the primary precipitates growth. Thus, as demonstrated in Figure 6.14 (f), given sufficient time at each ageing temperature the secondary precipitates will completely dissolve in order to contribute the growth of the considerably larger primary $Cr_{23}C_6$ precipitates (as discussed in Section 6.2.1).

The rate at which the secondary $Cr_{23}C_6$ precipitates coarsened likely follows the kinetic equation for Ostwald ripening kinetic as follows:

$$\bar{r}^3 - r_0^3 = kt \qquad 6.1$$

Where

$k \propto D\gamma X_e$

r_0 is the mean radius of the precipitate distribution at t=0

D is the diffusion coefficient of carbon/chromium through the austenite matrix

γ is the precipitate/matrix interfacial energy

X_e is the equilibrium solubility of very large particles

Diffusion short circuiting along dislocations and/or grain boundaries or precipitate-matrix interface-controlled diffusion can cause the coarsening rate to deviate from equation 6.1 [6]. However, due to the significant size of the austenite grains within HP reformer tubes, the rate at which the secondary $Cr_{23}C_6$ precipitates coarsen is likely to be controlled by volume diffusion of chromium and carbon through the austenite matrix (i.e. coarsening due to grain boundary diffusion is considered to be negligible).

As the rate at which chromium and carbon diffuse through the austenite matrix (i.e. D) is exponentially dependent on the ageing temperature, the rate at which the secondary precipitate distribution undergoes Ostwald ripening increases rapidly with the ageing temperature [6]. The significant acceleration secondary precipitates coarsening rate with respect to ageing temperature can be qualitatively observed in Figure 6.14 (a) – (f).

Unfortunately, quantitative measurement of the secondary precipitates average size and inter-particle spacing with respect to ageing temperature and time was unsuccessful. Image analysis of the secondary $Cr_{23}C_6$ precipitates was initially attempted using the backscattered electron images taken for the analysis of the primary precipitates (e.g. Figure 6.2, Figure 6.4 and Figure 6.6). However, due to the small size of the secondary precipitates (typically <0.5μm^2), the binary representation of these precipitates in image was extremely poor and accurate measurement of the size and area fraction of the secondary precipitate was not possible (discussed in further detail in section 7.4.3). Therefore, it was not possible to confirm if the rate at which the secondary $Cr_{23}C_6$ precipitates coarsened followed a linear relationship when plotting $\bar{r}^3$ versus time (i.e. confirming the secondary precipitates coarsening kinetics follows equation 6.1 $\bar{r}^3 - r_0^3 = kt$ *6.1*). Further analysis using a dual beam FIB-SEM is likely necessary in order to obtain a high quality and repeatable images of the secondary precipitate distribution to allow for quantitative measurement of these precipitates with respect to ageing time and temperature.

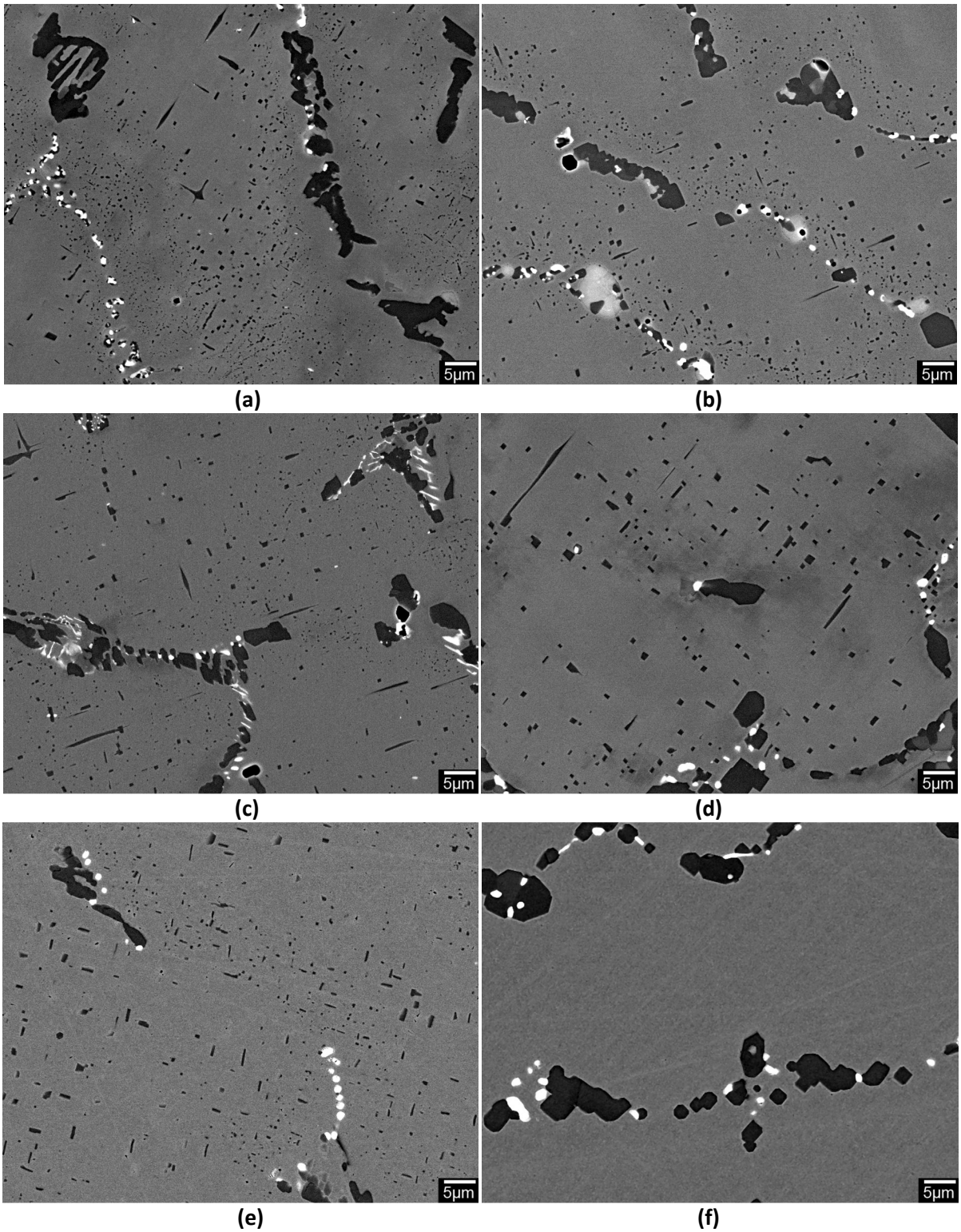

Figure 6.14 - Backscatter electron micrographs showing the secondary precipitates in the HP-Nb alloys after ageing at (a) & (b) 1000, (c) & (d) 1050 and (e) & (f) 1100°C for 1000 and 10,000 hours respectively.

Figure 6.15 (a) and (b) show higher magnification images of the secondary precipitates in the 1000°C-1000 hours sample. In two-dimensions, the $Cr_{23}C_6$ and NbC precipitates predominantly exhibited a cuboidal morphology. However, the $Cr_{23}C_6$ precipitates also commonly obtained plate (Figure 6.15 (a)) and needle-like (Figure 6.15 (b)) morphologies. As shown in Figure 6.15 (b), neighbouring needle-like precipitates were often similarly aligned. Widely spaced precipitates (i.e. precipitates not directly adjacent but located within the same grain) commonly exhibited orthogonal alignment. This needle-like or Widmanstätten morphology for $Cr_{23}C_6$ precipitates have previously been identified by Soares *et al.* [3] in laboratory aged HP-Nb alloys. Of the four compositionally unique HP-Nb alloys aged in that study, the presence of the Widmanstätten $Cr_{23}C_6$ was particularly prevalent in the alloy containing the highest chromium to carbon ratio leading the authors to suggest the chromium and carbon content in the as-cast matrix promotes this morphology. Unfortunately, in the present work, the HP-Nb1 and HP-Nb2 alloys were aged at differing temperatures making any comparison between the alloys difficult.

Secondary $Cr_{23}C_6$ stringers (multiple cuboidal $Cr_{23}C_6$ precipitates joined in series at each corner) were also rarely observed in the aged HP-Nb1 and HP-Nb2 alloys. The formation of $Cr_{23}C_6$ stringers reportedly grew through prismatic punching of dislocations within the austenite at the corners of the cuboidal $Cr_{23}C_6$ precipitates [3, 9, 13]. These dislocations provide a nucleation site for subsequent cuboidal $Cr_{23}C_6$ precipitates. Continued precipitation in this manner results in the formation of stringers which align with the $<110>_{Cr23C6}$ (hence $<110>_{\gamma}$ due to the cube-cube OR) direction.

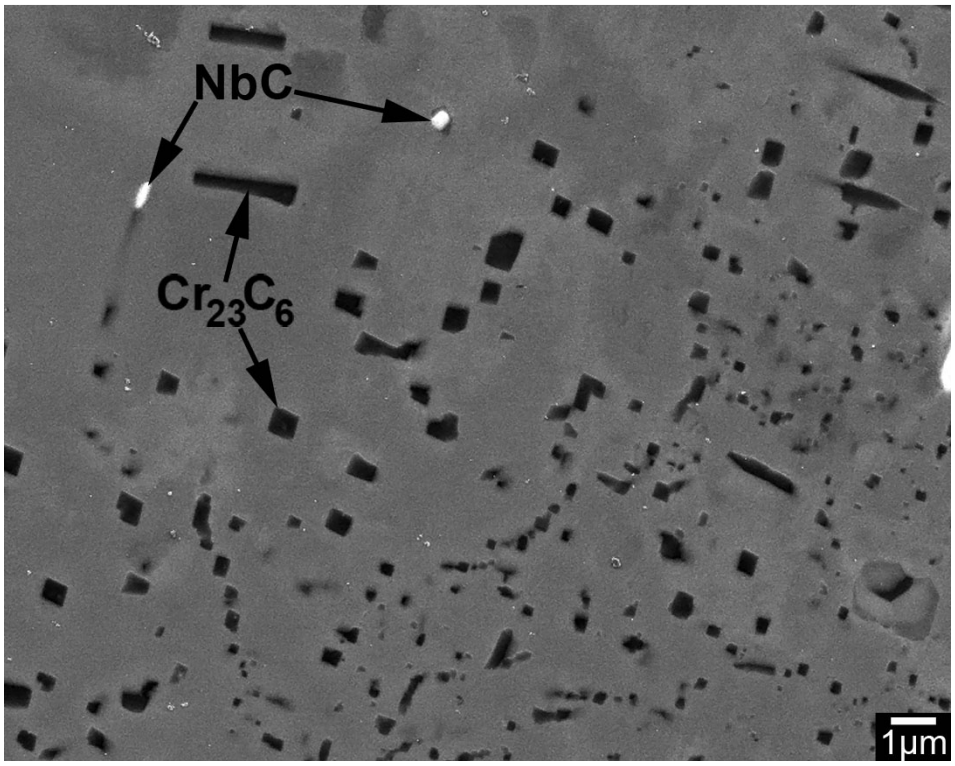

(a)

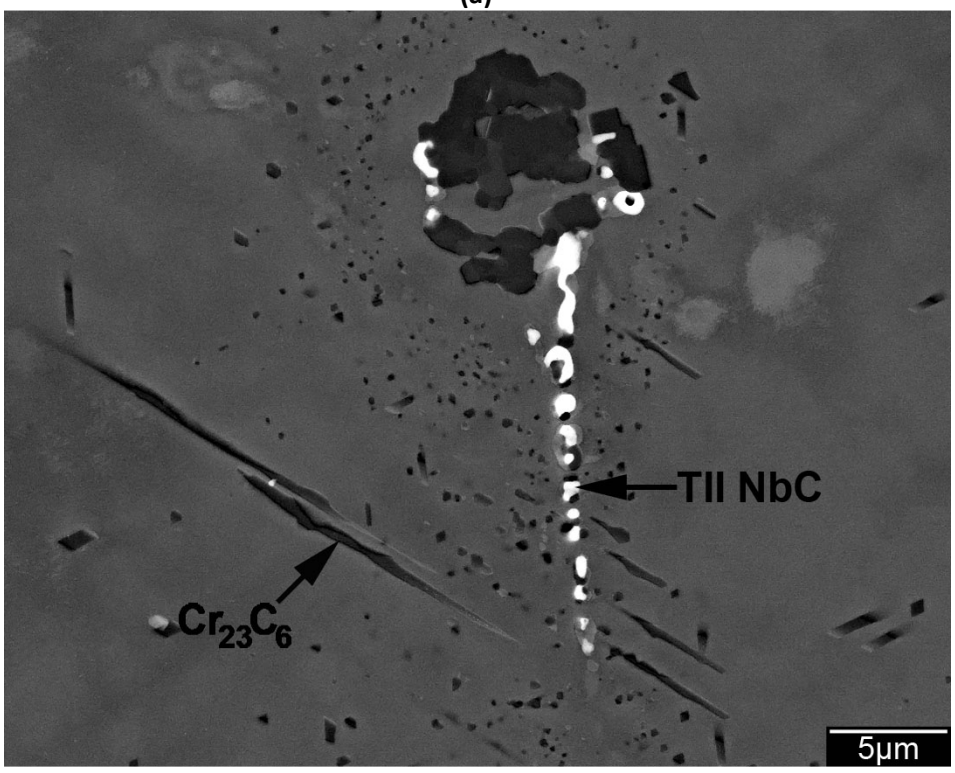

(b)

Figure 6.15 - Backscatter electron micrographs of the secondary precipitates showing (a) the cuboidal and plate $Cr_{23}C_6$ morphologies and the NbC; (b) large needle-like or Widmanstätten $Cr_{23}C_6$ precipitates emanating from the Type II lamellae.

Identification of the cuboidal, plate and needle-like (or Widmanstätten) secondary $Cr_{23}C_6$ was carried out using a combination of EDS and SAD. Due to the time consuming nature of this analysis, only secondary precipitates in the HP-Nb2 1000°C-1000, 3000 and 10,000 hours samples were analysed. EDS and EBSD analysis of the larger chromium-rich secondary precipitates in the HP-Nb1 samples aged at 1050 and 1100°C determined that the chromium-rich precipitates also obtain the $Cr_{23}C_6$ crystal structure. Based on the stability of the primary $Cr_{23}C_6$ precipitates with respect to ageing temperature and time, all chromium-rich secondary precipitates were expected to obtain the $Cr_{23}C_6$ crystal structure present after ageing the HP-Nb1 alloys at 1050 and 1100°C for 1000, 3000 and 10,000 hours.

Figure 6.16 (a) to (h) shows bright field images and SAD patterns taken from the cuboidal and plate or Widmanstätten morphologies. It must be noted that the elongated precipitate in Figure 6.16 (e) could either represent a plate or needle-like shape due to being only a cross section of a three-dimensional precipitate. The $Cr_{23}C_6$ crystal structure ($Fm\bar{3}m$) was confirmed for both morphologies. No significant difference in the lattice parameters or chemical composition was observed when comparing the two morphologies using EDS and SAD.

The SAD patterns presented for the two morphologies in Figure 6.16 (b) to (d) and (f) to (h) demonstrate the cube-cube ($<100>_{Cr23C6}//<100>_{\gamma}$) orientation relationship reported for the secondary $Cr_{23}C_6$ precipitates in the literature [3, 4, 14]. Numerous $Cr_{23}C_6$ cuboidal, plate and needle-like precipitates were analysed by tilting the foil to bring the $<100>_{\gamma}$ zone axes parallel to the beam direction. The OR could be easily confirmed by scanning the beam across the matrix/precipitate boundary of individual $Cr_{23}C_6$ precipitates within the thin area and observing the similarity of SAD patterns. Only one plate-like precipitate was found to exhibit no clearly apparent orientation relationship with the matrix. In this case, the alternative OR's could have occurred due to nucleation on an inclusion in the matrix.

Lath shaped $Cr_{23}C_6$ precipitates which exhibited a cube-cube OR identical to the plates or needle-like precipitates in the HP-Nb alloy have been observed in association with non-coherent twin boundaries in austenitic steels [9, 13]. Nucleation of the laths was believed to occur at the non-coherent twin interface, followed by growth of the $Cr_{23}C_6$ along the $<110>_{Cr23C6}$ direction into the austenite grain. The broad faces of the laths were reportedly parallel to the $\{111\}_{Cr23C6}$ planes. The similar alignment of neighbouring $Cr_{23}C_6$ laths in the HP-Nb alloys (Figure 6.15 (b)) suggests the growth of these

precipitates possibly occurs along the same <110>$_{Cr23C6}$ crystallographic direction. Trace analysis performed on the plates (which obtained the cube-cube OR) to determine the growth direction was inconclusive. However, this analysis was based on a limited sample of two precipitates.

Due to the similar appearance of the $Cr_{23}C_6$ and NbC secondary precipitates in the TEM, and the relatively sparse population of secondary NbC in the matrix, the NbC precipitates were inherently difficult to locate within the thin foils. Therefore, no NbC precipitates were able to be identified using the TEM. However, based on EDS analysis and reported phases in the literature [3, 14], these precipitates were expected to also obtain the FCC ($Fm\bar{3}m$) NbC crystal structure.

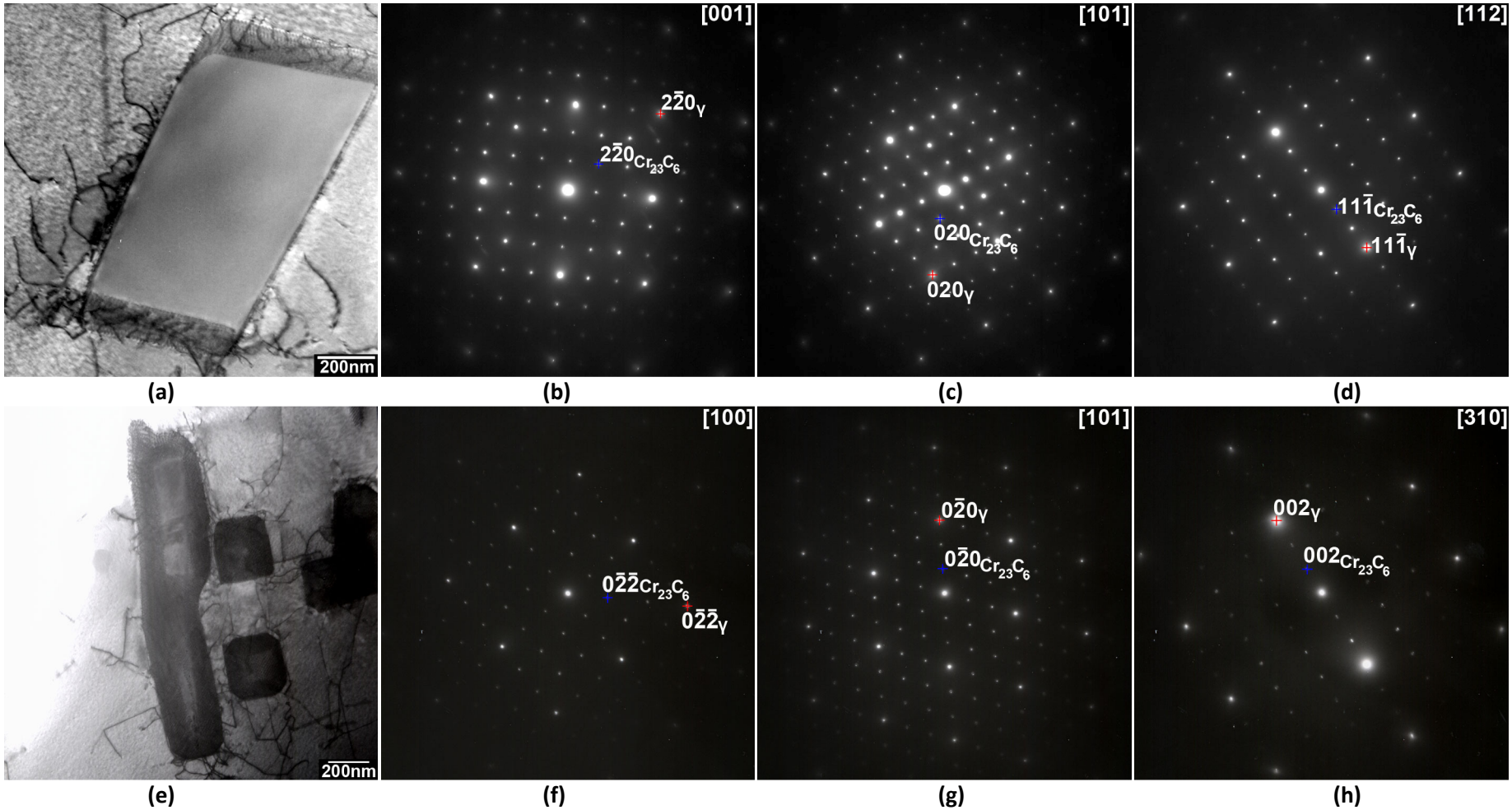

Figure 6.16 - (a) & (e) Brightfield TEM micrograph of the cuboidal and plate/needle-like morphology secondary precipitates. Selected area diffraction patterns of the (b) [001], (c) [101], (d) [112], (f) [100], (g) [101] and (h) [310] zone axes taken with the selected area aperture overlapping the $Cr_{23}C_6$ precipitates and directly adjacent austenite matrix in (a) & (e). The $[100]_{Cr23C6}//[100]_{\gamma}$ OR is clearly evident for both morphologies with reflections characteristic of the $Cr_{23}C_6$ and austenite crystal structures shown in each SAD pattern

In two-dimensions, the needle-like or Widmanstätten secondary precipitates typically showed no connection with the primary precipitates (Figure 6.15 (b)) and thus appeared to nucleate in the matrix similarly to the cuboidal precipitates. However, deep etching of the HP-Nb1 and HP-Nb2 alloys after ageing at 1000°C and 1050°C for 1000 hours revealed that these precipitates originated on the Type II NbC lamellae. Figure 6.17 shows a group of similarly aligned $Cr_{23}C_6$ laths all emanating from a colony of Type II NbC lamellae. The observation of the lath morphology in three-dimensions suggests the Widmanstatten appearance in 2-D are caused by sectioning effects. Not all Type II NbC colonies exhibited these $Cr_{23}C_6$ laths. However, in some cases, the laths' high aspect ratio could have caused these precipitates to fracture and subsequently fall out during deep etching. The regular occurrence of these laths adjacent to Type II NbC colonies in two-dimensions, suggests that these precipitates only nucleate on the Type II lamellae (i.e. nucleation and growth of the $Cr_{23}C_6$ lath morphology does not occur within the matrix). The strong alignment of neighbouring laths in the HP-Nb alloys suggests that after nucleation on the Type II lamellae interface growth proceeds along the $<110>_{Cr23C6}$ crystallographic direction.

In general, widespread precipitation of $Cr_{23}C_6$ was observed between the Type II NbC lamellae and austenite interfaces after ageing (see Section 6.3.5). This interfacial $Cr_{23}C_6$ was comprised of quasi-cuboidal and lath shaped precipitates. Since Cr_7C_3 precipitates were observed between the Type II NbC lamellae and austenite interfaces in the as-cast HP-Nb alloys, it is unknown if these $Cr_{23}C_6$ laths originate from the transformation (and subsequent growth) of the Cr_7C_3 precipitates or if these precipitates nucleate on the NbC interface after exposure to elevated temperatures. No $Cr_{23}C_6$ laths or interfacial precipitation was observed in association with the Type I NbC lamellae.

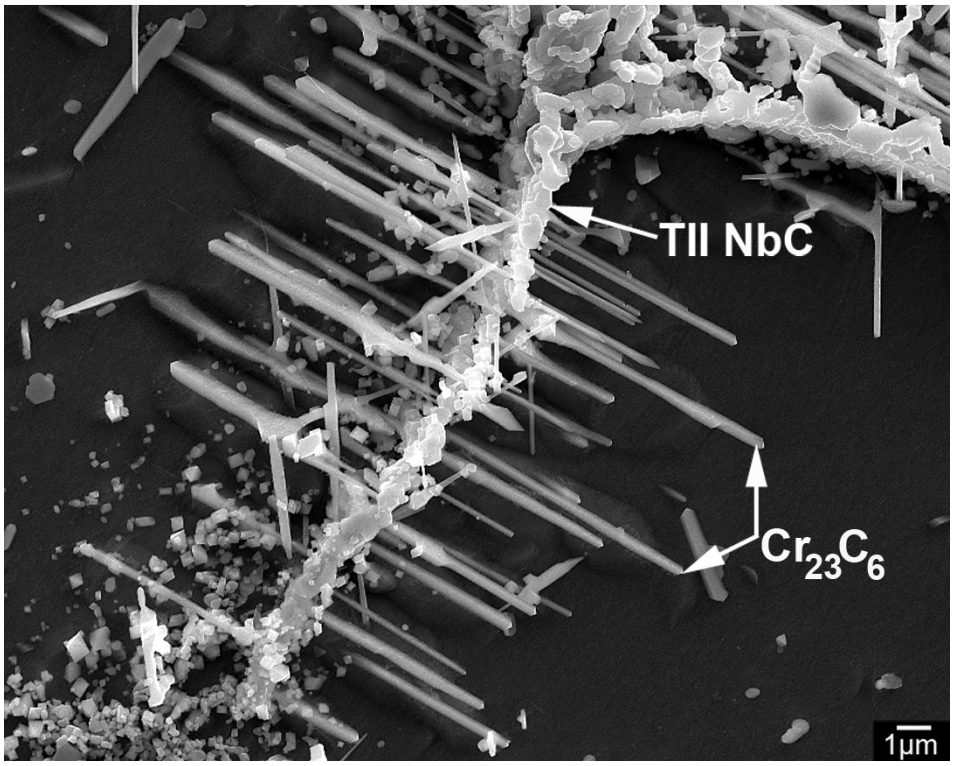

Figure 6.17 - Secondary electron micrograph of numerous aligned lath morphology $Cr_{23}C_6$ precipitates which are believed to originate from the Type II lamellae

The development of fine secondary precipitates within the austenite matrix during thermal ageing is considered to be beneficial to the HK and HP alloys creep properties as these precipitate reportedly restrict dislocation motion through the matrix during the tubes service life [3, 15]. Furthermore, secondary precipitates in the vicinity of the grain boundary precipitates are thought to inhibit the deformation typically concentrated in this area during creep [16].

Obviously, the increasingly coarse secondary precipitate distributions observed after ageing at for prolonged periods will to be detrimental to the HP-Nb alloys creep properties. Previous work by Hou and Honeycombe [10] on unmodified HK alloys (25wt.%Cr, 20wt.%Ni) suggested the high coarsening rate of the $Cr_{23}C_6$ precipitates (in comparison to the niobium- and titanium- rich MC precipitates) possibly causes these precipitates to be the least effective of the alloys carbides available for the strengthening of austenitic steels. The decreased 'effectiveness' of the $Cr_{23}C_6$ precipitates was believed to be due to the greater rate at which chromium diffuses through austenite matrix relative to niobium or titanium [10].

Consequently, Hou and Honeycombe [5] subsequently used additions of niobium, titanium and zirconium in an attempt to promote the formation of fine dispersions of secondary NbC and TiC precipitates in the HK alloys. TEM observations of the as-cast and aged modified HK alloys identified nano-sized (<50nm) MC precipitates which had nucleated on dislocations and stacking faults within the austenite matrix during casting. In addition to the MC precipitates being more than an order of magnitude finer than the secondary $Cr_{23}C_6$, Ostwald ripening of the MC dispersion was considerably slower in comparison to the rate observed for the $Cr_{23}C_6$ precipitates. The modified HK alloys superior creep resistance in comparison to the un-modified HK alloy was attributed to the increased dispersion strengthening effect provide by the intragranular MC precipitates.

Similar nano-sized intragranular NbC precipitates were also observed by Ibañez *et al.* [4] after ageing HP-Nb alloys (1.97wt.% Nb) at 900°C for 1000 hours. These precipitates were believed to have formed during isothermal ageing (rather than during casting as observed in the HK alloys [5]) and were typically observed in association on with dislocations and stacking faults. Interestingly, the secondary NbC precipitates remained stable during ageing whereas the primary NbC precipitates transformed to G-phase. Provided that these precipitates continue to remain stable during long-term ageing (with respect to the G-phase transformation), the nano-sized NbC precipitates would have a similar dispersion strengthening effect as observed in the HK alloys [5].

Similar intragranular nano-sized NbC precipitates were not present in the as-cast HP-Nb1 or HP-Nb2 alloys. While nano-sized NbC precipitates were observed when analyzing thin foils taken from the HP-Nb alloys after ageing for 1000 hours, these precipitates were extremely rare. No evidence was found to suggest the dispersion of NbC precipitates had transformed to η-carbides during ageing. Thus, the use of niobium to increase the stability of the secondary precipitate distribution in the HP-Nb1 and HP-Nb2 alloys was unsuccessful. The absence of these precipitates in the HP-Nb1 and HP-Nb2 alloys is possibly due to each alloy's niobium content being considerably lower (0.44 and 0.92wt.% respectively) in comparison to the alloys studied by Ibañez *et al.* (1.97wt.%) [4].

Typically, the HP alloy's creep properties are determined by performing accelerated creep testing on as-cast material which often last for significantly less than 10,000 hours [2, 3]. The current research shows that the size and distribution of the secondary precipitates within short-term accelerated testing is likely to be finer than actually exists during prolonged service periods (~100,000 hours). Therefore, previous creep tests have possibly been conducted on microstructures which would produce the greatest possible creep properties.

While long-term unstressed laboratory ageing followed by creep testing of the aged alloys will allow for better prediction of the HP alloys' long-term creep properties, the transformation and coarsening of the primary network may obscure the contribution of the secondary precipitates. Thus, additional ageing experiments where HP alloys were subjected to temperatures between 900-1100°C for 6 to 12 hours were carried out [14]. The heating rate for each sample was varied between approximately 5 to 200°C per minute. These heat treatments allowed the secondary precipitate distribution to be altered while keeping the properties of the primary precipitate network relatively constant. In general, higher temperature and heating rates resulted in coarser secondary precipitate distributions. Creep testing of these samples was planned, however, due to time limitations, the microstructural characterisation and accelerated creep testing could not be completed.

6.3 Evolution of the Niobium-Rich Precipitates during Isothermal Ageing

6.3.1 Identification of the Primary Precipitates Crystal Structure

As discussed in Section 6.1, remnants of the as-cast Type I and II NbC lamellae were observed in all aged samples. Identification of these precipitates was performed using EDS and EBSD. Typically, analysis was performed on 5-10 Type I and II NbC lamellae all of which belonged to separate colonies. Figure 6.18 (a) to (c) give representative examples of the EDS spectra and EBSD patterns taken from the NbC. Regardless of the ageing temperature, all remnants of the as-cast lamellae retained the face centered cubic ($Fm\bar{3}m$) NbC crystal structure.

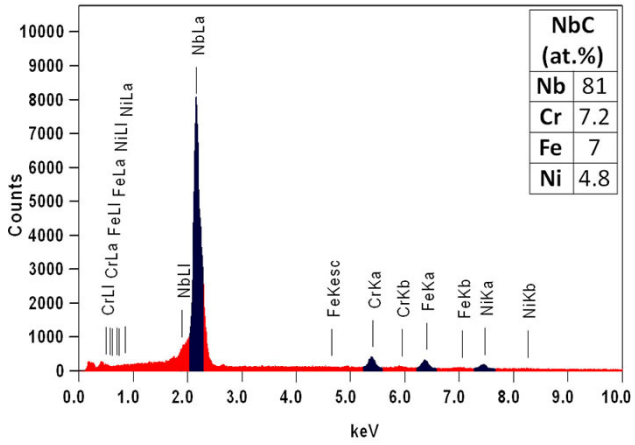

(a)

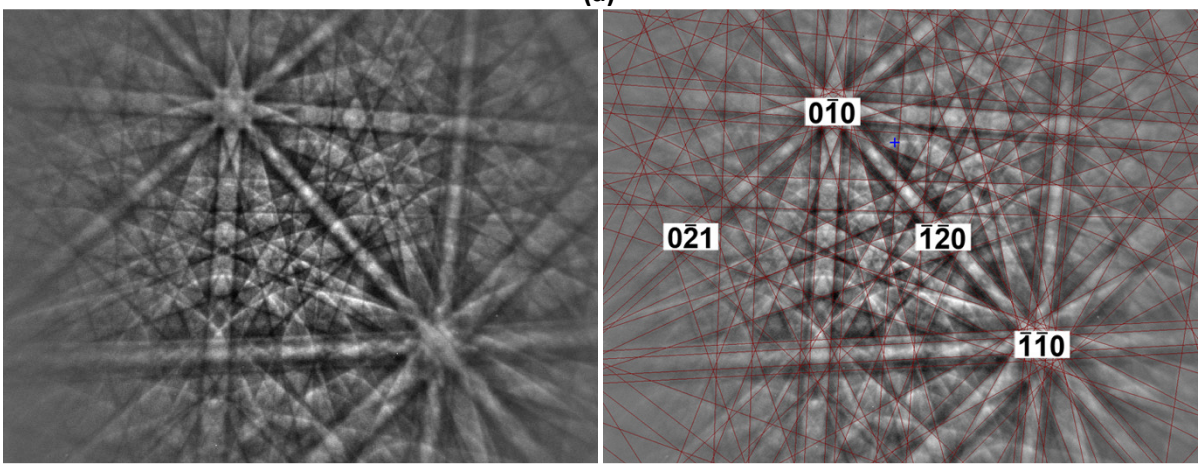

(b) (c)

Figure 6.18 - Representative (a) EDS spectrum (ignoring carbon) and (b) experimentally obtained and (c) Simulated pattern for the NbC crystal structure overlaying the EBSP in (b).

6.3.2 Identification of the η-carbide crystal structure (1000-1050°C)

Exposure of the HP-Nb1 and HP-Nb2 alloys to 1000 and 1050°C caused the Type I and Type II lamellae to partially transform to a Ni-Nb-Si-Cr rich phase. Partial transformation of the NbC was first observed after ageing the HP-Nb2 alloy at 1000°C for 1000 hours (Figure 6.2 (b)). This transformation continued during prolonged ageing at 1000°C. In contrast, the transformation rate was significantly decreased when ageing at 1050°C with the Ni-Nb-Si-Cr rich phase only observed after ageing for 10,000 hours (at least at the tube's mid-wall position – Chapter 8). The NbC crystal structure remained completely stable in the 1100°C aged samples.

The transformation of the NbC precipitates in HP alloys during exposure to temperatures between 700-1050°C has been well documented in the literature [1, 3, 4, 14, 18-20]. Generally, the transformation product was identified as G-phase ($Ni_{16}Nb_6Si_7$) which exhibits a face centred cubic structure with a lattice parameter of 1.12nm [1, 3, 4, 14]. While the transformed phase in the HP-Nb1 and HP-Nb2 alloys contained the Ni, Nb and Si typical of G-phase, the chromium concentration (determined by EDS as 33.4% - Figure 6.19 (b)) was well above the concentration reported for G-phase in the literature (typically <5%) [3, 4, 14]. This elevated chromium concentration was constant regardless of the original NbC morphology (i.e. the transformation product associated with the Type I and Type II lamellae was chemically similar). As the precipitates are surrounded by a Cr-Ni-Fe rich matrix, the additional chromium was initially thought to be attributed to excitation of the austenite matrix by the electron probe. However, based on the composition of the matrix, any excitation of the surrounding the matrix would also increase the concentration of iron and nickel above the concentrations shown in Figure 6.19 (b). Since the high chromium levels were also observed when analysing precipitates believed to be significantly greater size than the probes interaction volume (~1-2µm diameter at 20keV [21]), the composition shown in Figure 6.19 (b) was considered to be representative of the transformed phase in the HP-Nb1 and Nb2 alloys.

The diamond cubic ($Fd\bar{3}m$) η-carbide or M_6C crystal structure has also been identified in the HP-Nb alloy after long-term laboratory ageing [18] and in ex-service material [1, 19, 20]. The reported compositions of the η-carbide in the literature showed good agreement with the Ni-Nb-Si-Cr rich phase in the HP-Nb1 and HP-Nb2 alloys. Therefore, the NbC-to-η-carbide transformation appears to

be occurring in the HP-Nb1 and HP-Nb2 alloys rather than the NbC-to-G-phase transformation identified by Soares *et al.* [3] and Ibañez *et al.* [4] after similar laboratory ageing.

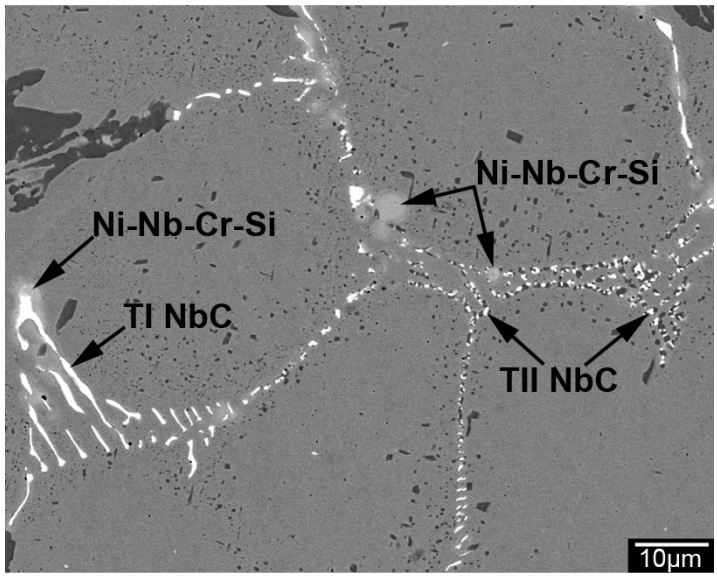

(a)

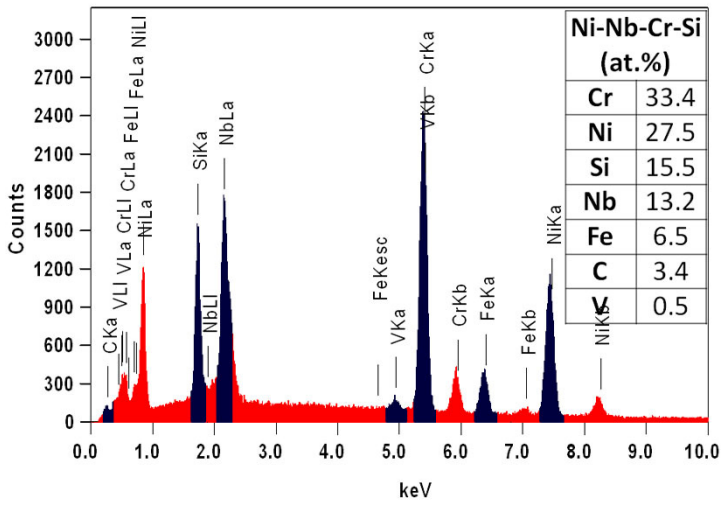

(b)

Figure 6.19 - (a) Backscatter electron micrograph showing the transformation of the Type I and II lamellae to a Ni-Nb-Cr-Si rich phase. (b) Chemical composition of the transformed phase as determined by EDS.

To make a thorough investigation of the decomposition of NbC, a list of candidate phases was selected from the Pearson's Crystal Database [22] based on the chemical composition given in Figure 6.19 (b). Although the lattice parameter for the η-carbides previously identified in the HP-Nb alloys was not explicitly reported in the literature, it was noted to be similar to the Cr_3Ni_2SiC or Cr_3Ni_2Si parameters [20]. It must be noted that no phase was found in the Pearson's database which closely

matched the composition of the Ni-Nb-Si-Cr rich phase. Furthermore, only one phase was found which merely contained all four major elements ($Nb_3Cr_{1.6}Ni_{2.4}Si_6$). Therefore, a range of crystal structures which were elementally similar were selected and entered into the HKL Flamenco software in order to perform EBSD phase identification. Table 6.2 lists the phases which were chemically similar to the observed composition of the phase observed in the HP-Nb1 and HP-Nb2 aged samples.

Table 6.2 - List of candidate crystal structures used for EBSD identification of the Ni-Nb-Cr-Si rich phase.

Phase	Crystal System	Space Group	Lattice parameters- a, b, c (nm)			α, β, γ (°)			Ref.
$Ni_{16}Nb_6Si_7$	Cubic	$Fm\bar{3}m$	1.1249	1.1249	1.1249	90	90	90	22
$Ni_{16}Cr_6Si_7$	Cubic	$Fm\bar{3}m$	1.11	1.11	1.11	90	90	90	23
Cr_2Ni_2SiC	Cubic	$Fd\bar{3}m$	1.062	1.062	1.062	90	90	90	23
$Cr_{0.4}Ni_{0.6}Si$	Cubic	$P2_13$	0.4545	0.4545	0.4545	90	90	90	23
NbNiSi	Orthorhombic	Pnma	0.6223	0.3683	0.7088	90	90	90	24
CrNiSi	Orthorhombic	Pnma	0.5667	0.3613	0.6887	90	90	90	25
Nb_4NiSi	Tetragonal	P4/mmc	0.6188	0.6188	0.5052	90	90	90	26
$NbNiSi_2$	Tetragonal	I4/mmm	1.2571	1.2571	0.4988	90	90	90	27
$Nb_3Cr_{1.6}Ni_{2.4}Si6$	Tetragonal	$P4_2$/mbc	1.6571	1.657	0.4943	90	90	90	28
$Cr_{0.65}Ni_{0.25}Si_{0.1}$	Tetragonal	$P4_2$/mnm	0.8787	0.8787	0.457	90	90	90	29
NbCrNi	Hexagonal	$P6_3$/mmc	0.4856	0.4856	0.7945	90	90	120	30

Figure 6.20 (a) shows a representative EBSP taken from the transformed phase in the HP-Nb2 alloy after ageing at 1000°C for 1000 hours. Based on the crystallographic parameters shown in Table 6.1, the experimentally determined EBSP exhibited good agreement with the simulated patterns for $Ni_{16}Nb_6Si_7$ and Cr_3Ni_2SiC (i.e. the G-phase and η-carbide crystal structures). However, due to the crystallographically similar space groups and lattice parameters, it was not possible to positively distinguish the best match between the two candidate phases using EBSD. While the chemical composition suggested the phase observed in the HP-Nb2 alloy matched the η-carbide, further analysis was considered necessary to differentiate between these two candidate crystal structures.

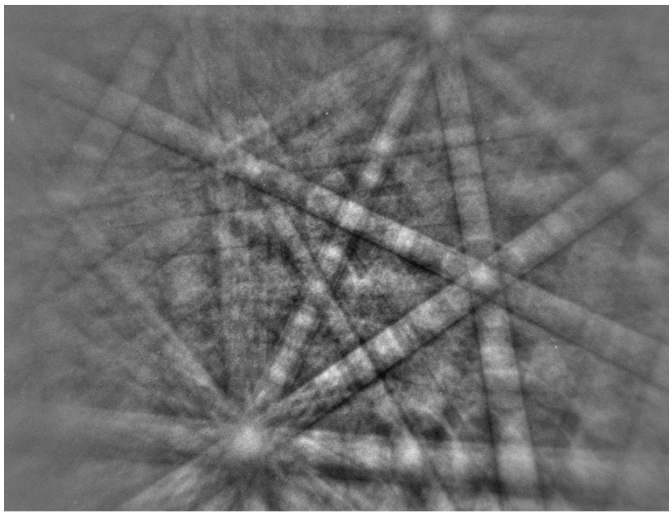

(a)

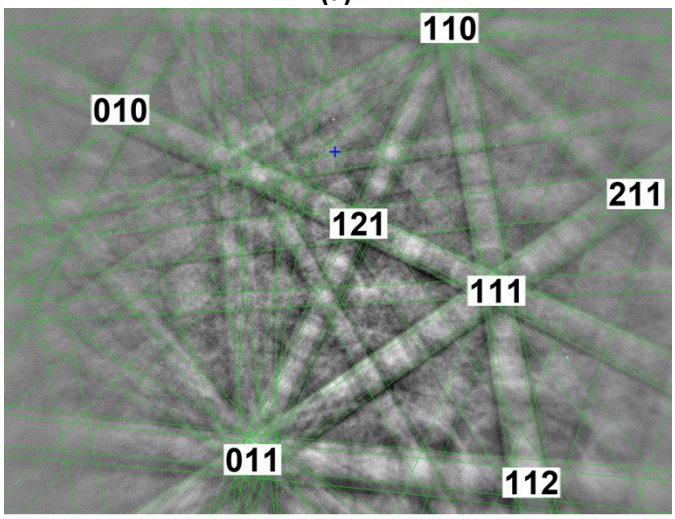

(b)

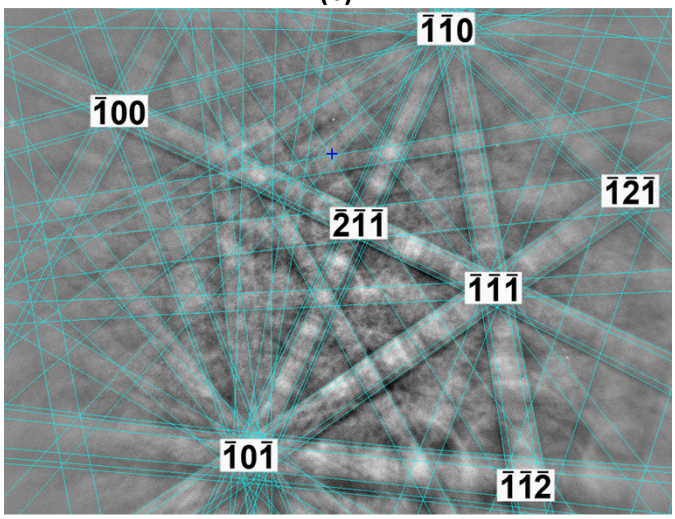

(c)

Figure 6.20 - (a) Representative EBSP taken from the Ni-Nb-Si-Cr rich phase in the 1000 and 1050°C and the simulated patterns for the (b) η-carbide and (c) G-phase crystal structures which are shown overlaying the experimental pattern in (a).

As a result of the EBSD ambiguity, SAD analysis of the Ni-Nb-Si-Cr rich phase in the HP-Nb2 1000°C-1000h and 3000h samples was performed using a Philips CM200 TEM operating at 200keV. All foils were produced using the methods described in Chapter 3. Figure 6.21 (a) gives a bright-field image of a transforming Type II lamellae where both $Cr_{23}C_6$ and the Ni-Nb-Si-Cr rich phase were identified between the NbC and austenite interfaces. SAD analysis of the transformed phase confirmed the diamond cubic η-carbide crystal structure. Figure 6.21 (b) to (d) show indexed [001], [101] and [112] zone axes taken from the precipitate labelled in Figure 6.21 (a) with the experimentally determined lattice parameters given in Table 6.3.

Considerable care needs to taken when distinguishing between the $Cr_{23}C_6$, η-phase and G-phase structures when analyzing zone axis patterns (ZAP). Differentiating between the $Cr_{23}C_6$, G-phase and η-carbide crystal structures by comparing experimentally determined lattice parameters (Table 6.3) with those reported in the literature is not reliable due to their similarity. All three phases obtain face centred cubic structures (Table 6.2) with only the space group differing between the $Cr_{23}C_6$ ($Fm\bar{3}m$), G-phase ($Fm\bar{3}m$) and η-carbide ($Fd\bar{3}m$) crystal structures. Based solely on the [101] and [112] patterns shown in Figure 6.21 (c) and (d), the diamond cubic modification of the FCC lattice is relatively unapparent. Although the {020} and {402} reflections are kinematically forbidden in the $Fd\bar{3}m$ <101> and <112> ZAP, these forbidden reflections were clearly observable when analysing the η-carbides (labelled in Figure 6.21 (c) and (d)). Since these reflections are allowed for the $Fm\bar{3}m$ space group, differentiation between each crystal structure using these reflections is not possible.

While the space group could not be easily determined using the [101] and [112] ZAP, the diamond cubic structure is readily distinguishable using the [001] ZAP. As shown in Figure 6.21 (b) the expected $<001>_{FCC}$ {040}, {220} and {400} reflections are clearly apparent. However, the {020} reflections (i.e. allowed reflections in the $Fm\bar{3}m$ space group) are barely visible. Based on kinematic diffraction the {020} and {420} type reflections are forbidden for the $Fd\bar{3}m$ space group [31-36]. However, dynamic diffraction allows the re-emergence of weak reflections (through double diffraction) in the <001> ZAP. Although no double diffraction route exists within the zero order Laue zone (ZOLZ) to produce these forbidden reflections, double diffraction involving the allowed {23 1 1} and {23 3 1} reflections located on the first order Laue zone (FOLZ) [33, 34, 36] causes the {020} reflections to be faintly observable in Figure 6.21 (b). The {420} reflections (also a result of double

diffraction) cannot be resolved in Figure 6.21 (b) due to the insufficient film exposure time used during capture of the pattern.

As previously mentioned the {020} and {402} reflections are kinematically forbidden for $Fd\bar{3}m$ <101> and <112> ZAPs. However, as shown in Figure 6.21 (c) and (d), these forbidden reflections were clearly observable with the intensity of these reflections being notably greater than observed for the forbidden reflections in the [001] zone. The reflections arise due to double diffraction routes existing within the ZOLZ. For example, double diffraction from the {113} reflections are the primary source for the forbidden {020} reflections in the <101> ZAP [33, 36]. Therefore, after confirmation of the weak {020} reflections associated with the <001> ZAP, the presence of the {020} and {420} reflections give further confirmation of the diamond cubic η-carbide crystal structure. Use of these double diffraction reflections for identification of η-carbides in Ni-based superalloys is commonly reported in the literature [32-35]. Further confirmation of the $Fd\bar{3}m$ space group using convergent beam electron diffraction has also been presented by Muddle [36] for Fe-W-C η-carbides in sintered W-Ni-Fe alloys.

Although a carbon peak was detected within the HP-Nb2 η precipitates, the EDS analysis presented in Figure 6.19 (b) at best gives a qualitative indication of the presence of carbon. Based on the measured composition these precipitates appear to obtain the $M_{12}C$ composition. However, it must also be noted that Cr-Ni rich silicides (Table 6.2) with crystal structure and lattice parameters identical to the η-carbide have also been identified in the literature [23]. Therefore, the η crystal structure does not necessitate the presence of carbon (i.e. the precipitates observed in the HP-Nb2 alloy which obtain the $Fd\bar{3}m$ space group could equally be classified as silicides). While the precipitates have been labelled as η-carbides, further analysis (such as electron energy loss spectroscopy) is necessary to quantitatively confirm the carbon content of these precipitates in HP-Nb2.

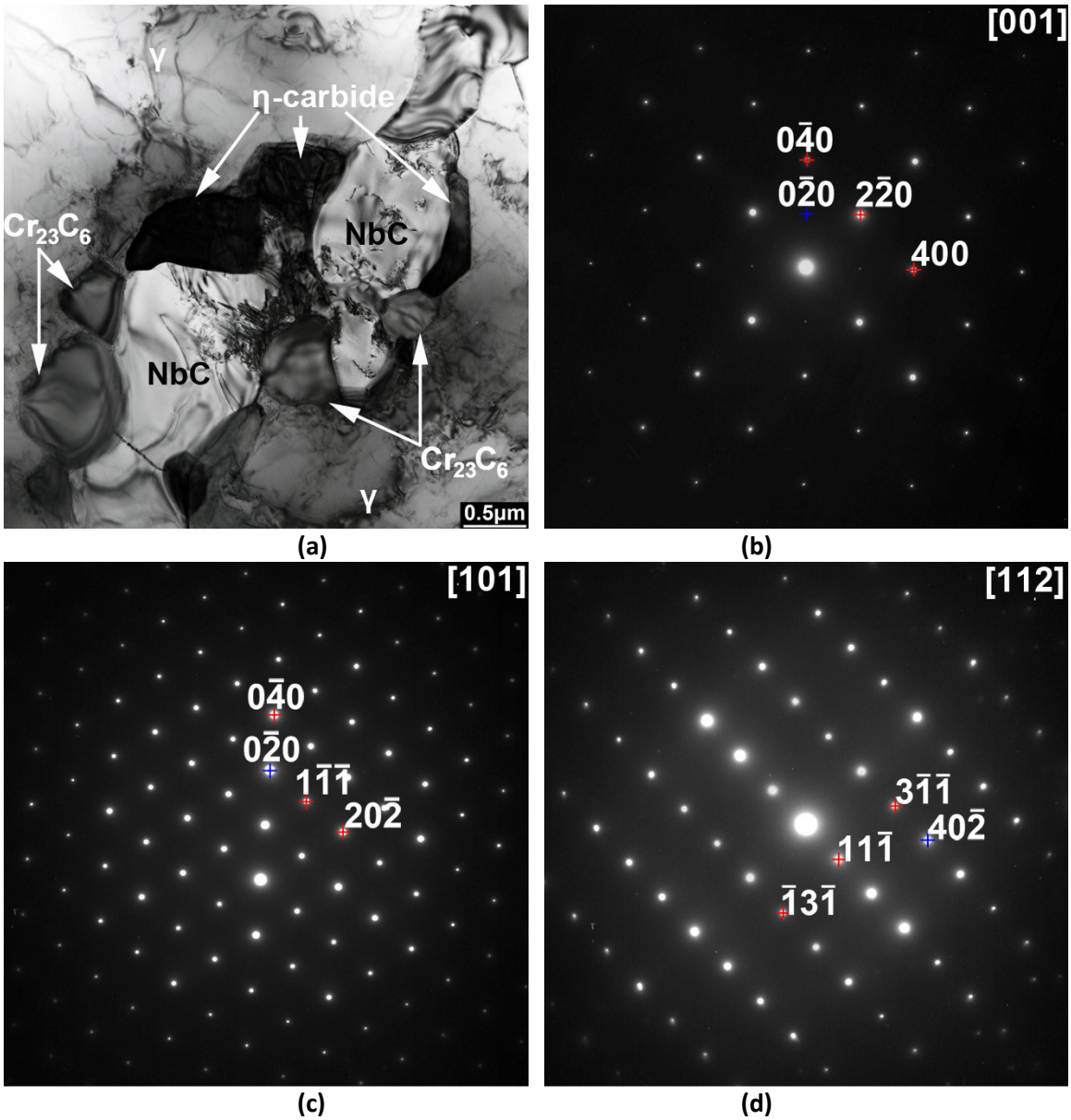

Figure 6.21 – (a) Bright field transmission electron micrograph of the Type II lamellae with η-carbide and $Cr_{23}C_6$ located between the NbC and austenite interfaces. Indexed selected area diffraction patterns taken from the (b) $[001]_{\eta\text{-carbide}}$, (b) $[101]_{\eta\text{-carbide}}$ and $[112]_{\eta\text{-carbide}}$ zone axes.

Table 6.3 – Crystal structure, lattice parameters and chemical composition of the η-carbide and interfacial $Cr_{23}C_6$ as determined by SAD and EDS analysis of the HP-Nb2 alloys after ageing at 1000°C for 1000 and 3000 hours.

	Structure	Space Group	Lattice parameter a=b=c (nm)	EDS Composition (at.%)					
				Cr	Ni	Si	Nb	Fe	V
η-phase	FCC	$Fd\bar{3}m$	1.084	33.3	30.3	16.6	14	5	0.8
$Cr_{23}C_6$	FCC	$Fm\bar{3}m$	1.067	85.6	4	-	-	10.4	-

In order to rule out the possibility that the NbC-to-η-carbide transformation was not specific to the HP-Nb2 alloy, the HP-Nb1 alloy was also aged at 1000°C for 1000 hours (Figure 6.22 (a)). Although TEM analysis was not performed on the transformed phase in the HP-Nb1 alloy, EDS and EBSD phase identification was performed to confirm the diamond cubic η-carbide crystal structure (Figure 6.22 (a) and (b)) . Based on the TEM analysis performed on the HP-Nb2 aged samples, the compositional similarity between the transformed phase in the HP-Nb1 and HP-Nb2 alloys (Figure 6.19 (b) and Figure 6.22 (b)) was considered sufficient evidence to identify the η-carbide as opposed to the G-phase.

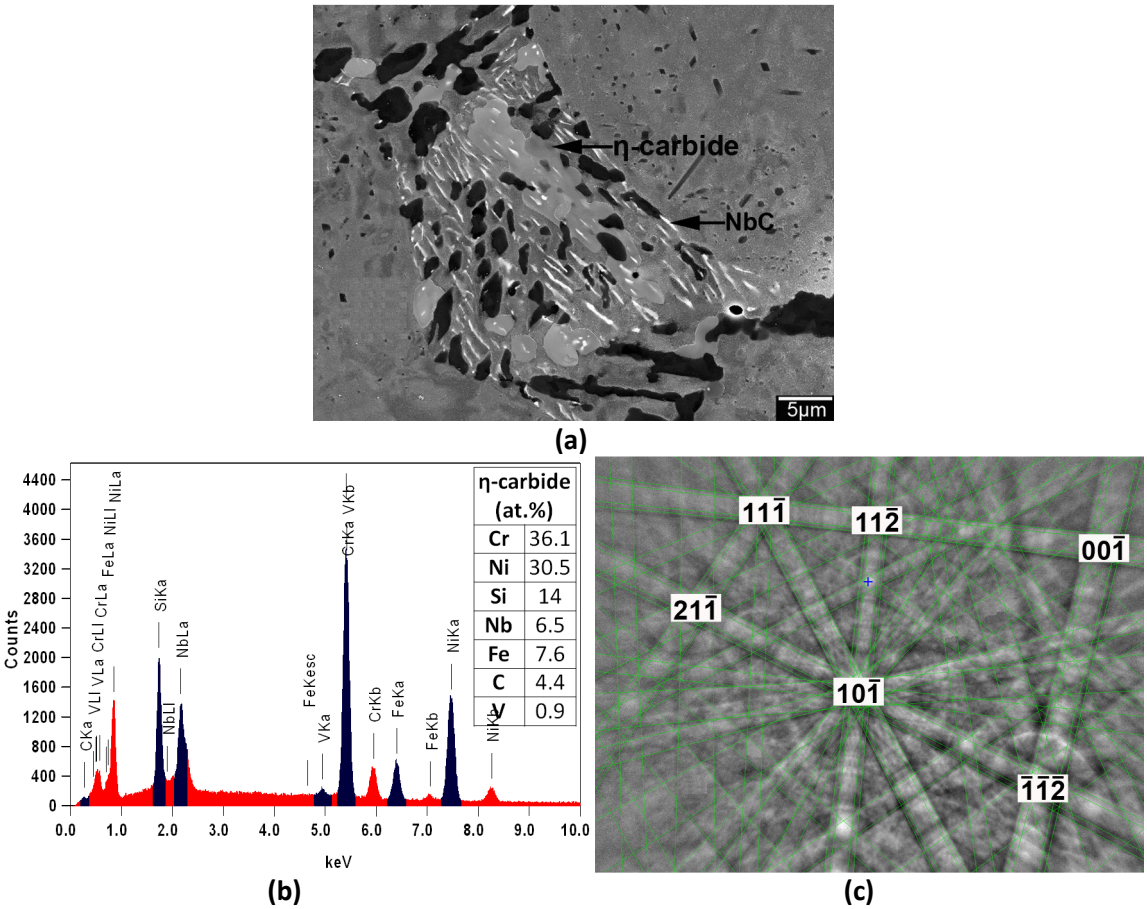

Figure 6.22 - (a) Composite electron micrograph of a transforming Type I colony in the HP-Nb1 alloy after ageing at 1000°C for 1000 hours. Phase identification of the η-carbide was performed using (b) EDS and (c) EBSD.

6.3.3 NbC-to-η-carbide Transformation versus NbC-to-G-phase Transformation

To provide further comparison between of the η-carbide and G-phase crystal structures in HP-Nb alloys, TEM analysis was performed on an ex-service HP-Nb alloy (service history unknown) removed from the Shell Middle Distillate Synthesis Plant in Bintulu Malaysia. SEM analysis determined the service conditions experienced by this HP-Nb tube had caused the NbC to predominantly transform to G-phase. However, η-carbide precipitates were also observed (although very rarely), suggesting that the two phases can co-exist in the HP-Nb alloy. Backscatter electron imaging and EDS analysis of the tube suggested the NbC transformation was nearly complete at the time of the tubes removal from service.

Figure 6.23 (a) shows a bright field TEM image of the G-phase precipitates in the ex-service material (beam direction parallel to the $[001]_{G\text{-}phase}$ zone axis) where remnants of the transforming NbC are surrounded by G-phase. The [001], [011] and [112] patterns taken from the G-phase precipitate are also given in Figure 6.23 (b) - (d). In contrast to the η-carbide structure, the allowed (200) reflections for G-phase's $Fm\bar{3}m$ space group were clearly visible in the [001] ZAP (labelled in Figure 6.23 (b)). The experimentally determined lattice parameters for the G-phase precipitate are presented in Table 6.1. Comparison of the EDS analysis presented in Table 6.3 and Table 6.1 further stresses the marked compositional difference between the η-carbide and G-phase precipitates. Both the G-phase chemical composition and lattice parameter closely matched previously reported values [3, 4, 14]. Therefore, based on the quantitative confirmation of each phase in the HP-Nb alloys, the NbC is capable of transforming to the distinctly different η-carbide and G-phase precipitates during thermal ageing.

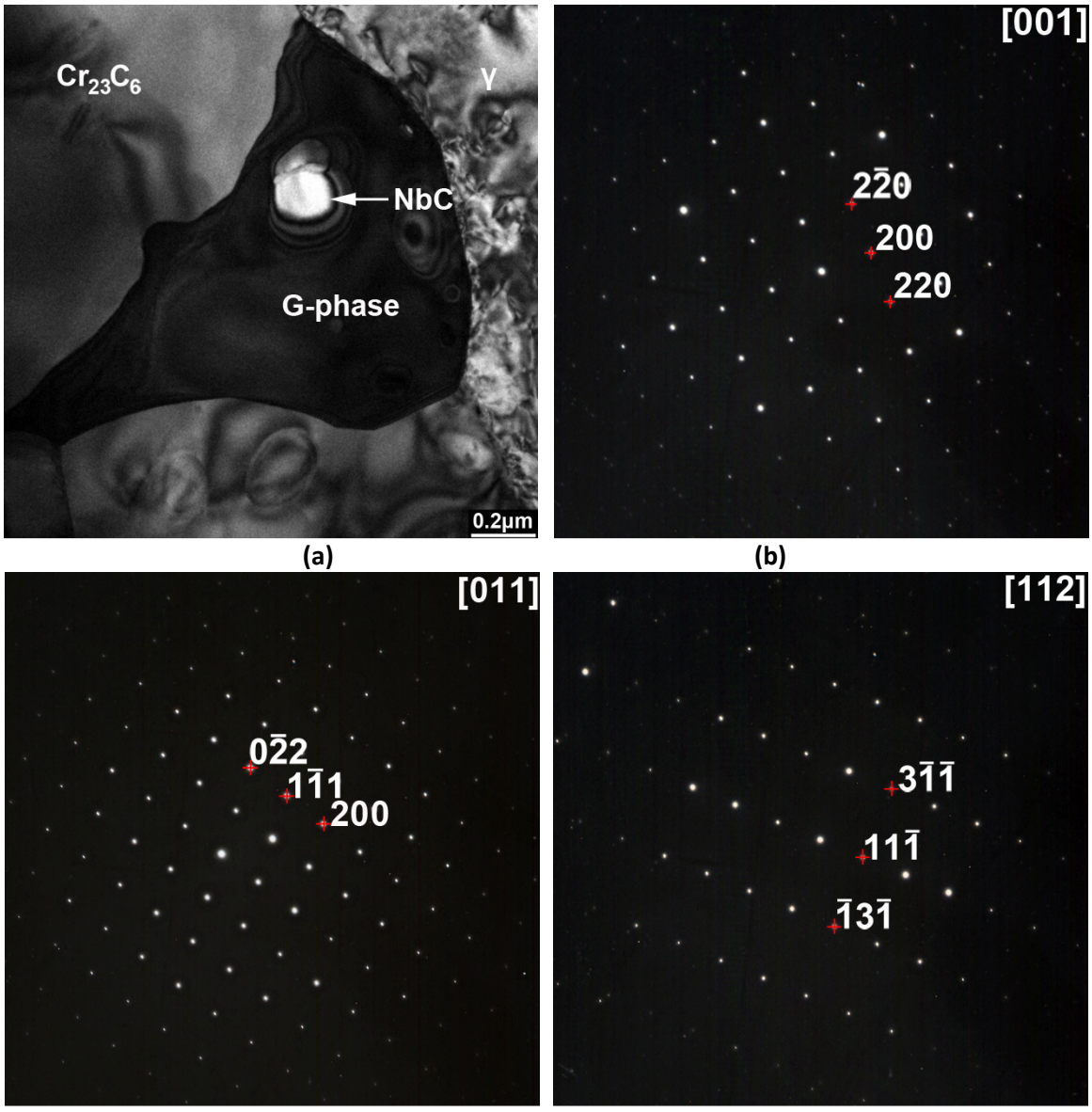

Figure 6.23 – (a) Bright field transmission electron micrograph of G-phase precipitates in the Shell Bintulu ex-service HP-Nb alloy. Indexed selected area diffraction patterns taken from the (b) $[001]_{G\text{-}phase}$, (b) $[101]_{G\text{-}phase}$ and $[112]_{G\text{-}phase}$ zone axes.

Table 6.4 – Crystal structure, lattice parameter and chemical composition of the G-phase precipitate in Figure 6.23 (a) as determined by SAD and EDS analysis.

	Structure	Space Group	Lattice parameter a=b=c (nm)	EDS Composition (at.%)				
				Ni	Si	Nb	Fe	Cr
G-phase	FCC	$Fm\bar{3}m$	1.127	51.7	20.4	19.5	5.5	2.9

The G-phase ($Ni_{16}Nb_6Si_7$) crystal structure identified in the Shell-Bintulu ex-service material was the only Ni-Nb-Si rich phase identified by Soares *et al.* [3] and Ibañez *et al.* [4] after conducting unstressed laboratory ageing studies on statically cast HP-Nb alloys. In total, Soares *et al.* and Ibañez *et al.* subjected five HP-Nb alloys with varied niobium and silicon contents to unstressed ageing at 700, 900 and 1100°C. The NbC-to-G-phase transformation was observed in all samples exposed to unstressed ageing 700 and 900°C. This transformation resulted in the near complete replacement of the as-cast primary NbC with comparatively larger G-phase precipitates after 1000 hours. Conversely, the NbC remained stable after ageing at 1100°C indicating the maximum temperature limit for the G-phase transformation lies between 900-1100°C. The G-phase crystal structure was identified in the 700 and 900°C samples using a combination powder X-ray diffraction (XRD), SAD and EDS. Based on the reported chemical composition and lattice parameters, it is unlikely the authors confused the η-carbide and G-phase structures.

In order to further characterise the NbC-to-G-phase transformation with respect to temperature, Soares *et al.* and Ibañez *et al.* performed numerous additional ageing treatments at temperatures between 700-1100°C. Three compositionally different alloys (1.97wt.% Nb, 1.63-2.62wt.% Si) were subjected to ageing for periods between 1 to 1000 hours. In this case, the phases in each aged sample were determined exclusively by performing XRD analysis on residues extracted using Berzelius' solution. The authors specifically noted that the $(440)_{G\text{-}phase}$ interplanar spacing of 0.198nm was used to identify G-phase. Regardless of the alloy composition, G-phase was the only reported phase in association with the NbC after ageing between 700-1000°C for up to 1000 hours. The X-ray data was subsequently used to construct time-temperature-transformation (TTT) curves for the G-phase transformation. Although G-phase was not reported when ageing above 1000°C for the 1000 hours ageing periods studied, the TTT curves were used to predict an upper limit for the G-phase transformation of between 1000-1050°C.

The complete absence of G-phase in the HP-Nb1 and HP-Nb2 alloys after ageing at 1000 and 1050°C suggests the upper temperature limit for the G-phase transformation within these alloys differs from the alloys studied by Soares *et al.* and Ibañez *et al*.. For direct comparison with these two earlier studies, the HP-Nb1 and HP-Nb2 alloys were aged at 900°C for 1000 hours. Ageing at 900°C was expected to cause the complete transformation of the as-cast primary NbC network to G-phase. However, in both alloys the NbC transformed to a mixed network of η-carbides and G-phase (Figure 6.24 (a) and (b)). Although the NbC transformation was not complete after 1000 hours at 900°C,

significantly less NbC remained in comparison to the sample aged at 1000°C. The volume fraction of NbC, η-carbide, and G-phase typically varied between the transformed NbC colonies. Overall, backscatter electron observations of the transformed NbC indicated the NbC-to-η-carbide transformation was slightly more prevalent after ageing (G-phase precipitates appeared slightly lighter in comparison to the η-carbides). EDS analysis of individual groups of precipitates supported the observed η-carbide prevalence. The marked compositional difference between the two phases was considered as strong evidence that allowed the G-phase and η-carbide crystal structures to be distinguished using EDS in the HP-Nb1 and HP-Nb2 900°C samples.

Transformation of the NbC colonies solely to either η-carbide or G-phase precipitates was not observed. The η-carbide and G-phase precipitates within individual colonies were often located directly adjacent to each other. Based on two-dimensional observations of the 900°C samples, there appears to be no preferential formation of either η-carbide or G-phase precipitates with respect to the original NbC morphology or location within the colony (i.e. adjacent to the primary $Cr_{23}C_6$). Further short-term ageing experiments (between 100-500 hours) are necessary to determine the factors that influence the type of transformation each individual lamella undergoes.

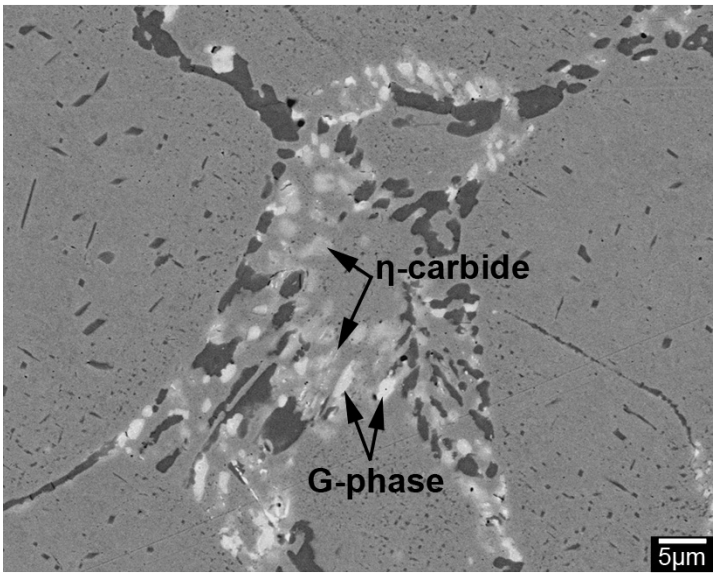

(a)

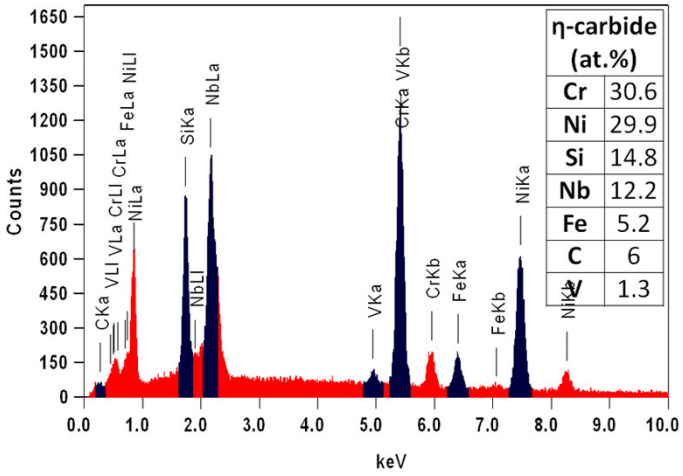

(b)

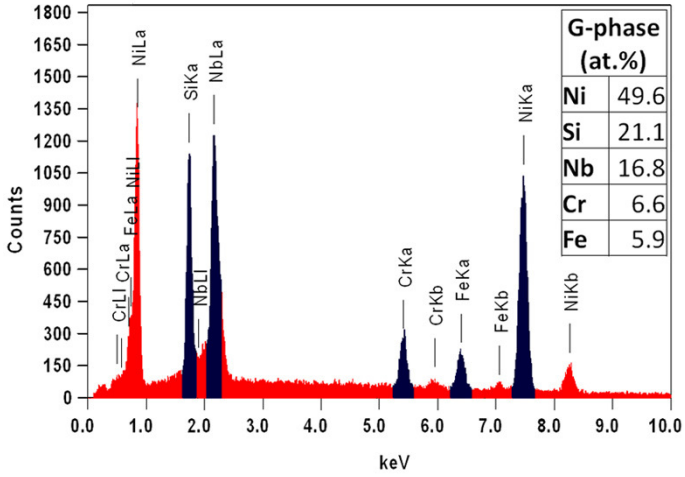

(c)

Figure 6.24 - (a) Backscatter electron micrograph of the HP-Nb1 alloy after ageing at 900°C for 1000 hours where the near complete transformation of the as-cast NbC colony to a mixed network of η-carbide and G-phase precipitates has occurred. (b) & (c) Representative EDS spectra taken from the η-carbide and G-phase precipitates.

As previously stated, identification of the G-phase precipitates in the Soares *et al.* and Ibañez *et al*. alloys was performed using X-ray powder diffraction. Unless considerable care is taken, XRD analysis of multiphase alloy systems (i.e. the HP-Nb alloy) can be inaccurate as a result of numerous peak overlaps in the XRD spectra. Such confusion -specifically between the η-carbide and G-phase crystal structures- was documented by the group of same authors in an earlier paper on the HK-Nb alloy (the 25Cr/20Ni alloy series which preceded the HP alloys) [15]. The confusion reportedly arose when using XRD as the peaks corresponding to the Ni-Si-Nb rich phase showed good agreement with powder diffraction data produced from both the $Fd\bar{3}m$ Nb_3Ni_2Si (η-carbide) and $Fm\bar{3}m$ $Ni_{16}Nb_6Si_7$ (G-phase) crystal structures.

To further demonstrate the complex nature of the XRD spectra produced from aged HP-Nb alloys containing η-carbide and G-phase precipitates, XRD analysis was performed on the HP-Nb2 1000°C-3000h aged sample and HP-Nb Shell Bintulu ex-service materials. These alloys were specifically selected as the η-carbide and G-phase crystal structures had already been confirmed using SAD. Moreover, the ex-service Shell Bintulu tube contained both η-carbide and G-phase precipitates. Samples from each alloy were prepared by dissolving the austenite with glyceregia, and subsequently crushing the remaining precipitate networks into a fine powder suitable for XRD analysis. Observations of the alloys after short-term etching (less than 1 minute) determined the austenite matrix was preferentially attacked by the glyceregia etchant while the η-carbide, G-phase, NbC and $Cr_{23}C_6$ precipitates remained completely intact. Peak identification was carried out manually by comparing the experimental spectra with individual spectra presented for each respective phase in the Pearson's Crystal Database [22] and with spectra simulated using Desktop Microscopist[1].

The XRD spectra produced from the HP-Nb2 1000°C-3000h aged sample and ex-service Shell Bintulu tube are shown in Figure 6.25 (a) and (b). In the Shell Bintulu tube, the peaks corresponding to η-carbide in were frequently overlapped by the $Cr_{23}C_6$, NbC and G-phase peaks. For example, the $(440)_{\eta\text{-carbide}}$ peak (47.6°) is overlapped by the $(531)_{\text{G-phase}}$ peak (47.8°) resulting in the observed double peak in Figure 6.25 (b). As shown in Figure 6.25 (a), the peak corresponding to the $(333)_{\eta\text{-carbide}}$ planes is the only η-carbide peak where significant overlapping does not occur in the HP-Nb2 1000°C-3000h aged sample. However, a slight overlap of the $(333)_{\eta\text{-carbide}}$ peak was observed in the ex-service material. Unfortunately, the phase that caused this overlap was unable to be identified with the

[1] Lacuna Laboratories, Beaverton, Oregon, USA.

available XRD data. Further SEM analysis was only identified the $Cr_{23}C_6$, NbC, η-carbide and G-phase precipitates across the tube wall thickness.

The common overlap between the $Cr_{23}C_6$, NbC, η-carbide and G-phase peaks when analyzing modified HP alloys could lead to phases being overlooked when performing XRD. Thus, the preceding observations emphasize the importance of using other identification techniques which are capable of sampling numerous groups of precipitates across the tube's wall thickness in combination with XRD. For example, EDS could be performed to identify candidate compounds (similar to Table 6.2) which can be subsequent simulated and compared with the XRD spectrum.

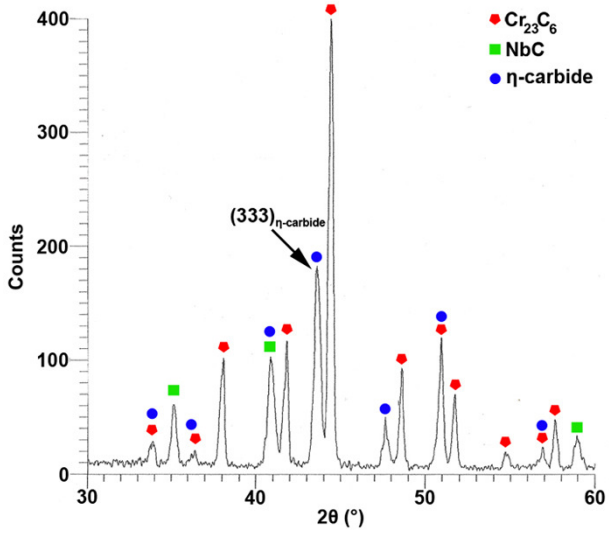

Figure 6.25 - XRD spectra taken from the primary and secondary precipitates present in the (a) HP-Nb2 1000°C-3000h and (b) ex-service Shell Bintulu HP-Nb tube.

While there is a limited number of laboratory aged HP-Nb studies reported in the literature [3, 4, 14, 18], numerous studies have been published on ex-service HP-Nb material (e.g., 1, 18-20, 37-40)). Typically, these ex-service studies consisted of optical, SEM and EDS analysis of the precipitates present in the ex-service materials. However, more comprehensive studies involving SEM and TEM analysis of the ex-service material were published by Nishimoto [18], Kenik et al. [19] and Thomas *et al.* [20]

Table 6.5 summaries the service conditions, phases identified and characterisation techniques specific to each ex-service material. It must be noted that the service temperature definition differed between authors. In general, the average tube skin temperature and maximum tube skin temperature were used to describe the temperature experienced by each tube during service. Accurate measurement of the tube material temperature is inherently difficult due to temperature gradients existing along the tubes length, around the diameter and through the tubes wall thickness [41]. The furnace temperature and internal gas stream temperature also fluctuates during the tubes service life often leading to tube temperature variations as large as 150°C [19]. Therefore, the service conditions stated in Table 6.5 can only be considered as approximations of the tubes wall temperature during service.

Similar to the laboratory ageing experiments, the NbC transformation product varied depending on the service temperature experienced by each tube. The NbC-to-G-phase transformation was solely observed in tubes exposed to 815°C and 890°C, whereas mixed NbC/η-carbide/G-phase networks were typically reported for tubes exposed to 875-905°C. At service temperatures between 920-1100°C, the NbC-to-η-carbide transformation dominated. These observations suggest the NbC-to-G-phase transformation dominates at lower temperatures (T<875°C) whereas the NbC-to-η-carbide transformation dominates at higher temperatures (T>920°C). The coexistence of η-carbide and G-phase when ageing at temperatures between approximately 875-920°C suggests a progressive transition from the G-phase to the η-carbide transformations occurs over this temperature range.

Table 6.5 - Summary of the phases reported in the literature for ex-service HP-Nb alloys (sorted based on the service temperature).

Reference	Sample ID	Service Temperature (°C)	Hoop Stress (MPa)	Exposure time (hrs)	Phases identified	Characterisation Techniques
38	EX	815	-	26,000	$Cr_{23}C_6$, NbC, G-phase	OM, SEM, EDS
38	EX	815	-	131,400	$Cr_{23}C_6$, G-phase	OM, SEM, EDS
1	SE-B	875	12.3	108,306	$Cr_{23}C_6$, NbC, η-carbide, G-phase	OM, SEM, EDS
1	SE-A	888	14.6	108,306	$Cr_{23}C_6$, η-carbide, G-phase	OM, SEM, EDS
39	F01	890 (max)	6.4	85,000	$Cr_{23}C_6$, NbC, G-phase	OM, SEM, EDS
1	SE-C	899	4.96	75,000	$Cr_{23}C_6$, η-carbide, G-phase	OM, SEM, EDS
1	SE-D	899	8	148,920	$Cr_{23}C_6$, NbC, η-carbide	OM, SEM, EDS
1	SE-H	905	13.6	131,000	$Cr_{23}C_6$, η-carbide, M2(C,N)	OM, SEM, EDS
1	SE-I	905	13.6	143,000	$Cr_{23}C_6$, η-carbide, G-phase	OM, SEM, EDS
1	SE-J	905	13.6	143,000	$Cr_{23}C_6$, η-carbide, G-phase	OM, SEM, EDS
20	ES	920	10	70,000	$Cr_{23}C_6$, NbC, η-carbide, NbCrN	OM, SEM, TEM, EDS, SAD, XRD
19	HPNb	927-1066	-	105,000	$Cr_{23}C_6$, NbC, η-carbide	OM, SEM, TEM, EDS, SAD, XRD
18	HP35C	1100 (max)	-	26,277	$Cr_{23}C_6$, η-carbide	SEM, TEM, SAD

Although the dominant factors influencing the NbC-to-G-phase and NbC-to-η-carbide transformation in the HP-Nb alloys are unclear in the literature, the factors governing the η-carbide and G-phase transformations in other alloy systems has been investigated in further detail [42-44]. Williams and Titchmarsh [42] reported the formation of both phases due to neutron irradiation of niobium stabilised FV548 austenitic steels (17wt.% Cr, 12wt.% Ni). Preferential transformation to either G-phase or η-carbides was determined to be dependent on the alloys thermal history prior to irradiation. The G-phase transformation occurred preferentially in material aged at 850°C, whereas the η-carbide transformation dominated in material which was subjected to a solution heat treatment (1150°C) prior to irradiation. In the aged material, the carbon content dissolved in the austenite matrix was found to be comparatively lower in comparison to the solution heat treated

material. Therefore, the carbon-free G-phase was believed to be favoured in specimens where the matrix was carbon-lean whereas the η-carbides formed when the matrix was carbon-rich. Experiments conducted with 'model' alloys produced to contain low (0.02wt.%) and high (0.22wt.%) carbon contents supported the authors theory with the phase preference changing from G-phase in the low carbon alloy to η-carbides in the high carbon alloy.

The high cooling rates induced during centrifugal casting of the HP-Nb tubes results in the as-cast austenite matrix being relatively supersaturated with carbon. Direct evidence of this carbon saturation within the as-cast matrix is provided by the substantial secondary carbide network which rapidly forms during ageing of the HP-Nb alloys. Extensive secondary precipitation was also observed in the statically cast HP-Nb alloys analysed by Soares et al [3] and Ibañez et al. [4] suggesting any reduction in the dissolved carbon content in these alloys (due to the comparatively slower cooling rates) in comparison to the HP-Nb1 and HP-Nb2 alloys was negligible. Based on the Williams and Titchmarsh [42] study, the comparatively high levels of dissolved carbon in the as-cast HP-Nb matrix would be expected to promote the NbC-to-η-carbide transformation. However, the maximum ageing temperature for their 'model' alloys was 850°C. As previously discussed, the NbC-to-η-carbide transformation in the HP-Nb alloys was only observed when ageing at temperatures above 850°C. Unfortunately, ageing of other low carbon alloy systems similar to the FV548 alloy studied by Williams and Titchmarsh at temperatures where the NbC-to-η-phase transformation may proceed (i.e. T>850°C) has not been reported in the literature. Consequently, it is unknown if the NbC-to-G-phase transformation continues to proceed when ageing the low carbon alloys at higher ageing temperatures. Without further knowledge of these higher temperature phase transformations in low carbon alloys, it is difficult to determine if the comparatively high carbon content in the HP-Nb matrix is the dominant factor that promotes the NbC-to-η-carbide transformation.

The η-carbide and G-phase precipitates have also been identified in low carbon (0.04wt.%) 20Cr-25Ni alloys after ageing at temperatures between 600-850°C [43-46]. Powell *et al.* [44] argued that identification of the η-carbides and G-phase precipitates had often been confused in aged 20Cr/25Ni/Nb alloys and stated that alternate studies recent to their 1988 article [43] predominantly observed G-phase while earlier studies [45, 46] reported the M_6C (η) carbide despite all studies analysing steels with similar composition and thermal history. Unfortunately, this confusion surrounding the identification of the two phases causes it to be difficult to reliably conclude what conditions would cause preferential formation of either phase.

In addition to carbon, nitrogen has also been noted to influence the formation of molybdenum-rich η-carbides ($(FeCr)_{21}Mo_3C_6$) in 316 stainless steels [47]. The formation of Mo-rich η-carbides in 316 containing 0.069wt.% nitrogen after ageing for 1 hour at 900°C. In contrast, η-carbides were not observed in a similar alloy containing 0.037wt.% nitrogen after ageing for 1000 hours. While little evidence of the effects of nitrogen on the Nb-rich η-carbides exists in the literature, the nitrogen content was notably kept below 0.012wt.% in the statically cast HP-Nb alloys studied by Soares *et al.* [3] (i.e. the laboratory aged alloys where only G-phase was identified). The nitrogen contents in the HP-Nb1 and HP-Nb2 alloys (as determined by LECO combustion analysis) was 0.049 and 0.089wt.% respectively. Currently it is unknown if these marginally higher nitrogen contents in HP-Nb1 and HP-Nb2 alloys (in comparison to those studied by Soares *et al.*) promoted the formation of η-carbides. The nitrogen content in the HP-Nb2 alloy was almost twice that of the HP-Nb1 alloy, yet the specific NbC transformations that occurred in each alloy with respect to temperature were the same. Ageing of the HP-Nb1 and Nb2 alloys at 900°C for 1000 hours caused the η-carbide and G-phase transformations to proceed in both alloys, whereas exposure to 1000°C for 1000 hours resulted in only the η-carbide transformation proceeding in each alloy.

In contrast to the statically cast HP-Nb alloys studied by Soares *et al.*, the HP-Nb1 and Nb2 alloys were commercially produced (i.e. the HP-Nb1 and HP-Nb2 alloys were produced using the same method as used for HP-Nb reformer tubes). Thus, if the nitrogen content influences the η-carbide and G-phase transformations, the phase transformations during service exposure of centrifugally cast HP-Nb tubes are expected to be similar to those observed in the HP-Nb1 and HP-Nb2 alloys.

The reported nitrogen contents in the ex-service alloys (which contained η-carbides) ranged between 0.05-0.26wt.%. Unfortunately, the ex-service alloys which exhibited comparatively high nitrogen contents and solely contained η-carbides were also the alloys which experienced higher service temperatures (T>905°C). Thus, the influence of nitrogen on the NbC/η-carbide transformation in the ex-service alloys is masked by the increased service temperature.

As discussed further in Chapter 8, ageing of the alloys of the alloys in air caused decarburisation and nitridation to occur during long-term ageing. The effects of the furnace atmosphere largely manifested within 2-3mm of the exposed surfaces (depending on the ageing temperature). While the NbC-to-η-carbide transformation was accelerated in the regions of tube affected by the furnace atmosphere when ageing at 1000 and 1050°C, no significant evidence of nitrogen was observed

when performing EDS analysis on the η-carbides. Therefore, it was considered unlikely that nitrogen solely contributed to the accelerated kinetics of the η-carbide transformation in these regions.

In order to further rule out the ageing atmosphere being the cause of the η-carbide transformation, as-cast HP-Nb1 and HP-Nb2 samples were encapsulated in evacuated quartz tubes and subjected to ageing at 1000°C for 1000 hours. Figure 6.26 (a) gives a representative backscatter scanning electron micrograph of the Type II morphology undergoing the NbC-to-η-carbide transformation. Although only a brief SEM/EDS study was performed on these aged samples, the NbC-to-η-carbide transformation was solely observed in association with Type I and II lamellae for both the HP-Nb1 and HP-Nb2 alloys. Therefore, the absorption of nitrogen from air ageing atmosphere is not thought to be responsible for the formation of η-carbides in place of G-phase.

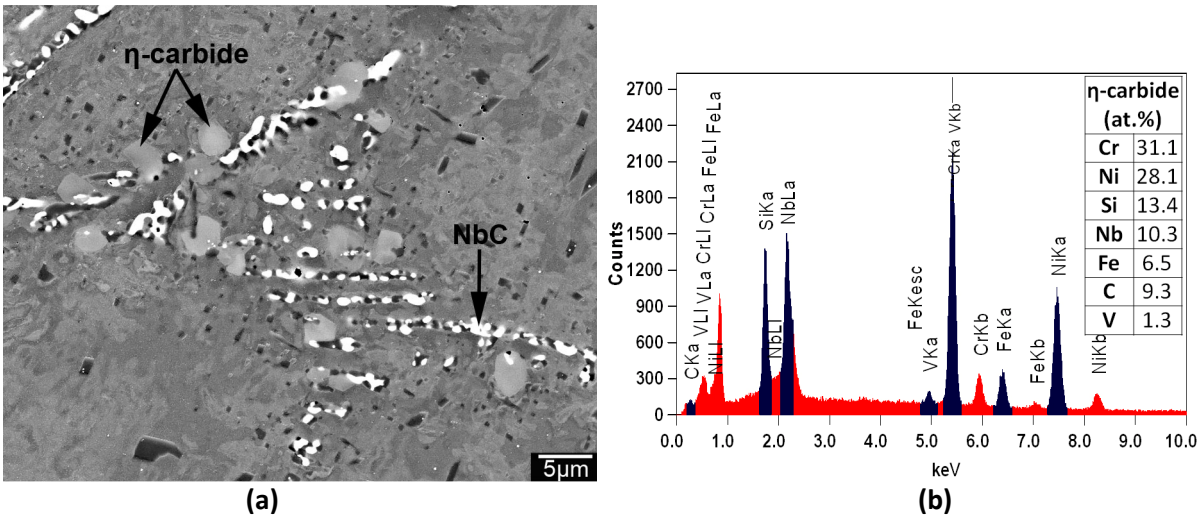

(a) (b)

Figure 6.26 - (a) Representative backscatter electron micrograph of the HP-Nb1 and Nb2 alloys after ageing at 1000°C for 1000 hours where the as-cast Type II NbC colony has partially transformed to η-carbides. (b) Representative EDS spectra taken from the η-carbides.

Based on the preceding evidence, the NbC-to-G-phase and NbC-to-η-carbide phase transformations in the HP-Nb alloys are believed to be dictated by the ageing temperature. At temperatures below 875°C, the NbC-to-G-phase transformation dominates resulting in the complete transformation of the primary NbC network to G-phase. Ageing at temperatures between 875-920°C causes the NbC-to-G-phase and NbC-to-η-carbide transformations occur in parallel. The η-carbide volume fraction is expected to progressively increase with the ageing temperature until the NbC-to-η-carbide transformation becomes dominant. However, it must be strongly stressed that the stated temperature ranges are an approximation based on limited data from ex-service and laboratory aged

samples. Further laboratory ageing of the HP-Nb alloys between 700-1050°C (i.e. the temperature range over which these transformations have been observed) followed by phase identification and quantitative image analysis to determine the area fraction of G-phase and η-carbide over the 850-950°C temperature range and the percentage of NbC transformed with respect to ageing temperature and time is necessary to define the η-carbide and G-phase TTT curves.

While the NbC-to-G-phase and NbC-to-η-carbide transformations are potentially influenced by the carbon and nitrogen concentrations in the as-cast alloys, the extent to which these elements influence each transformation in the HP-Nb alloys could not be quantified based on comparison with similar alloy systems presented in the literature. Based on the observations in the current work, it is believed that the composition will mainly alter the temperature range over which these transformations occur rather than complete suppression of either the η-carbide or G-phase transformations in the HP-Nb alloy. However, further ageing experiments on 'model' HP alloys which specifically contain comparatively low and high carbon and nitrogen contents are necessary in order to gain further insight into the role of the alloy's chemical composition with respect to ageing temperature and time.

Interestingly, the specific temperature ranges over which each phase transformation occurs potentially provides an additional microstructural marker through which the tubes thermal history during service could be judged. Accurate knowledge of the G-phase and η-carbide TTT curves would possibly allow for the average temperature specific to each region of the pipe to be estimated. This estimated temperature could be subsequently combined with diametric strain measurements, the pressure history and other microstructural indicators such as the void fraction to assess the remaining life of the entire tube set. Alternatively, the presence of G-phase (T<875°C), η-carbides (T>920°C) or NbC precipitates (T>1050°C) in ex-service material could be used to indicated if the tube has operated at the specified design temperature.

6.3.4 Evolution of the Type I NbC Lamellae with respect to Ageing Temperature and Time

As discussed in Chapter 4, the as-cast primary NbC network was comprised of two significantly different morphologies of individual plate lamella (designated as Type I and Type II lamellae). The Type I lamellae obtained a cube-cube OR with the austenite matrix while no consistent OR was observed between the Type II lamellae and austenite matrix. Observations of the HP-Nb alloys revealed that the appearance of the two morphologies was considerably different after exposure to 1000-1100°C (e.g. Figure 6.27 and Figure 6.32). Therefore, the observed morphological and crystallographic differences in the as-cast condition directly influenced the evolution of the Type I and II morphologies during ageing.

Figure 6.27 (a) to (d) shows scanning electron micrographs of the Type I lamellae after exposure to 1000°C for 1000 and 10,000 hours. The transformation of the Type I lamellae to η-carbides was clearly observable after 1000 hours. Generally the transformation rate varied significantly between individual colonies with the volume fraction of η-carbide for colonies on the grain boundaries being greater in comparison to colonies located on dendrite boundaries. The transformation kinetics also varied markedly between individual lamellae within each colony. As shown in Figure 6.27 (a), the transformation of the labelled lamellae appears significantly advanced in comparison to the lamellae shown in Figure 6.27 (b). When observing two-dimensional polished sections, no clear positional preference within the colony was observed with respect to the observed transformation of each lamella.

Continued transformation of the NbC to η-carbide occurred during pronged exposure of the HP-Nb2 alloy to 1000°C with the volume fraction of η-carbide progressively increasing after 3000, 6000 and 10,000 hours. After 10,000 hours, the NbC-to-η-carbide transformation had caused sections of the grain boundaries (GB) to be completely covered by alternating $Cr_{23}C_6$/η-carbide precipitates. For colonies located on the dendrite boundaries, the transformation rate variance between individual lamellae (observed after 1000 hours) remained after prolonged ageing (Figure 6.27 (c) and (d)). As shown in Figure 6.27 (c), few Type I colonies experienced near complete transformation of the NbC lamellae to η-carbides with the size of the resulting η-carbide often encompassed the entire as-cast NbC colony. In contrast, the isolated transformation of the lamellae in Figure 6.27 (d) is nearing completion while the NbC lamellae adjacent to these η-carbides showed negligible evidence of the

transformation. For colonies located on the dendrite boundaries, localised transformation of lamellae similar to Figure 6.27 (b) was more commonly observed than the completely transformed colonies after 10,000 hours.

Regardless of the colony's location (i.e. GB or DB), the total volume fraction of η-carbides markedly increased when comparing the 1000 and 10,000 hour samples. The grain boundary η-carbides were typically larger than those located on dendrite boundaries (~10-20µm GB, 5-15µm DB). Unfortunately, due to the similar backscatter electron contrast of the η-carbides and austenite, segmentation of the η-carbides for quantitative image analysis proved inaccurate when performed on backscatter electron images (similar to those shown in Figure 6.2). Therefore, measuring the transformed fraction for each Type I colony and determining the variance was not possible. However, image analysis of the NbC determined that approximately 50% of the as-cast NbC area fraction had transformed to η-carbides after 10,000 hours.

Small (<0.5µm diameter) silicon-oxygen rich particles were commonly found in association with the η-carbides after in the 1000°C-1000h sample (Figure 6.27 (a))). These particles were observed within the Type I and II NbC colonies. The Si-O rich particles were still present in the 1000°C-10,000 hour, but prolonged ageing had caused their number to reduce. Due to the small size of these particles phase identification was not possible using EBSD. These particles were not observed within the thin area of the TEM samples. The size of these particles also caused the EDS analysis to be inaccurate as the beam excited X-rays from the surrounding η-carbide. However, the silicon peak was higher than typically expected for η-carbides (with respect to the Cr, Ni and Nb peaks). Moreover, the oxygen peak was not observable when analysing the η-carbides at the mid-wall position.

Currently it is unknown if these precipitates exist in the as-cast condition or solely after ageing. In the as-cast condition, evidence of the Si-O particles was found between the Type I lamellae/austenite interface. However, the particles were typically less than 0.1µm in diameter and thus the EDS spectra produced from the surrounding phases completely masked the signal from the particles of interest. Pitting located between the NbC/austenite interfaces (induced during sample preparation) further complicated the identification of these particles. Since these particles were not able to be located in the TEM samples, further analysis of the as-cast Type I and II lamellae is necessary to prove if these Si-O rich particles exist in the as-cast condition and subsequently coarsen during ageing or if nucleation and growth of these particles occurs on the NbC/austenite interfaces. Further analysis is

also necessary to determine relationship between these particles and the NbC-to-η-phase transformation.

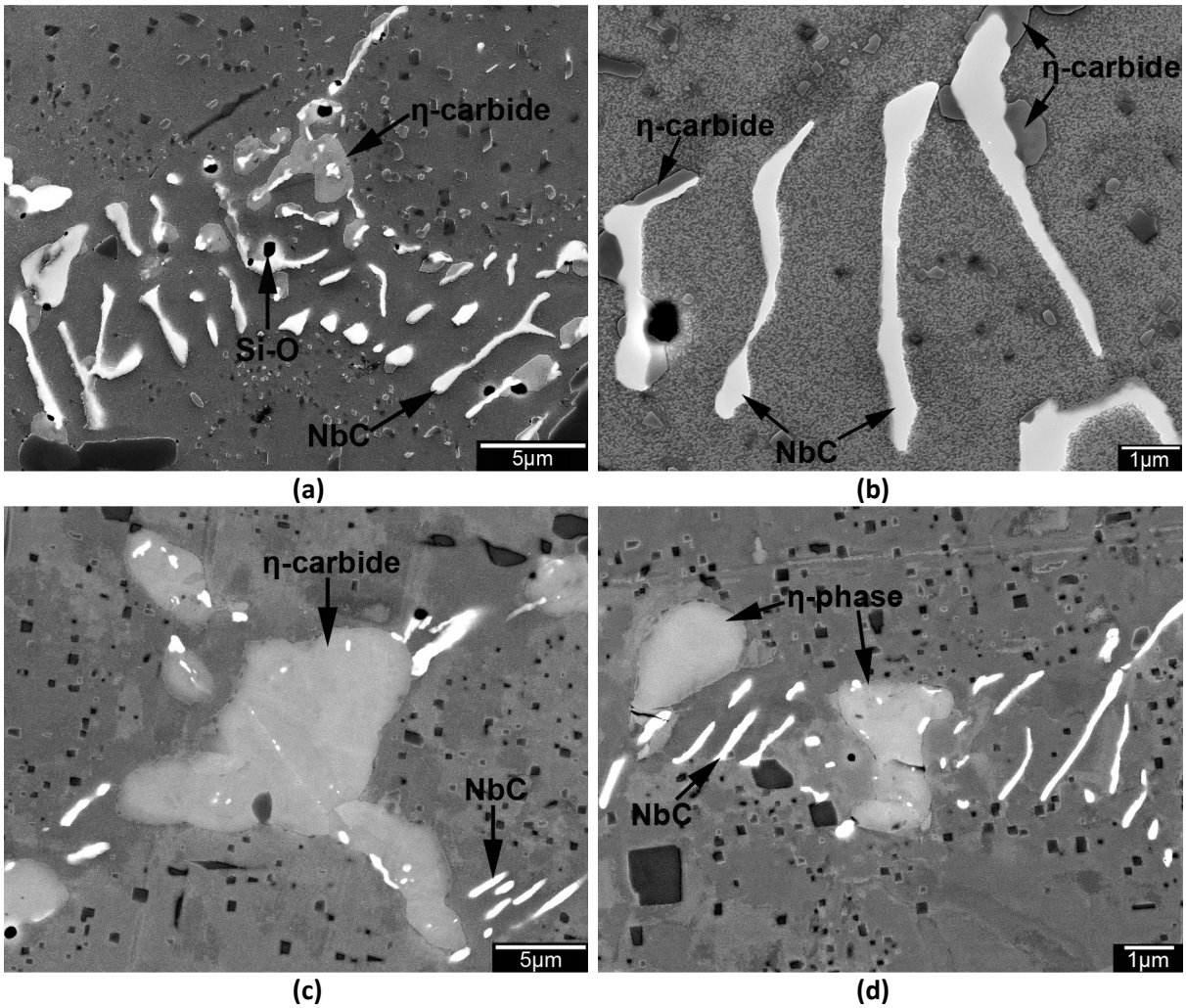

Figure 6.27 – Composite scanning electron micrographs showing the transformation of the Type I lamellae to η-carbides in the HP-Nb2 alloy after ageing at 1000°C for (a)-(b) 1000 and (c)-(d) 10,000 hours.

Figure 6.28 (a) and (b) shows the Type I lamellae after ageing at 1050°C for 1000 and 10,000 hours. In contrast to the 1000°C samples, the NbC remained completely stable during the first 1000 hours of ageing and the as-cast lamellar morphology was completely retained (Figure 6.28 (a)). The NbC-to-η-carbide transformation was only observed in the 1050°C-10,000 hour sample. Similar to the transformation at 1000°C, the transformation was relatively variable with the localised formation of large η-carbide precipitates in certain regions of the Type I colony while lamellae located directly adjacent to these η-carbides remained stable. Generally the untransformed lamellae were larger than those observed in the as-condition indicating that, in the absence of the η-carbide transformation, the lamellae undergo coarsening during prolonged ageing.

Interestingly, the η-carbides often exhibited highly faceted interfaces which were closely aligned with the faceting observed on the secondary $Cr_{23}C_6$ matrix precipitates. Although similar facets were also exhibited by the η-carbides in the 1000°C samples, faceted interfaces were much more prevalent in the 1050°C-10,000 hours sample. Transmission electron microscope studies conducted on similar cuboidal $Cr_{23}C_6$ precipitates in austenitic steels determined the cuboidal facets aligned with the {110} and {111} planes [9, 13]. Therefore, the faceted interfaces observed on the η-carbide interfaces may also obtain similar habit planes. However, trace analysis is necessary to confirm if the η-carbide facets align with a consistent and rational habit plane.

Figure 6.28 (c) and (d) show the Type I lamellae after ageing at 1100°C where, regardless of the ageing time, the NbC crystal structure remained completely stable. The size of the lamellae after 1000 hours appeared similar in size to those observed at 1050°C. However, the lamellae were notably larger after 10,000 hours (Figure 6.28 (c)). Although the lamellar morphology was still observable after ageing at 1100°C for 1000 hours, the lamellae appeared much more fragmented in comparison to the as-cast and 1050°C lamellae. During prolonged ageing, the lamellar NbC precipitates transitioned to a blocky morphology with coarsening and dissolution of the fragmented lamellae resulting in a significant reduction in the total number of blocky precipitates remaining within each colony after 10,000 hours.

Regardless of the ageing temperature or time, precipitation of secondary $Cr_{23}C_6$ on the Type I lamellae/austenite interface was not observed.

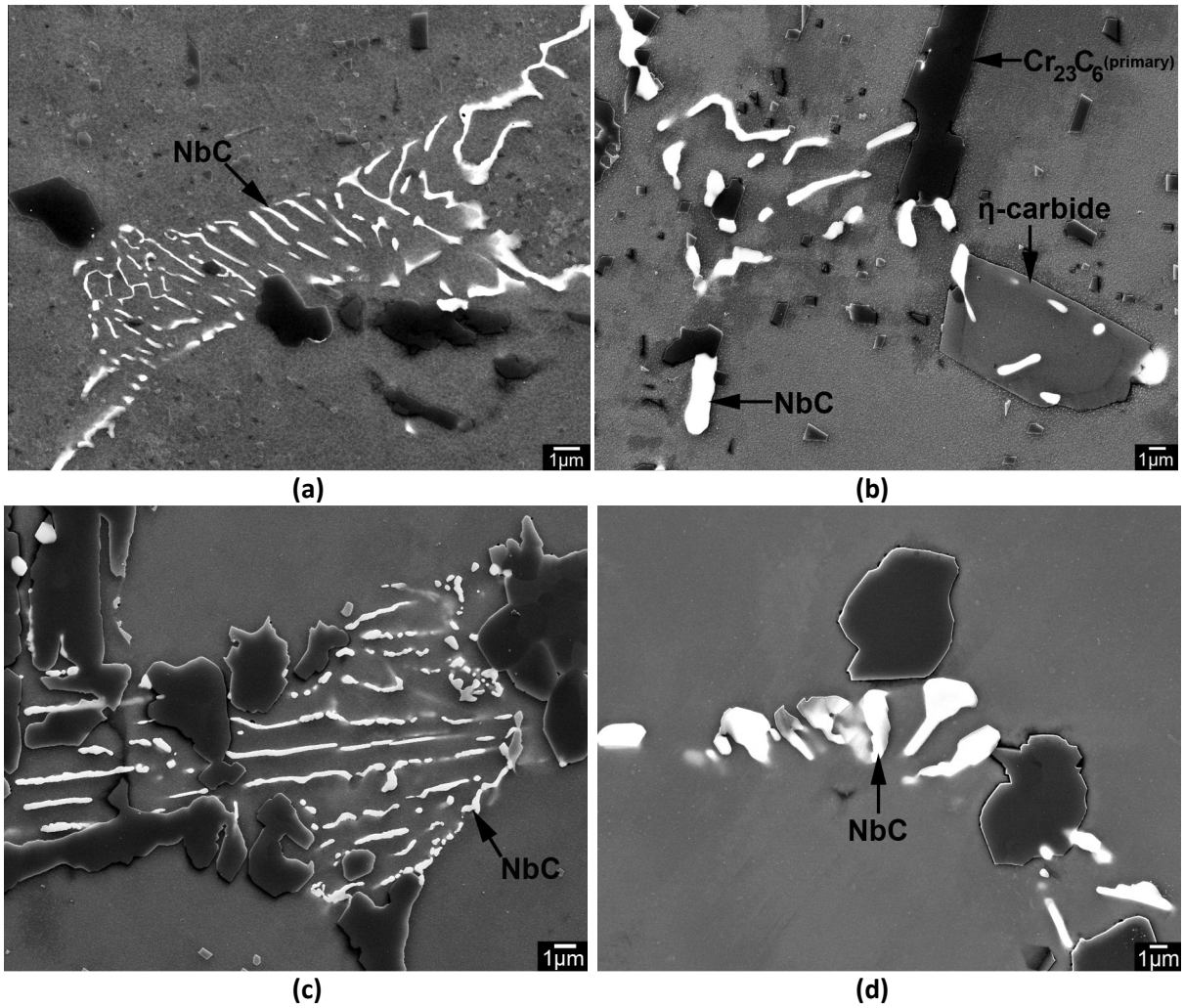

Figure 6.28 – Composite scanning electron micrographs showing the evolution of the Type I lamellae after exposure of the HP-Nb1 to 1050 and 1100°C for (a) & (c) 1000 and (b) & (d) 10,000 hours respectively.

As previously stated, the NbC-to-η-carbide transformation rate varied significantly between individual lamellae that were located within the same colony when ageing of the HP-Nb alloy at 1000 and 1050°C. Determining the cause of this variance was inherently difficult based on observations made from two-dimensional sections of the lamellae. For example, the lamellae which appeared stable in two dimensions may have been undergoing the η-carbide transformation out of the sectioning plane. Therefore, deep etching of the 1000°C-1000h aged sample was performed to provide further insight into the microstructural evolution of the Type I and II NbC lamellae during ageing. Deep etching of the 1050°C-1000h samples was also carried out to provide comparison between the morphological evolutions of the Type I lamellae when the NbC-to-carbide transformation present and absent respectively. Progressive etching experiments confirmed the

glyceregia etchant preferentially attacked the austenite matrix while leaving the primary precipitate network intact. Etching was performed by submersing the samples in glyceregia for a maximum of 2 hours.

Figure 6.29 (a) and (b) show the three-dimensional morphology of the Type I lamellae after ageing at 1000°C for 1000 hours. The varied transformation rate observed in two-dimensions was also evident in three-dimensions. This variance is demonstrated in Figure 6.29 (a) where transformed and untransformed lamellae lie directly adjacent. Unfortunately, the factors causing greater instability of certain lamellae with respect to others could not be further deduced from the deep etched samples.

As shown in Figure 6.29 (a) and (c), the untransformed NbC in the 1000 and 1050°C samples appear to retain the as-cast lamellar morphology. However, higher magnification images reveal the stepped appearance of the plate's broad faces. While these faces appeared featureless when observed at similar magnifications in the as-cast condition, ledges were observed on the broad faces of the lamellae when observed using the TEM. As no evidence of the NbC-to-η-carbide transformation was observed in the 1050°C-1000h sample, these ledges are not thought to be associated with the η-carbide transformation. Instead these ledges are likely related to the coarsening of the NbC lamellae which remain stable during ageing. Further analysis of the Type I lamellae using the TEM is necessary to rule out these features being associated with the NbC-to-η-carbide transformation.

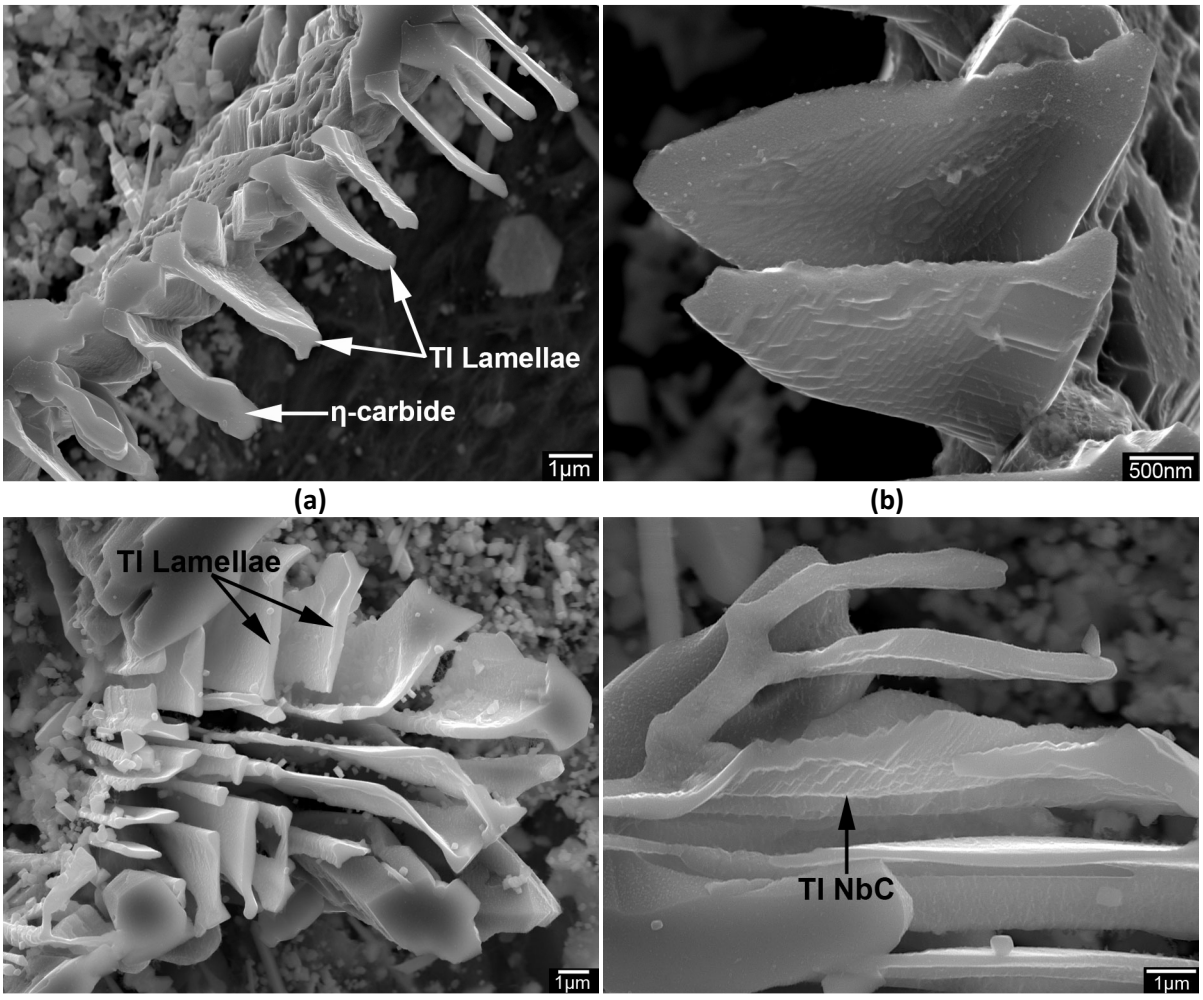

Figure 6.29 – Secondary electron micrographs showing the three-dimensional morphology of the Type I lamellae after ageing for 1000 hours at (a)-(b) 1000°C and (c)-(d) 1050°C

6.3.5 Evolution of the Type II NbC Lamellae with respect to Ageing Temperature and Time

The evolution of the Type II lamellae during ageing was considerably more complex than observed for the Type I lamellae (Figure 6.30 (a) - (d)). After 1000 hours, partial transformation of the Type II lamellae to the η-carbide had occurred. In addition to the NbC-to-η-carbide transformation, the NbC/austenite interface was densely populated with $Cr_{23}C_6$ precipitates similar in size to the secondary matrix precipitates (typically <1μm^2). The η-carbide transformation combined with the interfacial $Cr_{23}C_6$ precipitate often resulted in an apparent fragmentation of Type II lamellae when viewed in two-dimensions. These fragmented NbC precipitates were rejoined by η-carbide and $Cr_{23}C_6$ precipitates causing the complex mixed lamellae after 1000 hours (Figure 6.30 (a) and (b)). As shown in Figure 6.30 (b), the Si-O rich particles were observed in association with the Type II lamellae after ageing for 1000 and 10,000 hours.

Similar to the Type I lamellae, this transformation rate varied across individual colonies of Type II lamellae with localised transformation the NbC resulting in η-carbides of typically less than 3μm in diameter after 1000 hours exposure. The transformation rate was also greater for colonies located on and directly adjacent to grain boundaries (as opposed to those located on dendrite boundaries). Due to the complexity of the Type II lamellae after ageing, it was not possible to determine the type of lamellae which contained the greater area fraction of η-carbide based on qualitative comparisons.

Figure 6.30 (c) and (d) show the Type II lamellae after ageing for 10,000 hours at 1000°C. Increased exposure of the HP-Nb2 alloy caused further transformation of the Type II lamellae to η-carbides and coarsening of the interfacial $Cr_{23}C_6$. Generally, the η-carbides in association with the Type I lamellae after 10,000 hours were slightly smaller (5-10μm) in comparison to the η-carbides associated with the Type I lamellae (5-15μm). Although the transformation rate of Type II lamellae located on the grain boundaries was greater than on dendrite boundaries, the transformation was not complete after 10,000 hours. Prolonged ageing has caused the remaining NbC to appear spheroidized when observing the precipitates in two dimensions. Based on comparison between the interfacial and matrix $Cr_{23}C_6$ distributions, coarsening of the interfacial $Cr_{23}C_6$ precipitates occurred at a greater rate in comparison to the matrix $Cr_{23}C_6$. The average interfacial precipitate size typically ranged from 0.5-1.5μm^2 whereas the matrix precipitation was less than 0.5 μm^2.

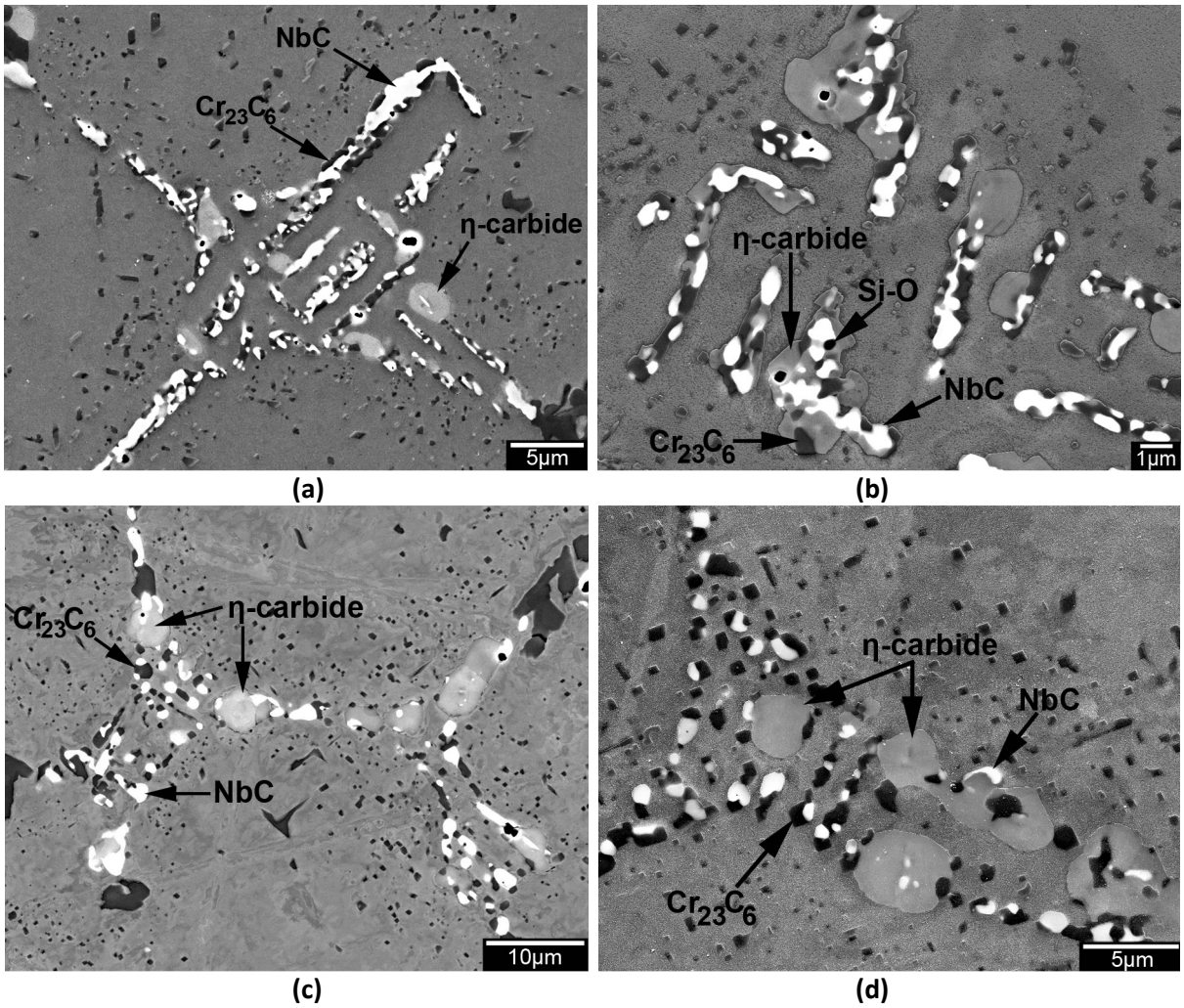

Figure 6.30 – Composite scanning electron micrographs showing the transformation of the Type II lamellae to η-carbides and extensive interfacial $Cr_{23}C_6$ precipitation which occurs between the NbC/austenite interfaces after ageing the HP-Nb2 at 1000°C for (a)-(b) 1000 and (c)-(d) 10,000 hours.

The interfacial $Cr_{23}C_6$ often exhibited a quasi-cuboidal morphology with the $Cr_{23}C_6$/austenite interfaces showing similar faceting to the matrix $Cr_{23}C_6$, whereas the $Cr_{23}C_6$/NbC interfaces followed the original curvature of the as-cast Type II lamellae (Figure 6.31 (a)). The cube-cube ($[100]_{Cr23C6}//[100]_{\gamma}$) OR characteristic of the primary (Section 6.2.1), secondary (Section 6.2.2) $Cr_{23}C_6$ networks was also observed between the interfacial $Cr_{23}C_6$ and adjacent austenite (Figure 6.31 (b)). However, not all precipitate/matrix pairs which obtained the OR exhibited the same pattern alignment shown in Figure 6.31 (b). Slight divergences (<5°) from the ideal $[100]_{Cr23C6}//[100]_{\gamma}$ OR were observed in some cases. This divergence from the ideal OR is possibly due to constraints caused by the NbC/$Cr_{23}C_6$ interface or due to the original orientation of the as-cast Cr_7C_3 influencing the $Cr_{23}C_6$ precipitates orientation with respect to the matrix.

The interfacial $Cr_{23}C_6$ precipitates are believed to be largely attributed to the transformation of the sub-micron Cr_7C_3 precipitates located between the as-cast Type II-NbC/austenite interfaces. Further precipitation of $Cr_{23}C_6$ at the NbC/austenite interface potentially contributes to the increased number of interfacial $Cr_{23}C_6$ observed after ageing. Precipitation of $Cr_{23}C_6$ at the interface of NbC precipitates transforming to G-phase was observed by Ibañez *et al.* [4]. This interfacial $Cr_{23}C_6$ was reportedly induced by the rejection of carbon from the transforming NbC precipitate. However, the transforming NbC precipitates appeared similar to the Type II colonies observed in the HP-Nb2 alloys after ageing. Therefore, while carbon rejection from the transforming NbC precipitate likely contributes to the nucleation and growth of the interfacial $Cr_{23}C_6$, transformation of existing as-cast Cr_7C_3 is considered the predominant cause of this interfacial precipitation. The interfacial $Cr_{23}C_6$ was typically lower in the regions of the Type II colony which contained η-carbides, suggesting the carbon expelled from the transforming NbC lamellae was somewhat contained within the η-carbide.

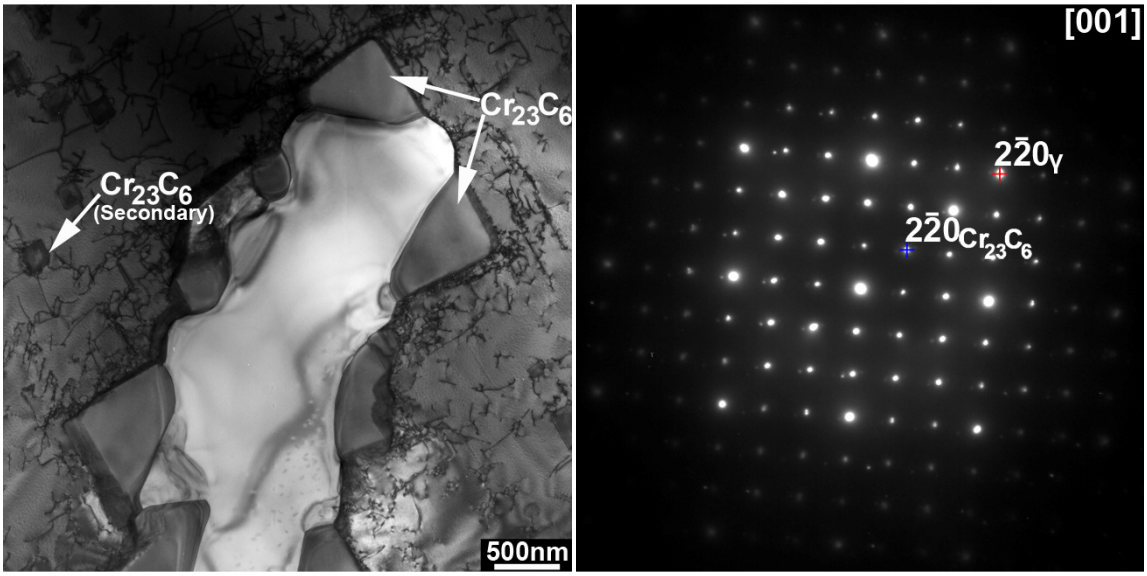

(a) **(b)**

Figure 6.31 – (a) Bright field transmission electron micrograph of the Type II lamellae in the HP-Nb2 alloy after ageing at 1000°C for 1000 hours. Widespread precipitation of $Cr_{23}C_6$ can be observed between the NbC and austenite interfaces. This interfacial precipitation obtains the same $<100>_{Cr23C6}//<100>_{\gamma}$ (demonstrated by the SAD pattern in (b)) OR with the austenite as the primary and secondary matrix $Cr_{23}C_6$ precipitates.

Figure 6.32 (a) and (b) show the Type II lamellae after ageing at 1050°C for 1000 and 10,000 hours respectively. The NbC-to-η-carbide transformation was only observed in the 1050°C-10,000h sample. Similar to the Type I morphology, the η-carbide transformation did not occur evenly across the Type II colony. Generally, for the lamellae undergoing the η-carbide transformation, the NbC was largely consumed after 10,000 hours. The spherical Si-O rich particles associated with the η-carbides in the 1000°C samples were not observed in association with the η-carbides in the 1050°C-10,000 hours sample. The NbC which did not transform to η-carbides underwent coarsening during long-term ageing at 1050°C.

Figure 6.32 (c) and (d) show the Type II lamellae after ageing at 1100°C for 1000 and 10,000 hours. In contrast to ageing at 1000 and 1050°C, the NbC crystal structure remained completely stable regardless of the ageing time. However, the comparatively fewer and larger precipitates shown in Figure 6.32 (d) show the NbC coarsened considerably when ageing for 10,000 hours.

Extensive precipitation of $Cr_{23}C_6$ between the NbC/austenite interfaces was observed for both ageing temperatures after 1000 hours (Figure 6.32 (a) to (d)). As for the Type II lamellae in the 1000°C samples, the interfacial $Cr_{23}C_6$ precipitates were believed to be attributed to the transformation of existing interfacial Cr_7C_3 precipitates that were present between the NbC/austenite interfaces in the as-cast condition and to the nucleation of additional secondary precipitates on the NbC interface. Prolonged ageing at 1050 and 1100°C caused these precipitates to coarsen considerably (Figure 6.32 (b) and (d)).

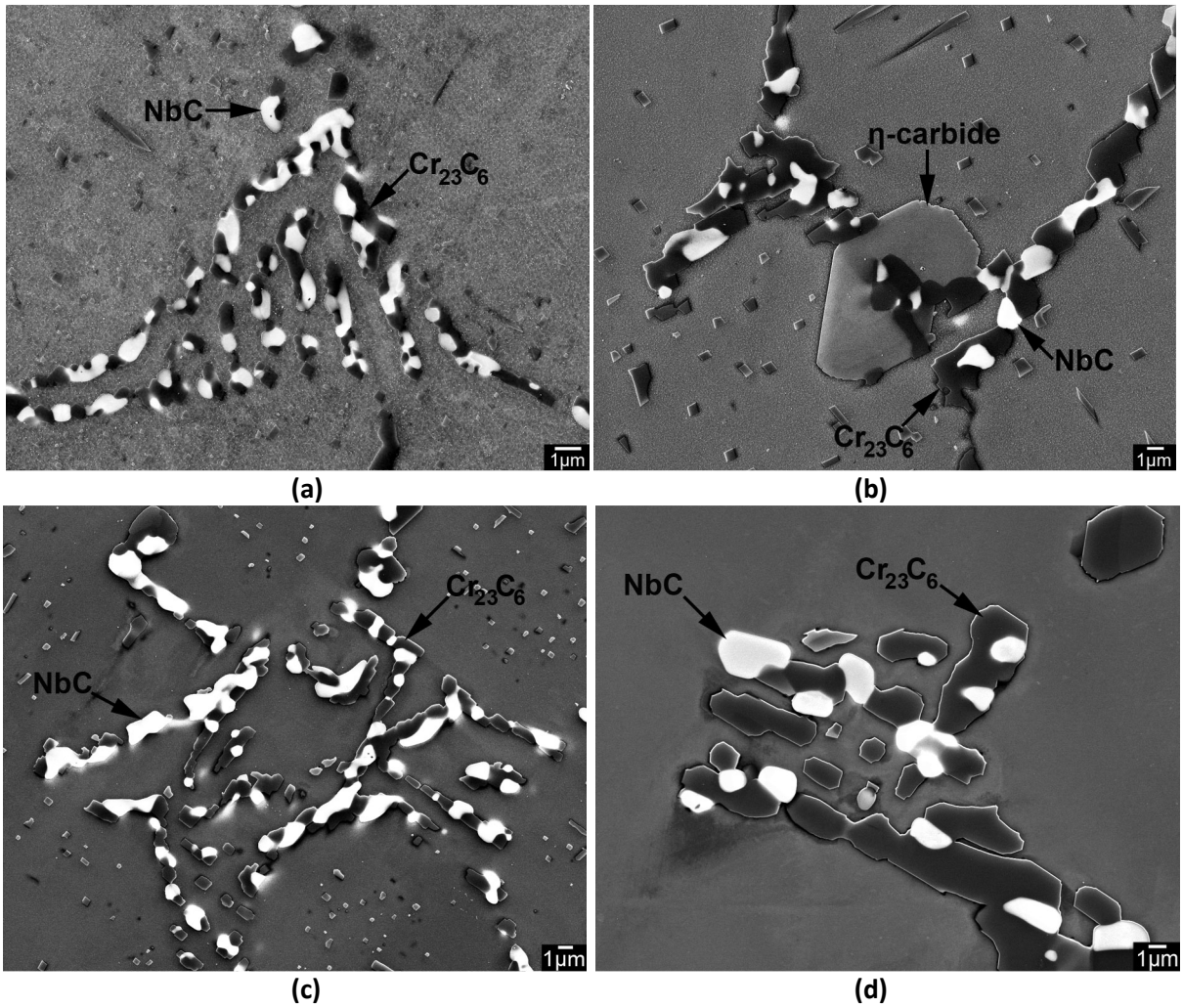

Figure 6.32 - Composite scanning electron micrographs showing the evolution of the Type II lamellae after exposure of the HP-Nb1 to 1050 and 1100°C for (a) & (c) 1000 and (b) & (d) 10,000 hours respectively.

The increased complexity of the Type II lamellae after ageing becomes more apparent when observing the precipitates in three-dimensions. After 1000 hours exposure to 1000°C the Type II lamellae still exhibited an overall plate-like appearance (Figure 6.33 (a) and (b)). The NbC-to-η-phase transformation and interfacial $Cr_{23}C_6$ precipitation observed in two-dimensions caused the complete loss of the lamellae's as-cast porosity. In two-dimensions, ageing of the Type II lamellae appeared to increase the fragmentation of the lamellae. However, the replacement of the NbC with larger η-carbides and the interfacial $Cr_{23}C_6$ has resulted in an overall reduction of the lamellae's fragmentation in three-dimensions. Due to the complexity of the Type II lamellae after ageing, distinguishing between the NbC, η and $Cr_{23}C_6$ precipitates in the deep etched samples was not possible. Therefore, the NbC-to-η-carbide transformation variance was unobservable in the deep etched samples.

Figure 6.33 (c) and (d) show the Type II lamellae after ageing at 1050°C for 1000 hours. Similar to the lamellae in the 1000°C-1000h sample, the overall porous appearance of the as-cast Type II colonies had reduced due to the significantly increased volume fraction of interfacial $Cr_{23}C_6$ which often linked adjacent NbC lamellae (Figure 6.33 (d)). In the absence of the η-carbide transformation, regions of the web-like Type II NbC morphology could still be clearly observed after ageing (labelled in Figure 6.33 (d)). Therefore, the apparent fragmentation of the Type II lamellae in two-dimensions was not necessarily a result of the fragmentation of the lamellae in three-dimensions. Alternatively, the two-dimensional fragmentation of the lamellae may have become more obvious as a result of the significant increase in the size and number of interfacial $Cr_{23}C_6$ precipitates in association with these lamellae after ageing.

Although deep etching provided further insight into the evolution of the Type I and II lamellae during ageing, the cause of the η-carbide transformation variance was not observable. Thus, serial sectioning is considered necessary to determine fully characterise the NbC-to-η-carbide with respect to the Type I and II NbC colonies. Conducting EDS and EBSD mapping of each serial sections would provide significant insight into what compositional and crystallographic factors cause certain NbC lamellae to exhibit greater stability during ageing.

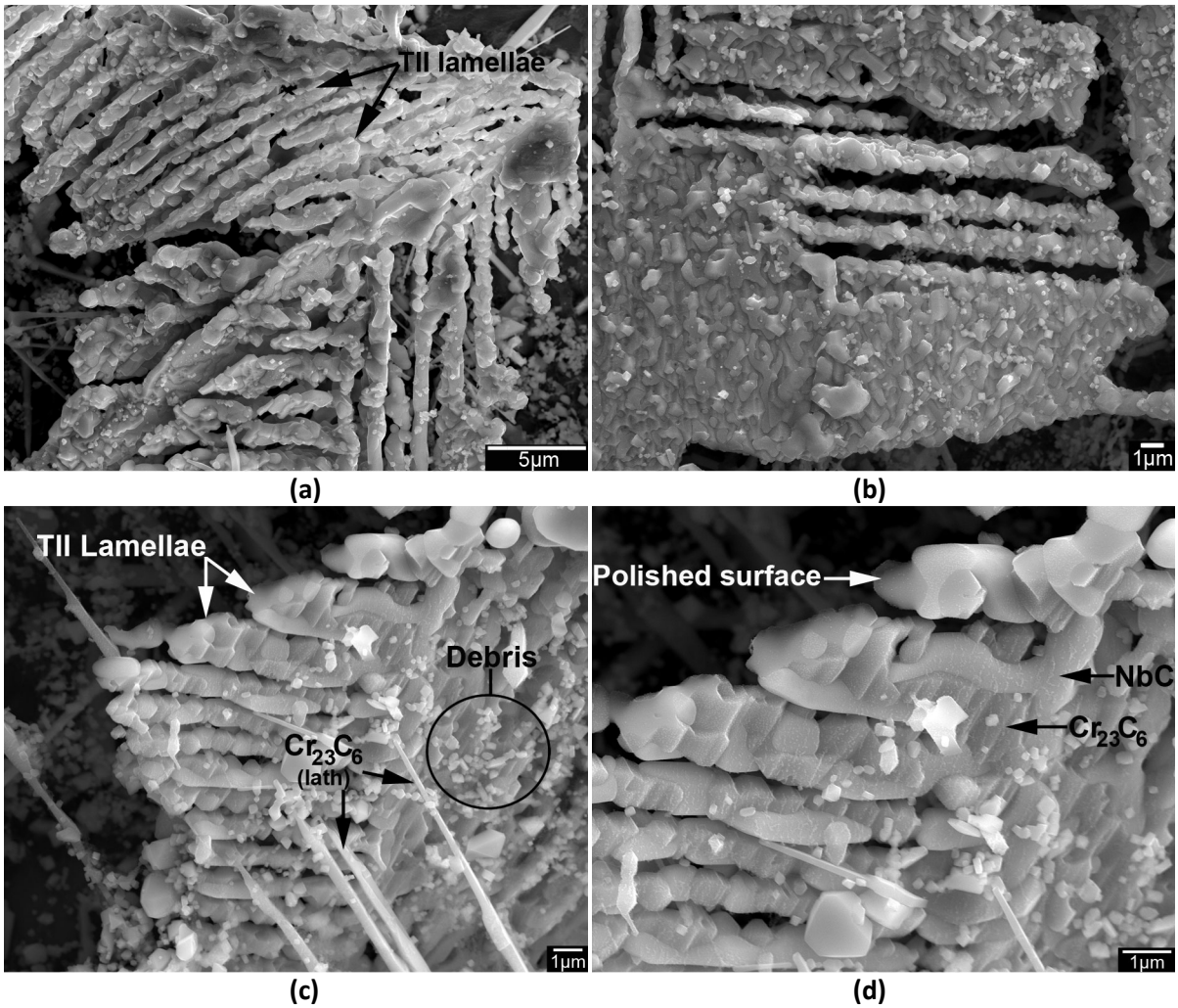

Figure 6.33 – Secondary electron micrographs showing the three-dimensional morphology of the Type II lamellae after ageing for 1000 hours at (a)-(b) 1000°C and (c)-(d) 1050°C

Summary and Conclusions

Two compositionally unique HP-Nb alloys were subjected to unstressed isothermal ageing at 1000, 1050 and 1100°C for up to 10,000 hours (the HP-Nb1 and HP-Nb2 in Chapter 4). Detailed analysis was carried out using a combination of OM, SEM, EDS, EBSD, TEM, SAD, and XRD in order to characterise the microstructural evolution of the HP-Nb1 and HP-Nb2 alloys with respect to ageing temperature and time. Specific attention was paid to the mid-wall position, as this microstructure was representative of the microstructure within the creep samples that were separately subjected to accelerated creep testing by Quest Integrity Group.

A summary of the phases present in each aged condition have already been shown in Table 6.1 and will not be repeated here. However, the microstructural evolution specific to the phases present in the aged HP-Nb1 and HP-Nb2 alloys can be summarised as follows:

Primary Cr-rich precipitates

- Complete transformation of the as-cast Cr_7C_3 to $Cr_{23}C_6$ for all ageing temperatures occurred within the first 1000 hours of exposure to 1000, 1050 and 1100°C.
- After transformation, the primary $Cr_{23}C_6$ coarsened considerably during prolonged ageing with both the average size and area fraction increasing. Generally, the coarsening rate increase with the ageing temperature.
- The considerable coarsening of the primary $Cr_{23}C_6$ network was enabled by the dissolution of the secondary $Cr_{23}C_6$ precipitates.
- The $Cr_{23}C_6$ precipitates were comprised of numerous grains typically with disorientations of less than 10°. However, grains with high angle disorientations (>15°) were also less frequently observed.
- The $Cr_{23}C_6$ typically obtained a $[100]_{Cr23C6}//[100]_{\gamma}$ OR with the austenite matrix. This OR becoming more prevalent during prolonged ageing.

Secondary Cr-rich precipitates

- Regardless of the ageing temperature, extensive secondary precipitation occurred in the austenite matrix within the first six hours of exposure.
- Generally the precipitates were $Cr_{23}C_6$, however, secondary NbC precipitates that were similar in size to the $Cr_{23}C_6$ (<0.5μm^2) were also occasionally observed.
- These precipitates were mainly concentrated within the austenite matrix directly adjacent to the primary precipitate network. The density of the secondary precipitates decreased with increasing distance from the primary precipitates. This preferential formation of the secondary precipitates adjacent to the primary network reportedly occurs due to the high dislocation density in these regions that is induced by the primary precipitates during casting.
- The secondary distribution became increasingly coarser with respect to ageing temperature and time. The dissolution of this network during prolonged ageing supported the coarsening of the primary $Cr_{23}C_6$ network.
- Typically the precipitates obtained a cuboidal morphology, but Widmanstätten $Cr_{23}C_6$ precipitates (which originated from the Type II NbC lamellae) were also observed.
- Identical to the primary $Cr_{23}C_6$ precipitates, the secondary $Cr_{23}C_6$ obtained a $<100>_{Cr23C6}//<100>_{\gamma}$, $\{100\}_{Cr23C6}//\{100\}_{\gamma}$ OR with the matrix.

Primary Nb-rich precipitates

- The NbC-to-η-carbide transformation was observed in all samples aged at 1000°C and in the 1050°C-10,000h sample. This transformation was independent of the as-cast NbC morphology (i.e. both the Type I and Type II NbC lamellae transformed to η-carbides)
- The diamond cubic ($Fd\bar{3}m$) η-carbide crystal structure was confirmed using SAD rather than the more commonly identified G-phase ($Fm\bar{3}m$) crystal structure.
- Spherical Si-O rich particles were found in association with the η-carbides in the 1000°C samples. The crystal structure of these precipitates and their role in the η-carbide transformation is currently unknown.
- Typically, the NbC-to-η-carbide transformation rate was greater for NbC lamellae located on the grain boundaries as opposed to those located on the dendrite boundaries.

- The η-carbides in association with the Type I lamellae were slightly larger than those associated with the Type II lamellae after ageing for 10,000 hours at 1000°C
- Interestingly, a mixed network of the η-carbide and G-phase was identified when ageing at 900°C for 1000 hours. The η-carbide/G-phase transformation preference in the HP-Nb alloy is believed to be largely determined by the ageing temperature.
- While the carbon and nitrogen content in each alloys is expected to influence the η-carbide and G-phase transformations, further testing is necessary to determine the extent to which these elements influence the two transformations.
- The NbC crystal structure remained stable when ageing at 1100°C although significant coarsening of the NbC occurred during prolonged ageing.
- Regardless of the ageing temperature, widespread precipitation of $Cr_{23}C_6$ was observed solely between the Type II lamellae and austenite interfaces after ageing. These precipitates were believed to have predominantly originated from the Cr_7C_3 which are present between the Type II/austenite interfaces in the as-cast condition. Coarsening of the interfacial $Cr_{23}C_6$ occurred at slightly greater rate in comparison to the secondary matrix $Cr_{23}C_6$ precipitates. The interfacial precipitates also obtained the same $[100]_{Cr23C6}//[100]_{\gamma}$ OR as the primary and secondary $Cr_{23}C_6$ precipitates.

Based on the Nb-Ni-Si rich phases identified in the current research and previous studies conducted on laboratory aged and ex-service HP-Nb alloys, the G-phase transformation is expected to proceed preferentially at temperatures below 875°C where as the η-carbide transformation is expected to preferentially occur at temperatures above 920°C. At temperatures between 875-920°C the η-carbide and G-phase transformations occur in parallel, with the volume fraction of each phase being dependent on the ageing temperature and time (i.e. the G-phase volume fraction will be greater at lower temperatures while the η-carbide volume fraction will be greater at higher temperatures). While the alloy composition is expected to play a role in both transformations, it is believed that the composition will mainly alter the temperature range over which these transformations occur rather than complete suppression of either the η-carbide or G-phase transformations in the HP-Nb alloys.

Chapter References

[1] Berghof-Hasselbacher, E., Gawenda, P., Schorr, M. & Schutze, M. (2008). *Atlas of Microstructures.* St. Lous: Materials Technology Institute.

[2] Davis, J. R. (Ed.). (1997). *ASM Specialty Handbook: Heat-Resistant Materials.* Materials Park, Ohio: ASM International, pp. 200-218.

[3] de Almeida Soares, G. D., de Almeida, L. H., da Silveira, T. L. & Le May, I. (1992). *Niobium Additions in HP Heat-Resistant Cast Stainless Steels.* Materials Characterization, 29: pp. 387-396.

[4] Ibañez, R. A. P., Soares, G. D. A., de Almeida, L. H. & Le May, I. (1993). *Effects of Si Content on the Microstructure of Modified-HP Austenitic Steels.* Materials Characterization, 30: pp. 243-249.

[5] Hou, W. T. & Honeycombe, R. W. K. (1985). *Structure of Centrifugally cast austenitic steels: Part 2 Effects of Nb, Ti and Zr.* Materials Science and Technology, 1(5): pp. 390-397.

[6] Porter, D. A., Easterling, K. E. & Sherif, M. Y. (2009). *Phase Transformations in Metals and Alloys.* 3rd ed. Boca Raton, Florida: CRC Press, pp. 42-45.

[7] Wahab, A. A. & Kral, M. V. (2005). *3D analysis of creep voids in hydrogen reformer tubes.* Materials Science & Engineering A, 412: pp. 222-229.

[8] Wahab, A. A., Hutchinson, C. R. & Kral, M. V. (2006). A three-dimensional characterization of creep void formation in hydrogen reformer tube. Scripta Materialia, 55: pp. 69-73.

[9] Lewis, M. H. & Hattersley, B. (1965). PRECIPITATION OF $M_{23}C_6$ IN AUSTENITIC STEELS. Acta Metallurgica, 13: pp. 1159-1168.

[10] Hou, W. T. & Honeycombe, R. W. K. (1985). Structure of Centrifugally cast austenitic steels: Part 1. HK 40 as cast and after creep between 250 and 1000 degree C. Materials Science and Technology, 1(5): pp. 385-389.

[11] Ratke, L. & Voorhees, P. W. (2002). Growth and Coarsening: Ostwald Ripening in Material Processing. Berlin, New York: Springer, p. 118.

[12] Zaghloul, M. B., Shinoda, T. & Tanaka, R. (1977). Relation between Structure and Creep Rupture Strength of Centrifugally Cast HK40 Steel. Transactions of the Iron and Steel Institute of Japan, 17(1): pp. 28-36.

[13] Beckitt, F. R. & Clark, B., R. (1967). *THE SHAPE AND MECHANISM OF FORMATION OF $M_{23}C_6$ CARBIDE IN AUSTENITE.* Acta Metallurgica, 15: pp. 113-129.

[14] de Almeida, L. H., Ribeiro, A. F. & Le May, I. (2003). *Microstructural Characterization of modified 25Cr-35Ni centrifugally cast steel furnace tubes.* Materials Characterization, 49: pp. 219-229.

[15] Barbabela, G. D., de Almeida, L. H., da Silveira, T. L., Le May, I. (1991). *Phase Characterization in Two Centrifugally Cast HK Stainless Steel Tubes.* Materials Characterization, 26: pp. 1-7.

[16] Caballero, F. G., Imizcoz, P., Lopez, V., Alvarez, L. F. & Garcia de Andrés, C. (2007). *Use of titanium and zirconium in centrifugally cast heat resistant steel.* Materials Science and Technology, 23: pp. 528-534.

[17] Mcleod, A., Buchanan, K. G., Kral, M. V. (2011). *(unpublished work).* University of Canterbury – Christchurch.

[18] Nishimoto, K., Saida, K., Inui, M. & Takahashi, M. (2001). Changes in microstructure of HP-modified, heat-resisting cast alloys under long-term aging. Repair weld craking of service exposed, HP-modified, heat-resisting cast alloys (2nd report). Welding International, 15(7): pp. 1-9.

[19] Kenik, E. A., Maziasz, P. J., Swindeman, R. W., Cervenka, J., Le May, I. (2003). Structure and phase stability in a cast modified-HP austenite after long-term ageing. Scripta Materialia, 49: pp. 117-122.

[20] Thomas, C. W., Stevens, K. J. & Ryan, M. J. (1996). Microstructure and properties of alloy HP50-Nb: comparison of as cast and service exposed materials. Materials Science and Technology, 12: pp. 469-475.

[21] Goldstein, J., Newbury, D., Joy, D., Lyman, C., Echlin, P., Sawyer, L. & Michael, J. (2003). *Scanning Electron Microscopy and X-Ray Microanalysis.* 3rd ed. New York: Springer Science + Business Media Inc., p. 69.

[22] Villars, P. (Ed.) & Cenzual, K. (Ed) (2008). *Pearson's Crystal Data: Crystal Structure Database for Inorganic Compounds.* (Version 1.0) [Computer software]. Materials Park, Ohio, U. S. A.: ASM International®.

[22] Spiegel, F. X., Bardos, D. & Beck, P. A. (1963). *Ternary G and E Silicides and Germanides of Transition Elements.* Transactions of the Metallurgical Society of AIME, 227: pp. 575-579.

[23] Gladyshevskii, E. I. & Borusevich, L. K. (1963). *THE Cr-Ni-Si TERNARY SYSTEM.* Russian Journal of Inorganic Chemistry, 8: pp. 997-1000.

[24] Jeitschko, W., Jordan, A. G. & Beck, P. A. (1969). *V and E Phases in Ternary Systems with Transition Metals and Silicon or Germanium.* Transactions of the Metallurgical Society of AIME, 245: pp. 335-339.

[25] Landrum, G. A., Hoffmann, R., Evers, J. & Boysen H. (1998). *The TiNiSi Family of Compounds: Structure and Bonding.* Inorganic Chemistry, 37: pp. 5754-5763.

[26] Gladyshevskii, E. I. & Kuz'ma, Yu, B. (1965). *The compounds Nb_4FeSi, Nb_4CoSi, Nb_4NiSi and their crystal structures.* Journal of Structural Chemistry, 6(1): pp. 60-63.

[27] Markiv, V. Y. (1966). *The crystal structures of the compounds $R(M, X)_2$ and RMX_2 in Zr-Ni-Al, Ti-Fe-Si systems.* Acta Crystallographica A, 21: pp. 84-85.

[28] Vilasi, M., Francois, M., Podor, R. & Steinmetz, J. (1998). *New silicides for new niobium protective coatings.* Journal of Alloy and Compounds, 264(1-2): pp. 244-251.

[29] Gladyshevskii, E. I., Krypyankevych, P. I. & Kuz'ma, Yu, B. (1962). *THE CRYSTAL STRUCTURE OF LOW-SILICON TERNARY COMPOUNDS IN THE Cr - Ni - Si and Cr- Co- Si SYSTEMS.* Journal of Structural Chemistry, 3: pp. 402-410.

[30] Ganglberger E., Nowotny H. & Benesovsky F. (1965). *Ternäre Phasen mit $MgZn_2$-Typ.* Monatshefte für Chemie, 96: pp. 1658-1659.

[31] Tokonami, M. & Horiuchi, H. (1980). *On the Space Group of Spinel, $MgAl_2O_4$.* Acta Crystallographica A, 36(1): pp. 122-126.

[32] Zhang, Y. G., Han, Y. F. & Chaturvedi, M. C. (1995). *TEM Studies of ETA carbide Precipitate Particles in a DS Cast Ni_3Al Base Superalloy.* Materials Characterization, 34: pp. 205-212.

[33] Raghanvan, M., Steeds, J. W. & Petkovic-Lutton, R. (1982). *Convergent Beam Diffraction Analysis of Dispersoids in Oxide Dispersion Strengthened Alloys.* Metallurgical Transactions A, 13: pp. 953-957.

[34] Raghanvan, M., Berkowitz, B. J. & Scanlon, J. C. (1982). *Electron Microscope Analysis of Heterogeneous Precipitates in Hastelloy C-276.* Metallurgical Transactions A, 13: pp. 979-984.

[35] Quanyan, W., Song, H., Swindeman, R. W., Shingledecker, J. P. & Vasudevan, V. K. (2008). *Microstructure of Long-Term Aged IN617 Ni-Base Superalloy.* Metallurgical and Materials Transactions A, 39: 2569-2585.

[36] Muddle, B. C. & Edmonds, D. V. (1985). *PRECIPITATION IN A LIQUID PHASE SINTERED W-Ni-Fe ALLOY.* Acta Metallurgica, 33(12): pp. 2119-2128.

[37] Mostafaei, M., Shamanian, M., Purmohamad, H., Amini, M. & Saatchi, A. (2011). *Microstructural degradation of two cast heat resistant reformer tubes after long term service exposure.* Engineering Failure Analysis, 18: pp. 164-171.

[38] Shi, S. & Lippold, J. C. (2008). *Microstructural evolution during service exposure of two cast, heat-resistant stainless steels – HP-Nb modified and 20-32Nb.* Materials Characterization, 59: pp. 1029-1040.

[39] Alvino, A., Daniela, L., Giacobbe, F., Mazzocchi, V. & Rinaldi, A. (2010). *Damage characterization in two reformer heater tubes after nearly 10 years of service at different operative and maintenance conditions.* Engineering Failure Analysis, 17: pp. 1526-1541.

[40] Quickel, G., Jaske, C., Rollins, B. & Beavers, J. (2009). *Failure Analysis and Remaining Life Assessment of Methanol Reformer Tubes.* Journal of Failure Analysis and Prevention, 9: pp. 511-516.

[41] Thomas, C. W., Tack, A. J. & Briggs, N. (1997). *Stress relaxation properties of alloy HP50Nb and their application to life assessment of reformer furnace tubing.* International Journal of Pressure Vessels and Piping, 70: pp. 59-68.

[42] Williams, T. M. & Titchmarsh, J. M. (1981). *SILICON-RICH PHASES IN AUSTENITIC ALLOYS.* Journal of Nuclear Materials, 98: pp. 223-226.

[43] Ecob, R., C., Lobb, R. C. & Kohler, V. L. (1987). *The formation of G-phase in 20/25 Nb stainless steel AGR fuel cladding alloy and its effect on creep properties.* Journal of Materials Science, 22: 2867-2880.

[44] Powell, D. J., Pilkington, R. & Miller, D. A. (1988). *Precipitation characteristics of 20%Cr/25%Ni-Nb stabilised stainless steel.* Acta Metallurgica, 36(3): pp. 713-724.

[45] Sumerling, R. & Nutting, J. (1965). *Precipitation in 20%Cr-25%Ni steel stabilized with niobium.* Journal of the Iron and Steel Institute, 203: pp. 398-405.

[46] Dewey, R. A. P., Summer, G. & Brammar, I. S. (1965). *Precipitation of carbides in low-carbon austenitic stainless steel containing 20wt-%Cr-25wt-%Ni-0.7wt-%Nb.* Journal of the Iron and Steel Institute, 203: pp. 938-944.

[47] Sourmail, T. (2001). *Precipitation in creep resistant austenitic stainless steels.* Materials Science and Technology, 17: pp. 1-14.

Chapter 7 Mid-Wall Microstructural Evolution of the HP-NbTi Alloys during Unstressed Isothermal Ageing

In parallel with the HP-Nb1 and HP-Nb2 alloys, the HP-NbTi1 alloy was subjected to unstressed isothermal ageing at 1000, 1050 and 1100°C for 500, 1000, 3000, 6000 and 10,000 hours respectively. The following chapter discusses in detail the microstructural analysis carried out on the aged HP-NbTi1 samples. In this chapter, emphasis has once again been placed on the characterisation of the mid-wall microstructure. Emphasis was placed on this region of the tube as it coincided with microstructure that was present within the creep samples that were separately subjected to accelerated creep testing by Quest Integrity Group. Although the commercial sensitivity of the creep properties measured from the aged HP-Nb and HP-NbTi samples prohibits these results being presented in this thesis, it is well known that the creep resistance of the HP-NbTi alloy is superior to the HP-Nb alloy (Chapter 2). Consequently, this chapter compares the aged HP-Nb and HP-NbTi microstructures and discusses the microstructural features which contribute to the HP-NbTi alloy's superior creep resistance.

Since ageing of the HP-NbTi alloy was performed in the same air atmosphere, the significant nitridation, oxidation and decarburization observed in the HP-Nb alloys also occurred at the exposed surfaces of the HP-NbTi alloy. The effects of the air ageing atmosphere on the HP-NbTi1 alloy closely paralleled those observed in the HP-Nb1 and HP-Nb2 alloys. Therefore, the additional phase transformations observed in the HP-NbTi alloy with respect to ageing temperature and time has also been presented in Chapter 8.

7.1 Overview of the HP-NbTi Mid-Wall Microstructural Evolution during Unstressed Isothermal Ageing

In contrast to the microstructural evolution of the HP-Nb alloys, the microstructural evolution of the HP-NbTi alloy during isothermal ageing was considerably less pronounced. The apparent increase in the stability of the HP-NbTi microstructure was mainly due to the addition of titanium which markedly increased the stability of the primary (NbTi)C precipitates. As a result, the mid-wall microstructural evolution in the HP-NbTi1 alloy (note: the NbTi2 alloy was not subjected to long-term ageing) was relatively similar when comparing the samples aged at 1000, 1050 and 1100°C. Sections 7.1.1 - 7.1.3 give an overview of the observed microstructural evolution in the HP-NbTi1 alloy after isothermal ageing for up to 10,000 hours. A summary of the phases observed in each aged sample (labelled in Figure 7.3, Figure 7.5 and Figure 7.7) is also presented in Section 7.1.4.

For comparison with the aged microstructures, optical and scanning electron micrographs of the as-cast microstructure taken from Chapter 5 have been presented again in Figure 7.1 (a) and (b). These micrographs are representative of the as-cast HP-NbTi mid-wall microstructure. As discussed in detail in Chapter 5, the as-cast HP-NbTi microstructure consisted of a interdendritic network of Cr_7C_3 and (NbTi)C primary carbides surrounded by an austenite matrix which was free of precipitation. The addition of titanium caused the lamellar NbC precipitates observed in the as-cast HP-Nb microstructure to adopt a blocky morphology in the HP-NbTi alloy.

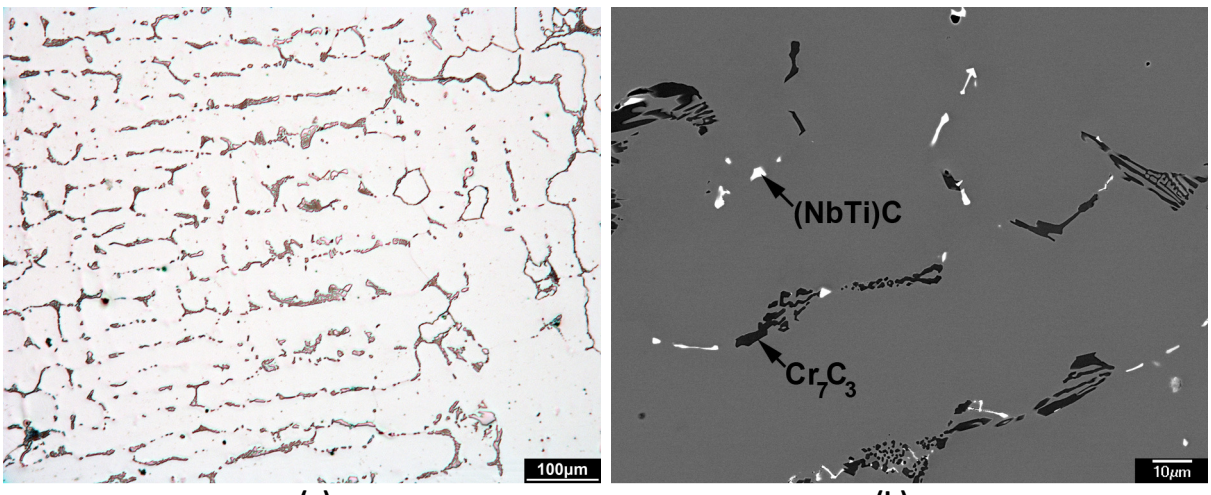

(a) (b)

Figure 7.1 - (a) Optical and (b) backscatter electron micrographs of the HP-NbTi1 alloy in the as-cast condition.

7.1.1 Unstressed Isothermal Ageing of the HP-NbTi1 alloy at 1000°C

Figure 7.2 (a) and (b) show optical micrographs of the HP-NbTi1 alloy after ageing at 1000°C for 1000 and 10,000 hours respectively. Figure 7.2 (a) shows the extensive modification to the as-cast HP-NbTi1 microstructure which occurred after exposure to 1000°C for 1000 hours. The as-cast interdendritic primary carbide network remained largely intact after ageing, but widespread secondary precipitation was observed within the previously precipitate-free austenite matrix. Identical to the HP-Nb alloys, prolonged ageing caused the primary and secondary precipitates in the HP-NbTi1 alloy to coarsen. While coarsening of the secondary precipitates was observable when qualitatively comparing the optical micrographs taken from the 1000 and 10,000 hour aged samples, coarsening of the primary carbide network was less apparent at the given magnifications.

Figure 7.3 (a) to (d) further depict the evolution of the HP-NbTi1 microstructure during ageing at 1000°C. Complete transformation of the primary Cr_7C_3 to $Cr_{23}C_6$ occurred within the first 1000 hours of exposure with the $Cr_{23}C_6$ crystal structure remaining stable during prolonged ageing at 1000°C. The primary $Cr_{23}C_6$ gradually coarsened at the expense of the secondary precipitates with increasing ageing time (discussed in detail in Section 7.4).

Regardless of the ageing time, the (NbTi)C primary precipitates remained stable when ageing at 1000°C with no evidence of the η-carbide or G-phase transformations observed at the mid-wall position. No noticeable change in the precipitates morphology was observable during long-term ageing when viewing the precipitates in two-dimensions (Figure 7.3 (a) to (d)). The aluminium oxide inclusions and surrounding spherical titanium-rich nucleus (which provided the nucleation site for the blocky (NbTi)C precipitates during solidification) were still present after ageing for 10,000 hours (not shown in Figure 7.3 (a) to (d)). The titanium concentration gradient which existed within the region of the as-cast (NbTi)C precipitates directly surrounding the spherical nuclei was also relatively unchanged after 10,000 hours.

Ageing of the HP-NbTi alloy caused an extensive network of $Cr_{23}C_6$ secondary precipitates to rapidly form within the austenite matrix (Figure 7.3 (a)). Identical to the secondary precipitates in the HP-Nb1 and HP-Nb2 alloys, these precipitates were typically concentrated within the matrix lying directly adjacent to the primary carbide network (reportedly due to the high dislocation densities present in these regions in the as-cast condition [1-3]). The density of the secondary precipitates

progressively decreased with increasing distance from the primary carbides. The secondary precipitate distribution observed in Figure 7.3 was predominantly composed of $Cr_{23}C_6$ precipitates which exhibited a cuboidal morphology. Although less common, needle shaped or Widmanstätten $Cr_{23}C_6$ precipitates were also observed in each aged sample. With increased ageing time the secondary $Cr_{23}C_6$ precipitates underwent coarsening and dissolution (Figure 7.3 (d)). The dissolving secondary precipitates contributed to the coarsening of the primary $Cr_{23}C_6$.

Based on comparison of backscatter electron micrographs similar to those presented in Figure 7.2 (a) to (d) and Chapter 6, the secondary NbC precipitates were equally rare in the aged HP-NbTi1 alloy (typically less than 1% of the total secondary precipitate population) as observed in the 1000°C HP-Nb2 aged samples. No evidence of nano-scale niobium rich secondary precipitates (similar to those reported in Nb-Ti modified HK alloys [1]) was found when observing the aged HP-NbTi1 alloy using the FE-SEM. However, as discussed in Section 7.4, numerous nano-sized (NbTi)C precipitates were observed when performing TEM on thin foils taken from the aged HP-NbTi alloy. These precipitates were typical more resistant to coarsening during prolonged aged in comparison to the $Cr_{23}C_6$ precipitates.

Regardless of the ageing time, the MnS inclusions observed in the as-cast condition remained stable when ageing at 1000°C. No significant change in the size of number of inclusions was observable when viewing backscatter electron micrographs similar to those in Figure 7.3 (a) to (d). It must be noted that these inclusions often exhibit similar in appearance to voids created by precipitates falling out during mechanical polishing of the samples. Thus, as accurate identification of these inclusions was often difficult when observing the aged microstructures with backscatter electrons, quantitative measurement of the size and area fraction of MnS was not possible.

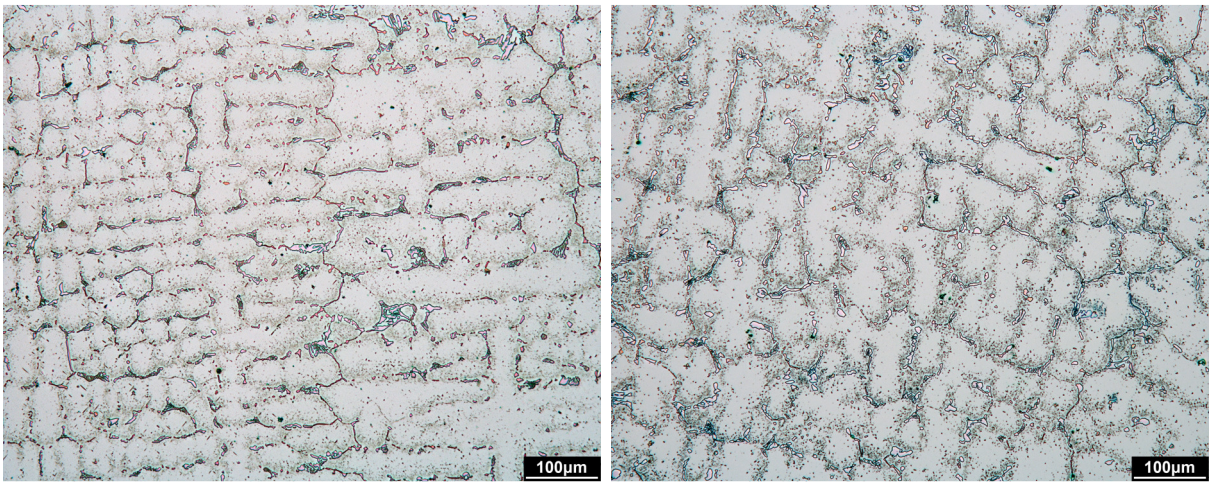

(a) (b)

Figure 7.2 - Low magnification (100x) optical micrographs of the HP-NbTi1 alloy after unstressed isothermal ageing at 1000°C for (a) 1000 and (b) 10,000 hours. (Glyceregia etchant).

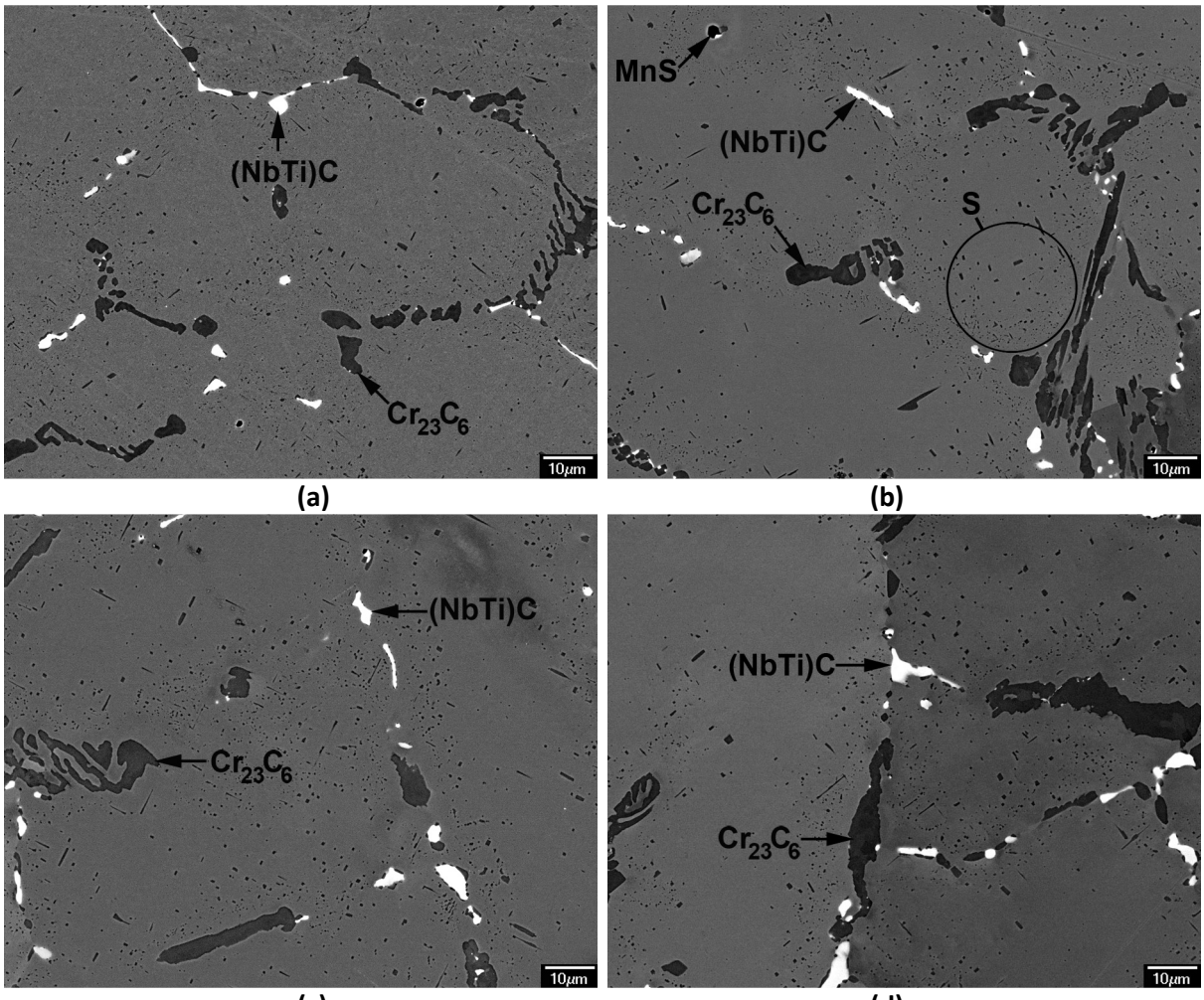

(a) (b)

(c) (d)

Figure 7.3 - Backscatter electron micrographs of the HP-NbTi1 alloy after unstressed isothermal ageing at 1000°C for (a) 1000, (b) 3000, (c) 6000 and (d) 10,000 hours. (As polished).

7.1.2 Unstressed Isothermal Ageing of the HP-NbTi1 alloy at 1050°C

Figure 7.4 (a) and (b) show representative optical micrographs of the HP-NbTi1 alloy after exposure to 1050°C for 1000 and 10,000 hours. The primary network remains after ageing for 1000 and 10,000 hours with widespread secondary precipitation within austenite matrix is also visible in each sample. At the magnification shown in Figure 7.4 (a) and (b) (100x), the confinement of the secondary precipitates to the matrix directly adjacent to the primary carbides is clearly evident. Optical observations of the 1050°-1000 and 10,000h samples indicated the primary and secondary precipitates had undergone significant coarsening during ageing.

Representative backscatter electron micrographs of the HP-NbTi1 alloy after ageing for 500, 1000, 3000 and 10,000 hours are shown in Figure 7.5 (a) to (d). The as-cast primary Cr_7C_3 precipitates completely transformed to $Cr_{23}C_6$ within the first 500 hours of exposure to 1050°C (Figure 7.5 (a)). The $Cr_{23}C_6$ crystal structure remained stable during prolonged ageing (Figure 7.5 (d)). As shown in Figure 7.5 (a) and (d), the primary chromium carbides coarsened significantly during ageing at 1050°C with the average size and area fraction of these precipitates after 10,000 hours being approximately three times greater than observed for the chromium-rich primary precipitates in the as-cast condition.

Identical to the 1000°C samples, the primary (NbTi)C precipitates remained stable in the 500, 1000 and 3000h samples with the as-cast blocky morphology remaining in the aged samples. Coarsening of these precipitates during the first 3000 hours of exposure to 1050°C was unapparent when observing the precipitates at similar magnifications to those shown in Figure 7.5 (a) to (d). Regardless of the ageing time, the spherical aluminium-titanium rich nuclei (present in the as-cast condition) were observed in all HP-NbTi1 samples aged at 1050°C.

Partial transformation of the (NbTi)C to NbCr(CN) (Z-phase) was observed at the mid-wall position in the 1050°C-10,000h sample (labelled in Figure 7.5 (d)). This transformation became increasingly prevalent with distance from the mid-wall position with the Z-phase precipitates being most common at the inner and outer diameter positions. Further analysis of the microstructural evolution at the inner and outer diameter positions determined this transformation was due to the continued absorption of nitrogen from the furnace atmosphere. The subsequent diffusion of nitrogen towards the mid-wall position progressively induced the (NbTi)C-to-Z-phase transformation during ageing (i.e.

the nitrogen concentration gradient with respect to wall position caused the fraction of (NbTi)C which had transformed to Z-phase to decrease with increasing distance from the exposed surfaces). The concentration of nitrogen at the mid-wall position in the 1050°-10,000h sample was sufficient to cause the observed partial transformation of (NbTi)C precipitates. As with the atmosphere induced phase transformations observed in the HP-Nb1 and HP-Nb2 alloys, further detailed analysis and discussion of the (NbTi)C/Z-phase transformation has been presented separately in Chapter 8.

As shown in Figure 7.5 (a), the secondary precipitate distribution was largely composed of cuboidal and Widmanstätten $Cr_{23}C_6$ precipitates. Identical to the HP-NbTi1 samples aged at 1000°C, the cuboidal morphology was strongly dominant in all samples aged at 1050°C. Regardless of the ageing time or wall position, the secondary precipitates were concentrated within the matrix directly adjacent to the primary precipitate network. The increased ageing temperature resulted in the secondary precipitates being comparatively coarser than the network observed in the 1000°C sample after 1000 hours. Ostwald ripening of the secondary precipitates occurred during prolonged ageing with the coarsening rate at 1050°C being greater in comparison to the samples aged at 1000°C. As observed in the HP-NbTi1 1000°C samples, secondary niobium or titanium rich precipitates were rare when observing the samples aged at 1050°C with the JEOL 7000F field-emission scanning electron microscope (representing significantly less than 1% of the total secondary precipitate population). The secondary (NbTi)C precipitates became increasingly rare during prolonged ageing at 1050°C.

Regardless of the ageing time, the MnS inclusions (observed in the as-cast condition) remained relatively constant during ageing at 1050°C.

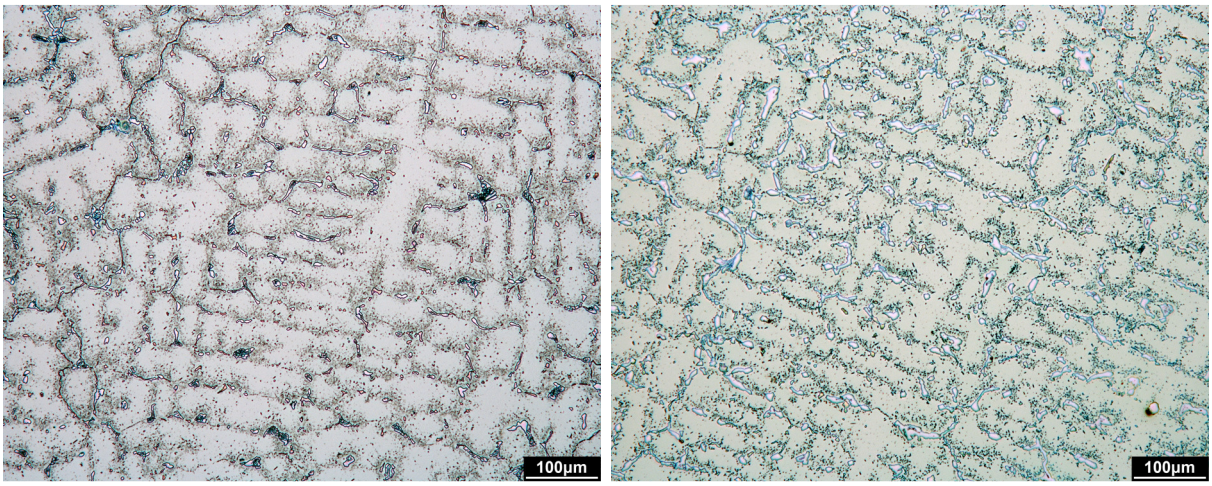

(a) (b)

Figure 7.4 - Low magnification (100x) optical micrographs of the HP-NbTi1 alloy after unstressed isothermal ageing at 1050°C for (a) 1000 and (b) 10,000 hours. (Glyceregia etchant).

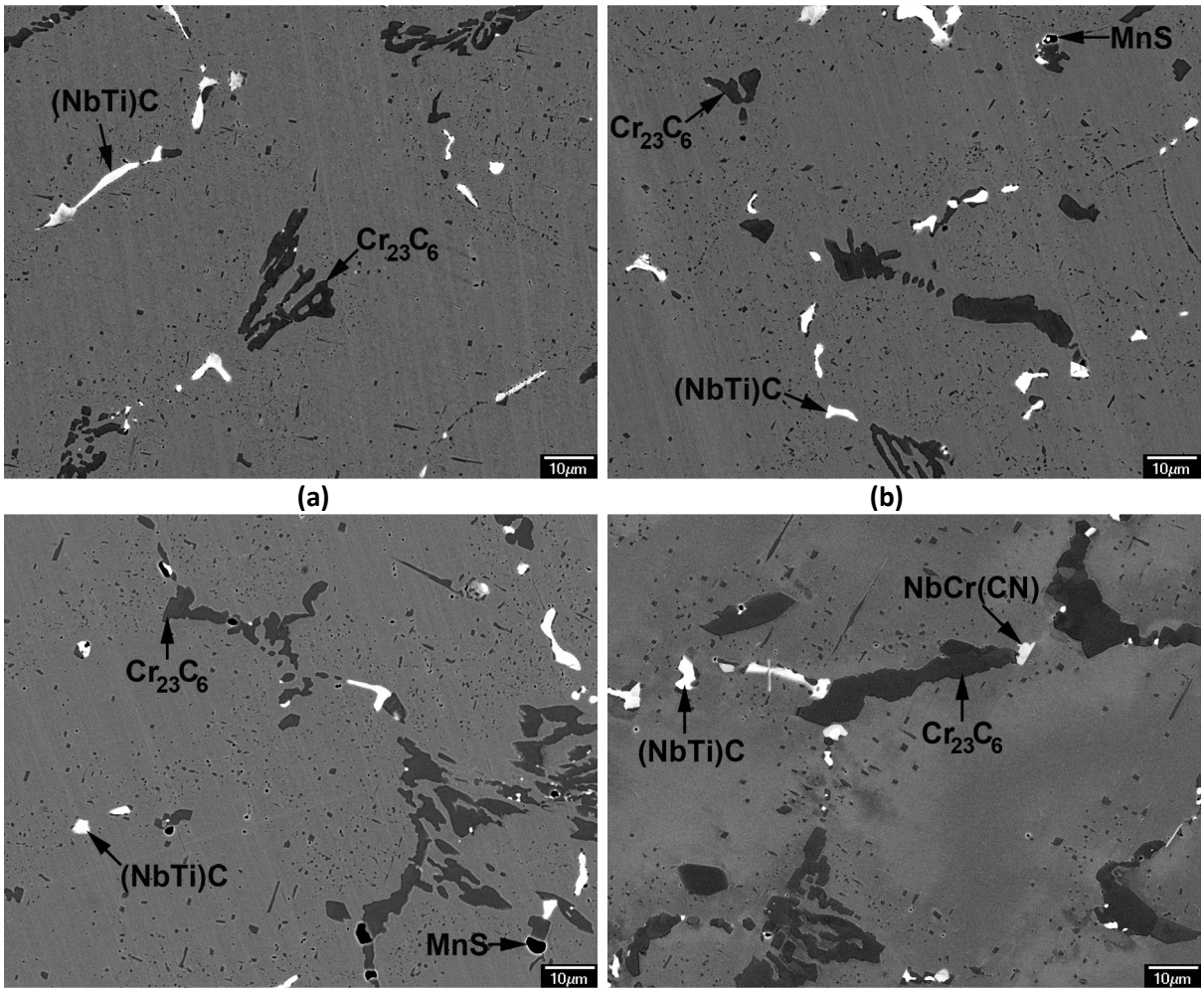

(a) (b)

(c) (d)

Figure 7.5 - Backscatter electron micrographs of the HP-NbTi1 alloy after unstressed isothermal ageing at 1050°C for (a) 500, (b) 1000, (c) 3000 and (d) 10,000 hours. (As polished).

7.1.3 Unstressed Isothermal Ageing of the HP-NbTi1 alloy at 1100°C

Similar to the HP-Nb alloys, ageing at 1100°C for 1000 and 10,000 hours caused the most pronounced microstructural evolution when observing the microstructure optically (Figure 7.6 (a) and (b)). Optical comparison of the as-cast (Figure 7.1 (a)) and 1100°C-10,000h (Figure 7.6 (b)) samples demonstrates the significant coarsening which the primary precipitate network undergoes during long-term ageing at 1100°C. Exposure of the HP-NbTi1 alloy to 1100°C induced the formation of secondary precipitates adjacent to the primary precipitates within the first 1000 hours of exposure (Figure 7.7 (a)). However, Ostwald ripening of the secondary precipitates during prolonged ageing at 1100°C caused the near complete loss of these precipitates after 10,000 hours (Figure 7.7 (b)).

Representative backscatter electron micrographs taken from the mid-wall position of the HP-NbTi1 alloy after ageing at 1100°C for 1000, 3000, 6000 and 10,000 hour are presented in Figure 7.7 (a) to (d). The transformation of the as-cast primary Cr_7C_3 to $Cr_{23}C_6$ was complete within the first 1000 hours of ageing. As shown in Figure 7.7 (a) and (d), the primary $Cr_{23}C_6$ precipitates underwent significant coarsening during prolonged ageing at 1100°C. The coarsening of the primary $Cr_{23}C_6$ when ageing the HP-NbTi1 alloy at 1100°C was considerably greater in comparison ageing at 1000 and 1050°C.

The primary (NbTi)C precipitates remained stable when ageing at 1100°C (regardless of the ageing time). The initial as-cast (NbTi)C blocky morphology also remained relatively stable during ageing (when viewing two dimensional sections of the aged HP-NbTi1 samples). However, the primary (NbTi)C precipitates appeared to coarsen marginally during long-term ageing at 1100°C (3.5μm^2 in the as-cast condition to 4.6 μm^2 after 10,000 hours exposure - Section 7.3). The aluminium-titanium rich nuclei, present in the as-cast condition, were commonly observed in all samples aged at 1100°C. Furthermore, the titanium-rich region of the (NbTi)C precipitates directly surrounding the nuclei also remained similar when comparing the as-cast and 10,000 hour samples.

Similar to the HP-Nb alloys, ageing at 1100°C resulted in the secondary $Cr_{23}C_6$ precipitate network being noticeably sparser after 1000 hours (Figure 7.7 (a)) when comparing to the networks observed in the samples aged at 1000°C (Figure 7.3 (a)) and 1050°C (Figure 7.4 (b)). The secondary precipitates were predominantly composed of cuboidal $Cr_{23}C_6$ precipitates but Widmanstätten shaped plates

were also observed. Niobium or titanium rich precipitates which could be resolved using the FE-SEM were rare and typically represented less than 1% of the total secondary precipitate population.

As shown in Figure 7.7 (d) the secondary precipitates had almost completely disappeared after 10,000 hours. Typically less than 10 $Cr_{23}C_6$ precipitates were present when observing fields of view similar to that in Figure 7.7 (d). The chromium and carbon ejected from the dissolving secondary precipitates (as a result of Ostwald ripening) was believed to have diffused to and subsequently combined with the primary $Cr_{23}C_6$ precipitates (hence driving the continued coarsening of this network during long-term ageing).

The MnS inclusions (observed in the as-cast condition) were also present in all of the 1100°C aged HP-NbTi samples. Qualitative observations of these inclusions using backscatter electron micrographs suggest these precipitates remained relatively constant during ageing at 1100°C.

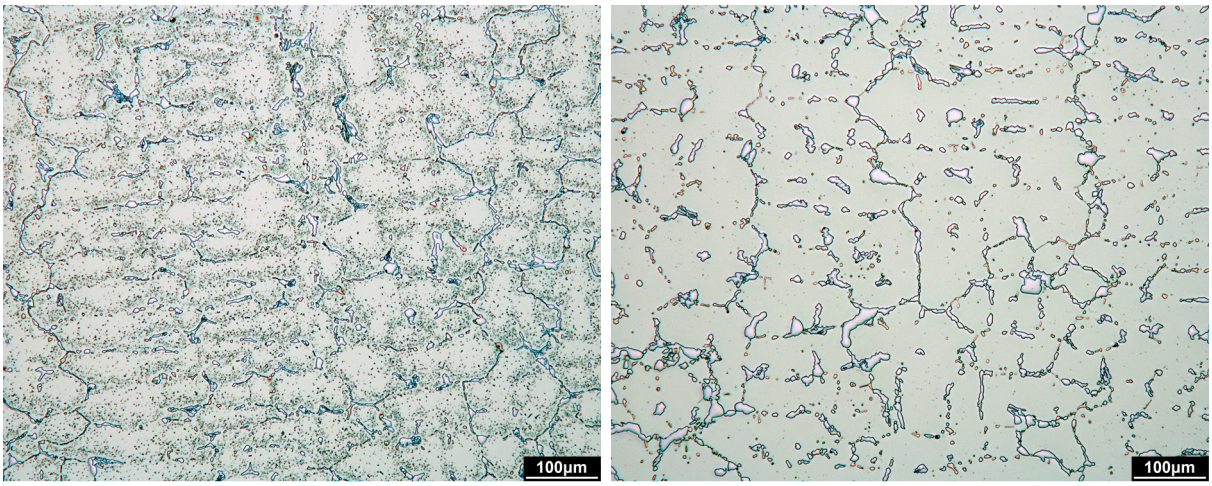

(a) (b)

Figure 7.6 - Low magnification (100x) optical micrographs of the HP-NbTi1 alloy after unstressed isothermal ageing at 1100°C for (a) 1000 and (b) 10,000 hours. (Glyceregia etchant).

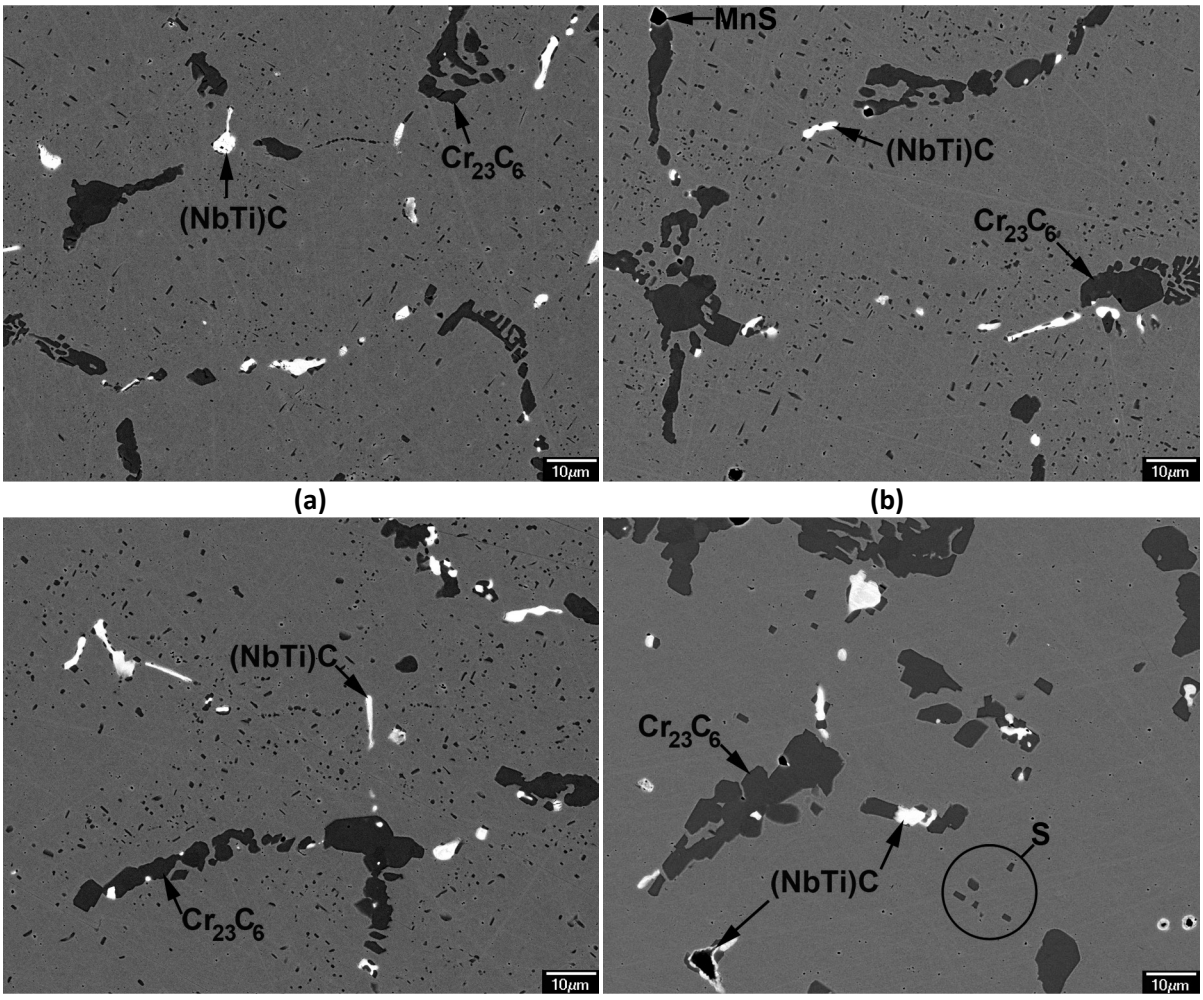

(a) (b)

(c) (d)

Figure 7.7 - Backscatter electron micrographs of the HP-NbTi1 alloy after unstressed isothermal ageing at 1100°C for (a) 1000, (b) 3000, (c) 6000 and (d) 10,000 hours. (As polished).

7.1.4 Summary of the Phases observed in the Aged HP-NbTi1 Samples

Table 7.1 summarizes the primary and secondary phases identified in the HP-NbTi1 aged samples with respect to ageing temperature and time. Identification of the primary precipitates in all aged samples was carried out using a combination of EDS, and EBSD. EDS analysis was performed using JEOL JSM 6100 and 7000F scanning electron microscopes equipped with the Oxford eXL and JEOL JED-2300 EDS detectors respectively. EBSD analysis was performed using the HKL Technology EBSD system (also attached to the JEOL JSM 6100 SEM). The phase database produced in the HKL Technology's Flamenco software for the as-cast material was also used for the aged HP-NbTi1 samples. All SEM observations were conducted using an accelerating voltage of 20keV.

Identification of the secondary precipitates in the 1000°C-1000 and 10,000 hour samples was carried out using a combination of EDS and SAD. All transmission electron microscopy was carried out using a Philips CM200 operated at 200keV and equipped with an Oxford INCA x-sight EDS system. Analysis of the secondary precipitates in the 1050 and 1100°C samples was carried out using the JEOL 7000F scanning electron microscopes and JEOL JED-2300 EDS detector. Based on the backscatter electron contrast and EDS analysis performed on the larger chromium-rich secondary precipitates, it is strongly believed the secondary precipitates in the 1050 and 1100°C samples obtain the $Cr_{23}C_6$ and (NbTi)C crystal structures.

Table 7.1 - Summary of the primary and secondary precipitate phases identified in the aged HP-NbTi1 alloy with respect to ageing temperature and time.

<table>
<tr><th rowspan="2">T (°C)</th><th rowspan="2">Network</th><th colspan="6">Ageing Time (hours)</th></tr>
<tr><th>AC</th><th>500</th><th>1000</th><th>3000</th><th>6000</th><th>10,000</th></tr>
<tr><td rowspan="2">1000</td><td>Primary</td><td>Cr_7C_3, NbC, MnS</td><td colspan="5">$Cr_{23}C_6$, (NbTi)C, MnS</td></tr>
<tr><td>Secondary</td><td>No precipitates</td><td colspan="5">$Cr_{23}C_6$, (NbTi)C</td></tr>
<tr><td rowspan="2">1050</td><td>Primary</td><td>Cr_7C_3, NbC, MnS</td><td colspan="3">$Cr_{23}C_6$, (NbTi)C, MnS</td><td rowspan="2">No samples</td><td>$Cr_{23}C_6$, (NbTi)C, NbCr(CN), MnS</td></tr>
<tr><td>Secondary</td><td>No precipitates</td><td colspan="3">$Cr_{23}C_6$, (NbTi)C</td><td>$Cr_{23}C_6$, (NbTi)C</td></tr>
<tr><td rowspan="2">1100</td><td>Primary</td><td>Cr_7C_3, NbC, MnS</td><td colspan="4">$Cr_{23}C_6$, (NbTi)C, MnS</td><td>$Cr_{23}C_6$, (NbTi)C, MnS</td></tr>
<tr><td>Secondary</td><td>No precipitates</td><td colspan="4">$Cr_{23}C_6$, (NbTi)C</td><td>$Cr_{23}C_6$</td></tr>
</table>

7.2 Evolution of the Chromium-Rich Primary Precipitates during Unstressed Isothermal Ageing

7.2.1 Phase Identification

EDS and EBSD phase identification (Figure 7.8 and Figure 7.9 (a) and (b)) confirmed that exposure of the HP-NbTi1 alloy to 1000, 1050 and 1100°C had caused the as-cast Cr_7C_3 to rapidly transform to $Cr_{23}C_6$. Short-term ageing experiments (6, 12 and 24 hours at 1000°C) determined the Cr_7C_3-to-$Cr_{23}C_6$ transformation was complete within the first six hours of exposure. Interestingly, EDS analysis identified the presence of low concentrations (generally less than 0.7at.%) of tungsten within the $Cr_{23}C_6$ composition. No significant tungsten peak was observed within the $Cr_{23}C_6$ primary precipitates in the HP-Nb alloys. Similar to iron and nickel, tungsten reportedly substitutes for chromium in the $Cr_{23}C_6$ structure [4]. However, the effects of tungsten on the $Cr_{23}C_6$ precipitates during thermal exposure it is relatively unknown in the literature.

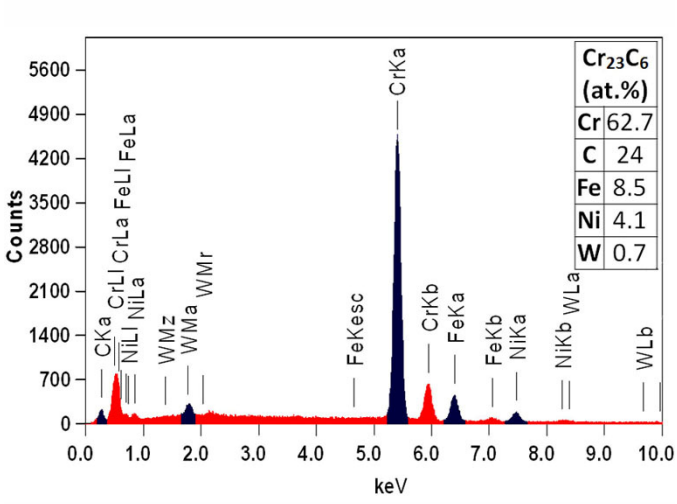

Figure 7.8 – Representative chemical composition taken from the primary $Cr_{23}C_6$ precipitates in the aged HP-NbTi1 alloy (as determined by EDS).

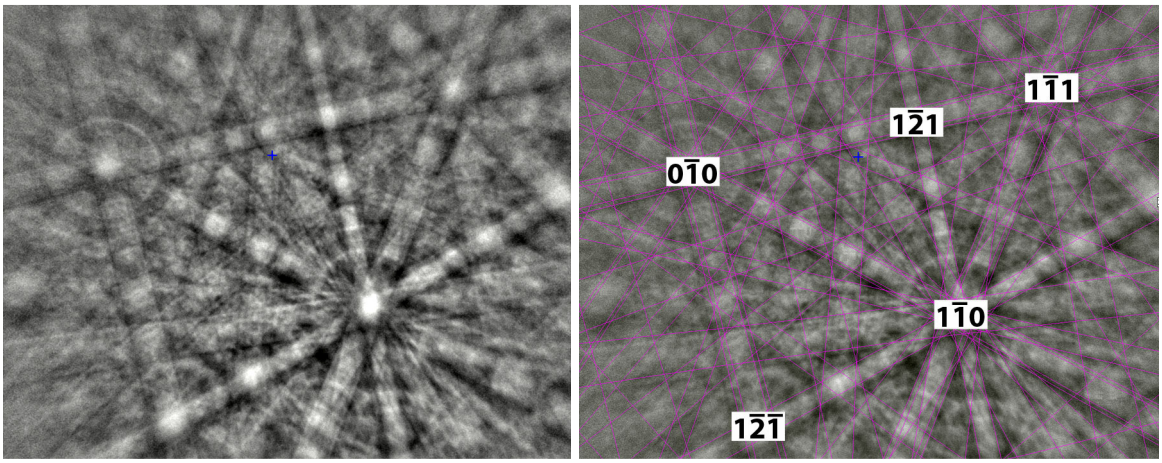

(a) **(B)**

Figure 7.9 – (a) experimentally determined EBSP and (B) Simulated pattern (overlaying the EBSP in (c)) for the primary $Cr_{23}C_6$ precipitates in the HP-NbTi1 alloy.

7.2.2 Coarsening of the $Cr_{23}C_6$ Primary Precipitates during Prolonged Ageing

As discussed in Section 7.1, optical and scanning electron microscope observations of the HP-NbTi alloys indicated the primary $Cr_{23}C_6$ coarsened during long-term ageing. As a result, quantitative image analysis was used to measure the growth of the primary precipitates in the aged HP-NbTi1 alloys with respect to ageing temperature and time (the secondary $Cr_{23}C_6$ precipitates were excluded from this analysis). Image analysis of the aged HP-NbTi alloys was carried out using the same methodology used for the aged HP-Nb alloys (Chapter 6).

Figure 7.10 (a) - (c) show the average size, area fraction and calculated coarsening rate (average size/ageing time) of the $Cr_{23}C_6$ precipitates plotted with respect to ageing temperature and time. Generally the evolution of the $Cr_{23}C_6$ precipitates in the HP-NbTi alloy closely followed that observed in the HP-Nb alloys (Chapter 6). Detail discussion of the primary $Cr_{23}C_6$ coarsening mechanisms for the HP-Nb alloys has already been presented in Chapter 6 and these mechanisms are believed to be identical in the HP-NbTi1 alloy. Therefore, only a summary of the $Cr_{23}C_6$ image analysis results for the HP-NbTi1 aged samples will be presented as follows:

- Irrespective of the ageing temperature, both the average size and area fraction increased with time. In agreement with the coarsening rates calculated for the HP-Nb alloys, the greatest coarsening rate was observed within the first 1000 hours of ageing (Figure 7.10 (c)).

The high coarsening rate observed within the first 1000 hours is believed due to a combination of the higher carbon content contained within the Cr_7C_3 crystal structure in comparison to the $Cr_{23}C_6$ (~33 and 21at.% respectively) structure and the relatively high carbon content dissolved in the as-cast matrix (as evidenced by the extensive secondary intragranular precipitation) which allows the initial rapid growth of the $Cr_{23}C_6$ precipitates.

- The continued increase in the primary $Cr_{23}C_6$ precipitates average size and area fraction during prolonged ageing is believed to be largely driven by Ostwald ripening of the primary and secondary precipitates. The observed Ostwald ripening of the secondary precipitate distribution in parallel to the primary $Cr_{23}C_6$ precipitates suggests both precipitate types must initially compete for the chromium and carbon which is released from the precipitates which are dissolving. However, as the secondary precipitates never become comparable in size to the primary precipitates, secondary precipitates that initially underwent coarsening will begin to dissolve once local composition gradients begin to favour the growth of the primary precipitates. Thus, given enough time at each ageing temperature all secondary precipitates will dissolve to support the continued growth of the primary $Cr_{23}C_6$ precipitates (as illustrated in Figure 7.7 (d)).

- Due to the strong dependence of diffusion on temperature, Ostwald ripening of the primary precipitate $Cr_{23}C_6$ network increased considerably with ageing temperature. For example, the average size and area fraction of $Cr_{23}C_6$ precipitates after ageing at 1100°C for 1000 hours were greater in comparison to the $Cr_{23}C_6$ precipitates present after ageing at 1000°C for 10,000 hours (Figure 7.10 (a)).

- For the first 3000 hours, the greatest increase in the $Cr_{23}C_6$ area fraction occurred when ageing at 1100°C (Figure 7.10 (a)). However, the area fraction in the HP-NbTi samples aged at 1050 and 1100°C converged after ageing for 10,000 hours. This convergence was also observed in the HP-Nb alloy after ageing at 1050 and 1100°C for 10,000 hours. This convergence in both alloys when ageing at 1050 and 1100°C was believed to be attributed to the severe decarburization and oxidation which occurred as a result of the furnace atmosphere during ageing. Decarburization and oxidation is believed to have partially diverted the flow of carbon and chromium (released from the dissolving secondary precipitates) to the samples exposed surfaces (Chapter 8). Thus, less carbon and chromium

was available to contribute to the primary $Cr_{23}C_6$ precipitates growth. The effect of the furnace atmosphere on the secondary precipitates was believed to be greatest when ageing at 1100°C resulting in the convergence of the $Cr_{23}C_6$ precipitate's area fraction in the samples aged at 1050 and 1100°C.

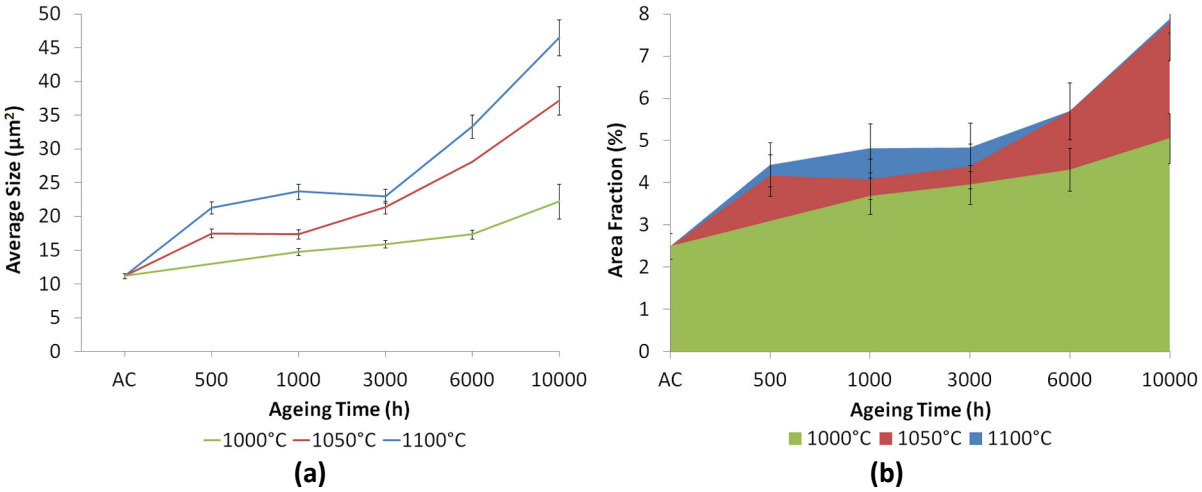

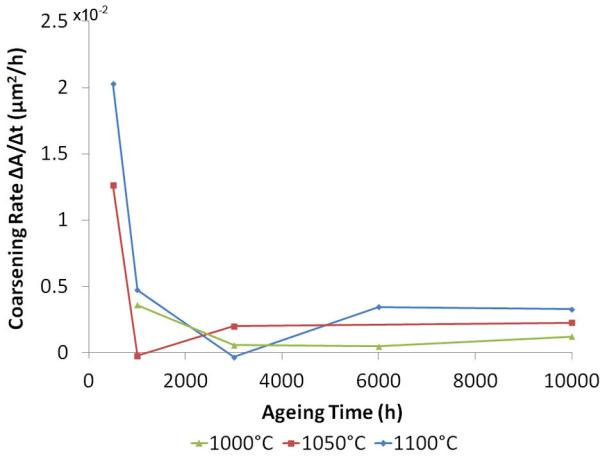

Figure 7.10 - The evolution of the primary $Cr_{23}C_6$ (a) average size, (b) area fraction and (c) coarsening rate (precipitate size/ageing time) with respect to the ageing temperature and time. All properties were measured through quantitative image analysis of micrographs similar to those shown in Figure 7.3, Figure 7.5 and Figure 7.7

7.2.3 Crystallographic Analysis of the Primary $Cr_{23}C_6$ Precipitates

Identical to the $Cr_{23}C_6$ precipitates in the HP-Nb alloy, slight variations in contrast were typically present when observing the primary $Cr_{23}C_6$ precipitates in the HP-NbTi alloy using secondary and backscatter electrons in the SEM (Figure 7.9 (a)). EBSD analysis of the $Cr_{23}C_6$ in the HP-NbTi1 1000°C aged samples confirmed the observed contrast was due to these precipitates containing the same sub-grain structure as described from the $Cr_{23}C_6$ precipitates in the aged HP-Nb alloy (Chapter 6). Generally, these sub-grains obtained disorientations of less than 10° with adjoining grains. However, high angle disorientations (>15°) were also less commonly observed between neighbouring grains.

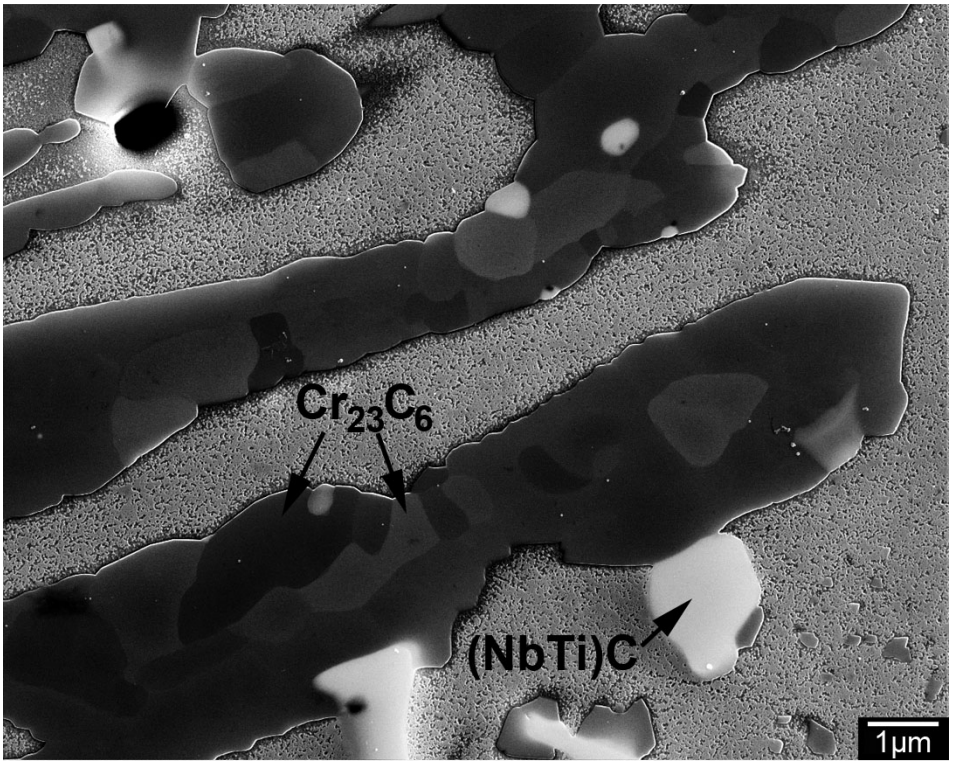

Figure 7.11 – Composite scanning electron micrograph of the primary $Cr_{23}C_6$ after ageing the HP-NbTi at 1000°C for 1000 hours. The contrast variations within each precipitate

The presence of these grains within the primary $Cr_{23}C_6$ precipitates in the HP-NbTi alloy strongly indicated that these precipitate would also obtain the same cube-cube ($<100>_{Cr23C6}//<100>_{\gamma}$, $\{100\}_{Cr23C6}//\{100\}_{\gamma}$) orientation relationship (OR) with the austenite matrix as observed in the HP-Nb alloy. Thus, EBSD was used to investigate the $Cr_{23}C_6$/austenite OR in the aged HP-NbTi1 samples. This analysis was performed using the same methodology implemented for the primary $Cr_{23}C_6$ precipitates in the HP-Nb alloys (Chapter 6). While the $Cr_{23}C_6$/austenite OR was confirmed in all of the aged HP-NbTi samples, emphasis was placed on the analysis of the samples aged at 1000°C. Since the $Cr_{23}C_6$/austenite crystallography was found to be identical in the HP-Nb and HP-NbTi alloys, analysis of the prevalence of the cube-cube OR was only conduced on the HP-NbTi samples which were aged at 1000°C for 1000 and 10,000 hours.

Detailed discussion of the $Cr_{23}C_6$ and austenite OR with respect to ageing time has already been presented in Section 6.2.1 of Chapter 6. Due to the relative indifference between the precipitate-matrix crystallography in the HP-Nb and HP-NbTi alloys it was considered unnecessary to repeat the same detailed discussion in the current chapter. However, the $Cr_{23}C_6$/austenite OR in the HP-NbTi alloy can be summarized as follows:

- Regardless of the ageing temperature and time, the primary $Cr_{23}C_6$ precipitates (located on grain and dendrite boundaries) typically obtained a cube-cube OR with the austenite in the aged HP-NbTi1 samples.

- After ageing the HP-NbTi1 alloy at 1000°C for 1000 hours 57% of the primary $Cr_{23}C_6$ precipitates obtained a cube-cube OR with the matrix.

- Prolonged ageing at 1000°C caused the prevalence of the cube-cube OR to increase to 67% after 10,000 hours. This increase in the prevalence of the cube-cube OR between the $Cr_{23}C_6$ and austenite in the HP-NbTi alloy was almost identical to the increase observed in the HP-Nb alloy during ageing at 1000°C (57- 70%).

7.2.4 Comparison of the Primary Chromium-Rich Precipitates in the HP-Nb and HP-NbTi Alloys during Long-Term Isothermal Ageing

As discussed in Sections 7.2.1 to 7.2.3, the evolution of the primary $Cr_{23}C_6$ precipitates in the HP-Nb and HP-NbTi alloy was similar during long-term isothermal ageing. Figure 7.12 (a) and (b) show histograms which directly compare the average size and area fraction of the chromium-rich precipitates in the as-cast HP-Nb1, HP-Nb2 and HP-NbTi1 alloys and after ageing each alloy at 1000, 1050 and 1100°C for 10,000 hours. As shown in Figure 7.12 (a), the average size of the as-cast Cr_7C_3 in the HP-NbTi1 alloy was greater in comparison to both the HP-Nb1 and HP-Nb2 alloys. Regardless of the ageing temperature, this difference was approximately mirrored when comparing the average size of the $Cr_{23}C_6$ precipitates in the HP-Nb1, HP-Nb2 and HP-NbTi1 alloys after ageing for 10,000 hours.

The influence of the as-cast Cr_7C_3 on the $Cr_{23}C_6$ in the aged samples is also apparent when comparing the area fraction of chromium-rich precipitates in each alloy (Figure 7.12 (b)). For example, the marginally greater Cr_7C_3 area fraction in the HP-NbTi1 alloy in comparison to the HP-Nb2 alloy (ΔA=0.4%) remained relatively unchanged after ageing each alloy at 1000°C for 10,000 hours (ΔA=0.6%). The greater Cr_7C_3 area fraction in the as-cast HP-Nb1 compared to the HP-Nb2 and HP-NbTi1 alloys is also retained by the $Cr_{23}C_6$ after ageing each alloy for 10,000 hours (regardless of the ageing temperature).

The preceding observations show that the difference in the chemical composition of the HP-Nb1, HP-Nb2 and HP-NbTi1 alloys (e.g. titanium and tungsten) had no significant effect on the evolution of the $Cr_{23}C_6$ precipitate network regardless of the ageing conditions experienced by each alloy. Thus, the overall refinement of the chromium-rich primary precipitate network in the aged structures is determined by the properties of the as-cast primary Cr_7C_3 network. As discussed in Chapters 4 and 5, the addition of niobium and titanium to the HP-Nb and HP-NbTi alloy causes the partial substitution of the as-cast Cr_7C_3 network with niobium-rich MC precipitates. The level of substation is directly dependent on the quantity of niobium and titanium additions [2, 5, 6]. Hence, the alloy's chemical composition is known to affect the properties of the as-cast Cr_7C_3 primary precipitate network. However, the as-cast primary precipitate network is has also been shown to be affected by the cooling rate experience by the tube during centrifugal casting [7, 8]. Zaghoul *et at.* [7] reported a 3

percent reduction in the volume fraction of Cr_7C_3 precipitates in as-cast unmodified HK alloys when increasing the cooling rate during casting from 240 to 804°C/minute. Similarly, Wu *et al.* [8] reported a 2.8 percent reduction in the volume fraction of Cr_7C_3 precipitates after centrifugally casting unmodified HK alloys using graphite (lower cooling rate) and cast iron (higher cooling rate) molds. Thus, the effects of differing alloying additions on the properties of the primary Cr_7C_3 precipitates in the HP-Nb and HP-NbTi alloys are possibly insignificant in comparison to the cooling rate during casting.

Unfortunately, due to the differing casting conditions experienced by the HP-Nb1, HP-Nb2 and HP-NbTi1 alloys during casting (as suggested by each tubes differing grain distributions – Chapters 4 and 5), it not possible to determine if the differing alloying contents significantly alter the refinement of the as-cast primary precipitate network. However, it is believed that any modification to the properties of the primary Cr_7C_3 precipitates as a result of the differing alloying additions in the HP-Nb and HP-NbTi alloys will likely be insignificant in comparison to the effect of the casting conditions.

Previous work by Wahab and Kral [9, 10] on an ex-service HP-NbTi alloy reformer tube determined that creep void nucleation and growth preferentially occurs on low registry $Cr_{23}C_6$/austenite interfaces. Thus, alloys that contain a greater proportion of $Cr_{23}C_6$ precipitates which obtain a cube-cube OR with the matrix would be expected to exhibit superior creep properties. However, as discussed in Section 7.2.3, the alloys' chemical composition had no apparent effect on the crystallographic relationship between the primary $Cr_{23}C_6$ precipitates and austenite matrix after ageing the HP-Nb and HP-NbTi alloys. For both alloys, the primary $Cr_{23}C_6$ precipitates were agglomerates of sub-grains which generally obtained a cube-cube OR with matrix regardless of the ageing conditions. For both alloys, 57 percent of $Cr_{23}C_6$ precipitates obtained a cube-cube OR with the matrix after ageing at 1000°C for 1000 hours. Similar increases in the prevalence of this OR were observed for each alloy during prolonged ageing (70% HP-Nb2, 67% HP-NbTi1). Although the percentage of precipitates which obtained the cube-cube OR in the HP-NbTi1 alloy was slightly lower in comparison to the HP-Nb alloy after ageing for 10,000 hours, this difference was believed be due to random statistical sampling error rather than an actual difference in the prevalence of the cube-cube OR in each alloy.

Based on the preceding evidence, the chromium-rich primary precipitates are not believed to contribute to the HP-NbTi alloy's superior creep resistance in comparison to the HP-Nb alloy.

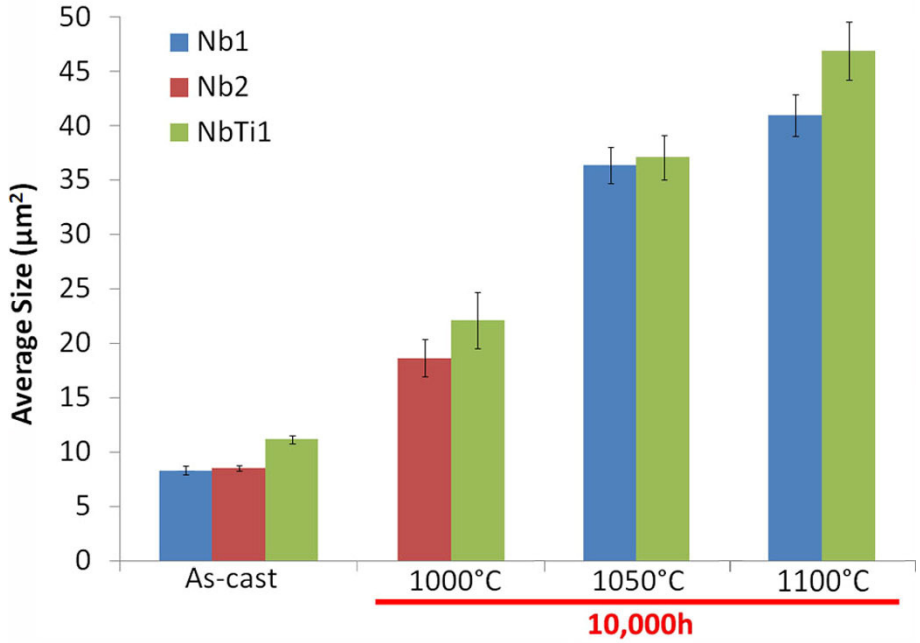

(a)

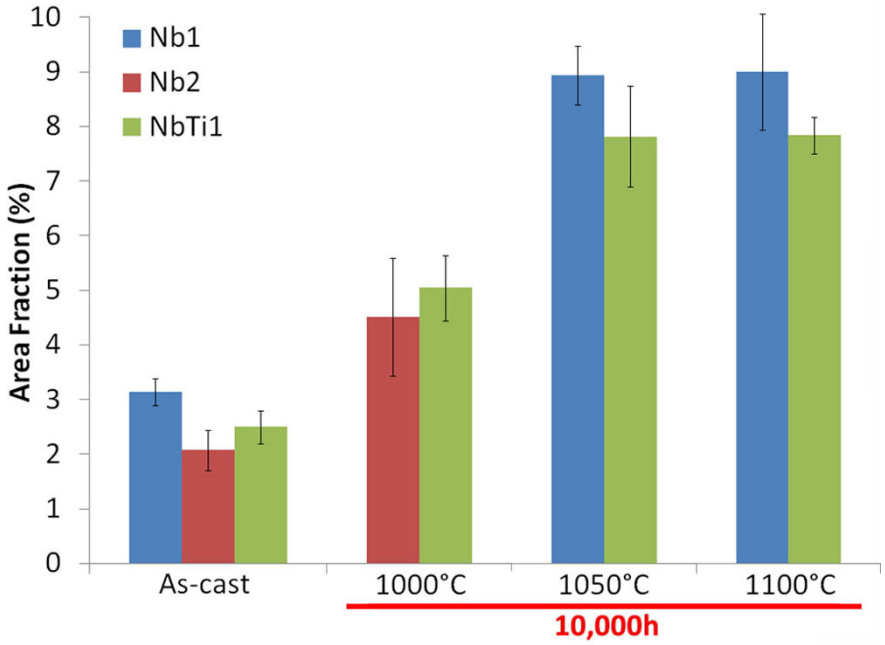

(b)

Figure 7.12 - Histograms comparing the (a) average size and (b) area fraction of the chromium-rich 'primary' precipitates in the HP-Nb and HP-NbTi alloys in the as-cast condition (Cr_7C_3) and after ageing at 1000, 1050 and 1100°C for 10,000 hours ($Cr_{23}C_6$).

7.3 Evolution of the Niobium-Rich Primary Precipitates during Unstressed Isothermal Ageing

7.3.1 Phase Identification

Figure 7.13 and Figure 7.14 (a) and (b) give representative examples of the EDS spectra and EBSD patterns taken from the primary niobium-rich precipitates in the aged HP-NbTi samples. Typically, the primary niobium-rich precipitates in the HP-NbTi alloys retained the FCC ($Fm\bar{3}m$) (NbTi)C crystal structure after ageing at 1000, 1050 and 1100°C. No evidence of the η-carbide or G-phase transformations (as observed in the HP-Nb alloys) was found at the mid-wall position of the HP-NbTi1 tube. However, transformation of the primary (NbTi)C to Z-phase was observed at the mid-wall position after ageing at 1050°C for 10,000 hours. This transformation was believed to have only occurred due to the absorption of nitrogen from the furnace atmosphere during ageing. Thus, detailed discussion of the (NbTi)C-to-Z-phase transformation will be presented separately in Chapter 8.

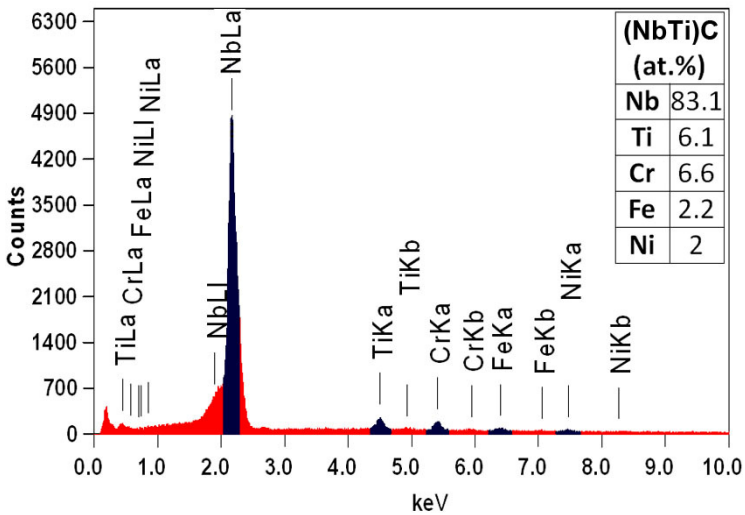

Figure 7.13 – EDS spectrum representative of the (NbTi)C precipitates in the aged HP-NbTi samples.

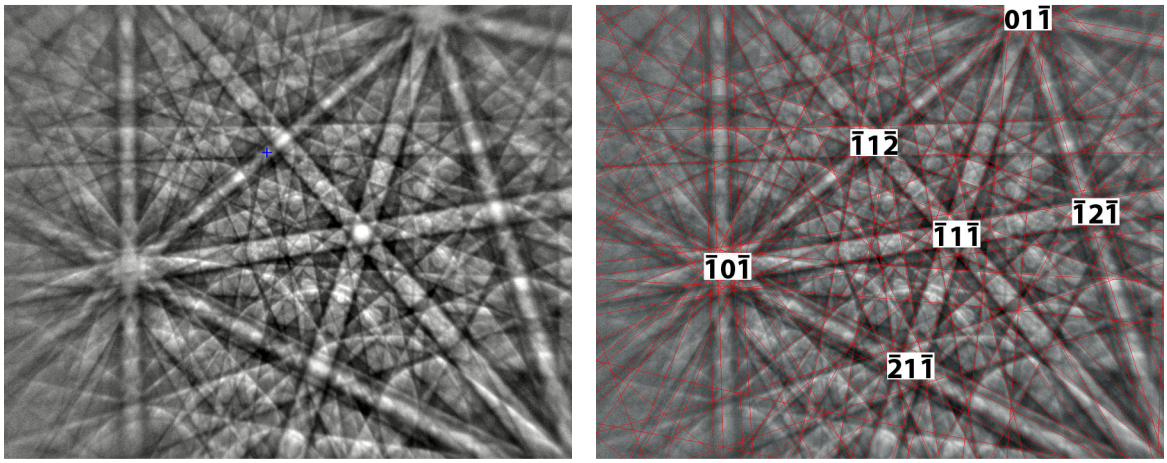

(a) (a)

Figure 7.14 – Representative (a) experimentally determined EBSP and (b) simulated EBSP pattern (shown overlaying (a)) taken from the primary (NbTi)C precipitates in the aged HP-NbTi samples.

7.3.2 The Effects of Titanium on the MC Precipitates

Figure 7.15 (a) to (c) show higher magnification scanning electron micrographs of the (NbTi)C precipitates in the HP-NbTi1 alloy after ageing at 1000°C for 1000 and 10,000 hours. The blocky (Type III) as-cast morphology remained relatively unchanged regardless of the ageing temperature and time. While the nodular (Type IV) morphology was observed in the aged HP-NbTi1 samples, the low occurrence of these precipitates in the as-cast structure (less than 1% of the (NbTi)C population) caused these precipitates to be relatively insignificant in the aged microstructures. Therefore, emphasis was placed on the characterisation of the blocky (NbTi)C precipitates with respect to ageing temperature and time.

In general, the primary (NbTi)C precipitates in the HP-NbTi alloy were considerably more stable during ageing in comparison to the NbC precipitates in the HP-Nb alloy. As discussed in Chapter 6, the NbC-to-η-carbide transformation was observed in the HP-Nb alloys when ageing at 1000°C. This transformation resulted in approximately 50% of the as-cast NbC network (by area fraction) undergoing transformation to η-carbide after ageing at 1000°C for 10,000 hours. In contrast to the NbC in the HP-Nb alloys, the (NbTi)C precipitates remained stable after ageing of the HP-NbTi1 alloy at 1000°C for 10,000 hours (Figure 7.3 (d)). Therefore, the addition of titanium to the MC composition clearly increased the stability of these precipitates with respect to the η-carbide transformation when ageing at 1000°C.

The increased stability of the (NbTi)C precipitates with respect to the NbC-to-G-phase transformation has also been reported when ageing HP-NbTi alloys at 900-1000°C for 1000 hours [3, 11]. Comparison between the G-phase transformation rates in HP-Nb and HP-NbTi alloys aged at 900°C for 1000 hours [3] determined that the transformation of the NbC precipitates (HP-Nb) occurred at a greater rate in comparison to the (NbTi)C precipitates (HP-NbTi). During the (NbTi)C-to-G-phase transformation, de Almeida *et al.* identified TiC particles in the centre of transforming G-phase precipitates using the TEM indicating that titanium was insoluble in G-phase. Thus, rejection of the titanium from the transforming (NbTi)C precipitate is believed to be necessary in order for the G-phase transformation to progress.

Although the (NbTi)C-to-η-carbide transformation was not observed at the mid-wall position of the aged HP-NbTi samples, the furnace atmosphere caused the (NbTi)C-to-η-carbide transformation to proceed at the tube's inner and outer diameter positions when ageing the HP-NbTi alloy at 1000 and 1050°C. EDS analysis of the η-carbide precipitates observed at the inner and outer diameter positions determined these precipitate do not contain any significant concentration of titanium. Consequently, during transformation the titanium possibly acts to stabilize the (NbTi)C precipitates against the η-carbide transformation in the same manner as observed for the G-phase transformation.

Image analysis of the primary (NbTi)C determined that these precipitates underwent coarsening during ageing of the HP-NbTi. However, the growth of these precipitate was relatively insignificant in comparison to the primary $Cr_{23}C_6$ precipitates. For example, ageing the HP-NbTi1 alloy at 1000°C for 10,000 hours caused the $Cr_{23}C_6$ precipitates average size and area fraction to increase by 98 and 104% respectively (Figure 7.12 (a) and (b)), whereas the average size of the (NbTi)C precipitates remained relatively constant while the area fraction increased by 9%. Ageing at 1100°C caused the greatest increase in the average size and area fraction of (NbTi)C precipitates (31% and 18% increases respectively). Though, this growth appears relatively insignificant when compared to the 140% and 232% increases in the $Cr_{23}C_6$ precipitates average size and area fraction during ageing at 1100°C.

The relatively low coarsening rate exhibited by the primary (NbTi)C precipitates in the HP-NbTi alloy is believed attributed to the low availability of niobium and titanium in the austenite matrix. As discussed in Section 7.4.2, nano-sized niobium-titanium rich secondary precipitates formed in the matrix within the first 1000 hours of exposure to 1000, 1050 and 1100°C. Thus, the niobium and titanium dissolved within the as-cast austenite was likely consumed by the nucleation and growth of

these precipitates. Ostwald ripening of the niobium-titanium rich secondary precipitates was relatively insignificant during ageing at 1000°C (increasing from 20-50nm to 50-100nm in diameter). However, the secondary precipitates completely dissolved during prolonged ageing at 1100°C. Thus, the significantly greater growth of the primary precipitates when ageing at 1100°C suggests these precipitates largely rely on the supply of titanium and niobium from dissolving secondary precipitates. In contrast to niobium and titanium, chromium is highly abundant in the austenite matrix (typically between 20-25wt.%). Thus, coarsening of the primary $Cr_{23}C_6$ is likely to be limited by the rate at which carbon is released from the secondary precipitate distribution.

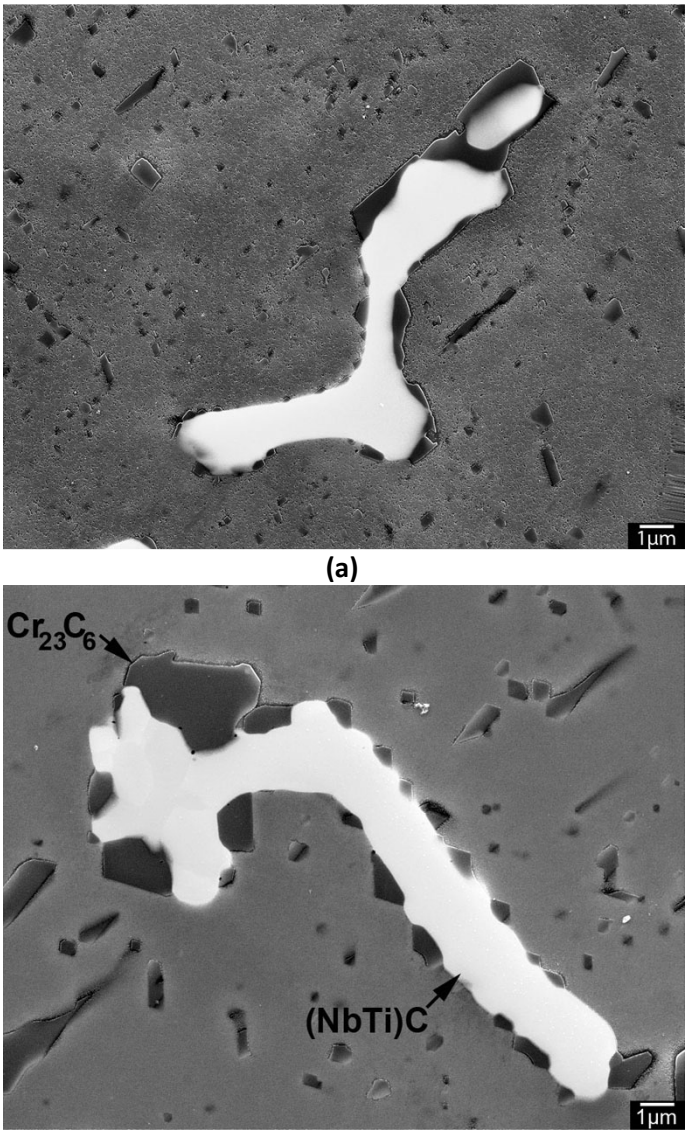

Figure 7.15 – Composite scanning electron micrographs showing the (NbTi)C precipitates and $Cr_{23}C_6$ located between the (NbTi)C and austenite interfaces after ageing at 1000°C for (a) 1000 and (b) 10,000 hours.

Figure 7.16 (a) and (b) show scanning electron micrographs of the titanium-rich nuclei and surrounding (NbTi)C precipitates (present in the as-cast condition) after ageing at 1000 and 1100°C for 1000 hours respectively. Regardless of the ageing temperature and time the titanium-rich nuclei remained stable. However, the edges of the initially spherical titanium-rich nuclei often appeared increasingly irregular with ageing temperature and time (Figure 7.16 (b)).

As discussed in Chapter 5, the region of the (NbTi)C precipitate directly surrounding the titanium-rich nuclei was typically enriched in titanium. The concentration of titanium in the (NbTi) precipitates decreased rapidly with increasing distance from the nucleus. The darkened contrast within the (NbTi)C precipitate in Figure 7.16 (a) shows the localised enrichment of titanium in the region directly surrounding the nucleus after ageing at 1000°C for 1000 hours. The localised enrichment within the (NbTi)C directly surrounding the nuclei was observed in all of the aged HP-NbTi1 samples.

The titanium enrichment within the region of the as-cast (NbTi)C precipitate directly surrounding the nucleus was expected to reduce during long-term ageing of the HP-NbTi1 alloy with the titanium diffusing to the branches of each precipitate where titanium concentration was lower in the as-cast condition (typically between 3-5at.%). However, regardless of the ageing temperature, (NbTi)C precipitates exhibiting a similar contrast to the precipitate shown in Figure 7.16 (a) were commonly observed after ageing at for 10,000 hours. EDS analysis of the (NbTi)C precipitate surrounding the nuclei determined the titanium enrichment of these regions often remained similar after ageing. Moreover, the titanium concentration within the (NbTi)C branches typically remained between 3-5at.% after ageing.

The preceding observations suggested the as-cast compositional gradient within the (NbTi)C precipitates did not significantly reduce during long-term ageing. Andrén *et al.* reported limited diffusion of metal atoms through MX carbides or carbo-nitrides during sintering of WC-Co, WC-MC-Co, TiC-TiN-Mo2C-Ni/Co and (Ti, W, Ta)(C, N)-(Co,Ni) cemented carbides and cermets during sintering at temperatures between 1300-1500°C [12]. The diffusion of carbon and nitrogen has also been reported to be relatively low through the MX crystal structure in 347 stainless steel during exposure to temperatures between 1000 and 1100°C [13]. Thus, the consistent observation of significant titanium concentration gradients within the (NbTi)C precipitates after ageing the HP-NbTi1 alloys for 10,000 hours suggests the diffusion of metallic elements through the (NbTi)C (i.e. MX) crystal structure during ageing at 1000, 1050 1100°C was similarly low.

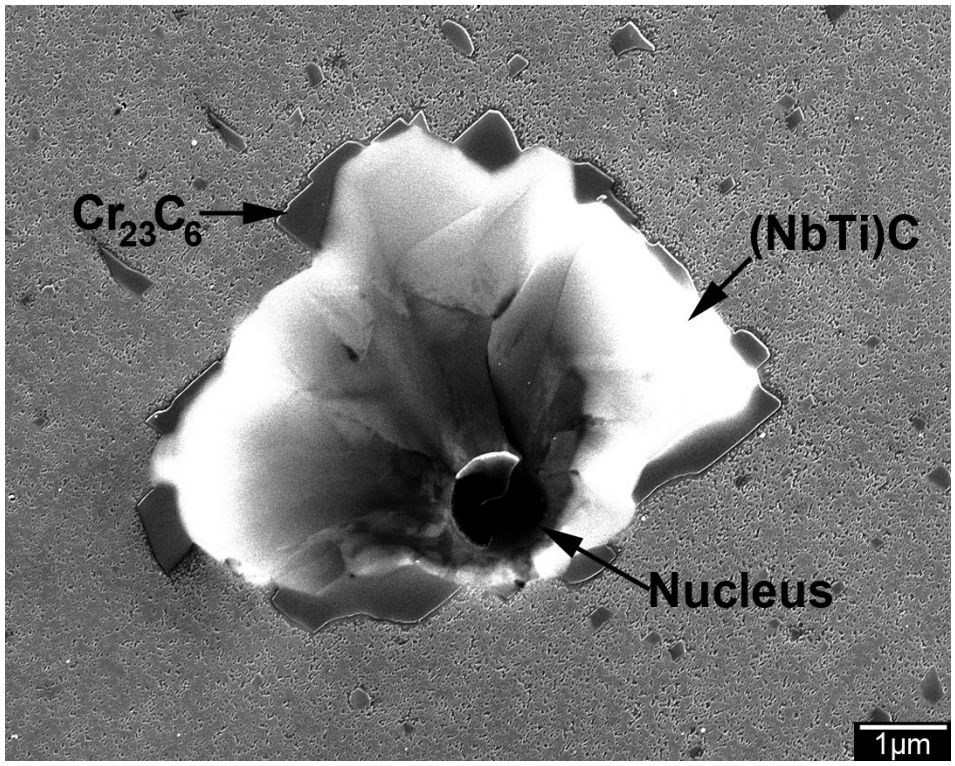

(a)

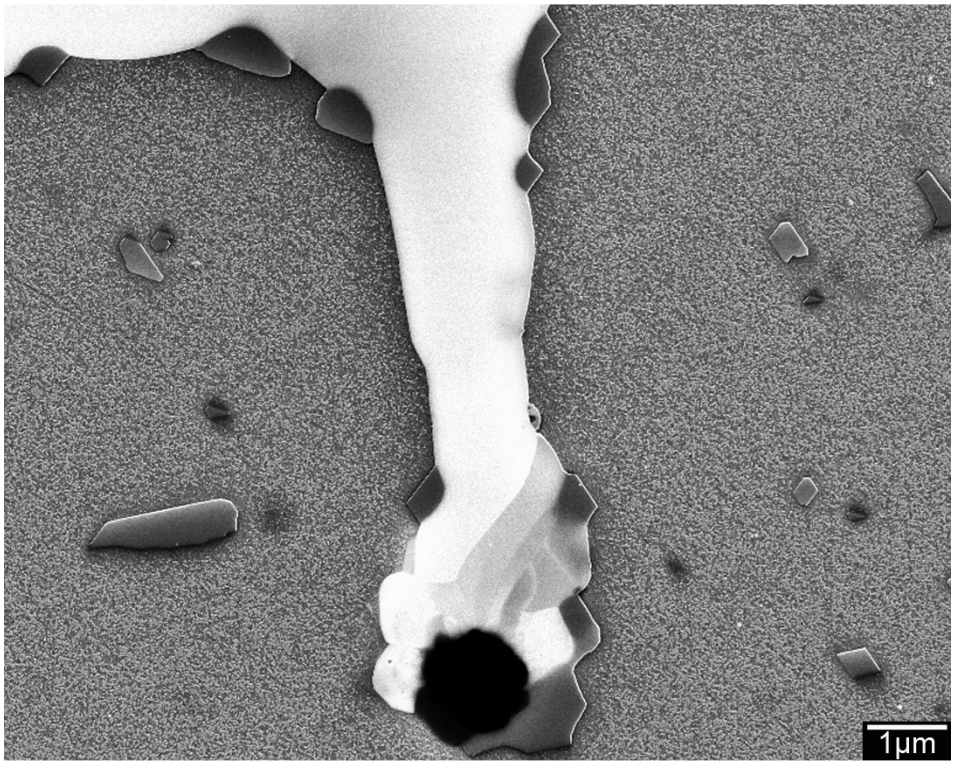

(b)

Figure 7.16 – Composite scanning electron micrographs showing the titanium-rich nucleus (which contains the aluminium oxide inclusion) and surrounding (NbTi)C primary precipitate in the (a) 1000°C-1000h and (b) 1100°C-1000h samples.

7.3.3 Interfacial $Cr_{23}C_6$ Precipitates

Similar to the Type II NbC lamellae in the HP-Nb alloys, numerous $Cr_{23}C_6$ precipitates were observed between the (NbTi)C and austenite interfaces after ageing the HP-NbTi1 alloy at 1000, 1050 and 1100°C. Figure 7.17 shows the interfacial $Cr_{23}C_6$ precipitates observed after ageing the HP-NbTi alloy at 1000°C for 1000 hours. Regardless of the ageing temperature, the interfacial $Cr_{23}C_6$ precipitates were typically similar in size to the secondary $Cr_{23}C_6$ (0.5-1μm^2) in the austenite matrix after 1000 hours of ageing. Although, larger precipitates (1-5μm^2) were also observed between the (NbTi)C and austenite interfaces, these larger precipitates were less common. After ageing it was relatively unusual to observe (NbTi)C precipitates with interfaces completely free of $Cr_{23}C_6$ precipitates (typically less than 15% of the (NbTi)C population).

As discussed in Chapter 5, the as-cast (NbTi)C interface was typically highly populated with Cr_7C_3 precipitates. During ageing, these precipitates transform to $Cr_{23}C_6$ resulting in the interfacial precipitates shown in Figure 7.17. However, the (NbTi)C/austenite interface potentially also acts as an energetically favourable nucleation site for secondary precipitation of $Cr_{23}C_6$. Thus, additional secondary precipitation of secondary $Cr_{23}C_6$ on this interface cannot be ruled out. Overall, the population of chromium-rich precipitates located between the (NbTi)C and austenite interface increased after ageing suggesting these precipitates form through a combination of the Cr_7C_3-to-$Cr_{23}C_6$ transformation and secondary precipitation of $Cr_{23}C_6$ on previously unoccupied regions of the as-cast (NbTi)C interface.

The characteristics of the interfacial $Cr_{23}C_6$ precipitates during long-term ageing closely paralleled those observed for the secondary $Cr_{23}C_6$ precipitate network. As shown in Figure 7.15 (a) and (b), the interfacial $Cr_{23}C_6$ precipitates were noticeably coarser after 10,000 hours. The rate at which the interfacial precipitates coarsened increased with the ageing temperature. In general, the interfacial precipitates appeared to be larger than the matrix precipitates after ageing at 1000, 1050 and 1100°C for 10,000 hours. Interestingly, the greatest size and area fraction of interfacial precipitates (based on qualitative comparisons of the 10,000 hour samples) was observed after ageing at 1100°C for 10,000 hours where the secondary $Cr_{23}C_6$ network had almost completely dissolved. Generally, the gradual dissolution of the secondary matrix $Cr_{23}C_6$ precipitates during prolonged ageing resulted in an overall reduction in the area fraction of the secondary precipitates. While the number of interfacial

precipitates reduced with increasing ageing time, coarsening of the remaining precipitates caused an apparent increase in the area fraction of interfacial $Cr_{23}C_6$ precipitates with increasing ageing time. Thus, the interfacial $Cr_{23}C_6$ precipitates typically exhibited greater stability during ageing in comparison to the secondary $Cr_{23}C_6$ precipitates.

The $Cr_{23}C_6$ precipitates often shared faceted interfaces with the austenite when viewed in two-dimensions. These faceted interfaces typically aligned with facets exhibited by the cuboidal $Cr_{23}C_6$ precipitates which were located in the directly adjacent austenite. Alignment of the cuboidal $Cr_{23}C_6$ facets with the $\{110\}_{Cr23C6}$ and $\{111\}_{Cr23C6}$ planes has been well documented in the literature for austenitic steels [14, 15]. Therefore, the similar alignment of the faceting on the interfacial and secondary $Cr_{23}C_6$ precipitates suggests the interfacial $Cr_{23}C_6$/austenite interfaces obtain identical habit planes. However, TEM trace analysis is necessary to confirm the habit plane of the $Cr_{23}C_6$/austenite interfaces. In contrast to the faceted $Cr_{23}C_6$/austenite interface, the $Cr_{23}C_6$/(NbTi)C interface followed the curvature of the (NbTi)C precipitate.

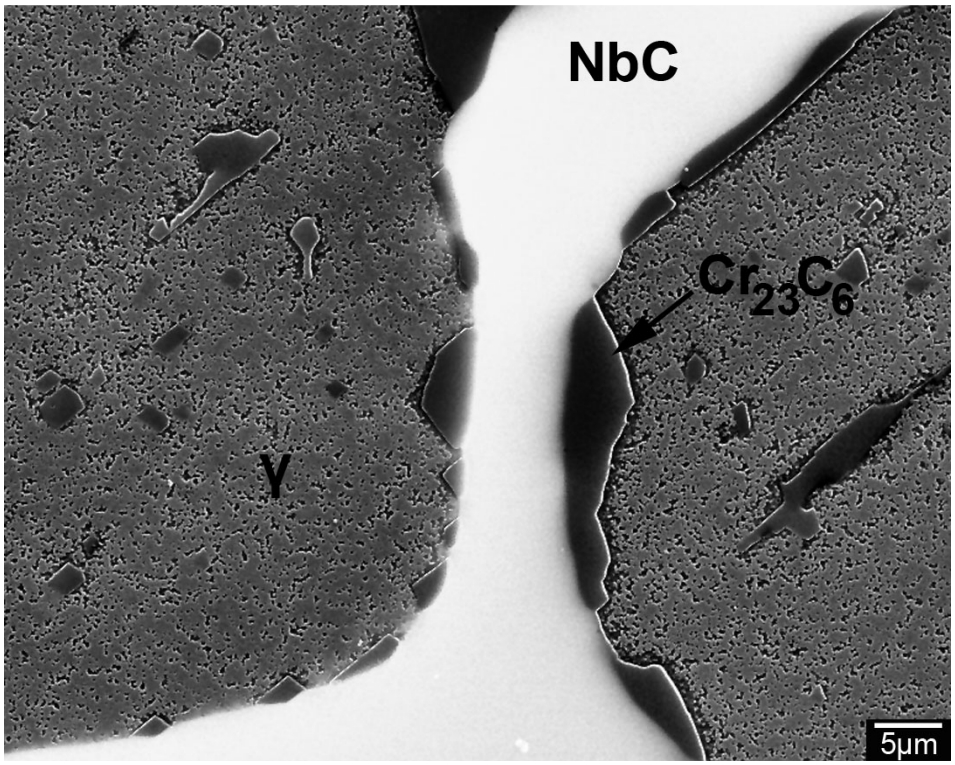

Figure 7.17 – Composite scanning electron micrograph showing the interfacial $Cr_{23}C_6$ precipitates located between the (NbTi)C and austenite interfaces

Figure 7.18 (a) shows a bright field transmission electron micrograph of the interfacial $Cr_{23}C_6$ precipitates after ageing at 1000°C for 1000 hours. Confirmation of the $Cr_{23}C_6$ ($Fm\bar{3}m$) crystal structure was carried out using EDS and SAD (Figure 7.18 (b)). The interfacial precipitates' experimentally determined chemical composition and lattice parameters were typically indistinguishable from the secondary $Cr_{23}C_6$ precipitates located within the austenite matrix (Section 7.4.1). Identical to the primary and secondary $Cr_{23}C_6$ precipitates, the interfacial precipitates also obtained a cube-cube orientation relationship (OR) with the matrix (Figure 7.18 (b)). The SAD pattern shown in Figure 7.18 (b) is centred with the beam direction closely parallel to the $[100]_\gamma$ zone axis. The slight asymmetry of the $Cr_{23}C_6$ reflections within the SAD pattern suggested the interfacial $Cr_{23}C_6$ precipitates were slightly misoriented with respected to the matrix. Typically, the measured misorientation was less than 3 degrees. Similar misorientation was not observed between the intragranular $Cr_{23}C_6$ precipitates and austenite matrix (i.e. the intragranular $Cr_{23}C_6$ OR was exactly cube-cube). However, similar divergence from the ideal cube-cube OR was exhibited by the interfacial $Cr_{23}C_6$ precipitates located between the Type II NbC lamellae and austenite interfaces in the aged HP-Nb alloys (Chapter 6). This misorientation was believed to be possibly induced by crystallographic constraints caused by the NbC/$Cr_{23}C_6$ interface.

Although the interfacial precipitates observed in the HP-NbTi1 1050 and 1100°C aged samples were not subjected to TEM analysis, EDS and EBSD analysis of the larger secondary precipitates after 10,000 hours exposure indicated that the chromium-rich secondary precipitates within these samples obtained the $Cr_{23}C_6$ crystal structure and OR with the austenite matrix.

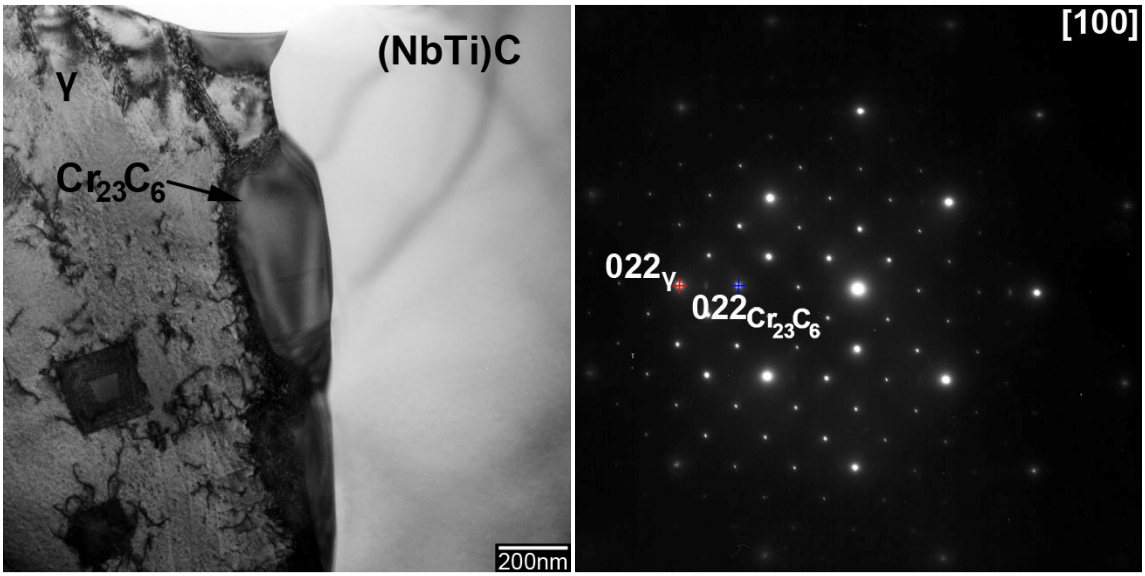

(a) **(b)**

Figure 7.18 - (a) Bright field TEM micrograph of the interfacial $Cr_{23}C_6$ precipitates located between the (NbTi)C/austenite interfaces in the 1000°C-1000h sample. (b) Representative [100] SAD pattern taken with the selected area aperture overlapping the interfacial-$Cr_{23}C_6$ and directly adjacent austenite in (a). The divergence from $[100]_{Cr23C6}//[100]_{\gamma}$ OR is shown by the non-symmetrical intensities of the $Cr_{23}C_6$ reflections in comparison to the austenite reflections.

The extent of $Cr_{23}C_6$ precipitation between the (NbTi)C and austenite interfaces becomes more obvious when viewing the (NbTi)C interface in three-dimensions. The (NbTi)C precipitates shown in Figure 7.19 (a) and (b) give representative examples of (NbTi)C precipitates where the interface was relatively highly populated with $Cr_{23}C_6$. (NbTi)C precipitates with interfaces relatively free of $Cr_{23}C_6$ were also observed but appeared to be significantly less common.

Ageing of the HP-NbTI1 alloy at 1000°C caused the dendritic appearance of the interfacial Cr_7C_3 observed in the as-cast HP-NbTi alloys (Chapter 5) to be completely lost within 1000 hours of exposure. The as-cast morphology was replaced with larger tetrahedral and wedge shaped $Cr_{23}C_6$ precipitates (Figure 7.19 (b)). When located on similarly oriented (NbTi)C interfaces, the exposed facets of the tetrahedral and wedge shaped $Cr_{23}C_6$ precipitates (i.e. the interfaces shared with the austenite) often shared similar alignment. This alignment in three-dimensions further suggests these faceted interfaces adhere to a consistent habit plane or set of habit planes.

The coarsening of the interfacial precipitates during long-term ageing (as observed in two-dimensions in Figure 7.15 (c)) is clearly apparent when viewing the interfacial precipitates in three-dimensions after ageing of the HP-NbTi1 alloy at 1000°C for 10,000 hours. After 10,000 hours of

exposure the tetrahedral and wedged shaped morphologies remained. The high degree of faceting of the exposed $Cr_{23}C_6$ interfaces and alignment of these interfaces is evident in Figure 7.19 (a) and (b). While the size of the interfacial precipitates had increased after markedly 10,000 hours, the number of precipitates had significantly reduced. Therefore, it was not possible to determine if the percentage of the (NbTi)C interfacial covered by $Cr_{23}C_6$ precipitates had increased or decreased based on qualitative comparison of the deep etched 1000 and 10,000 hour aged samples. Regions of the (NbTi)C interface without interfacial precipitation appeared smooth and featureless when observed using the JEOL 7000F field emission scanning electron microscope.

The high population of $Cr_{23}C_6$ precipitates located between the (NbTi)C and austenite interfaces would likely have implications on the (NbTi)C-to-η-carbide and (NbTi)C-to-G-phase transformations. Both transformations rely on the diffusion of elements such as silicon, nickel and titanium across the (NbTi)C/austenite interface. As shown in Figure 7.15 and Figure 7.19, the considerable coverage of the (NbTi)C interface with $Cr_{23}C_6$ precipitates reduces the (NbTi)C/austenite interfacial area available for the transfer of these elements. The low concentrations of Si and Ti typically observed in the $Cr_{23}C_6$ suggest the diffusion of these elements through the interfacial precipitates is negligible. Hence, since it is unlikely that these elements rapidly diffuse through the $Cr_{23}C_6$ crystal structure, these relatively stable precipitates will act as a barrier to diffusion reducing the total flow of Ti, Si, and Ni to the transforming (NbTi)C precipitate. Thus, the presence of these interfacial precipitates would potentially restrict the (NbTi)C-to-η-carbide and (NbTi)C-to-G-phase transformations during ageing.

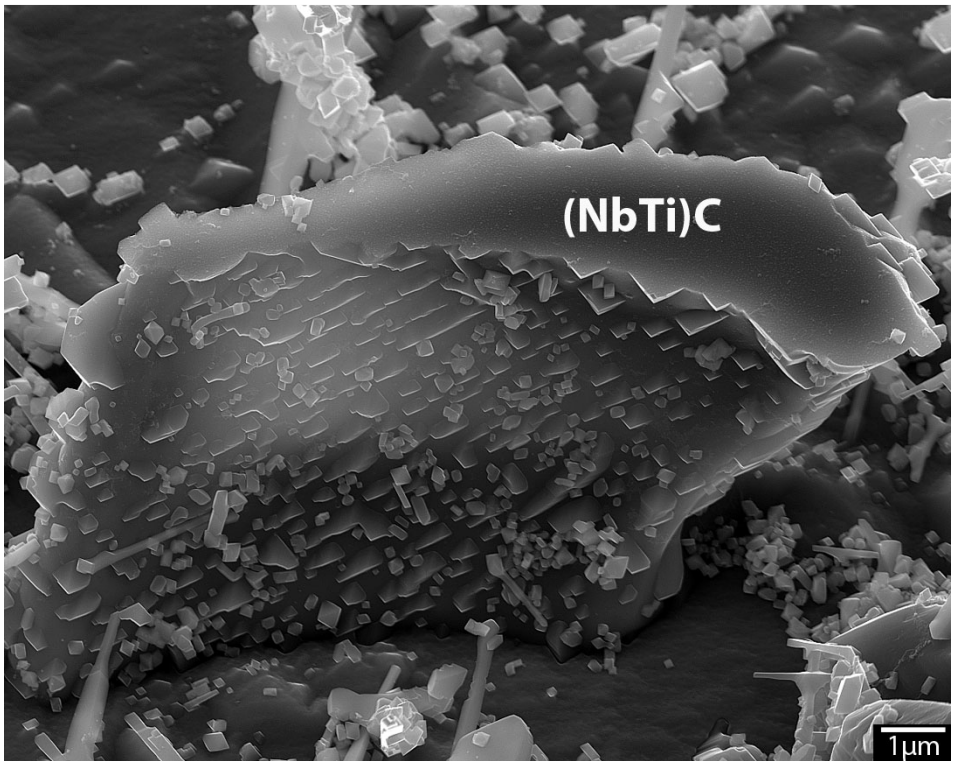

(a)

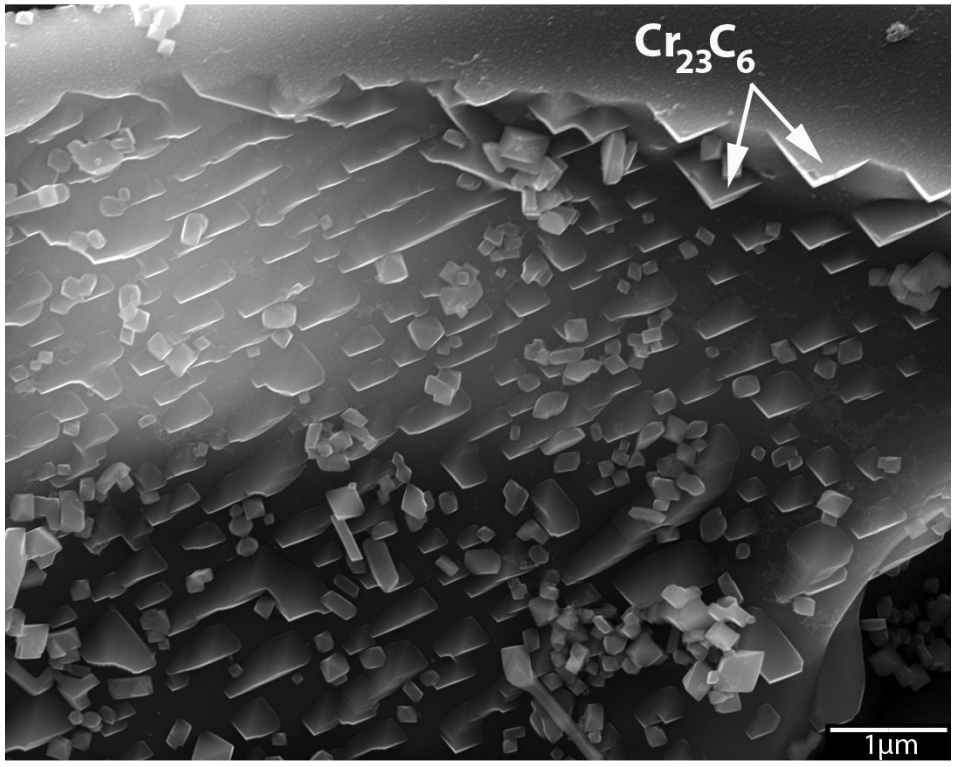

(b)

Figure 7.19 – (a) & (b) Secondary electron micrographs showing the three-dimensional morphology of the (NbTi)C and interfacial-$Cr_{23}C_6$ precipitates after ageing the HP-NbTi1 alloy at 1000°C for 1000 (deep etched in glyceregia).

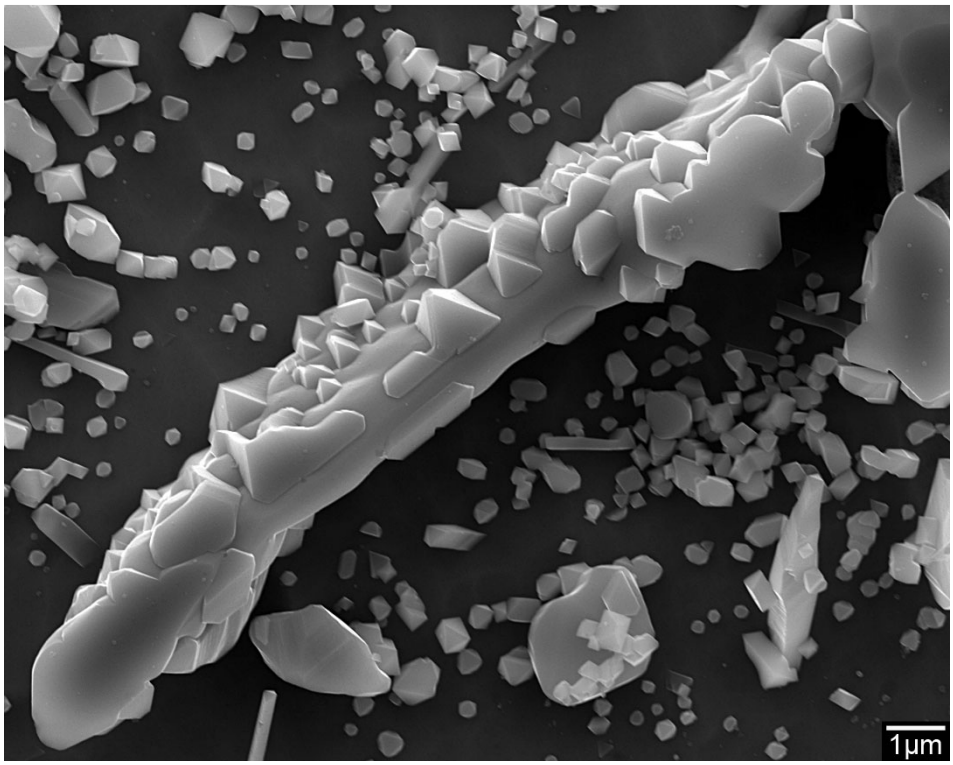

(a)

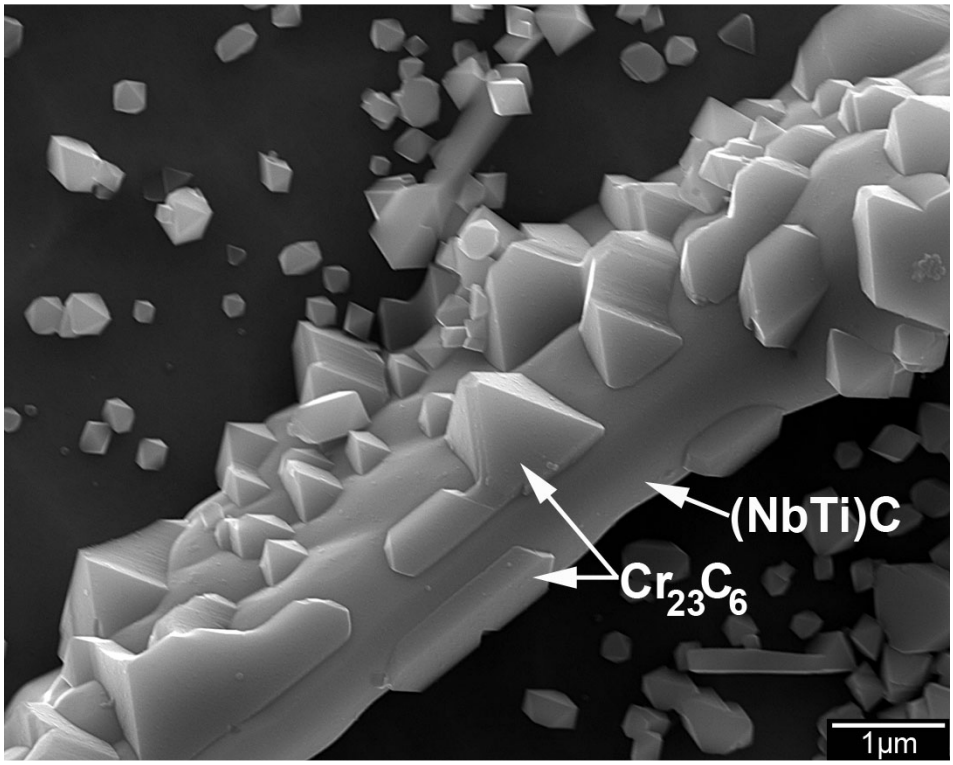

(b)

Figure 7.20 – (a) & (b) Secondary electron micrographs showing the three-dimensional morphology of the (NbTi)C and interfacial-$Cr_{23}C_6$ precipitates after ageing the HP-NbTi1 alloy at 1000°C for 1000 (deep etched in glyceregia).

7.3.4 Comparison of the Evolution of the Niobium-Rich Primary Precipitates in the HP-Nb and NbTi alloys

Figure 7.21 (a) to (d) show representative backscatter electron micrographs which directly compare the HP-Nb and NbTi alloys in the as-cast condition and after exposure to 1000°C for 10,000 hours. Micrographs of the alloys after long-term exposure to 1000°C has been shown in Figure 7.21 (b) and (d) as this temperature is within the normal operating temperatures that reformer tubes experience in service and it is also the temperature at which the NbC precipitates underwent the most significant change during ageing.

The effects of titanium on the niobium-rich primary precipitates are clearly apparent in the as-cast condition (Figure 7.21 (a) and (c)) where the addition of titanium to the primary NbC precipitates causes the lamellar morphology observed in the HP-Nb alloy to change to a blocky morphology in the HP-NbTi alloy (Chapters 4 and 5). During ageing at 1000°C, the additional 3-5wt.% of titanium within the (NbTi)C caused these precipitates to remain completely stable during ageing at 1000°C whereas the partial transformation of the NbC precipitates to η-carbide occurred in the HP-Nb alloy (Figure 7.21 (b) and (d)). In general, the η-carbide precipitates in the HP-Nb alloy after ageing at 1000°C for 10,000 hours were often similar in size to the entire as-cast NbC colonies.

Titanium has also been noted to reduce the MC-G-phase transformation in the HP-NbTi alloy in comparison to the HP-Nb alloy when ageing at 900°C for 1000 hours [3]. The total area fraction of G-phase was also considerably greater in comparison to the NbC when ageing the HP-Nb alloys at 900°C [2, 18].

In general the effect of the MC-to-G-phase and MC-to-η-carbide transformations on the HP-Nb and HP-NbTi alloys' creep properties is not well known in the literature. HK-Nb alloy tubes surviving 60,000 hours of service without failure and having G-phase present have been documented in the literature [19]. Similarly, the co-existence of G-phase and η-carbide precipitates has been reported in HP-Nb and HP-NbTi alloy tubes which survived service at temperatures between 875-982°C without failure for between 65,000-143,000 hours [20]. Such prolonged service periods suggest that G-phase and η-carbide preciptiates are not drastically detrimental to the alloys' creep properties.

Accelerated creep tests on laboratory aged HP-Nb samples with G-phase present have also shown increased creep properties in comparison to those aged above the upper limit of G-phase formation [2]. However, other studies that performed laboratory ageing followed by accelerated creep testing on HP-NbTi alloys that contained G-phase [3, 11] suggested that there is a volume expansion associated with the transformation to G-phase which increases the precipitate's interfacial energy. This increase was believed to result in the preferential creep damage (e.g. creep voids) observed at the G-phase/austenite interface. Unfortunately, similar laboratory ageing and accelerated creep testing of HP-Nb alloys with and without η-carbide precipitates has not been reported in the literature. Thus, these effects of this phase on the HP-Nb and HP-NbTi alloys' creep resistance are even less clear than for the G-phase precipitates.

If the accumulation of creep damage (e.g. creep void nucleation and growth) does preferentially occur on the G-phase/austenite and/or η-carbide/austenite interfaces, the relatively large area fraction that these phases rapidly form during ageing potentially provides ample interfacial area within the HP-Nb alloy for creep void nucleation. In contrast, the titanium within the HP-NbTi alloy reduces the G-phase transformation and completely suppresses the η-carbide transformation when ageing at 900 and 1000°C respectively. Therefore, the consistent increase in the stability of the primary niobium-rich precipitates in the HP-NbTi alloy during thermal exposure would potentially result in less damage prone precipitates in comparison to the HP-Nb alloy.

Although the significant difference between evolution of the niobium-rich primary precipitates' in the HP-Nb and HP-NbTi alloys during long-term ageing is obvious in Figure 7.21 (b) and (d), significant further analysis is necessary to determine if the observed greater stability exhibited by the (NbTi)C precipitates (with respect to the G-phase and η-carbide transformations) during ageing contributes to the HP-NbTi alloy's super creep resistance in comparison to the HP-Nb alloy. Analysis of the location of creep voids in ex-service and accelerated creep samples that contain G-phase and η-carbide precipitates (and are within the tertiary creep regime) is necessary to determine if the G-phase/austenite and η-carbide/austenite interfaces are prone to creep damage. However, since the shape, location and volume fraction of voids has been shown to be widely different when comparing voids in ex-service and accelerated creep testing samples [21], emphasis should be placed on the characterization of voids in ex-service tubes.

Comparing the creep properties of HP-Nb and HP-NbTi alloys that have been aged at differing temperatures in order to obtain (or suppress) the G-phase and η-carbide transformations will likely

to be misleading as the secondary precipitate distribution within each alloy is also dependent on the ageing temperature. Thus, the varying secondary precipitate distributions may mask the effect of the G-phase and η-carbide transformations on each alloy's creep properties.

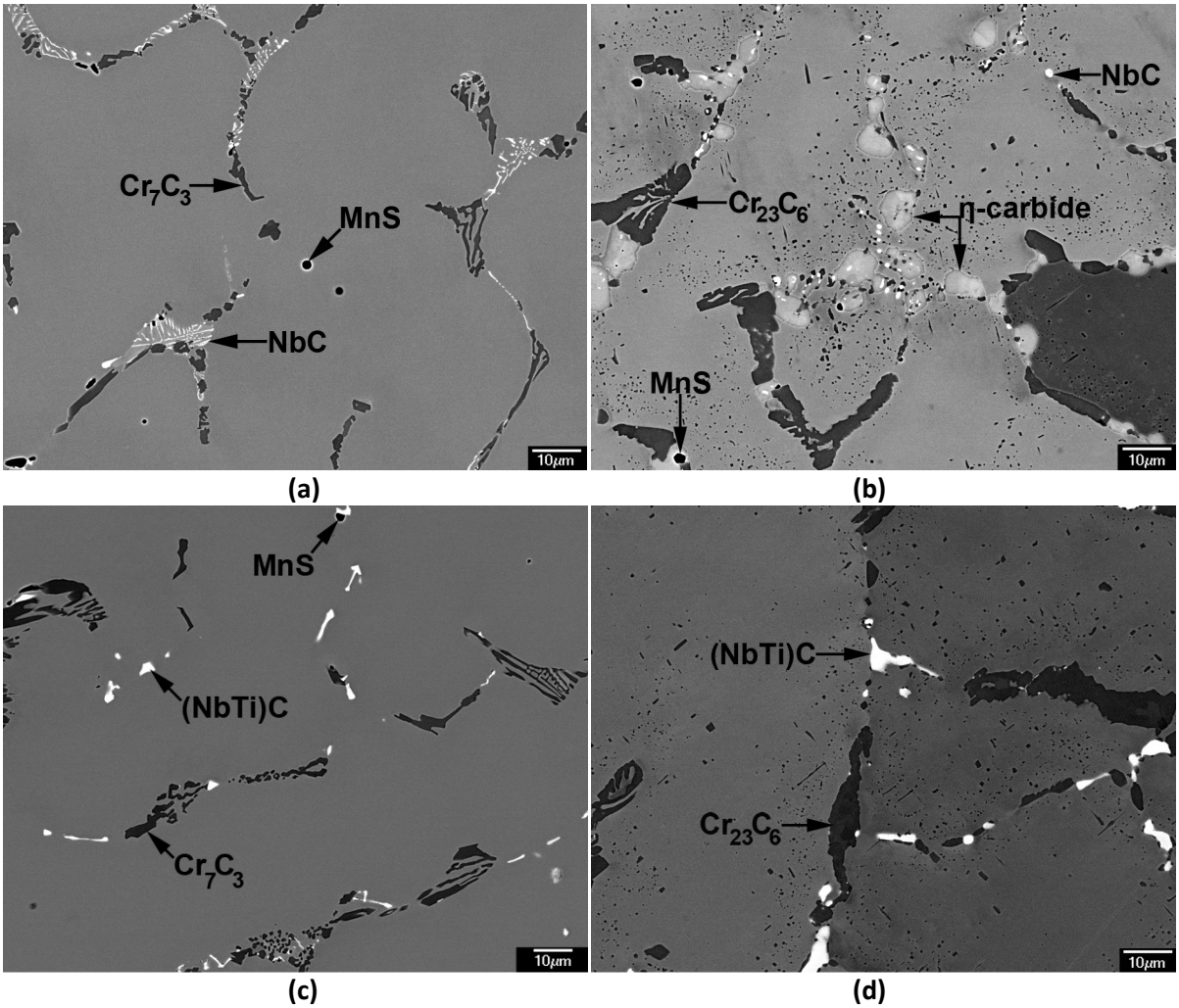

Figure 7.21 - Backscatter electron micrographs of the HP-Nb2 and HP-NbTi1 alloys in the (a) & (c) as-cast condition and (b) & (d) after ageing at 1000°C for 10,000 hours respectively

7.4 Secondary Precipitate Distribution

7.4.1 Chromium-Rich Secondary Precipitates

Figure 7.22 (a) to (f) show the secondary precipitates present in the HP-NbTi1 alloy after ageing at 1000, 1050 and 1100°C for 1000 and 10,000 hours respectively. The secondary precipitates in all aged samples were preferentially located within the austenite directly adjacent the larger primary precipitates (reportedly due to the higher dislocation density observed in these regions of the as-cast matrix [1-3]). The density of the secondary precipitates reduced with increasing distance from the primary precipitates often resulting in the centres of the austenite dendrite arms being comparatively free of secondary precipitate.

Short-term ageing of the HP-NbTi1 alloy (6, 12 and 24 hours) determined the secondary precipitate formed within the first 6 hours of exposure to 1000°C. No obvious difference in the number and average size of the secondary precipitates was observable when comparing the secondary precipitates in the samples aged for 6 and 24 hours suggesting the network becomes relatively stable within the first 6 hours of exposure (i.e. the initial nucleation and growth of the secondary precipitate distribution appeared to be complete).

The characteristics of the secondary precipitates in the HP-NbTi1 alloy during prolonged ageing mirrored those observed for the HP-Nb1 and HP-Nb2 alloys (Chapter 6). When comparing Figure 7.22 (a), (c) and (e), the secondary precipitate distribution present after 1000 hours exposure can be seen to become increasingly coarser with increasing ageing temperature. Regardless of the ageing temperature, prolonged ageing of HP-NbTi1 alloy caused Ostwald ripening of the secondary precipitates. The Ostwald ripening rate was strongly dependent on the ageing temperature (Figure 7.22 (b), (d) and (f)).

As shown in Figure 7.22 (f), the secondary precipitates had almost completely disappeared after ageing at 1100°C for 10,000 hours. The increased dissolution of the secondary precipitates in the 1100°C samples was believed to be caused by a combination of the comparatively higher diffusion rate of chromium and carbon through the austenite matrix and decarburization of the HP-NbTi1 alloy

which occurred during long-term ageing at 1100°C. Interestingly, the secondary precipitates were completely dissolved in the HP-Nb1 alloy whereas coarse secondary $Cr_{23}C_6$ precipitates were still observable in the HP-NbTi1 alloy after ageing at 1100°C for 10,000 hours. The remaining secondary precipitates at the mid-wall position of the HP-NbTi1 alloy were believed to be due to the as-cast HP-NbTi1 alloy having a greater wall thickness than the HP-Nb1 alloy (~2mm larger). Thus, the additional tube wall thickness caused the decarburization at the mid-wall position to be slightly less severe in the HP-NbTi alloy after ageing for 10,000 hours.

Based on SEM observations of the aged HP-NbTi1 samples, the secondary precipitates distribution was mainly composed of $Cr_{23}C_6$ precipitates that obtained either cuboidal or needle-like (Widmanstätten) morphologies. Irrespective of the ageing temperature, the cuboidal morphology was significantly more common than the Widmanstätten morphology. The number of Widmanstätten precipitates appeared to be relatively similar with respect to the ageing temperature (based on qualitative comparison of the secondary precipitates observed in backscatter electron images). $Cr_{23}C_6$ stringers (multiple cuboidal $Cr_{23}C_6$ precipitates joined in series at each corner - Chapter 6), were also rarely observed in all of the HP-NbTi1 aged samples.

As observed in the HP-Nb1 and HP-Nb2 aged samples, Widmanstätten $Cr_{23}C_6$ precipitates that were located in the same austenite grain typically exhibited parallel or orthogonal alignment (Figure 7.22 (a) to (f)) suggesting the plates obtained a specific habit or growth plane. Deep etching of the HP-Nb alloys suggested that these plates, which appeared as laths in three-dimensions, nucleated on the Type II NbC lamellae (i.e. the lamellae which did not obtain a consistent OR with the as-cast austenite). Evidence of similar nucleation of the laths on the (NbTi)C precipitates (which also did not share a consistent OR with the as-cast austenite) was similarly observed after deep etching the HP-NbTi1 alloy (Figure 7.23). However, the laths in HP-NbTi1 aged samples were comparatively more slender than the HP-Nb laths causing them to be particularly susceptible to fracture during deep etching. Thus, retaining suitable precipitates for analysis in the deep etched samples was inherently difficult.

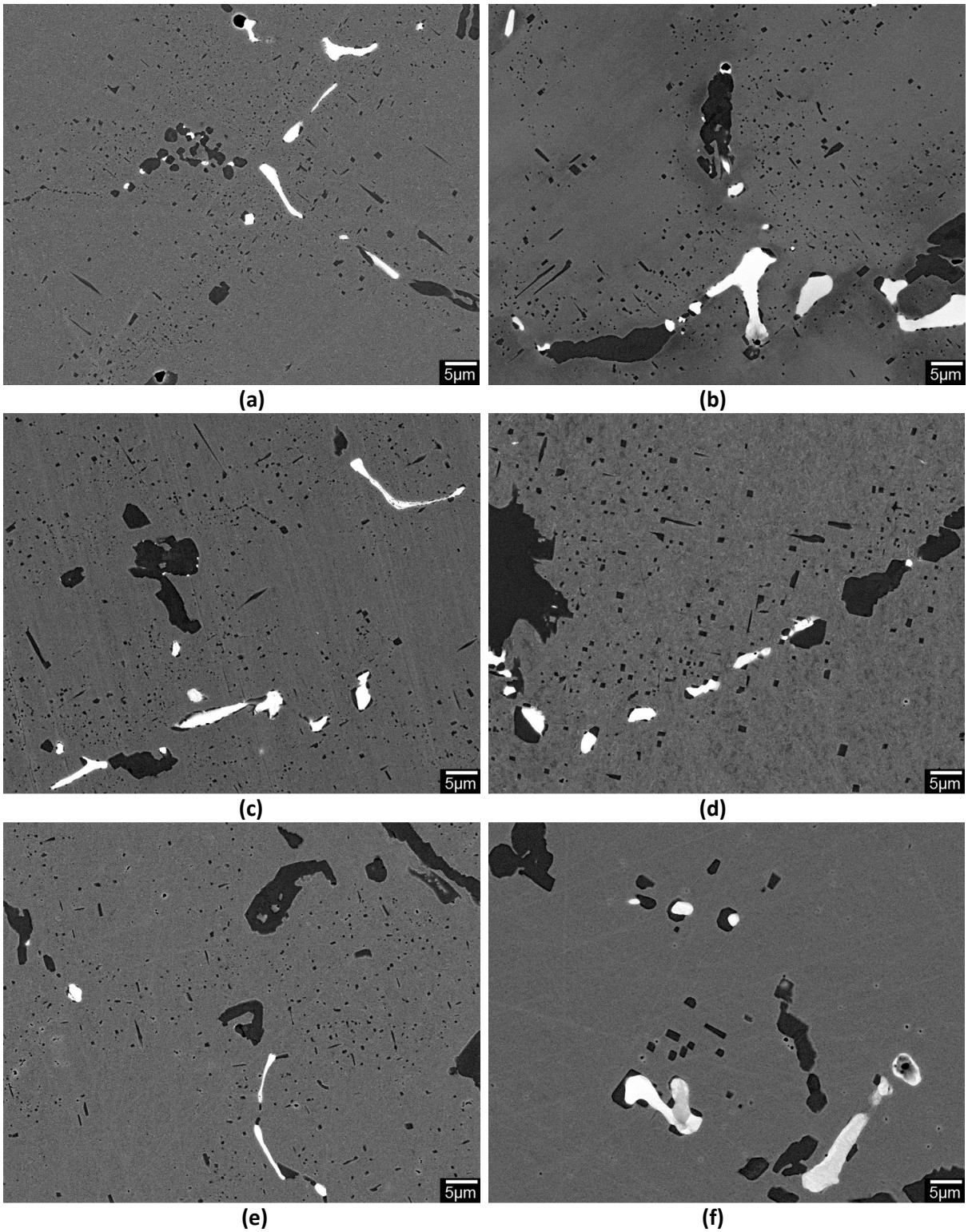

Figure 7.22 - Backscatter electron micrographs showing the secondary precipitates in the HP-NbTi1 alloy after ageing for 1000 and 10,000 hours at (a) & (b) 1000, (c) & (d) 1050 and (e) & (f) 1100°C.

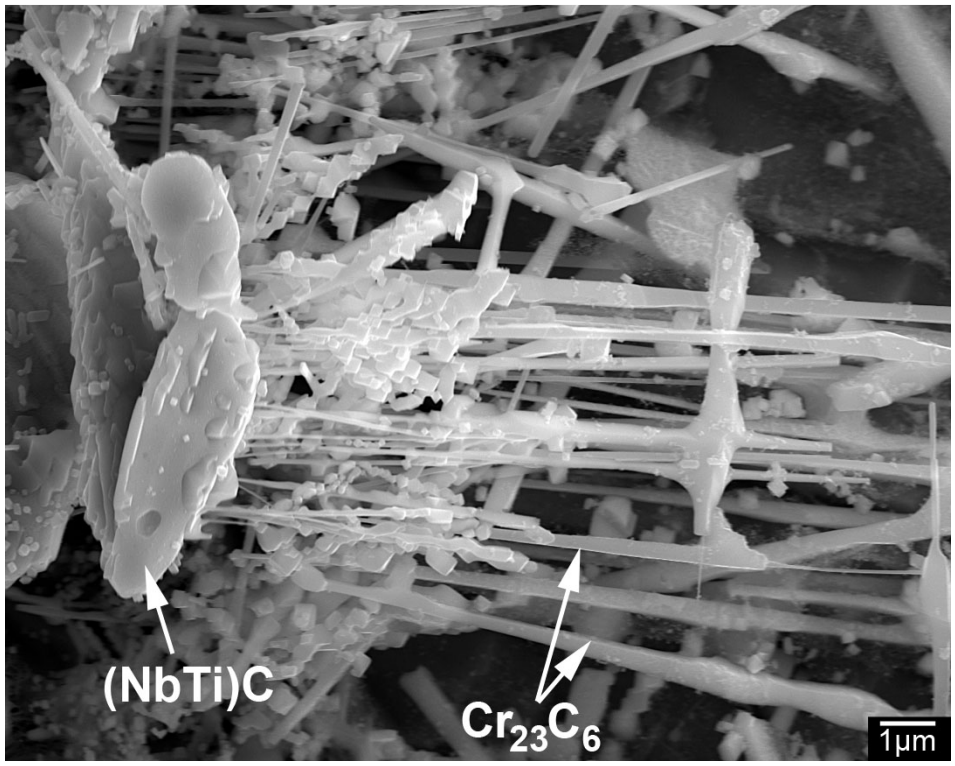

Figure 7.23 – Secondary electron micrograph showing the lath-shaped $Cr_{23}C_6$ which appeared to emanate from the primary (NbTi)C precipitates in the aged HP-NbTi alloy.

Identification of cuboidal (Figure 7.24 (a)) and Widmanstätten (Figure 7.24 (c)) precipitates $Cr_{23}C_6$ crystal structure was performed using EDS and SAD (Table 7.2; Figure 7.24 (b) and (d)). The cube-cube $Cr_{23}C_6$/austenite orientation relationship characteristic of the primary and secondary $Cr_{23}C_6$ precipitates in the HP alloys is also shown for both morphologies. Analysis of the $Cr_{23}C_6$/austenite OR was conducted on secondary precipitates after ageing at 1000 and 1100°C for 1000 and 10,000 hours, with the cube-cube $Cr_{23}C_6$/austenite OR observed for all precipitates (regardless of morphology).

TEM observations of the cuboidal $Cr_{23}C_6$ secondary precipitates revealed the presence of multiple small spots (less than 50nm in diameter) located within the $Cr_{23}C_6$ precipitates (Figure 7.24 (a)). EDS analysis indicated these spots were rich in niobium. Unfortunately CBED of the particles was not possible as any information produced by the niobium-rich phase was typically masked by the surrounding $Cr_{23}C_6$. The niobium-rich precipitates were not common to all cuboidal precipitates observed in the TEM and were not observed within the Widmanstätten precipitates. However, it must be stressed that the precipitates analysed in the TEM are a thin section of a larger three-

dimensional precipitate. Therefore, although $Cr_{23}C_6$ precipitates which did not contain these niobium-rich precipitates were observed, these precipitates may have existed but been out of the foils sectioning plane. The niobium-rich precipitates appeared to remain stable during prolonged ageing with similar size precipitates observed within the secondary $Cr_{23}C_6$ precipitates after ageing the HP-NbTi1 alloy at 1000°C for 10,000 hours. Analysis of the HP-Nb2 aged samples identified similar niobium-rich precipitates within the cuboidal secondary $Cr_{23}C_6$ precipitates (i.e. these spots were not unique to the HP-NbTi1 alloy). However, the niobium-rich precipitates were significantly less common in the HP-Nb alloys.

Further TEM analysis of the secondary precipitates in the HP-Nb and HP-NbTi aged samples is necessary to ascertain if these niobium-rich precipitates are common to the cuboidal and Widmanstätten $Cr_{23}C_6$ precipitates and also to determine their crystal structure and origin. Since beam induced damage of the $Cr_{23}C_6$ often appears similar to the niobium-rich precipitates, care must be taken when searching for these precipitates using the TEM. Generally, the niobium-rich precipitates became easily visible in the bright field image when the beam direction was aligned with a low index $Cr_{23}C_6$ zone axis (for example, $[100]_{Cr23C6}$). To avoid beam damage to the precipitate it is suggested the similarly oriented matrix adjacent to the precipitate is used to bring the $Cr_{23}C_6$ zone axes parallel to the beam direction. $Cr_{23}C_6$ precipitates located within the aligned austenite grain can subsequently be scanned for the niobium-rich precipitates when viewing bright field image of the sample.

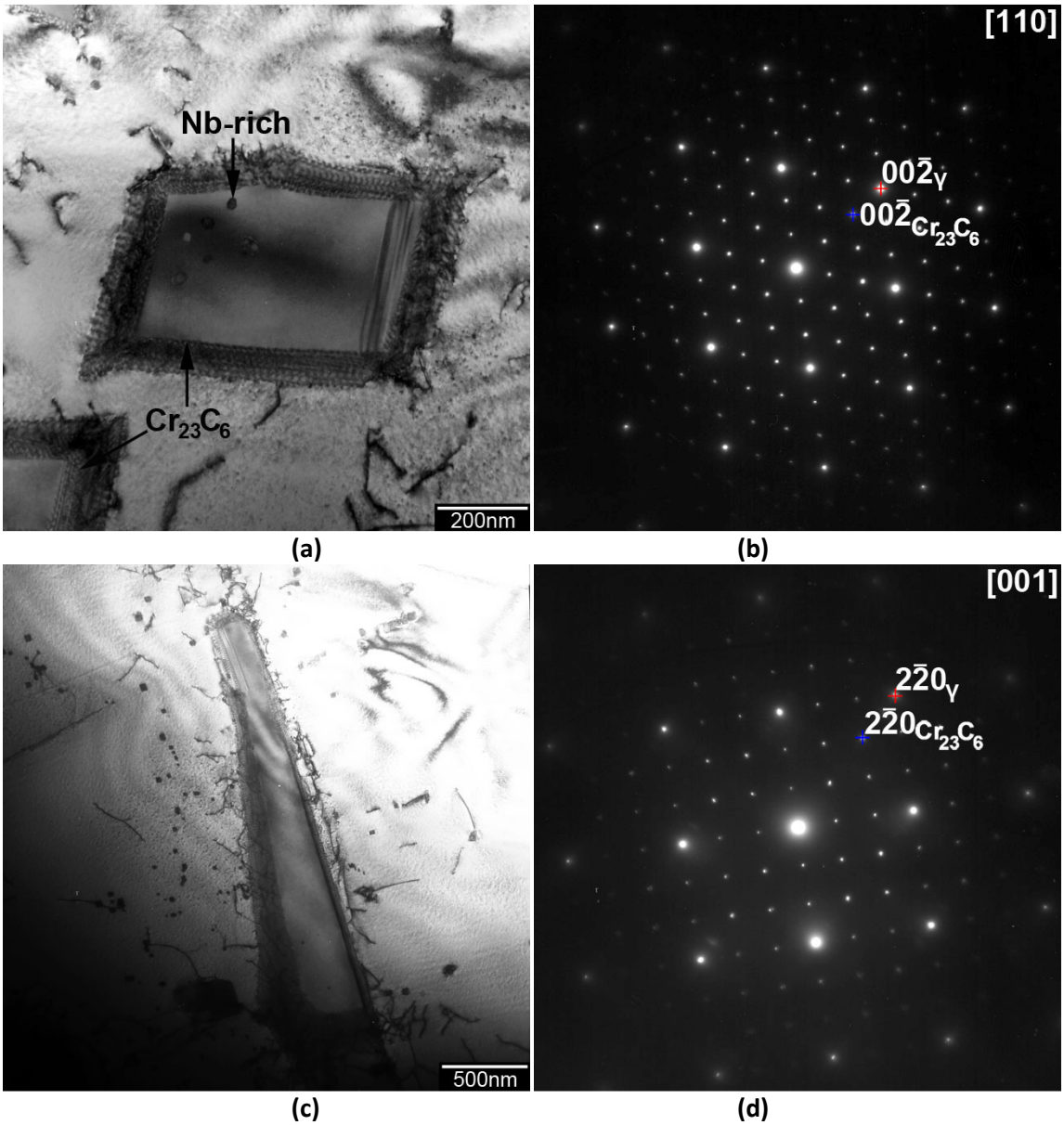

Figure 7.24 – (a) & (c) Bright field TEM micrographs of the cuboidal and Widmanstätten secondary precipitates. (b) & (d) Selected area diffraction patterns of the [110] and [001] zones axes respectively. The $[100]_{Cr23C6}//[100]_\gamma$ OR is clearly evident for both morphologies with reflections characteristic of the $Cr_{23}C_6$ and austenite crystal structures shown in each SAD pattern.

Table 7.2 – Crystal structure, average lattice parameter and chemical composition of the secondary cuboidal and Widmanstätten $Cr_{23}C_6$ as determined by SAD and EDS analysis of the HP-NbTi1 alloy after ageing at 1000°C for 1000 hours.

	Structure	Space Group	Lattice parameter a=b=c (nm)	EDS Composition (at.%)			
				Cr	Fe	Ni	W
$Cr_{23}C_6$	FCC	$Fm\bar{3}m$	1.073	84.9	9.4	4.5	1.2

7.4.2 Niobium-Rich Secondary Precipitates

In addition to the $Cr_{23}C_6$, niobium-rich secondary precipitates (believed to be (NbTi)C) were sporadically observed when viewing the aged samples with the JEOL 7000F field-emission scanning electron microscope. Regardless of the ageing temperature, the niobium-rich secondary precipitates were comparable in size to the $Cr_{23}C_6$ (Typically 0.5-1μm^2). The aged HP-NbTi1 samples typically contained fewer niobium-rich precipitates in comparison to the aged HP-Nb1 and Nb2 samples. However, for both alloys these precipitates were estimated to represent less the 1% of the total secondary precipitate population. During long-term ageing of the HP-Nb and HP-NbTi alloys, the niobium-rich secondary precipitates in the HP-NbTi1 alloy became increasingly rare.

High magnification TEM observations of thin foils produced from the HP-NbTi1 aged samples revealed the existence of nano-scale precipitates (Figure 7.25 (a) and (b)). Further observations of the as-cast alloys determined that these precipitates were not present in the as-cast condition (i.e. they formed during ageing). The small size of these precipitates (typically 20-50nm in diameter) caused these precipitates to be below the resolution of the JEOL 7000F SEM. EDS spectra taken from the precipitates indicated that the precipitates were niobium and titanium rich (Figure 7.26 (a) and (b)). Due to the small size of the precipitates, the electron beam typically excited silicon, chromium, iron and nickel X-rays from the surrounding austenite matrix (Figure 7.26 (b)). As shown in Figure 7.25 (a), the Nb-Ti rich precipitates were generally an order of magnitude smaller than the cuboidal secondary $Cr_{23}C_6$ precipitates in the 1000°C-1000h sample. The presence of these nano-sized Nb-Ti rich precipitates in the HP-NbTi1 alloy likely led to the previously mentioned lower occurrence of the larger NbC precipitates (0.5-1μm^2).

The (NbTi)C precipitates were commonly observed in association with dislocations suggesting that the dislocations present in the as-cast matrix [1] also act as nucleation site for these precipitates during ageing (Figure 7.25 (b)). The precipitates typically exhibited cuboidal or spheroidal morphologies. Based on observations of these precipitates in three separate austenite grains, the nano-scale precipitates appeared to be present in similar abundance to the larger $Cr_{23}C_6$ precipitates. Further TEM analysis of these precipitates is necessary to determine if the nano-precipitates cluster within the austenite adjacent to the primary precipitate network as observed for the $Cr_{23}C_6$ precipitates (i.e. where the highest dislocation density is believed to be present in the as-cast microstructure).

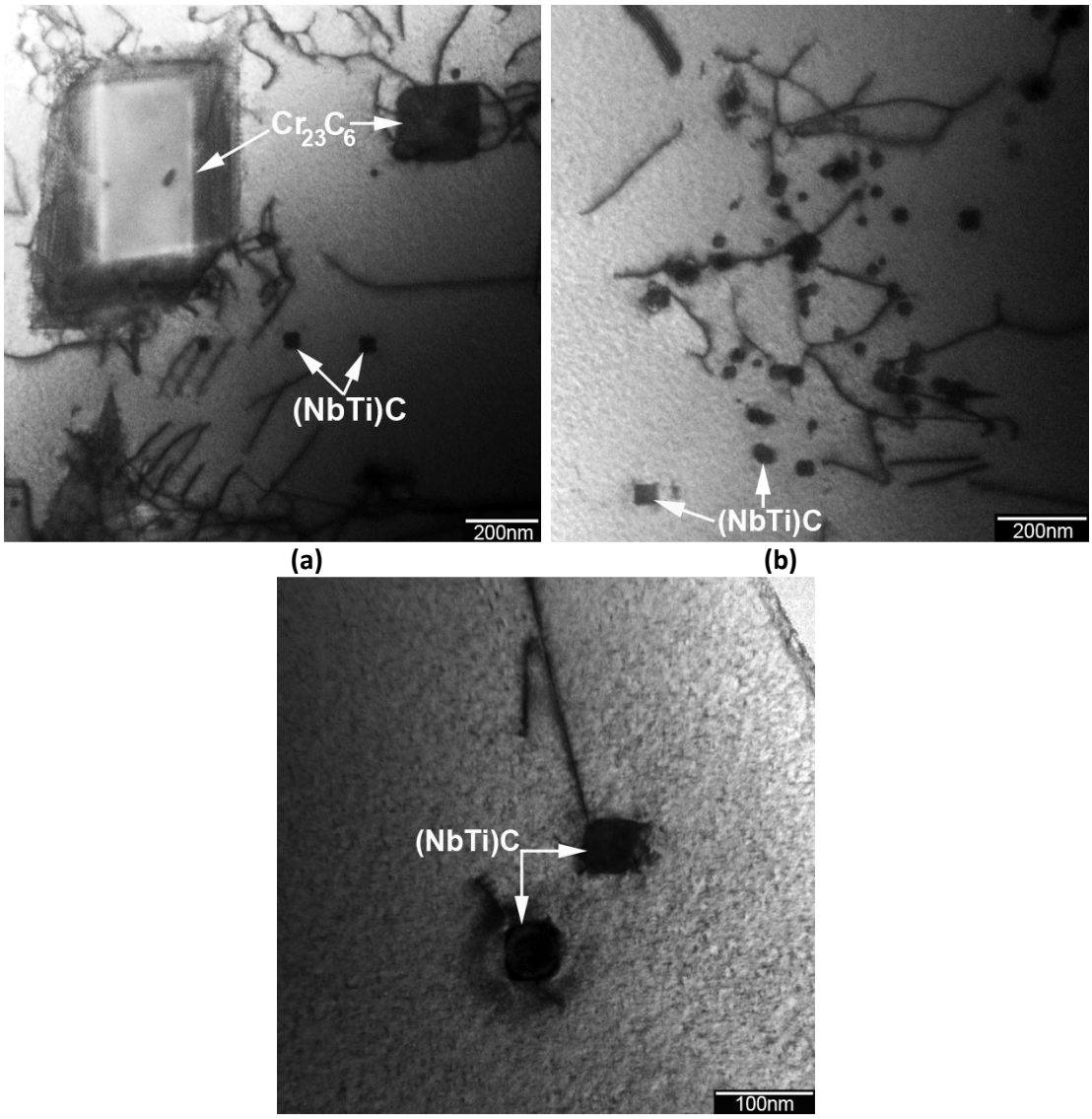

Figure 7.25 – Bright field transmission electron micrographs of the secondary $Cr_{23}C_6$ and (NbTi)C precipitates in the HP-NbTi1 alloy after ageing at 1000°C for (a) & (b) 1000 and (c) 10,000 hours.

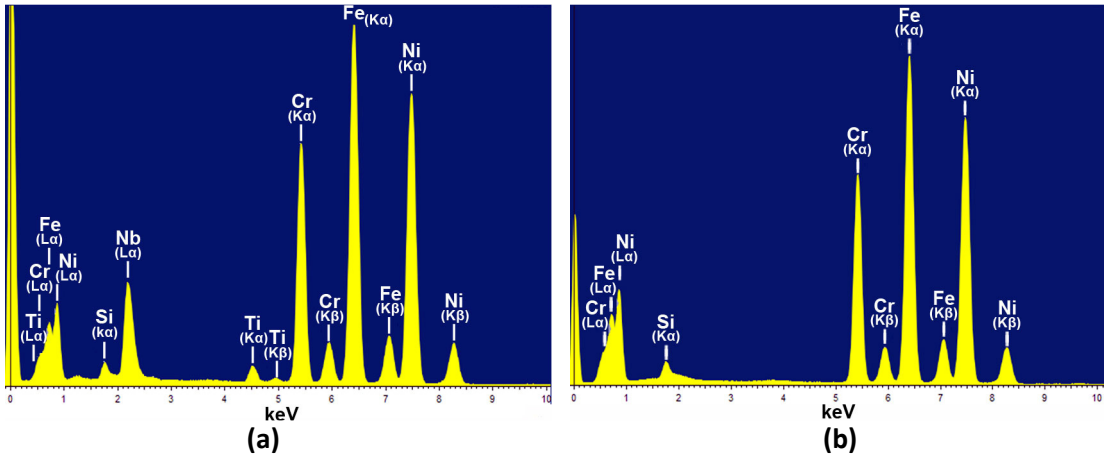

Figure 7.26 – EDS spectra from the (a) Niobium-titanium rich precipitates and (b) surrounding austenite.

Figure 7.25 (c) shows a bright field TEM micrograph of the Nb-Ti secondary precipitates after ageing at 1000°C for 10,000 hours. The number of Nb-Ti precipitates reduced during prolonged ageing at 1000°C. Although the remaining nano-precipitates were slightly coarser after 10,000 hours (typically between 50-100nm in diameter), these precipitates appeared to coarsen at a slower rate in comparison to the $Cr_{23}C_6$ precipitates. However, when ageing the HP-NbTi1 alloy at 1100°C the Nb-Ti precipitate distribution to completely dissolve after 10,000 hours.

Based on similar precipitates reported the HK alloys modified with niobium and titanium [22], the Nb-Ti rich precipitates in the aged HP-NbTi alloys were expected to obtain the $Fm\bar{3}m$ (NbTi)C crystal structure. Unfortunately, identification of the nano-precipitates crystal structure using CBED was unsuccessful. When performing CBED analysis of the precipitates, the diffraction information produced by each precipitate was completely obscured by the surrounding austenite (regardless of the beam diameter). CBED was attempted on precipitates in both the 1000 and 10,000 hour samples without success.

When observing the bright field image of the precipitates it was noticed that all of the Nb-Ti nano-precipitates heavily diffracted the electron been when a low index austenite zone axis was parallel to the beam direction. For example, the precipitates shown in Figure 7.25 (a) to (c) are all shown with the beam direction parallel to $<100>_{\gamma}$. It was believed the observed diffraction contrast was possibly induced as a result of the precipitates sharing an orientation relationship with the matrix (similar to the cube-cube OR between the Type I NbC lamellae and austenite). Therefore, identification of the nano-precipitates was also attempted by performing SAD on the precipitates and directly adjacent matrix. Analysis was performed by tilting the sample to bring a low index austenite zone axis parallel to the beam direction. SAD patterns were subsequently captured with selected area aperture centered to overlap single and multiple Nb-Ti precipitates. While additional weak reflections (un-associated with the austenite) were observed within each SAD pattern, no sense could be made from positions of these reflections.

In previous work, nano-scale MC precipitates (Nb-rich) have been identified in HK-Nb and HK-NbTiZr alloys [22]. The precipitates were observed in the as-cast condition and after creep testing of the alloys at temperatures between 800-1000°C. TEM observations of these precipitates in the as-cast and aged condition indicated the MC precipitates had nucleated on dislocations (both alloys) and stacking faults (HK-NbTiZr alloy). The extensive distribution of secondary MC precipitates present in

the as-cast condition was believed to have formed during cooling from the casting temperature. The number of secondary precipitates increased markedly when the alloys were subjected to accelerated creep testing. While coarsening of the MC precipitates occurred during prolonged exposure (~3500hours at 900°C), the coarsening rate was considerably slower in comparison to the $Cr_{23}C_6$ precipitates. This reduced coarsening rate was attributed to the slower diffusion of niobium and titanium through the austenite matrix in comparison to chromium.

Nano-scale Nb-rich precipitates 20-50nm in size have also been identified in HP-NbTiY alloys after accelerated creep testing at 980°C and 41.3MPa [23]. Interestingly, of the three compositionally unique NbTiY alloys studied, these precipitates were only identified in the alloy containing the lowest the titanium content. The enhanced creep performance of this alloy was partially attributed to the nano-scale precipitates.

Although very rare occurrences of the niobium-rich precipitates were observed in HP-Nb1 and HP-Nb2 alloy after ageing at 1000°C for 1000 hours, the small number of these precipitates suggested a similar distribution of nano-scale secondary precipitates did not exist in the HP-Nb alloys. It is currently unknown if the instability of the NbC crystal structure in the HP-Nb alloys when ageing at 1000°C caused the secondary precipitates to dissolve or transform within the 1000 hour ageing period. However, no evidence of η-carbide or G-phase precipitates was observed in the aged HP-Nb matrix suggesting the NbC precipitates (if initially present) had not transformed to either of these phases during ageing.

While no significant evidence of the nano-scale precipitates were observed in aged HP-Nb samples, the cumbersome nature of TEM analysis caused these observations to be based on the analysis of very limited fraction of the mid-wall microstructure. In order to confirm the absence of these precipitates in the aforementioned samples, additional high resolution TEM analysis and dark field imaging is considered necessary. TEM analysis of HP-Nb and HP-NbTi tubes which have experienced slightly different casting conditions and/or have different compositions is also necessary to completely characterise which HP alloy variants contain these precipitates.

7.4.3 Comparison of the Secondary Precipitate Distributions in the HP-Nb and NbTi Alloys

The secondary precipitate distribution present in HK and HP alloys modified with niobium and titanium have been reported as being finer and more evenly distributed in comparison to alloys modified with solely niobium [1, 3, 11, 16]. The enhanced creep strength of the HP-NbTi alloys in comparison to the HP-Nb alloys have been partially attributed to the increased refinement of the secondary precipitate distribution [3, 11, 16]. Assessment of the relative refinement of the secondary precipitate distribution in previous work on HP-Nb and NbTi alloys was performed by qualitatively comparing optical and scanning electron micrographs (similar to Figure 7.28 and Figure 7.29) of each alloy after isothermal ageing at 900°C for 1000 hours. Based on observations of the aged HP-NbTi1 alloy, the nano-sized (NbTi)C secondary precipitates (observed using the TEM) are below the resolution limits of the optical and scanning electron microscopes. Thus, it is believed that previous judgments of the secondary precipitate distributions in the HP-Nb and NbTi alloys using the optical or scanning electron microscopes has been largely based on the average size and inter-particle spacing of the secondary $Cr_{23}C_6$ precipitates.

Similar qualitative comparisons of the secondary precipitates in the aged HP-Nb1, HP-Nb2 and HP-NbTi1 alloys after aging at 1000, 1050 and 1100°C for 1000 hours (using backscatter electron images taken over a magnification range of 1000-7000x). As shown in Figure 7.28 and Figure 7.29, the secondary precipitate distribution varied significantly with respect to dendrite arm space. As a result, there was no conclusive evidence that the average size and inter-particle spacing of the secondary precipitates in the HP-NbTi1 alloy were lower in comparison to the secondary precipitates in the HP-Nb1 and HP-Nb2 alloys based on qualitative comparison of each alloy after ageing at 1000, 1050 and 1100°C.

Quantitative analysis of the secondary precipitates was attempted by performing image analysis on the $Cr_{23}C_6$ secondary precipitates using backscatter electron FE-SEM images taken over a range of magnifications (3000-7000x). However, preliminary analysis of the these images determined the high variability of the secondary precipitates with respect to grain and dendrite position and the high degree to which the polish quality could affect the visibility of the secondary precipitates caused image analysis to be highly unreliable.

Typically, the final polish varied significantly between samples even while maintaining strict control of the polishing conditions. The polished quality also varied between individual austenite grains within each sample. Poor polish quality typically resulted in many of the finer secondary precipitates (<0.5μm^2) being completely omitted during thresholding. Alternatively, fine secondary precipitates that were selected during thresholding were often similar in size to clusters of random noise within the austenite matrix, making them indistinguishable during counting.

Figure 7.27**Error! Reference source not found.** (a) and (b) show a backscatter electron image and a binary image of the secondary precipitates in the HP-Nb alloy after ageing at 1000°C for 1000 hours. In general, binary representation of each precipitate's shape did not accurately reproduce the morphology of the precipitates observed in the backscatter electron image. Additional artifacts included over or under estimation of the precipitates' size; fragmentation of actual individual precipitates into multiple separate binary precipitates and coalescence of multiple actual precipitates into a single binary precipitate. Figure 7.27 (c) gives examples of each artifact with the precipitates highlighted in either green or gold showing when the precipitate's size has been over or under estimated. Precipitates highlighted in blue give examples of single precipitates that have been fragmented into multiple separate precipitates after thresholding whereas the precipitates highlighted in orange represent one or more precipitates that have coalesced after thresholding. Finally, the 'precipitates' shown in red are produced through clusters of noise within the austenite matrix as result of contrast variations typically caused by the polish quality varying with respect to position in each sample.

As a result of aforementioned artifacts, large proportions of the secondary precipitate distribution after short-term would not be accurately captured during image analysis. Thus, it was typically impossible to obtain repeatable and comparable quantitative measurements of the secondary precipitates' average size and inter-particle spacing when mechanically polishing each sample.

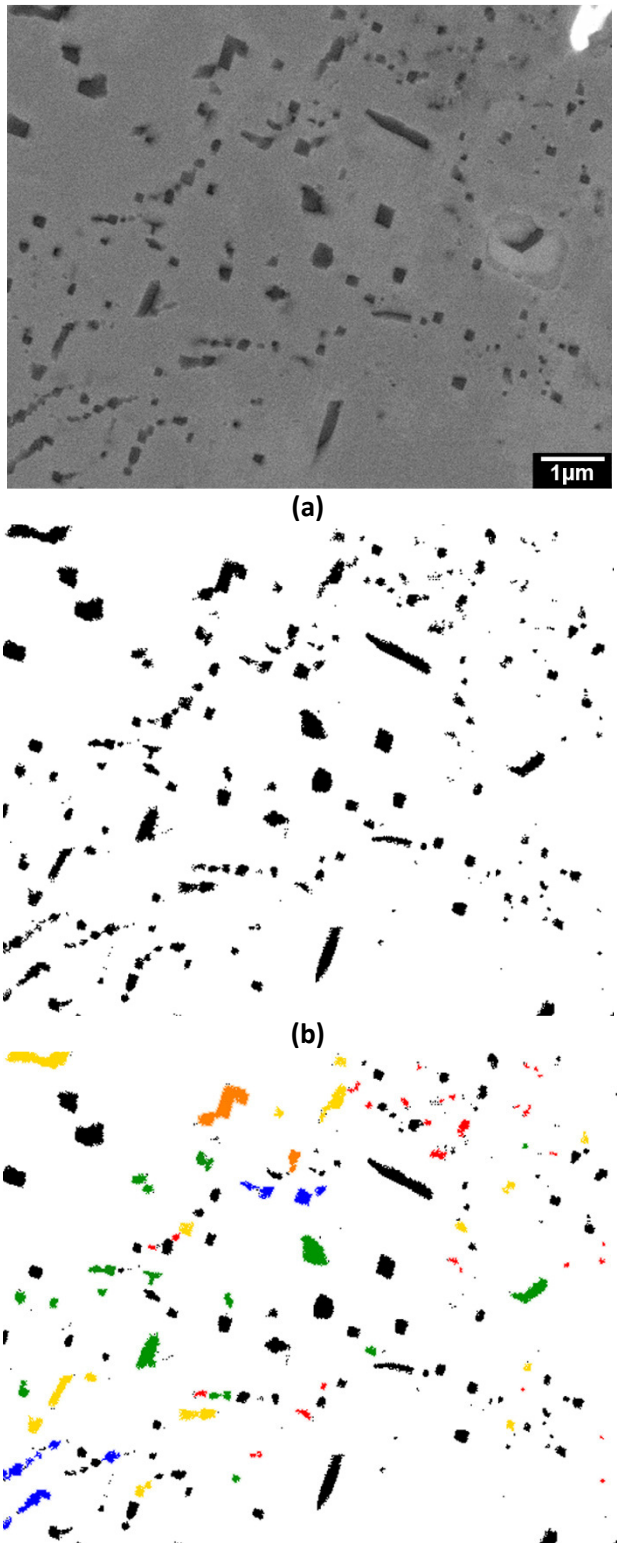

Figure 7.27 - (a) backscatter electron micrograph of the secondary precipitates in the HP-Nb alloy after ageing at 1000°C for 1000 hours. (b) Binary image of the secondary precipitates after thresholding (a). (c) The binary image coloured with green and gold representing when a precipitate's size has been significantly over or under estimated, blue and orange representing precipitates that have been fragmented or individual precipitates that have coalesced after thresholding and red denoting clusters of noise within the matrix that is similar in size to the secondary precipitates

Generally, the secondary $Cr_{23}C_6$ precipitates were finest and most abundant within the matrix closely adjacent to the primary precipitates. The number precipitates decreased with increasing distance from the primary precipitate network. Consequently, the non-uniform distribution of the secondary precipitates within the austenite matrix caused the measured average size and inter-particle spacing to be heavily dependent on the location that the image was taken with respect to the primary precipitates. In an attempt to obtain comparable images from each aged sample, images of the secondary precipitates were taken at a constant distance from the primary precipitates (e.g. images centred at 20μm from the primary precipitates). However, significant variance was still present when comparing images taken from separate dendrite arms within the same sample. While this variance is possibly a true characteristic of the secondary precipitate distributions within the HP alloys, it is also potentially a result of the non-uniformity of the secondary precipitate distribution in three-dimensions. Consequently, it is extremely difficult to obtain images from consistently comparable regions of separate dendrite arms when viewing the microstructure in two-dimensions.

Serial sectioning of the aged samples follow by high resolution FE-SEM imaging is considered necessary to obtain an accurate representation of the secondary precipitates in each alloy. Such analysis would allow for the measurement of the secondary precipitate distribution over entire dendrite arms. Thus, negating any dendrite position induced measurement errors. It must be noted that this analysis will only characterise the secondary $Cr_{23}C_6$ precipitate distribution as the nano-sized MC precipitates were typically below the resolution limit of the FE-SEM. Due to the time consuming nature of this analysis, quantitative analysis of the secondary distributions in the aged HP-Nb and NbTi alloys using serial sectioning was outside the scope of the current project.

Additionally, the differing casting conditions experienced by the alloys in the current research will affect the secondary precipitate distributions which form in each alloy during ageing. Increasingly finer secondary $Cr_{23}C_6$ precipitate distributions have been reported in un-modified HK alloys that experienced greater cooling rates during casting [22]. The differing secondary precipitate distributions within each tube were believed to be a result of the carbon content dissolved within the austenite matrix increasing with the cooling rate during casting. Since the differing cooling rates experienced by the HP-Nb1, HP-Nb2 and HP-NbTi1 alloys during casting could similarly alter the secondary $Cr_{23}C_6$ precipitate distributions in each alloy, any effect induced by the differing alloying content could be masked by the casting conditions. Hence, in order to obtain an accurate comparison of the secondary $Cr_{23}C_6$ precipitate distributions within the HP-Nb and NbTi alloys (i.e. to

determine if the alloying content affects the secondary distribution), both alloys must experience the same casting and ageing conditions.

While an accurate quantitative comparison of the secondary $Cr_{23}C_6$ precipitate distribution in the HP-Nb and HP-NbTi alloy was not possible, the niobium-rich secondary precipitates were clearly different when comparing the HP-Nb and HP-NbTi alloy. Overall, niobium precipitates that were similar in size to the $Cr_{23}C_6$ secondary precipitates were equally rare in both alloys (significantly <1% of the total secondary population). However, analysis of thin foils taken from the HP-Nb and HP-NbTi aged samples determined that nano-sized niobium-rich precipitates were very rare in the HP-Nb alloy whereas an extensive distribution of these precipitates formed in the HP-NbTi alloy during ageing. For the HP-NbTi alloy, these precipitates formed within 1000 hours and were comparative more resistant to coarsening during prolonged ageing in comparison to the $Cr_{23}C_6$ precipitates.

Based on the preceding discussion, the HP-NbTi alloy's increase creep resistance in comparison to the HP-Nb alloy is believed to be largely attributed to the dispersion strengthening effect induced by the nano-size niobium-rich secondary precipitates.

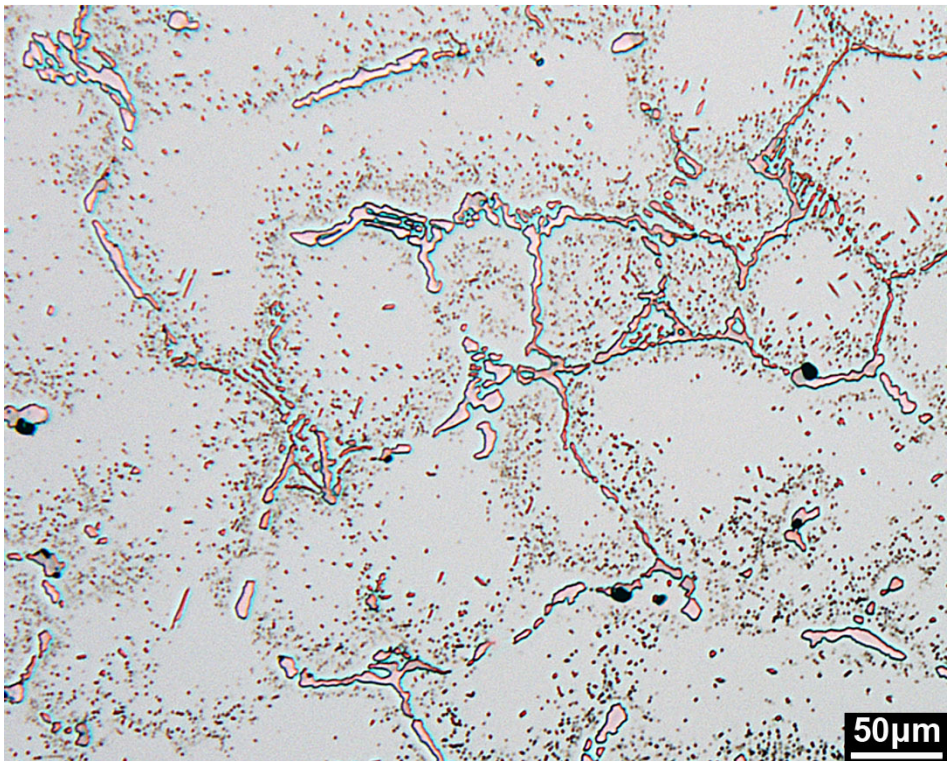

(a)

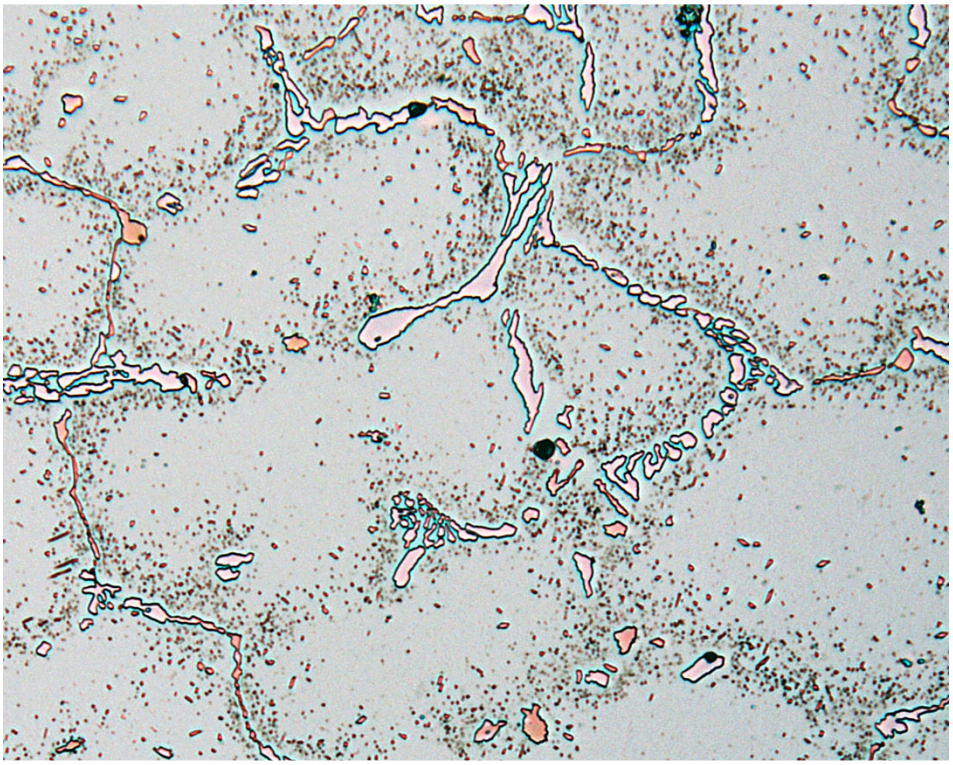

(b)

Figure 7.28 - Optical micrographs of the (a) HP-Nb2 and (b) HP-NbTi1 alloy after ageing at 1000°C for 1000 hours.

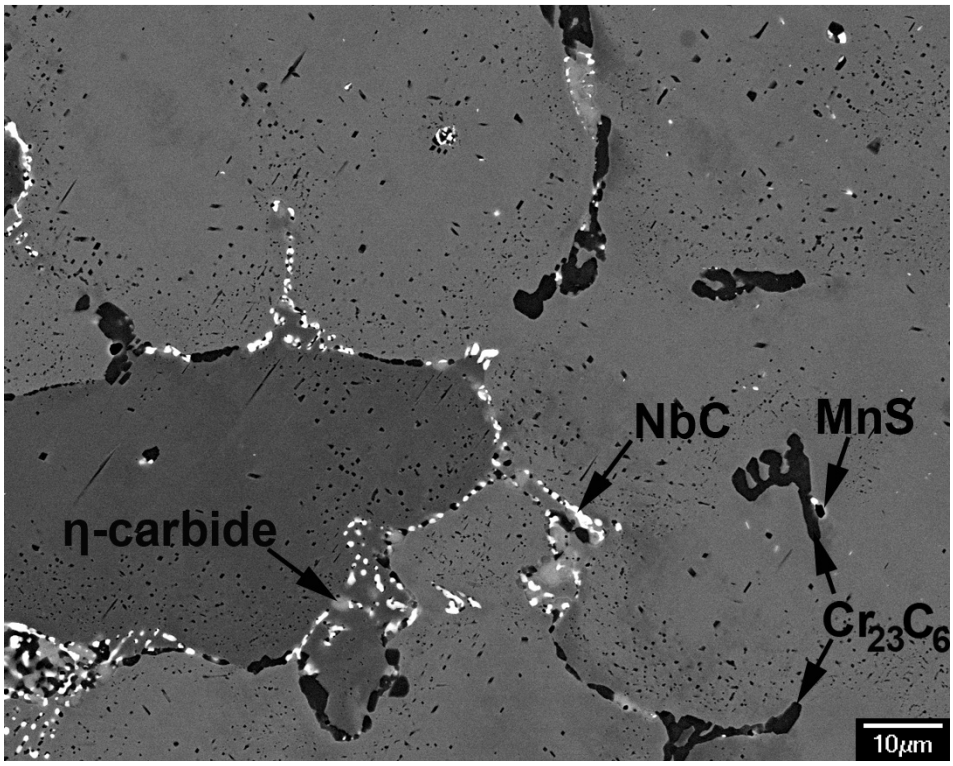

(a)

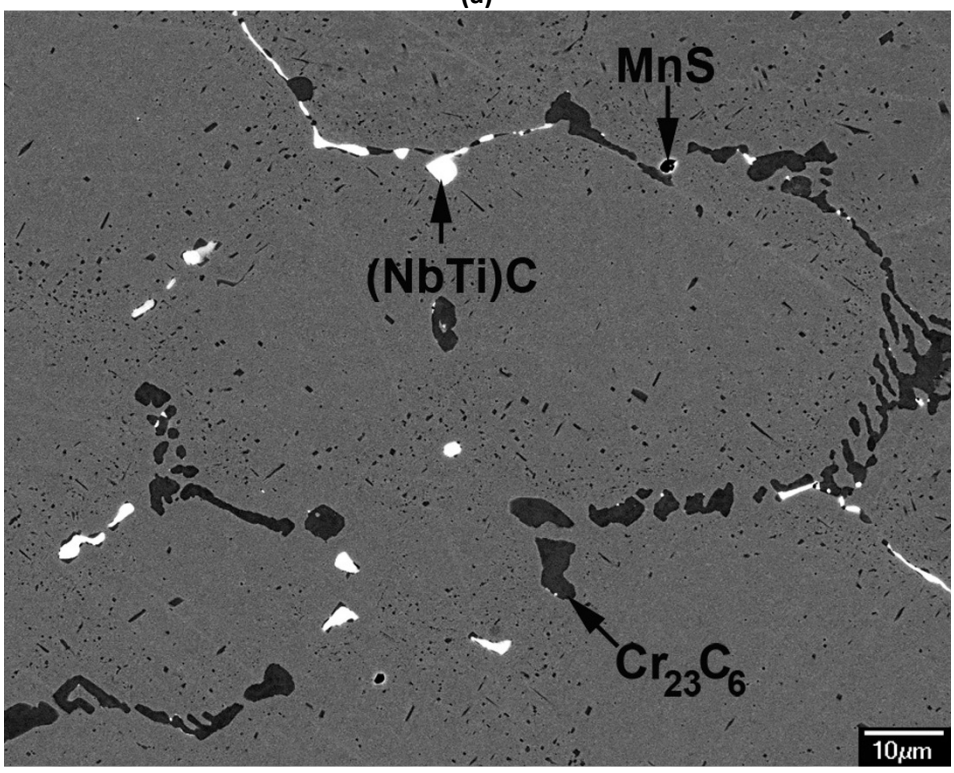

Figure 7.29 – Backscatter electron micrographs comparing the secondary precipitates in the (a) HP-Nb and (b) HP-NbTi alloys after ageing at 1000°C for 1000 hours.

7.5 Comparison of the HP-Nb and HP-NbTi Alloys Short-Term Creep Properties

As discussed in Chapter 1, the as-cast and isothermally aged HP-Nb and HP-NbTi samples (discussed in Chapters 4-8) were also subjected to accelerated creep testing at Quest Integrity Group's (QIG) Wellington laboratories. This accelerated testing was conducted independently of the microstructural analysis of the as-cast and aged samples performed at the University of Canterbury. The creep properties (e.g. creep ductility and rupture life) obtained from QIG's accelerated creep testing program forms the basis of their proprietary LifeQuest^{TM} Reformer software suite [24]. This software uses the HP-Nb and HP-NbTi alloys' long-term creep properties (generated from the aged samples) to predict the remaining life of service exposed reformer tubes based on creep strain measurements taken from each tube's inner and outer diameters. Since the remaining life prediction for each tube is heavily reliant on the creep properties obtained from QIG's accelerated creep testing of the aged HP-Nb and HP-NbTi samples, the results from this testing program were considered to be commercially sensitive. Thus, the relationship between the creep properties and microstructural evolution could not be published or discussed in this thesis.

All tube segments used for the microstructural analysis (presented in the current thesis) and QIG's accelerated creep testing program were aged without the application of any mechanically induced stress. However, isothermally ageing each alloy in the absence of stress is clearly not realistic in comparison to tubes in actual service, which typically experience stresses between 5-15MPa. For example, Peng *et al.* [25] determined that the application of stress during ageing increased the coarsening rate of intragranular MX precipitates in a 22Cr-25Ni-Mo-Nb-N alloy in comparison to material aged without stress. Since the dispersion strengthening effect provided by secondary precipitates is influenced by the average size and spacing of the precipitate distribution [26], the increased coarsening rate experienced by the secondary precipitates during stressed ageing will cause the material's creep resistance to decrease at a greater rate in comparison to the unstressed material. Hence, life predictions based solely on the creep data obtained from testing unstressed material will overestimate the creep resistance of material which experiences actual service exposure, unless some compensation is made.

Since the creep data derived from QIG's accelerated testing program on the samples subjected to unstressed isothermal ageing will be used to predict the remaining creep lives of service exposed tubes (i.e. where stress induced damage to the tubes life cannot be neglected), further creep testing was considered necessary to determine the creep properties of material that had experienced both simulated service creep conditions and unstressed ageing conditions. This testing will verify the hypothesis that the creep properties of service exposed HP alloy tubes can be accurately modelled using data produced from accelerated testing of samples that had been pre-aged without stress. If any significant discrepancy exists between the unstressed and stressed aged samples, this testing would provide compensative factors that could be applied in QIG's life prediction models.

Unfortunately, due to a series of major earthquakes that occurred in Christchurch between 2010 and 2012, only limited testing of aged unstressed samples was completed within the timeframe of the current project. No testing of aged stressed samples was possible. **Error! Reference source not found.** summarizes the accelerated creep testing conditions of the aged samples completed at the University of Canterbury. Clearly, a major objective of this project was not achieved, i.e., the comparison of unstressed and stressed materials. However, the state-of-the-art creep testing apparatus developed specifically for this project (Appendix B) revealed the considerable difference between the HP-Nb and HP-NbTi alloys' creep responses and enabled a comparison of the properties in context with the microstructural analysis presented in the current research.

Table 7.3 – Summary of the ageing and accelerated creep testing conditions used for the University of Canterbury creep testing program.

Alloy	Ageing Conditions		Accelerated Creep Testing Conditions		Number of Samples
	Temperature (°C)	Stress (MPa)	Temperature (°C)	Stress (MPa)	
HP-Nb1	1000	0	1030	17.5	4
HP-NbTi2	1000	0	1030	17.5	2

Accelerated testing of the aged samples was conducted at 1030°C and 17.5MPa (i.e. the same conditions used by Quest Integrity Group – Chapter 1). These temperatures and stresses were calculated to cause rupture of the specimens within 1000-3000 hours (based on the creep properties specified by each manufacturer – Appendix A). Such aggressive acceleration of the creep testing conditions (representing 1-3% of the tube actual service life) in order to obtain rupture of the creep samples within 3000 hours is commonly practiced when testing the HK and HP alloys [1, 26, 27].

Attempting to evaluate the accelerated creep testing conditions using deformation mechanism maps (similar to that shown for 316 stainless steel in Figure 7.30) to ensure that the deformation mechanisms (e.g. diffusional flow or power-law creep) during testing accurately replicated mechanisms experienced during service was not possible as deformation mechanism maps currently do not exist for the HK or HP alloys. Estimating the creep mechanisms within the HP-Nb and HP-NbTi alloys with respect to temperature and stress using deformation mechanism maps other nickel-based alloys was avoided as the significant microstructural differences between these alloys and the HP alloys (for example, equiaxed versus columnar grain structures; and the presence of secondary phases within the HP alloy) would likely cause such predictions to be grossly inaccurate.

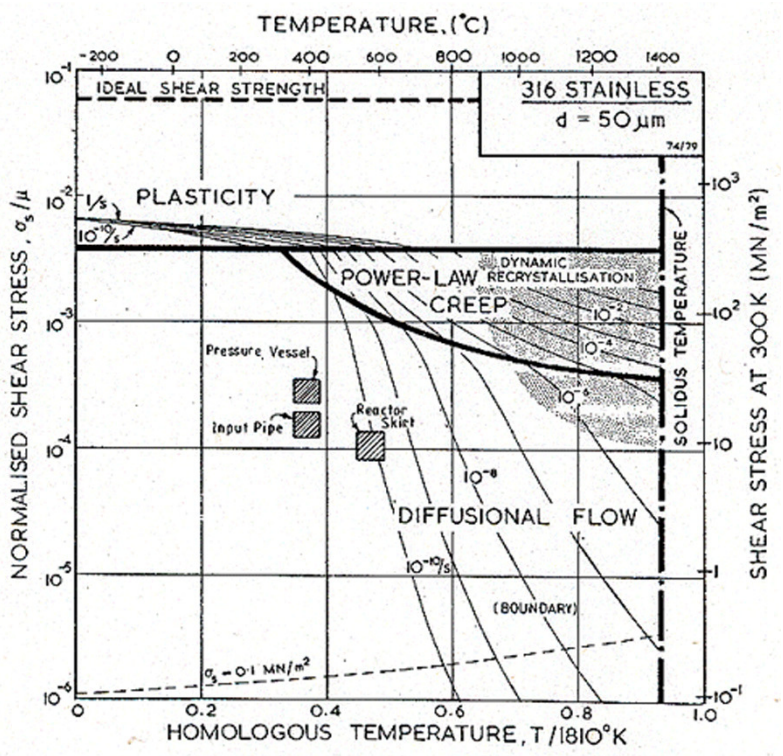

Figure 7.30 – Deformation mechanism map for 316 stainless steel with an average equiaxed grain size of 50μm (diameter) [28]

Accelerated creep testing of the aged HP-Nb1 and HP-NbTi2 alloys was carried out using creep testing apparatus shown in Figure 7.32. The design, manufacture and calibration of each testing apparatus (specifically for the current research) are presented separately in Appendix B. Setup and operation of each creep test was conducted in accordance to the guidelines set in ASTM E139 - Standard Test Methods for Conducting Creep, Creep-Rupture, and Stress-Rupture Tests of Metallic Materials [29].

Cylindrical dog bone type test samples (Figure 7.31 (b) and Appendix B) were machined from the mid-wall position of the aged HP-Nb1 and HP-NbTi2 tubes with the length of each sample running parallel to the tube's longitudinal direction (Figure 7.31 (a)). Prior to commencing each creep test, the gage length of the samples was polished using 9, 6, and 1µm diamond until the diameter of each sample's gauge length was 5 $^{+}/_{-}$ 0.01mm. The samples were subsequently ultrasonically cleaned in a bath of ethanol and dried thoroughly before placing four samples into the testing apparatus. Heating of the samples to the testing temperature was carried out at a rate of approximately 4.5°C/minute. Greater heating rates were not possible as it would have induced unacceptable thermal stresses within the isothermal furnace liner (or heat pipe) which surrounded the samples (Appendix B). Use of an isothermal furnace liner enabled the temperature within the entire furnace to be maintained at $1030^{+}/_{-}1$°C throughout the duration of each test. As specified in the ASTM standard, during heating, 15% of the total test load (~49.1N) was applied to each sample to ensure that the thermal expansion of the furnace insulation surrounding the load transfer rods did not significantly affect the axial application of the full testing load.

Prior to the application of the full testing load, the samples were held at the testing temperature (1030°C) for 30 minutes in order to normalize the temperature within the furnace chamber. The minimum 1 hour holding time recommended in ASTM E139 was considered to be detrimental for 2 reasons:

1. The primary creep response occurs rapidly and the test needs to commence as quickly as possible in order to measure these responses.
2. The isothermal furnace liner rapidly normalized the temperature within the chamber after 10-15 minutes of reaching the testing temperature causing such a prolonged holding period to be unnecessary.

During the holding stage the linear variable differential transducer (LVDT) extensometers were individually attached to each creep sample (as show in Appendix B). A tensile force of 343.5N was then applied to each sample (to achieve a tensile stress of 17.5MPa within each sample's gauge length) followed by zeroing of the LVDT extensometers. The samples' elastic response during loading was not recorded as only the plastic (i.e. creep deformation) response was required. The extension of each sample, chamber temperature (taken from two thermocouples) and room temperature was automatically appended to a .txt file at 10 minute intervals using data acquisition software developed

in LabVIEW[1]. This software provided real-time monitoring of each sample's extension and the furnace temperature and historical visualisation of the creep curve allowing the testing to be continuously monitored.

Post processing of creep data was performed using a combination of Microsoft Excel and a program developed in MATLAB[2]. These programs were used to plot the elongation of each sample with respect to time and to calculate each sample's minimum creep rate, creep ductility (elongation at fracture) and rupture time.

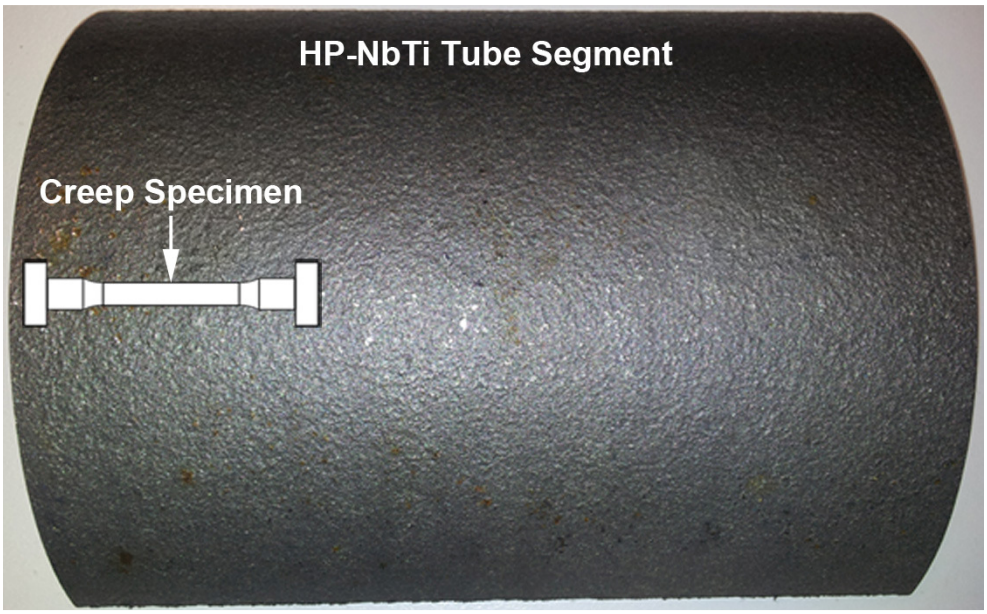

(a)

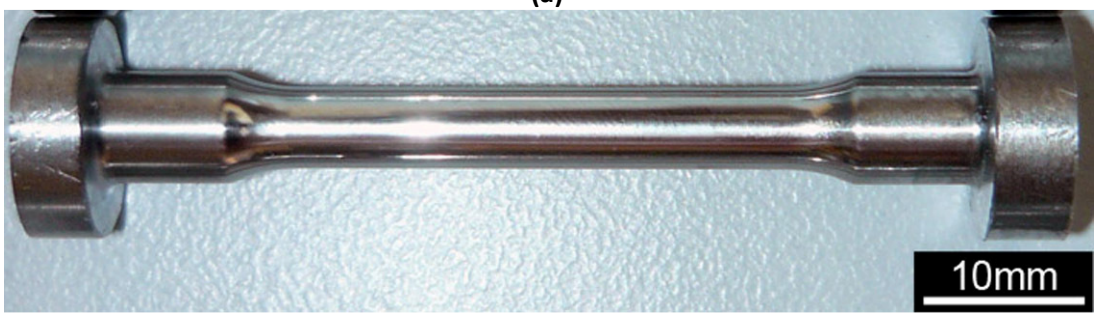

(b)

Figure 7.31 – (a) Segment of the HP-NbTi2 tube and overlaid schematic of the creep specimen showing the parallel orientation of the specimens gauge length with respect to the tubes longitudinal direction. (b) Standard creep specimen.

[1] LabVIEW System Design Software is a platform developed by National Instruments Corporation (Austin, Texas, U.S.A.) specifically for data acquisition and control systems.

[2] MATLAB is a software platform developed by MathWorks® (Natick, Massachusetts, USA) for numerical computation, visualization and programming.

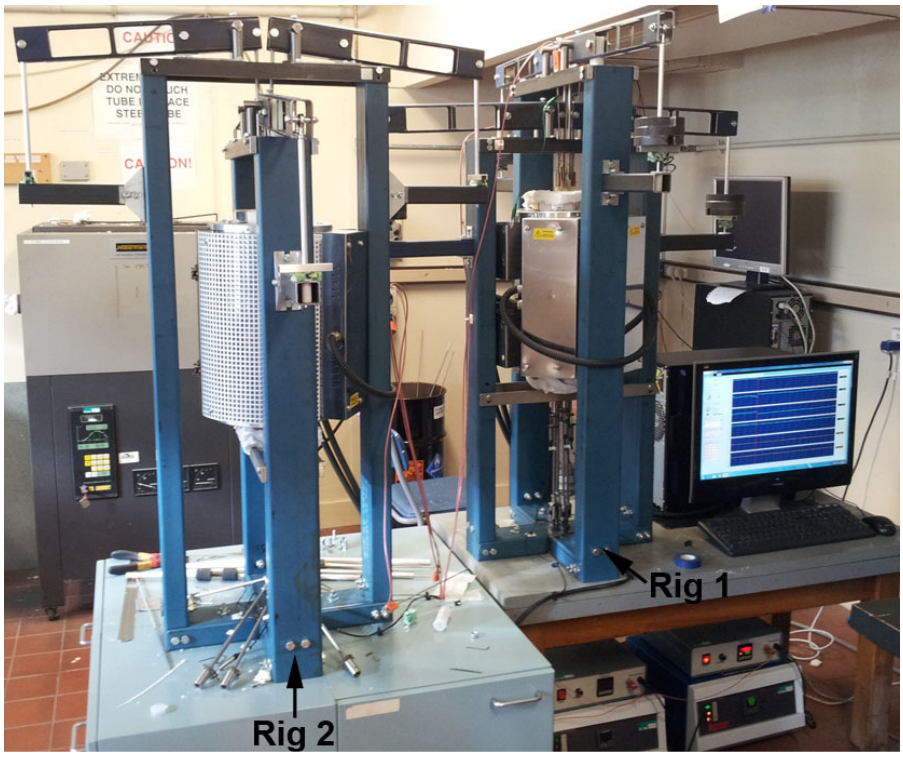

Figure 7.32 – Accelerated creep testing apparatuses.

Table 7.4 summarizes the rupture time, creep elongation and minimum creep rates measured from the HP-Nb1 and HP-NbTi2 alloys during testing at 1030°C and 17.5MPa. In general, the HP-Nb1 alloy exhibited significantly greater creep ductility and higher minimum creep rates. However, the HP-NbTi2 alloy exhibited a greater rupture life. Figure 7.33 shows representative examples of the HP-Nb1 (blue) and HP-NbTi2 (red) alloys' creep deformation plotted with respect to time where clear difference between each alloy's creep ductility, minimum creep rate and rupture life can be easily observed. The high creep ductility exhibited by the HP-Nb alloy was typically attributed to the significant creep deformation that occurred during tertiary creep.

Figure 7.34 directly compares the creep ductility and minimum creep rates for the HP-Nb and HP-NbTi samples. Both the creep ductility and minimum creep rate can be seen to be significantly greater for the HP-Nb samples in comparison to the HP-NbTi samples. Typically, the creep ductility for the HP-Nb alloy was between 18.2-18.6%. However, one sample's elongation was considerably greater at 29.7%. As shown visually in Figure 7.33, the HP-Nb alloys elongation largely occurred during tertiary creep with the samples' deformation during the primary and secondary creep stages typically contributing less than 10% of the HP-Nb alloys total elongation. In contrast, the HP-NbTi alloy's total creep ductility barely exceeded 10%. As shown in Figure 7.34, the HP-NbTi alloys

minimum creep rate was typically more than 50% lower than the HP-Nb alloys minimum creep rate. The time to rupture for the HP-NbTi alloy was between 50-135% greater than for the HP-Nb alloy.

Table 7.4 – Summary of the accelerated creep testing results measured from the HP-Nb1 and HP-NbTi2 alloys.

Alloy	Sample	Rupture Time (h)	Elongation (%)	Minimum creep rate (s-1)
HP-Nb1	1	2413.8	18.8	0.001
	2	1926	18.2	0.0014
	3	1814	29.7	0.0015
	4	2324.9	18.6	0.0014
HP-NbTi2	1	3608.3	7.9	0.0004
	2	4253.1	10.3	0.0006

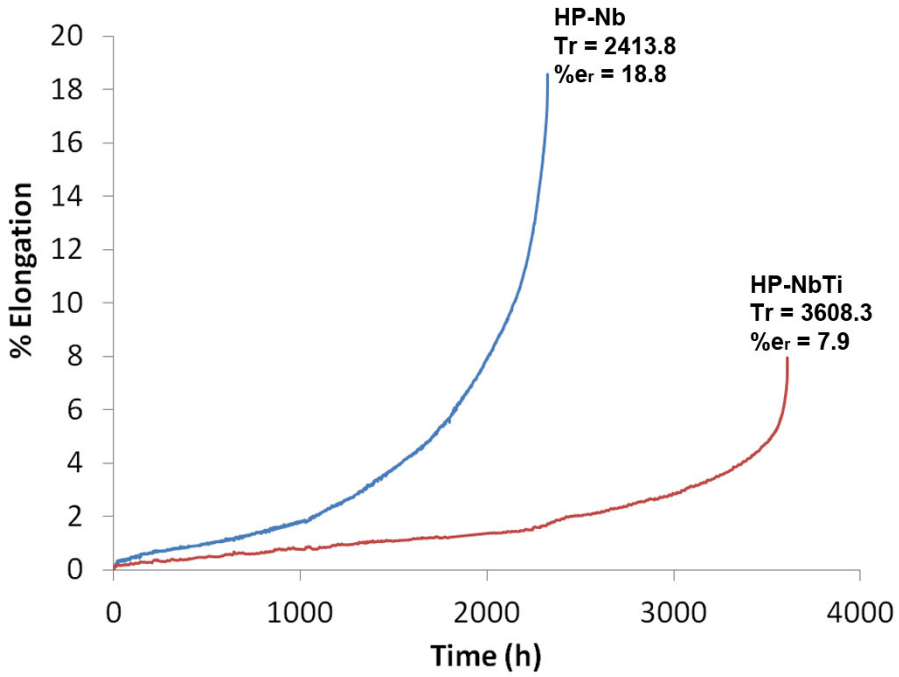

Figure 7.33 – Comparison of the HP-Nb and HP-NbTi alloys' creep response when testing at 1030°C and 17.5MPa.

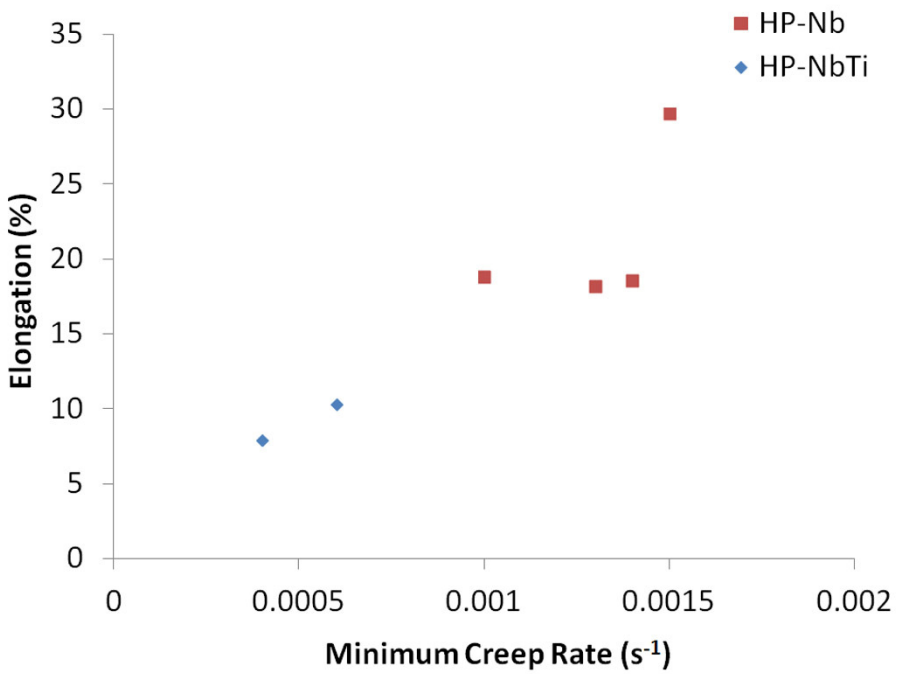

Figure 7.34 – Comparison of the HP-Nb and HP-NbTi alloys elongation and minimum creep rate when testing at 1030°C and 17.5MPa.

As discussed in Sections 7.2 to 7.4 the most significant difference between the aged HP-Nb and HP-NbTi alloys' microstructures when ageing at 1000°C was observed when comparing the niobium-rich primary and secondary precipitates. After ageing of the HP-Nb alloy at 1000°C for 1000 hours the lamellar NbC primary precipitates had partially transformed to η-carbides whereas the blocky (NbTi)C primary precipitates remained completely stable in the HP-NbTi alloy. Widespread precipitation of ~50nm niobium-rich secondary precipitates also occurred solely in the HP-NbTi alloy during ageing. In contrast, the size and distribution of the chromium-rich primary and secondary precipitates were relatively similar for each alloy regardless of the ageing time. Hence, the difference in each alloy's minimum creep rate and creep ductility as shown in Figure 7.33 and Figure 7.34 is believed to be largely attributed to the characteristics of the niobium-rich precipitates in each alloy.

Only a few previous studies have attempted to relate creep properties to inter- and intragranular precipitate phases in similar alloys. Hou and Honeycombe [1] attributed the IN519 (25Cr-25-Ni-Nb) and IN519TZ (25Cr-25-Ni-Nb-Ti-Zr) alloys' superior creep resistance in comparison to unmodified HK alloy largely to the fine distribution of intragranular MC precipitates that formed solely within the IN519 alloys. The mixed MC/$Cr_{23}C_6$ secondary precipitate distribution within the IN519 alloys reportedly provided greater resistance to creep dislocations in comparison to the $Cr_{23}C_6$ secondary precipitate distribution in the HK alloy. Previous work by Powel *et al.* [30, 31] reported that both the minimum creep rate and creep ductility became increasingly greater after subjecting a 20Cr-25Ni-Nb stainless steel to ageing at 650°C for 5000 and 10,000 hours. Although G-phase was identified on the grain boundaries of the alloy after ageing, the higher minimum creep rate and ductility was attributed to coarsening of the intragranular Nb(CN) precipitates during prolonged ageing. Thus, in the present study, the HP-NbTi alloy's lower minimum creep rate and creep ductility is attributed to a fine and relatively stable secondary precipitate distribution in comparison to the HP-Nb alloy.

Kakehi [32] reported a similar increase in the creep ductility and minimum creep rate exhibited by a single crystal nickel based superalloy after modifying the ageing and cooling conditions to alter the primary and secondary precipitate distributions. Slow furnace cooling of the alloy resulted in a matrix completely devoid of secondary γ' precipitates whereas force-air quenching of the material induced numerous secondary γ' precipitates within the matrix. Typically, the secondary γ' precipitate distribution was believed to have a greater effect on the alloy's creep strength in comparison to the primary γ' precipitates. Regardless of the crystallographic orientation with respect to the tensile load during accelerated creep testing, the minimum creep rate and creep ductility were greater for the

furnace cooled material, which did not contain secondary precipitates within the matrix. The creep ductility and minimum creep rates were reportedly greatest for the furnace cooled material when testing of the single crystal material was conducted with the <111> orientation parallel to the tensile load direction. The high creep rate and ductility within the furnace cooled material was attributed to the relative ease through which matrix dislocations glided through the furnace cooled material's precipitate-free matrix and the weak level of strain hardening within the matrix.

Interestingly, the creep ductility of an ex-service HP-Nb alloy reformer tube (70,000, ~920°C and 10MPa) during accelerated creep testing was consistently greater in comparison to the creep ductility observed when testing the HP-Nb alloy in the as-cast condition [26]. The secondary precipitate distribution was significantly coarser in the ex-service material in comparison to the material after the short-term thermal exposure typical of accelerated creep testing. However, in parallel to the coarsening of the secondary precipitates, the primary $Cr_{23}C_6$ precipitates had undergone significant coarsening and the NbC had partially transformed to η-carbide during service exposure, which did not occur to the same extent during accelerated testing of the as-cast material.

In general, decoupling the effects of the primary and secondary precipitates on the HP-Nb and HP-NbTi alloys creep properties is inherently difficult. Hou and Honeycombe [1] suggested the morphology of the primary precipitates played a role in determining the alloys creep ductility. The lamellar MC precipitates in the IN519 alloy were believed to give "greater opportunity" for the formation of creep voids and the subsequent growth of cracks in comparison to the blocky primary precipitates in the IN519TZ alloy. Shinoda *et at.* [6] independently observed the preferential void formation on the tips of the lamellar primary NbC precipitates in a HK-Nb alloy after accelerated creep testing at temperatures between 950-1100°C and stresses between 15-50MPa. The greater elongation of the HK-Nb (~9%) alloy in comparison to the plain HK alloy (~5%) was attributed to the relatively higher number of voids that formed in the modified alloy. Additionally, the prolonged tertiary creep stage exhibited by the HK-Nb alloy was attributed to the complex path through which these voids had to propagate within the colonies of lamellae in order to coalesce and form macroscopic cracks.

Figure 7.35 (a) and (b) show light optical micrographs taken from the failed HP-Nb and HP-NbTi creep samples. Metallographic samples were cut approximately 3mm from the fracture surface of the failed HP-Nb and HP-NbTi creep samples and prepared for metallographic analysis using the methods described in Chapter 3. In contrast to the analysis of creep voids in the HK-Nb and HK-NbTi alloys by

Shinoda *et al.* [6], the voids within the failed HP-Nb and HP-NbTi samples were almost always located between the $Cr_{23}C_6$ and austenite interfaces. While voids located between the NbC, η-carbide (HP-Nb) or (NbTi)C (HP-NbTi) and austenite interfaces were less commonly observed, these voids usually also shared an interface with a $Cr_{23}C_6$ precipitate. Rarely, creep voids located solely adjacent to the NbC, η-carbide or (NbTi)C precipitates were observed. Serial sectioning of an ex-service HP-NbTi alloy tube by Wahab and Kral [9, 10] determined that creep voids which appeared to share an interface with the (NbTi)C precipitates in two-dimensions typically encountered at least one $Cr_{23}C_6$ precipitate at some point along each void's perimeter in three-dimensions. Thus, the voids solely in contact with the NbC, NbC, η-carbide or (NbTi)C precipitates in the failed HP-Nb and HP-NbTi creep samples analyzed in the current study may have similarly come into contact with $Cr_{23}C_6$ precipitates out of the sectioning plane. The preferential location of voids between the $Cr_{23}C_6$ and austenite interfaces within both alloys suggests that the NbC and η-carbide precipitates did not significantly contribute to the HP-Nb alloy's greater ductility in comparison to the HP-NbTi alloy when testing each alloy at 1030°C and 17.5MPa.

Based on the preceding discussion, the HP-NbTi alloy's lower minimum creep rate during accelerated testing is believed to be largely attributed to the greater dispersion strengthening effect provided by this alloy's mixed $Cr_{23}C_6$-(NbTi)C secondary precipitate distribution in comparison to the HP-Nb alloy's $Cr_{23}C_6$ secondary precipitate distribution. The increased creep resistance of the HP-NbTi alloy's matrix resulting from the mixed $Cr_{23}C_6$-(NbTi)C secondary precipitate distribution possibly restricts the level of creep deformation that occurs in the regions of the matrix highly populated with secondary precipitates, thus forcing the creep deformation to largely be accommodated by the regions of the matrix that contain comparatively few secondary precipitates (e.g. the precipitate-free zones surrounding the primary precipitates). The greater concentration of creep deformation within limited regions of the matrix possibly leads to the overall reduction in the HP-NbTi alloy's macroscopic creep ductility in comparison to the HP-Nb alloy.

As discussed in Section 7.4.2, the niobium-rich secondary precipitates coarsened at a considerably slower rate in comparison to the $Cr_{23}C_6$ secondary precipitates when ageing at 1000°C. Thus, the dispersion strengthening effect provided by the niobium-rich precipitates in the HP-NbTi alloy during short-term accelerated creep testing would be expected to help maintain the HP-NbTi alloy's superior creep resistance during long-term ageing in comparison to the HP-Nb alloy. However, Ostwald ripening of the secondary $Cr_{23}C_6$ precipitate distributions in the HP-Nb and HP-NbTi alloys

during long-term ageing would be expected to result in an overall increase in each alloy's minimum creep rate and creep ductility. Since the effects of the η-carbide on the HP-Nb alloy's creep properties are relatively unknown, it is currently unknown if the progression of the NbC-to-η-carbide phase transformation will affect the HP-Nb alloy's creep properties.

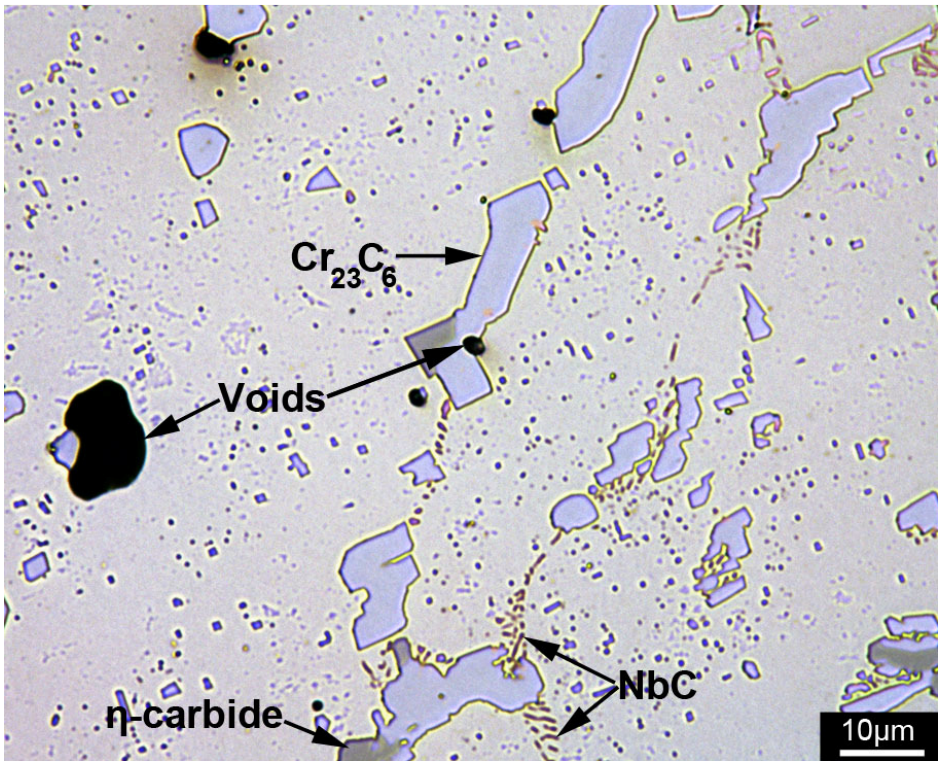

(a)

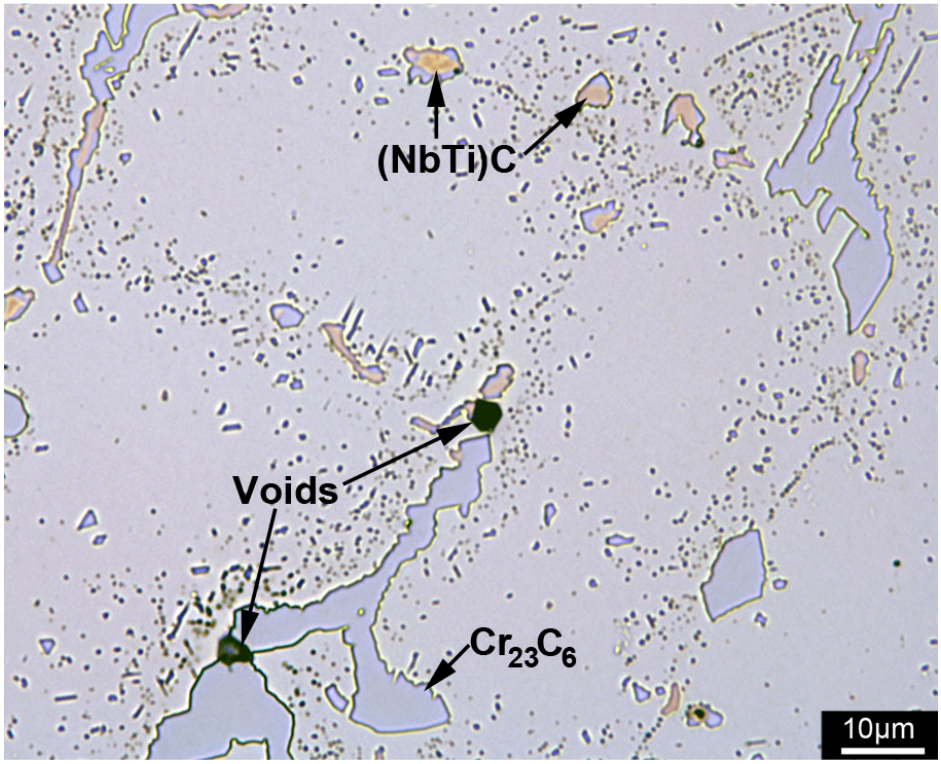

(b)

Figure 7.35 – Light optical micrographs of the failed (a) HP-Nb and (b) HP-NbTi creep samples showing the preferential formation of voids at the $Cr_{23}C_6$/austenite interface.

Summary and Conclusions

The as-cast HP-NbTi1 alloy was subjected to unstressed isothermal ageing at 1000, 1050 and 1100°C for 500, 1000, 3000, 6000 and 10,000 hours. Detailed characterisation of the aged HP-NbTi1 microstructures with respect to ageing temperature and time was carried out using a combination of OM, SEM, EDS, EBSD, TEM, and SAD. In agreement with the analysis performed on the aged HP-Nb alloys (Chapter 6), specific attention was also paid to the microstructural evolution at the mid-wall position of the HP-NbTi1 tube since the creep samples subjected to accelerated creep testing by Quest Integrity Group were taken from this region of the aged samples.

Many aspects of the HP-NbTi1 mid-wall microstructural evolution mirrored those observed in the HP-Nb alloys. The similarities mainly applied to the primary and secondary chromium-rich precipitates. Thus, several of the following points about the chromium-rich precipitates have already been summarized in Chapter 6. The evolution of the primary and secondary precipitates with time and temperature can be summarised as follows:

Primary Cr-rich precipitates

- The as-cast Cr_7C_3 completely transform to $Cr_{23}C_6$ within 1000 hours at all ageing temperatures. Further short-term ageing experiments (<24 hours) determined the Cr_7C_3-to-$Cr_{23}C_6$ transformation was complete within 6 hours when ageing at 1000°C.
- The primary $Cr_{23}C_6$ coarsened significantly during prolonged ageing. Generally, the coarsening rate increased with ageing temperature. No significant difference in the $Cr_{23}C_6$ coarsening rate with respect to ageing temperature was observed when comparing the HP-Nb and HP-NbTi alloys.
- The $Cr_{23}C_6$ precipitates were comprised of numerous grains typically with disorientations of less than 10°. Although rare, high angle disorientations (>15°) were also observed.
- The $Cr_{23}C_6$ commonly obtained a $[100]_{Cr23C6}//[100]_{\gamma}$ (cube-cube) OR with the austenite matrix. Analysis of the $Cr_{23}C_6$/austenite OR in the 1000°C-1000h and 1000°C-10,000h samples indicated the cube-cube OR became increasingly common with ageing time (57-67% respectively).
- Comparison of the $Cr_{23}C_6$ precipitates within the HP-Nb and HP-NbTi alloys indicated that these precipitates do not contribute to the HP-NbTi alloy's superior creep resistance.

Secondary Cr-rich precipitates

- Regardless of the ageing temperature, extensive secondary precipitation occurred within the austenite matrix. Short-term ageing experiments showed that the secondary precipitates were established within the first 6 hours of ageing.
- The scanning electron microscope level of resolution indicated that the precipitates were predominantly $Cr_{23}C_6$.
- The $Cr_{23}C_6$ precipitates were mainly concentrated within the austenite matrix directly adjacent to the primary precipitate network. The density of the secondary precipitates decreases with increasing distance from the primary precipitates. The preferential formation of the secondary precipitates adjacent to the primary network reportedly occurs due to the high dislocation density in these regions that is induced by the primary precipitates during casting.
- The secondary distribution became increasingly coarse with respect to ageing temperature and time.
- The gradual dissolution of the secondary $Cr_{23}C_6$ network during prolonged ageing due to Ostwald ripening supported the coarsening of the primary $Cr_{23}C_6$ network.
- Typically the precipitates obtained a cuboidal morphology, but Widmanstätten $Cr_{23}C_6$ precipitates (which were thought to have nucleated on the (NbTi)C/austenite interfaces) were also observed.
- Identical to the primary $Cr_{23}C_6$ precipitates, the secondary $Cr_{23}C_6$ obtained a $<100>_{Cr23C6}//<100>_{\gamma}$, $\{100\}_{Cr23C6}//\{100\}_{\gamma}$ OR with the matrix.
- No significant difference in the size and number of $Cr_{23}C_6$ secondary precipitates was observed when qualitatively comparing the aged HP-Nb and HP-NbTi alloys.
- Bright field TEM observations of the HP-NbTi1 samples identified the presence of 50 - 100nm Nb-rich particles within the cuboidal $Cr_{23}C_6$ precipitates.

As discussed in Chapter 5, the addition of titanium to the niobium-rich precipitates in the as-cast HP-NbTi alloys modified the lamellar morphology (observed in the HP-Nb alloys) to a blocky morphology. This change in the as-cast microstructure resulted in notable differences when comparing the evolution of the primary niobium-rich precipitates in the aged HP-Nb and HP-NbTi. The following summarises the evolution of the primary and secondary (NbTi)C precipitates in the HP-NbTi alloys:

Primary NbTi-rich precipitates

- In contrast to the HP-Nb alloys, the η-carbide transformation was not observed when ageing the HP-NbTi1 alloy at 1000°C.
- Aside from the 1050°C-10,000h aged sample, the (NbTi)C precipitates located at the mid-wall position remained completely stable in all other aged samples. The (NbTi)C precipitates in the 1050°C-10,000h sample transformed to Z-phase (NbCr(CN)) as a direct result of the air ageing atmosphere.
- Long-term ageing at 1000 and 1100°C caused the average size and area fraction of the (NbTi)C precipitates to increase. However, the coarsening rate of the (NbTi)C precipitates was considerably less when compared to the primary $Cr_{23}C_6$ precipitates.
- The as-cast blocky morphology remained relatively stable with respect to ageing temperature and time when viewed in two-dimensions.
- Extensive precipitation of $Cr_{23}C_6$ was observed between the (NbTi)C and austenite interfaces after ageing. These precipitates were believed to have predominantly originated from the as-cast interfacial Cr_7C_3 precipitates. Transformation of the as-cast Cr_7C_3 to $Cr_{23}C_6$ was believed to have occurred within the first 6 hours of ageing.
- The dendritic morphology characteristic of as-cast interfacial Cr_7C_3 precipitates was largely replaced by tetrahedral and wedge shaped $Cr_{23}C_6$ precipitates within the first 1000 hours of exposure (when viewed in three-dimensions). The $Cr_{23}C_6$/austenite interfaces exhibited similar faceting to the secondary matrix $Cr_{23}C_6$, suggesting the interfacial precipitates obtain the same {110} and/or {111} habit planes.
- The interfacial precipitates obtained the same $[100]_{Cr23C6}//[100]_{\gamma}$ OR as the primary and secondary $Cr_{23}C_6$ precipitates. However, small divergences (<3°) from the idea cube-cube OR was typically observed when performing SAD analysis of the interfacial $Cr_{23}C_6$.
- Irrespective of the ageing temperature, the interfacial precipitates were typically coarser than the secondary matrix precipitates after 10,000 hours.

Secondary NbTi-rich precipitates

- Secondary (NbTi)C precipitates similar in size to the $Cr_{23}C_6$ precipitates were observed using JEOL 7000F field emission scanning electron microscope but the number of (NbTi)C precipitates was insignificant in comparison to the $Cr_{23}C_6$ (<1% of the total secondary precipitate population).
- TEM analysis of thin foils determined the presence of 50-100nm NbTi-rich precipitates in the HP-NbTi alloys aged at 1000°C for 1000 and 10,000 hours and 1100°C for 1000 hours. These precipitates were below the limit of resolution in the FE-SEM.
- Although SAD and CBED analysis of the 50-100nm NbTi-rich precipitates failed to identify the crystal structure, the precipitates are believed to obtain the (NbTi)C ($Fm\bar{3}m$) crystal structure (based on previous reports of similar precipitates in the HK-NbTi alloys).
- The NbTi-rich precipitates were typically less than 50nm in diameter after ageing at 1000°C for 1000 hours. Marginal coarsening of these precipitates occurred during further ageing of the HP-NbTi1 at 1000°C with the average diameter typically between 50-100nm after ageing for 10,000 hours. The precipitates were believed to have completely dissolved after ageing at 1100°C for 10,000 hours.
- The 50-100nm NbTi-rich precipitates appeared to be present in similar abundance to the larger $Cr_{23}C_6$ precipitates in the 1000°C-1000h aged sample. The number of precipitates reduced during prolonged ageing at 1000°C.
- The common association of these precipitates with dislocations suggested the dislocations had acted as the nucleation sites for the (NbTi)C.

Overall the enhanced creep properties of the HP-NbTi alloy in comparison to the HP-Nb alloy are attributed to the formation of a nano-sized secondary (NbTi)C precipitate distribution in the HP-NbTi alloy. While the increased stability of the primary (NbTi)C precipitates in the HP-NbTi alloy in comparison to the primary NbC in the HP-Nb alloy during ageing may also contribute to the HP-NbTi alloys superior creep properties, significant further analysis of the susceptibility of G-phase and η-carbides precipitates to creep damage is necessary to determine the effects of these phases with respect to the HP alloys' creep properties.

Chapter References

[1] Hou, W. T. & Honeycombe, R. W. K. (1985). *Structure of Centrifugally cast austenitic steels: Part 2 Effects of Nb, Ti and Zr.* Materials Science and Technology, 1(5): pp. 390-397.

[2] de Almeida Soares, G. D., de Almeida, L. H., da Silveira, T. L. & Le May, I. (1992). *Niobium Additions in HP Heat-Resistant Cast Stainless Steels.* Materials Characterization, 29: pp. 387-396.

[3] de Almeida, L. H., Ribeiro, A. F. & Le May, I. (2003). *Microstructural Characterization of modified 25Cr-35Ni centrifugally cast steel furnace tubes.* Materials Characterization, 49: pp. 219-229.

[4] Davis, J. R. (Ed.). (2000). *ASM Specialty Handbook: Nickel, Cobalt and Their Alloys.* Materials Park, Ohio: ASM International.

[5] Kirchheiner, R. & Woelpert, P. (2001). *Niobium in centrifugally cast tubes for petrochemical applications.* Proceedings of the International Symposium Niobium, Orlando, U.S.A.

[6] Shinoda, T., Zaghloul, M. B, Kondo, Y. & Tanaka, R. (1978). *The Effect of Single and Combined Additions of Ti and Nb on the Structure and Strength of the Centrifugally Cast HK40 Steel.* Transactions of the Iron and Steel Institute of Japan, 18: pp. 139-148.

[7] Zaghloul, M. B., Shinoda, T. & Tanaka, R. (1977). *Relation between Structure and Creep Rupture Strength of Centrifugally Cast HK40 Steel.* Transactions of the Iron and Steel Institute of Japan, 17(1): pp. 28-36.

[8] Wu, X. Q., Jing, Y. G., Zheng, Z. M., Yao, W. Ke. & Hu, Z. Q. (2000). *The eutectic carbides and rupture strength of 25Cr20Ni heat-resistant steel tubes centrifugally cast with different solidification conditions.* Materials Science and Engineering A, 293: pp. 252-260.

[9] Wahab, A. A. & Kral, M. V. (2005). *3D analysis of creep voids in hydrogen reformer tubes.* Materials Science & Engineering A, 412: pp. 222-229.

[10] Wahab, A. A., Hutchinson, C. R. & Kral, M. V. (2006). *A three-dimensional characterization of creep void formation in hydrogen reformer tube.* Scripta Materialia, 55: pp. 69-73.

[11] Ribeiro, A. F., de Almeida, L. H., dos Santos, D. S., Fruchart, D. & Bobrovnitchii, G. S. (2003). *Microstructural modifications induced by hydrogen in a heat resistant steel type HP-45 with Nb and Ti additions.* Journal of Alloys and Compounds, 356-357: pp. 693-696.

[12] Andrén, H. -O., Rolander, U. & Lindahl, P. (1994). *Phase Compostion in Cemented Carbides and Cermets.* International Journal of Refractory Metals & Hard Materials, 12: pp. 107-113.

[13] Erneman, J., Schwind, M., Liu, P., Nilsson, J. -O., Andrén, H. -O. & Årgren, J. (2004). *Precipitation reactions caused by nitrogen uptake during service at high temperatures of a niobium stabilised austenitic stainless steel.* Acta Materialia, 52: pp. 4337-4350.

[14] Lewis, M. H. & Hattersley, B. (1965). PRECIPITATION OF $M_{23}C_6$ IN AUSTENITIC STEELS. Acta Metallurgica, 13: pp. 1159-1168.

[15] Beckitt, F. R. & Clark, B., R. (1967). *THE SHAPE AND MECHANISM OF FORMATION OF $M_{23}C_6$ CARBIDE IN AUSTENITE.* Acta Metallurgica, 15: pp. 113-129.

[16] Caballero, F. G., Imizcoz, P., Lopez, V., Alvarez, L. F. & Garcia de Andrés, C. (2007). *Use of titanium and zirconium in centrifugally cast heat resistant steel.* Materials Science and Technology, 23: pp. 528-534.

[17] Piekarski, B. (2001). *Effect of Nb and Ti additions on microstructure, and identification of precipitates in stabilized Ni-Cr cast austenitic steels.* Materials Characterization, 47: 181-186.

[18] Ibañez, R. A. P., Soares, G. D. A., de Almeida, L. H. & Le May, I. (1993). *Effects of Si Content on the Microstructure of Modified-HP Austenitic Steels.* Materials Characterization, 30: pp. 243-249.

[19] Barbabela, G. D., de Almeida, L. H., da Silveira, T. L & Le May, I. (1991). *Role of Nb in Modifying the Microstructure of Heat-Resistant Cast HP Steel.* Materials Characterization, 26:pp. 193-197.

[20] Berghof-Hasselbacher, E., Gawenda, P., Schorr, M. & Schutze, M. (2008). *Atlas of Microstructures.* St. Lous: Materials Technology Institute.

[21] Wahab, A. A. (2007). *Three-Dimensional Analysis of Creep Void Formation in Steam-Methane Reformer Tubes.* Unpublished doctoral dissertation, University of Canterbury, Christchurch, New Zealand.

[22] Hou, W. T. & Honeycombe, R. W. K. (1985). *Structure of Centrifugally cast austenitic steels: Part 2 Effects of Nb, Ti and Zr.* Materials Science and Technology, 1(5): pp. 390-397.

[23] Nunes. F. C., de Almeida, L. H., Dille, J., Delplancke, J. -L., Le May, I. (2007). *Microstructural Changes caused by yttrium addition to NbTi-modified centrifugally cast HP-type stainless steels.* Materials Characterization, 58: pp. 132-142.

[24] Quest Integrity Group (2013). *Reformer Care: A Complete Asset Integrity Solution.* Retrieved January 2013, from http://www.questintegrity.com/technology/steam-reformer-tube-inspection

[25] Peng, B., Zhang, H., Hong, J., Gao, J., Zhang, H. Li, J. & Wang Q. (2010). *The evolution of precipitates of 22Cr-25Ni-Mo-Nb-N heat-resistant austenitic steel in long-term creep.* Materials Science and Engineering A, 527: pp. 4424-4430.

[26] Thomas, C. W., Stevens, K. J. & Ryan, M. J. (1996). *Microstructure and properties of alloy HP50-Nb: comparison of as cast and service exposed materials.* Materials Science and Technology, 12: pp. 469-475.

[27] de Almeida Soares, G. D., de Almeida, L. H., da Silveira, T. L. & Le May, I. (1992). *Niobium Additions in HP Heat-Resistant Cast Stainless Steels.* Materials Characterization, 29: pp. 387-396.

[28] Frost, H. J., & Ashby, M. F. *Deformation-Mechanism Maps: The Plasticity and Creep of Metals and Ceramics* [website]. Retrieved February 2013, from http://engineering.dartmouth.edu/defmech/

[29] American Society for Testing and Materials. (2011). *Standard Test Methods for Conducting Creep, Creep-Rupture, and Stress-Rupture Tests of Metallic Materials.* ASTM E139-11, E28.04.

[30] Powell, D. J., Pilkington, R. & Miller, D. A. (1985). *Influence of thermal ageing on creep properties of a 20/25/Nb-stabilized steel.* Paper presented at the Stainless Steels '84 Conference and published in the Institute of Metals (Book n 320): pp. 382-390.

[31] Powell, D. J., Pilkington, R. & Miller, D. A. (1988). *Precipitation characteristics of 20%Cr/25%Ni-Nb stabilised stainless steel.* Acta Metallurgica, 36(3): pp. 713-724.

Chapter 8 Effects of the Ageing Atmosphere on the Microstructural Evolution of the HP-Nb and HP-NbTi

As-cast HP-Nb and HP-NbTi alloys were isothermally aged at 1000, 1050 and 1100°C in a furnace containing an air atmosphere for up to 10,000 hours. The use of an air atmosphere during ageing (as opposed to an inert atmosphere such as argon) caused significant decarburization and nitridation of the HP-Nb and NbTi alloys. This decarburization and nitridation induced multiple phase transformations at each tube's inner and outer diameters which generally did not occur at the mid-wall position. For example, Figure 8.1 (b) shows the HP-Nb1 1050°C-10,000h sample has a coarsened primary precipitate network and lack of the secondary precipitates that normally featured within the HP-Nb and HP-NbTi aged samples (Figure 8.1 (a)). For most samples, the effects of the air atmosphere were mainly confined to material adjacent to the free surfaces.

Comparative analysis of the affected and unaffected regions within the aged HP-Nb and NbTi samples determined that, depending on the ageing temperature, the furnace atmosphere induced the $Cr_{23}C_6$-to-$Cr_2(CN)$ and MC-to-Z-phase (NbCr(CN)) primary precipitate transformations and promoted the MC-to-η-carbide ($(CrNiNbSi)_6C$) transformation. The furnace atmosphere also accelerated dissolution of the secondary precipitates within the affected regions of both alloys. Regardless of the alloy and ageing temperature, the effects of the ageing atmosphere were mainly confined to within 1mm of the exposed surfaces after 1000 hours of exposure. While prolonged ageing caused the affected area to grow significantly, the affected area typically did not encroach on the microstructure within the creep samples' (which was machined approximately from the mid-wall position of the aged tubes) that were subjected to accelerated creep testing by Quest Integrity Group (separate from this thesis). However, precipitates located at the mid-wall positions in the 1050 and 1100°C 10,000 hour samples were affected by the air atmosphere (although to a lesser degree than at the surface, as shown in Figure 8.1). The HP-Nb1 and HP-NbTi1 1050 and 1100°C-10,000h samples were the only samples where the mid-wall microstructure was believed to be significantly affected by the furnace atmosphere.

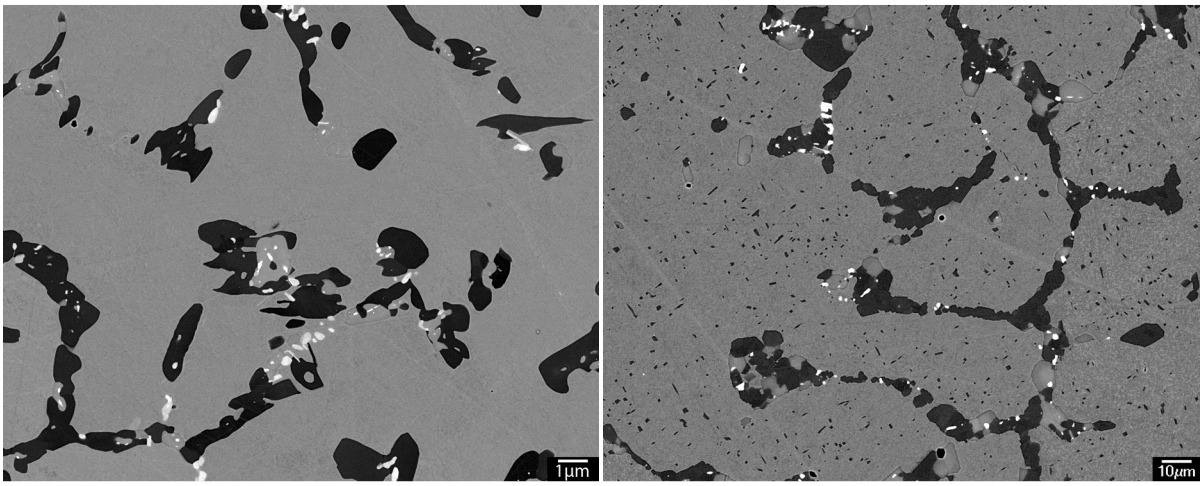

(a) **(b)**

Figure 8.1 – Backscatter electron micrographs comparing the (b) outer diameter and (a) mid-wall microstructures in the HP-Nb1 alloy after ageing at 1050°C for 10,000 hours.

As discussed in Chapters 6 and 7, Quest Integrity Group conducted accelerated creep testing on the aged HP-Nb and HP-NbTi samples. The samples were machined with the gauge length within the relatively unaffected mid-wall microstructures. Ultimately, the creep properties (e.g. minimum creep rate, rupture strength and creep ductility) measured from the aged samples is intended to augment Quest Integrity's LifeQuest^{TM} database [1]. This database is used by Quest when performing life assessments on HP-Nb and NbTi reformer tubes in order to predict each tube's remaining service life (as discussed in Chapter 1). As a result, in the current research effort was mainly placed on understanding the microstructural evolution at the mid-wall position of the HP-Nb and NbTi alloys. Thus, the separate microstructural (this thesis) and mechanical properties (Quest Integrity Group) studies could subsequently be used for the development of an understanding of the relationship between the HP alloy's microstructure and creep properties. In general, the microstructural evolution at the mid-wall position was thought to be more representative of the microstructural evolution that would occur within the HP-Nb and NbTi alloys during actual service in steam reforming furnaces (based on comparison with ex-service material [2]) as opposed to the evolution that was observed within the affected regions of the HP-Nb1, HP-Nb2 and HP-NbTi1 aged samples. The $Cr_2(CN)$, Z-phase and η-carbide phases induced by the furnace atmosphere during laboratory ageing have only very rarely been reported within ex-service HP-Nb and NbTi tubes [2, 3]. For example, of the ten tubes analyzed by Berghof-Hasselbacher *et al.*, these phases were only identified in three tubes all of which experienced service lives of greater 95,000 hours (10.8 years).

Although the identification of $Cr_2(CN)$, Z-phase and η-carbide phases in the literature was relatively rare, it must be noted that published studies on the microstructural analysis of ex-service tubes is relatively limited. Consequently, it is currently unclear if these phases form in similar abundance during service to what was observed in the laboratory aged samples. Since the $Cr_2(CN)$, Z-phase and η-carbide phases have been identified within ex-service HP-Nb and HP-NbTi tubes, it was considered important to characterize the phases observed within the affected regions of the laboratory aged HP-Nb1, HP-Nb2 and HP-NbTi1 alloys. It is also believed that these phases will become more commonly reported within ex-service HP-Nb and HP-NbTi tubes (particularly for tubes which have be operated at between 1000-1100°C) as the number comprehensive studies conducted on tubes nearing the end of their service life increases (which typically ranges from 50,000-150,000 hours [2]). Thus, any insight gained from the analysis of the phases within the affected regions of the laboratory ageing aged samples will also become increasingly important.

It is also important to realise that these phases will form during the time frame of a typical accelerated creep test (1000-2000 hours) if an air atmosphere is present within the furnace. As these phases will likely affect the samples creep resistance, it is necessary to determine if the extent to which the atmosphere modifies the microstructure during accelerated testing (e.g. number of phase transformations, penetration depth and area fraction of each phase) is sufficient to cause the testing to become unrepresentative of the tubes actual creep resistance during service in steam-methane reforming furnaces.

The following chapter details the analysis performed on the affected regions in the HP-Nb1, HP-Nb2 and HP-NbTi1 aged samples. Analysis of the affected microstructures was predominantly carried out using the optical and scanning electron microscopes, with a combination of EDS and EBSD used to identify of the phases present in each sample. Although the analysis performed on these atmosphere-affected regions of the tubes was not as comprehensive as the mid-wall position, significant effort was made to identify the types of phase transformations which were induced by the furnace atmosphere, the factors influencing these transformations, and the depth of penetration for each phase with respect to ageing temperature and time. It must be noted that the microstructural evolution in the HP-Nb and HP-NbTi alloys as a result of the furnace atmosphere was relatively complex and consequently is often difficult to follow. Figure 8.12, 8.17, 8.19 and 8.22 are intended to provide a pictorial overview to assist the reader with understanding the region of affected material and the phases that exist within the affected region.

8.1 Overview of the Affected Area with the HP-Nb and HP-NbTi Aged Samples

The effects of the furnace atmosphere on the microstructures at the inner and outer diameter positions of the HP-Nb1, HP-Nb2 and HP-NbTi1 tubes was first observed after ageing at 1000, 1050 and 1100°C for 1000 hours. The exposure of each alloy to the air atmosphere during the first 1000 hours of ageing typically resulted in the dissolution of the primary and secondary precipitates within 200µm of the exposed surfaces followed by the transformation of the primary chromium and niobium rich carbides to nitrides and accelerated the Ostwald ripening of the secondary precipitates within a band approximately 200-500µm from the exposed surfaces (depending on the ageing temperature). Continued ageing intensified the abundance of the nitride phases within the already affected regions and also caused the transformation of the primary chromium and niobium-rich precipitates from carbides to nitrides to occur at increasingly greater distances from the exposed surfaces.

Initial observations of the affected area strongly suggested the dissolution of the primary precipitates directly adjacent to the exposed surfaces and carbide-to-nitride primary phase transformations were a direct result of the oxygen and nitrogen rich furnace atmosphere. However, due to the centrifugal casting technique, variations in the as-cast tubes grain structure and chemical composition were known to exist with respect to wall position (Chapters 4, 5). Although it was considered unlikely the unique phase transformations at the inner and outer diameter were a result of any casting induced compositional variance, it was necessary to confirm that none of these wall position dependent phase transformations were related to the casting process. Fortunately, as shown schematically in Figure 8.2, both the HP-Nb1 and HP-NbTi1 samples aged at 1050°C for 10,000 hours contained affected regions which spanned the across the tubes wall thickness. This region allowed for the phases in both the affected and unaffected regions to be analysed while keeping the wall position constant (i.e. removing any influence of wall position on the microstructural evolution).

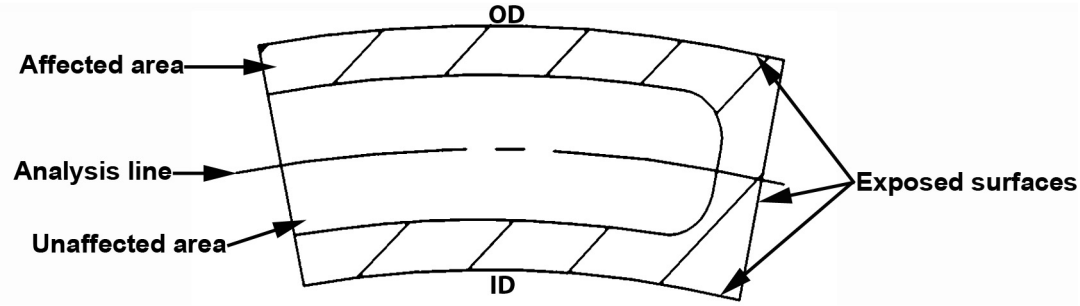

Figure 8.2 – Schematic showing the affected region observed in the HP-Nb1 and HP-NbTi1 1050°C-10,000h samples

Analysis of the 1050°C-10,000h samples confirmed that the transformation of the primary chromium and niobium rich carbides to nitrides and the accelerated Ostwald ripening of the secondary precipitates was a direct result of the exposure each alloy to the oxygen-nitrogen rich furnace atmosphere during ageing. Further analysis of the HP-Nb and HP-NbTi aged samples determined that the affected material at the inner and outer diameter positions could be separated into two distinctly different zones which are shown schematically in Figure 8.3 (a). For the purposes of this thesis, the two separate affected zones will be referred to as Zones A-I and A-II (where A-I and A-II abbreviate affected zones 1 and 2 respectively). The unaffected region of the tubes (i.e. the mid-wall position discussed in Chapters 6 and 7) will be referred as Zone UA (where UA abbreviates unaffected). Figure 8.3 (b) to (d) give representative backscatter electron micrographs of the markedly different microstructures observed within Zones A-I, A-II and UA respectively. The general characteristics of each zone can summarized as follows:

Zone A-I – All aged HP-Nb and HP-NbTi samples exhibited a thin band (typically <0.2mm) directly adjacent to the exposed surfaces where the primary and secondary chromium carbides had completely dissolved and only spheroidized Z-phase (NbCr(CN)) precipitates remained when ageing at 1000 and 1050°C. When ageing at 1100°C, only spheroidized NbC or (NbTi)C precipitates (commonly referred to as MC) remained present within Zone A-I. A chromium-rich oxide scale along the exposed surfaces and silicon-rich oxides extending from the exposed surfaces into the austenite matrix were typical of Zone A-I. The formation of these oxides caused the concentration of chromium and silicon remaining in the matrix within Zone A-I to be significantly lower in comparison to Zones A-II and UA (typically 25-40% less Cr and 75-80% less Si). Regardless of the ageing temperature and

time, the width of Zone A-I typically remained between 200-300µm. Detailed discussion of Zone A-I with respect to ageing temperature and time will be presented in Section 8.2.

Zone A-II – Defined as the regions of the tube where the furnace atmosphere caused the primary $Cr_{23}C_6$ and MC phases to transform to the nitrogen-rich $Cr_2(CN)$ and NbCr(CN) or (NbTi)Cr(CN) (commonly referred to as Z-phase [4]) phases (depending on the ageing temperature). The MC/η-carbide transformation and Ostwald ripening of the secondary precipitates was also accelerated in the region of the tubes affected by the furnace atmosphere. Since the number of primary phase transformations observed within Zone A-II was dependent on the ageing conditions, the size of Zone A-II has been defined here as the maximum depth (measured from the Zone A-I/A-II interface) at which the transformation of either the primary carbides ($Cr_{23}C_6$ and/or MC) to nitrogen-rich phases was observed. Zone A-II continuously increased in size with increasing exposure time and was generally significantly larger (between 2-6mm depending on the ageing conditions) in comparison to Zone A-II. Detailed analysis and discussion of the phase transformations which occurred in Zone A-II with respect to the alloy content and ageing conditions will be presented in Section 8.3.

Zone UA – Defined as the unaffected mid-wall region of the aged samples where no atmosphere induced phase transformations occurred or modification to other microstructural features (such as the accelerated dissolution of the secondary precipitates) could be distinguished. Detailed analysis of Zone UA was presented in Chapters 6 and 7.

In general, the types of phase transformations observed within the affected area appeared to be dictated by the ageing temperature and relatively independent of the alloying content. For example, ageing at 1050°C for 10,000 hours caused the $Cr_{23}C_6$-to-Cr_2N, MC-to-Z-phase (NbCr(CN)) and MC-to-η-carbide transformations to occur within the affected area of both the HP-Nb1 and HP-NbTi1 alloys. However, the depth to which each phase transformation occurred was influenced by the alloying content. For example, the MC-to-η-carbide transformation typically occurred more readily (and consequently was observed to a greater depth) in the HP-Nb alloy in comparison to the HP-NbTi alloy, whereas the opposite was true for the MC/Z-phase transformation. Due to the similarities between the atmosphere affected regions of the aged HP-Nb and HP-NbTi alloys, the two alloys will be discussed in parallel in this chapter as opposed to the previous chapters, which separately presented the as-cast and mid-wall aged microstructures specific to each alloy.

The analysis of Zones A-I and A-II presented in Sections 8.2 and 8.3 only considers the microstructural modification that was believed to be caused by the exchange of elements between the furnace atmosphere and the tubes inner and outer diameter surfaces (i.e. all analysis was performed on sections of the tube where the influence of the additional mid-wall exposed surface shown in Figure 8.2 was considered to be negligible). Analysis of material within 5mm of this additional exposed surface would artificially increase the thickness of the affected regions at the tube's inner and outer diameter positions in comparison to sections of the aged samples at distances greater than 5mm from this additional surface. Since this additional surface would not be exposed in an actual tube, the microstructural modifications caused solely by the exposure of the inner and outer diameter surfaces to the furnace atmosphere was considered to be more representative of the evolution which would occur if a complete (un-sectioned) tube was aged in an air atmosphere. Hence, this section of the aged samples was not included when determining the properties of each zone with respect to ageing temperature and time, even though the exposed surface spanning across the mid-wall position was initially used to identify the phases induced by the furnace atmosphere.

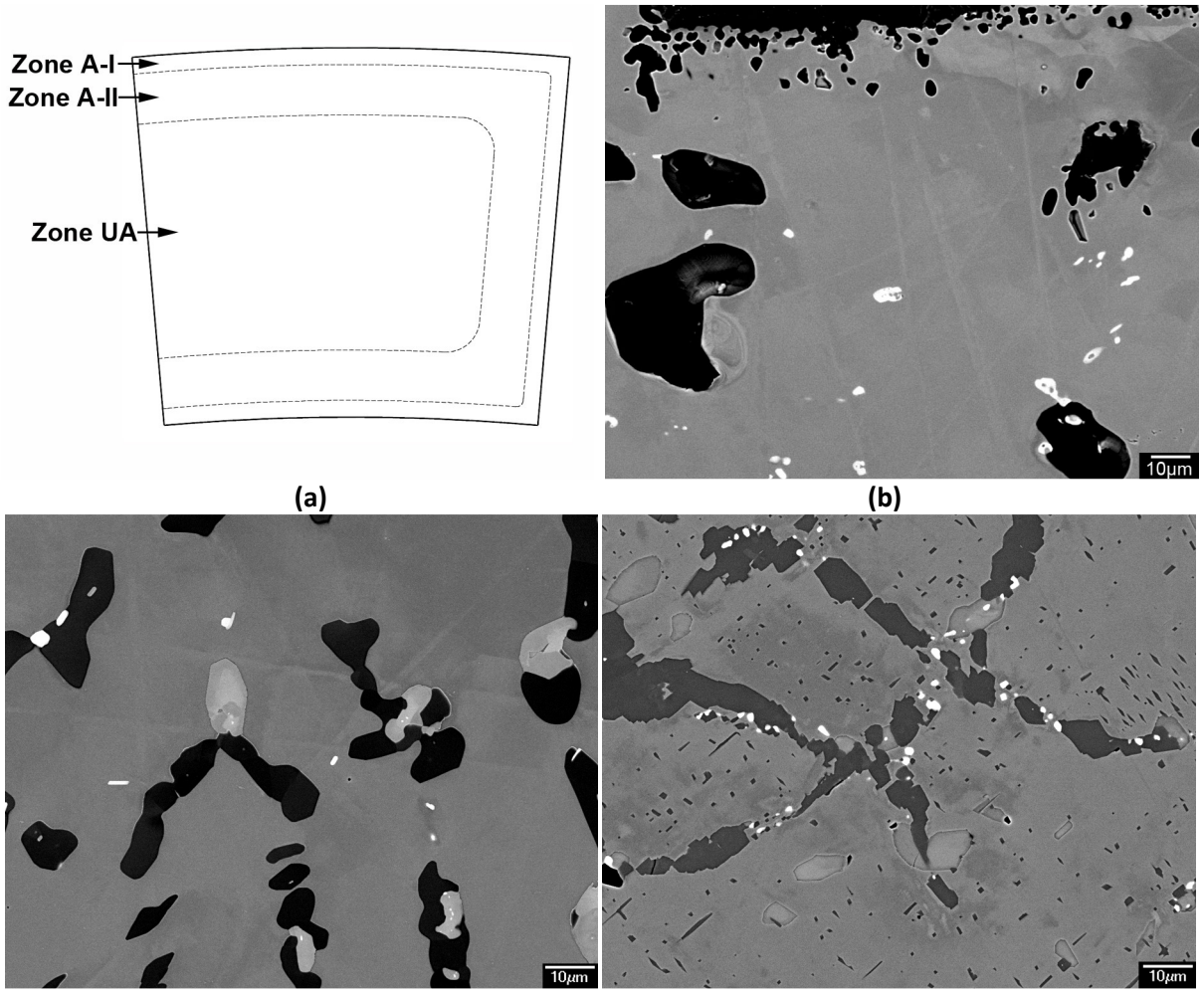

Figure 8.3 – (a) Schematic depicting the three unique regions which formed within the HP-Nb and HP-NbTi alloys as a result of ageing in an air atmosphere. (b) - (d) Backscatter electron micrographs showing representative examples of Zone A-I, Zone A-II and Zone UA in the HP-NbTi1 1050°C-10,000h aged sample respectively.

8.2 Zone A-I

As stated in Section 8.1, Zone A-I was defined as the material directly adjacent to the exposed surfaces were the chromium-rich primary and secondary chromium carbides completely dissolved leaving only spheroidized Z-phase or MC precipitates. The low magnification backscatter electron micrographs shown in Figure 8.4 (a) to (d) give representative examples of Zone A-I in the HP-Nb1, HP-Nb2 and HP-NbTi1 aged samples. The dimensions given in Figure 8.4 (a) to (d) indicate the approximate average size of Zone A-I in each alloy. The size of Zone A-I in the HP-Nb1 and HP-Nb2 alloys (100% columnar grain structures) typically ranged between 150-250µm in thickness and was relatively constant regardless of the ageing conditions and wall position. In contrast, the size of Zone A-I in the HP-NbTi1 (80% columnar, 20% equiaxed grain structure) alloy remained constant with respect to the ageing conditions but varied with respect to wall position. The average thickness of Zone A-I at the outer diameter (i.e. the region of the tube which contained columnar grains) was similar to the HP-Nb alloys (150-250µm). However, the equiaxed grain structure located at the HP-NbTi1 tubes inner diameter reduced the average thickness of Zone A-I to range between 100-150µm (Figure 8.4 (c)). The reduced thickness of Zone A-I at the inner diameter of the HP-NbTi1 samples is believed to be related to the fallout of entire equiaxed grains which increased the oxide spalling rate at the inner diameter. Rarely, regions of greater thickness (typically between 200-400µm - Figure 8.4 (b)) were observed at the outer diameter of both alloys.

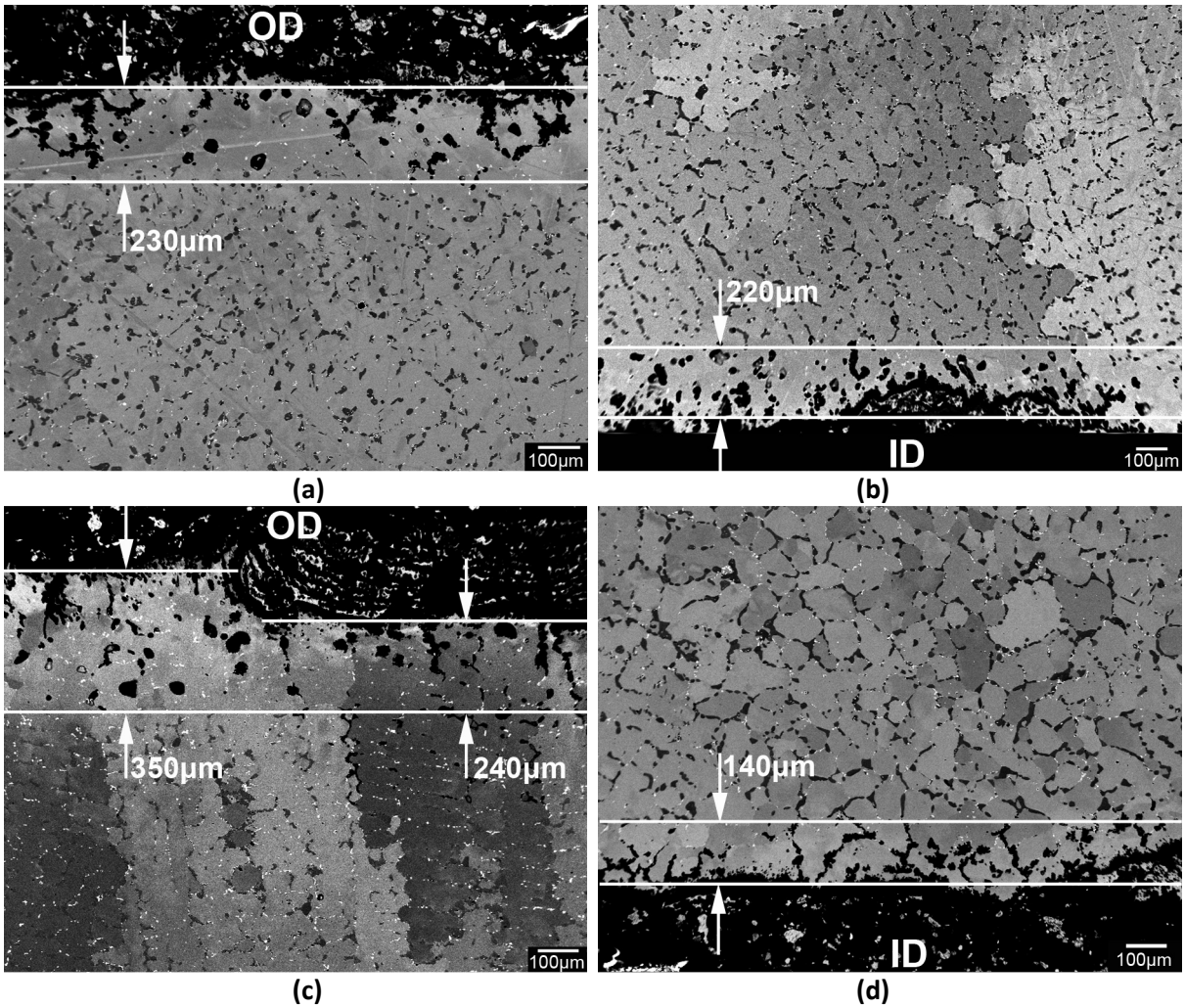

Figure 8.4 – Low magnification backscatter electron micrographs showing the representative examples of Zone A-I taken at the outer and inner diameter of the (a) & (b) HP-Nb1 1100°C-10,000h and the (b) & (c) HP-NbTi1 1100°C-10,000h aged samples respectively.

Figure 8.5 (a) and (b) show representative backscatter electron micrographs of Zone A-I in the HP-Nb and HP-NbTi aged samples. In the as-cast condition, the interdendritic network of Cr_7C_3 and NbC/(NbTi)C (or MC) precipitates extends to the inner and outer walls of the HP-Nb and HP-NbTi tubes. However, ageing of the HP-Nb and NbTi alloys within the air atmosphere resulted in the complete absence of the primary and secondary chromium carbides within Zone A-I (regardless of the ageing temperature). As shown in Figure 8.5 (a), only spheroidized niobium-rich precipitates remained within Zone A-I after ageing (arrowed). Ageing of the HP-Nb and HP-NbTi alloys at 1000 and 1050°C caused the as-cast primary MC precipitates located within Zone A-I to transform to Z-phase within the first 1000 hours (NbCr(CN)-see Section 0). The tetragonal (*P*4/*nmm* O2) Z-phase crystal structure remained stable within Zone A-I during prolonged ageing of both alloys at 1000 and

1050°C. Conversely, the MC ($Fm\bar{3}m$) crystal structure (present in the as-cast condition) remained completely stable when ageing at 1100°C.

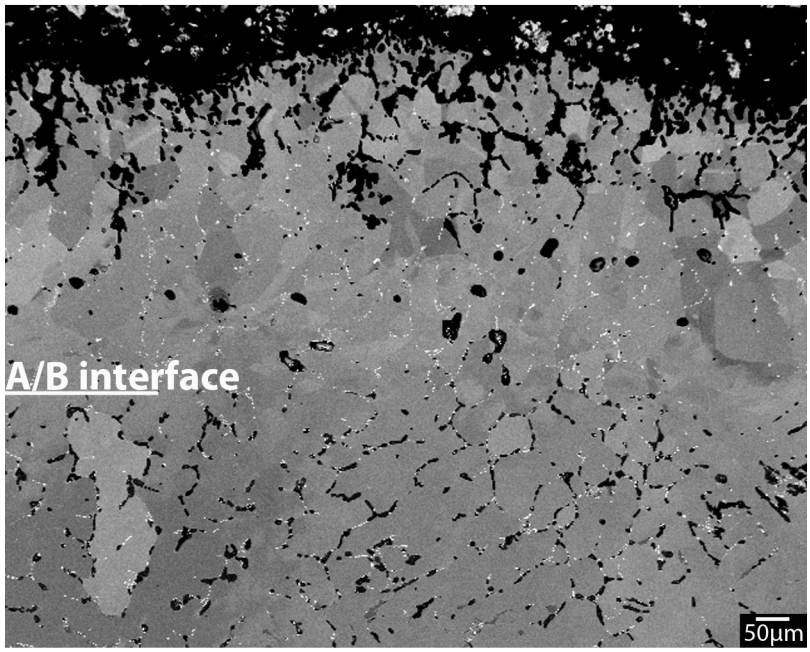

(a)

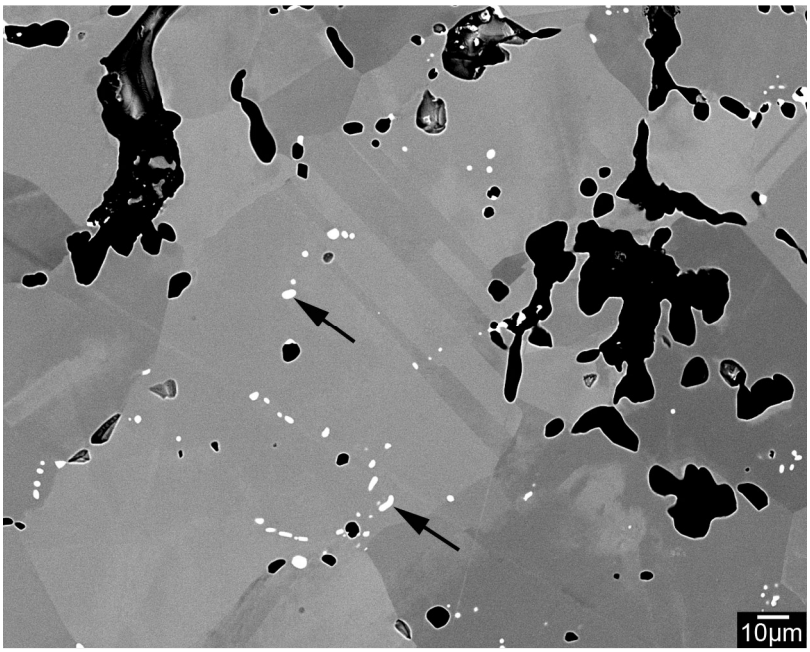

(b)

Figure 8.5 – Backscatter electron micrographs of Zone A-I in the HP-Nb and HP-NbTi aged samples showing (a) & (b) the complete absence of the chromium carbides (dark grey in (a)) within Zone A-I and the remaining niobium-rich precipitates (arrowed).

Figure 8.6 shows representative examples of the chromium and silicon rich oxide scales observed at the exposed surfaces of the HP-Nb and HP-NbTi alloys. EDS was used to determine the chemical composition of the oxides in all aged samples (Figure 8.7 (a) and (b)). Generally the composition of the oxides in the all of the aged samples matched the compositions reported for the Cr_2O_3 and SiO_2 crystal structures identified in similar studies conducted on HP alloys [5-7]. Regardless of the ageing conditions, the Cr_2O_3 was typically confined to the surfaces of the HP-Nb and HP-NbTi aged samples (Figure 8.6). The thickness of the Cr_2O_3 layer appeared relatively non-uniform along the surfaces of the aged HP-Nb and HP-NbTi metallographic samples. This variance was due to the spallation of the Cr_2O_3 layer during cooling of the samples from all ageing temperatures. In contrast to surface confined chromium-rich oxide layer, the silicon-rich oxides were typically present below the Cr_2O_3 layer and extended into the austenite matrix. Because the SiO_2 often exhibited a dendritic appearance similar to the as-cast Cr_7C_3 precipitates (Figure 8.6), it is possible that these oxides replaced the interdendritic primary Cr_7C_3 precipitates which completely dissolved in Zone A-I during ageing at 1000, 1050 and 1100°C.

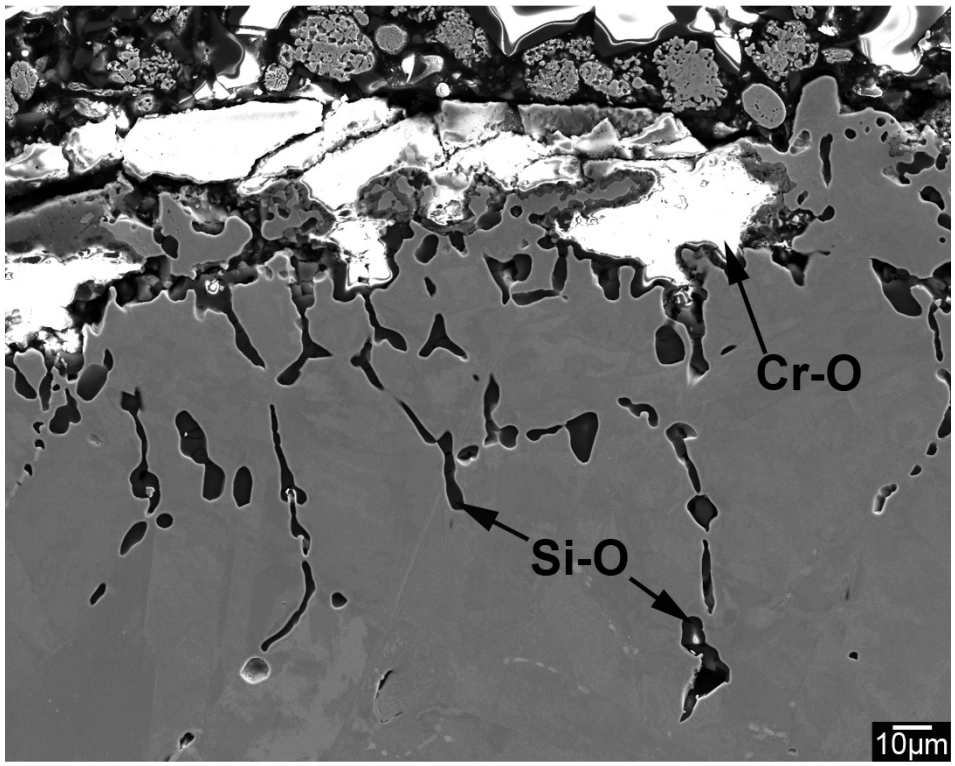

Figure 8.6 – Secondary electron micrograph showing the silicon and chromium rich oxides observed at the exposed surfaces of the HP-Nb and HP-NbTi alloys.

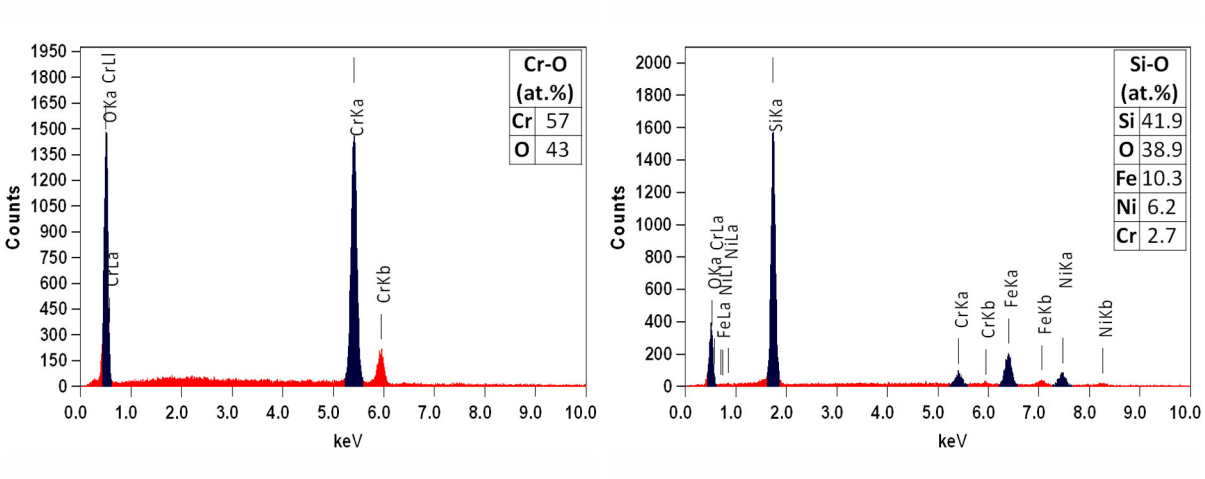

(a) **(b)**

Figure 8.7 – EDS spectra taken from the (a) chromium-rich and (b) silicon-rich oxides shown in Figure 8.6.

As show in Figure 8.5 (a) and (b), the chromium-rich primary and secondary precipitates were completely absent within Zone A-I after exposure of the HP-Nb and HP-NbTi alloys to 1000, 1050 and 1100°C for 1000 hours. Dissolution of these precipitates is believed to be caused by the significant loss of chromium from the austenite matrix due to the formation of the Cr_2O_3 oxide scale at the exposed surface. As shown in Table 8.1, the concentration of chromium in the austenite matrix was significantly reduced in Zone A-I in comparison to Zone UA supporting the idea that the formation Cr_2O_3 oxide layer caused the dissolution of the chromium rich precipitates (Table 8.1). Additionally, the formation of SiO_2 within Zone A-I reduced the concentration of silicon in the surrounding austenite matrix relative to the silicon concentration observed in Zone UA. The chemical composition of the austenite matrix within Zone A-I remained relatively constant regardless of the ageing temperature and time indicating that any chromium and silicon which diffused from the mid-wall position to Zone A-I was likely consumed by the continuous growth of the oxide scales during ageing.

Table 8.1 – Comparison of the average chemical composition of the austenite matrix at Zone A-I and Zone UA as determine by energy dispersive X-ray spectroscopy.

at.%	Ni	Fe	Cr	Si
Zone A-I	41.5	43.5	14.4	0.7
Zone UA	35.1	40.2	22.0	2.7

Interestingly, twinning of the austenite grains within Zone A-I was common in all aged samples (arrowed in Figure 8.8). These twins were not observed within Zone A-II or at the mid-wall position of the aged samples (i.e. they were solely confined to Zone A-I). Moreover, twinning of the austenite grains at the outer and inner diameter was not clearly apparent in the as-cast condition. The cause of these twins within Zone A-I is currently unknown.

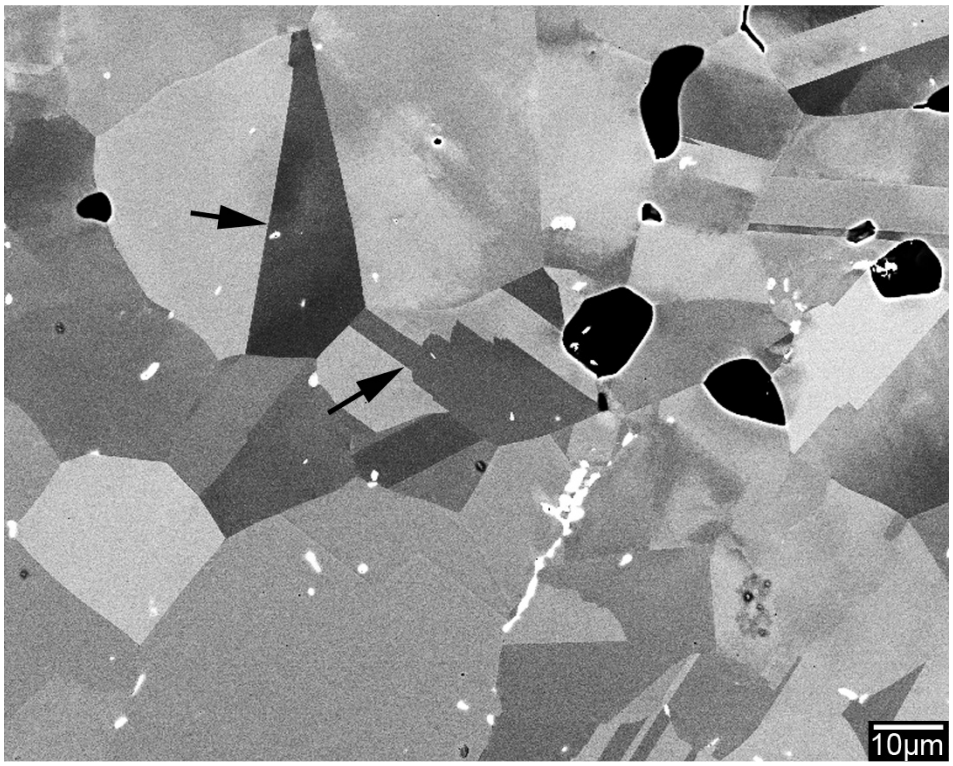

Figure 8.8 – Backscatter electron micrograph showing representative examples of the twinning commonly observed within the austenite grains located in Zone A-I of the aged HP-Nb and HP-NbTi samples.

8.3 Zone A-II

As stated in Section 8.1, Zone A-II was defined as the regions of the tube where the furnace atmosphere caused the progressive transformation of the chromium and niobium rich primary carbides to nitrides and accelerated dissolution of the secondary $Cr_{23}C_6$ precipitates. The evolution of Zone A-II was comparatively more complex than Zone A-I as the size and number of phases within Zone A-II was dependent on the ageing temperature and time. Analysis of the HP-Nb1, HP-Nb2 and HP-NbTi1 aged samples with respect to the ageing temperature and time determined that the following primary phase transformations were induced by the furnace atmosphere:

Ageing at 1000 and 1050°C

NbC	→	NbCr(CN)	Z-phase	(HP-Nb1 and HP-Nb2)
(NbTi)C	→	(NbTi)Cr(CN)		(HP-NbTi1)
(NbTi)C	→	η-carbide		(HP-NbTi1)

Ageing at 1000, 1050 and 1100°C

$Cr_{23}C_6$	→	$Cr_2(CN)$	(all alloys)

In contrast to the HP-NbTi alloys, the NbC-to-η-carbide transformation occurred independently of the furnace atmosphere at the mid-wall position of the HP-Nb alloy (Chapter 6). However, the furnace atmosphere accelerated the NbC-to-η-carbide phase transformation within the Zone A-II of the HP-Nb2 and HP-Nb1 alloys during ageing at 1000 and 1050°C respectively. For all three alloys, accelerated of the dissolution of the secondary $Cr_{23}C_6$ precipitates was also observed within Zone A-II (in comparison to the dissolution occurring at the mid-wall position).

Sections 8.3.1- 8.3.3 present detailed discussion of the $Cr_{23}C_6$-to-$Cr_2(CN)$, MC-to-Z-phase and MC-to-η-carbide phase transformations for both alloys with respect to ageing temperature and time. Accelerated dissolution of the secondary precipitates within Zone A-II is discussed in Section 8.3.4. It must be noted that the characterization of Zone A-II has mainly been conducted on the HP-Nb and HP-NbTi samples which were aged at 1000, 1050, and 1100°C for 1000 and 10,000 hours. Detailed characterization of the samples after 1000 hours was considered important due to the accelerated creep testing of HP alloys generally being performed in an air atmosphere and lasting for 1000-2000 hours. Thus, the extent to which the furnace atmosphere affected aged samples within the first 1000 hours can also be expected during accelerated creep testing of all centrifugally cast HP-Nb and HP-NbTi alloys at temperatures between 1000-1100°C.

8.3.1 $Cr_{23}C_6$-to-$Cr_2(CN)$ Phase Transformation

Ageing of the HP-Nb1, HP-Nb2 and HP-NbTi1 alloys in air caused the $Cr_{23}C_6$ precipitates adjacent to the exposed surfaces to progressively transform to $Cr_2(CN)$. The transformation of $Cr_{23}C_6$ to $Cr_2(CN)$ was confined to precipitates located on grain and dendrite boundaries (i.e. the larger 'primary' precipitates) and did not occur to the intragranular (secondary) $Cr_{23}C_6$ distribution. In contrast to the MC-to-Z-phase and MC-to-η-carbide transformations, the $Cr_{23}C_6$-to-$Cr_2(CN)$ transformation was the only atmosphere induced phase transformation that occurred in both alloys at all three ageing temperatures.

While the $Cr_{23}C_6$-to-$Cr_2(CN)$ transformation rate was largely dictated by the ageing temperature, the manner in which the transformation progressed from the exposed surfaces to the mid-wall position of the HP-Nb and HP-NbTi alloys was similar when ageing both alloys at 1000, 1050 and 1100°C. Initially, the $Cr_{23}C_6$-to-$Cr_2(CN)$ transformation was confined within a narrow band (<0.1mm thick) located at the Zone A-I/A-II interface where the primary $Cr_{23}C_6$ precipitates had completely transformed to $Cr_2(CN)$. During prolonged ageing, the band of $Cr_2(CN)$ precipitates uniformly grew towards the mid-wall position. Figure 8.9 (a) and (b) show an example of this band at the outer diameter of the HP-Nb1 and HP-NbTi1 tubes after ageing at 1050°C for 10,000 hours. All $Cr_{23}C_6$ precipitates which were located within the dimensioned regions in Figure 8.9 (a) and (b) had completely transformed to $Cr_2(CN)$. As shown in Figure 8.9 (c) and (d), the transition from the $Cr_2(CN)$

to the untransformed primary $Cr_{23}C_6$ (at the mid-wall position) occurred relatively rapidly. Typically, the transition occurred over a relatively narrow band (<100µm) where a mixed network of separate $Cr_{23}C_6$ and $Cr_2(CN)$ precipitates and rarely partially transformed $Cr_{23}C_6$ was observed (as shown in Figure 8.10 (c) and (d)). Either side of this transition region the precipitate networks were populated entirely with $Cr_{23}C_6$ (mid-wall position) or $Cr_2(CN)$ (inner and outer diameter positions) precipitates.

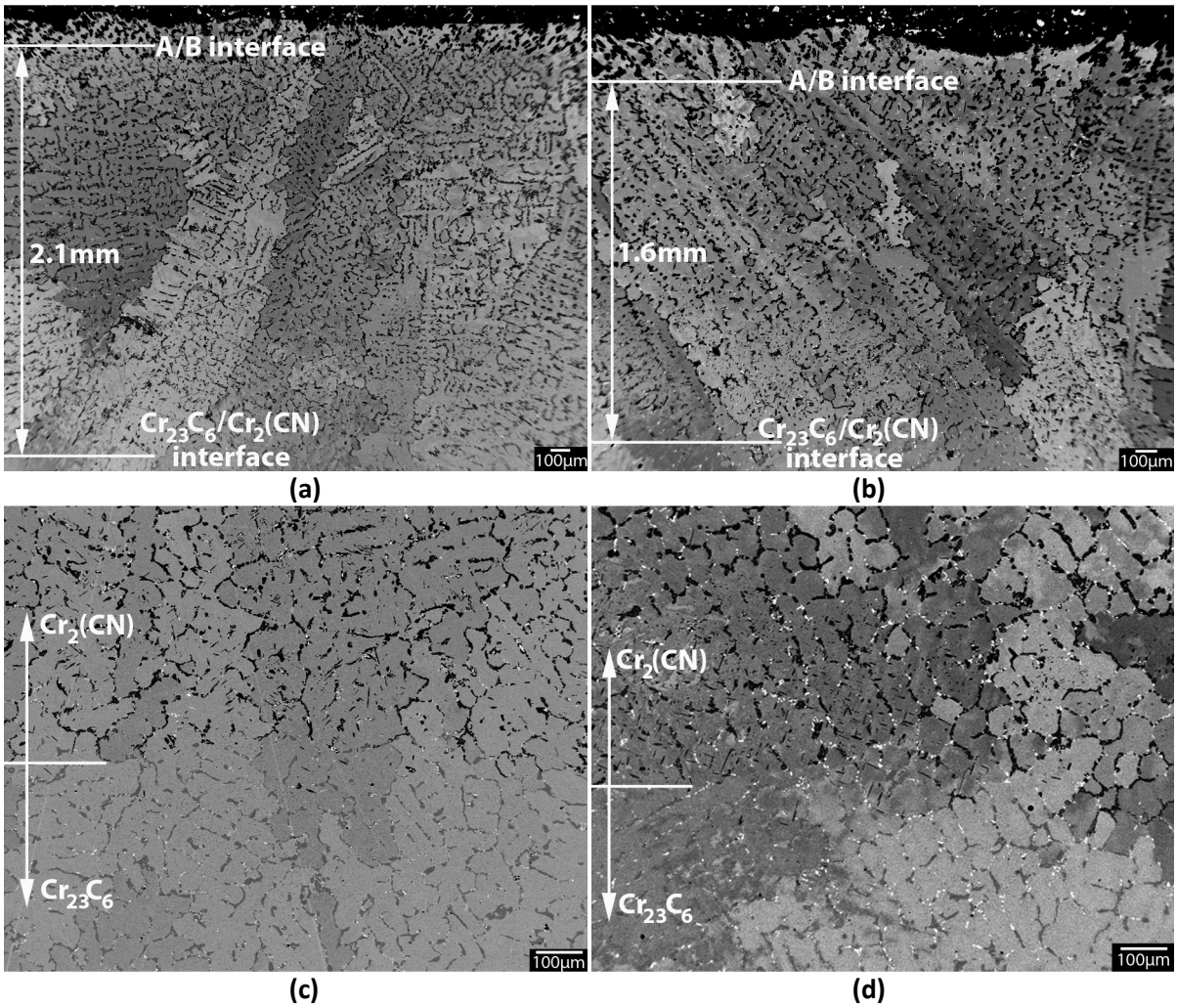

Figure 8.9 – (a) & (b) Low magnification (50x) backscatter electron micrographs showing the extent of the $Cr_{23}C_6/Cr_2(CN)$ transformation at the outer diameter of the HP-Nb1 and NbTi1 alloys after ageing at 1050°C for 10,000 hours. (c) & (d) Higher magnification images (100x) showing the relatively abrupt $Cr_{23}C_6/Cr_2(CN)$ interface.

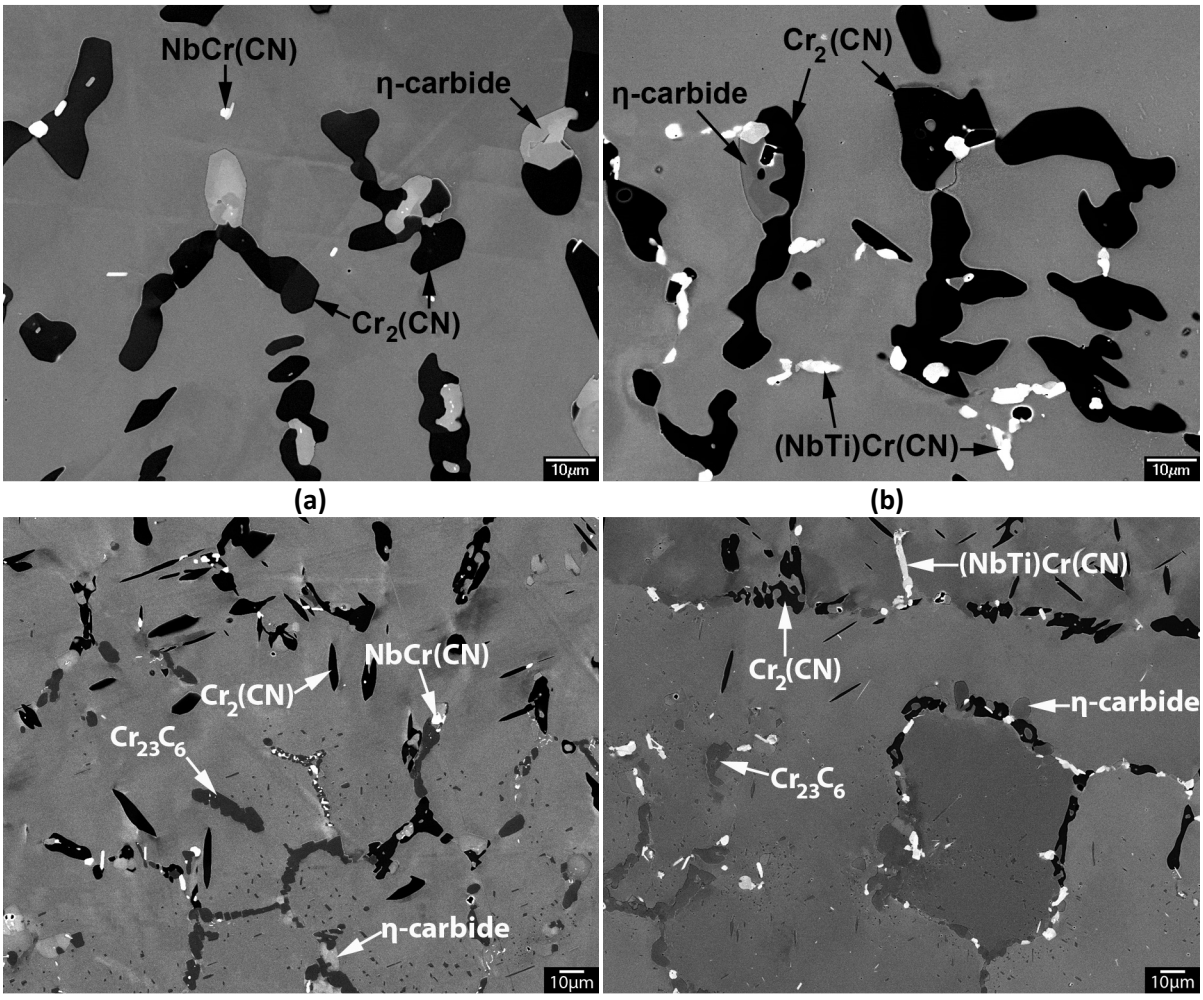

Figure 8.10 – Backscatter electron micrographs showing (a) & (b) the complete transformation of the primary $Cr_{23}C_6$ to $Cr_2(CN)$ within the dimensioned regions in Figure 8.9 (a) and (b). (c) & (d) The transition from $Cr_2(CN)$ to $Cr_{23}C_6$ (as labelled in Figure 8.9 (c) and (d)).

Identification of the Cr_2N ($P\bar{3}1m$) phase in all aged samples was carried out using a combination of EDS and EBSD (Figure 8.11 (a) to (d)). Aside from the small quantity of tungsten (typically less than 0.5at.%) contained within the $Cr_2(CN)$ precipitates in the HP-NbTi1 alloy, the composition of the $Cr_2(CN)$ precipitates was relatively similar in each alloy with respect to ageing temperature and time. Regardless of the ageing temperature and time, carbon and nitrogen peaks were both commonly observed when performing EDS on the $Cr_2(CN)$ precipitates. The ratio of the carbon and nitrogen peaks varied when comparing precipitates with respect to distance from the exposed surfaces. Precipitates closely adjacent to the exposed surfaces typically contained lower carbon and greater nitrogen concentrations. With increasing distance from the exposed surfaces, the carbon concentration gradually increased while the nitrogen concentration decreased. For example, the EDS spectra shown in Figure 8.11 (c) and (d) are representative of precipitates located within 0.5mm of

the exposed surfaces in each sample. Typically, EDS indicated that precipitates located near the exposed surfaces contained much less carbon (between 2-4at.%) than nitrogen (between 15-17at.%). In contrast, the carbon and nitrogen concentrations in $Cr_2(CN)$ precipitates located near the $Cr_2(CN)/Cr_{23}C_6$ transition interface were relatively similar (10-12at.%). The relatively greater nitrogen content of $Cr_2(CN)$ precipitates located directly adjacent to the exposed surfaces was due to the nitrogen being largely absorbed from the nitrogen-rich furnace atmosphere (the as-cast alloys contained <0.09wt.% N).

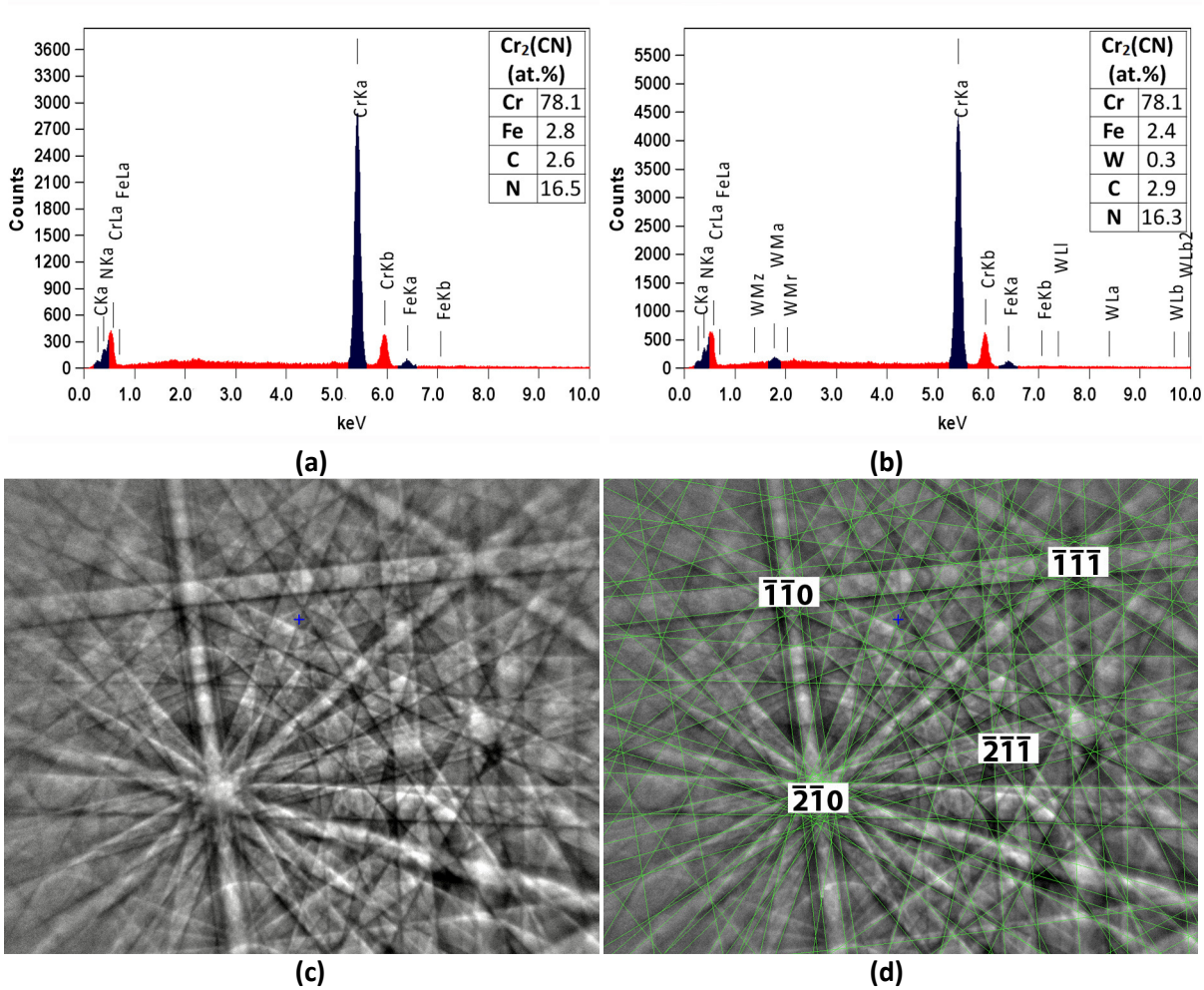

Figure 8.11 – (a) & (b) EDS spectra representative of the $Cr_2(CN)$ precipitates in Figure 8.10 (a) & (b). (c) Experimentally determined electron backscatter diffraction pattern (EBSP) and (d) the simulated pattern for the $Cr_2(CN)$ ($P\bar{3}1m$) crystal structure overlaying the pattern in (c).

Table 8.2 and Table 8.3 summarize the ageing conditions where the $Cr_{23}C_6$-to-$Cr_2(CN)$ transformation was observed at the inner and outer diameters of the HP-Nb1, HP-Nb2 and HP-NbTi1 alloys. Figure 8.12 (a) and (b) show the average depth to which $Cr_2(CN)$ precipitates were observed in the HP-Nb and HP-NbTi alloys after ageing at 1000, 1050, 1100°C for 1000 and 10,000 hours. A minimum of 5 measurements were taken along both the inner and outer diameters using the same method as shown in Figure 8.9 (a) and (b). Typically, the average depth would vary by less than 0.2mm when comparing individual measurements at the inner or outer diameters.

In general, the $Cr_{23}C_6$-to-$Cr_2(CN)$ transformation rate was greatest when ageing at 1050°C with $Cr_2(CN)$ precipitates observed in both the HP-Nb1 and HP-NbTi1 alloys after 1000 hours exposure. Therefore, the depth to which the $Cr_{23}C_6$-to-$Cr_2(CN)$ transformation was observed and the total area fraction of $Cr_2(CN)$ precipitates to be highest after ageing at 1050°C for 10,000 hours. Regardless of the ageing temperature, the $Cr_{23}C_6$-to-$Cr_2(CN)$ transformation rate was relatively similar when comparing the inner and outer diameter positions of the HP-Nb1 and HP-Nb2 alloys. Conversely, the transformation rate was markedly greater at the inner diameter position in the HP-NbTi1 alloy. The increased transformation rate at the HP-NbTi1 tube's inner wall is evidenced in Figure 8.12 (b) by the consistently greater depth to which $Cr_2(CN)$ precipitates were observed in comparison to the outer wall after ageing at 1000, 1050 and 1100°C.

As discussed in Chapter 5, the HP-NbTi1 alloy was the only tube sample that contained equiaxed grains at the inner diameter. Generally, the significantly smaller size of the equiaxed grains in comparison to the columnar grains caused the chromium-rich precipitates to be predominantly located on the equiaxed grain boundaries. As a result, the increased $Cr_{23}C_6$-to-$Cr_2(CN)$ transformation rates within the equiaxed region of the HP-NbTi tubes is believed to be attributed to the comparatively higher equiaxed grain boundary area. The higher grain boundary area likely cause the overall diffusion rate of nitrogen to be greater at the tube's inner wall.

Table 8.2 – Summary stating the ageing conditions where $Cr_2(CN)$ precipitates were identified at the inner and outer diameters of the HP-Nb1 and HP-Nb2 alloys with respect to ageing temperature and time.

T (°C)	Wall Position	Ageing Time (h)			
		1000	3000	6000	10,000
1000 (Nb2)	OD	$Cr_{23}C_6$			$Cr_2(CN)$
	ID				
1050 (Nb1)	OD	$Cr_2(CN)$		No samples	$Cr_2(CN)$
	ID				
1100 (Nb1)	OD	$Cr_{23}C_6$	$Cr_2(CN)$		$Cr_2(CN)$
	ID				

Table 8.3 – Summary stating the ageing conditions where $Cr_2(CN)$ precipitates were identified at the inner and outer diameters of the HP-NbTi1 alloy with respect to ageing temperature and time.

T (°C)	Wall Position	Ageing Time (h)			
		1000	3000	6000	10,000
1000	OD	$Cr_{23}C_6$			
	ID	$Cr_{23}C_6$	$Cr_2(CN)$		
1050	OD	$Cr_{23}C_6$		No samples	$Cr_2(CN)$
	ID	$Cr_2(CN)$			
1100	OD	$Cr_{23}C_6$			$Cr_2(CN)$
	ID	$Cr_{23}C_6$	$Cr_2(CN)$		

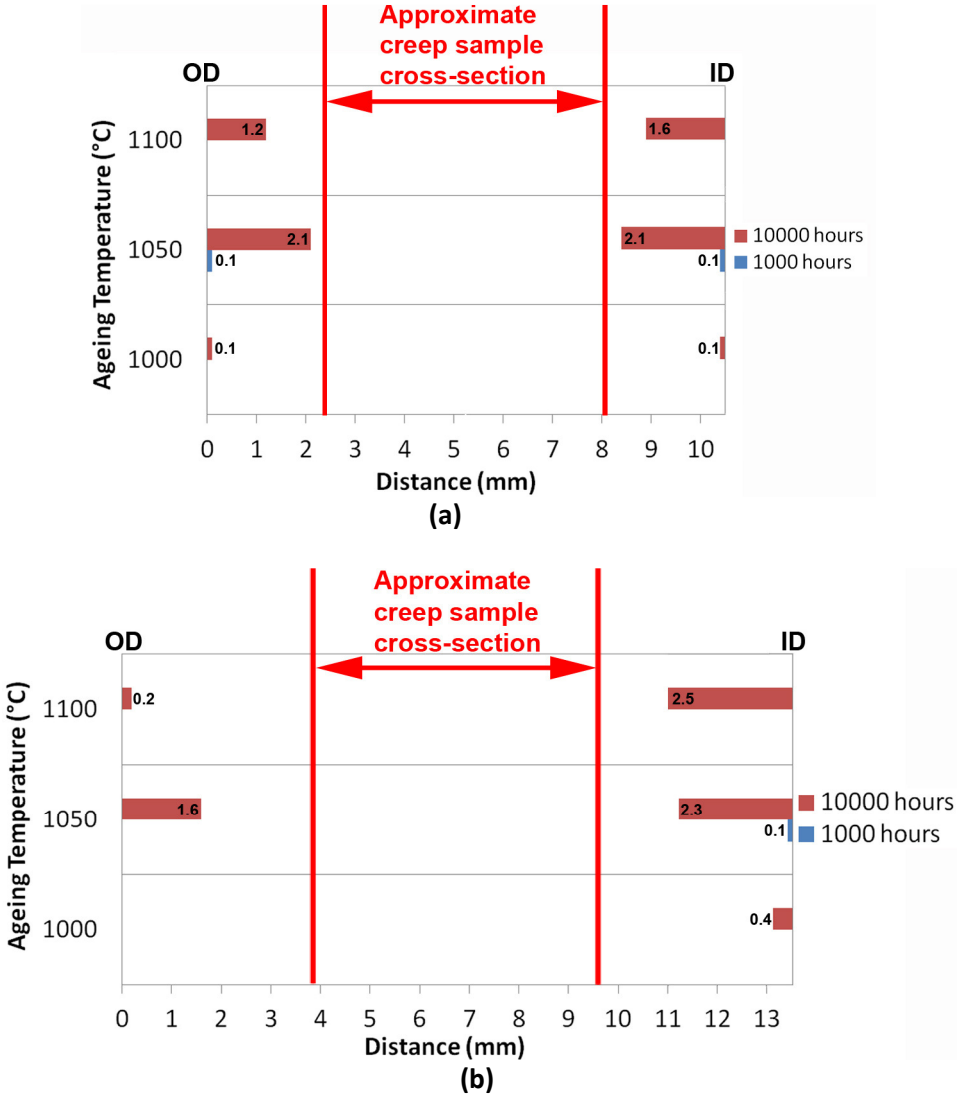

Figure 8.12 – Histograms showing the depth (measured from the exposed surfaces) that the $Cr_2(CN)$ precipitates were observed after ageing the (a) HP-Nb1/Nb2 and (b) HP-NbTi1 alloy at 1000, 1050 and 1100°C for 1000 and 10,000 hours.

Rarely, $Cr_2(CN)$ precipitates were randomly observed along the columnar grain boundaries at the mid-wall position of the HP-Nb1 1100°C-10,000h aged sample (Figure 8.13 (a) and (b)). These grain boundary $Cr_2(CN)$ precipitates were not observed at the mid-wall position of any other aged HP-Nb or HP-NbTi aged sample. For all other HP-Nb and HP-NbTi aged samples, the $Cr_2(CN)$ precipitates were confined to a 0.1-2.5mm thick band (depending on the ageing conditions) directly adjacent to the exposed surfaces (Figure 8.9 (a) to (d)). While a slightly enhanced transformation rate was observed for $Cr_{23}C_6$ precipitates located on grain boundaries at the $Cr_{23}C_6/Cr_2(CN)$ transition regions shown in Figure 8.10 (c) and (d), this increased transformation rate only increased the depth at which the grain boundary $Cr_2(CN)$ precipitates were observed in comparison to those on dendrite

boundaries by less than 100µm. In contrast, the grain boundary $Cr_2(CN)$ precipitates located at the mid-wall position of the HP-Nb1 1100°C 10,000 hour sample were often observed at distances of 2.5mm ahead of the $Cr_{23}C_6/Cr_2(CN)$ transition interface. It is currently unknown why $Cr_2(CN)$ precipitates located at such large distances ahead of the transition in interface shown in Figure 8.9 (a) and (b) were only observed in the HP-Nb1 1100°C 10,000 hour aged sample.

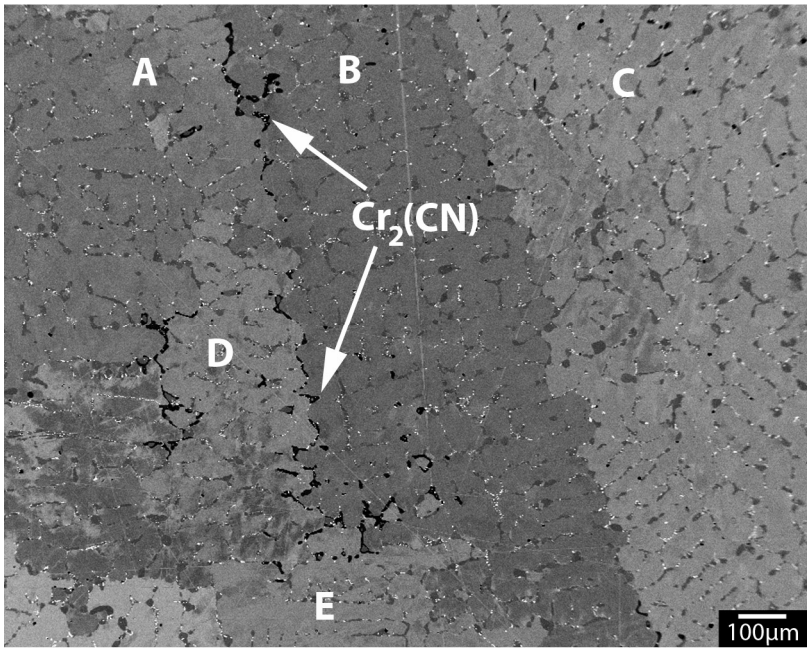

(a)

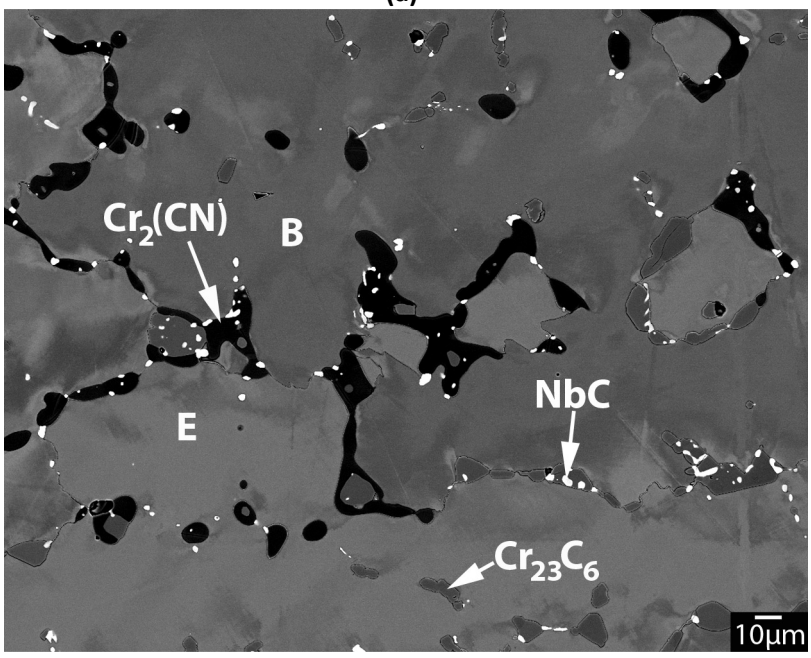

(b)

Figure 8.13 – (a) & (b) Backscatter electron micrographs showing the $Cr_2(CN)$ located on the columnar grain boundaries at the mid-wall position HP-Nb1 1100°C 10,000h aged sample. The labels A, B, C, D and E in each figure denote individual columnar grains.

While the as-cast HP-Nb and HP-NbTi alloys contained low concentrations of nitrogen (<0.09wt.%), the initial confinement of the $Cr_{23}C_6$-to-$Cr_2(CN)$ transformation adjacent to the exposed surfaces and the progression of this transformation toward the tube's mid-wall position suggests that the formation of the $Cr_2(CN)$ within the HP-Nb and HP-NbTi alloys is due to the nitrogen-rich furnace atmosphere. Based on the preceding analysis it is currently unknown if the nitrogen absorbed from the atmosphere remains contained completely within the austenite matrix surrounding the $Cr_{23}C_6$ precipitates until the concentration reaches a certain threshold level (currently unknown) which induces the $Cr_{23}C_6$-to-$Cr_2(CN)$ transformation or if the $Cr_{23}C_6$ precipitates gradually absorb the nitrogen from the matrix until a threshold concentration of nitrogen within the $Cr_{23}C_6$ precipitate is reached (also unknown) leading to the $Cr_2(CN)$ transformation. No noticeable nitrogen peak was observed when performing EDS analysis on the $Cr_{23}C_6$ precipitates located at the $Cr_{23}C_6/Cr_2(CN)$ interface suggesting nitrogen was not absorbed in significant quantities by these precipitates prior to the $Cr_2(CN)$ transformation.

Previous work on Cr_2N precipitates in austenitic steels has mainly focused on the nucleation and growth mechanisms of Cr_2N precipitates which formed on grain and twin boundaries and also within the matrix during isothermal ageing [4, 8-11]. Typically, the samples analysed in these studies were encapsulated in evacuated quartz tubes with the carbon and nitrogen contents set prior to isothermal ageing (below 0.02wt.% C [4, 8, 10] and between 0.08 and 0.3wt.% [9] N). Relatively limited work in the widely available literature has been conducted on the transformation of existing $Cr_{23}C_6$ precipitates to $Cr_2(CN)$ as a result of nitrogen absorption during isothermal ageing of austenitic steels.

Erneman *et al.* [12] analysed the precipitates formed in a 347 stainless steel (17wt.% Cr, 11wt.% Ni, 0.78wt.% Nb, 0.065wt.% C) due to nitrogen absorption during creep testing at 700 and 800°C. Prior to creep testing, the samples were subjected to a solution heat treatment at 1100°C for 3 minutes which induced the formation of Nb(CN) precipitates within the austenite matrix. Subsequent to the solution heat treatment, creep testing was carried out at 700 and 800°C with stresses ranging between 20-120MPa for a maximum of 69,752 and 77,782 hours respectively. The diffusion of nitrogen when testing at 700°C was believed to be low with only a relatively uniform distribution of Nb(CN) precipitates identified across the creep samples circular cross-section regardless of the ageing time. However, ageing at 800°C was sufficient to cause the formation of zones within the 347 steel that were similar to Zones A-I, A-II and UA observed in the aged HP-Nb and HP-NbTi alloys. A

chromium-rich oxide scale was identified at the creep sample's outer surface. Beneath the oxide layer was decarburized band approximately 50-100µm thick which contained Nb(CN), Z-phase and Cr_2N precipitates. This band was followed by an intermediate zone (located between 0.1-1.2mm from the surface of the 8mm diameter samples) where Nb(CN), Z-phase and Cr_2N and $Cr_{23}C_6$ precipitates were identified. Finally, a network comprised of Nb(CN) which had partially transformed to Z-phase and $Cr_{23}C_6$ precipitates was identified at the center of the creep samples.

Thermodynamic calculations performed by Erneman *et al.* [12] using DICTRA for the 347 steel predicted the formation of the Cr_2N phase would occur when the alloy's total nitrogen concentration was above 0.2wt.%. Nitrogen concentrations above 0.4wt.% were predicted to cause the decomposition of $Cr_{23}C_6$ and rapidly increase the volume fraction of Cr_2N. Wavelength dispersive X-ray analysis performed on the creep samples after 77,782 hours of exposure to 800°C determined that the presence of Cr_2N with respect to the measured concentration of nitrogen within the austenite matrix corresponded well with the thermodynamically calculated phases. The nitrogen concentration within solution was between than 0.4-0.6wt.% in regions of the sample where Cr_2N was present but not $Cr_{23}C_6$. In regions of the sample that contained both Cr_2N and $Cr_{23}C_6$ the concentration of nitrogen within the austenite was between 0.1-0.4wt.%. Only $Cr_{23}C_6$ was present at the core region of the samples where the nitrogen concentration within the austenite was approximately 0.1wt.%.

The preceding observations suggest that the $Cr_{23}C_6$-to-Cr_2(CN) transformation proceeds within the HP-Nb and HP-NbTi alloys once the local nitrogen concentration within the austenite exceeds a certain threshold level (possibly 0.4wt.%). The initial transformation of the $Cr_{23}C_6$ at the Zone A-I/A-II interface is a direct result of these precipitates being located closest to the furnace atmosphere (i.e. the nitrogen source) resulting in the minimum threshold level of nitrogen first being reached within austenite surrounding these precipitates (or within the $Cr_{23}C_6$ precipitates). Continued absorption of nitrogen at the exposed surfaces and diffusion of the nitrogen toward the mid-wall position results in the observed progression of the $Cr_{23}C_6$-to-Cr_2(CN) transformation towards the mid-wall position. The relatively rapid transition from Cr_2(CN) to $Cr_{23}C_6$ precipitates (Figure 8.9, Figure 8.10) suggests these precipitates can only co-exist over a narrow range of nitrogen concentrations.

As previously discussed, Erneman *et al.* [12] determined the absorption of nitrogen from the atmosphere was relatively low when testing the 347 stainless steel at 700°C but significantly increased when testing at 800°C resulting in the layered distribution of Cr_2N, Z-phase Nb(CN) and

$Cr_{23}C_6$ precipitates across the creep sample's cross-section. The markedly greater $Cr_{23}C_6$-to-Cr_2(CN) transformation rate observed when ageing the HP-Nb and HP-NbTi alloys at 1050°C in comparison to ageing at 1000°C suggested a similar increase in the nitrogen absorption rate occurred with respect to the ageing temperature. However, as shown in Figure 8.12 (a) and (b), the $Cr_{23}C_6$-to-Cr_2(CN) transformation rate decreased when the ageing temperature is increased from 1050 to 1100°C. Interestingly, the decreased $Cr_{23}C_6$-to-Cr_2(CN) transformation rate occurred despite the MC precipitates remaining completely stable when ageing at 1100°C whereas the MC precipitates transformed to nitrogen-rich Z-phase precipitates when ageing at 1050°C. Hence, the nitrogen which was absorbed during at 1100°C only participated in the $Cr_{23}C_6$-to-Cr_2(CN) transformation.

The decrease in the $Cr_{23}C_6$-to-Cr_2(CN) transformation rate when increasing the temperature from 1050 to 1100°C is unlikely related to a decreased nitrogen absorption rate since diffusion is so strongly influenced by temperature. Instead, the $Cr_{23}C_6$-to-Cr_2(CN) transformation is believed to be similar to the NbC-to-G-phase [13] and NbC-to-η-carbide (Chapter 6) phase transformations in the HP-Nb alloy. Generally, the transformation rate for both the NbC-to-G-phase and NbC-to-η-carbide transformations was greatest when ageing at temperatures between 900-1000°C. Each transformation became increasingly more sluggish when ageing at temperatures above 1000°C and neither transformation proceeded when ageing the HP-Nb alloy at temperatures above 1050°C (i.e. the NbC remained completely stable). Hence, the considerably lower volume fraction of Cr_2(CN) observed in the HP-Nb and HP-NbTi alloys after ageing at 1100°C for 10,000 hours is likely attributed to the $Cr_{23}C_6$-to-Cr_2(CN) transformation becoming progressively more sluggish when increasing the ageing temperature above 1050°C. However, it must be noted that the NbC-to-G-phase and NbC-to-η-carbide phase transformation rates were observed within alloys where the chemical composition could be assumed to be relatively constant during ageing. Hence, these phase transformations were primarily influenced by the ageing temperature. In contrast, the chemical composition at the exposed surfaces of the HP-Nb and HP-NbTi alloys continuously evolved during ageing. Consequently, the $Cr_{23}C_6$-to-Cr_2(CN) phase transformation was dependent on both the ageing temperature and local chemical composition.

The $Cr_{23}C_6$-to-Cr_2(CN) transformation rate could be explained by considering the driving force (i.e. undercooling) and nitrogen absorption rate with respect to temperature. When ageing at 1050°C, the combination of a high driving force for the $Cr_{23}C_6$-to-Cr_2(CN) transformation and ample absorption of nitrogen (and subsequent diffusion towards the tube's mid wall position) from the atmosphere

results in the greatest $Cr_{23}C_6$-to-Cr_2(CN) transformation rate (in comparison to ageing at 1000 and 1100°C). While reducing the ageing temperature to 1000°C will cause the driving force to increase, the transformation rate is impeded by the comparatively lower absorption of nitrogen. Conversely, the absorption of nitrogen likely increases when increasing the ageing temperature to 1100°C, but the undercooling reduces resulting in a lower driving force for the $Cr_{23}C_6$-to-Cr_2(CN) transformation. However, the preceding explanation of the $Cr_{23}C_6$-to-Cr_2(CN) transformation rate with respect to temperature is likely over simplified as it does not take into account the concentration of chromium in the austenite matrix with respect to the ageing temperature.

If the $Cr_{23}C_6$-to-Cr_2(CN) transformation rate is predominantly influenced by the inward diffusion of nitrogen, the depth at which this transformation occurs with respect to temperature and time would be expected to follow a parabolic rate law [18]. Thus, the penetration depth (ξ) to which internal nitrides form as a function of exposure time (t) can be analytically calculated by applying Carl Wagner's equation (initially proposed for internal oxidation [18]) to the internal nitridation rate observed in the HP alloys:

$$\xi^2 = 2k_N t \qquad 8.1$$

Where

ξ is the penetration depth of internal nitrides with respect to ageing time (at constant temperature)

k_N denotes the parabolic nitridation rate constant

The internal nitridation process can be said to obey a parabolic rate law if the penetration depth increases linearly (from ξ = 0 when t=0) with respect to √t. Figure 8.14 shows a plot of the Cr_2N penetration depth plotted against the square root of exposure time for the HP-Nb1 alloys after ageing at 1050 and 1100°C. Although additional depth measurements with respect to ageing time are necessary to more accurately visualise the ξ - √t relationship, the points shown in Figure 8.14 suggest that the kinetics of the $Cr_{23}C_6$-to-Cr_2(CN) transformation when ageing the HP alloy in air is not necessarily controlled by the inward diffusion of nitrogen (i.e. a linear relationship is unlikely).

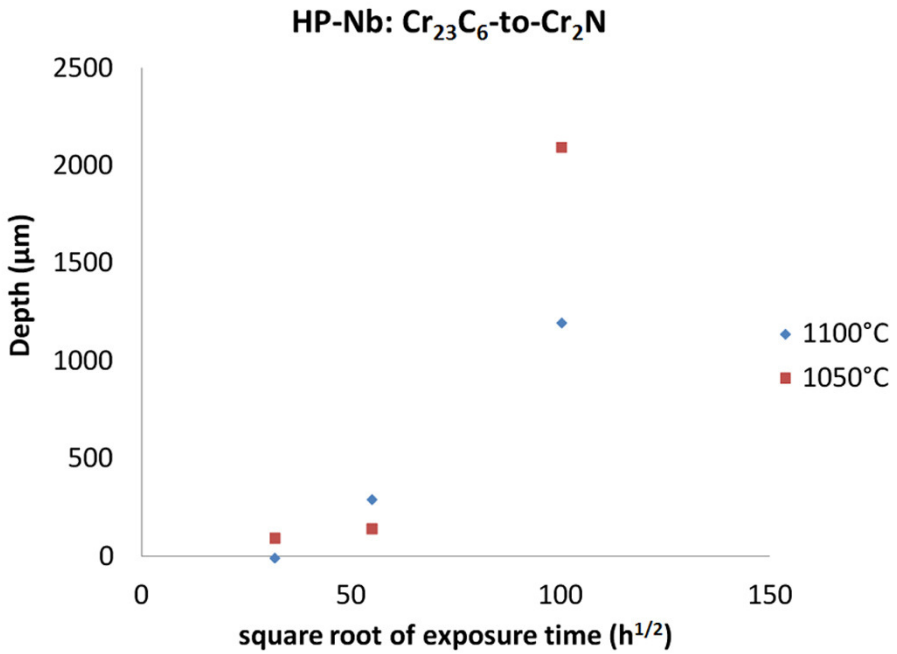

Figure 8.14 – Penetration depth of internal Cr_2N precipitates at 1050 and 1100°C in the HP-Nb alloy with respect to the square root of time.

The deviation of the $Cr_{23}C_6$-to-Cr_2(CN) transformation rate from parabolic rate law (i.e. Wagner's equation) is possibly due to the HP alloys protective chromium-oxide scale restricting the absorption of nitrogen during ageing. Internal nitridation of Ni-based alloys in oxygen-free atmospheres (where surface oxidation is negligible) have been shown to follow a parabolic rate law [18]. However, internal nitridation of Ni-based alloys in within oxygen containing atmospheres typically occur as a result of spalling and cracking of the protective oxide scale (which are often to be considered impervious to nitrogen [18]). The significant volume fraction of Cr_2N precipitates after ageing for 10,000 hours indicates that while the oxide scale (discussed in Section 8.2) that forms on the HP alloys during ageing at 1000, 1050 and 1100°C is not impervious to nitrogen (likely due to scaling and cracking), it possibly acts to restrict the rate of nitrogen ingress during ageing resulting in the deviation of the $Cr_{23}C_6$-to-Cr_2(CN) transformation kinetics from the parabolic rate law.

Alternatively, the observed deviation from a parabolic rate law could be attributed to the continuous decrease in the chromium concentration within the austenite matrix during ageing. Figure 8.15 (a) and (b) show the chromium content in the austenite matrix with respect to distance from the outer diameter of the HP-Nb1 and HP-NbTi1 alloys after ageing at 1050 and 1100°C for 10,000 hours. Regardless of the ageing temperature, the chromium concentration was lowest at the outer diameter. As discussed in Section 8.2, the chromium content was significantly lower within Zone A-I

(i.e. at 0mm) due to the formation of chromium oxide on the surfaces of the samples during ageing. After ageing both alloys at 1050°C for 10,000 hours, the chromium content gradually increased with increasing distance from the outer wall, until becoming relatively constant after the $Cr_2(CN)/Cr_{23}C_6$ transition interface. In contrast, the chromium concentration increased at a greater rate with distance from the outer wall when ageing at 1100°C. Irrespective of the wall position, the chromium concentration was greater after ageing both alloys at 1100°C for 10,000 hours in comparison to ageing at 1050°C.

Although the loss of chromium from the aged austenite matrix is believed to be partially attributed to the diffusion of chromium from Zones A-II and UA to the comparatively chromium-lean Zone A-I in order to maintain the chromium rich oxide layer, the overall lower concentration of chromium in the austenite matrix after ageing at 1050°C for 10,000 hours was not believed to be due to an increase in the oxidation rate at 1050°C when compared to ageing at 1100°C. Alternatively, the difference is believed caused by the additional transformation of the primary MC precipitates to the chromium-rich η-carbide (30-40at.% Cr) and Z-phase (~50at.% Cr) precipitates which form prior to the $Cr_2(CN)$ precipitates when ageing at 1050°C (the MC precipitates remained completely stable when ageing at 1100°C). Each phase transformation requires chromium to be absorbed from the austenite matrix.

Since these additional phase transformations occur prior to the $Cr_{23}C_6$-to-$Cr_2(CN)$ transformation, the resulting reduction in the chromium content within the austenite matrix likely influences the stability of the $Cr_{23}C_6$ and $Cr_2(CN)$ precipitates. The solubility of nitrogen in Ni-Cr-Ti alloys and austenitic stainless steels have been shown to increase strongly with increasing chromium content [4, 18]. Thus, the consumption of chromium from the austenite matrix due to the MC-to-η-carbide and MC-to-Z-phase transformations and surface oxidation during ageing likely influences the rate at which the $Cr_{23}C_6$-to-$Cr_2(CN)$ occurs, hence causing the transformation kinetics to not strictly adhere to Wagner's equation for internal nitridation.

Unfortunately, due to the complexity of the $Cr_{23}C_6$-to-$Cr_2(CN)$ phase transformation in the HP-Nb and HP-NbTi alloys, it was not possible to determine dominant factors which influenced the transformation rate based on the current analysis. Thus, while it is understood that this discussion potentially raises more questions than answers, it is hoped that it will provide a platform for subsequent analysis (such as thermodynamic modelling of the phase equilibria with respect to alloy composition and ageing temperature) of the $Cr_{23}C_6$-to-$Cr_2(CN)$ phase transformation in the HP-Nb and HP-NbTi alloys.

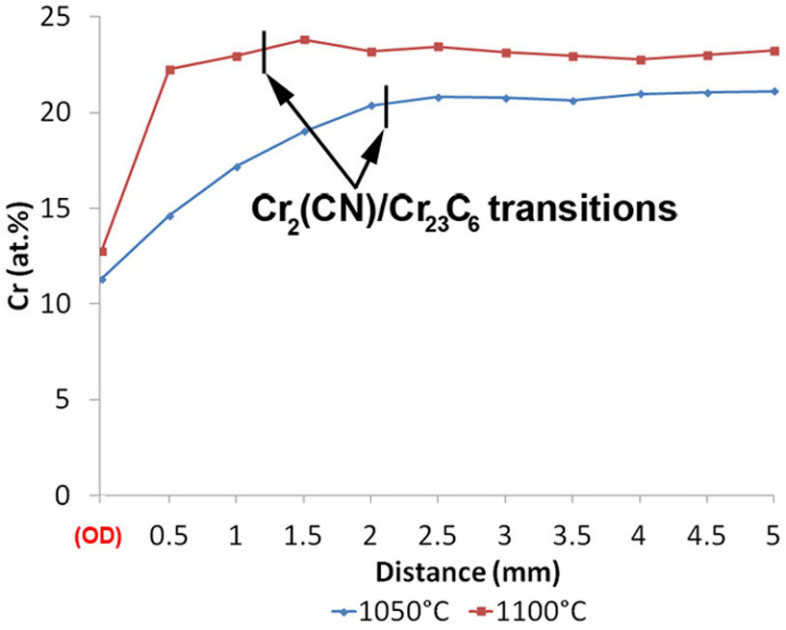

(a)

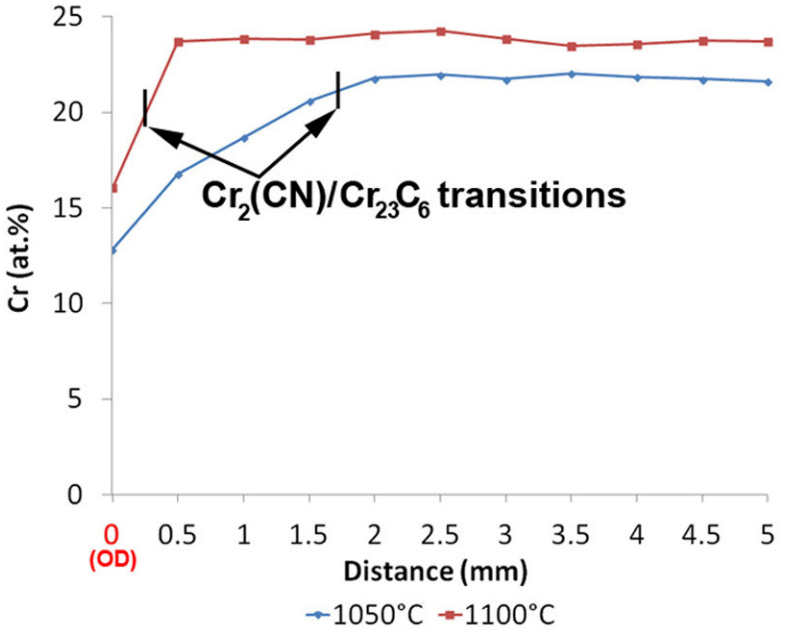

(b)

Figure 8.15 – Concentration of chromium within the austenite matrices of the (a) HP-Nb1 and (b) HP-NbTi1 samples aged at 1050 and 1100°C for 10,000 hours. Measurements were taken at 0.5mm increments from the outer diameter of the tubes using EDS.

8.3.2 MC-to-Z-phase Transformation

Figure 8.16 (a) to (d) give representative examples of the MC-to-Z-phase transformation which occurred within Zone A-II when ageing the HP-Nb1, HP-Nb2 and HP-NbTi1 alloys at 1000 and 1050°C. Unlike the $Cr_{23}C_6$ precipitates which solely transformed to $Cr_2(CN)$ during ageing, the NbC and (NbTi)C precipitates in the HP-Nb and HP-NbTi alloys could participate in either the MC-to-η-carbide or MC-to-Z-phase transformations during ageing at 1000 and 1050°C. Generally, each individual MC precipitate only participated in one of these transformations. For example, once a MC precipitate began to undergo the MC-to-Z-phase transformation, the MC precipitate would be completely consumed by the Z-phase precipitate (thus, being unable to also participate in the MC-to-η-carbide transformation). This Z-phase precipitate would subsequently remain stable during prolonged ageing. While the $Cr_{23}C_6$-to-$Cr_2(CN)$ transformation was observed within Zone A-II of the HP-Nb1 and HP-NbTi1 alloys after ageing at 1100°C, the MC precipitates in both alloys remained completely stable across the entire wall thickness.

The onset of the MC-to-Z-phase transformation was comparatively more rapid than the $Cr_{23}C_6$-to-$Cr_2(CN)$ transformation, with Z-phase precipitates commonly observed adjacent to the exposed surfaces after 1000 hours while the $Cr_{23}C_6$ in the same region remained stable. As a result, the depth at which the Z-phase transformation was observed with respect to ageing temperature and time was typically greater in comparison to the $Cr_{23}C_6$-to-$Cr_2(CN)$ transformation. For example, Figure 8.16 (a) and (b) show micrographs taken approximately 0.1mm ahead of the $Cr_{23}C_6$-to-$Cr_2(CN)$ transition interfaces shown in Figure 8.9 (c) and (d). The partial transformation of the primary MC precipitates to Z-phase (Figure 8.16 (c) and (d)) was observed while the primary $Cr_{23}C_6$ precipitates within this region of the tubes remained completely stable.

Generally, the (NbTi)C precipitates in the HP-NbTi1 alloy that had undergone the Z-phase transformation retained a similar blocky morphology (Figure 8.16 (d)). However, the Z-phase precipitates in the HP-Nb alloy did not obtain the original lamellar morphology (Figure 8.16 (c)). As discussed in Chapter 6, prolonged thermal exposure caused the lamellar NbC precipitates to spheroidize. Typically, spheroidization of the lamellar morphology occurred prior to the Z-phase transformation. Consequently, the Z-phase precipitates in the HP-Nb alloy obtained the spheroidized morphology.

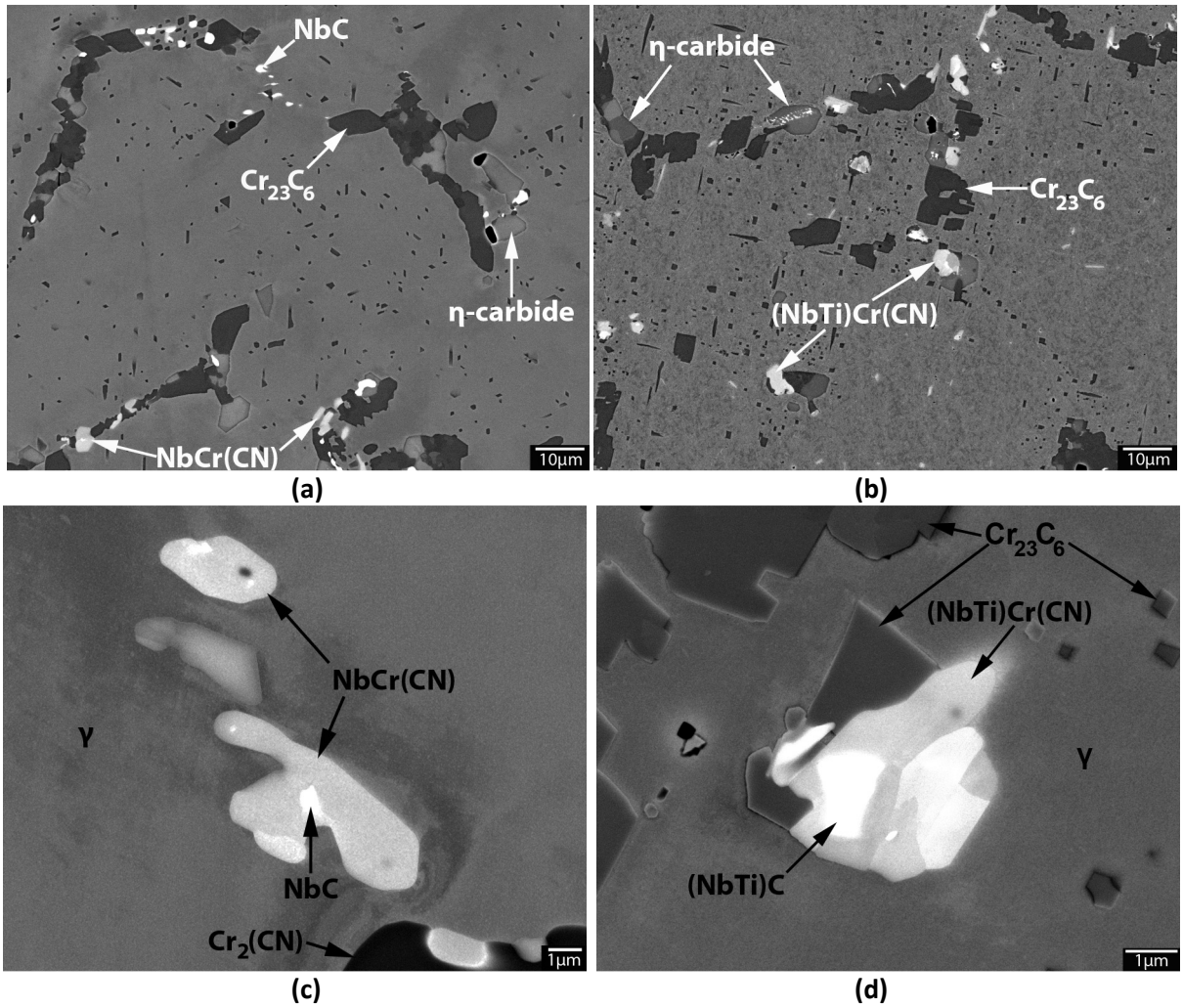

Figure 8.16 – Backscatter electron micrographs showing the mixed network of (a) $Cr_{23}C_6$, NbC, NbCr(CN), η-carbide, (b) $Cr_{23}C_6$, (NbTi)Cr(CN), and η-carbide observed in the HP-Nb1 and HP-NbTi1 1050°C-10,000h aged samples. (c) & (d) Higher magnifications NbC and (NbTi)C precipitates transforming to NbCr(CN) and (NbTi)Cr(CN) in the HP-Nb1 and HP-NbTi1 alloys respectively.

Figure 8.17 (a) and (b) give representative examples of EDS spectra taken from the Z-phase precipitates observed in the HP-Nb and HP-NbTi 1000 and 1050°C aged samples. For both alloys, the chemical composition of the Z-phase precipitates remained relatively constant with respect to the wall position and the ageing temperature and time. The titanium present within the (NbTi)C precipitates in the as-cast HP-NbTi1 alloy remained within the transformed Z-phase precipitates after ageing (typically between 2-5at.%). Similar to the as-cast NbC and (NbTi)C precipitates, is was not possible to obtain an accurate measurement of the carbon and nitrogen content within the Z-phase precipitates using the JEOL JED 2300 EDS detector. While it has been suggested that carbon can dissolve within Z-phase [12], no quantitative analysis of carbon or nitrogen within Z-phase was found in the widely available literature. Thus, further analysis using a technique that is more sensitive to

low concentrations of light elements (such as electron energy loss spectroscopy) is necessary to determine the carbon and nitrogen concentrations contained within these precipitates.

Identification of the Z-phase crystal structure in both alloys was carried out using EBSD. The Z-phase has a tetragonal (*P*4/*nmm* O2) crystal structure with a=b=0.3037nm and c=0.7391nm. The formula of Z-phase is typically been reported as $Cr_2Nb_2N_2$ [14] or NbCrN [15]. Z-phase precipitates containing titanium (in similar concentrations as shown in Figure 8.17 (a)) have not been previously identified in the literature. Figure 8.17 (c) and (d) gives representative examples of EBSPs taken from the Z-phase precipitates in the HP-Nb and HP-NbTi aged samples. In total, 10 EBSPs were obtained from separate precipitates located within the affected inner and outer diameter positions of each sample aged at 1000 and 1050°C. Regardless of the wall position, the NbC and (NbTi)C ($Fm\bar{3}m$) crystal structure was the only niobium-rich phase identified within the HP-Nb1 and HP-NbTi1 alloys when ageing at 1100°C.

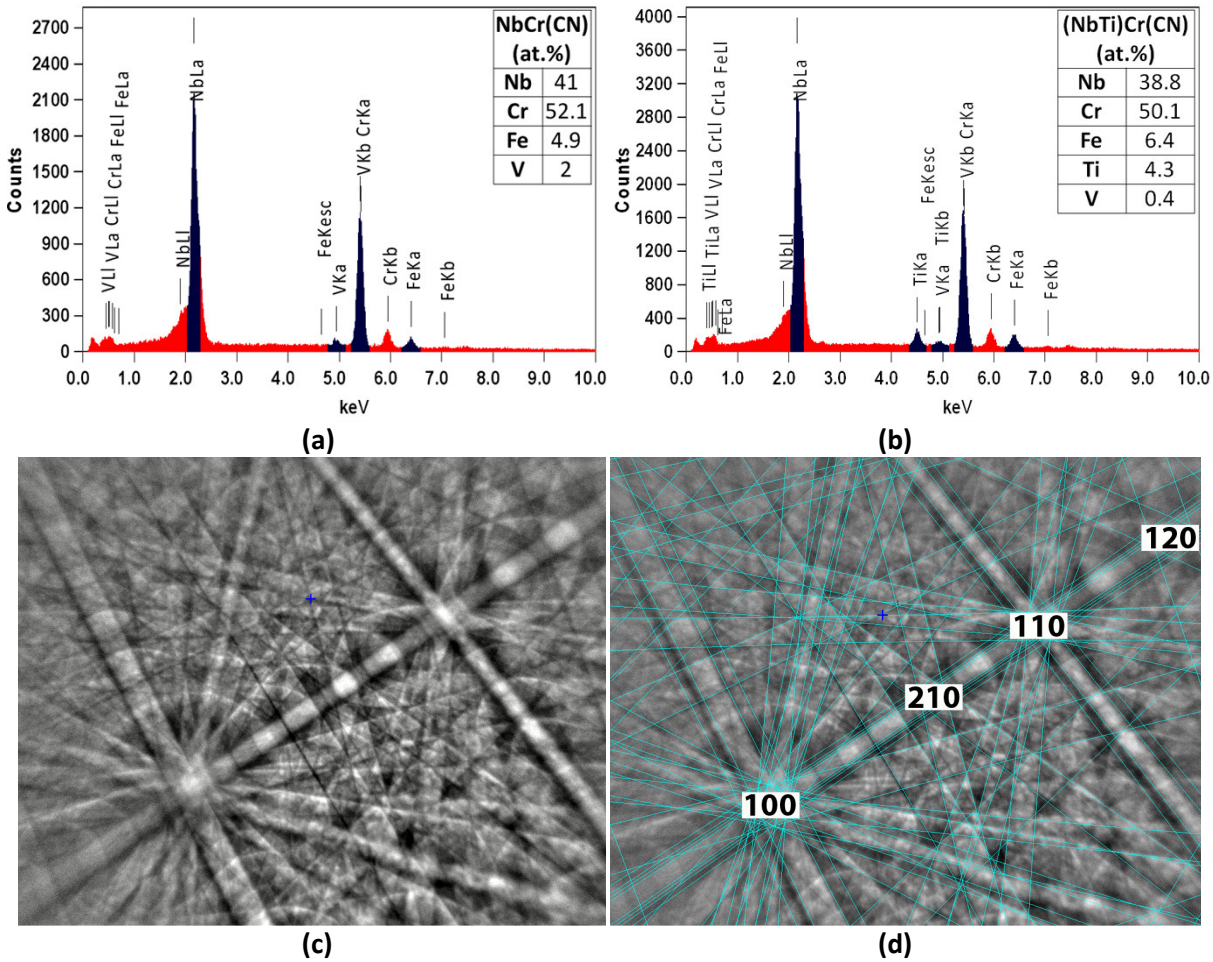

Figure 8.17 – (a) & (b) EDS spectra representative of the MCr(CN) precipitates in Figure 8.16 (a) - (d). (c) Experimentally determined electron backscatter diffraction pattern (EBSP) and (d) the corresponding simulated pattern for the MCr(CN) (*P*4/*nmm* O2) crystal structure.

Table 8.4 and Table 8.5 summarise the ageing conditions where the MC-to-Z-phase transformation was observed at the inner and outer diameters of the HP-Nb1, HP-Nb2 and HP-NbTi1 alloys. Similar to the $Cr_{23}C_6$-to-Cr_2(CN) transformation, the distance from the exposed surfaces at which the MC-to-Z-phase transformation was observed and the abundance of Z-phase precipitates at the inner and outer diameter positions in the HP-Nb and HP-NbTi alloys was greatest after ageing at 1050°C. This increase in the transformation rate was believed to be a result of the greater diffusion of nitrogen during ageing 1050°C in comparison to the diffusion rate 1000°C. As previously stated, the MC precipitates remained completely stable when ageing at 1100°C. Figure 8.18 (a) and (b) show the distance (measured from the Zone A-I/A-II interface) at which the MC-to-Z-phase transformation was observed. No easily observable interface existed between the regions of the aged samples that were affected and unaffected by the MC-to-Z-phase transformation (as was observed for the $Cr_{23}C_6$-to-

Cr_2(CN) transformation - Figure 8.9 (c) and (d)). Consequently, the distances in Figure 8.18 (a) and (b) were determined by carefully scanning the primary precipitate network at increasingly greater distances from the Zone A-I/A-II interfaces using a combination of backscatter electron imaging and EDS until Z-phase precipitates were no longer observed. The distances given in Figure 8.18 (a) and (b) are only considered to be accurate to a tolerance of $^{+}/_{-}$0.5mm.

As discussed in Section 8.3.1, $Cr_{23}C_6$ precipitates that had partially transformed to Cr_2(CN) were very rarely observed in the aged samples. However, MC precipitates which had partially transformed to Z-phase were commonly observed with the HP-Nb and HP-NbTi alloys. After ageing at 1000 and 1050°C for 1000 hours, a small band (<0.5mm) of MC precipitates that had partially transformed to Z-phase was located directly adjacent to the exposed surfaces in both the HP-Nb and HP-NbTi alloys. The depth from the exposed surfaces at which Z-phase precipitates were observed in the HP-Nb and HP-NbTi alloys progressively increased during prolonged ageing. For precipitates located directly adjacent to Zone A-I, the Z-phase transformation was nearing completion after ageing at 1000 and 1050°C for 10,000 hours. Generally, the fraction of individual MC precipitates that had transformed to Z-phase progressively decreased with increasing distance from the exposed surfaces. The transformed fraction for individual MC precipitates located within the region of the tubes containing Cr_2(CN) precipitates was typically greater than 50%. However, beyond the $Cr_{23}C_6$/Cr_2(CN) transition interface, the transformed fraction for MC individual precipitates rapidly decreased below 50%.

Typically, the MC-to-Z-phase transformation rate was relatively similar at the inner and outer diameter positions of the HP-Nb1 and HP-Nb2 alloys. However, although Z-phase precipitates were observed across the entire wall thickness of the HP-NbTi1 1050°C-10,000h aged sample, the transformation rate for individual precipitates was slightly greater at the inner diameter position. Further observations of the HP-NbTi1 aged samples determined the greater transformation rate at the inner diameter of this tube was typical of all samples after ageing at 1000 and 1050°C (based on qualitative comparison of the inner and outer diameter positions). The greater MC-to-Z-phase transformation at the inner diameter position of the HP-NbTi1 sample was believed to be due to the increased equiaxed grain boundary area at the tube's inner wall.

Interestingly, the MC-to-Z-phase transformation was typically observed at greater distances from the exposed surfaces in the HP-NbTi1 alloy in comparison to the HP-Nb1 and HP-Nb2 alloys when ageing each alloy at constant temperature. For example, Z-phase precipitates were observed across the entire wall thickness of the HP-NbTi1 1050°C-10,000h aged sample whereas the MC-to-Z-phase

transformation affected less than 50% of the HP-Nb1 1050°C-10,000h aged sample. It must be noted that the wall thickness of the HP-NbTi1 alloy was approximately 3mm greater than both HP-Nb alloys. Thus, the total depth at which the Z-phase precipitates were observed in the HP-NbTi1 alloy was considerably greater than the HP-Nb1 alloy (approximately 6.8 and 2.3mm respectively).

In addition to the reduced depth at which the MC-to-Z-phase transformation was observed in the HP-Nb alloy, the total number of MC precipitates which transformed to Z-phase precipitates within the affected area of the HP-Nb aged samples appeared to be significantly lower in comparison to the HP-NbTi1 aged samples (based on qualitative comparisons of the HP-Nb and HP-NbTi alloys after ageing at 1000 and 1050°C for 10,000 hours). The reduction in the number of MC precipitates which underwent the Z-phase transformation in the HP-Nb alloys was attributed to the partial transformation of the primary MC to η-carbides within the first 1000 hours of exposure to 1000 and 1050°C. This transformation continued during prolonged ageing, typically resulting in the MC being completely consumed by the η-carbide transformation. The MC-to-η-carbide transformation was particularly dominant when ageing the HP-Nb2 alloy at 1000°C with the majority of MC precipitates adjacent to the exposed surfaces transforming to η-carbides. As the MC-to-η-carbide transformation occurred more readily than the MC-to-Z-phase transformation in the HP-Nb alloys, the number of NbC precipitates remaining within the affected region of the tubes was relatively low when sufficient nitrogen was available within the austenite matrix to induce the MC-to-Z-phase transformation.

The MC-to-η-carbide transformation rate was reduced when ageing the HP-Nb1 alloy at 1050°C. Thus, a greater number of NbC precipitates were able to participate in the Z-phase transformation when the nitrogen concentration in the austenite matrix was sufficient. Additionally, the diffusion rate of nitrogen through the austenite matrix was thought to be greater at 1050°C (based on the observed increased MC-to-Z-phase transformation rate in both alloys) in comparison to 1000°C. Consequently, the total area fraction and depth at which Z-phase precipitates was comparatively greater when ageing the HP-Nb alloy at 1050°C as opposed to 1000°C Figure 8.18 (a).

As discussed in Chapter 7, the presence of titanium within the HP-NbTi alloy markedly increased the stability of the MC precipitates with respect to the η-carbide transformation when ageing at 1000 and 1050°C. As a result, the majority of the primary MC precipitates located adjacent to the exposed surfaces transformed to Z-phase prior to the onset of the η-carbide transformation (i.e. the number of MC precipitates which participated in the MC-to-Z-phase transformation increased due to the more sluggish MC-to-η-carbide transformation in the HP-NbTi alloy).

Table 8.4 – Summary stating the ageing conditions where NbCr(CN) (Z-phase) precipitates were identified at the inner and outer diameters of the HP-Nb1 and HP-Nb2 alloys with respect to ageing temperature and time.

<table>
<tr><th rowspan="2">T (°C)</th><th rowspan="2">Wall Position</th><th colspan="4">Ageing Time (h)</th></tr>
<tr><th>1000</th><th>3000</th><th>6000</th><th>10,000</th></tr>
<tr><td rowspan="2">1000 (Nb2)</td><td>OD</td><td rowspan="2">NbC</td><td colspan="3" rowspan="2">NbC, Z-phase</td></tr>
<tr><td>ID</td></tr>
<tr><td rowspan="2">1050 (Nb1)</td><td>OD</td><td rowspan="2">NbC</td><td rowspan="2">NbC, Z-phase</td><td rowspan="3">No samples</td><td rowspan="2">NbC, Z-phase</td></tr>
<tr><td>ID</td></tr>
<tr><td rowspan="2">1100 (Nb1)</td><td>OD</td><td colspan="2" rowspan="2">NbC</td><td rowspan="2">NbC</td></tr>
<tr><td>ID</td></tr>
</table>

Table 8.5 – Summary stating the ageing conditions where (NbTi)Cr(CN) (Z-phase) precipitates were identified at the inner and outer diameters of the HP-NbTi1 alloy with respect to ageing temperature and time.

<table>
<tr><th rowspan="2">T (°C)</th><th rowspan="2">Wall Position</th><th colspan="4">Ageing Time (h)</th></tr>
<tr><th>1000</th><th>3000</th><th>6000</th><th>10,000</th></tr>
<tr><td rowspan="2">1000</td><td>OD</td><td colspan="3" rowspan="2">(NbTi)C, Z-phase</td></tr>
<tr><td>ID</td></tr>
<tr><td rowspan="2">1050</td><td>OD</td><td colspan="2" rowspan="2">(NbTi)C, Z-phase</td><td rowspan="2">No sample</td><td rowspan="2">(NbTi)C, Z-phase</td></tr>
<tr><td>ID</td></tr>
<tr><td rowspan="2">1100</td><td>OD</td><td colspan="3" rowspan="2">(NbTi)C</td></tr>
<tr><td>ID</td></tr>
</table>

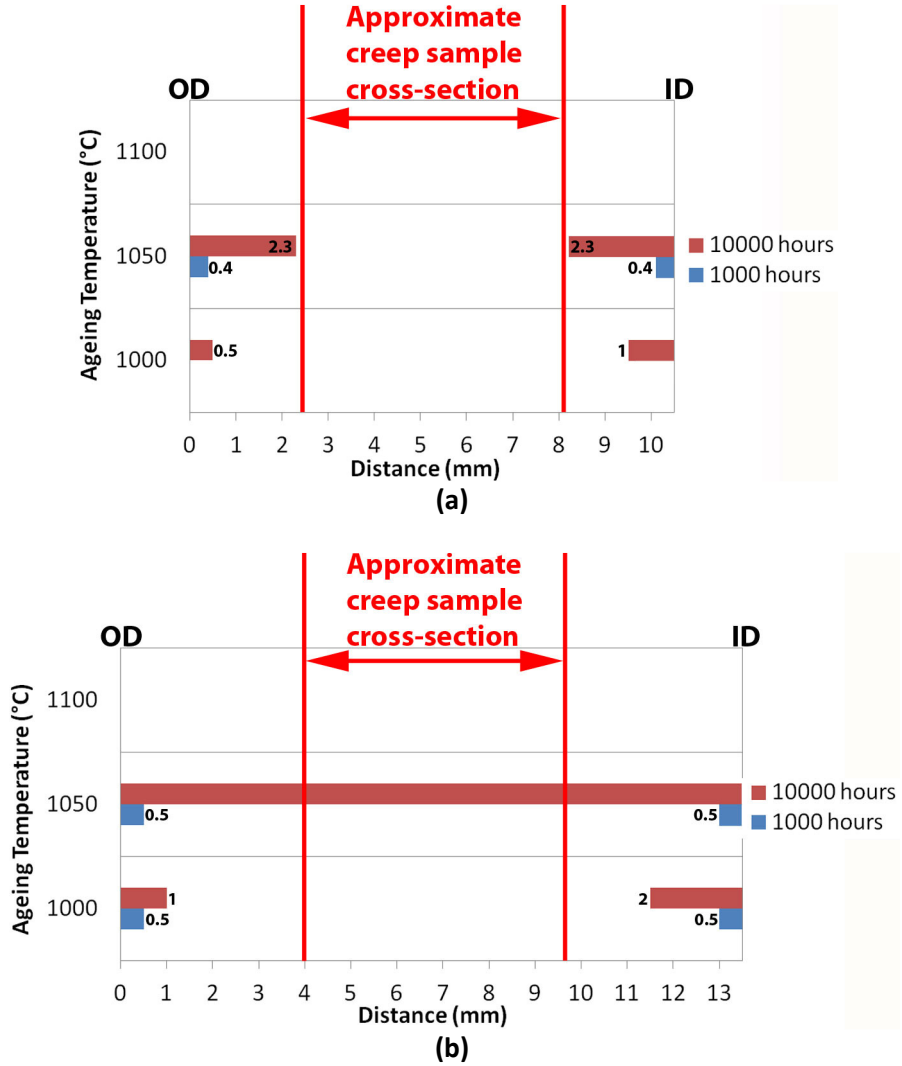

Figure 8.18 – Histograms showing the distance measured from the exposed surfaces that the Z-phase precipitates were observed after ageing the (a) HP-Nb1/Nb2 and (b) HP-NbTi1 alloys at 1000, 1050 and 1100°C for 1000 and 10,000 hours.

The initial transformation of MC precipitates to the nitrogen-rich Z-phase at the inner and outer diameter surfaces which were exposed to the nitrogen-rich furnace atmosphere and the subsequent progression of the MC-to-Z-phase transformation towards the mid-wall position strongly indicated this transformation only occurred within the HP-Nb and HP-NbTi alloys as a result of the furnace atmosphere. Hence, as with the $Cr_{23}C_6$-to-$Cr_2(CN)$ transformation, MC-to-Z-phase transformation is believed to have occurred due to the continuous absorption of nitrogen from the furnace atmosphere while ageing the HP-Nb and NbTi alloys at 1000 and 1050°C.

Similar to the $Cr_{23}C_6$-to-$Cr_2(CN)$, Wagner's equation for internal nitridation (equation 8.1) can be applied to the MC-to-Z-phase transformation in order to determine if the transformation kinetics are

determined by the inward diffusion of nitrogen. Figure 8.19 shows the depth at which Z-phase precipitates were observed in the HP-NbTi alloy with respect to ageing time when ageing at 1000 and 1050°C. When ageing at 1000°C, the penetration depth can be seen to increase linearly with respect to the square root of time. The linear relationship between ξ and √t confirms the MC-to-Z-phase transformation obeys a parabolic rate law and thus that the transformations kinetics are likely controlled by the inward diffusion of nitrogen. While the penetration depth appears to similarly show a linear relationship with respect to the square root of time when ageing at 1050°C for between 3000-10,000 hours, as shown by the relatively shallow penetration depth after ageing for 1000 hours, further work is necessary to confirm if a linear trend is observed when ageing for less than 3000 hours.

The NbC-to-η-carbide transformation dominated during ageing the HP-Nb alloy at 1000 and 1050°C significantly reducing the number of precipitates available to participate in the NbC-to-Z-phase transformation. Consequently, the area fraction and penetration depth of the Z-phase was considerably less in comparison to the HP-NbTi alloy. The dominance of the η-carbide transformation caused it to be inherently difficult to accurately determine the penetration depth with respect to time. Thus, further analysis is necessary to apply Wagner's internal nitridation equation to the Z-phase in the HP-Nb alloy.

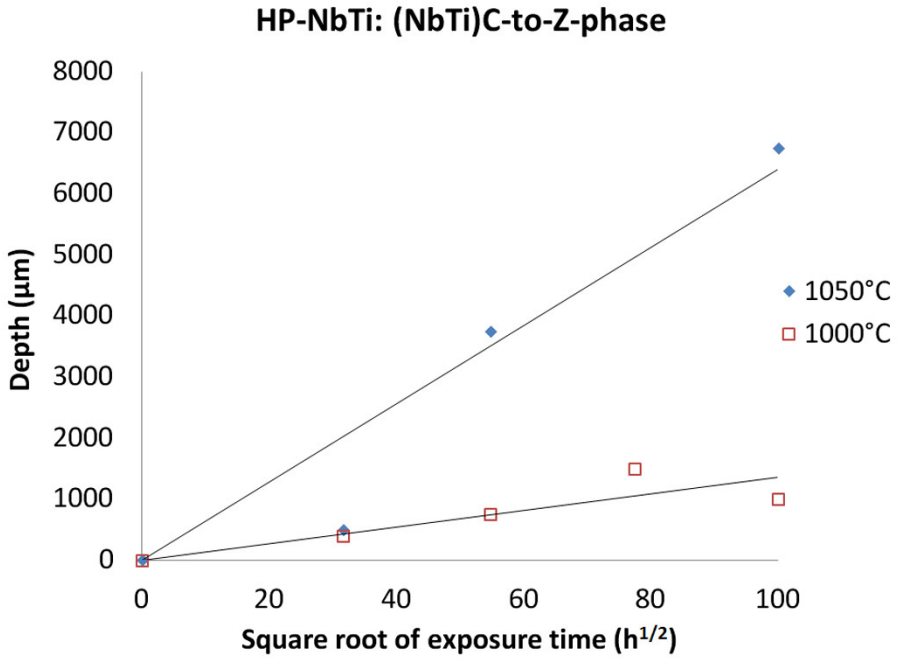

Figure 8.19 - Penetration depth of internal Z-phase precipitates at 1000 and 1050°C in the HP-NbTi alloy with respect to the square root of time.

8.3.3 MC-to-η-carbide Phase Transformation

Observations of the HP-Nb and HP-NbTi samples after ageing at 1000 and 1050°C determined that the furnace atmosphere also promoted the MC-to-η-carbide phase transformation within Zone A-II of each alloy. Figure 8.20 (a) to (d) show representative examples of the HP-Nb2 and HP-NbTi1 microstructures in Zone A-II and Zone UA after ageing at 1000°C for 10,000 hours. The influence of the furnace atmosphere on the MC-to-η-carbide transformation was dependent on both the alloying content and ageing temperature. In the HP-Nb2 alloy, the MC-to-η-carbide phase transformation proceeded independently of the furnace atmosphere when ageing at 1000°C (Chapter 6). However, comparison of the NbC precipitates undergoing the η-carbide transformation adjacent to exposed surfaces and at the mid-wall position when ageing at 1000°C determined the rate at which the transformation occurred was accelerated by the furnace atmosphere. As shown in Figure 8.20 (a), the MC-to-η-carbide transformation is nearing completion for precipitates located adjacent to Zone A-I with the η-carbides precipitates becoming comparable in size to the primary $Cr_{23}C_6$ precipitates after 10,000 hours. In contrast, the transformation of precipitates located at the mid-wall position (Zone UA) was considerably less advanced (Figure 8.20 (b)). Therefore, the furnace atmosphere appeared to accelerate the η-carbide transformation in the HP-Nb alloys during ageing.

In contrast to the HP-Nb alloys, the MC-to-η-carbide transformation only occurred in the HP-NbTi alloy as a direct result of the furnace atmosphere. Regardless of the ageing temperature and time, the MC-to-η-carbide phase transformation was not observed at the mid-wall position of the HP-NbTi alloy (Figure 8.20 (d)). Instead the η-carbide transformation was confined to MC precipitates situated within the affected regions at the inner and outer diameter positions (Figure 8.20 (c)).

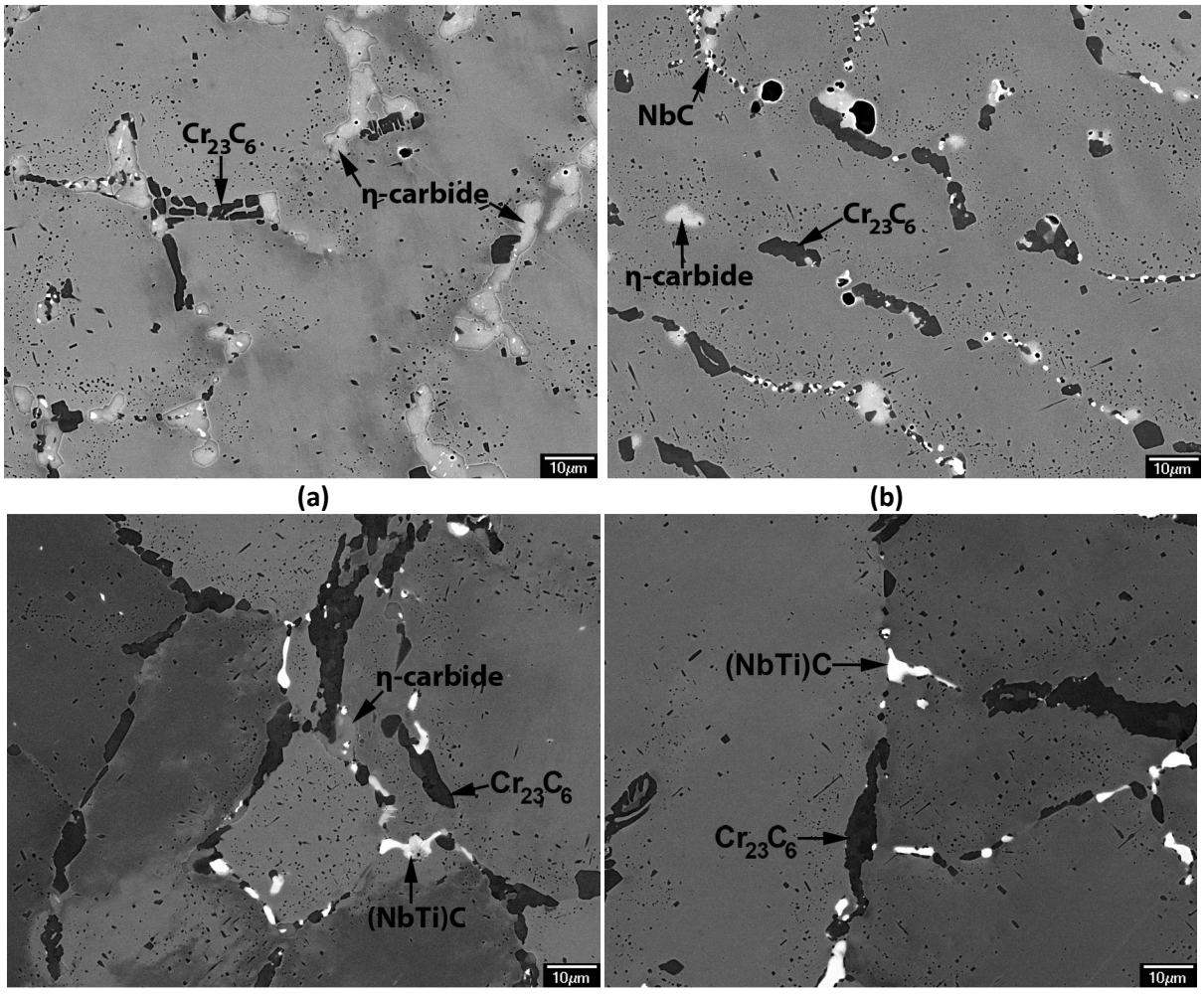

Figure 8.20 – Backscatter electron micrographs showing the phases present (a) & (c) in Zone A-II and (b) & (d) at the mid-wall position of the HP-Nb2 and HP-NbTi1 alloys after ageing at 1000°C for 10,000 hours

Table 8.6 and Table 8.7 show the ageing conditions where the furnace atmosphere induced the MC-to-η-carbide phase transformation at the inner and outer diameters of the HP-Nb1, HP-Nb2 and HP-NbTi1 alloys. Figure 8.21 (a) and (b) show the depth at which the η-carbide precipitates were observed after ageing each alloy for 1000 hours 10,000 hours. Overall, the MC-to-η-carbide transformation rate was greatest when ageing the HP-Nb2 alloy at 1000°C. This relatively high transformation rate was due to the MC-to-η-carbide transformation also occurring independent of the furnace atmosphere (Chapter 6). As a result, the η-carbides precipitates were observed across the entire wall thickness of the HP-Nb2 alloy within the first 1000 hours of exposure to 1000°C. The furnace atmosphere only acted to accelerate the transformation rate within the affected region of the HP-Nb2 tube. As shown in Figure 8.20 (a), this acceleration within the affected regions of the tube was typically evidenced through the significantly greater fraction of the primary NbC which had undergone the η-carbide transformation in comparison to the primary NbC located at the mid-wall position (Figure 8.20 (a)). While it was typically difficult to identify the extent to which the furnace atmosphere had affected the MC-to-η-carbide transformation when ageing the HP-Nb2 alloy at 1000°C, the depth at which noticeable acceleration was observed has been indicated in Figure 8.21 (a). Regardless of the ageing time, the MC-to-η-carbide transformation at the mid-wall position (Zone UA) was not believed to be significantly accelerated by the furnace atmosphere when ageing at 1000°C. In contrast to the HP-Nb2 samples aged at 1000°C, the MC-to-η-carbide transformation was initially confined to the inner and outer diameter positions of the HP-Nb1 alloy when ageing at 1050°C for 1000 hours. The MC-to-η-carbide transformation was only observed at the mid-wall position of the samples aged at 1050°C after 10,000 hours of exposure.

As discussed in Chapter 7, the addition of titanium to the MC precipitates in the HP-NbTi1 alloy considerably increased the stability of the MC precipitates with respect to the η-carbide transformation. Consequently, the MC-to-η-carbide transformation was considerably more sluggish within the HP-NbTi1 alloy. As shown in Figure 8.21 (b), η-carbide precipitates were solely observed at the inner and outer diameter positions of the HP-NbTi1 tube. The complete absence of η-carbide precipitates at the mid-wall position of the HP-NbTi aged samples regardless of the ageing temperature and time indicated these precipitates only formed as a result of the furnace atmosphere. In contrast to the HP-Nb alloys, the MC-to-η-carbide transformation rate was greatest when ageing at 1050°C (Figure 8.21 (b)).

Unsurprisingly, the total area fraction of η-carbide precipitates within Zone A-II of the HP-NbTi1 tube was significantly less in comparison to the HP-Nb1 and HP-Nb2 alloys. This decreased total area fraction would be expected as the considerable increase in the MC precipitates' stability with respect to the η-carbide transformation in the HP-NbTi1 alloys (due to the addition of titanium) caused the exposure time required to form η-carbides to be significantly greater than observed in the HP-Nb alloys. However, it must also be noted that the MC-to-η-carbide transformation faced comparatively greater competition with the MC-to-Z-phase transformation when ageing the HP-NbTi1 alloy at 1000 and 1050°C. As discussed in Section 0, MC precipitates located within 0.5mm of the exposed surfaces partially transformed to Z-phase after ageing at 1000 and 1050°C for 1000 hours. The depth at which the Z-phase transformation was observed progressively increased with ageing time. Thus, the MC-to-Z-phase transformation significantly reduced the number of MC precipitates available to participate in the MC-to-η-carbide transformation (which was first observed after 6000 hours). This situation was completely reversed in the HP-Nb alloys where the MC-to-η-carbide transformation more readily occurred, reducing the number of MC precipitates available to participate in the MC-to-Z-phase transformation.

Interestingly, unlike the $Cr_{23}C_6$-to-$Cr_2(CN)$ and MC-to-Z-phase transformations, only a marginal difference in the depth at which the MC-to-η-carbide transformation was observed when comparing the inner and outer diameter positions of the HP-NbTi1 tube (Figure 8.21 (b)). However, typically the transformed fraction of individual precipitates within the affected region at the inner diameter position was more advanced than precipitates located at the outer diameter position. The increased transformation rate at the inner diameter position was believed to be a result of the finer equiaxed grain structure (in comparison to the columnar grains) at the inner diameter being more susceptible to the effects of the furnace atmosphere. No noticeable difference in depth at which acceleration of the MC-to-η-carbide transformation was observed when comparing the inner and outer diameters of the HP-Nb1 and Nb2 alloys.

Regardless of the wall position, both the NbC and (NbTi)C precipitates remained completely stable during ageing at 1100°C.

Table 8.6 – Summary stating the ageing conditions where η-carbide precipitates was identified at the inner and outer diameters of the HP-Nb1 and HP-Nb2 alloys with respect to ageing temperature and time.

<table>
<tr><th rowspan="2">T (°C)</th><th rowspan="2">Wall Position</th><th colspan="4">Ageing Time (h)</th></tr>
<tr><th>1000</th><th>3000</th><th>6000</th><th>10,000</th></tr>
<tr><td rowspan="2">1000 (Nb2)</td><td>OD</td><td colspan="4" rowspan="2">NbC, η-carbide</td></tr>
<tr><td>ID</td></tr>
<tr><td rowspan="2">1050 (Nb1)</td><td>OD</td><td colspan="2" rowspan="2">NbC, η-carbide</td><td rowspan="4">No sample</td><td rowspan="2">NbC, η-carbide</td></tr>
<tr><td>ID</td></tr>
<tr><td rowspan="2">1100 (Nb1)</td><td>OD</td><td colspan="2" rowspan="2">NbC</td><td rowspan="2">NbC</td></tr>
<tr><td>ID</td></tr>
</table>

Table 8.7 – Summary stating the ageing conditions where η-carbide precipitates was identified at the inner and outer diameters of the HP-NbTi1 alloy with respect to ageing temperature and time.

<table>
<tr><th rowspan="2">T (°C)</th><th rowspan="2">Wall Position</th><th colspan="4">Ageing Time (h)</th></tr>
<tr><th>1000</th><th>3000</th><th>6000</th><th>10,000</th></tr>
<tr><td rowspan="2">1000</td><td>OD</td><td colspan="2" rowspan="2">(NbTi)C</td><td colspan="2" rowspan="2">(NbTi)C, η-carbide</td></tr>
<tr><td>ID</td></tr>
<tr><td rowspan="2">1050</td><td>OD</td><td colspan="2" rowspan="2">(NbTi)C</td><td rowspan="2">No sample</td><td rowspan="2">(NbTi)C, η-carbide</td></tr>
<tr><td>ID</td></tr>
<tr><td rowspan="2">1100</td><td>OD</td><td colspan="4" rowspan="2">(NbTi)C</td></tr>
<tr><td>ID</td></tr>
</table>

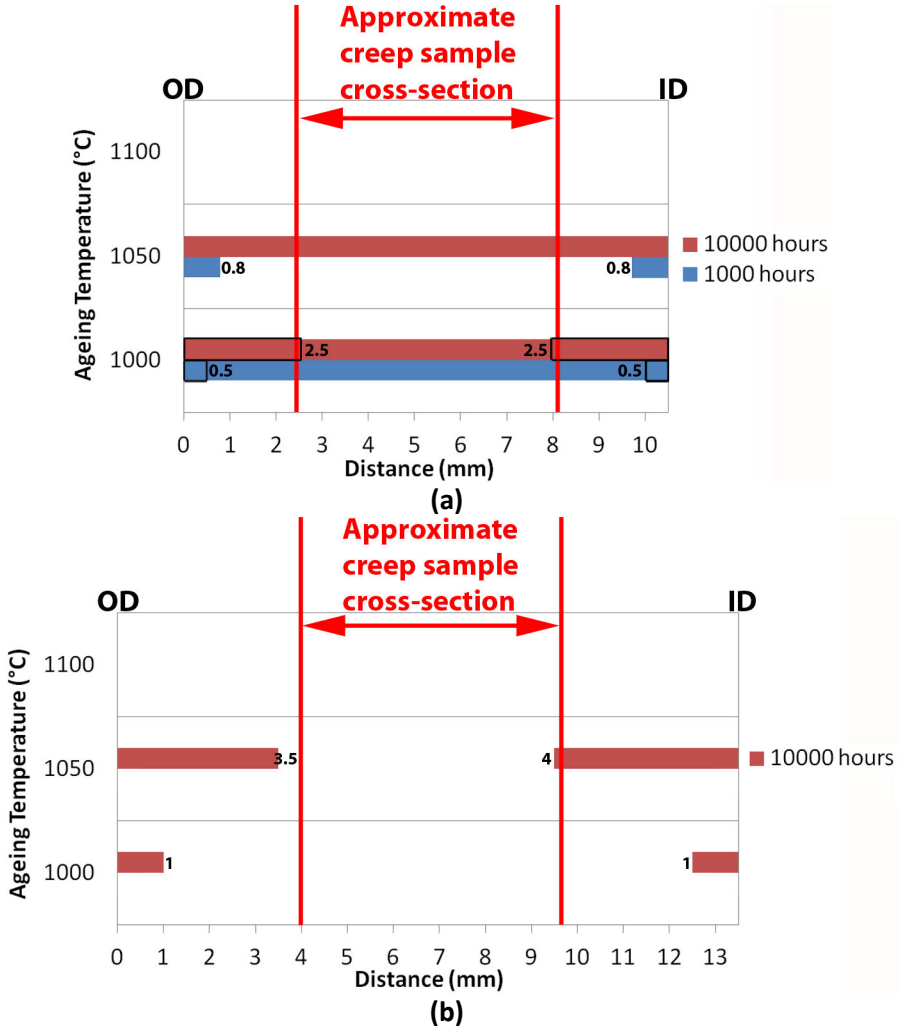

Figure 8.21 – Histograms showing the distance measured from the exposed surfaces that the η-carbide precipitates were observed after ageing the (a) HP-Nb1/Nb2 and (b) HP-NbTi1 alloy at 1000, 1050 and 1100°C for 1000 and 10,000 hours.

Identification of the η-carbide precipitates observed within the area of the HP-Nb1, HP-Nb2 and HP-NbTi1 tubes affected by the furnace atmosphere was carried out using a combination of EDS and EBSD (refer to Chapter 6 for representative EBSD patterns for the η-carbide crystal structure). Interestingly, η-carbide precipitates located within the affected regions of the aged samples exhibited greater chromium concentrations and lower niobium concentrations in comparison to the η-carbide observed at the mid-wall position of the HP-Nb2 1000°C aged samples (i.e. where the MC-to-η-carbide transformation was believed to occur completely independent of the furnace atmosphere). Figure 8.22 shows the concentration of chromium, nickel, silicon and niobium measured from η-carbide precipitates at increasingly greater distances from the exposed surfaces in the HP-Nb2 alloy after ageing at 1000°C for 10,000 hours. The average chromium concentration was

highest (41.1at.%) and niobium concentration lowest (6.4at.%) for η-carbide precipitates located directly adjacent to the exposed surfaces. The chromium concentration decreased while the niobium increased when analysing precipitates located at increasingly greater distances from the exposed surfaces. Typically, the concentration of chromium and niobium was relatively constant for precipitates located at distances greater than 1mm from the exposed surfaces (approximately 34at.% and 13at.% respectively).

Table 8.8 shows the average composition of the η-carbide precipitates in the HP-Nb1 (aged at 1050°C) and HP-NbTi1 (aged at 1000 and 1050°C) after ageing for 10,000 hours. In contrast to the η-carbide precipitates in the HP-Nb2 1000°C-10,000h sample, no compositional gradient was observed when comparing the composition of individual η-carbide precipitates with respect to wall position. Thus, all η-carbide precipitates within the HP-Nb1 1050°C-10,000h, HP-NbTi1 1000°C-10,000h and HP-NbTi1 1050°C-10,000h aged samples exhibited a chemical composition similar to the η-carbide precipitates observed directly adjacent to the exposed surfaces in the HP-Nb2 1000°C-10,000h aged sample.

While prolonged ageing of the HP-Nb1 alloy at 1050°C resulted in the partial transformation of MC precipitates to η-carbides across the tubes entire wall thickness (Figure 8.21 (a)), it was difficult to determine if the transformation at the mid-wall position would have proceeded if ageing had been conducted in an inert atmosphere. The sole observation of η-carbides within the affected area of the HP-Nb1 tubes after 1000 hours of exposure to 1050°C and progression of the transformation towards the mid-wall position during prolonged ageing suggested that the MC-to-η-carbide transformation within the 1050°C aged samples was mainly attributable to the furnace atmosphere. The consistent enrichment of the η-carbide precipitates with chromium across the entire wall thickness of the HP-Nb1 1050°C-10,000h sample provides further evidence to suggest that the MC-to-η-carbide transformation was likely to have been induced by the furnace atmosphere. Unfortunately, it was not possible to perform additional long-term ageing experiments at 1050°C with the HP-Nb1 alloy encapsulated within evacuated quartz tubes as performed for the HP-Nb 1000°C samples. Ageing of the encapsulated HP-Nb samples at 1000°C only required 1000 hours to confirm the presence of the MC-to-η-carbide across the tubes entire wall thickness. However, the comparatively more sluggish transformation rate observed at the mid-wall position of the HP-Nb1 alloy during ageing at 1050°C (10,000 hours) would have necessitated ageing of the encapsulated samples to also be performed for

10,000 hours in order to determine if the transformation would proceed without the furnace atmosphere.

The confinement of the MC-to-η-carbide transformation adjacent to the exposed surfaces and average chemical composition of the η-carbide precipitates in the HP-NbTi1 samples after ageing at 1050°C is believed to support the idea that this transformation was solely due to the furnace atmosphere.

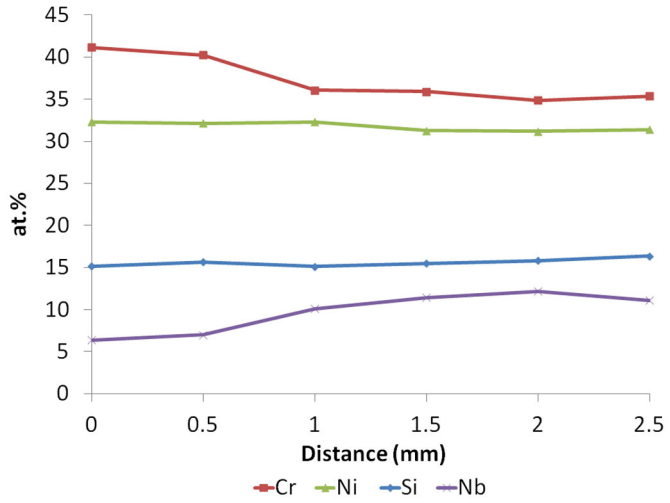

Figure 8.22 – Relative concentrations of chromium, nickel, silicon and niobium within the η-carbide precipitates located at increasingly greater distances from the exposed surfaces.

Table 8.8 – Average composition of the η-carbides precipitates after ageing the HP-Nb1, HP-Nb2 and NbTi at 1000 and 1050°C for 10,000 hours.

at.%	Cr	Ni	Nb	Si	Fe	V
Nb2 1000°C (MW)	33.8	31.2	13.1	15.6	5.4	1.0
Nb1 1050°C	40.1	29.5	7.8	17.4	4.6	0.7
NbTi1 1000°C	43.0	32.0	4.9	15.6	3.9	0.6
NbTi1 1050°C	42.7	29.8	5.5	17.4	4.5	0.3

The factors that promoted the MC-to-η-carbide transformation adjacent to the exposed surfaces were less apparent than observed for the $Cr_{23}C_6$-to-Cr_2(CN) and MC-to-Z-phase transformations**.** As discussed in Sections 8.3.1 and 0, the $Cr_{23}C_6$-to-Cr_2(CN) and MC-to-Z-phase transformations were believed to be directly induced by the absorption of nitrogen from the furnace atmosphere. However, no significant evidence of nitrogen was observed when performing EDS analysis on the η-carbide precipitates located within the affected regions of in the HP-Nb and NbTi alloys tubes. Hence, if nitrogen did promote the MC-to-η-carbide transformation in these alloys, the concentration of nitrogen within these η-carbide precipitates could not be resolved using the JEOL JED 2300 EDS detector.

Generally, the influence of nitrogen on the formation of η-carbides in austenitic steels is not well understood in the literature [4]. Nitrogen is believed to have a large influence on the formation of molybdenum-rich η-carbides with a nitrogen and molybdenum rich version of the η-carbide crystal structure having been identified in a 20Cr-25Ni-5Mo-0.2N steel after ageing at 850°C for 3000 hours [16]. Their *et al.* [17] identified similar precipitates after ageing a 316 stainless steel containing 0.069wt.% nitrogen at 900°C for 1 hour. However, Their *et al.* did not observe these precipitates after ageing a similar steel containing 0.037wt.% nitrogen at 900°C for 1000 hours. These studies suggested that nitrogen promotes the formation of molybdenum-rich η-carbides in austenitic steels. Thus, the higher nitrogen concentration within the affected regions of the HP-Nb and HP-NbTi alloys may have a similar effect on the formation of niobium-rich η-carbide. Unfortunately, similar studies on the influence of nitrogen on niobium-rich η-carbides were not found in the literature. Further analysis of 'model' HP-Nb alloys containing high and low concentrations of nitrogen is necessary to determine the effects of nitrogen on the MC-to-η-carbide transformation.

8.3.4 Accelerated Dissolution of the Secondary $Cr_{23}C_6$ Precipitates

In addition to the three primary precipitate network phase transformations, the furnace atmosphere also caused the accelerated dissolution of the secondary $Cr_{23}C_6$ precipitates within Zone A-II during ageing the HP-Nb1, HP-Nb2 and HP-NbTi1 alloys at 1000, 1050 and 1100°C. Figure 8.23 (a) to (c) shows representative examples of this dissolution within Zone A-II of the HP-Nb1 1050°C-10,000h sample. The accelerated dissolution shown in Figure 8.23 (a) to (c) was typical of Zone A-II in both alloys when ageing at 1000, 1050 and 1100°C. For comparison, Figure 8.23 (d) shows the numerous secondary precipitates which typically remained at the mid-wall position of the HP-Nb 1050°C-10,000h sample.

Generally, the dissolution of the secondary $Cr_{23}C_6$ precipitates was most severe within the region of the tubes where the primary $Cr_{23}C_6$ had transformed to $Cr_2(CN)$. As shown in Figure 8.23 (a) and (b), the secondary $Cr_{23}C_6$ precipitates have completely dissolved within this region of the tubes, commonly resulting in the austenite matrix being completely free of intragranular precipitates (Figure 8.23 (a)). However, clusters of acicular $Cr_2(CN)$ secondary precipitates (arrowed in Figure 8.23 (b)) were observed within the austenite matrix. These clusters were only found within regions where the primary $Cr_{23}C_6$ had transformed to $Cr_2(CN)$ and were most prevalent after ageing of the HP-Nb1 and HP-NbTi1 alloys at 1050°C. Typically, the regions containing these clusters of acicular $Cr_2(CN)$ secondary precipitates were located directly adjacent to Zone A-I and adjacent to the $Cr_2(CN)/Cr_{23}C_6$ transition interface shown in Figure 8.9 (c) and (d).

As the number of acicular $Cr_2(CN)$ secondary precipitates within each cluster was typically greater in comparison to the number of Widmanstätten $Cr_{23}C_6$ secondary precipitates observed over the same area, these precipitates were not believed to have formed through the transformation of existing Widmanstätten $Cr_{23}C_6$ secondary precipitates. Alternatively, the acicular $Cr_2(CN)$ secondary precipitates likely nucleate and grow separately within the austenite matrix once the nitrogen concentration reaches a minimum threshold level (currently unknown). Consequently, the concentration of these precipitates adjacent to Zone A-I can be expected as the nitrogen concentration would be greatest within the matrix directly adjacent to the exposed surfaces (i.e. adjacent to the source of nitrogen). However, the cause of these clusters adjacent to the $Cr_2(CN)/Cr_{23}C_6$ transition interface is less well understood. It is unlikely that the nitrogen concentration within the matrix adjacent to the transition interface would be greater than the

neighbouring regions which were closer to the exposed surfaces but did not contain any acicular $Cr_2(CN)$ secondary precipitates. Unfortunately, the nitrogen concentrations within the austenite matrix were unable to be detected by the JEOL JED-2300 EDS detector and the analysis of the nitrogen content using techniques more sensitive to light elements (such as electron energy loss spectroscopy) was not possible. Thus, the cause of the acicular $Cr_2(CN)$ secondary precipitates adjacent to the $Cr_2(CN)/Cr_{23}C_6$ transition interface is currently unknown.

As shown in Figure 8.23 (c), the transition of the primary $Cr_2(CN)$ precipitates to $Cr_{23}C_6$ precipitates was also accompanied by the appearance of secondary $Cr_{23}C_6$ precipitates. The distribution of secondary $Cr_{23}C_6$ precipitates adjacent to the $Cr_2(CN)$-to-$Cr_{23}C_6$ transition interface was sparser in comparison to the distribution observed at the mid-wall position (Figure 8.23 (c)). The secondary precipitate distribution became increasingly denser with increasing distance from the $Cr_2(CN)/Cr_{23}C_6$ transition interface. The sparser distribution near the transition interface was due to the closer proximity of these precipitates to the exposed surfaces (i.e. the influence of the furnace atmosphere accelerated the Ostwald ripening of these precipitates relative to precipitates located at the mid-wall position). Unfortunately, it was not possible to quantify the extent to which the furnace atmosphere had affected the secondary precipitate distributions in the HP-Nb and HP-NbTi alloys with respect to ageing temperature and time. Determining this depth requires comparison with samples where the secondary precipitate distributions were completely unaffected by the ageing atmosphere (i.e. reference samples aged in an inert atmosphere). Ageing additional samples of the HP-Nb1, HP-Nb2 and HP-NbTi alloys at 1000, 1050 and 1100°C for 10,000 hours was not possible within the current project's time frame.

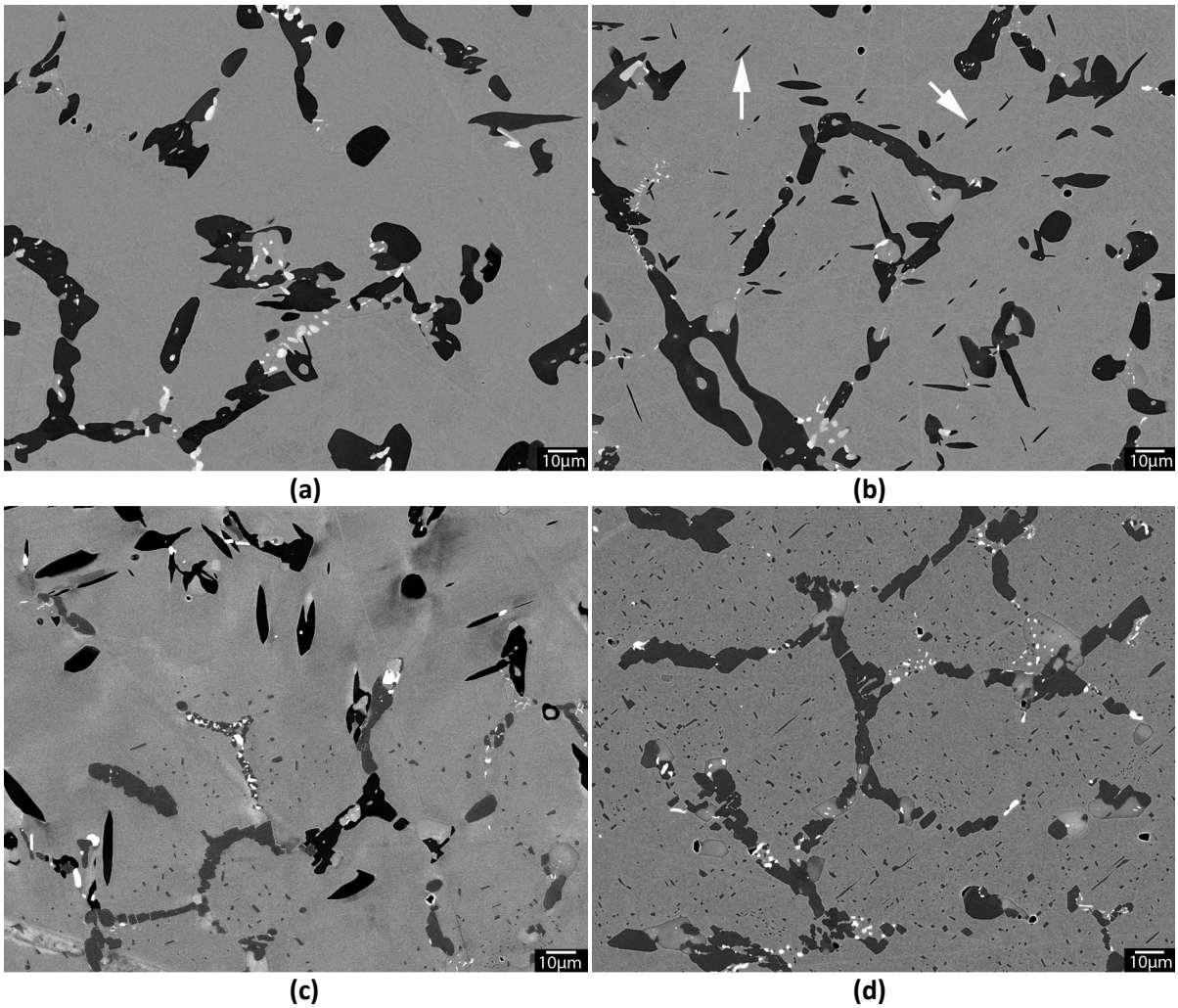

Figure 8.23 – Backscatter electron micrographs demonstrating the accelerated dissolution of the secondary $Cr_{23}C_6$ precipitates which occurred within Zone A-II (a) - (c) during ageing of the HP-Nb and NbTi alloys at 1000, 1050 and 1100°C. (d) Micrograph taken at the mid-wall position where the secondary precipitates were relatively unaffected.

Generally, the rate at which the dissolution of the secondary precipitates occurred increased with the ageing temperature. As discussed in Chapters 6 and 7, the accelerated dissolution induced by the furnace atmosphere was believed to have attributed to the dissolution of the secondary $Cr_{23}C_6$ precipitates across the entire wall thickness of the HP-Nb1 and HP-NbTi1 1100°C-10,000h aged samples. The accelerated dissolution of the secondary $Cr_{23}C_6$ precipitates adjacent to the exposed surfaces was believed to be largely due to furnace atmosphere causing significant decarburization of the HP-Nb1, HP-Nb2 and HP-NbTi1 alloys during ageing at 1000, 1050 and 1100°C. This belief was based on the transformation of the carbon-rich $Cr_{23}C_6$ and MC primary precipitates in favour of the carbon-lean $Cr_2(CN)$, Z-phase and η-carbide phases (EDS indicated the carbon content in each phase was less the 5at.%) and loss of the carbon-rich secondary precipitates. Unless the carbon from the

dissolving precipitates was lost to the furnace atmosphere it had to have been completely re-absorbed within the austenite matrix. The re-absorption of the carbon that was initially rejected from the austenite matrix resulting in the formation of the primary precipitate network during solidification and secondary precipitates during ageing is considered highly unlikely.

While carbon in the HP-Nb1, HP-Nb2 and HP-NbTi1 alloys was believed to have been lost to the air atmosphere within each furnace during ageing, due the limited amount of material available for metallographic analysis, analysis of the carbon content within the aged samples using destructive techniques such as ICP-AES (as performed on the as-cast samples) was not possible. As discussed in chapter 5, the carbon content along the length of the as-cast HP-NbTi2 tube varied by $^{+}/_{-}$ 0.02 wt.%. Thus, an average of multiple composition analyses performed on separate sections of the as-cast and aged samples would have been necessary to ensure that this variance would not have masked the change in the carbon content due to the furnace atmosphere.

Previous work by Voicu *et al.* [5] measured the carbon content within HP-Nb alloys in the as-cast condition and after ageing at 1000°C in air for approximately 6500 hours. Samples were machined from the mid-wall position and analysed using combustion analysis. Interestingly, this analysis indicated that the carbon content increased by 0.06wt.% during ageing. While the authors attributed this increase to the release of carbon from the $Cr_{23}C_6$ precipitates to the "bulk of the material" (i.e. to the matrix) during ageing, it is considered to be more likely due to statistical variations in the carbon content along the tubes length. In order to observe an increase in the "bulk" carbon content due to the dissolution of the $Cr_{23}C_6$ precipitates the authors would need to separate the $Cr_{23}C_6$ precipitate networks from the matrix prior to performing combustion analysis of each sample. Such separation would likely require the dissolution of the precipitate networks possibly using an etchant which specifically dissolves the widely different precipitate networks present within as-cast and aged HP-Nb alloys. However, the authors made no mention of any attempt to separate the precipitates and matrix suggesting the combustion analysis included both the matrix and precipitates. As it was unlikely the precipitate network was separated from the matrix prior to combustion analysis, the carbon initially contained within the chromium carbides would have been included when analysing the as-cast samples. Thus, neglecting any external source or sink for carbon (e.g. a carburizing or decarburizing ageing atmosphere), the carbon content in the aged samples would only vary as a result of the as-cast variation.

As shown in Figure 8.23 (c), the dissolution of the secondary precipitates closely followed the $Cr_{23}C_6$-to-$Cr_2(CN)$ phase transformation when ageing at 1050°C. The austenite matrix within affected region of the tubes was shown to contain a comparatively lower concentration of chromium in comparison to the mid-wall position (Section 8.3.1) as a result of surface oxidation and the transformation of the primary chromium and niobium rich carbides to chromium rich nitrides. As a result, the depletion of chromium from the austenite matrix could have also contributed to the accelerated the dissolution of the secondary precipitate network within the affected regions of the aged samples.

As discussed in Section 8.3.1, the chromium concentration within the austenite after ageing at 1050°C for 10,000 hours was significantly lower in comparison to the chromium concentration after ageing at 1100°C for 10,000 hours (Figure 8.15 (a) and (b)). The greater depletion of chromium from the austenite matrix during ageing at 1050°C was believed to be due to the MC-η-carbides and MC-Z-phase transformations only occurring when ageing at 1050°C. Interestingly, the chromium concentration at distances greater than 0.5mm from the exposed surfaces of the HP-Nb and HP-NbTi tubes after ageing at 1100°C for 10,000 hours was similar to the chromium concentration within the unaffected region of the 1000, 1050 and 1100°C samples after ageing for 1000 hours (typically 22-25wt.%). Therefore, the level of chromium depletion due to surface oxidation was believed to be relatively insignificant in comparison to the chromium depletion due to the MC-η-carbides and MC-Z-phase transformations. Although, the secondary $Cr_{23}C_6$ precipitates completely dissolved after ageing at 1100°C for 10,000 hours, the area fraction of primary $Cr_{23}C_6$ consistently increased suggesting that a significant proportion of the chromium released from the dissolution of the secondary precipitate distribution was absorbed by the primary precipitate network rather than diffusing to Zone A-I in order to support the chromium-rich oxide scale.

Further work is necessary to distinguish the level of chromium depletion from the austenite matrix due to oxidation and depletion due to the $Cr_{23}C_6$-to-Cr_2N, MC-to-η-carbide and MC-to-Z-phase phase transformations. Analysis of the matrix and precipitates' chemical composition (as discussed in Section 8.3.3 the chromium content in the η-carbide phase decreases with increasing distance from the surface) with respect to wall position, ageing temperature and time needs to be measured using EDS. In parallel, image analysis of each phase with respect to wall position, ageing temperature and time is also necessary in order to estimate the chromium depletion from the matrix due to the $Cr_{23}C_6$, Cr_2N, η-carbide, and Z-phase precipitates (i.e. each phase that contains chromium). The chromium depletion from the matrix due to each phase transformation can then be estimated and compared

with the measured chromium content. Any discrepancy between the measured chromium depletion and depletion predicted from image analysis can subsequently be used to determine the chromium depletion from the matrix due to surface oxidation.

8.4 Summary of the Phases formed within the HP-Nb and HP-NbTi Tubes due to the Furnace Atmosphere.

Table 8.9 and Table 8.10 gives a summary of the phases identified within the HP-Nb1, HP-Nb2 and HP-NbTi1 alloys after ageing at 1000, 1050, 1100°C for 1000 and 10,000 hours. Phases that were formed as a direct result of the furnace atmosphere (e.g. $Cr_2(CN)$, Z-phase) or influenced by the furnace atmosphere (e.g. η-carbide) have been highlighted in red. Comparing the phases present in each aged sample demonstrates that the types of phase transformations that occurred as a result of the furnace atmosphere when ageing at 1000, 1050 and 1100°C were similar for both alloys. Thus, the phase transformations were mainly dependent on the ageing temperature rather than the alloy content. However, as discussed in Sections 8.3.1 to 8.3.3, the depth at which each phase was observed and the total area fraction of each phase with respect to ageing temperature and time varied between each alloy. Table 8.11 summarizes the crystal structure information for the phases shown in Table 8.9 and Table 8.10.

Table 8.9 - Phases identified in the aged HP-Nb1 and HP-Nb2 samples.

T (°C)	Ageing Time (h)			
	1000	3000	6000	10,000
1000 (Nb2)	$Cr_{23}C_6$, NbC, η-carbide	$Cr_{23}C_6$, NbC, η-carbide, Z-phase		$Cr_{23}C_6$, NbC, η-carbide, Z-phase, $Cr_2(CN)$
1050 (Nb1)	$Cr_{23}C_6$, NbC, $Cr_2(CN)$, η-carbide	$Cr_{23}C_6$, NbC, $Cr_2(CN)$, η-carbide, Z-phase	No samples	$Cr_{23}C_6$, NbC, $Cr_2(CN)$, η-carbide, Z-phase
1100 (Nb1)	$Cr_{23}C_6$, NbC	$Cr_{23}C_6$, NbC, $Cr_2(CN)$		$Cr_{23}C_6$, NbC, $Cr_2(CN)$

Table 8.10 - Phases identified in the aged HP-NbTi1 samples.

T (°C)	Ageing Time (h)			
	1000	3000	6000	10,000
1000	$Cr_{23}C_6$, (NbTi)C, Z-phase	$Cr_{23}C_6$, (NbTi)C, Z-phase, $Cr_2(CN)$	$Cr_{23}C_6$, (NbTi)C, Z-phase, $Cr_2(CN)$, η-carbide	$Cr_{23}C_6$, (NbTi)C, Z-phase, $Cr_2(CN)$, η-carbide
1050	$Cr_{23}C_6$, NbC, Z-phase, $Cr_2(CN)$	$Cr_{23}C_6$, NbC, Z-phase, $Cr_2(CN)$	No sample	$Cr_{23}C_6$, (NbTi)C, Z-phase, $Cr_2(CN)$, η-carbide
1100	$Cr_{23}C_6$, (NbTi)C	$Cr_{23}C_6$, (NbTi)C, $Cr_2(CN)$		

Table 8.11 - Crystal structures identified within the HP-Nb and HP-NbTi alloys after ageing at 1000, 1050 and 1100°C for 10,000 hours in an air atmosphere.

Phase	Crystal System	Space Group	Lattice parameters a, b, c (nm)			α, β, γ (°)			Ref.
$Cr_{23}C_6$	Cubic	$Fm\bar{3}m$	1.065	1.065	1.065	90	90	90	11
NbC/(NbTi)C	Cubic	$Fm\bar{3}m$	0.446	0.446	0.446	90	90	90	Chapter4/5
η-carbide	Diamond cubic	$Fd\bar{3}m$	1.084	1.084	1.084	90	90	90	Chapter 6
$Cr_2(CN)$	Hexagonal	$P\bar{3}1m$	0.482	0.482	0.447	90	90	120	17
Z-phase	Tetragonal	$P4/nmm$	0.303	0.303	0.739	90	90	90	15

Figure 8.24 (a) and (b) shows the average size of the affected region (i.e. Zones A-I and A-II) in the HP-Nb1, HP-Nb2 and HP-NbTi1 alloys after ageing at 1000, 1050 and 1100°C for 1000 and 10,000 hours. Measurements were taken after ageing for 1000 hours as the extent to which these samples were affected by the furnace atmosphere during isothermal ageing gives a indication of the extent that the creep samples would be affected during accelerated creep testing of the HP-Nb and NbTi alloys (if testing is conducted in an air atmosphere). These measurements suggest that, at worst, accelerated testing of the HP-Nb and HP-NbTi alloys at 1050°C within an air atmosphere would be expected to modify each alloys microstructure to a depth of 0.8-1mm. However, analysis of the nitrogen concentration with respect to distance from the surface of 347 creep samples (800°C, 77,782 hours exposure) by Erneman *et al.* [12] using wavelength dispersive X-ray spectroscopy determined that the nitrogen content differed markedly when comparing the grip and gauge length sections of the sample. The maximum nitrogen concentration in the grip section was approximately 0.5wt.% whereas the maximum concentration in the gauge length was 1.5wt.% (observed directly adjacent to the exposed surfaces). This difference was attributed to the properties of the chromium-rich oxide layer at each section. The oxide layer at surfaces of the grip layer reportedly provided a constant barrier to the ingress of nitrogen. However, the deformation along the samples gauge length was believed to have caused cracking of the oxide layer, subsequently reducing the effectiveness of this layer in preventing the absorption of nitrogen. Thus, the thickness of the affected region within HP alloy creep samples will likely be greater than shown in Figure 8.24 (a) and (b) for samples which were subjected to unstressed isothermal ageing.

The marked microstructural modification that can occur over a large proportion of the creep samples gauge length during accelerated testing of the HP alloys in an air atmosphere raises serious questions to whether such testing yields an accurate representation of the tubes in-service creep resistance. While $Cr_2(CN)$ and Z-phase precipitates have been identified at the outer diameter of ex-service HP-

Nb and HP-NbTi tubes which experienced temperatures between 890-910°C for 95,000-131,000 hours [2], insufficient information has been published to determine the extent to which the ex-service tubes were affected (i.e. percentage of the tube wall affected by the atmosphere and area fraction of each phase within the affected area) by the steam-methane reforming furnaces' atmosphere (typically a mixture of CO_2, CO, N_2 and H_2O depending on the air/fuel ratio). Therefore, considerable further analysis needs to be carried out on laboratory aged and ex-service material to determine the effects of the atmosphere induced phases on the creep resistance of the HP-Nb and HP-NbTi alloys.

It is considered necessary to initially perform accelerated creep testing of as-cast, laboratory aged and ex-service HP-Nb and HP-NbTi samples within an air atmosphere and an inert (e.g. argon) atmosphere in order to determine whether the microstructural modification caused by the air atmosphere during the time-frame of an accelerated creep test results in a measurable change in the alloys' creep resistance. Significant further analysis of ex-service material is also necessary to determine the service conditions which cause the formation of the $Cr_2(CN)$ and Z-phase precipitates during service and the extent (i.e. depth, area fraction and distribution of the precipitates with respect to the tube-wall position) to which these phases form within each alloy. Such analysis is imperative to determine if the phase transformations that occur when performing accelerated creep testing within an air atmosphere can be considered to be representative of the tubes microstructural evolution during actual service.

Measurements of Zone A-I and A-II in the samples aged at 1050 and 1100°C for 10,000 hours determined that the total affected area after ageing at 1050 and 1100°C had encroached on the gauge length of the creep samples which were subjected to accelerated creep testing by Quest Integrity Group. Table 8.12 shows the type of microstructural modifications which were observed at the mid-wall position of the HP-Nb and HP-NbTi 1050 and 1100°C aged samples. While the modification to the primary precipitate network at the mid-wall position of the samples aged at 1050°C (as shown in Figure 8.16 (a) and (b)) was significantly less in comparison to the modification observed adjacent to the exposed surface (as shown in Figure 8.10 (a) and (b)), it is considered that the observed microstructural modification at the mid-wall position will likely influence the creep resistance of the HP-Nb and HP-NbTi alloys. While the effects of the MC-to-η-carbide and MC-to-Z-phase transformations (after ageing at 1050°C) on the HP-Nb and HP-NbTi alloys' creep resistance is currently unknown, the complete dissolution of the secondary precipitates during ageing of the HP-

Nb1 and HP-NbTi1 alloys at 1100°C as a result of the atmosphere will reduce each alloys creep resistance. It must be also noted that the effects of the furnace atmosphere on each samples microstructure will worsen during the subsequent accelerated creep testing and further atmosphere induced degradation of the alloys' creep properties is possible during this testing.

Currently, it is believed that the severely affected microstructures observed in the HP-Nb1 and HP-NbTi1 1050 and 1100°C samples are unlikely to be representative of service exposed material (based on comparison with the phases reported at the mid-wall position of ex-service HP-Nb and HP-NbTi alloys [2]). Thus, the creep properties (i.e. minimum creep rate, rupture strength and creep ductility) measured from these samples will also unlikely be representative of the creep properties exhibited by the HP-Nb and HP-NbTi alloys during actual service in a steam-methane reforming furnace. Thus, prior to the application of any creep results measured from these samples to predict the HP-Nb and HP-NbTi alloys actual service performance, it is currently recommended that further microstructural analysis and testing of samples which were aged within an inert atmosphere (e.g. argon) ex-service material which experienced temperatures between 1000-1100°C.

As the extent to which the furnace atmosphere affected the mid-wall microstructure was significantly less for all other laboratory aged HP-Nb1, HP-Nb2 and HP-NbTi samples, the microstructural evolution at the mid-wall position of these samples is considered to be similar to that observed in ex-service material (based on qualitative comparison between the laboratory aged HP-Nb1, HP-Nb2 and HP-NbTi1 samples and ex-service HP-Nb and HP-NbTi material presented by Berghof-Hasselbächer *et al.* [2]).

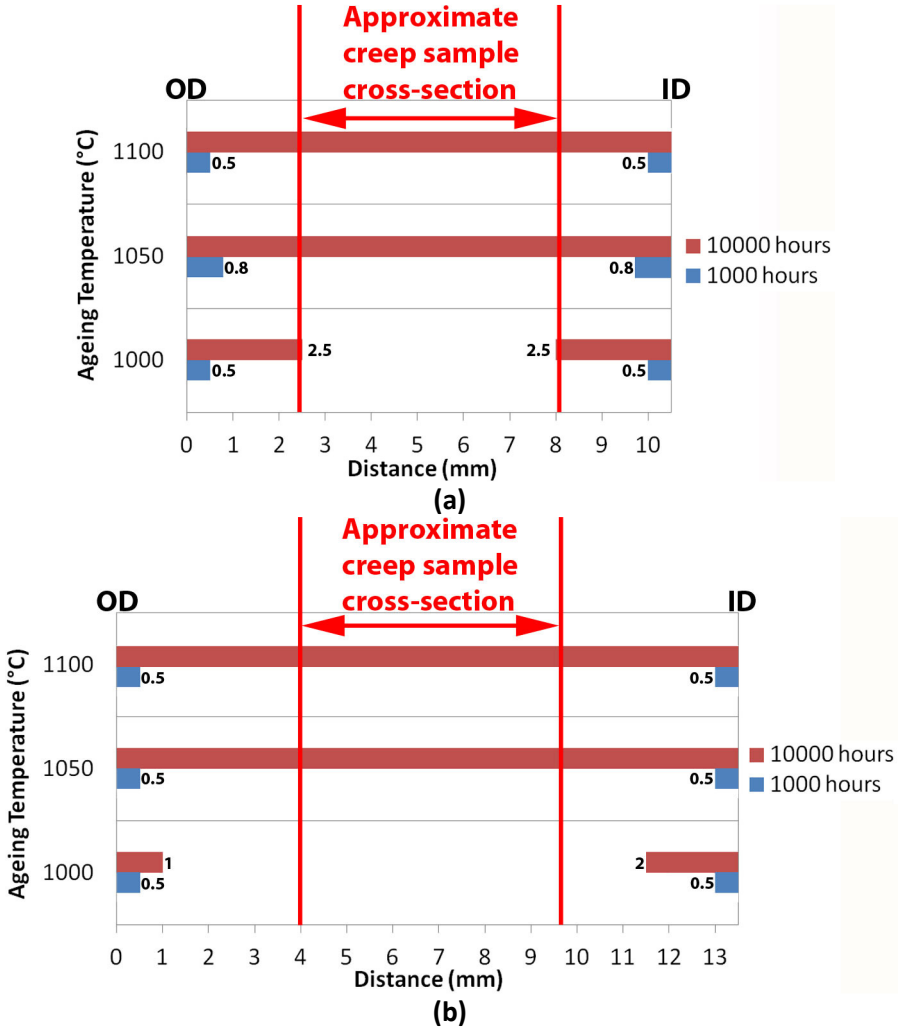

Figure 8.24 – Histograms showing the total size of the affected regions (measured from the tubes inner and outer diameters) in the (a) HP-Nb1/Nb2 and (b) HP-NbTi1 alloys.

Table 8.12 – Summary of the aged samples where the phase transformations induced by the furnace atmosphere had encroached on the accelerated creep samples gauge length.

Alloy	T (°C)	Ageing Time (h)	Atmosphere Induced Modification
HP-Nb1	1050	10,000	NbC/η-carbide transformation
	1100	10,000	Complete dissolution of secondary $Cr_{23}C_6$
HP-NbTi1	1050	10,000	(NbTi)C/Z-phase transformation
	1100	10,000	Complete dissolution of secondary $Cr_{23}C_6$

Conclusions

The furnace atmosphere significantly influenced the microstructural evolution of the HP-Nb and HP-NbTi alloys during exposure to temperatures between 1000-1100°C. This effect raises serious questions over the validity of performing isothermal ageing and accelerated creep testing of the HP alloys within air atmospheres. Overall, the creep resistance of the HP-Nb and HP-NbTi alloys is expected to decrease as a result of the furnace atmosphere induced transformations and subsequent coarsening of the primary precipitate network and the complete dissolution of the secondary precipitates. Currently, it is unknown if the atmosphere induced microstructural modifications observed at the inner and outer diameter positions of the laboratory aged samples are representative of the microstructural modifications which have been reported within ex-service HP-Nb and HP-NbTi tubes. Therefore, it is currently recommended that considerable further microstructural analysis be carried out on ex-service material to determine the extent to which the HP-Nb and HP-NbTi alloys microstructures are affected by the reforming furnace's atmosphere during service. Further accelerated creep testing of as-cast, laboratory aged and ex-service HP-Nb and HP-NbTi samples within an air atmosphere and an inert atmosphere is also recommended to determine if the microstructural modification caused by the air atmosphere during the time-frame of an accelerated creep test results in a measurable change in the alloys creep resistance. This testing will determine if it is necessary to strictly control the furnace atmosphere when subsequently performing accelerated testing on the HP alloys.

Chapter References

[1] Quest Integrity Group (2013). *Reformer Care: A Complete Asset Integrity Solution.* Retrieved January 2013, from http://www.questintegrity.com/technology/steam-reformer-tube-inspection

[2] Berghof-Hasselbacher, E., Gawenda, P., Schorr, M. & Schutze, M. (2008). *Atlas of Microstructures.* St. Lous: Materials Technology Institute.

[3] Thomas, C. W., Stevens, K. J. & Ryan, M. J. (1996). *Microstructure and properties of alloy HP50-Nb: comparison of as cast and service exposed materials.* Materials Science and Technology, 12: pp. 469-475.

[4] Sourmail, T. (2001). *Precipitation in creep resistant austenitic stainless steels.* Materials Science and Technology, 17: pp. 1-14.

[5] Voicu, R., Andrieu, E., Poquillon, D., Furtado, J. & Lacaze, J. (2009). *Microstructure evolution of HP40-Nb alloys during aging under air at 1000°C.* Materials Characterization, 60: pp. 1020-1027.

[6] Xu, N., Monceau, D., Young, D., & Furtado, J. (2008). *High temperature corrosion of cast heat-resistant steels in CO + CO2 gas mixtures.* Science, 50(8): pp. 2398-2406.

[7] Al-Meshari, A. & Little, J. (2009). *High temperature oxidation of centrifugally cast heat-resistant alloys.* Materials at High Temperatures, 26(3): pp. 233-239.

[8] Carvalho, P. A., Machado, I. F., Solórzano, G. & Padilha, A. F. (2008). *On Cr_2N precipitation mechanisms in high-nitrogen austenite.* Philosophical Magazine, 88(2): pp. 229-242.

[9] Lee, T. -H. & Kim, S. -J. (1998). *PHASE IDENTIFICATION IN AN ISOTHERMALLY AGED AUSTENITIC 22Cr-21Ni-6Mo-N STAINLESS STEEL.* Scripta Materialia, 39(7): pp. 951-956.

[10] Shankar, P., Sundararaman, D. & Ranganathan, S. (1994). *Cr_2N PRECIPITATION STAGES IN 316LN AUSTENITIC STAINLESS STEELS.* Scripta Metallurgica *et* Materialia, 31(5): pp. 589-593.

[11] Sundararaman, D., Shankar, P. & Ranganathan, S. (1996). *Electron Microscopic Study of Cr_2N Formation in Thermally Aged 316LN Austenitic Stainless Steels.* Metallurgical and Materials Transactions A, 27: pp. 1175-1186.

[12] Erneman, J., Schwind, M., Liu, P., Nilsson, J. -O., Andrén, H. -O. & Årgren, J. (2004). *Precipitation reactions caused by nitrogen uptake during service at high temperatures of a niobium stabilised austenitic stainless steel.* Acta Materialia, 52: pp. 4337-4350.

[13] Ibañez, R. A. P., Soares, G. D. A., de Almeida, L. H. & Le May, I. (1993). *Effects of Si Content on the Microstructure of Modified-HP Austenitic Steels.* Materials Characterization, 30: pp. 243-249.

[14] Raghavan, A., Klein, C. F. & Marzinsky, C. N. (1992). *Instabilities in stabilized austenitic stainless steels.* Metallurgical Transactions A, 24(9): pp. 2455-2467.

[15] Jack, D. H. & Jack, K. H. (1972). *Structure of Z-phase, NbCrN.* Journal of the Iron and Steel Institute (London), 210(10): pp. 790-792.

[16] Jargelius-Pettersson, R. F. A. & Rachel, F. A. (1998). *Precipitation trends in high alloyed austenitic stainless steels. Zeitschrift fuer Metallkunde/Materials Research and Advanced Techniques*, 89(3): pp. 177-183.

[17] Their, H., Bämuel, A., Schmidtmann, E. (1969). *Einfluß von Stickstoff auf das Ausscheidungs-verhalten des Stahles X 5CrNiMo 1713.* Arch Eisenhüttenw, 40(4): 333-339.

[18] Christ, H. J., Chang, S. Y. & Krupp, U. (2003). *Thermodynamic characteristics and numerical modelling of internal nitridation of nickel base alloys.* Materials and Corrosion, 54(11):pp. 887-894

Chapter 9 Summary and Concluding Remarks

9.1 Summary of Achievements

9.1.1 As-Cast HP-Nb and HP-NbTi Alloys

Two compositionally unique niobium-modified centrifugally cast tubes (referred to as the HP-Nb1 and HP-Nb2 alloys for the purposes of this thesis) were subjected to detailed microstructural analysis. The HP-Nb1 alloy was manufactured by Paralloy Limited U.K. (alloy designation H39W) whereas the HP-Nb2 alloy was manufactured by Kubota Metal Corporation Canada (alloy designation KHR35C). Each alloy had completely columnar grain structures, with the HP-Nb1 alloys grain size appearing significantly coarser than the HP-Nb2 alloy. A combination of EDS, EBSD, SAD, and CBED was used to confirm that the primary network was composed of alternating groups of chromium-rich Cr_7C_3 and niobium-rich NbC precipitates. These precipitates were generally located on dendrite boundaries rather than grain boundaries.

Analysis of the primary NbC precipitates in two- and three-dimensions using high resolution scanning electron microscopy revealed these precipitates obtained two distinctly different lamellar morphologies. The properties of Type I and Type II lamellar morphologies can be summarized as follows:

- The Type I NbC lamellae had solid lamellar plates which shared a relatively planar interface with the adjacent austenite;
- The Type II lamellae had web-like or reticulated plates with Cr_7C_3 identified between the Type II lamellae and austenite interfaces;
- Both NbC morphologies obtained a FCC ($Fm\bar{3}m$) MC crystal structure;
- The Type II lamellae was more prevalent than the Type I lamellae in both the HP-Nb1 and HP-Nb2 alloys;

The morphological difference was determined by the solidification conditions that each type of lamellae experience:

- Nucleation of the Type II lamellae occurs on the existing austenite dendrite followed by eutectic growth of the lamellae with the austenite. Consequently, the lamellae obtain a cube-cube ($<100>_{NbC}||<100>_{\gamma}$, $\{100\}_{NbC}||\{100\}_{\gamma}$) orientation relationship (OR) with the adjacent austenite matrix and the broad faces of the NbC lamellae also obtain a {100} habit plane.
- Nucleation and growth of the Type II lamellae was believed to have occurred in the liquid ahead of the γ/L interface, prior to the formation of the Type I lamellae. Local melt thermal and chemical gradients subsequently dominate growth of the Type II lamellae resulting in the observed array of undulations within the plates and overall planar growth. The differing solidification conditions experienced by the Type II lamellae causes no consistent, rational OR to be obtained between the Type II lamellae and austenite matrix. Moreover, although the lamellae often adhered to an overall growth plane in three-dimensions, the lamellae did not obtain a consistent habit plane.

Two different heats of HP-NbTi alloy were also investigated in the as-cast condition (referred to as the HP-NbTi1 and HP-NbTi2 alloys for the purposes of this thesis). Both HP-NbTi centrifugally cast tubes were manufactured by Schmidt + Clemens Spain S.A.U (alloy designation Centralloy® 4852Micro). The HP-NbTi1 alloys exhibited a mixed columnar/equi-axed grain structure (80% /20%), whereas the HP-NbTi2 alloy exhibited a completely columnar grain structure. Similar to the HP-Nb alloys, a combination of EDS, EBSD and SAD confirmed the HP-NbTi alloys' primary precipitate network was composed of chromium-rich Cr_7C_3 precipitates separated by blocky niobium-titanium rich (NbTi)C precipitates. In addition to the primary (NbTi)C precipitates, cuboidal titanium carbides were also present in the HP-NbTi2 alloy. Within the columnar regions of the tubes, the primary precipitates were predominantly located on dendrite boundaries rather than grain boundaries. However, in the equiaxed region of the HP-NbTi1 alloy, the primary precipitates were almost exclusively located on grain boundaries.

Detailed analysis of the primary (NbTi)C precipitates in two- and three-dimensions reveal that these precipitates obtain two distinct morphologies: the Type III and Type IV (NbTi)C morphologies. The following summarizes each morphology's attributes:

- Both (NbTi)C morphologies obtained a FCC ($Fm\bar{3}m$) MC crystal structure;
- The Type III blocky morphology was significantly more prevalent than the Type IV nodular morphology which was obtained by less than 1% of the total (NbTi)C population in both the HP-NbTi1 and HP-NbTi2 alloys;
- The Type III morphology exhibited multiple blocky branches in three-dimensions which radiated outwards from a centralised nucleus. This nucleus typically contained an oxide core on which the (NbTi)C precipitate nucleated;
- The Type IV (NbTi)C precipitate morphology was generally present as thick plates which exhibited significant undulations along the plates broad faces. In two-dimensions the Type IV (NbTi)C precipitates appeared similar to the Type II lamellae in the HP-Nb alloy but in three-dimensions, the plates did not exhibit the porosity of the Type II lamellae;
- For both morphologies, Cr_7C_3 precipitates were identified between the (NbTi)C and austenite interfaces. The Cr_7C_3 precipitates located between the Type III/austenite interfaces obtained a dendritic morphology whereas the Cr_7C_3 precipitates located between the Type IV/austenite interfaces obtained a faceted morphology.

Interestingly, (NbTi)C precipitates exhibiting both the Type III and IV morphologies were observed in the deep etched samples. These precipitates suggested the origin of the Type IV morphology was unlikely to be related to any difference in the nucleation site or precipitate/matrix crystallography as shown for the Type I and II NbC lamellae. Instead, the morphology preference was determined to be related to the local concentration of titanium within the melt during solidification. Nucleation and growth was believed to occur as follows:

- Initially, nucleation of the spherical titanium carbo-nitrides occurs on the aluminium oxide inclusions present within the melt;
- These Ti-rich spheres subsequently act as prolific nucleation sites for the Type III (NbTi)C precipitates, resulting in nucleation of multiple (NbTi)C grains;
- Grains favourably oriented with respect to local thermal and compositional gradients grow preferentially, resulting in the three-dimensional blocky branches;

- The Type IV morphology only emerges for branches located in regions of the melt which are relatively poor in titanium. As the growth of the branch progresses, the continual reduction of titanium within the melt likely reduces the (NbTi)C/L interfacial free energy, eventually allowing these precipitates to form the much greater interfacial area associated with the nodules.

Hence, during solidification, titanium causes all niobium-rich primary precipitates to nucleate and grow in the matrix ahead of the γ/liquid interface. The nucleation of all niobium-rich precipitates ahead of the γ/liquid interface suppresses the formation of the lamellar (Type I) morphology that was observed in the as-cast HP-Nb alloy. During growth of the (NbTi)C precipitates, the presence of titanium within the growing precipitate increases the interfacial energy between the precipitate and liquid. This increased interfacial energy causes the (NbTi)C precipitates to typically obtain the blocky morphology to reduce the precipitates total interfacial surface area, thus largely suppressing the growth of the Type II NbC morphology that was also believed to nucleate and grow ahead of the γ/liquid interface during solidification of the HP-Nb alloy.

No evidence of secondary precipitation was observed (through SEM and TEM observations) within the HP-Nb and HP-NbTi alloys' as-cast austenite matrix (i.e. the interdendritic primary carbides were the only precipitates observed in each as-cast alloy).

9.1.2 The Evolution HP-Nb and HP-NbTi alloys' Microstructures during Long-Term Isothermal Ageing

Detailed characterization of the HP-Nb1, HP-Nb2 and HP-NbTi1 alloys' microstructural evolution during long-term isothermal ageing was carried out using a combination of LOM, SEM, EDS, EBSD, TEM, SAD, and XRD. Initially, specific attention was paid to the aged samples' mid-wall position, as the creep samples that were subjected to accelerated creep testing by Quest Integrity Group were taken from this section of the aged samples.

In general, the evolution of the chromium-rich precipitates at the mid-wall position was similar in the HP-Nb and HP-NbTi alloys during ageing and can be summarized as follows:

- Complete transformation of the as-cast primary Cr_7C_3 to $Cr_{23}C_6$ for all ageing temperatures occurred within the first 6 hours of exposure to 1000, 1050 and 1100°C;
- The transformed $Cr_{23}C_6$ precipitates present after ageing for 1000 hours were agglomerates of numerous grains;
- Typically, neighbouring grains exhibited disorientations of less than 10°, however high angle disorientations (>15°) were also observed;
- Approximately 57% of the total population of $Cr_{23}C_6$ precipitates in both the HP-Nb and HP-NbTi alloys obtained a cube-cube ($<100>_{Cr23C6}//<100>_{\gamma}$, $\{100\}_{Cr23C6}//\{100\}_{\gamma}$) OR with the austenite matrix within the first 1000 hours of exposure to 1000°C;
- During prolonged ageing the $Cr_{23}C_6$ coarsened considerably with both the average size and area fraction increasing. Generally, the coarsening rate increased with ageing temperature and was believed to be enabled by the dissolution of the secondary $Cr_{23}C_6$ precipitates.
- The cube-cube OR became more prevalent during prolonged ageing. Ageing the HP-Nb2 and HP-NbTi1 alloys at 1000°C for 10,000 hours caused the prevalence of the OR to increase to 70 and 67% respectively. This increase in the number of precipitates which obtained the cube-cube OR with the matrix was believed to be beneficial to the alloys creep resistance.

Overall, the near identical evolution of the chromium-rich primary precipitates in the HP-Nb and HP-NbTi alloys suggested that these precipitates do not significantly contribute to the HP-NbTi alloy's superior creep resistance in comparison to the HP-Nb alloy.

In contrast to the evolution of the chromium-rich primary precipitates, the evolution of the niobium-rich primary precipitates varied significantly when comparing the in the HP-Nb and HP-NbTi alloys:

- Ageing the HP-Nb alloys at 900°C for 1000 hours resulted in the near complete transformation of the Type I and II colonies to a mixed network of G-phase ($Ni_{16}Nb_6Si_7$) and η-carbide $(CrNiNbSi)_6C$;
- Partial transformation of the primary NbC solely to η-carbide was observed after ageing the HP-Nb alloy at 1000°C for 1000 hours. The NbC-to-η-carbide transformation progressed

significantly during prolonged ageing at 1000°C. Rarely, the entire Type I and II NbC colonies were completely consumed by the η-carbide transformation after 10,000 hours;

- When ageing the HP-Nb alloy at 1050°C, the NbC-to-η-carbide transformation was considerably more sluggish with η-carbide precipitates only being observed after 10,000 hours;
- The NbC crystal structure remained stable when ageing the HP-Nb alloy at 1100°C although significant coarsening of the NbC occurred during prolonged ageing;
- In contrast to the NbC precipitates in the HP-Nb alloy, the (NbTi)C precipitates in the HP-NbTi alloy generally remained stable regardless of the ageing temperature and time. During prolonged ageing, the average size and area fraction of the (NbTi)C precipitates typically increased.

Currently, it is unclear if the η-carbide/austenite and G-phase/austenite interfaces are prone to creep damage (i.e. void nucleation and growth). Therefore, significant further research is necessary to determine how each of these phases affects the HP alloys' creep properties (e.g. minimum creep rate, creep ductility, rupture strength). If the presence of either η-carbide or G-phase precipitates is detrimental to the HP alloys' creep properties, the rapid formation of large volume fractions of these precipitates within the first 10,000 hours of exposure to temperatures between 900-1000°C would be expected to significantly reduce the service life of HP-Nb alloy reformer tubes in comparison to HP-NbTi alloy reformer tubes.

Widespread precipitation of $Cr_{23}C_6$ was observed between the Type II/austenite (HP-Nb), Type III/austenite (HP-NbTi) interfaces after ageing. SEM and TEM observations revealed these interfacial precipitates share similar characteristics to the primary and secondary precipitates including:

- The interfacial $Cr_{23}C_6$ precipitates transform from the Cr_7C_3 precipitates that are present between the MC and austenite interfaces in the as-cast HP-Nb and HP-NbTi alloys;
- The interfacial precipitates obtained the same cube- cube OR as the primary and secondary $Cr_{23}C_6$ precipitates;
- The $Cr_{23}C_6$/austenite interfaces exhibited similar faceting to the secondary matrix $Cr_{23}C_6$, suggesting these facets obtain the same {110} and/or {111} habit planes.

Extensive secondary precipitation of $Cr_{23}C_6$ occurred within the austenite matrix of the HP-Nb and HP-NbTi alloys during exposure to 1000, 1050 and 1100°C. The formation and growth of these precipitates was similar for both alloys and can be summarized as follows:

- The secondary $Cr_{23}C_6$ precipitate distribution was relatively well established after 500 hours with the average size of these precipitates ranging between 0.5-1μm^2;
- The secondary precipitates were concentrated within the austenite matrix directly adjacent to the primary precipitate network. The density of the secondary precipitates decreased with increasing distance from the primary precipitates;
- The precipitates predominantly obtained a cuboidal morphology, but Widmanstätten $Cr_{23}C_6$ precipitates were also observed in both alloys;
- The Widmanstätten $Cr_{23}C_6$ precipitates located in the same austenite grain typically exhibited parallel or orthogonal alignment suggesting the plates obtained a specific habit or growth plane;
- The Widmanstätten $Cr_{23}C_6$ precipitates were shown to be laths in three-dimensions that emanated from the Type II NbC lamellae in the HP-Nb alloy and the Type III and IV (NbTi)C precipitates in the HP-NbTi alloy;
- Identical to the primary $Cr_{23}C_6$ precipitates, both the cuboidal and Widmanstätten secondary $Cr_{23}C_6$ obtained a cube-cube OR with the matrix;
- During prolonged ageing, Ostwald ripening of the secondary $Cr_{23}C_6$ precipitates supported the coarsening of the primary $Cr_{23}C_6$ network, leading to the progressive loss of the secondary precipitates in each alloy;
- No significant difference in the size and number of $Cr_{23}C_6$ secondary precipitates was observed when qualitatively comparing the aged HP-Nb and HP-NbTi alloys suggesting that initial nucleation and growth of the secondary precipitate distribution and subsequent Ostwald ripening of these precipitates did not significantly differ with respect to alloying content.

Bright field TEM observations revealed presence of nano-scale Nb-rich particles (~50-100nm in diameter) in the HP-NbTi alloy. Regardless of the ageing temperature or time, these nano-scale precipitates were completely absent in the HP-Nb alloy. The Nb-rich precipitates in the aged HP-NbTi alloy were believed to obtain the (NbTi)C ($Fm\bar{3}m$) crystal structure. The nano-scale (NbTi)C

precipitates were typically less than 50nm in diameter after ageing of the HP-NbTi alloy for 1000 hours and were significantly more resistant to coarsening during prolonged ageing in comparison to the $Cr_{23}C_6$ secondary precipitates.

The HP-NbTi alloy's superior creep resistance is believed to be largely attributed to the greater dispersion strengthening effect provided by this alloy's mixed $Cr_{23}C_6$-(NbTi)C secondary precipitate distribution in comparison to the HP-Nb alloy's $Cr_{23}C_6$ secondary precipitate distribution. Although the increased stability of the primary (NbTi)C precipitates in the HP-NbTi alloy in comparison to the primary NbC precipitates in the HP-Nb alloy may also contribute to the HP-NbTi alloy's superior creep resistance, significant further work into the effects of the primary carbide's morphology and the effects of η-carbides on the each alloy's creep properties is necessary to quantify the relationship between the primary carbide network and creep properties.

Ageing of the as-cast HP-Nb and HP-NbTi alloys was conducted by isothermally aging at 1000, 1050 and 1100°C in a furnace containing an air atmosphere for up to 10,000 hours. The use of an air atmosphere during ageing (as opposed to an inert atmosphere such as argon) caused significant decarburization and nitridation of the HP-Nb and HP-NbTi alloys. This decarburization and nitridation induced multiple phase transformations at each tube's inner and outer diameters which generally did not occur at the mid-wall position. For most samples, the effects of the air atmosphere were mainly confined to material adjacent to the free surfaces (i.e. surfaces exposed to the air atmosphere). The following phase transformations were believed to be induced by the furnace atmosphere:

$Cr_{23}C_6$-to-Cr_2(CN)

- Occurred when ageing at 1000, 1050 and 1100°C;
- Transformation rate was relatively independent of the alloy composition;
- Most prevalent when ageing both alloys at 1050°C.

NbC /(NbTi)C-to-Z-phase (MCr(CN)).

- Proceeded in both alloys when ageing at 1000 and 1050°C;
- Transformation rate was dependent on the alloy composition;
- Most prevalent for both alloys when ageing at 1050°C, however the (NbTi)C precipitates in the HP-NbTi alloy were more susceptible to the Z-phase

transformation resulting in a significantly greater area fraction of Z-phase in the HP-NbTi alloy in comparison to the HP-Nb alloy;

- Did not occur in either alloy when ageing at 1100°C.

NbC/(NbTi)C-to-η-carbide (M_6C)

- Proceeded in both alloys when ageing at 1000 and 1050°C;
- While the NbC-to-η-carbide phase transformation in the HP-Nb alloy was shown to occur independently of the furnace atmosphere when ageing at 1000°C, this phase transformation was accelerated by the furnace atmosphere;
- Generally, more prevalent in the HP-Nb alloy in comparison to the HP-NbTi alloy;
- Did not occur in either alloy when ageing at 1100°C.

In addition to primary precipitate phase transformations, the furnace atmosphere also accelerated the dissolution of the secondary precipitate distribution within each alloy. Generally, the accelerated dissolution of the secondary precipitates did not affect the mid-wall position when ageing at 1000 and 1050°C. However, the furnace atmosphere was believed to have contributed to the complete dissolution of the secondary precipitates after ageing at 1100°C for 10,000 hours.

The significant influence of the furnace atmosphere on the microstructural evolution of the HP alloys during exposure to temperatures between 1000-1100°C raises doubt over the validity of performing isothermal ageing and accelerated creep testing of the HP alloys within air atmospheres since the microstructural modification which occurred to the HP-Nb and HP-NbTi alloys as a result of the furnace atmosphere will likely affect each alloys creep resistance. While similar phase transformations have been identified at the outer diameter of ex-service tubes, it is currently it is unknown if these phases were present to the extent as observed in the affected the inner and outer diameter positions of the laboratory aged samples.

9.2 Concluding remarks

The primary objective of the current research was to determine the effects of the single addition of niobium and dual additions of niobium and titanium on the HP alloy's microstructure in the as-cast condition and during long-term isothermal ageing.

For the HP-Nb alloy, the current research has provided significant further insight into the nucleation and growth of the primary NbC precipitates during solidification. The subsequent instability of the primary NbC precipitates with respect to the η-carbide and G-phase transformations during ageing at temperatures between 900-1000°C has also been discussed in detail.

For the HP-NbTi alloy, it is believed that this research has demonstrated the key role that titanium plays in modifying the HP-NbTi alloy's microstructure in the as-cast and aged conditions. Specifically, the influence of titanium on the nucleation and growth of the niobium-rich precipitates during solidification was discussed with respect to the morphology obtained by the in the as-cast niobium-rich precipitates in the HP-Nb and HP-NbTi alloys. During isothermal ageing, the 3-5wt.% titanium contained within (NbTi)C precipitates has been shown to completely suppress the MC-to-η-carbide transformation. Titanium was also believed be responsible for the formation of niobium-titanium rich secondary precipitates that were an order of magnitude finer than the chromium-rich secondary precipitates and more resistant to coarsening during prolonged ageing.

The current research has also shown that the average size, area fraction and crystallography of the chromium-rich primary precipitates during prolonged ageing were independent of the alloying content, strongly suggesting that the HP-NbTi alloy's superior creep resistance in comparison to the HP-Nb alloy is not related to the chromium-rich primary precipitate network.

Overall, the increased HP-NbTi alloy superior creep resistance in comparison to the HP-Nb alloy is believed to due to titanium's influence on stability of the primary MC precipitates and enabling of the fine dispersion of niobium-titanium-rich precipitates during ageing.

This research has also highlighted the significant interaction between the ageing atmosphere and the HP alloys' microstructure during long-term thermal exposure. The extensive modification of the HP-Nb and HP-NbTi alloys' microstructure during isotheral ageing demonstrated that further research

into the interaction between each alloy's microstructure and the atmospheres experienced by HP reformer tubes is necessary to determine if the creep properties measured by accelerated creep testing of the HP-Nb and HP-NbTi alloys are representative of each alloy's creep properties during actual service.

9.3 Future Work

9.3.1 As-cast Grain Distribution

Due to the centrifugal casting technique, the cross-section of the reformer tubes typically consists of small equiaxed (chill) grains, followed by columnar grains, and finally equiaxed grains. The ratio of columnar to equiaxed grains (at the tube's inner diameter) depends on the melt pouring temperature, mould material, and the rotational speed of the mould during pouring. Although the centrifugal casting technique has become the industry standard for the tubes manufacture, the optimum columnar-equiaxed grain structure with respect to the tube's creep strength remains relatively unclear. This uncertainty has largely arisen due to the difficulty of accurately measuring and comparing the creep properties of HP alloy reformer tubes which exhibit widely different grain structures.

Currently, measurement of the creep properties of HP alloy tubes are largely determined through uni-axial accelerated creep testing of samples which are machined from the center of the tubes wall thickness. As the creep samples gauge length often only encompasses a fraction (50-60%) of the tubes wall thickness, it is inherently difficult to produce test samples which fairly represent the mixed grain structures exhibited by reformer tubes. Even if creep samples were produced with sufficient cross-sectional area to completely encompass the tubes grain structure, the complex stress state and non-uniform temperature distribution through the tubes wall thickness during service will likely negate the validity of predicting the tubes in-service creep resistance by performing uni-axial accelerated testing on these samples.

Alternatively, the creep life of tubes cast with varying combinations of columnar and equiaxed grain structures could be measured by performing creep testing on pressurized tubes. Such testing would possibly also allow for the stresses induced by through-wall temperature gradients to be simulated by flowing pressurized gas through the pipe during testing. Such testing would provide further insight into the grain distribution which maximizes the tube's creep resistance. Additionally, the pressurized pipe tests could be halted prior to failure of the tube in order to perform sectioning and microstructural analysis of the creep void distributions with respect to grain structure.

9.3.2 NbC-to-G-phase and NbC-to-η-carbide Phase Transformations (HP-Nb)

While considerable effort was placed into the characterization of the NbC-to-G-phase and NbC-to-η-carbide transformations in the current research, it is necessary to define the η-carbide and G-phase TTT curves through further laboratory ageing of the HP-Nb alloys between 700-1050°C (i.e. the temperature range over which these transformations have been observed) followed by phase identification and quantitative image analysis to determine the area fraction of G-phase and η-carbide and the percentage of NbC transformed with respect to ageing temperature and time.

A detailed investigation into the effects of G-phase and η-carbide on the HP-Nb alloy's creep resistance is also considered essential to gain a complete understanding of the microstructural factors which affect the tube's service life. If the accumulation of creep damage preferentially occurs on the η-carbide/austenite and G-phase/austenite interfaces, the relatively large area fraction of these phases that rapidly form during ageing potentially provides ample interfacial area within the HP-Nb alloy for creep void nucleation.

The characterization of creep void distributions in ex-service and accelerated creep samples which contain G-phase η-carbide precipitates would provide further insight into if the G-phase/austenite or η-carbide/austenite interfaces are prone to creep damage. Emphasis should be placed on the characterization of the void distributions in ex-service tubes as the shape, location and volume fraction of voids can differ between ex-service and accelerated creep testing samples.

9.3.3 Quantitative Measurement of the Secondary $Cr_{23}C_6$ Precipitate Distribution

While quantitative image analysis of the secondary precipitates was attempted by performing image analysis on the $Cr_{23}C_6$ secondary precipitates using backscatter electron images, the high variability of the secondary precipitates with respect to grain and dendrite position and the high degree to which the polish quality could affect the visibility of these precipitates typically caused the measurement of the secondary precipitate distribution in each aged sample to be inaccurate when using this method. Generally, the non-uniform distribution of the secondary precipitates made it inherently difficult to obtain images from consistently comparable regions of separate dendrite arms when viewing the aged microstructures in two-dimensions. Thus, serial sectioning of the aged samples using a FIB (focused ion beam) with high resolution FE-SEM imaging is considered necessary in order to accurately measure and compare the non-uniform secondary precipitate distributions present within the HP-Nb and HP-NbTi alloys. Since the casting can alter the secondary precipitate distributions in each alloy, any modification to the secondary precipitate distribution as a result of the differing alloying content can be masked by the casting conditions. Hence, in order to obtain an accurate comparison of the secondary precipitate distributions within the HP-Nb and HP-NbTi alloys (i.e. to determine if the alloying content affects the secondary precipitates distribution), either multiple HP-Nb and HP-NbTi alloy tubes that have experienced a range of differing casting conditions must be analysed or more simply the sample of HP-Nb and HP-NbTi alloys must experience the same casting conditions.

9.3.4 Investigation of Atmosphere Induced Phase Transformation in Ex-Service HP alloys

Ageing the HP-Nb and HP-NbTi alloys within an air atmosphere caused multiple additional phase transformations to occur at each tube's inner and outer diameter (i.e. the material directly adjacent to the exposed surfaces) that typically did not occur at the tube's mid-wall position. While the additional phase transformations have also been identified at the outer diameter of ex-service HP-Nb and HP-NbTi tubes, it is currently unknown if the extent to which each alloy's microstructure is modified during service within a reforming furnace is similar to that experienced by the HP-Nb and HP-NbTi alloys during unstressed laboratory ageing or accelerated creep testing. Therefore, it is

recommended that considerable further microstructural analysis be carried out on ex-service material to determine the extent to which the HP-Nb and HP-NbTi alloys microstructures are affected by the furnace atmosphere during long-term service exposure. Since these additional phase transformations will likely affect the HP-Nb and HP-NbTi alloys' creep resistance, further accelerated creep testing of as-cast, laboratory aged and ex-service HP-Nb and HP-NbTi samples within an air atmosphere and atmospheres that are representative of those experienced by the tubes during actual service is also necessary to determine if the microstructural modification caused by the air atmosphere during the time-frame of an accelerated creep test results in a measurable change in the alloys creep resistance.

9.3.5 Comparison of the HP alloy's Creep Properties after Stressed and Unstressed Ageing

Unfortunately, due to numerous uncontrollable delays experienced during the manufacture of the accelerated creep testing rigs, it was not possible to test the samples which had been aged with and without the mechanical application of stress. Thus, in order to determine if the creep properties obtained from HP alloys that have been subjected to unstressed isothermal ageing can be used to predict the creep properties of HP reformer tubes during actual service, accelerated creep testing of the stressed samples that have experienced simulated service conditions should be carried out.

Appendix A Selected Properties of the HP-Nb and HP-NbTi Alloys

The following figures and tables show the typical physical and mechanical properties for the HP-Nb1, HP-Nb2, HP-NbTi1 and HP-NbTi2 alloys (as published by Kubota Metal Corporation [1], Paralloy [2] and Schmit-Clemens [3] respectively) that were considered relevant to the current research.

A.1 Kubota Metal Corporation Alloy KHR35C (HP-Nb1)

The following tables give the typical chemical composition; creep rupture strength with respect to temperature and time; and minimum creep rate with respect to stress and temperature for Kubota Metal Corporation's centrifugally cast KHR35C alloy [1]. This alloy was referred to as the "HP-Nb1" alloy in the current research.

Table A.1 – KHR35C chemical composition. Balance:Fe.

	C	Mn	Si	Cr	Ni	Nb	P	S
Min %	0.4			24	34	0.6		
Max %	0.5	1.5	1.5	28	37	1.5	<0.3	<0.3

Table A.2 – Stress required for creep rupture of the KHR35C alloy within the given temperatures and times.

		RUPTURE STRESS (KSI)							
Hours	**(°F)**	**1400**	**1500**	**1600**	**1700**	**1800**	**1900**	**2000**	**2100**
100	**AVG.**	-	-	10.5	8.24	6.24	4.55	3.15	2.05
	MIN.	-	-	9.11	7.14	5.42	3.96	2.75	1.79
1000	**AVG.**	-	10.79	8.37	6.28	4.51	3.06	1.94	1.14
	MIN.	-	9.34	7.26	5.45	3.92	2.67	1.69	0.99
10,000	**AVG.**	-	8.71	6.48	4.61	3.08	1.91	1.1	-
	MIN.	-	7.55	5.63	4.01	2.69	1.67	0.95	-
100,000	**AVG.**	9.26	6.86	4.85	3.22	1.97	1.11	0.63	-
	MIN.	8.02	5.96	4.22	2.81	1.72	0.96	0.52	-

Table A.3 – Stress required for a 0.001%/hour minimum creep rate with respect to temperature.

%/HOUR	(°F)	1700	1800	1900	1922	2012
0.001	**AVG.**	4.12	2.77	1.76	1.45	0.9

A.2 Paralloy Alloy H39W (HP-Nb2)

Table A.4 and Figure A.1 give the chemical composition and creep rupture strength of Paralloy's centrifugally cast H39W alloy [2]. This alloy was referred to as the "HP-Nb2" alloy in the current research.

Table A.4 – H39W chemical composition. Balance:Fe.

wt.%	C	Mn	Si	Cr	Ni	Nb
Nominal	0.4	1	1.5	25	35	1.2

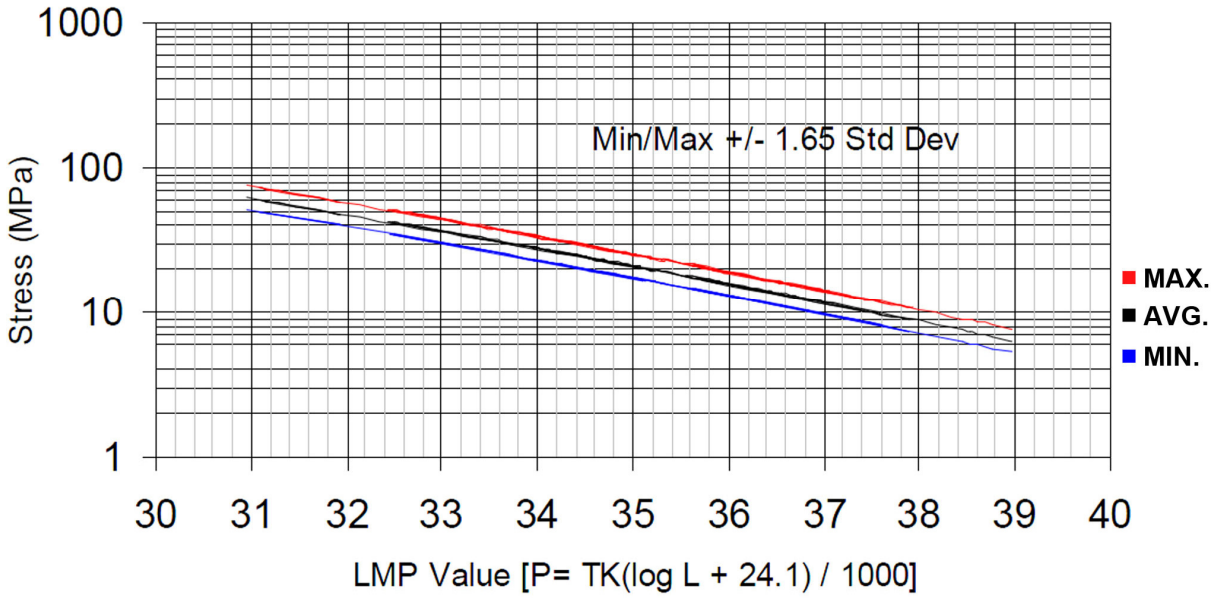

Figure A.1 – Larson-Miller stress rupture plot of Paralloy H39W (Directly reproduced from [2]).

A.3 Schmidt + Clemens Group Centralloy® G 4852 Micro (HP-NbTi1, HP-NbTi2)

Table A.5 and Figure A.2 give the chemical composition and creep rupture strength of Schmidt and Clemens Group centrifugally cast Centralloy® G 4852 Micro [3]. This alloy was referred to as the "HP-NbTi1" and "HP-NbTi2" alloys in the current research. As discussed in Chapter 5, the HP-NbTi1 and HP-NbTi2 were referred to separately as each tube was individually cast resulting in slight variance between the tubes chemical compositions, grain structures and precipitate networks.

Table A.5 – Centralloy® G 4852 Micro chemical composition

wt.%	C	Mn	Si	Cr	Ni	Nb	Ti
Nominal	0.45	1	1.5	25	35	1.5	Additions

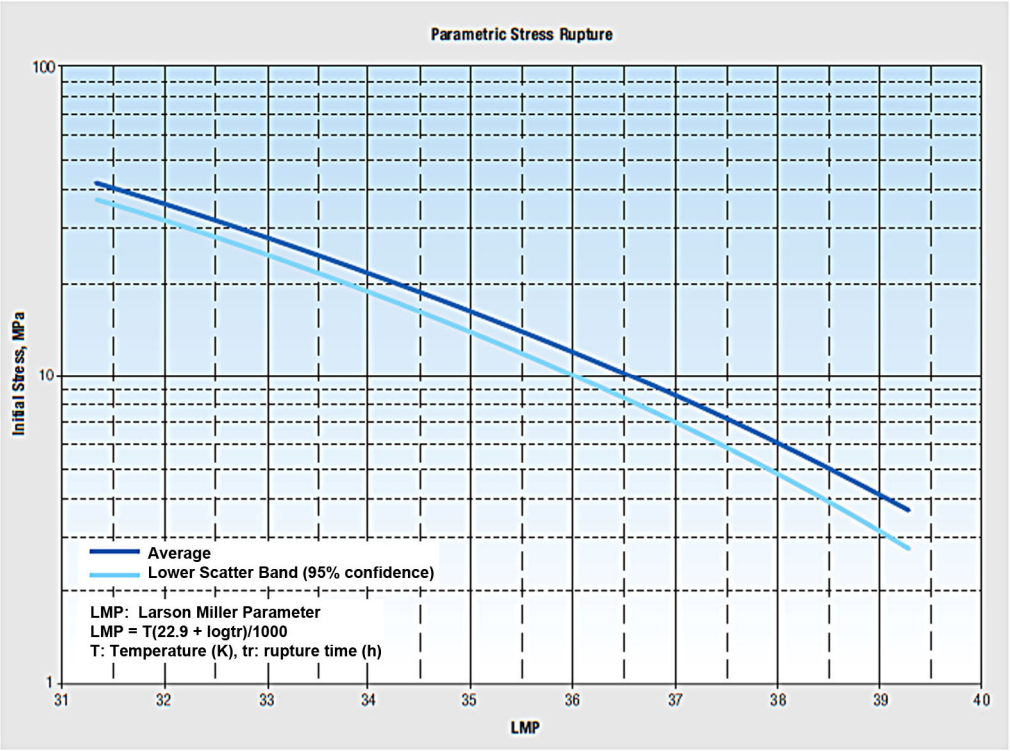

Figure A.2 – Larson-Miller stress rupture plot of the Centralloy® G 4852 Micro alloy (directly reproduced from [3])

References

[1] Kubota Metal Corporation (1999). *KHR 35C alloy data sheet.* Revision 06/99. Kubota Metal Corporation: Ontario, Canada.

[2] ASM International (2002). *Paralloy H39Wmaterial datasheet.* Alloy Digest Inc.: Orange, New Jersey, U.S.A.

[3] Schmidt + Clemens Group (2001). *Centralloy CA4852 Micro material data sheet.* Schmidt + Clemens Group: Lindlar, Germany.

Appendix B Design of the Accelerated Creep Testing Apparatus

In order to subject the HP-Nb and HP-NbTi alloys to accelerated creep testing two widely different creep testing apparatuses were designed and manufactured at the University of Canterbury. The first generation creep apparatus was designed and manufactured between 2009 and 2010 but was badly damaged during the 2011 Canterbury earthquakes. Based on lessons learnt from this design, a vastly improved testing apparatus which could test four samples simultaneously until failure was designed and manufactured during 2011-2012. All accelerated creep testing presented within Chapter 7 was subsequently carried out using the second generation apparatus.

The purpose of this appendix is to provide a brief overview of the design process used to produce each accelerated creep testing apparatus. Each apparatus has been designed to meet or exceed the specifications set out in the ASTM E139 (Standard Test Methods for Conducting Creep, Creep-Rupture, and Stress-Rupture Tests of Metallic Materials) standard [1]. The sample geometries which can be accommodated by each apparatus and maximum allowable testing conditions will be discussed. However, for brevity, the countless different modelling scenarios that were simulated within the ANSYS[1] finite element software package will not be shown in detail as it would cause this appendix to be unnecessarily long.

[1] ANSYS Inc. Canonsburg Pennsylvania, USA

B.1 Creep Apparatus Design Requirements

Table B.1 summarizes the initial design requirements for the accelerated creep testing apparatus. Brief explanations of the motive for each requirement are given in Sections B.1.1 - B.1.5.

Table B.1 – Preliminary design requirements for the accelerated creep testing apparatus

Testing Materials	High temperature austenitic stainless steels
Sample shape	Cylindrical or rectangular miniature dog-bones (ASTM E-139)
Testing temperature	700-1050°C
Load	Up to 100kg
Test duration	500-2000 hours
Samples per apparatus	4
Extensometer	Linear variable differential transducer (LVDT)

B.1.1 Material

Although the primary objective of the accelerated creep testing program in the current research was to test the HP-Nb and HP-NbTi alloys, it was also anticipated that this testing apparatus would be used by other postgraduate students at the University of Canterbury. Thus, the apparatus also had to be designed to accommodate additional austenitic materials such as the wrought INCOLOY® 800H and 800HT[2] and Centralloy® ET 45 Micro[3] alloys. Fortunately, the HP alloy's high creep resistance relative to other austenitic stainless steels (hence, resulting in the greatest stress being placed on the components when testing HP alloys) made the accommodation of these additional alloys within the current apparatus relatively easy.

[2] INCOLOY® 800H and 800HT are austenitic alloys (UNS N08810/ UNS N08811) produced by Special Metals Corporation, New Hartford, New York, U.S.A.
[3] Centralloy® ET 45 Micro is an austenitic alloy produced by Schmidt-Clemens, Spain, S.A.U.

B.1.2 Sample Shape

A cylindrical dog-bone type creep sample shape was selected for the current research (Figure B.1 (a)) partly due to the ease of machining this shape from the HP alloy tube's wall thickness in comparison to rectangular samples. Additionally, cylindrical samples were exclusively used within Quest Integrity Group's accelerated creep testing program. Thus, the use of cylindrical samples provided easily comparable results between the two separate creep testing programs which were associated with the current research.

The dimensions for the cylindrical shaped creep sample (Figure B.1 (a)) were based on the "Small-Size" samples specified within the ASTM E139 [1] and ASTM E8 [2] standards. Generally, the diameter of the reduced section and gauge length were kept similar to the dimensions given in ASTM E8 but the fillet radii adjacent to the sample's gauge length was increased from 6mm to 10mm in order to minimize the stress concentration associated with the change in the section size.

In contrast to the accelerated creep testing of the HP alloys for the current research, rectangular dog-bone shaped samples (Figure B.1 (b)) have been predominantly used when testing the wrought INCOLOY® 800H and 800HT alloys at the University of Canterbury. Consequently, the sample grips had to be designed to accommodate both sample shapes. Additionally, as multiple samples would be tested simultaneously, the interchange between the two sample shapes had to be simple enough to allow for testing of each sample shape to occur in parallel. For the rectangular sample, the sample grips were designed to accommodate a scaled down version of the "Pin-Loaded" sample specified within ASTM E8 (Figure B.1 (b)).

Scaled-down creep samples were necessary due to the limited space available within the furnace chamber, the need to obtain stresses up to 50MPa without using excessively large weights and to ensure that the stressed induced within the sample grips was kept to a tolerable level.

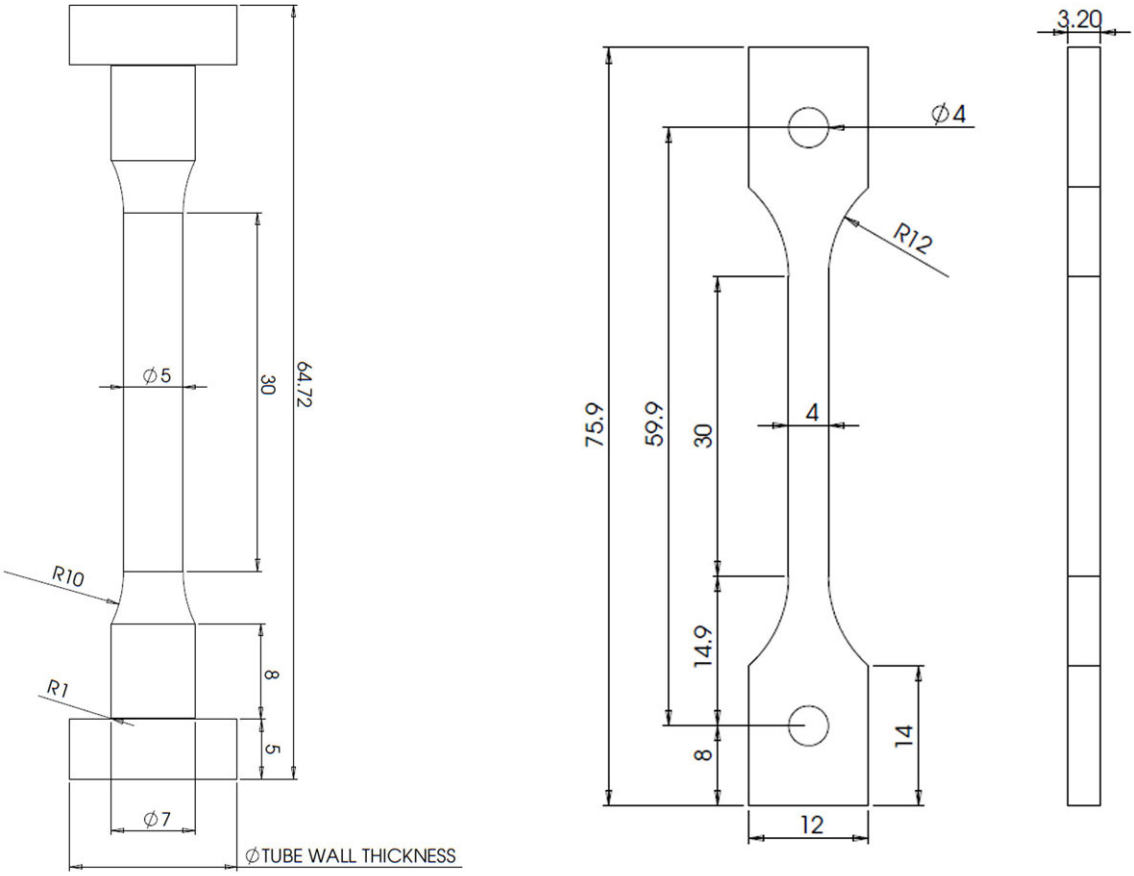

(a) **(b)**

Figure B.1 – Dimensions of the (a) cylindrical and (b) rectangular creep samples

B.1.3 Testing Temperature, Stress and Duration

During service within steam-methane reforming furnaces, HP alloy tubes typically operate at temperatures between 800-1050°C and stresses between 5-20MPa for durations of up to 100,000 hours (~11.4 years). Obviously, testing for such prolonged periods within a laboratory is impractical and thus the testing temperature and/or stress must be increased in order to obtain failure of the creep sample within an acceptable timeframe. In general, when testing the HP alloys, the testing temperature ranges between 1000-1050°C and stress between 10-20MPa in order to obtain failure of the sample within 500-2000 hours. As a result, the creep testing apparatus for the current research had to be designed to continuously and stably operate at temperatures and stresses of up to 1050°C and 20MPa (an approximately 40kg tensile load for the sample shown in Figure B.1 (a)) for up to 2000 hours.

Since it was anticipated that this apparatus would be used for testing of other alloys, the required temperature range was increased to between 700-1050°C and the stress increased a maximum of 50MPa (~100kg) for the cylindrical sample and 77MPa (~100kg) for the rectangular sample. In addition to the preceding requirements, the maximum allowable temperature variance was limited to $^{+}/_{-}$ 1°C. Such strict temperature control between individual samples was possible when a sodium filled isothermal furnace liner (also known as a heat pipe) was used as a working tube within the tube furnace. These relatively aggressive operating conditions necessitated the use of Ni-based super-alloys and ceramics for the sample grip components under stress within the heated region. Additionally, high temperature N-type thermocouples were necessary to ensure that the temperature control remained stable throughout the duration of each accelerated test.

Generally, a constant uni-axial load is applied to the samples during accelerated creep testing. The application of this load is most commonly achieved using statically hangings weight or a lever arm system. Both methods considered when designing the testing apparatus for the current research, however applying the load using a lever arm system ultimately became the preferred method (discussed in further detail in Sections B.2 and B.3).

B.1.4 Samples per Apparatus

Due to the considerable length of time required to cause rupture of a single creep sample, it was decided that the testing apparatus would be designed to simultaneously test multiple creep samples. Initially, it was aimed to have up to six samples contained within the testing chamber. However, increasing the number of samples too significantly resulted in excessively large furnace cavities. Large furnace cavities typically caused the temperature variation between individual samples to be greater than the specified $^{+}/_{-}$ 1°C tolerance. During detailed design of the apparatus it was found that the optimum number of samples was four.

B.1.5 Extensometer

An extensometer is a device that measures the sample's elongation during the creep test. While a number of devices are currently available to measure the sample's elongation (e.g. laser extensometers or strain gauges), linear variable differential transducers (LVDTs) were selected for this research due to their relatively low cost (<$1000) and high resolution (~1µm). Essentially, a LVDT is a type of transformer used to measure small levels of linear displacement. The LVDT consists of a magnetic core (or pushrod) which is surrounded by a separate cylindrical sheath which contains multiple AC excited solenoid coils (Figure B.2). Linearly displacing the pushrod changes the inductance across the pair of solenoids which varies the output voltage. Hence, by knowing the relationship between the pushrods displacement and the output voltage, accurate linear measurements (e.g. of the sample's elongation) can be deduced.

LVDTs have been successfully used to measure the elongation of creep samples in two previous accelerated creep testing apparatus that were also designed and manufactured at the University of Canterbury. Thus, a considerable amount of knowledge about the correct design and operation of LVDT extensometers was already available [4, 5] prior to the design of the testing apparatus for the current research. An extensive review of the advantages of LVDT extensometers has already been presented by Dr. Takanori Sato [4] and will not be repeated here.

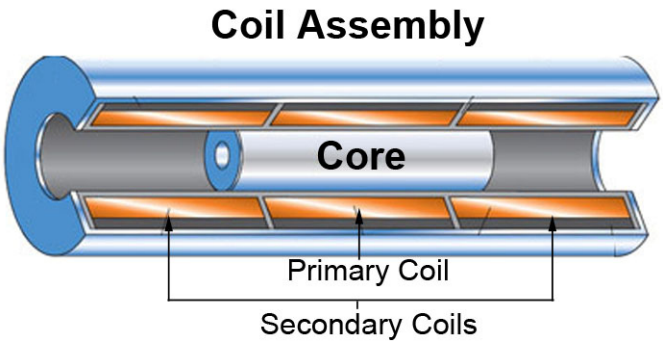

Figure B.2 – Schematic showing the internal mechanism of a linear variable differential transducer (LVDT) [3].

B.2 Design of the First Generation Accelerated Creep testing Apparatus

As stated in the introduction to this appendix, two separate designs of creep apparatus were manufactured throughout the course of the current research. Figure B.3 and B.4 show CAD drawings of the design of the first generation accelerated creep testing apparatus which was designed and manufactured specifically for this research at the University of Canterbury in 2009. The design of this creep testing rig was loosely been based on upon an existing rig at the University of Canterbury which simultaneously tested two creep samples connected in series [5]. As shown in B.4, the capacity of the apparatus designed for the current research was increased to allow for simultaneous testing of four creep samples in series. The following points briefly summarize the main features the first creep testing apparatus:

- Simultaneous constant load testing of four creep samples in series. Loading of the samples is applied using a hanging weight.

- Slotted grip design which allows for the accommodation of both flat (rectangular) and round dog-bone shaped test samples by simply changing the sample clamps.

- Real-time high resolution (1µm) strain measurement of each creep sample (using linear variable differential transformers-LVDT)

- Sodium filled isothermal furnace liner allowing $^{+}/_{-}1$°C temperature control along the testing length (400mm),

- Maximum testing temperature: 1050°C,

- Maximum testing load: 500N.

Unfortunately, this test apparatus was in operation during the February 2011 Canterbury Earthquake, resulting in irreparable damage which largely rendered the apparatus unusable. While significant effort was made to ensure the design of this apparatus complied with the ASTM E139 standard, the finite element stress analysis of the sample grips (performed in ANSYS) and detailed design the testing frame will not be discussed here as this apparatus has been superseded by the second generation creep testing apparatus (discussed in Section B.3) and as a result is no longer in operation.

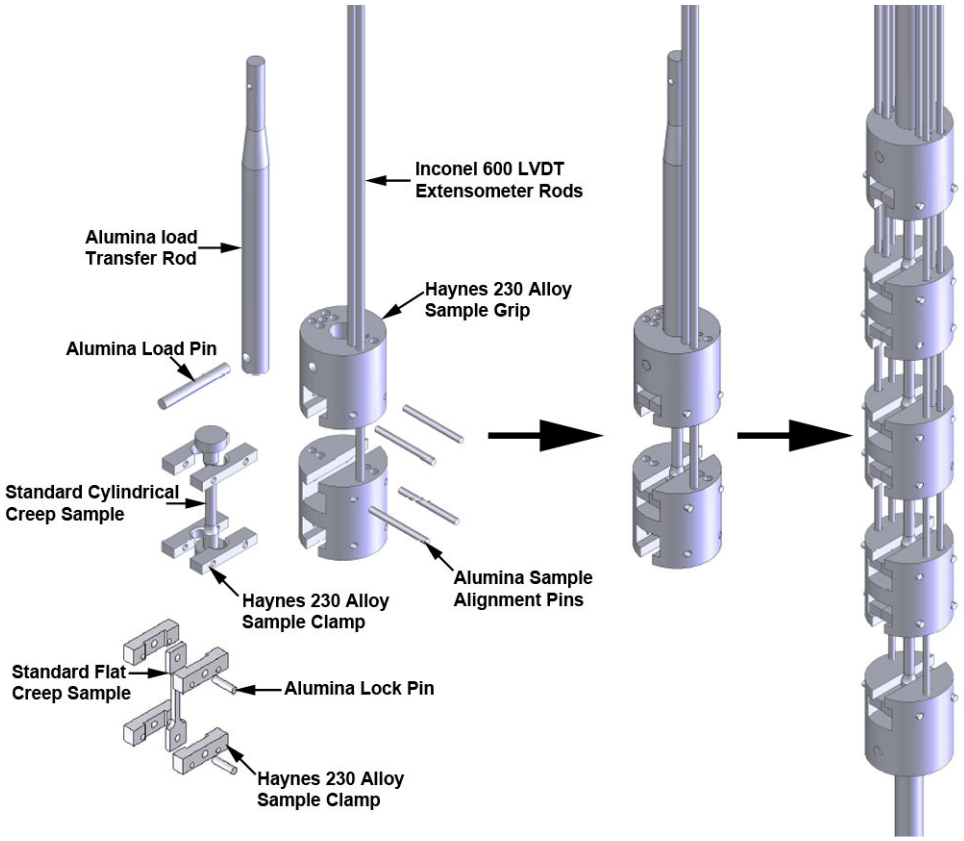

Figure B.3 – CAD design depicting the sample grip assembly.

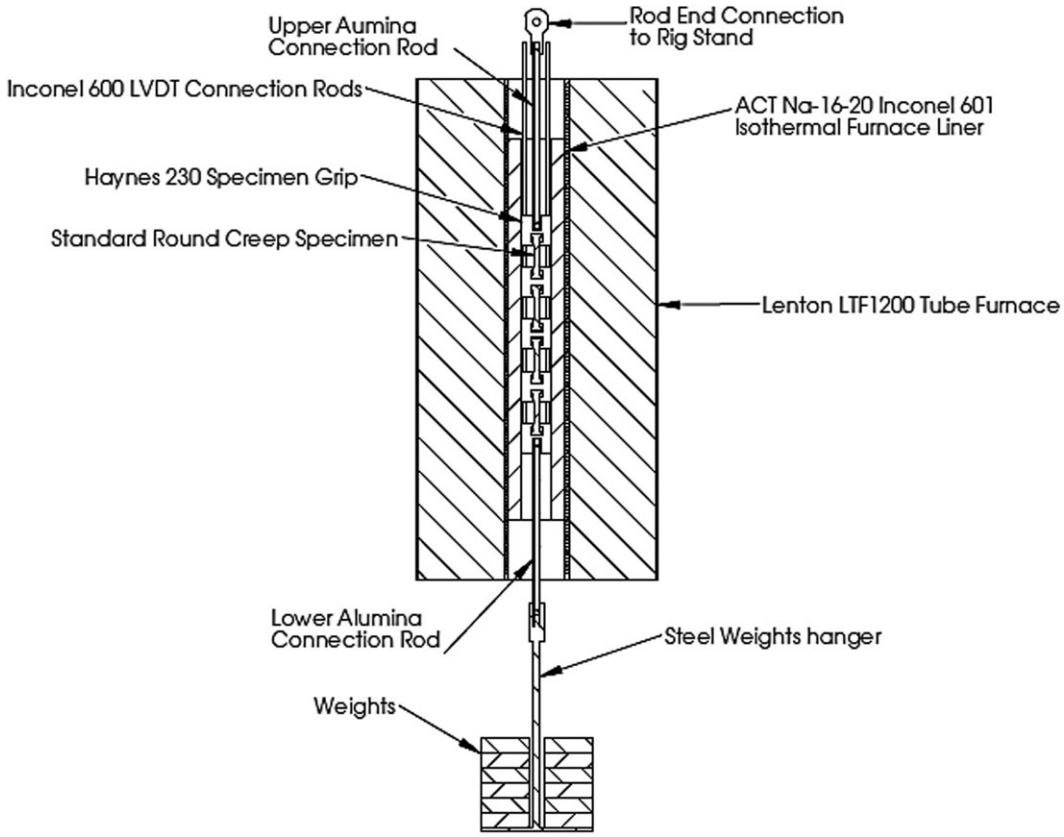

Figure B.4 – Schematic showing a cross-section of the first accelerated creep testing apparatus.

B.3 Accelerated Creep Apparatus – Second Generation

While the first generation apparatus was capable of testing four samples simultaneously, the arrangement of the samples in series meant that the load applied to each sample would be released after rupture of just one sample had occurred. Hence, testing all four samples to rupture was not possible within that apparatus. Since testing of the HP alloys until failure was considered necessary, it was decided that the creep samples within the second generation apparatus would be individually loaded. This requirement necessitated considerable modification to the design of the apparatus in order to maintain four creep samples within the furnace chamber. The following sections briefly describe the design of the second generation creep testing apparatus.

B.3.1 Overview of the Sample Grip Design

Figure B.5 shows the design of the second generation sample grips. The limited space within the furnace chamber required the outer diameter of the second generation grips to be reduced. As a result, using the slotted grip design from the first generation rig was not possible as the stresses within the scaled down grip became too high. Therefore, an alternative design using cylindrical shaped sample clamps which were held within a larger outer grip was developed (as shown in Figure B.5). Separating the sample clamps from the outer grip was primarily carried out to allow the grips to easily accommodate both cylindrical and rectangular creep samples. Moreover, by designing the grips in this manner, samples with alternate dimensions or shapes could easily be accommodated by manufacturing the appropriate sample clamps (as opposed to requiring a wholesale change to the grip design). Solely having to manufacture the smaller and simpler sample clamps as opposed to the large sample grips was particularly beneficial as the cost of the raw grip material and its subsequent machining represented a significant proportion of the total cost of the apparatus.

All main components of the grips were manufactured from the Haynes® 230®[4] alloy. A basic requirement of the grip material is that it exhibits a sufficiently greater creep resistance than the material being subjected to accelerated creep testing so that the grips can be considered to be rigid. Additionally, the grip material must also be easily machined to shape. Although certain ceramics (such as alumina) may exhibit significantly higher creep resistances than metallic materials, machining ceramics to the tolerances required for creep sample grips was prohibitively expensive. Moreover, the brittle nature of many ceramics (in comparison to metals) would result in the grips being less tolerant to any shock loading which could occur during sample exchange. While the Haynes® 230® alloy only exhibited a marginally greater creep resistance than the HP alloy, this alloy was selected due the combination of an excellent high temperature strength, oxidation resistance and reasonable machinability.

The load pins and load transfer rod that connected the grips to the frame and weights were made from alumina (Al_2O_3). Alumina was successfully used for this purpose in the first generation apparatus and was found to remain dimensionally stable (i.e. rigid) when testing at temperatures between 1000-1050°C). In addition, alumina also has a considerably lower thermal conductivity in comparison to Ni-based super-alloys. Finite element modelling of the heat transfer rate along metallic load transfer rods indicated that heat lost through these rods would induce a temperature gradient along the sample's gauge length. This temperature gradient was completely eliminated by using alumina load transfer rods.

[4] Haynes® 230® is a Ni-Cr-W-Mo super-alloy produced by Haynes International, Inc., Kokomo, Indiana, U.S.A.

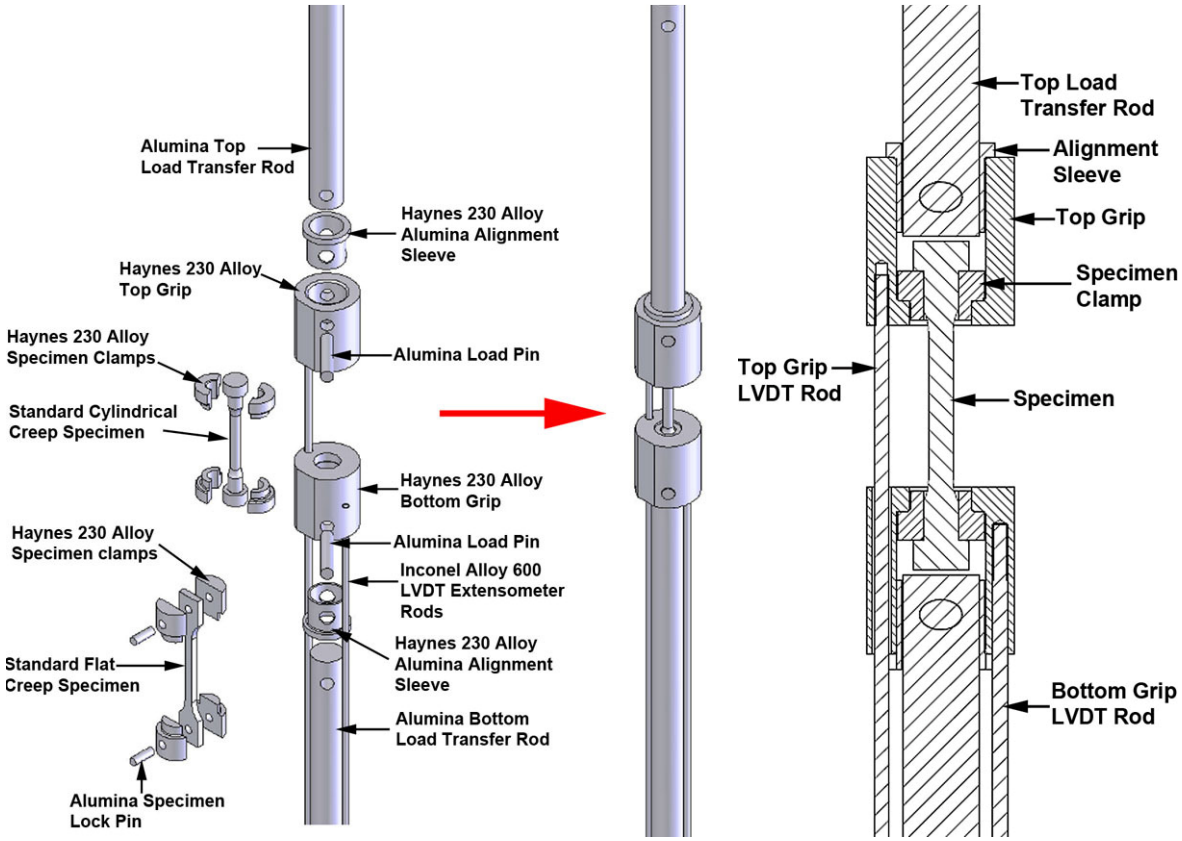

Figure B.5 – CAD drawings showing the design of the second generation creep sample grips.

B.3.2 Finite element Modelling of the Sample Grips

Since the Haynes® 230® grip material only exhibited a marginally greater creep resistance than the HP alloys, it was important to accurately model the stresses within the sample grips to ensure that the grip's creep deformation during testing was negligible. Therefore, finite element modelling of the grips was carried out using the ANSYS finite element analysis (FEA) software. Two unique finite element models were produced to simulate the elastic response of the sample clamps and grip base (Model 1 – Figure B.6 - B.8) and the stress within the grip material contacting the alumina load pin (Model 2 – Figure B.9 –Figure B.12). The simulation of the stress within the sample clamps and grip base was separated from the simulation of the stress surrounding the alumina pin in order to simplify the modelling process.

Overall, the FEA modelling had three main objectives:

1) To allow for the calculation of the stress state within several grip geometries in order to determine the optimum design that minimized the stress distribution within the grip assembly.

2) To ensure that the stress distribution within the grip assembly was below a predetermined threshold limit so that the assembly could be assumed to be rigid during testing. This threshold limit was based on the stress required (at a given temperature) to cause the Haynes® 230® material to undergo a 1% creep deformation over 10,000 hours of exposure.

3) To simulate the effects of manufacturing inaccuracies (such as non-concentric positioning of the creep sample with respect to the sample grip) on the stress state within the creep sample. Such inaccuracies would induce bending moments within the sample causing the loading of the sample to no longer be under a uni-axial tensile load. This modelling allowed the important manufacturing tolerances to be set to a level where the bending stresses within the sample did not exceed 1% of stress induced when the sample was under a pure uni-axial tensile load.

For brevity, the simulation results from the numerous different grip geometries will not be shown here as many of these changes involved subtle adjustments to the grips dimensions. Additionally, a detailed presentation of the numerous simulations of the stress distributions within the grip assembly with respect to load and anticipated manufacturing defects will not be discussed here in detail. However, the modelling conditions and results for the final grip design under a 40kg load (~20 and 31MPa stress for the cylindrical and rectangular shaped samples respectively) has been given below as an example to show the stress distribution (Figure B.6 – Figure B.12) within the grip assembly during a typical creep test conducted in the current research. It must be stressed that these models only show the elastic response of the grip assembly under 40 kilograms of load. The elastic response was used when designing both the first and second generation grips to ensure that the stress experienced by the grips (with respect to temperature) would not result in significant deformation of the grips over the duration of a typical accelerated creep test. While the true stress distribution within the grip assemblies was not expected to remain constant throughout the accelerated creep testing period (e.g. the peak stresses would gradually relax and redistribute the load), prolonged exposure of the first generation grips suggested that the elastic FEA modelling over

estimated the magnitude of the peak stresses within grips during testing. Thus, when designing the grips for the current generation, it was believed that the same elastic modelling approach would also provide a conservative estimate of the grip's actual deformation during testing.

Model 1

In order to obtain a solution to the FEA model within a reasonable time period, a number of minor simplifications were made to the sample grips. Figure B.6 (a) and (b) show the minor changes (namely the removal of the alumina load pin hole and top fillet radius) made to the sample grips for Model 1. Simulations of the actual grip design using coarse meshes determined that these simplifications had not adverse affect on the stress state shown in Figure B.8.

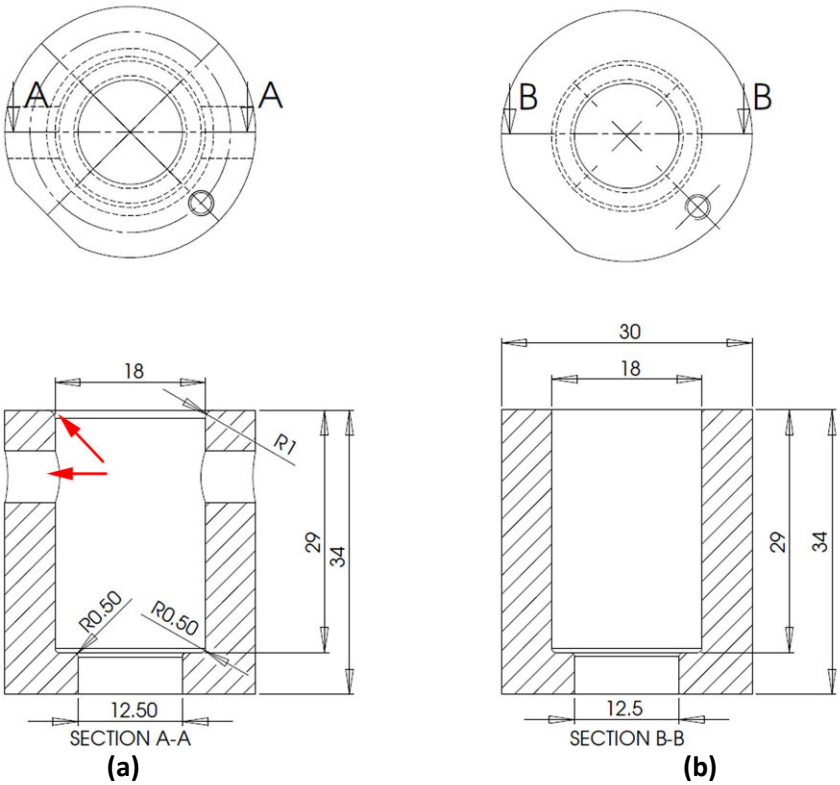

(a) **(b)**

Figure B.6 – CAD drawings showing cross-sections of the (a) actual sample grip and (b) simplified sample grip which was used to model the stress within the sample, sample clamps and base of the sample grip (Model 1). The red arrows in (a) show the simplifications made to the sample grip for the FEA model in (b).

Figure B.7 (a) and (b) show the boundary conditions that were applied to the FEA model to simulate the actual loading conditions in service. The “frictionless” contact model within ANSYS Workbench was used to simulate the contact between the sample, sample clamps and sample grip. Since the elastic response of the sample grip assembly was being modeled, frictionless contact could be used as sliding contact between the contact faces was believed to be negligible.

Meshing of the components within the model was completed using tetrahedral elements. The mesh convergence was confirmed by designating consistent points on each component and refining the mesh until the stress at each point became independent of the mesh size.

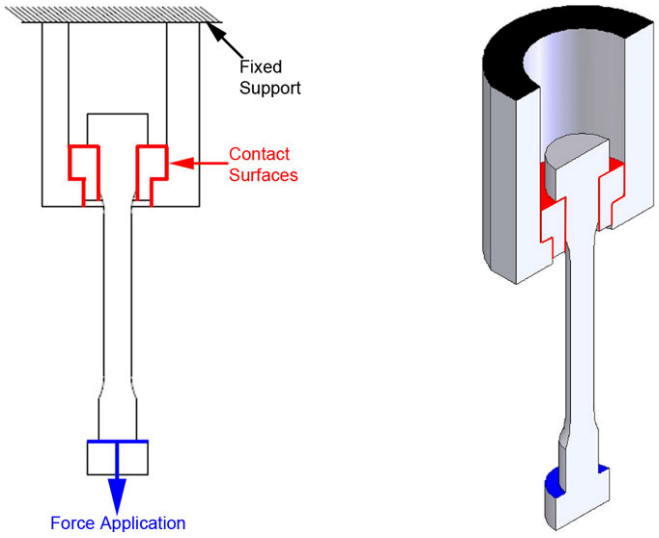

(a) **(b)**

Figure B.7 – (a) Two dimensional cross-section schematic of the Model 1 showing the boundary conditions used for the FEA simulation of the stress within the sample clamp and grip. (b) Cross-section of the three-dimensional CAD model inputted into ANSYS indicating the surfaces over which the boundary conditions in (a) were applied.

Figure B.8 gives a stress contour plot showing the elastic stress distribution within the sample, sample clamps and sample grip when applying a static load of 40kg. Peak contact stresses of approximately 6MPa occurred within the material directly adjacent to the sample clamps and sample grip contact faces. Generally, it was not believed that these peak stresses would significantly contribute to the total deformation of the grips during creep testing as they occurred within a very small volume of the grip material. Thus, it was believed that the stress distribution indicated by the

white lines in would likely result in the most significant deformation of the grip assembly during testing.

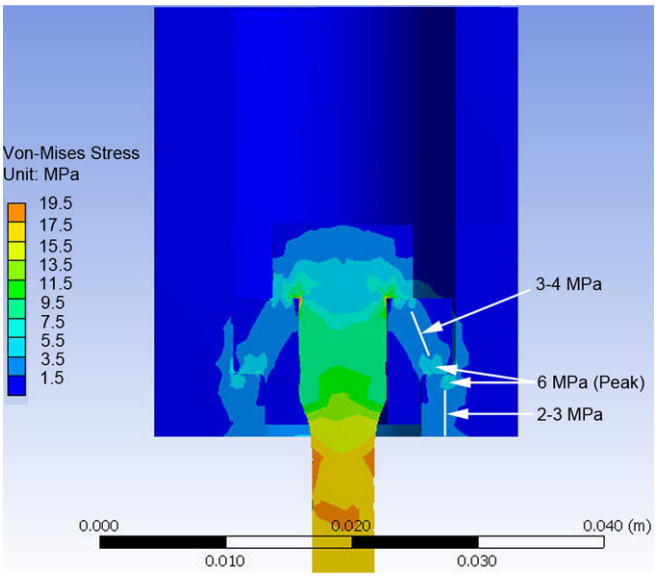

Figure B.8 – Stress contour plot showing the Von-Mises stress within the creep sample, sample clamps and sample grip when applying a static load of 40kg.

Model 2

Figure B.9 and Figure B.10 show the simplifications made to the sample grip and alumina load connections. Simulating the 'true' and 'model' grip geometries with course meshes determined that the removal of the sample hole at the base of the sample clamp (arrowed in Figure B.9 (a)) did not affect the stress distribution within the grip material surrounding the alumina load pin. In contrast, the simplification made to the alumina load pin (Figure B.10 (b)) caused the stress distribution within the alumina pin to be un-representative of the true stress distribution experienced by the alumina pin and load transfer rod assembly (Figure B.10 (a)). However, additional FEA modelling of solely the alumina pin and load transfer rod indicated the stress within these components was insignificant. Typically, the factor of safety on the alumina was an order of magnitude lower than alumina's room temperature ultimate tensile strength (high temperature properties are not widely available). Similar alumina components within the first generation apparatus remained completely rigid when using similarly high factors of safety. Thus, accurate modelling of the stress distribution within the alumina components in the second generation apparatus was considered unnecessary.

Based on comparisons of the 'true' and 'model' pin geometries using course meshes, the simplification of the alumina pin also marginally decreased the stress within the sample grip. Although the decrease appeared to be negligible, this decrease was still accounted for when determining the maximum permissible load with respect to temperature.

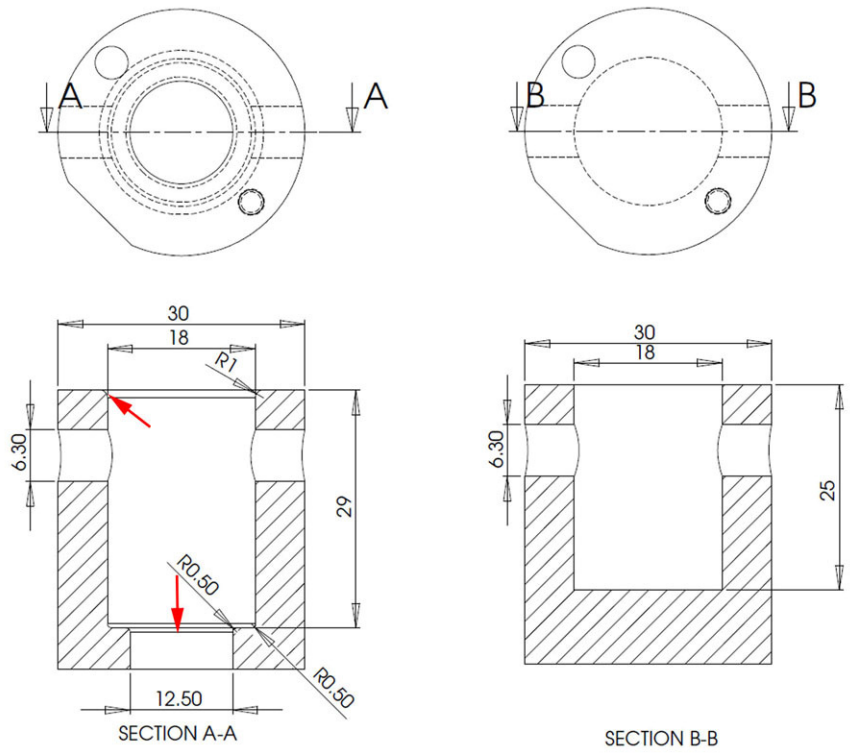

(a) **(b)**

Figure B.9 – CAD drawings showing cross-sections of the (a) actual sample grip and (b) simplified sample grip which was used to model the stress within the grip material contacting the alumina load pin. The red arrows in (a) show the simplifications made to the sample grip for the FEA model in (b).

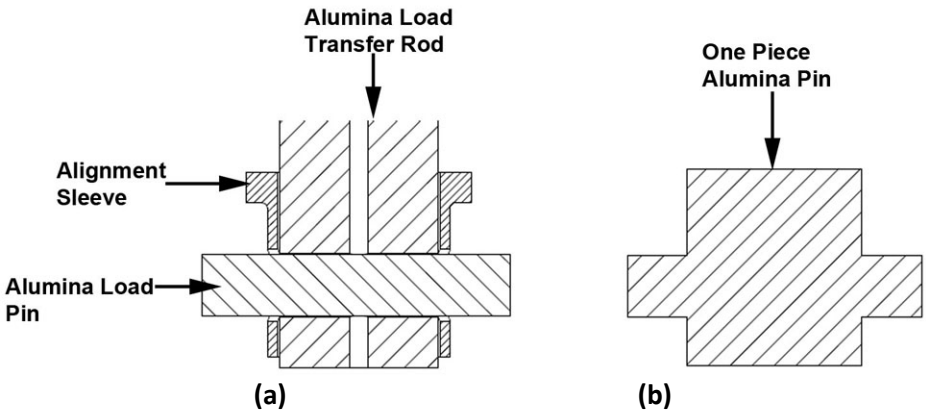

(a) **(b)**

Figure B.10 – CAD drawings showing cross-sections of the (a) actual alumina load pin and load transfer rod connection and (b) the simplified alumina pin connection which was used to model the stress within the grip material contacting the alumina load pin.

Figure B.11 (a) and (b) show the boundary conditions that were applied to FEA model to simulate the actual loading conditions experienced by the alumina pin joint during service. Identical to Model 1, the “frictionless” contact model within ANSYS Workbench was used to simulate the contact between the sample grip and alumina pin as sliding contact between the contact faces was believed to be negligible. Meshing of the components within Model 2 was completed using tetrahedral elements. The mesh convergence was verified using the same method describe for Model 1.

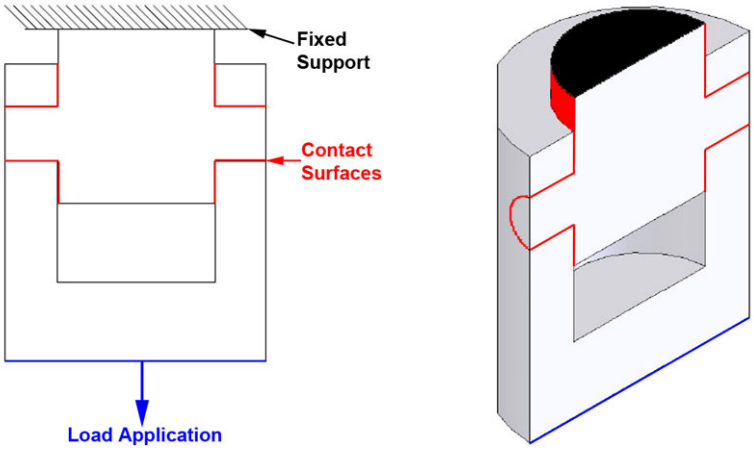

(a) **(b)**

Figure B.11 – (a) Two dimensional cross-section schematic of Model 2 showing the boundary conditions used for the FEA simulation of the stress induced within the grips due to the alumina load pin connection. (b) Cross-section of the three-dimensional CAD model inputted into ANSYS indicating the surfaces over which the boundary conditions in (a) were applied.

Figure B.12 (a) and (b) gives stress contor plots showing the Von-Mises stress distribution within the region of the sample grip which contacts the alumina load pin. While relatively high contact stresses of between 8-15MPa can be observed at the inner edge of the through hole within the sample grip (Figure B.12 (a)), this stress rapidly dissipates with distance from the inner edge (Figure B.12 (b)). Identical to Model 1, it was not believed that this peak stress would significantly contribute to the creep deformation within this region of the sample grips. Thus, the majority of the creep deformation would likely occur as a result of the 3-6MPa stresses located within the bulk material above the hole.

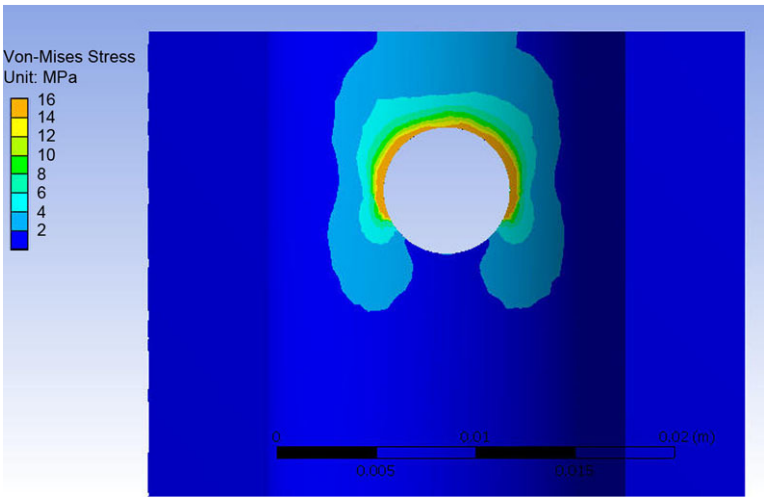

(a)

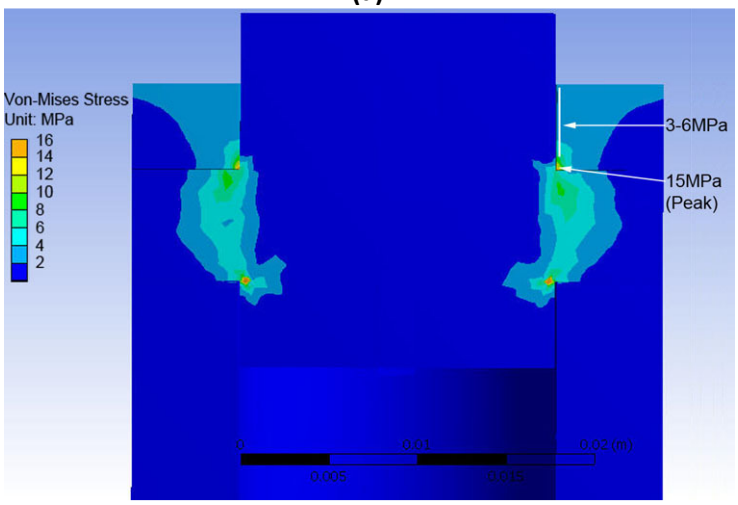

(b)

Figure B.12– (a) & (b) Stress contour plots showing the Von-Mises stress within the grip material surrounding the alumina load pin when applying a static load of 40kg.

The two previous models were completed for static loads ranging between 20-100kg. The stress distributions in the grip assembly with respect to load were then used to determine the maximum load that could be applied to the sample grip assembly with respect to the testing temperature (Figure B.13). To ensure conservatism, the maximum stress within the bulk material (not including the larger peak contact stresses) were used to determine the maximum allowable load which could be applied to the grip assembly with respect to temperature. Provided that these stresses were below the stress required (at a given temperature) to cause the Haynes® 230® material to undergo a 1% creep deformation over 10,000 hours of exposure, it was assumed that the creep deformation which occurred within the sample grips over the 1000-2000 accelerated testing duration was relatively negligible. This assumption was confirmed after finding no detectable difference between

the sample grip dimensions before and after performing a 300 hour commissioning test at 1040°C and 40kg (~1.5x the recommended weight at 1040°C). Subsequent measurements of the grips after performing accelerated testing of the HP alloys also did not detect any significant change to the grips dimensions during testing. It is recommended that the grip assembly's dimensions are measured after each creep test and compared to the original drawing. If the dimensions of any component differ from those specified by more the 0.1mm, the component must be replaced before commencing a new test.

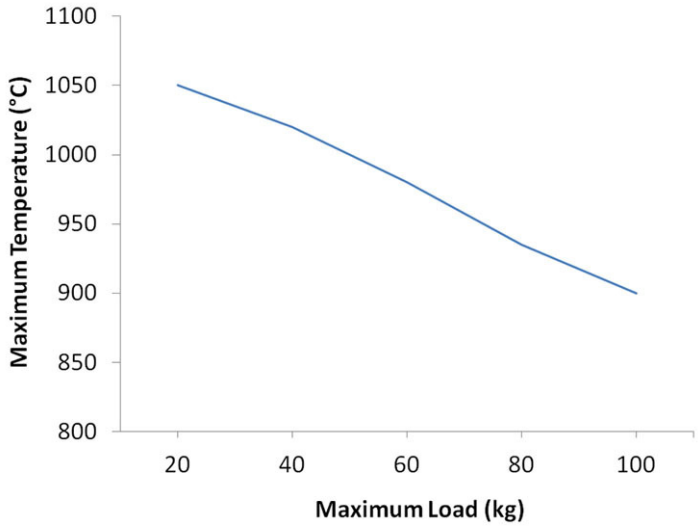

Figure B.13 – Maximum allowable load which can be applied to the grip assembly with respect to the testing temperature

B.3.3 Grip Layout and Sample Collision Prevention

Due to the time consuming nature of creep testing, one of the primary objectives when designing the creep testing apparatus was to test multiple creep samples simultaneously within a single furnace. Achieving this objective was relatively easy when designing the first generation apparatus as the four samples were simply connected in series within an approximately 600mm long tube furnace. As a result of the samples being connected in series, the grip assembly only required a single set of alumina load transfer rods and hanging weights and thus a relatively small diameter (<75mm) tube furnace. Conversely, the four individually loaded samples in the second generation apparatus required a much larger diameter tube furnace which could accommodate the additional alumina load transfer rods and force application systems associated with each sample. In general, the temperature control becomes increasingly difficult when increasing the size of the furnace cavity. Moreover, the cost of the furnace and isothermal furnace liner (IFL) markedly increases with the size of the cavity. Thus, it was important to minimize the total heated volume while also ensuring the sample grip assemblies were sufficiently spaced to prevent any interference between the samples during testing.

Figure B.14 (a) shows the layout of the four creep sample grip assemblies within the furnace. In order to minimize the internal bore of the tube furnace and the size of the isothermal furnace liner, the sample grips were separated into upper and lower pairs that were orthogonally orientated. This compact arrangement was spaced so that contact between individual grip assemblies was not possible while the sample remained intact. However, contact was possible between neighbouring grip assemblies when rupture of the samples occurred. As a result, a collision prevention system (shown in Figure B.14 (b)) was designed to limit the grips movement so that, once rupture of a sample occurred, the freed grip assemblies could only make contact with the Ni-based super-alloy (Inconel 601) collision prevention rods. Hence, contact could not be made between the freed grip assemblies and neighbouring alumina load transfer rods that are attached to a sample that has not failed. The spacing between the sample grip assemblies and collision prevention rods prior to rupture of the samples was sufficient so that these rods did not interfere with the grip assemblies during testing.

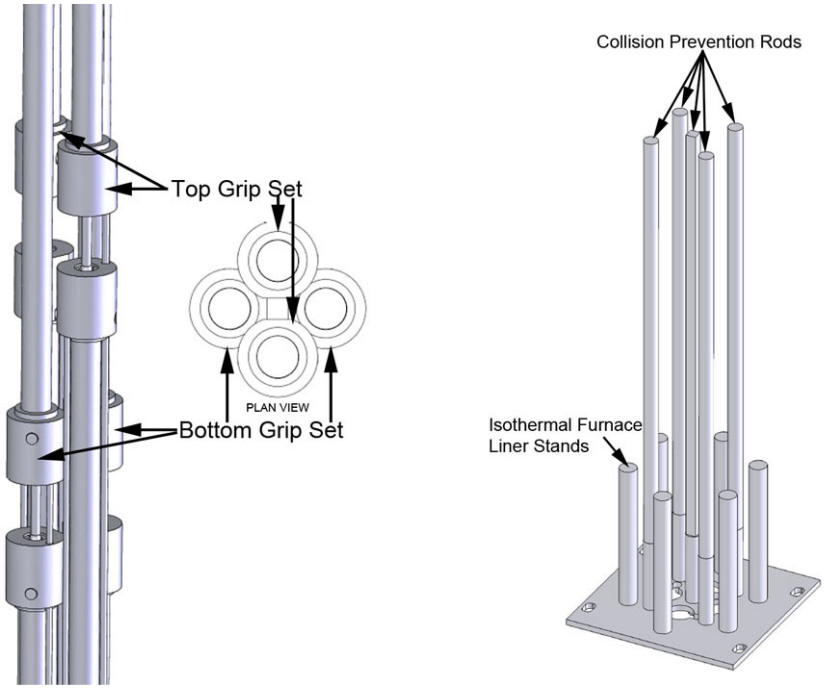

(a) **(b)**

Figure B.14 – CAD drawings showing the (a) layout of the sample grip assemblies and (b) sample collision prevention system.

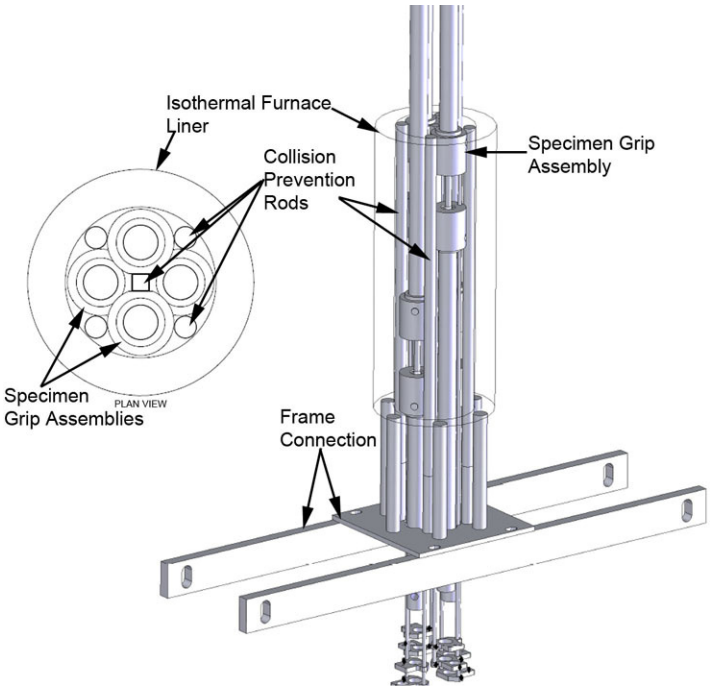

Figure B.15 – CAD drawing showing the sample grip assemblies and collision prevention system within the isothermal furnace liner.

B.3.4 Extensometers

As discussed in Section B.1.5, linear variable differential transducers (LVDT) were used to measure the samples' elongation. Since LVDTs cannot withstand temperatures above 120°C, the LVDTs had to be placed far outside the heated region of the furnace. Therefore, Ni-based super-alloy (Inconel 600) rods were attached to the top and bottom grip assemblies (as shown in Figure B. 16 (a) to (c)). These rods translated the displacement of the sample grips outside of the furnace cavity. At the base of these rods two clamps were separately fixed to the rods. These clamps connected the LVDT coil assembly and pushrod to the super-alloy rods which were connected to the top and bottom grips respectively (Figure B.16 (b)). Thus, any linear displacement of the grips due to the sample's elongation was translated through the LVDT rods and detected by the LVDT extensometer (as shown in Figure B.16 (b) and (c)).

Although the direct attachment of the super-alloy extensometer rods directly to the sample's gauge length (as opposed to the grips) is more desirable, measurement of the sample's elongation based on the displacement of the grips was allowed by ASTM E139 [1] standard when using miniature creep samples (Figure B.16 (a) and (b)). Designing re-usable fixtures which reliably measure the sample's elongation without slipping and do not introduce a stress concentration within the sample's gauge length is very difficult when testing at temperatures above 1000°C.

The LVDT extensometers could measure elongations of up to 12mm. Calibration of the each LVDT was carried out using a micrometer with an accuracy of 1μm. Observation of the LVDTs dimensional stability with respect to time determined that these extensometers fell well within the acceptable ranges specified in ASTM E139 (e.g. noise levels should not exceed 5% of the total calibrated range and the peak noise on the raw creep data should not exceed 7.5 % of the total creep or total plastic strain for the test).

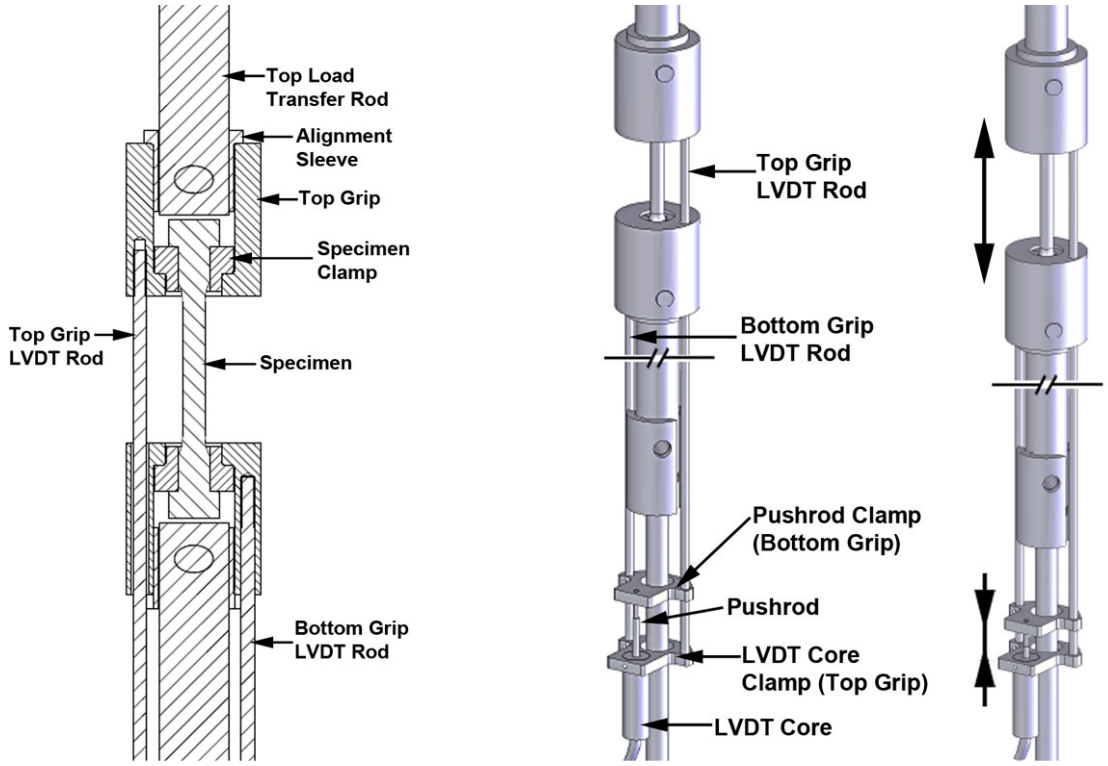

Figure B.16 – CAD drawings showing (a) the attachment of the LVDT rods to the grip assemblies and (b) & (c) the LVDT and clamp assembly attached to the rods which measured the samples elongation.

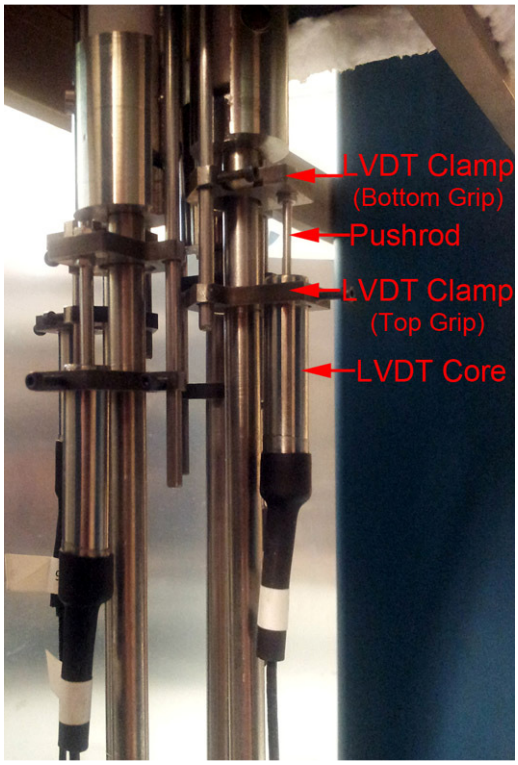

Figure B.17 – LVDT extensometer assemblies.

B.3.5 Creep Apparatus Frame and Load Arms

Figure B.18 (a) to (c) show the frame that was designed to apply the load to each sample and also provide stable mounting for the furnace and isothermal furnace liner. The primary structure of the frame was manufactured from 125 x 50mm rectangular hollow section (RHS). Although a much smaller gauge of RHS would have been sufficient to withstand the relatively low forces experienced the frame (typically <10kg of weights when used for sample), the 125 x 50mm RHS was used to give the frame a high level of rigidity. This rigidity was necessary to ensure that the frame completely absorbed the shock loading which occurred when the rupture of a creep sample released the lever arm causing the weights to impact the lever arm travel limiter (Figure B.19). To minimize the transmission of any shockwaves created by the weights impacting the travel limiter, nylon connecting bushes were used to connect the lever arm assemblies to the RHS uprights and also to connect RHS uprights to the RHS base (Figure B.18 (a)). The most signification nylon connecting bushes were used to connect the RHS uprights to the RHS base (Figure B.19 (b)). These bushes effectively isolated the base connections, 316 stainless steel tensile bars and most importantly the LVDT extensometers from any vibrations created by the lever arm loading system. Hence, as a result of the damping provided by these bushes, vibrations created by the failure of one sample were generally not detected by the LVDTs attached to the other three samples.

While hanging weights were used to apply the load to the samples in the first generation apparatus (Figure B.4), the compact arrangement of the sample grips in the second generation apparatus made it impossible to individually attach sufficient weights to each sample which could induce stresses of up to 50MPa within the sample's gauge length. Thus, lever arms were used to individually apply the testing load to each sample. Each lever arm was designed to rotate on a knife edge pivot point and apply a ten-fold load magnification factor to the sample. It must also be noted that the self weight of the lever arm was designed place a 5kg load on each sample. This self weight load was designed specifically to provide the 10-15% pre-load (of the total testing load) to each sample while heating the furnace to the testing temperature (as required by ASTM E139).

Although the rotation of the lever arm due to the sample's elongation during testing causes the load applied to the sample to gradually reduce, the maximum reduction in load was typically less than 1% of the total applied load. While a threaded connection which allowed for the height of the lever arm

to be adjusted was used to fix the base connections to the frame, this adjustment generally produced unacceptable noise in the extensometer readings and thus was typically avoided.

Due to the high cost and delicate nature of the alumina load transfer rods, the alumina rods did not directly attach to the base of the frame or lever arms. Instead the alumina load transfer rods were attached to 316 stainless steel tensile load bars which subsequently connected to the base and lever arms (Figure B.18 (a) and Figure B.19). The tensile load bars were connected to the base of the frame and lever arms using self-aligning rod-end bearings (Figure B.19). The self-aligning characteristic of these bearings eliminated the transmission of any bending moments from the frame to the samples, thus achieving pure tensile loading of each sample. These bearings were also used to attach the weights hangers to the lever arms.

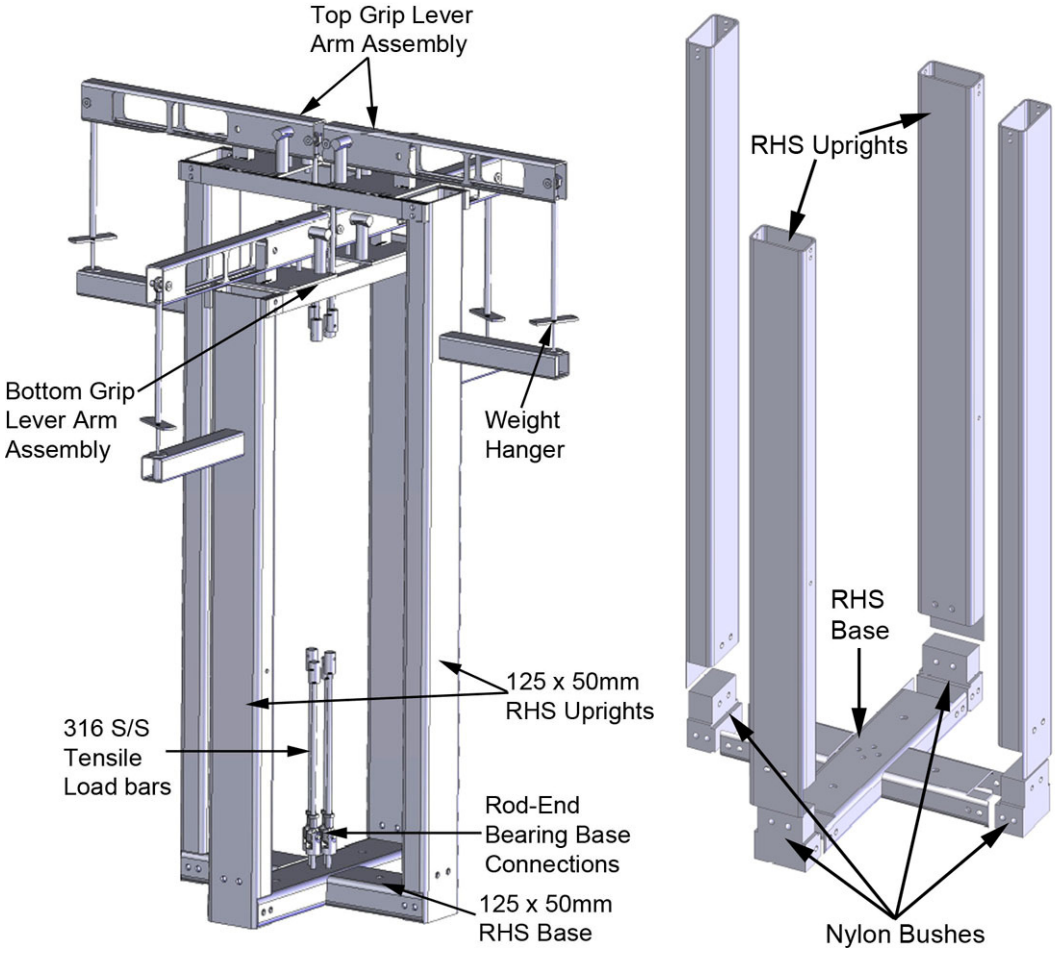

(c)

Figure B.18 – (a) CAD drawing showing the creep apparatus frame and (b) the nylon bushes used to minimize the transmission of vibrations to the LVDTs and (c) the actual assembled creep apparatus.

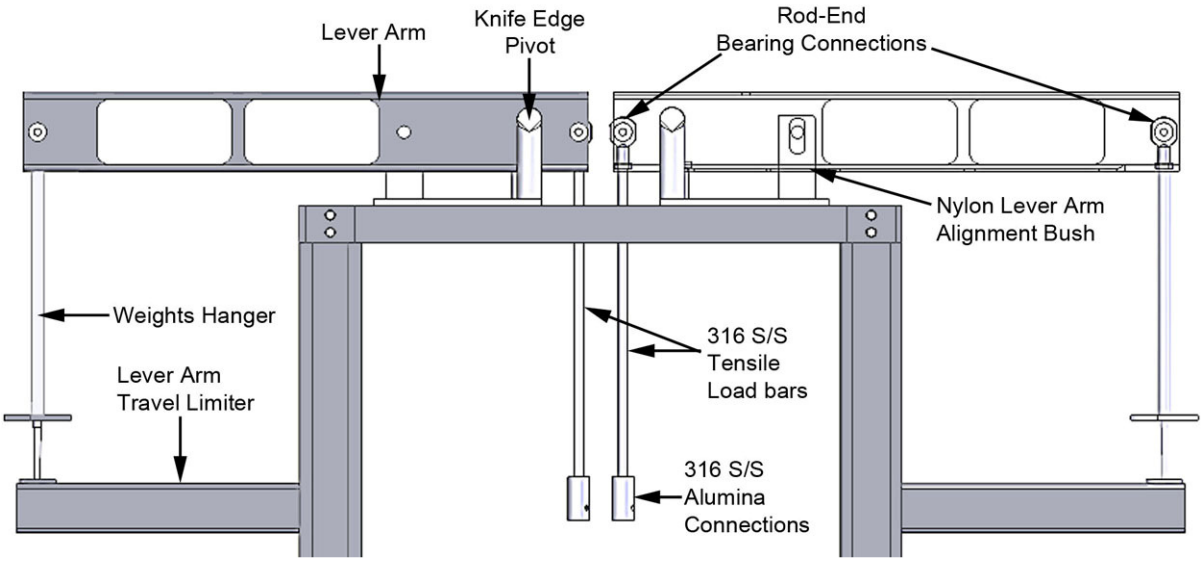

Figure B.19 – CAD drawing showing the lever arm loading mechanisms from the top samples

B.3.6 Furnace and Isothermal Furnace Liner

In order to achieve the 700-1050°C testing temperature range, a Lenton CSC 12/90/300 split tube furnace was selected. This furnace used ceramic resistance elements to obtain a maximum continuous operating temperature of 1150°C. Due to the furnace's 100mm diameter bore, a temperature gradient of between 3-5°C was typical within the furnace cavity when operating at temperatures between 700-1050°C. Therefore, a sodium filled isothermal furnace liner produced by Advanced Cooling Technologies Inc.[5] (also known as a heat pipe) was used as a working tube within the furnace to bring the temperature gradient between individual samples to $^{+}/_{-}$ 1°C. The sample grip assemblies were completely contained within the isothermal furnace liner. While the furnace liner significantly improved the temperature profile within the furnace, it also limited the testing temperature range to between 700-1050°C.

[5] Advance Cooling Technologies Inc (ACT), Lancaster, Pennsylvania, U.S.A

Summary

As part of the current research project, multiple accelerated creep testing apparatus were designed and manufactured at the University of Canterbury. The first generation is no longer in operation due to the damage that occurred during the 2011 Canterbury Earthquakes. As a result, a second generation apparatus was designed and manufactured to carry out the accelerated testing in the current research. The second generation apparatus has the following specifications:

- Simultaneous constant load testing of four samples to rupture,
- Accommodation of both cylindrical and rectangular shaped samples,
- Real-time high resolution (1µm) strain measurement for each sample using LVDT extensometers,
- Strict $^{+}/_{-}$ 1°C temperature control within the heated region,
- Maximum testing load of 100kg,
- Maximum testing temperature of 1050°C.

References

[1] American Society for Testing and Materials. (2011). *Standard Test Methods for Conducting Creep, Creep-Rupture, and Stress-Rupture Tests of Metallic Materials.* ASTM E139-11, E28.04.

[2] American Society for Testing and Materials. (2011). *Standard Test Methods for Tensile Testing of Metallic Materials.* ASTM E8/ E8M-11, E28.04.

[3] *LVDT Basics* [Image]. Retrieved January 2013, from http://www.macrosensors.com/lvdt_tutorial.html

[4] Sato, T. (2008). *Power-Law Creep Behavoiur in Magnesium and its Alloys*. Appendix A. Unpublished doctoral thesis. University of Canterbury, Christchurch, New Zealand.

[5] Drabble, D. (2010). *The effect of grain boundary engineering on the properties of incoloy 800H/800HT.* Unpublished doctoral thesis. University of Canterbury, Christchurch, New Zealand.

Appendix C Time-Temperature-Transformation Diagrams

The following appendix shows the time-temperature-transformation plots produced for the $Cr_{23}C_6$-to-Cr_2N, NbC-to-Z-phase, (NbTi)C-to-Z-phase, NbC-to-η-carbide and (NbTi)C-to-η-carbide phase transformations after ageing the HP-Nb and HP-NbTi alloys in an air atmosphere at 1000, 1050 and 1100°C for 1000 to 10,000 hours. It must be noted that further work is necessary in order to plot the C-curves for each alloy with respect to ageing temperature, time and the alloy's chemical composition. Furthermore, as shown in Figure C.2 (a) and (b) for the $Cr_{23}C_6$-to-Cr_2N transformation, the grain distribution can have a significant effect on each phase's transformation kinetics. Consequently, due to the variable grain distributions that separately cast HP reformer tubes typically exhibit, further analysis on the phase transformation rates with respect to the tube's grain distribution is also necessary. Discussion of the effects of grain distribution on the phase transformation kinetics in the HP-Nb and HP-NbTi alloys characterized in the current study has been presented in Chapter 8.

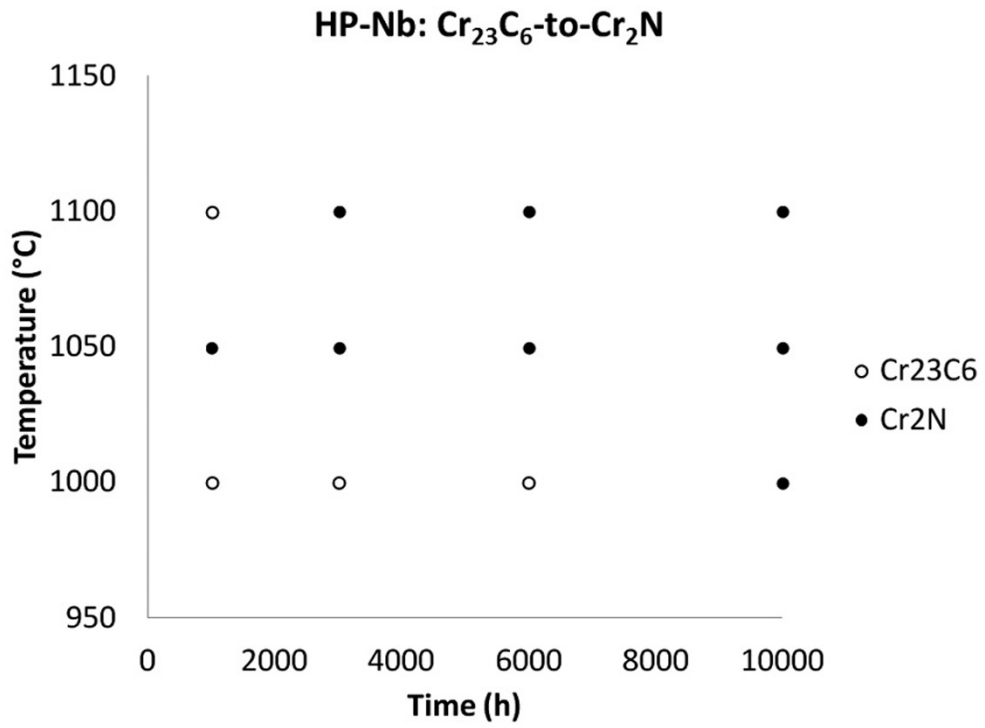

Figure C.1 – Time-temperature-transformation curve plotted for the $Cr_{23}C_6$-to-Cr_2N transformation in the HP-Nb alloy after ageing in air at 1000, 1050 and 1100°C for up to 10,000 hours.

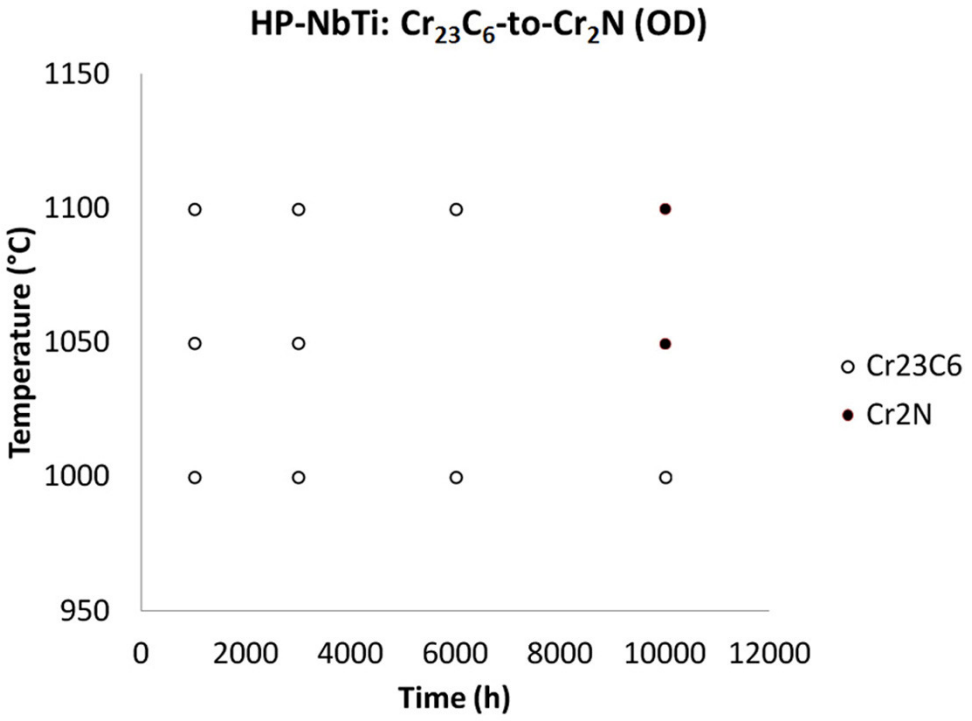

(a)

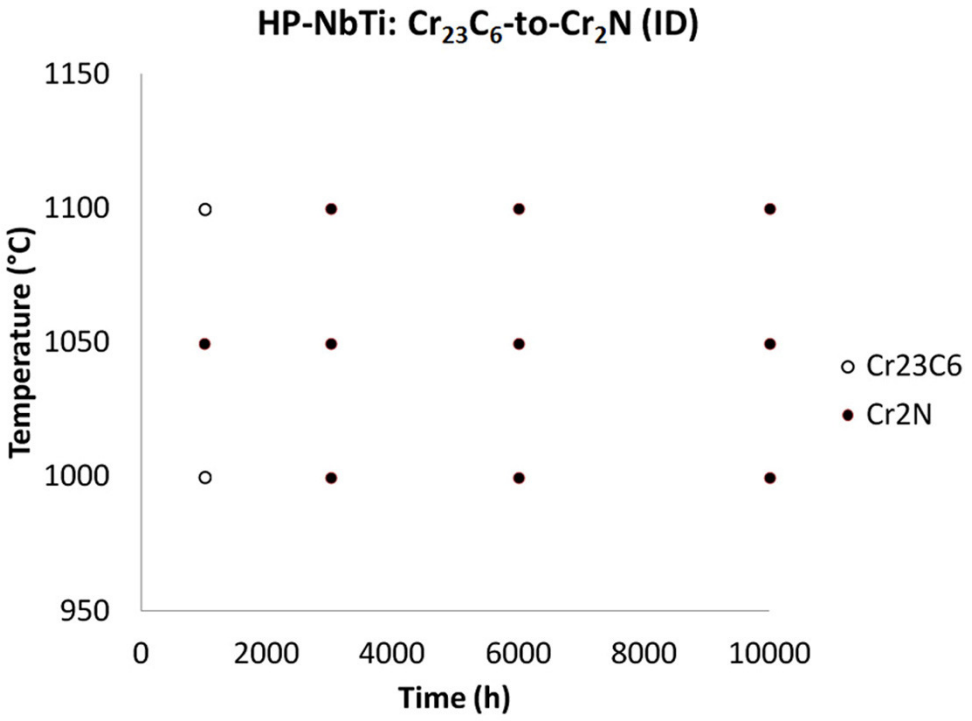

(b)

Figure C.2 – Time-temperature-transformation diagram for the $Cr_{23}C_6$-to-Cr_2N transformation at the (a) outer and (b) inner diameter positions of the HP-NbTi alloy after ageing in air at 1000, 1050 and 1100°C for up to 10,000 hours. As discussed in Chapter 8 the greater transformation kinetics at the tubes inner diameter are due to the equiaxed grain structure as opposed to the columnar grain structure at the tube's outer diameter

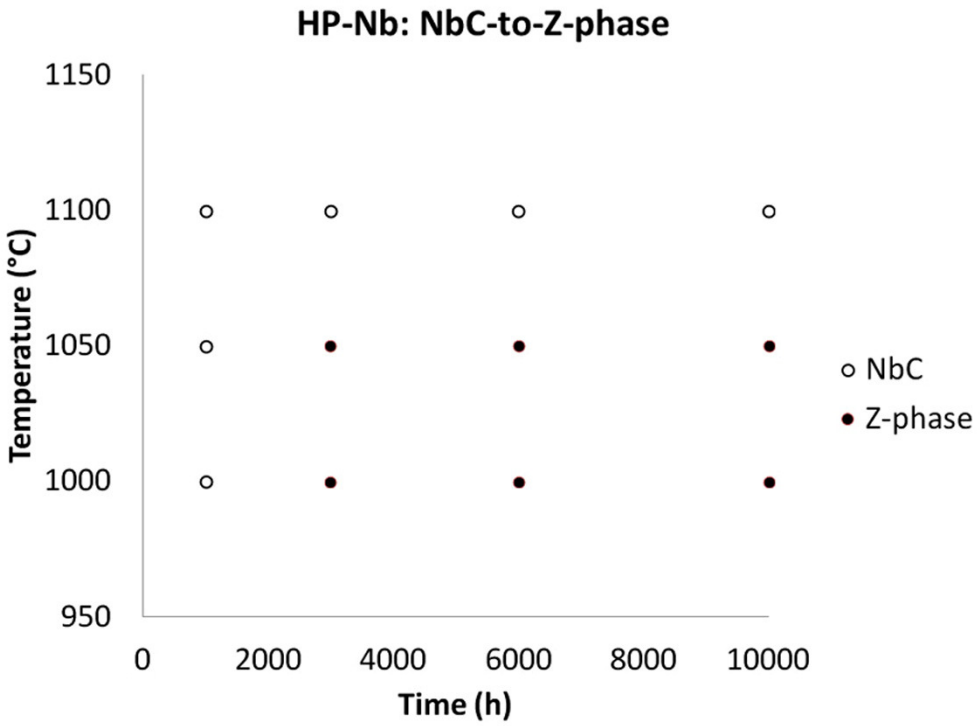

(a)

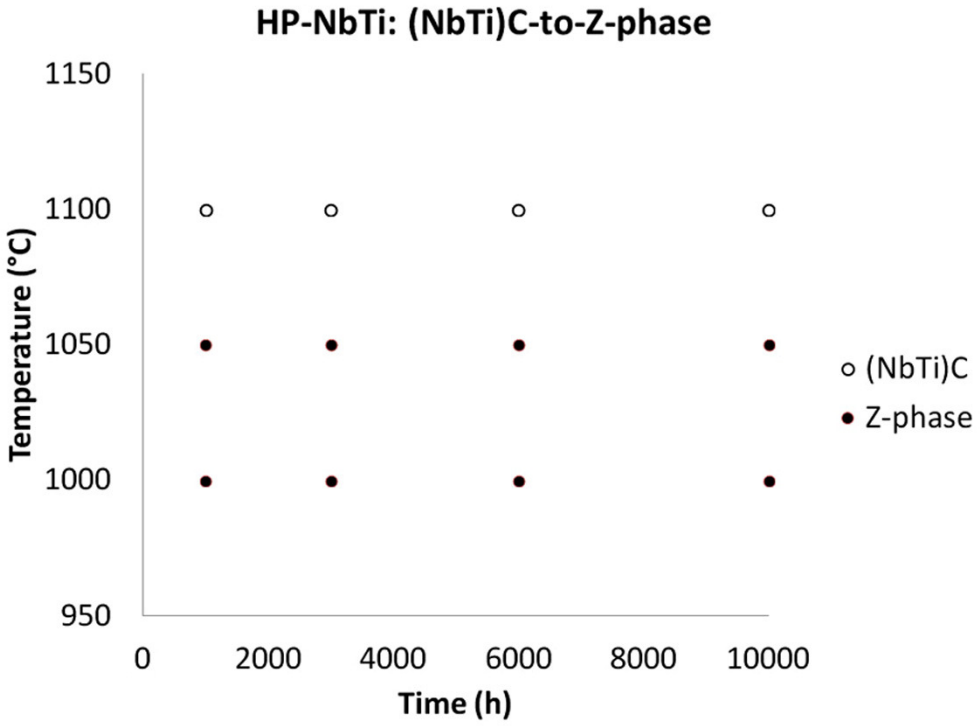

(b)

Figure C.3 – Time-temperature-transformation diagram for the MC-to-Z-phase transformation in the (a) HP-Nb and (b) HP-NbTi alloys after ageing in air at 1000, 1050 and 1100°C for up to 10,000 hours.

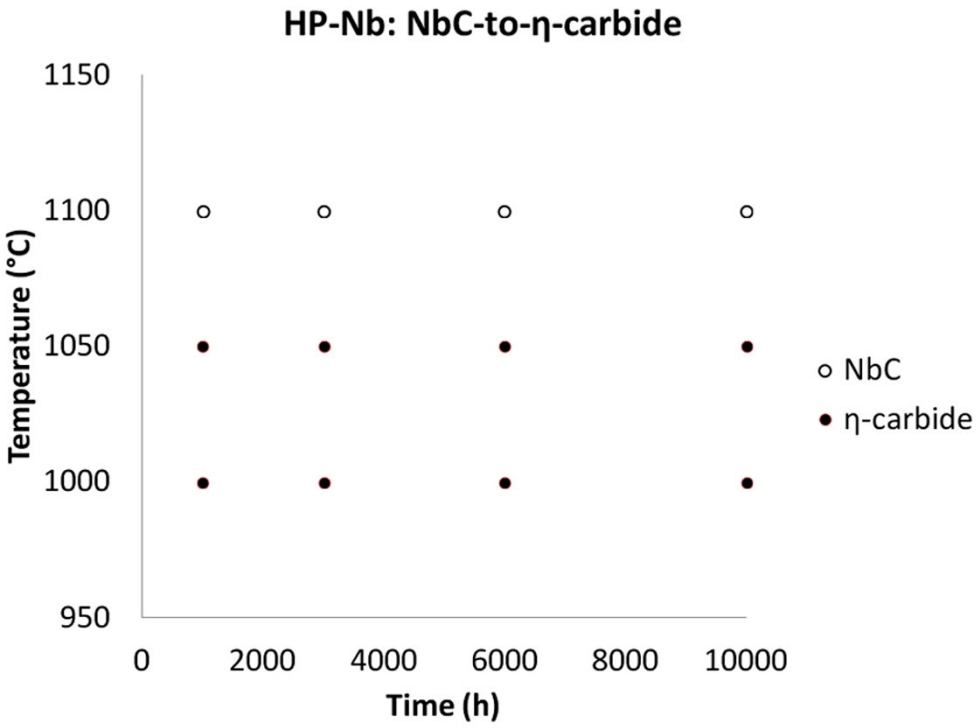

(a)

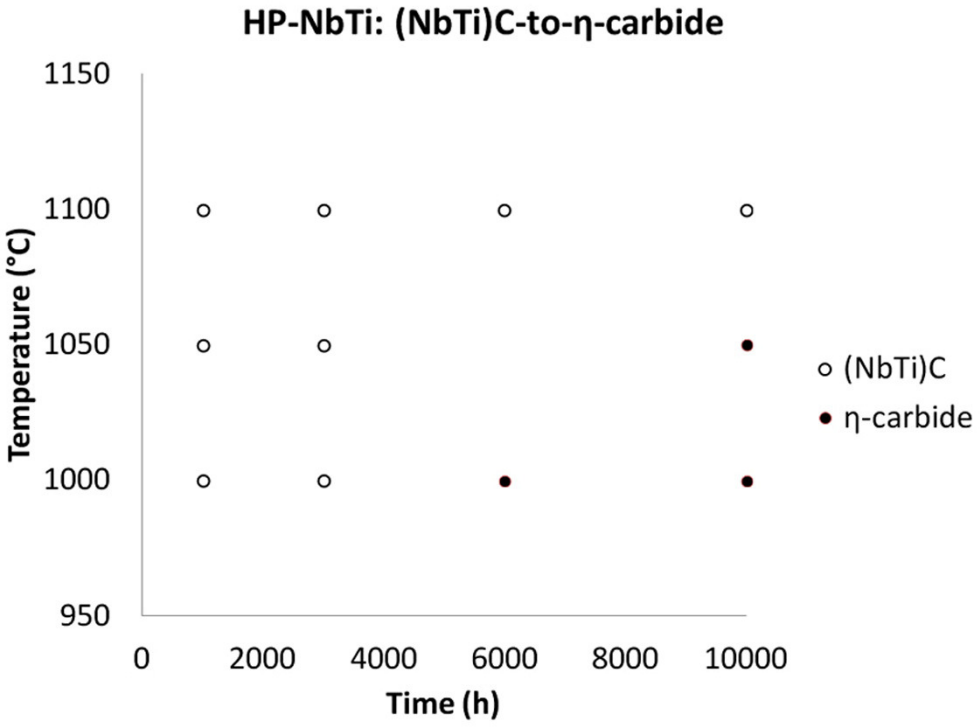

(b)

Figure C.3 – Time-temperature-transformation diagram for the MC-to-η-carbide transformation in the (a) HP-Nb and (b) HP-NbTi alloys after ageing in air at 1000, 1050 and 1100°C for up to 10,000 hours.

Appendix D Publications

During the course of this research a journal paper and conference proceeding was published. Each paper is attached in the following pages of this Appendix.

Buchanan, K.G. and Kral, M.V. (2012) *Crystallography and Morphology of Niobium Carbide in As-Cast HP-Niobium Reformer Tubes*, published in Metallurgical and Materials Transactions A 43(6): 1760-1769.

Knowles, D.; Buchanan, K. G and Kral, M. V. (2009) *Condition Assessment Strategies in Centrifugally Cast HP Steam Reformer Tube Alloys,* published in the Proceedings of the 2nd International ECCC Conference: Creep & Fracture in High Temperature Components – Design & Life Assessment, Dübendorf, Switzerland.

Crystallography and Morphology of Niobium Carbide in As-Cast HP-Niobium Reformer Tubes

KARL G. BUCHANAN and MILO V. KRAL

The microstructures of two as-cast heats of niobium-modified HP stainless steels were characterized. Particular attention was paid to the interdendritic niobium-rich carbides formed during solidification of these alloys. At low magnifications, these precipitates are grouped in colonies of similar lamellae. Higher magnifications revealed that the lamellae actually obtain two distinct morphologies. The type I morphology exhibits broad planar interfaces with a smooth platelike shape. Type II lamellae have undulating interfaces and an overall reticulated shape. To provide further insight into the origin of these two different morphologies, the microstructure and crystallography of each have been studied in detail using high resolution scanning electron microscopy, transmission electron microscopy, various electron diffraction methods (electron backscatter diffraction (EBSD), selected area diffraction (SAD), and convergent beam electron diffraction (CBED)), and energy dispersive X-ray spectroscopy.

DOI: 10.1007/s11661-011-1025-0

I. INTRODUCTION

HEAT-RESISTANT Fe-Cr-Ni-C austenitic stainless steels have become the dominant alloys for use in steam reforming and pyrolysis applications by the petrochemical industry. For example, depending on the process requirements, centrifugally cast alloy reformer tubes typically operate at temperatures between 1123 K and 1323 K (850 °C and 1050 °C) and internal pressures between 2 and 5 MPa for up to 100,000 hours. The combination of high temperatures and moderate stresses causes creep to be the dominant failure mechanism experienced in service. Initially, the HK (25 pct Cr, 20 pct Ni) alloy series replaced HT (18 pct Cr, 37 pct Ni) superalloys, providing tubes with comparable creep performance while reducing cost (due to the decrease in Ni). Subsequently, the HK series was superseded by the HP series (25 pct Cr, 35 pct Ni), which has shown higher creep strength and oxidation resistance than its predecessors. Extensive work has been carried out to optimize the microstructure of all of these alloys to maximize their high-temperature strength.

In the as-cast condition, the standard 25Cr-35Ni HP microstructure consists of a dendritic network of primary Cr_7C_3 (commonly known in the literature as M_7C_3) in an austenite matrix, which is relatively free of precipitation. On exposure to service temperatures, the primary Cr_7C_3 transforms to $Cr_{23}C_6$ and extensive secondary precipitation of $Cr_{23}C_6$ occurs within the matrix. The grain boundary carbide network is believed to inhibit grain boundary sliding, while the secondary matrix carbides obstruct dislocation motion.[1] However, due to the rapid diffusion of chromium through the austenite matrix (in comparison to vanadium, niobium, and titanium), the high coarsening rate of $Cr_{23}C_6$ causes it to possibly be the least effective of the available carbides for strengthening high-temperature stainless steels.[2] Addition of niobium, a strong carbide forming element, was reported to cause partial replacement of Cr_7C_3 with NbC (MC), refining and fragmenting the primary carbide network. The amount of replacement, refinement, and fragmentation of the as-cast carbide network is a function of the niobium content.[3] Accelerated creep testing showed that niobium-modified HP alloys have increased rupture life and lower minimum creep rates in comparison to the standard HP composition (*i.e.*, without niobium).[3] However, due to the decomposition of niobium carbide to *G* phase ($Ni_{16}Nb_6Si_7$) during exposure to elevated temperatures, the long-term strengthening effect of niobium is relatively unknown.

In the present work, the microstructures of two as-cast niobium-modified HP alloys were characterized with specific attention being paid to the primary NbC precipitates. Past studies described these precipitates as having a lamellar or "Chinese-script" morphology.[3–5] However, the present high-resolution scanning electron microscope observations of the primary NbC revealed that the lamellae actually take on two significantly different morphologies. The type I lamellae exhibit broad planar interfaces with a smooth platelike shape. Type II lamellae have undulating interfaces and an overall reticulated shape. The morphology of the NbC is likely to influence the NbC/G-phase transformation during the alloys exposure to service temperatures and subsequently affect the creep properties. Therefore, to provide further insight into the origin of these two different morphologies, the microstructure and crystallography of each have been studied in detail using high resolution scanning electron microscopy, transmission

KARL G. BUCHANAN, Doctoral Candidate, and MILO V. KRAL, Professor, are with the Department of Mechanical Engineering, University of Canterbury, Private Bag 4800, Christchurch, New Zealand. Contact e-mail: milo.kral@canterbury.ac.nz
Manuscript submitted December 1, 2010.
Article published online January 19, 2012

electron microscopy, various electron diffraction methods (electron backscattered diffraction (EBSD), selected area diffraction (SAD), and convergent beam electron diffraction (CBED)), and energy dispersive X-ray spectroscopy.

II. EXPERIMENTAL PROCEDURE

Two melts of HP-niobium steel were centrifugally cast in the form of tubes by Kubota Metal Corporation (designated KHR35C) and Paralloy (designated H39W). The chemical composition of each melt is listed in Table I. Samples of reformer tube were mounted for radial view (through wall) using Buehler Probemet and underwent grinding steps using 240, 400, and 600 grit silicon carbide paper and polishing steps using 9-, 3-, and 1-μm diamond paste. Prolonged final polish (4 to 5 hours) using 0.02-μm colloidal silica was necessary to remove the surface deformation induced by the previous polishing steps. For EBSD and energy dispersive X-ray spectroscopy (EDS), samples were etched for 20 seconds in glyceregia (30-mL glycerol, 30-mL HCl, and 10 mL HNO_3) and examined at 20 keV using a JEOL* JSM 6100[6] scanning electron microscope (SEM) equipped with the Oxford eXL EDS system and HKL Technology EBSD system (Oxford Instrument, Bucks, UK).[7] Samples for high resolution scanning electron microscopy were observed in the as-polished condition, after etching for 45 seconds and after deep etching for up to 90 minutes in glyceregia. Observations of these samples were carried out at 20 keV using a JEOL 7000F[6] field emission scanning electron microscope equipped with a JEOL JED-2300 EDS detector.

*JEOL is a trademark of Japan Electron Optics Ltd., Tokyo.

For transmission electron microscopy (TEM), 3-mm-diameter discs were mechanically punched and ground to approximately 100 μm using 1200 and 4000 grit silicon carbide paper. Prior to ion milling, the specimens were electropolished in a solution of 6 pct (by volume) perchloric acid, 35 pct *n*-butyl alcohol, and 59 pct methanol at approximately –40 °C, a voltage of 40 V, and current of 25 mA using a E.A. Fishione automatic twin-jet electropolishing apparatus (www.fischione.com/9003 Corporate Circle Export, PA). Strict control of the electrolyte temperature (within ±5 °C) to maintain the potential of 40 V and 25 mA reduced the prevalence of pitting. Optimally, electropolishing was stopped just prior to perforation of the foil. Subsequent perforation and thinning to electron transparency was carried out using the Gatan precision ion polishing system[8] with an initial accelerating voltage of 3.5 keV and sputtering angle of 6 deg. Milling was halted once the perforation began to noticeably increase in size. The accelerating voltage was reduced to 1.5 keV and the sputtering angle to 4.5 deg to grow the perforation to a suitable size (~0.2- to 0.5-mm diameter). Final cleaning of the sample at 0.5 keV and sputtering angle at 4.5 deg was carried out for 30 minutes. Analytical transmission electron microscopy (TEM) was carried out using a PHILIPS** CM200[9] operated at 200 keV and equipped with an Oxford INCA x-sight EDS system.[7]

**PHILIPS is a trademark of FEI Company, Hillsboro, OR.

EBSD patterns (or EBSPs) were recorded in spot mode and indexed using crystallographic parameters from the Pearson's Handbook.[10] EBSPs were obtained from the primary NbC precipitates and the austenite matrix directly adjacent to each precipitate. Using HKL Technology's[7] Flamenco software, the Euler angles (φ_1, φ_2, Φ) describing the crystallographic orientation of the phase with respect to a reference axis system could be calculated. These angles were used to calculate a 3 × 3 orientation matrix for each analysis point, and subsequently, the misorientation between any two points could be calculated using the following matrix operation:

$$[\mathrm{A}][\mathrm{B}]^{-1} = [\mathrm{M}]$$

where A and B are the orientation matrices of locations in phases A and B and M is the misorientation matrix:

$$[\mathrm{M}] = \begin{bmatrix} m_{11} & m_{12} & m_{13} \\ m_{21} & m_{22} & m_{23} \\ m_{31} & m_{32} & m_{33} \end{bmatrix}$$

The orientation relationship (OR) between location A and B is then:

$$\begin{array}{lll} [m_{11}\, m_{21}\, m_{31}]_A & // & [1\ \ 0\ \ 0]_B \\ [m_{21}\, m_{22}\, m_{23}]_A & // & [0\ \ 1\ \ 0]_B \\ [m_{31}\, m_{32}\, m_{33}]_A & // & [0\ \ 0\ \ 1]_B \end{array}$$

The misorientation angle θ and axis [u v w] between points A and B can also be calculated using the following equation:

$$\theta = \cos^{-1}\left(\frac{m_{11} + m_{22} + m_{33} - 1}{2}\right)$$

$$[u\, v\, w] = [m_{23} - m_{32} \quad m_{31} - m_{13} \quad m_{12} - m_{21}]$$

Table I. Chemical Composition of the As-Cast HP-Niobium–Modified Alloys as Determined by Inductively Coupled Plasma Spectroscopy (Weight Percent)

Wt Pct	C	Ni	Cr	Nb	Si	Mn	Mo	V	W	Co	Fe
KHR35C	0.41	33	25	0.77	1.26	0.6	0.24	0.07	0.35	0.11	bal
H39W	0.38	32.2	24.5	0.92	1.53	1.09	0.12	0.06	0.08	0.17	bal

By considering the 24 crystallographic equivalents for the cubic system, the disorientation (*i.e.*, the variant with the smallest value of θ about axis UVW) can be determined.[11] Alternatively, the Euler angles can be converted to a quaternion representation of the crystals' orientation with respect to the reference axis. The misorientation and disorientation can be calculated following the procedures used by Sutton and Balluffi[12] and Hanson.[13] A minimum of two precipitate-matrix pairs were analyzed within each dendritic group of NbC precipitates, and over 100 groups were analyzed. Since separate plates within a particular dendritic group were similarly orientated, an average orientation was calculated for each group.

TEM trace analysis was performed on nine NbC precipitates (each from a separate dendrite group) following the processes described by Hirsch *et al.*[14] and Loretto.[15] The purpose of the trace analysis was to determine whether the plates obtained a particular crystallographic "habit plane." A minimum of three and maximum of four zone axes were indexed for each precipitate and, after correction for rotation, superimposed onto the TEM bright-field image taken at each orientation.

III. RESULTS AND DISCUSSION

Figures 1(a) and (b) show the through-wall grain structure of the two as-cast HP-niobium alloys. Depending on the centrifugal casting conditions (for example, pouring temperature and cooling rate), reformer tubes exhibit either a completely columnar or a mixed columnar-equiaxed grain structure.[16,17] The high cooling rate induced during casting of these alloys has resulted in 100 pct columnar grain structures. Qualitatively, the KHR35C alloy can be seen to have a significantly larger grain size than the H39W alloy. Figures 2(a) and (b) are scanning electron micrographs showing the as-cast microstructure of each alloy. The dendritic structure, typical of these centrifugally cast alloys, contains alternating interdendritic groups of the primary carbides Cr_7C_3 (dark gray) and NbC (white) in an austenitic matrix. EBSD was employed to identify all three as-cast phases. At the magnifications shown in Figures 2(a) and (b), the primary NbC precipitates can be seen to exhibit the typical lamellar or "Chinese–script" morphology, as described by previous studies.[3–5]

Observations of the primary NbC at higher magnifications revealed the existence of two significantly different morphologies of individual plate lamella (Figures 3(a) and (b)). Type I lamellae, shown in Figure 3(a), exhibit a relatively planar interface with the austenite. In contrast, type II lamellae exhibit significant undulations along their surfaces, as shown in Figure 3(b). In two dimensions, the type II lamellae appear somewhat fragmented. SAD and CBED analysis of thin foils confirmed that both morphologies have the feck NbC (or MC) crystal structure. However, EDS consistently revealed small concentrations of molybdenum in type II (Table II) but none in type I. During solidification, partitioning molybdenum could have

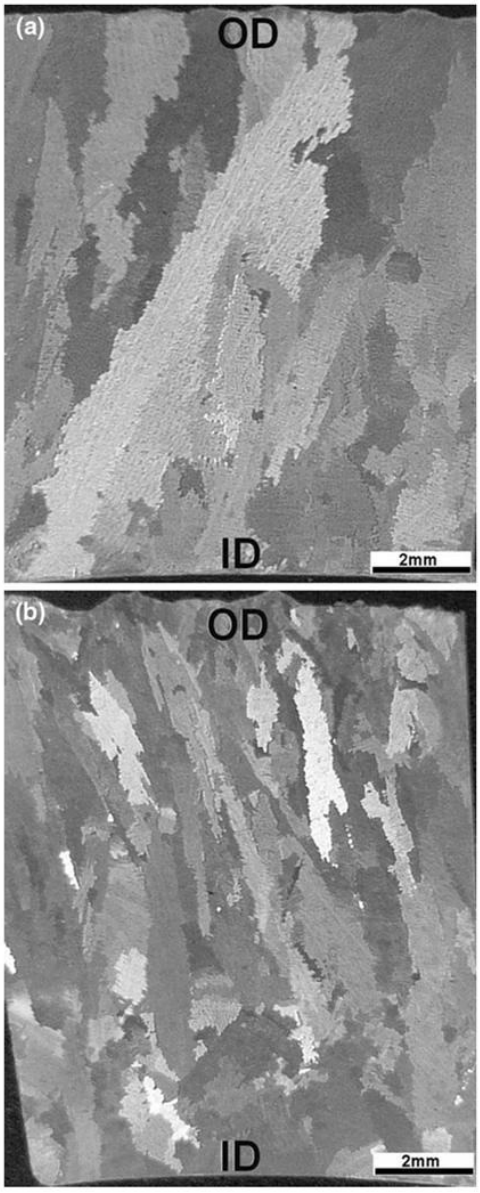

Fig. 1—Low-magnification optical micrographs showing the macrostructure of (*a*) KHR35C and (*b*) H39W (etchant: Marbles reagent).

influenced the growth morphology of the NbC precipitate; however, further investigation is required to investigate this theory. Small concentrations (<5 wt pct) of elements such as titanium (commonly utilized in combination with niobium in the HP-micro variant) were reported to cause the NbC morphology to change from lamellar to blocky.[4,5] Similar changes to (TaTiNb)C precipitates were attributed to small concentrations of hafnium and zirconium in directionally solidified Ni-based alloys.[18,19] Such additions are thought to increase the MC/matrix interfacial energy, causing the precipitates for the blocky morphology to

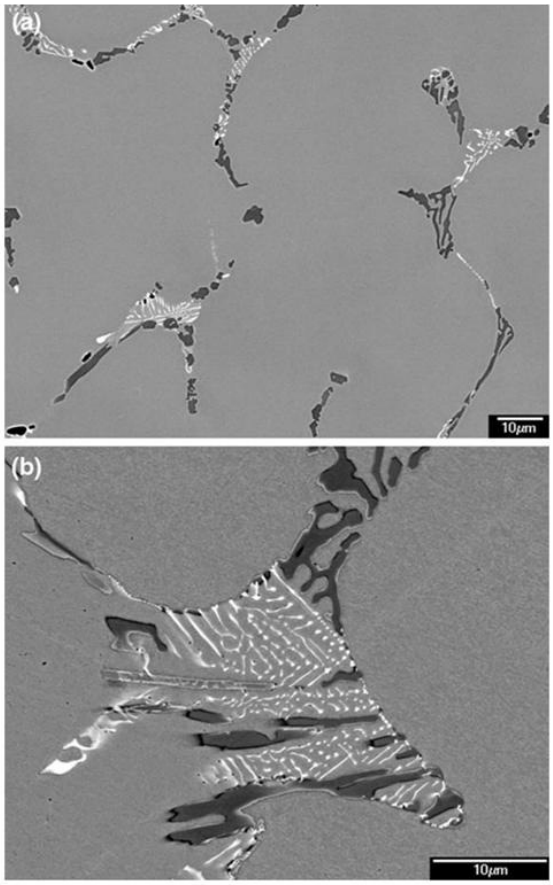

Fig. 2—Backscatter electron images of as-cast HP-niobium in the as-polished condition, with NbC appearing white and Cr_7C_3 as dark gray in an austenite matrix.

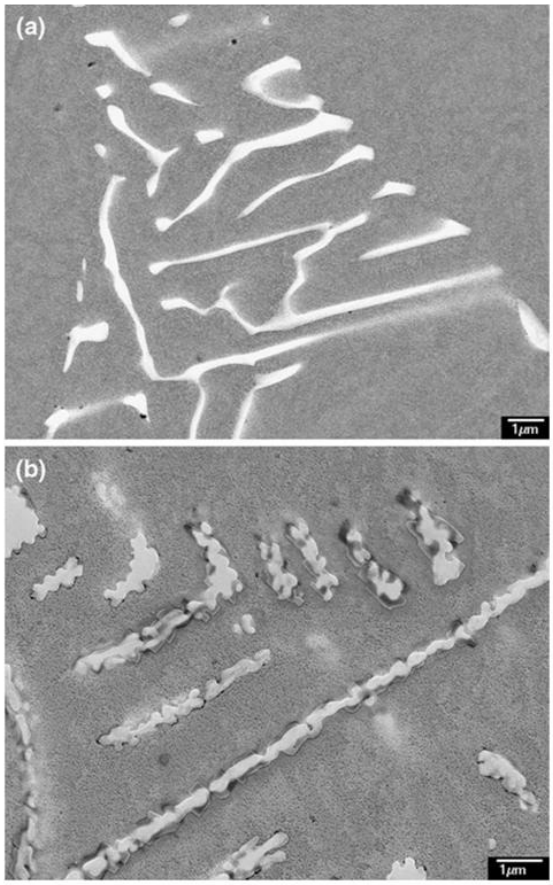

Fig. 3—Scanning electron micrographs showing the two-dimensional morphology of (*a*) type I lamellae and (*b*) type II lamellae.

minimize the interfacial area. Thus, local differences in the Mo concentration may have a smiliar modifying effect on the NbC morphology.

A small (typically <0.5-μm diameter) chromium-carbon–rich phase was observed between the type II NbC and austenite phases (Figures 4(a) and (b)). Convergent beam electron diffraction (CBED) analysis of this phase confirmed the orthorhombic Cr_7C_3 crystal structure (the same structure as the larger primary Cr-rich carbides). The Cr_7C_3/austenite interface was highly faceted. Although the dendritic groups of primary Cr_7C_3 and NbC are commonly interlinked (Figures 2(a) and (b)), it is believed that the interfacial Cr_7C_3 is independent of the primary Cr_7C_3 network (*i.e.*, the interfacial Cr_7C_3 is not caused by two-dimensional sectioning of small segments of the primary Cr_7C_3 network).

Studies of material subjected to unstressed aging for 1000 hours at 1173 K (900 °C)[20] previously reported the presence of $Cr_{23}C_6$ precipitates (typically 1 to 5 μm in diameter) on the interface of NbC lamella, which had partially transformed to *G* phase. This $Cr_{23}C_6$ precipitation was said to have formed due to the rejection of carbon from the transforming NbC precipitate into the chromium-rich austenite. However, the present work suggests that these $Cr_{23}C_6$ precipitates are just as likely to have arisen due to transformation of the pre-existing interfacial Cr_7C_3 to $Cr_{23}C_6$.

The difference between morphologies becomes more apparent after deep etching (Figures 5(a) through (d)). Progressive etching experiments on the as-cast material determined that deep etching with glyceregia caused the sole dissolution of the austenite matrix while leaving the primary carbides completely intact; *i.e.*, the carbide morphologies observed were not influenced by the etching process.

Type I lamellae are revealed as smooth solid plates in three dimensions (Figure 5(a)), where the broad faces exhibit varying degrees of curvature. Small steps or facets on the broad faces of the plates (which would be associated with the curvature) were not resolved using an SEM (Figure 5(b)).

Figures 5(c) and (d) show the weblike or reticulated shape of the type II lamellae in three dimensions. The fragmentation of the lamellae observed in two dimensions (Figure 3(b)) corresponds to the three-dimensional pores within the plane of the plates. The undulations commonly occurred at a near-constant length scale

Table II. SAD and CBED Determined Crystal Structure and EDS Chemical Composition for Each NbC Morphology

Type	Crystal System	Space Group	a (nm)	Nb	Cr	Fe	Ni	V	Mo
I	fcc	$Fm\bar{3}m$	0.438	87.9	7.6	2.3	1.5	0.7	—
II	fcc	$Fm\bar{3}m$	0.440	87.2	7.4	2.5	1.7	0.6	0.6

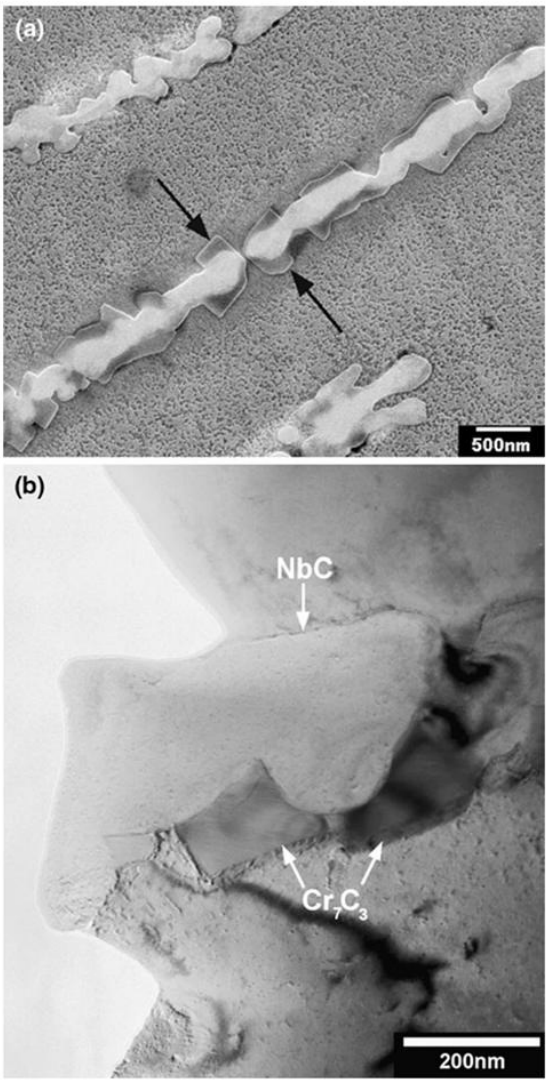

Fig. 4—(*a*) Scanning electron and (*b*) bright-field transmission electron micrographs showing the Cr_7C_3 located on the precipitate/matrix interface of type II lamellae.

causing the pore size of plates within and between separate groups to also remain consistent (typically 0.2 to 0.5 μm). Many lamellae adhered to a particular plane of growth causing the overall platelike morphology. After deep etching, the interfacial Cr_7C_3 could not be distinguished from the type II lamellae due to the lack of contrast between the two phases in scanning electron microscopy. For the H39W alloy, the type II lamellae appeared to be more prevalent than the type I lamellae (approximately, 65 pct type II–35 pct type I). However, the type I and II lamellae appeared to be equally abundant in the KHR35C alloy (*i.e.*, 50 pct type II–50 pct type I). Neither morphology appeared to be preferentially located, *e.g.*, at dendrite, grain boundaries, or relative position within the tube wall.

The type II lamellae exhibits a higher surface area to volume ratio in comparison to the type I lamellae; however, further work (such as serial sectioning) would be required to quantify this ratio. Exposure of the alloy to temperatures between 973 K and 1323 K (700 °C and 1050 °C) causes the NbC/G-phase transformation to occur. Therefore, the total surface area and properties (*i.e.*, interfacial structure and free energy) of the as-cast NbC/austenite interface will likely influence the kinetics of the *G*-phase transformation. This transformation does not occur during thermal exposure to temperatures above 1323 K (1050 °C) (*i.e.*, the NbC phase remains stable). However, the high surface area to volume ratio could cause the type II morphology to be unstable, causing the lamellae to undergo spheroidization to reduce the total interfacial energy.

Accelerated creep testing showed that laboratory aged samples with *G* phase present increased creep ductility in comparison to samples without *G* phase.[3] Thus, the characteristics of the *G*-phase transformation are important to predicting the service behavior of these alloys. However, since the existence of these two morphologies was previously unknown in HP-niobium–modified alloys, no effort to date was made to determine the transformation characteristics specific to each morphology. Characterization of unstressed laboratory aged material is currently underway[21] to provide further insight into the importance of the morphologies.

In a study of niobium-modified HK alloys, Wen-Tai and Honeycombe[5] established the existence of a cube-cube crystallographic OR between the primary NbC and austenite:

$$\langle 100\rangle_{\mathrm{NbC}} || \langle 100\rangle_{\gamma}$$
$$\{100\}_{\mathrm{NbC}} || \{100\}_{\gamma}$$

Calculation of the OR using EBSD and the matrix operations described in the experimental procedure confirmed that all type I lamellae located at dendrite boundaries obtain this cube-cube OR (on all sides of the lamella) with the austenite matrix. In cases where the lamellae were located on grain boundaries, the OR was exhibited with the grain, which contained the associated colony of lamellae (*i.e.*, the grain where nucleation of the colony occurred). The histogram in Figure 6(a) shows the magnitude of disorientation for each precipitate-matrix pair. Thirty-one out of the 40 precipitate type I groups analyzed were found to deviate from this ideal

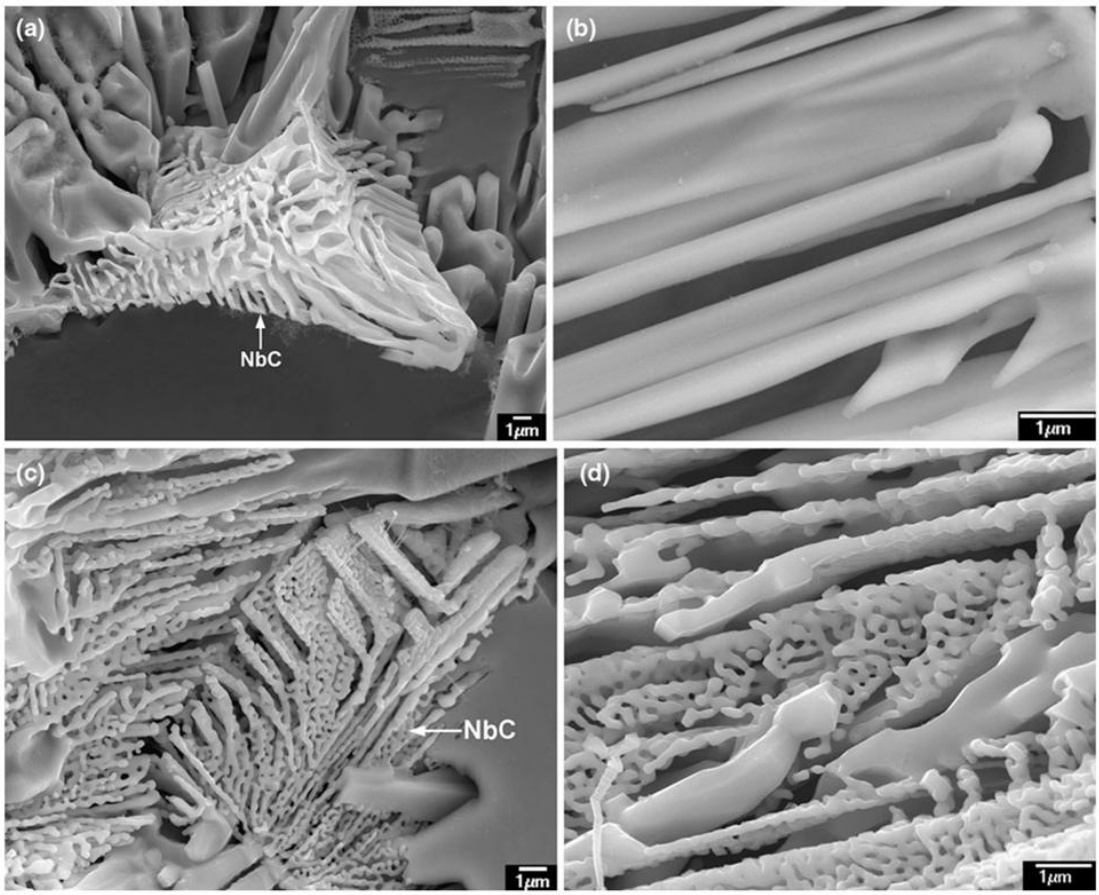

Fig. 5—Three-dimensional morphology of (*a*) and (*b*) type I lamellae and (*c*) and (*d*) type II lamellae.

relationship by less than 5 deg. All precipitates within a single group had the same crystallographic OR with a typical variance of less than 1 deg.

A similar analysis for the type II lamellae yielded complex expressions of OR such as

$$[\overline{25}\,\overline{1}325]_{NbC} \| [10\,0]_{\gamma}$$
$$[11\overline{2}50]_{NbC} \| [010]_{\gamma}$$

Although a consistent (but complex) crystallographic orientation relationship may exist between this example precipitate-matrix pair, rational pairs of parallel planes and directions from this information are not obvious. Therefore, calculation of the disorientation for each precipitate-matrix pair was performed to determine if clustering around a common angle occurred. Crystallographic orientation relationships with disorientations matching this common disorientation angle could then be confirmed or rejected by plotting the crystal pair with respect to each other in a stereographic projection and checking if the candidate poles were coincident.

Precipitates within each single group of type II lamellae were found to share a similar orientation with respect to the matrix (typical disorientation variance of less than 1 deg). However, between groups, the disorientation varied significantly (Figure 6(b)). The high level of variance between groups of these precipitates indicates that they are not likely to obtain a consistent orientation relationship with the matrix. Though there may seem to be slight clustering around 55 deg, it must be noted that these plots only display the magnitude of disorientation and not the axis of rotation. This axis was found to vary considerably when comparing precipitate-matrix pairs with a disorientation of approximately 55 deg.

TEM trace analysis of linear/planar features was performed to determine if the type I and II lamellae obtain a specific crystallographic habit plane. For the type I lamellae, traces were taken along the broad faces of lamella, which had a sufficient linear edge (such as the precipitate shown in Figure 7(a)). The traces taken from four widely separated zone axes for this precipitate are plotted on the stereographic projection shown in Figure 7(b). Each trace can be seen to intersect at the (100) pole. The linear edges of three type I lamellae were examined, all of which exhibited a {100} habit plane.

The traces determined from the type II lamella shown in Figures 8(a) and (b) are plotted in Figure 8(c). As the precipitates had no linear edge from which to take the

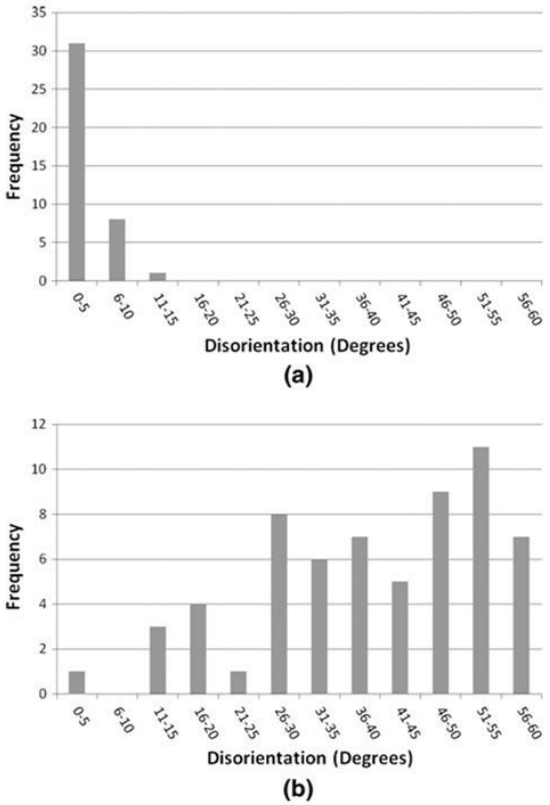

Fig. 6—Histograms showing the frequency of occurrence of disorientation measured between NbC-matrix pairs for the (*a*) type I lamellae and (*b*) type II lamellae.

traces, an estimated centerline for each lamella was defined as the trace direction. As shown in Figure 8(c), the general area of intersection of the traces shows no strong association with any low index habit plane. Furthermore, the area of intersection for each set of traces was inconsistent. Trace analysis was performed on five type II lamellae, each showing similar inconsistencies, indicating that it is unlikely that these plates obtain a rational habit plane over large areas. However, the complex shape of these precipitates and the presence of the interfacial Cr_7C_3 causes great difficultly when attempting to consistently determine the trace direction when viewing the precipitate from different crystallographic orientations. Analysis of deviations in the measured trace direction of approximately 5 deg resulted in a worst case intersection deviation on the stereographic projection of 10 to 15 deg. Therefore, the sum of small errors in defining the trace for each zone could be largely attributed to the resulting ambiguities on the stereographic projection.

While the type II morphology was not reported for Nb-rich MC precipitates in HP or HK alloys, similar morphologies were observed in directionally solidified and single-crystal Ni-based alloys.[22 24] Tin and Pollock[22,23] identified three distinctly different morphologies (blocky, Chinese-script, and nodular), which Ta-rich MC precipitates exhibited in various single-crystal Ni-based alloys. In all alloys with carbon additions, the script and nodular lamellae were dominant, with only few blocky precipitates typically observed. The ratio of script to nodular precipitates varied significantly with respect to overall alloy composition. However, no single alloying element could be attributed to altering the script-nodular preference. While both morphologies existed throughout the cross section, the nodular TaC precipitates were the sole precipitates situated around freckle chain defects. These defects are a direct result of compositional gradients within the "mushy zone," indicating the importance of local melt composition with respect to morphology. While the overall solidification conditions were kept constant, local variations were present due to the turbine blades complex geometry. However, these local variations did not significantly affect the script-nodular preference.

The morphological dependence of MC carbides with respect to the solidification conditions was studied extensively in directionally solidified (DS) Ni-based alloys.[24 30] Typically, individual studies kept the overall alloy composition constant while varying the solidification conditions at the γ/L interface. Due to the large range of Ni-based alloys, the MC composition varied significantly between studies (for example, (TaTi)C,[24] (TiMo)C,[25] (NbTi)C,[29] and (NbTiW)C[32]). Although composition is known to affect the MC morphology,[4,18,19] generally all MC compositions followed similar trends with respect to the solidification conditions.

Previous work has shown that the thermal gradient at the γ/L interface (G_L) and overall growth rate (R) play an important role in determining the morphology of the advancing γ/L interface, thus influencing the MC growth characteristics. In general, blocky morphologies dominated at high G_L/R ratios while low ratios promoted script morphologies similar to the type I lamellae. When G_L remained constant, the MC precipitates formed blocky morphologies at growth rates below 5 μm/s, which progressively transitioned to script morphologies at growth rates between 5 to 100 μm/s.[19,23 26,28] The exact growth rate where the transition occurred in each Ni-based alloy was specific to the composition of the MC precipitate. Under splat cooling conditions, fine faceted blocks (thought to be present in the melt prior to quenching) were dominant.[19,27] Melt treatments such as superheating were also reported to induce the blocky to script transition.[30]

Low growth rates ($R < 1$ μm/s) induced planar growth fronts where nucleation and growth of the blocky precipitates occurred in the liquid ahead of the advancing γ/L interface. These blocky MC precipitates typically exhibited the equilibrium octahedral shape.[19,23,26,27] Cellular growth fronts occurred at intermediate growth rates ($1 < R < 5$ μm/s) with the MC precipitates exhibiting irregular blocky or elongated platelet morphologies.[19,24,27 29] This irregular shape often appeared to be a transitional morphology where both blocky and scriptlike features could be identified. In some cases, the irregular morphologies contained

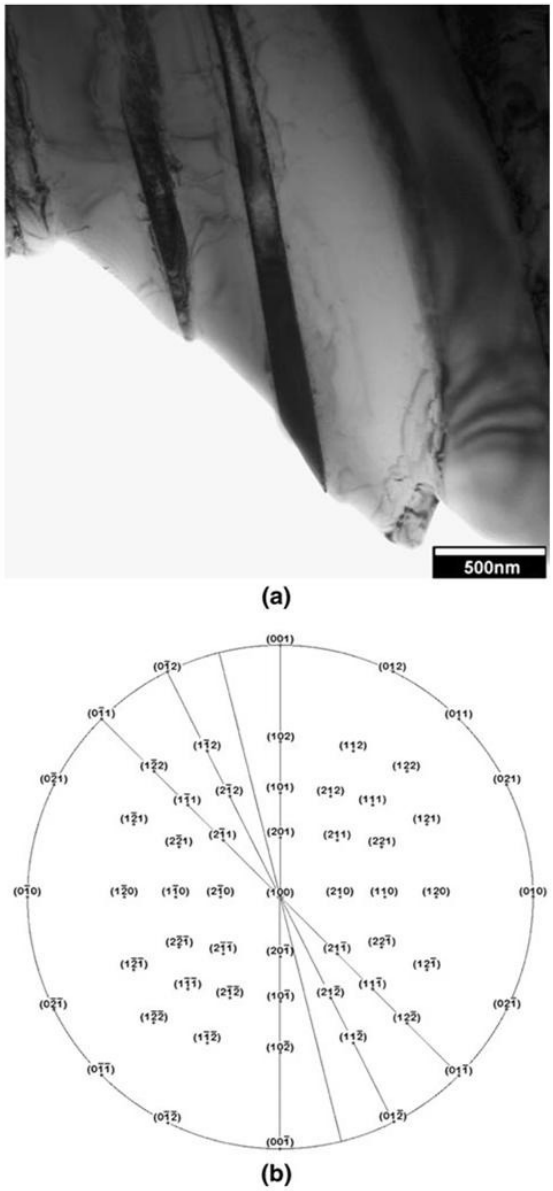

Fig. 7—(*a*) Representative bright-field transmission electron micrograph of the type I lamellae. (*b*) Stereographic projection centered about $(100)_{NbC}$ showing the intersection of four traces taken from (a).

titanium-nitrogen or hafnium-rich cores, which had heterogeneously nucleated on aluminum or magnesium oxide melt inclusions.[25,26,29] Dendritic growth fronts associated with higher growth rates ($R > 5\ \mu$m/s) resulted in higher levels of solute supersaturation within the interdendritic regions, promoting the formation of a MC/γ eutectic. The favorable conditions for the growth of dendritic carbide branches result in the Chinese-script morphology.[19,24,27,28] Existing octahedral precipitates were also observed to preferentially grow along the $\langle 100 \rangle_{MC}$ direction, resulting in arrowhead-shaped plates or rods.[19,23,26]

Although script morphologies similar to the type I lamellae were commonly observed in DS Ni-based alloys, morphologies similar to the type II lamellae were rare. Nodular rods rich in titanium and tantalum were observed on the grain boundaries of a DS alloy when the growth rate was reduced below 0.5 μm/s.[24] These rods were thought to have grown ahead of the γ/L interface into the solute-rich liquid until the MC + γ eutectic composition was reached. Coarsening of the rod due to the eutectic reaction subsequently formed the nodules. However, no significant compositional or structural analysis was performed on the blocky, script, or nodular morphologies observed in this alloy. Thus, it is difficult to attribute the nodular rod formation to either the local solidification rate or local melt composition.

Based on the preceding observations, the type I lamellae are believed to be formed during eutectic solidification. Initially, rejection of niobium and carbon to the melt during dendritic growth of the austenite occurs until the MC + γ eutectic composition is reached. Nucleation of the type I lamella likely occurs on the existing austenite dendrite, setting the NbC/austenite orientation relationship. The {100} habit plane is formed during cooperative growth of the NbC lamellae and austenite, thus allowing the precipitates to obtain a high surface area while minimizing the total free energy associated with the boundary. These observations are consistent with those exhibited by the TaC, (TaTiNb)C, and (TiNb)C script morphologies in Ni-based alloys.[18,22,23,31 33] Preferred orientation relationships and habit planes were also observed in other alloy systems containing lamellar precipitates (for example, the Bagaryatsky or Pitsch–Petch relationships of pearlite[34]), where selection of these unique ORs and habit planes is thought to be influenced by the nucleation site, interfacial energy, and relative growth rates of the constituents.[35]

For the type II lamellae, nucleation and growth is not well understood. Similar to the blocky morphology in Ni-based alloys, the type II lamellae did not obtain an OR with the matrix, suggesting that these precipitates also form in the liquid ahead of the γ/L interface. The higher type II prevalence in the H39W alloy indicates that higher niobium contents (when comparing the H39W and KHR35C alloys, Table I) further promote nucleation in the liquid. The differing solidification conditions (as suggested by the differing grain sizes) may also influence the morphology preference; however, controlled solidification studies (where the solidification rate, thermal gradient, alloy composition, and inclusion content are systematically varied) are necessary to determine the factors that dominate the final morphology preference. While the overall alloy composition and solidification conditions likely influence the relative proportion of the type II lamellae, the present evidence (*i.e.*, no consistent NbC/γ OR, overall planar growth, and undulations within the plates) suggests that the morphology is determined by the nucleation site and local solidification conditions.

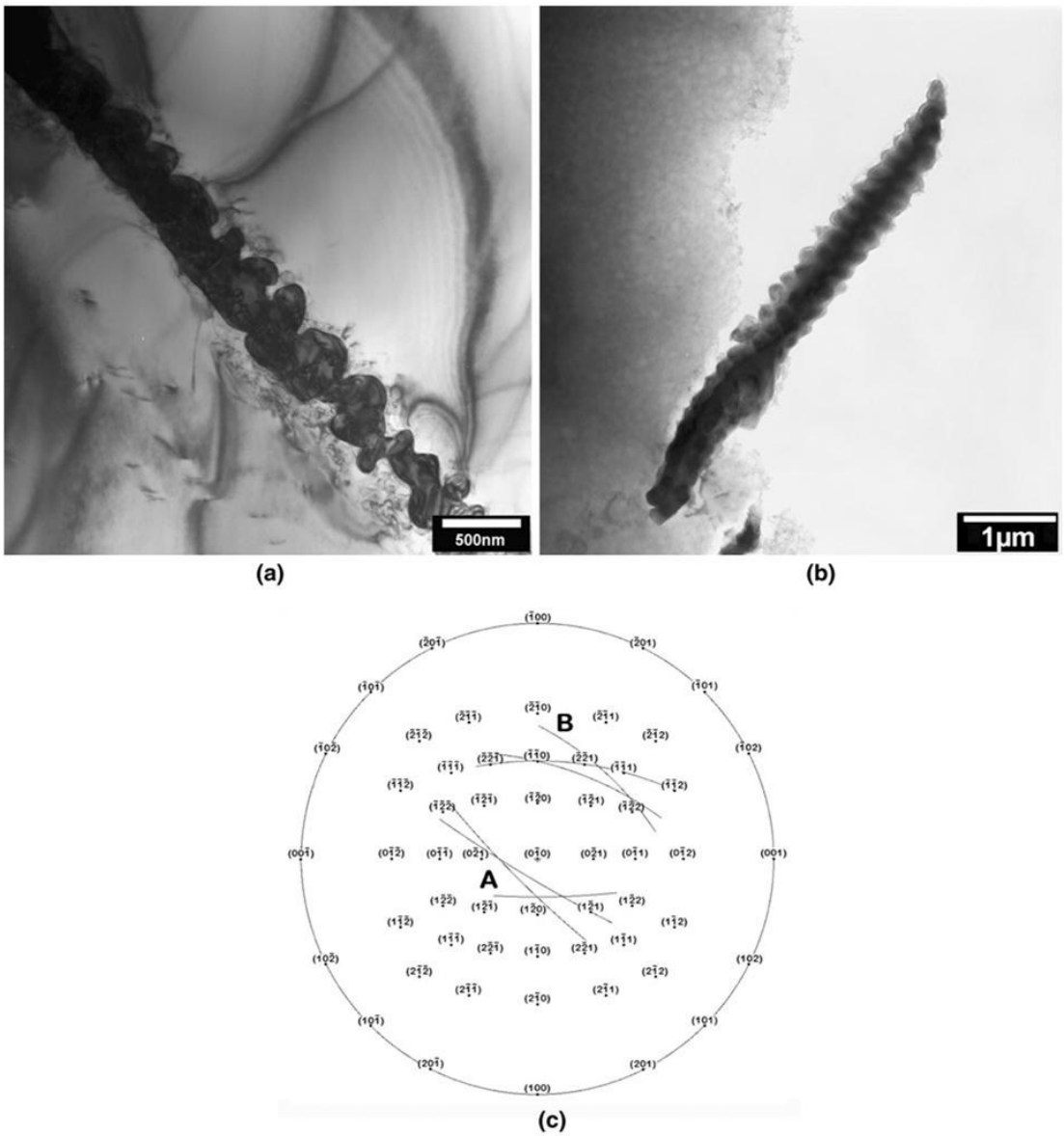

Fig. 8—(*a*) and (*b*) Representative bright-field transmission electron micrographs of the type II lamellae. (*c*) Stereographic projection centered about $(0\bar{1}0)_{NbC}$ showing the intersections of the three traces from precipitate (a) and of the three traces from precipitate (b).

Nucleation of the type II lamellae possibly occurs heterogeneously on oxide inclusions. Spherical TiC nuclei surrounded by blocky (NbTi)C precipitates were observed in the HP-micro alloy (Nb and Ti additions) and IN718 Ni-based alloys.[17,29,36] Submicron aluminium, magnesium, and zirconium oxide inclusions were detected within these TiC nuclei, indicating the presence of Al_2O_3, MgO, or ZrO melt inclusions.[17,29,36] Nucleation of blocky (TiMo)C precipitates on alumina inclusions was also observed in directionally solidified IN100 alloys.[25] While no evidence of oxide inclusions associated with the type II lamellae was found, it is unlikely these submicron inclusions are isolated to the HP-micro alloy. The surrounding TiC nuclei in the HP-micro alloys typically causes the inclusions to be easily distinguishable within the blocky (NbTi)C. Therefore, the absence of titanium could make it inherently difficult to locate these oxide inclusions in the HP-niobium alloys.

During growth of the blocky morphology in HP-micro, the addition of titanium possibly increases the MC/L interfacial energy. Therefore, the blocky morphology is formed to minimize the surface area to volume ratio. The type II NbC may be associated with a lower interfacial energy, allowing for the precipitates to form with significantly higher surface areas. The array of undulations within the plane of the plates is also possibly

influenced by partitioning molybdenum concentrating at the advancing NbC/melt interface. Once a threshold concentration capable of affecting the growth profile is reached, the growth direction may be forced to alter. Similar modifications of eutectic morphologies (faceted to fibrous) due to elemental poisons (such as sodium or strontium in the Al-Si system) are well known in the literature.[35] The overall planar growth of the type II lamellae is likely related to a preferred growth direction aligning with local melt thermal and chemical gradients.

IV. SUMMARY AND CONCLUSIONS

The primary NbC distribution was found to consist of two different morphologies. Both had an fcc crystal structure (a = 0.44 nm). No location preference of either morphology was observed with respect to dendrite boundary, grain boundary, or wall position. The attributes for each morphology can be summarized as follows.

Type I:

1. solid lamellar plates, which share a relatively planar interface with the adjacent austenite;
2. $\langle 100\rangle_{NbC}||\langle 100\rangle_{\gamma}$, $\{100\}_{NbC}||\{100\}_{\gamma}$ orientation relationship; and
3. exhibited a {100} habit plane.

Type II:

1. weblike or reticulated plates, which often adhered to an overall growth plane, but exhibited no crystallographically rational habit plane;
2. no consistent, rational NbC/matrix orientation relationship;
3. more prevalent than the type I lamellae, particularly so in the H39W alloy, which contained a higher niobium content;
4. molybdenum present in the NbC composition; and
5. Cr_7C_3 identified between the NbC and austenite.

The preceding observations suggest that the morphological difference is determined by the solidification conditions that each type of lamellae experience. In the case of type I lamellae, nucleation occurs on the existing austenite dendrite followed by eutectic growth of the lamellae with the austenite. The type II lamellae likely nucleate in the liquid ahead of the γ/L interface, prior to the formation of the type I lamellae. Local melt thermal and chemical gradients subsequently dominate growth of the type II lamellae, resulting in the observed array of undulations within the plates and overall planar growth.

ACKNOWLEDGMENTS

The authors appreciatively acknowledge the support of Quest Integrity Limited (NZ), Shell Global Solutions (Netherlands), and the New Zealand Foundation for Science and Technology (Contract No. QREL0702) for funding of this work. The authors are also grateful to Drs. Takanori Sato and Catherine Bishop (University of Canterbury), Dr. Chris Hutchinson (Monash University), and Professor John Cahn (University of Washington) for many helpful discussions.

REFERENCES

1. E.A.A.G. Ribeiro, R. Papaleo, and J.R.C. Guimaraes: *Metall. Trans. A*, 1986, vol. 17A, pp. 691–96.
2. W.-T. Hou and R.W.K. Honeycombe: *Mater. Sci. Technol.*, 1985, vol. 1, pp. 390–97.
3. G.D. de Almeida Soares, L.H. de Almeida, T.L. da Silveira I. Le May: *Mater. Charact.*, 1992, vol. 29, pp. 387–96.
4. L.H. De Almeida, A.F. Ribeiro, and I. Le May: *Mater. Charact.*, 2002, vol. 49, pp. 219–29.
5. H. Wen-Tai and R.W.K. Honeycombe: *Mater. Sci. Technol.*, 1985, vol. 1, pp. 385–89.
6. www.jeol.com.
7. www.oxford-instruments.com.
8. www.gatan.com.
9. www.fei.com.
10. P. Villars and L.D. Calvert: *Pearson's Handbook of Crystallographic Data for Intermetallic Phases*, 2nd ed., ASM INTERNATIONAL, Materials Park, OH, 1991.
11. V. Randle: *The Measurement of Grain Boundary Geometry*, Institute of Physics Pub, Bristol, PA, 1993, pp. 24–28.
12. A.P. Sutton and R.W. Balluffi: *Interfaces in Crystalline Materials*, Oxford Science Publications, Gloucestershire, 1996, pp. 17–20.
13. A. Hanson: *Visualizing Quaternions*, Morgan Kaufmann, San Francisco, CA, 2006, pp. 52–54.
14. P.B. Hirsch, A. Howie, R.B. Nicholson, D.W. Pashley M.J. Whelan: *Electron Microscopy of Thin Crystals*, 1st ed., Butterworths, London, 1965, pp. 311–15.
15. M.H. Loretto: *Electron Beam Analysis of Materials*, 2nd ed., Chapman & Hall, London, 1994, pp. 252–53.
16. X.Q. Wu, H.M. Jing, Y.G. Zheng, Z.M. Yao, W. Ke, and Z.Q. Hu: *Mater. Sci. Eng.*, 2000, vol. A293, pp. 252–60.
17. F.G. Caballero, P. Imizcoz, V. Lopez, L.F. Alvarez, and C. García de Andrēs: *Mater. Sci. Technol.*, 2007, vol. 23, pp. 528–34.
18. Q.Z. Chen, N. Jones, and D.M. Knowles: *Acta Mater.*, 2002, vol. 50, pp. 1095–1112.
19. A.K. Bhambri, T.Z. Kattamis, and J.E. Morral: *Metall. Trans. B*, 1975, vol. 6B, pp. 523–37.
20. R.A.P. Ibanez, G.D. de Almeida Soares, L.H. de Almeida, and I. Le May: *Mater. Charact.*, 1993, vol. 30, pp. 243–49.
21. K.G. Buchanan and M.V. Kral: University of Canterbury, Christchurch, New Zealand, unpublished research, 2011.
22. S. Tin, T.M. Pollock, and W. Murphy: *Metall. Mater. Trans. A*, 2001, vol. 32A, pp. 1743–53.
23. S. Tin and T.M. Pollock: *Metall. Mater. Trans. A*, 2003, vol. 34A, pp. 1953–67.
24. W.R. Sun, J.H. Lee, S.M. Seo, S.J. Choe, and Z.Q. Hu: *Mater. Sci. Eng.*, 1999, vol. A271, pp. 143–49.
25. R. Fernandez, J.C. Lecomte, and T.Z. Kattamis: *Metall. Trans. A*, 1978, vol. 9A, pp. 1381–86.
26. J. Chen, J.H. Lee, C.Y. Jo, S.J. Choe, and Y.T. Lee: *Mater. Sci. Eng.*, 1998, vol. A247, pp. 113–25.
27. L. Liu, F. Sommer, and H.Z. Fu: *Scripta Metall.*, 1994, vol. 30, pp. 587–91.
28. S.M. Seo, I.S. Kim, J.H. Lee, C.Y. Jo, H. Miyahara, and K. Ogi: *Mater. Sci. Technol.*, 2008, vol. 24, pp. 110–14.
29. A. Formenti, A. Eliasson, A. Mitchell, and H. Fredriksson: *High Temp. Mater. Process.*, 2005, vol. 24, pp. 239–58.
30. F.S. Yin, X.F. Sun, J.G. Li, H.R. Guan, and Z.Q. Hu: *Scripta Mater.*, 2003, vol. 48, pp. 425–29.
31. K.A. Al-Jarba and G.E. Fuchs: *Mater. Sci. Eng.*, 2004, vol. A373, pp. 255–67.
32. J. Yang, Q. Zheng, X. Sun, H. Guan, and Z. Hu: *J. Mater. Sci.*, 2006, vol. 41, pp. 6476–78.
33. V.A. Wills and D.G. McCartney: *Mater. Sci. Eng.*, 1991, vol. A145, pp. 223–32.
34. D.S. Zhou and G.J. Shiflet: *Metall. Trans. A*, 1992, vol. 23A, pp. 1259–69.
35. R. Elliott: *Int. Met. Rev.*, 1977, vol. 22, pp. 161–86.
36. F.C. Nunes, L.H. de Almeida, J. Dille, J.L. Delplancke, and I. Le May: *Mater. Charact.*, 2007, vol. 58, pp. 132–42.

ECCC Creep Conference, 21–23 April 2009, Zurich

Condition Assessment Strategies in Centrifugally Cast HP Steam Reformer Tube Alloys

David Knowles+, Karl Buchanan#, Milo Kral#
+Shell Global Solutions International, PO Box 38000, 1030 BN Amsterdam
#Dept Mechanical Engineering, Private Bag 4800, Christchurch 8140, New Zealand

Abstract

In steam methane reforming one of the key reliability aspects relates to ensuring the integrity and reliable operation of the catalyst filled radiant tubes. The tubes experience temperatures beyond 900°C for a considerable length of time, which makes creep the prime mode of failure. Predicting and assessing creep damage rates is challenging for a number of reasons: the alloys are not subject to any international specifications, the tubes are cast and their microstructures evolve substantially in service. These factors are known to lead to considerable scatter in creep life, strain and ductility response.

This paper describes the initial steps of a current approach to managing tube life and outlines the early stages of a study aimed at development of a methodology to utilise appropriate inspection in combination with judicious creep strain/rupture testing to provide an effective strategy for long-term assessment and management of reformer tube integrity. The work involves creep testing and microstructural characterisation of service-exposed material to incorporate the influences of material changes

Keywords: Centrifugally cast alloys, creep strain, microstructure

1. Introduction

In steam methane reforming one of the key reliability aspects relates to ensuring the integrity and reliable operation of the catalyst filled radiant tubes. These tubes are generally exposed to metal temperatures beyond 900°C for a considerable length of time, which makes creep the prime mode of failure. Generally non-standardised materials with a range of chemistries are employed, the tubes being fabricated by centrifugal casting. This cast structure along with in-service aging is known to lead to substantial variations in creep strain/life response. Furthermore the variation in local metal temperature along the length of individual tubes are known to be significant so that the remnant life of the tube is very sensitive to the location at which any inspection measurements are made.

Temperature estimates using radiation thermometry plays a key role in day-to-day management of the furnace, but this is a specialist technique and is subject to a number of potential errors; generally it does not capture the long-term trends in temperature at local regions along the tube length. At the present time there are a number of complementary inspection techniques that can be adopted during routine outages to assess the condition of the tubes, of which measuring diametral growth is a widely adopted technique often in parallel with ultrasonic or eddy current inspection.

This paper describes the initial outline of a study aimed at development of a methodology to utilise appropriate inspection measurements in combination with judicious creep strain/rupture

testing to provide an effective strategy for long-term assessment and management of reformer tube integrity. The work involves creep testing and microstructural characterisation of service-exposed material to incorporate the influences of material changes.

2. Inspection Techniques

2.1 Material inspection

If one considers a controlled failure process in a reformer tube, the prime 'damage' mechanisms relate to microstructural modification and creep. To date a non-destructive, volumetric measure of microstructural change (as opposed to surface replication) has not been adopted in general use. In relation to bulk creep damage assessment a number of techniques have evolved over recent decades and have been utilised with mixed success. To better understand the applicability of these techniques it is important to keep in mind the general nature of a typical strain/time plot in the creep regime, Figure 1

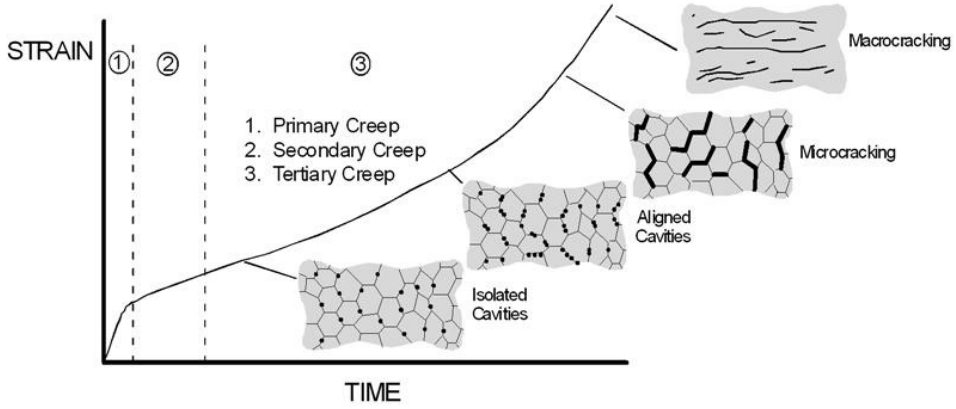

Figure 1. Typical creep strain versus time curve for a metallic material.

Generally the initial primary creep regime (1) can be ignored as it does not play a role in the damage process and its influence on dimensional changes in actual cast tubes is limited. In regions (2/3) strain evolves and damage accumulates due to a number of processes – multiplication of dislocations, intergranular stress generation, grain boundary cavity formation, cavity linkage, micro and macro cracking to name a few. Most inspection techniques aim to measure changes at a material microstructural level and focus on these damage processes beginning with cavity formation. However it is important to recognise that the early stages of cavity formation are difficult to measure and this manifestation of damage is rarely observed in the first 1/3rd of a component's life.

Typical non-destructive inspection techniques fall into three general categories (often used in combination):

1. Measurement of strain—principally through diametric growth in the cast tubes
2. Eddy current inspection
3. Ultrasonic inspection

Given the complex cast microstructure in these tubes, consisting of extensive regions of columnar grains and a varying extent of more equiaxed grains on the inner surface, for the latter two processes it is acknowledged that successful application requires both a validated procedure and well informed interpretation/understanding of the results.

The eddy current technique has been found to be particularly useful at finding more extensive defects in tubes that are in the final stages of life (and hence not suitable for a further campaign), but the interpretation of the output from the inspection is subjective. Uncertainties can be reduced substantially by implementing baseline inspection on the tubes prior to their entering service.

The perceived advantage of the strain-based approach is that, in principle, it can be used to monitor the earlier stage of creep damage (strain) accumulation, which is complementary to the aforementioned measures. For improved accuracy it is desirable to measure changes in the internal diameter along the whole length of each tube using laser profilometry. The benefits to this technique stem from the fact that the internal surface of the tubes is bored and not subject to any corrosion in service. If no prior inspections have been carried out then the growth in any region of the tube can be compared to a base line from the cold section of the tube outside the radiant box. The main draw back of internal inspection is simply that access is only available during a catalyst change-out and hence the opportunity for inspection can be very limited.

External dimension profiling can be carried out rapidly during any planned shutdown, but its accuracy is more limited owing to:

- Variation in the outer diameter of the tubes owing to the measurement being on the as-cast surface (no final machining) and
- The potential for surface oxidation

In practice this latter concern is not significant; primarily the initial surface wall loss is due to oxidation of the rough surface cast finish. The substantial variation in external diameter negates the ability to compare tube growth, using cold regions as a benchmark. Owing to this fact, base lining of the tubes either prior to entering service, or early in life, is seen as a critical step and considered as best practice. Regular inspection then allows a clear measure of strain evolution to be recorded for every tube as a function of any position along their length i.e., effective mapping of strain evolution throughout the radiant box can be undertaken.

2.2 Temperature

A final inspection technique, which warrants mention, is that of temperature, a critical parameter in any reformer tube life assessment study. Temperature measurement is normally achieved using radiation thermometry. While this can provide accurate results it is known to be prone to a number of large potential sources of error, if not applied with insight, including:

- Emissivity errors,
- Reflection errors– from furnace wall and neighbouring tubes,
- Size of source effects,
- Adsorption and emission errors.

These issues are described in depth by Saunders [1], which provides excellent background on the subject.

A less well recognised advantage of regular measurement of diametral growth is that, to a first approximation, it provides a time-averaged measure of the thermal exposure along the length of the reformer tube which is an alternative and often more accurate indicator of the non uniformity of the temperature profile within the furnace. This is clearly indicated in Figure 2 where an inspection has highlighted the extremely localised nature of accelerated tube growth in the coffin section (towards the outlet of the tube). In this case the location of concern could not be monitored with optical pyrometry, owing to difficult access, but allowed appropriate selection of the location from which to take creep specimens.

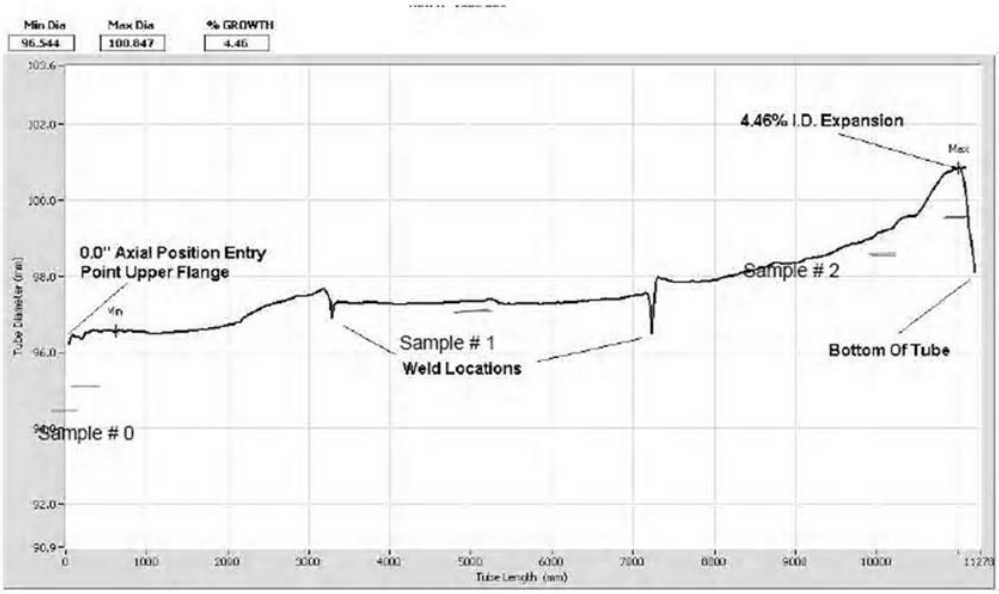

Figure 2. Internal laser profilometry from a service exposed reformer tube. Clearly marked are the weld locations and the region of highest diametral growth, which, in this instance is in the 'coffin' section of the furnace.

3. Strain/Life Interpretation

The traditional approach to reformer tube design life assessment has followed the approach as described in API 530 [2] whereby the Larson-Miller Parameter is used as a time-temperature parameter to allow prediction of the required rupture life when the tube wall is subjected to specific combination of stress and temperature.

$$LMP = f(\sigma) = (T + 273)\left[C + \log(t_R)\right]$$

where σ is stress, T is temperature (°C), t_R is time to rupture, and C is a constant. In principle this approach can be used to determine accumulated tube life; a Robinson life-fraction summation technique can be applied if one has access to regular and accurate temperature measurement. Larson-Miller Parameter data is generally available from the tube supplier which can be used for

this purpose. However this approach should be treated with some caution as it is acknowledged that there are a number of significant drawbacks:

1. Remnant life estimates are based on tube metal temperatures and primary hoop stress but do not consider the secondary through-wall stresses generated due to temperature gradients.
2. Aside from temperature measurement the previously mentioned inspection techniques provide no input to the assessment process and hence the opportunity does not exist to optimise life consumption estimates.
3. Larson Miller data is based on relatively short-term testing (rarely beyond 1 year) and microstructural modifications (in-service aging) in long-term exposure are known to modify significantly the creep performance [3].

In older generation HK alloys, due to the reduced high temperature strength, thicker walled tubes were employed, and the through-wall stresses were known to contribute significantly to life consumption via creep relaxation. In thinner tubes fabricated using HP alloys it is generally acknowledged that this effect is reduced substantially. Its influence is, obviously, very dependent upon the number of cycles which a unit will see and the manner in which the unit is shut down/started up. Thomas et al [4] have described a strain based approach, centred on the ductility exhaustion method in R5 [5] which discusses this topic in some detail. For ductile materials it has been found that the contribution of these cycles to life reduction is minor, though further consideration of this aspect is warranted.

Strain-based approaches to creep life assessment has not historically gained much attention in the petrochemical/refining sector, but the introduction of the Omega method in API 579 [6] has changed this position somewhat in recent years. In terms of uniaxial stress the Omega method is simply described by:

$$\dot{\varepsilon} = \dot{\varepsilon}_o \exp\left[-\Omega \varepsilon_c\right]$$

where $\dot{\varepsilon}_o$ is the starting creep rate, ε_c is the accumulated creep strain at the given stress and Ω is a stress/temperature dependent material parameter which describes the shape of the creep curve. This approach is essentially a specific continuum damage mechanics formulation as discussed in detail in many texts such as Penny and Marriott [7], damage (D) being related to an acceleration in creep strain rate via the relation:

$$D = 1 - \frac{\dot{\varepsilon}_o}{\dot{\varepsilon}} = 1 - e^{-\Omega \varepsilon_c}$$

If one ignores the initial region of primary creep then this form of relation can easily be fitted to a typical creep strain curve as illustrated in Figure 3 and, in principle, measurement of diametral growth (given stress, time and temperature) can then directly be related to a position on the creep curve, hence current life consumption can be calculated. If temperature and stress vary then integration of strain increments can be achieved by use of the strain rate acceleration factor, which is represented in the above description of damage. From a material perspective a significant drawback in the model is that it cannot consider time related development of microstructure. While this isn't a major concern when testing thermally stabilised wrought alloys it is an important consideration in these centrifugally cast materials, which see much higher temperatures.

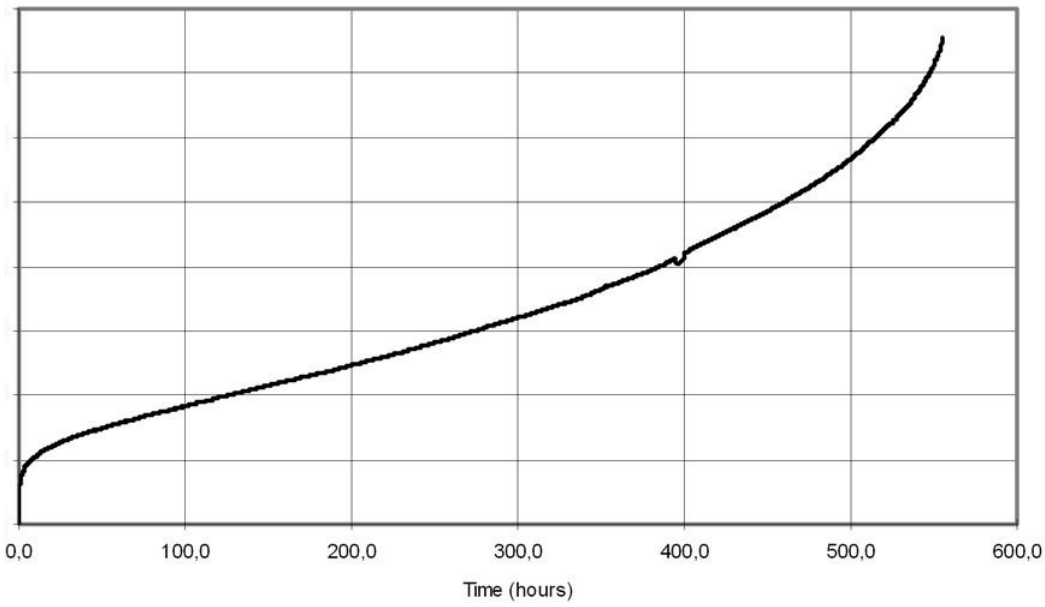

Figure 3. Short-term creep strain vs. time curve for typical 25/35 microalloyed ex service tube (alloy A) tested at 1000deg C. Note ductility at failure greater than 14%.

In practice a wide range of creep models could be adopted to fit the general form of the creep strain curve and hence make better use of in-situ diametric growth measurement, but it is important to ensure these do not over model the situation! A major factor is that the alloys we are trying to assess are somewhat unique to each supplier, they have additions of a range of microalloying additions, and are cast, and hence any parameters used to describe their creep strain response are subject to substantial variation. Compounding this is the need to recognise that the time/temperature evolution of the microstructure in service will further modify the form of the creep curve and the rate of damage evolution. In practice this means that the mechanical response of any given tube in service is very sensitive to how the tubes are thermally exposed and hence aging is a parameter that requires careful consideration in any creep modelling.

4. Role of Material Aging

To graphically illustrate the influence of microstructural condition one should compare the results of Figure 3 with Figure 4. These tests are from two different ex-service materials. In both instances the tubes had experienced minimal in-service creep damage as measured by strain, however while the 1065 °C test gave the expected life and ductility, the tube tested at 1000 °C failed at less than 50% of the expected life with a ductility lower than 1%.

As a first consideration there appear to be two major parameters that influence this variability in creep. Gaining a better understanding of these influences can provide a dual benefit:

- Opportunity for improved specification in procuring new tubes which are less prone to degradation in ductility
- Refinement in prediction of the creep strain response i.e. optimisation of the creep strain versus life relation.

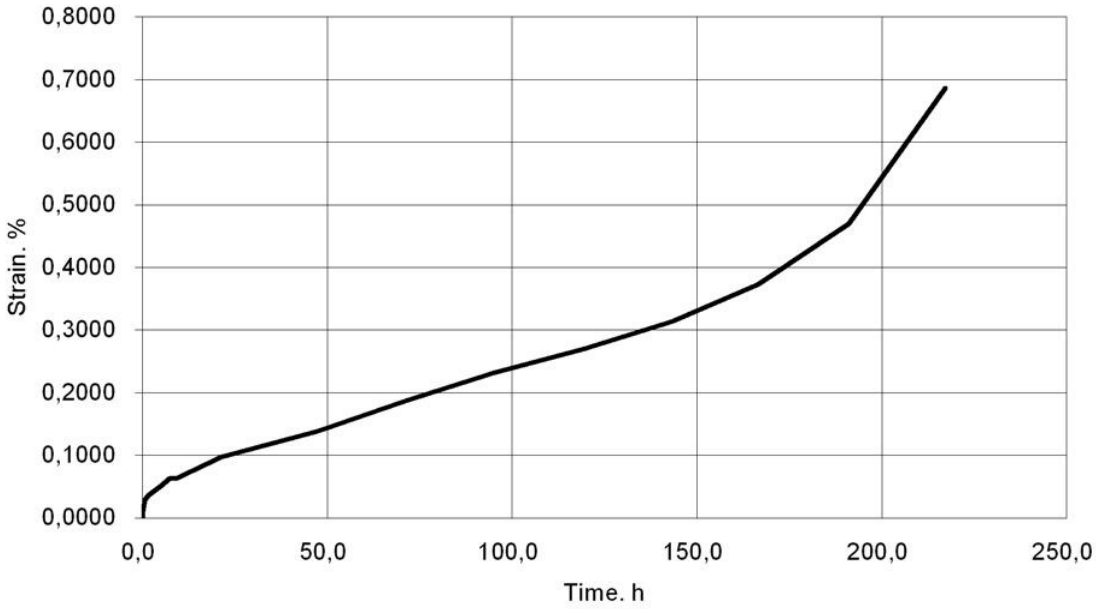

Figure 4. Short-term creep strain vs. time curve for ex service 25/35 microalloyed tube (alloy B) tested at 1065 deg C. Note ductility at failure less than 1.0%.

The book, Atlas of Microstructures [8] has provided an informative review of microstructures that can be generated in this genre of alloys as a function of thermal exposure, but does not make a clear link to mechanical response. In the current study we are aiming to use a combination of service exposed materials and limited laboratory pre-aged HP niobium modified and HP micro-alloyed material to gain a better understanding of the relations between microstructure versus creep response in both the as received and service aged conditions.

At the current time only limited work has been undertaken, but to illustrate the approach we use can consider alloys A and B, with creep responses shown in Figure 3 and Figure 4 respectively, and where more detailed investigation of the microstructure using optical, scanning electron and transmission electron microscopy techniques has been initiated. Table 1gives the chemical composition of the investigated alloys.

Table 1. Material composition (wt%).

	C	Cr	Ni	Nb	Mn	Si	Ti	W
Alloy A*	0.34	25.78	34.39	0.84	1.09	1.11	0.02	0.46**
Alloy B	0.35-0.4	23-28	33-38	N/A	1.0-1..5	1.0-2.0	+	+

OES,** XRF ,Balance: Fe

+For alloy B manufacturer's compositions provided. Ti and W are deliberate alloying additions, with undefined compositions

Figure 5 shows low magnification optical micrographs of the two alloys, both taken from the mid-wall location in the tube. Both alloys show the typical dendritic microstructure characteristic of these cast materials. In comparison, alloy B's microstructure has a smaller dendrite arm spacing, and the primary carbide network is much more continuous.

Higher magnification optical images in Figure 6 reveal several differences. In alloy B, the primary carbides are mainly chromium carbides. Cuboidal titanium carbides, revealed as the dark grey phase in Figure 6a, ranging in size from 3-8 microns are also present. However, the volume fraction of these titanium carbides in alloy B appears to be much less than the (NbTi)C precipitates (dark grey phase in Figure 6b) in the A alloy and they are less integral to the primary carbide network. Further the B alloy intragranular (secondary) precipitate population is strikingly more refined than in the A alloy.

Figure 7 shows SEM micrographs of the alloys. The primary carbide network of the B alloy retains its original lamellar/acicular appearance, while the A alloy primary carbides are relatively coarse and blocky. The secondary precipitate distribution in the B alloy is significantly refined in comparison the higher ductility material as noted in the optical micrographs. The white phase in the A alloy is (Ti,Nb)C carbides.

Based upon the preliminary microstructural differences observed, the relatively low ductility of the B alloy is thought to be mainly due to the continuous, acicular/lamellar primary carbide network and the higher density of finely distributed carbides in the matrix which would render the matrix more resistant to shape change during creep. This more creep resistant matrix would impart large stresses at the interdendritic regions which may then be forced to deform locally to accommodate shape change, reducing overall macroscopic ductility.

Clearly these initial findings are only related to two specific examples, but the aim is to generate sufficient creep strain and microstructural information to allow categorisation of a typical range of alloys into subgroups for which suitable creep strain vs. life parameters can be derived. What is apparent from this work is that relatively minor changes in microstructure can impart significant differences in the alloy's ductility

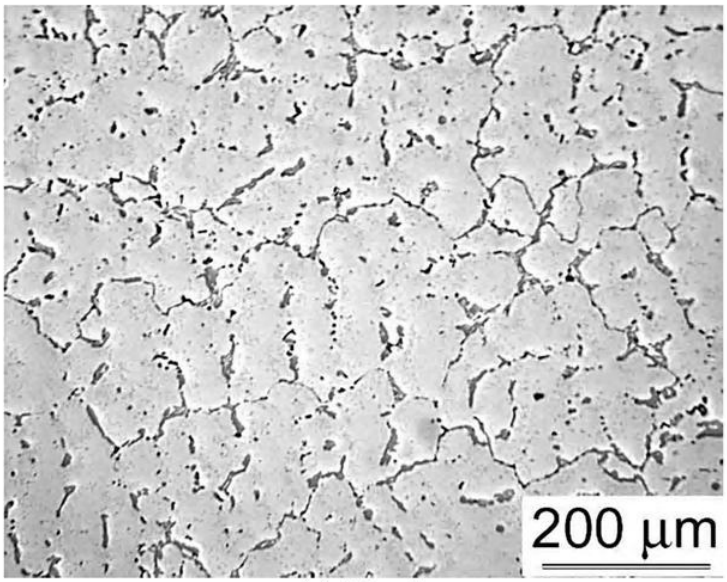

(a) Alloy A

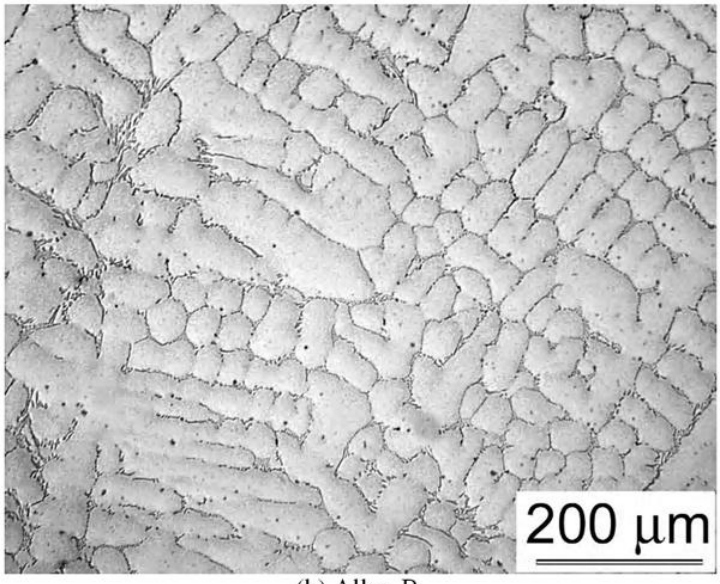

(b) Alloy B.

Figure 5. Optical micrographs. Etched with glyceregia, 100x original magnification.

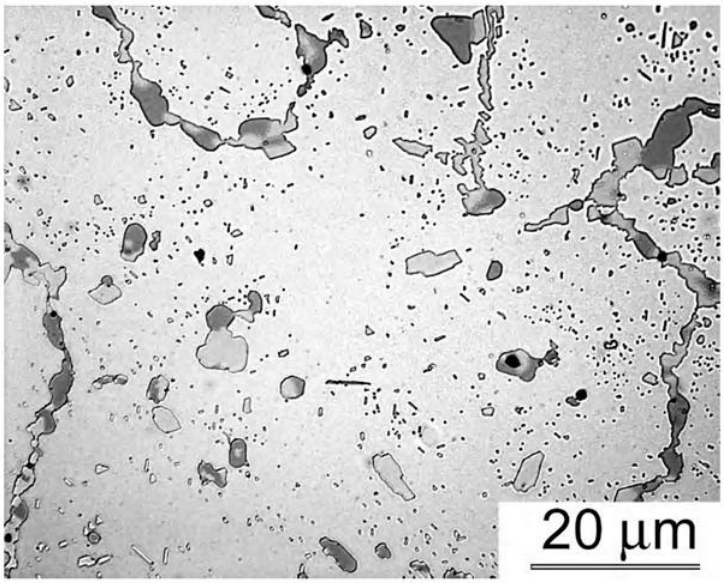

(a) Alloy A

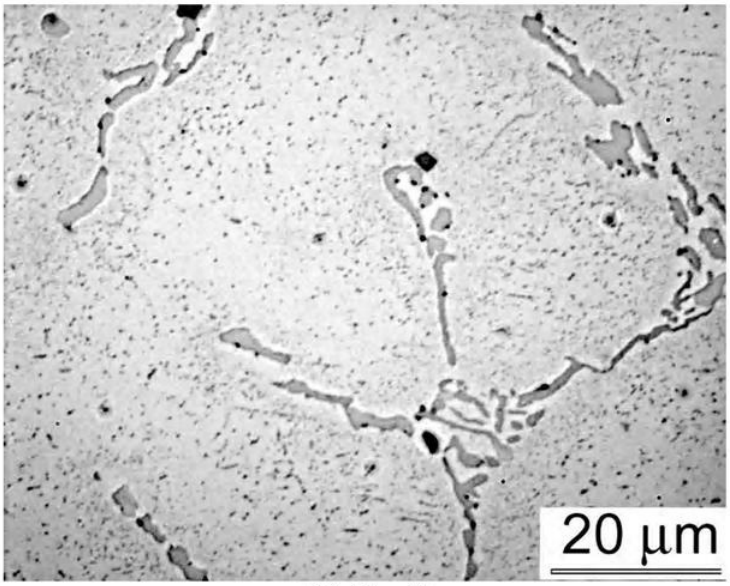

(b) Alloy B

Figure 6. Optical micrographs. Etched with glyceregia, 1000x original magnification.

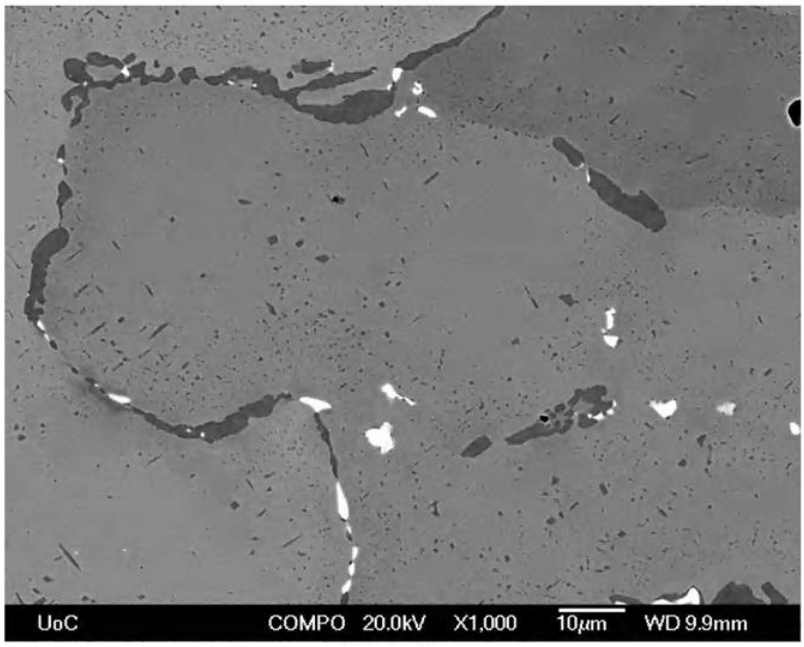

(a) A alloy

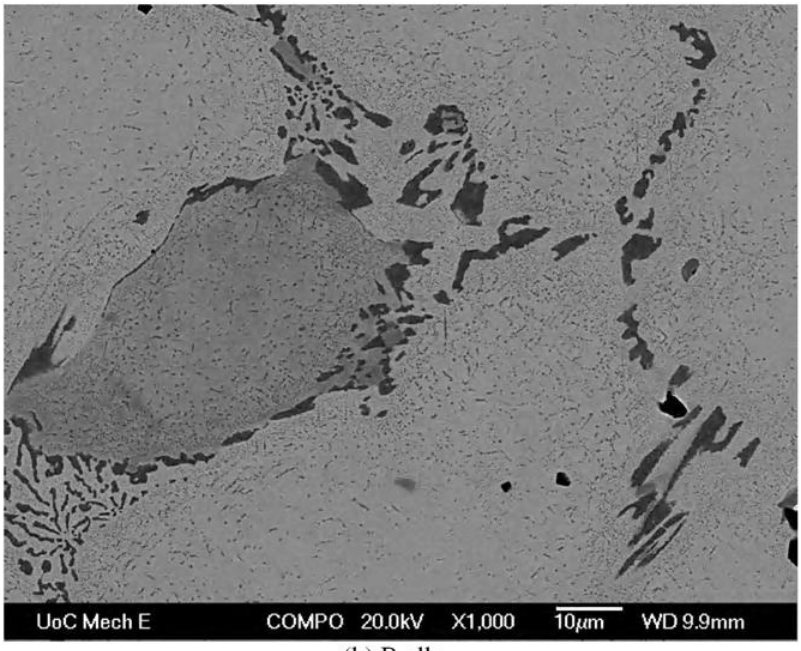

(b) B alloy

Figure 7. Backscattered scanning electron images, as-polished.

5. Tube life management

The brief observations and comparisons of microstructure vs. creep strain response described above illustrate clearly the uncertainty that faces the current operator of such tubes. Without further information (which will arise from better understanding of the materials) a pragmatic approach to life assessment has to be adopted which combines the best features of a number of inspection and life assessment techniques. The combination of these will depend somewhat on the manner in which the furnace is operated. However for a typical hydrogen manufacturing unit the following could be considered as a measured approach to optimise reliability while avoiding unnecessary replacement.

1. The tubes should be base-lined by suitable inspection (particularly diametric growth) prior to first use—this is particularly recommended if regular external dimension profiling is to be undertaken. Careful consideration should be given to associating which tubes relate to individual heats at the foundry (recognising that elements such as Ti are added separately to each individual casting)
2. At a predefined (relatively low) strain, during a turn around inspection, the worst tube can be removed from service and undergo accelerated (strain based) creep testing. If necessary one tube from each heat of the furnace tube sets could be selected.
3. Based on the outcome of creep testing a remnant life estimate can be made, a refined creep strain/life model employed and an upper creep ductility defined (based on microstructure and creep results on the actual tube) which will allow much more accurate tube condition assessment.
4. Regular temperature measurement and strain monitoring (when allowable) continues
5. Tubes are finally removed at the recalculated strain (ideally supported by a second inspection method which can identify the later stages of creep damage)

The main advantage of this approach are that one can set lower bound expectations on tube performance, monitor the early stages of creep damage (using strain) and then, by sample removal, obtain an actual sample (s) of service exposed material (s) on which to base the expected creep strain and rupture ductility for the remaining tube set. Generally a single tube will, along its length, contain a range of material thermal exposure and strain, hence a comprehensive set of testing from different locations on a single tube could provide considerable information in relation to the condition of the remaining tube set in the furnace. A further refinement could be to split the tubes into individual heats for consideration if this is thought necessary. Of course accurate thermography throughout life is paramount to identifying anomalies in operation and significant temperature excursions that may modify the material microstructure.

Finally it should be remembered that short – term creep testing using methods such as Omega remain dependent upon applicability of the models to extrapolate from short-term testing to long-term life. Given the limitations and complexity required to address the role of microstructural aging it still remains necessary to ensure that representative databases to describe the behaviour of thermal aged cast alloys are available.

6. Conclusion

A short summary of available inspection techniques to monitor condition in steam methane reformers has been made. Owing to its ability to monitor the early stages of creep evolution strain measurement, in the form of diametric growth is seen as providing information that complements the other common techniques.

At the present time the lack of understanding in terms of the microstructure/creep property relation for this genre of cast alloys, where some low ductility failures are known to occur, precludes gaining the perceived value from accurate and regular strain measurement. A significant body of research is still required to address this shortfall, both in terms of microstructural understanding and in creep strain related data base generation (for a range of alloy aged conditions).

At the present time the most satisfactory approach to life management of a tube set is to use a combination of appropriate inspection techniques, accurate temperature measurement and sample removal and creep testing.

Acknowledgements.

The authors are grateful to Shell Global Solutions International for permission to publish this paper.

References

[1] P. Saunders, Radiation Thermometry, Fundamentals and Applications in the Petrochemical Industry, SPIE press.

[2] API STD 530, Calculation of Heater Tube Thickness in Petroleum Industries, American Petroleum Institute, Washington DC, 2004.

[3] C. Thomas, The effect of Aging on the Strength of Reformer Tube Materials, 51st Annual Ammonia Saftey Symposium, AIChE Technical Manual, vol 47 pp 35 to 45, 2006.

[4] C.W.Thomas, A.J.Tack and N. Briggs , International Journal of Pressure Vessel and Piping, 70, pp 59-68 1997.

[5] British Energy R5 code, Assessment procedure for the high temperature response of structures.

[6] API Recommended Practice 579, Fitness For Service, American Petroleum Institute, Washington DC, 2000.

[7] R.K. Penny and D. L. Marriott Design for Creep, Chapman and Hall, 2nd Edition 1995

[8] E. Berghof-Hasselbacher, P Gawenda, M Schorr, M. Schutze and J. Hoffman, Atlas of Microstructures, Dechema, Materials Technology Institute.